Jaime Klapp
Leonardo Di G. Sigalotti
Abraham Medina
Abel López
Gerardo Ruiz-Chavarría *Editors*

Recent Advances in Fluid Dynamics with Environmental Applications

Springer

Environmental Science and Engineering

Environmental Engineering

Series editors

Ulrich Förstner, Hamburg, Germany
Wim H. Rulkens, Wageningen, The Netherlands
Wim Salomons, Haren, The Netherlands

Jaime Klapp · Leonardo Di G. Sigalotti
Abraham Medina · Abel López
Gerardo Ruiz-Chavarría

Editors

Recent Advances in Fluid Dynamics with Environmental Applications

Springer

Editors
Jaime Klapp
Instituto Nacional de Investigaciones
   Nucleares
Ocoyoacac
Mexico

Leonardo Di G. Sigalotti
Departamento de Ciencias Básicas
UAM Azcapotzalco
Mexico City
Mexico

Abraham Medina
SEPI ESIME Azcapotzalco
Instituto Politécnico Nacional
Mexico City
Mexico

Abel López
SEPI ESIME Azcapotzalco
Instituto Politécnico Nacional
Mexico City
Mexico

Gerardo Ruiz-Chavarría
Facultad de Ciencias
Universidad Nacional Autónoma de México
Mexico City
Mexico

Preface

Fluid dynamics has had significant advances in recent years as a result of the current vertiginous development of computational power. This expansion has nowadays enabled the implementation of numerical high-resolution simulations as never before. For instance, fluid dynamic cosmological simulations are presently being run using up to 10^{12} particles, and turbulence simulations with up to 10^{11} mesh elements. Experimental advances are also present. Just to mention, some computer methods to reconstruct the topography of a liquid's free surface have been developed in recent times bringing into play high-definition digital images. With these tools, phenomena like wave turbulence or wave breaking are at the present being investigated. The development of different computer architectures offers now the possibility to work out fluid dynamics equations with alternative methods. Recent simulations with Smoothed Particle Hydrodynamics have been done using both multicore architectures and GPUs. The advantage of this approach is that the method is meshless, so it is suitable for modeling systems with moving and irregular boundaries.

Today the Mexican fluid dynamics community is involved in the research of novel topics using the advancements mentioned above. To name but a few topics, we draw attention to the studies in microfluidics and their relation to real problems like secondary oil recovery, while—in a different vein—studies in the field of magnetohydrodynamics are now being conducted on the mutual conversion of mechanical and electromagnetic energy.

The papers included in this book are selected contributions of two meetings held in Mexico during 2014. The first one was the Spring School "Enzo Levi" on May 12–13, 2014. The second event was the Annual Meeting of the Division of Fluid Dynamics of the Mexican Physical Society on November 18–20, 2014. In both meetings, an important fraction of the Mexican community working on fluid dynamics gathered, including students, researchers, and lecturers of several institutions from all over Mexico. We are pleased to acknowledge the contributions and attendance of all colleagues of the institutes and universities that were present in

one or both meetings. Among several institutions we would like to mention: UNAM, CINVESTAV, CICESE, IPN, UAM-A, ININ, and UNACH.

The 2014 "Enzo Levi" Spring School was hosted by the recently created Aeronautical University of Querétaro (UNAQ). This university was established with the aim to provide technical assistance to the aeronautical industries located in the Mexican state of Querétaro.

The number of participants attending the "Enzo Levi" conference was approximately 150. During this meeting, a total of 11 lectures were delivered by renowned scientists from Mexico and abroad. The topics covered by the lectures were diverse: waves produced by ships, aerogenerator designs, drag reduction in planes, turbulence at low temperatures, fluid mechanics in cosmology, and in coastal systems, among other topics. Of the lectures delivered during the meeting, some of them stand out. We would like to mention those given by Jens Sorensen, a distinguished professor of the Technical University of Denmark. His first lecture dealt with aerodynamic principles and then was centered on renewable energy, in particular on how to increase wind power. His second lecture was devoted to wind farms and the problems associated with the wakes produced by turbines. Marc Rabaud from the University Paris-Sud delivered two lectures on the wakes produced by fast boats and small obstacles, respectively. In the first case, the gravity is relevant while in the second case both gravity and capillarity are involved. With respect to aeronautics, Fausto Sánchez Cruz, from the University of Nuevo León, spoke about the development of winglets to reduce the drag on aircrafts and on the modifications of the wing end to dissipate or attenuate the wingtip vortices. In a succeeding lecture, Hugo Carmona Orvañanos spoke about the Coanda effect and its application to the reduction of the takeoff length. Enrico Fonda from New York University spoke on two aspects of turbulence, namely, experiments at low temperatures to attain high Reynolds numbers and on vorticity in superfluids. The lecture by Jorge Cervantes from Instituto Nacional de Investigaciones Nucleares (ININ) concerned fluid dynamics in the frame of cosmology in which relativistic and non-relativistic effects were reviewed. Finally, Erick Lopez Sanchez from UNAM spoke on numerical simulations of vortices in tidal induced flows in a channel flushing to the sea.

During the 2014 "Enzo Levi" Spring School, the UNAQ local organizer arranged an open house event where participants visited the aeronautical school premises including laboratories, test workshops, and toured around various airplanes donated to the institution for student training. This experience allowed visitors and local participants, researchers, and students of different institutes to establish fruitful academic links in the vibrant field of applications of fluid mechanics to aerodynamics.

The annual meeting of the Mexican Division of Fluid Dynamics was held during three days at the recently established Mesoamerican Centre for Theoretical Physics in Tuxtla Gutierrez, Chiapas, a state located south of the country. This conference was attended by approximately 250 participants. Conference activities included: oral sessions, a gallery of fluid motion and open lectures on fluid mechanics aimed at an audience of informed non-specialists in the specific topic of the talk.

Prominent scientists from Mexico and other countries delivered lectures on new trends in fluids dynamics. In relation to the contents of lectures, Tomas Bohr, from the Physics Department of the Technical University of Denmark, talked on the analogy between quantum mechanics and the behavior of a bouncing drop on the surface of a vibrating fluid. Yves Couder from the University of Paris Diderot also commented on the mentioned analogy. Tomas Bohr made a critical review of the double slit experiments. In a succeeding lecture, Joseph Niemela of the International Centre for Theoretical Physics (ICTP) gave a talk on experiments in turbulence for high Reynolds and Taylor numbers, which conveys to a better understanding of this phenomenon. For its part, Chantal Staquet from Joseph Fourier University in France talked about the statistical properties of internal waves in the ocean, their nonlinear interactions, and their importance in geophysical flows. Another lecture concerning waves was given by Francisco Ocampo Torres from CICESE, a research institute located at the Baja California Peninsula, in the north of Mexico. He spoke about the interactions between the ocean and the atmosphere, with emphasis on the surface waves and their role in the oceanic and atmospheric circulation. It is also important to mention the talk given by Nicolas Mujica from the University of Chile, related to a vibrating granular material and the occurrence of phase transitions. Finally, Vadim Kourdioumov of Centro de Investigaciones Energéticas, Madrid, gave a lecture on the propagation of flames in narrow channels. Some of these lectures have been included in this book.

The book contains review and research papers, covering a wide spectrum of topics in fluid dynamics. It is divided into four parts, each one having papers based on invited lectures and a selection of works presented in the annual 2014 meeting. The first part is devoted to vortices and circulation phenomena. It contains contributions like vortices produced by deformable objects (a flexible plate and a flexible cylinder). Three papers treating some applications to aerodynamics, for example, structures generated behind flapping foils or the study of the Coanda effect to increase the lift of airplanes. The part includes also a paper about the vortices created in tidal induced flows and two papers on the technique known as Background Oriented Schlieren. Finally, a paper of the crossflow in a non-isothermal open cavity is included. The second part is entitled "Environmental Applications". This part includes experimental and numerical investigations of the modeling of hydrodynamic processes in lagoons, offshore, and in atmospheric systems in Latin American countries such as Colombia and Mexico. In addition, the part includes a paper on fractals and rainfalls and other one on the evaluation of a cooling system. The third part is devoted to the fluid–structure interaction. In this part there are papers on magnetohydrodynamics, microfluidics, applications to the automotive industry, and an introduction to novel techniques like the fractional Navier–Stokes equation. There are in addition papers on the formation of Rayleigh jets, the trajectories of water and sand jets, the flow of viscoelastic fluids, and so on. In this part of the book there are contributions that reflect some of the new trends of the research developed by the Mexican community of fluid dynamics. The last part is entitled "General Fluid Dynamics and Applications". In this part a relevant paper of Tomas Bohr is included which deals with the analogy between

a bouncing drop and quantum mechanics. There are also two papers on astronomical applications of fluid dynamics, namely the dynamics of novae and the X-ray outflow in active galactic nuclei. This part contains a paper written by Nicola Mujica and Rodrigo Soto on the dynamics of non-cohesive granular media. Other papers deal with fundamental problems such as heat propagation or the use of new computing capabilities. Such is the case of a paper in which the method of Smoothed Particle Hydrodynamics is programmed to run in parallel using GPUs and multicore architectures.

The book is aimed at senior and graduate students, and scientists in the field of physics, engineering, and chemistry that have an interest in fluid dynamics from the experimental and theoretical points of view. The material includes recent advances in experimental and theoretical fluid dynamics and is adequate for both teaching and research. The invited lectures are introductory and avoid the use of complicated mathematics.

The editors are grateful to the institutions that made possible the International Enzo Levi Spring School 2014, and the XX National Congress of the Fluid Dynamics Division of the Mexican Physical Society, particularly the Consejo Nacional de Ciencia y Tecnología (CONACYT), the Sociedad Mexicana de Física (SMF), the Aeronautical University of Queretaro (UNAQ), the Mesoamerican Centre for Theoretical Physics in Tuxtla Gutierrez, Chiapas, the Universidad Nacional Autónoma de México (UNAM), the ESIME of the Instituto Politécnico Nacional (IPN), Cinvestav-Abacus, the Universidad Autónoma Metropolitana-Azcapotzalco (UAM-A), and the Instituto Nacional de Investigaciones Nucleares (ININ).

Mexico City   Jaime Klapp
January 2016   Leonardo Di G. Sigalotti
                                                                                         Abraham Medina
                                                                                               Abel López
                                                                           Gerardo Ruiz-Chavarría

Contents

Contributors

A. Aguayo Ortiz Facultad de Ciencias, UNAM, Delegación Coyoacán, D.F., Mexico

A. Aguilar-Corona Faculty of Mechanical Engineering, Universidad Michoacana de San Nicolás de Hidalgo, Ciudad Universitaria, Morelia, Michoacán, Mexico

A. Aguirre-Guzman Laboratorio de Física de la Atmósfera Y El Espacio Ultraterrestre, Universidad de Carabobo, Valencia, Venezuela

Anders Andersen Department of Physics, Technical University of Denmark, Kgs. Lyngby, Denmark

J. Arellano Facultad de Ingeniería, Universidad Autónoma de San Luis Potosí, San Luis Potosí, Mexico

A. Barreiro EPhysLab Environmental Physics Laboratory, Universidad de Vigo, Ourense, Spain

H. Barrios-Piña Tecnológico de Monterrey, Guadalajara, Jalisco, Mexico

Tomas Bohr Department of Physics, Technical University of Denmark, Kgs. Lyngby, Denmark

R. Cantero-Rodelo Faculty of Environmental Sciences, Universidad de la Costa, Barranquilla, Colombia

H. Cardoso Sakamoto Facultad de Ciencias, UNAM, Delegación Coyoacán, D.F., Mexico

J.E. Hiroki Cardoso Facultad de Ciencias, UNAM, Ciudad Universitaria, D.F., Mexico

H. Carmona Universidad Aeronáutica en Querétaro, Colón, Mexico

J.M. Casillas Navarrete Instituto Politécnico Nacional SEPI-ESIME. U.P. Azcapotzalco, Delegación Azcapotzalco, Mexico

A. Cházaro Universidad Aeronáutica en Querétaro, Colón, Mexico

A.J.C. Crespo EPhysLab Environmental Physics Laboratory, Universidad de Vigo, Ourense, Spain

A. Cros Physics Department CUCEI, Universidad de Guadalajara, Guadalajara, Jalisco, Mexico

A. Cuevas-Otero DEPFI-UNAM, Mexico City, Mexico; SEPI-ESIA, IPN, Mexico City, Mexico

S. Cuevas Instituto de Energías Renovables, Universidad Nacional Autónoma de México, Temixco, Morelos, Mexico

Y.N. Domínguez-del Ángel Departamento de Matemáticas Aplicadas y Sistemas, DMAS, Universidad Autónoma Metropolitana, Mexico, D.F., Mexico

G. Domínguez Instituto Mexicano Del Petróleo, Del. Gustavo A. Madero, Mexico, D.F., Mexico

J.M. Domínguez EPhysLab Environmental Physics Laboratory, Universidad de Vigo, Ourense, Spain

L. Díaz Barriga Arceo ESIQIE, Instituto Politécnico Nacional, México D.F., Mexico

C. Echeverría Arjonilla Facultad de Ciencias, UNAM, Coyoacán, Mexico D.F., Mexico

N. Falcón Laboratorio de Física de la Atmósfera Y El Espacio Ultraterrestre, Universidad de Carabobo, Valencia, Venezuela

A. Figueroa Centro de Investigación en Ciencias, Universidad Autónoma del Estado de Morelos, Cuernavaca, Morelos, Mexico

J. Flores-Velázquez Coordinación de Riego y Drenaje, Instituto Mexicano de Tecnología del Agua, Jiutepec, Mor, Mexico

M.A. Fontelos Campus de Cantoblanco, Instituto de Ciencias Matemáticas (CSIC —UAM—UC3M—UCM), Madrid, Spain

B. Franco Llamas Physics Department CUCEI, Universidad de Guadalajara, Guadalajara, Jalisco, Mexico

C. Fuentes Instituto Mexicano de Tecnología del Agua, Jiutepec, Morelos, Mexico; Instituto Mexicano de Tecnología del Agua. Paseo Cuauhnahuac 8532 Progreso, Jiutepec, MOR, Mexico

S.R. Galván-González Faculty of Mechanical Engineering, Universidad Michoacana de San Nicolás de Hidalgo, Ciudad Universitaria, Morelia, Michoacán, Mexico

L.B. Gamboa Universidad Autónoma de Yucatán Periférico Norte, Mérida, Yucatán, Mexico

A.R. Garcia Centro de Ciencias de la Atmósfera, UNAM, Circuito de la Investigación Cientìfica s/n, Mexico, D.F., Mexico

O. García-Feal EPhysLab Environmental Physics Laboratory, Universidad de Vigo, Ourense, Spain

C.D. García-Molina Facultad de Ciencias, Universidad Nacional Autónoma de México Ciudad Universitaria, Mexico, D.F., Mexico

J. García Harvard-Smithsonian Center for Astrophysics, Cambridge, MA, USA

A. Gómez López Facultad de Ingeniería, Universidad Nacional Autónoma de México, México, DF, Mexico

M. Gómez-Gesteira EPhysLab Environmental Physics Laboratory, Universidad de Vigo, Ourense, Spain

J.G. González-Santos Posgrado en Ciencias Naturales e Ingeniería, Universidad Autónoma Metropolitana, Mexico, D.F., Mexico

G.J. Gutiérrez Paredes Instituto Politécnico Nacional SEPI-ESIME. U.P. Azcapotzalco, Delegación Azcapotzalco, Mexico

G.L. Gutiérrez-Urueta Facultad de Ingeniería, Universidad Autónoma de San Luis Potosí, Zona Universitaria Poniente, Av. Manuel Nava 8, San Luis Potosí, Mexico

J. Hernández Universidad Aeronáutica en Querétaro, Colón, Mexico

L.A. Ibarra-Bracamontes Faculty of Mechanical Engineering, Universidad Michoacana de San Nicolás de Hidalgo, Ciudad Universitaria, Morelia, Michoacán, Mexico

A. Iturbe Universidad Aeronáutica en Querétaro, Colón, Mexico

C.A. Jiménez García Instituto Politécnico Nacional SEPI-ESIME. U.P. Azcapotzalco, Delegación Azcapotzalco, Mexico

J. Klapp Departamento de Física, Instituto Nacional de Investigaciones Nucleares, Ocoyoacac, Estado de México, Mexico; ABACUS-Centro de Matemáticas Aplicadas y Cómputo de Alto Rendimiento, CINVESTAV-IPN, Ocoyoacac, Estado de México, Mexico

Benny Lautrup Niels Bohr International Academy, The Niels Bohr Institute, Copenhagen, Denmark

A. López Villa Instituto Politécnico Nacional SEPI-ESIME. U.P. Azcapotzalco, México D.F., Mexico

M. López-L Universidad del Norte, Barranquilla, Colombia

A.A. López-Lambraño Facultad de Ingeniería, Universidad Autónoma de Baja California (UABC), Mexicali, BC, Mexico

A. López-Ramos Escuela de Ingenierías y Arquitectura Facultad de Ingeniería Civil, Universidad Pontificia Bolivariana-Seccional Montería, Montería, Córdoba, Colombia

E.J. López-Sánchez Facultad de Ciencias, Universidad Nacional Autónoma de México Ciudad Universitaria, Mexico, D.F., Mexico; ESIME-Azcapotzalco, Instituto Politécnico Nacional, Mexico, D.F., Mexico

B.E. Mar-Morales Centro de Ciencias de la Atmósfera, UNAM, Circuito de la Investigación Científica s/n, Mexico, D.F., Mexico

N. Martínez-Gutiérrez Faculty of Mechanical Engineering, Universidad Michoacana de San Nicolás de Hidalgo, Ciudad Universitaria, Morelia, Michoacán, Mexico

A. Medina ESIME Azcapotzalco, Instituto Politécnico Nacional, Santa Catarina, Mexico, D.F., Mexico

G. Mejía-Rodríguez Facultad de Ingeniería, Universidad Autónoma de San Luis Potosí, Zona Universitaria Poniente, Av. Manuel Nava 8, San Luis Potosí, Mexico

C. Monreal-Jiménez Facultad de Ingeniería, Universidad Autónoma de San Luis Potosí, Zona Universitaria Poniente, Av. Manuel Nava 8, San Luis Potosí, Mexico

G. Monsivais Galindo Instituto de Física, UNAM, Delegación Coyoacán, D.F., Mexico

J.G. Morales-Nava Facultad de Ingeniería Arquitectura Y Diseño, Universidad Autónoma de Baja California, Ensenada, BC, Mexico

N. Mujica Facultad de Ciencias Físicas y Matemáticas, Departamento de Física, Universidad de Chile, Santiago, Chile

M. Núñez-López Escuela Superior de Física y Matemáticas ESFM-IPN, Mexico, D.F., Mexico

W. Ojeda B Coordinación de Riego y Drenaje, Instituto Mexicano de Tecnología del Agua, Jiutepec, Mor, Mexico

A. Ortiz Facultad de Ingeniería, Universidad Autónoma de Baja California, Blvd. Unidad Universitaria, Mexicali, Mexico

G.E. Ovando-Chacon Depto. de Metal Mecánica Y Mecatrónica, Instituto Tecnológico de Veracruz, Veracruz, Mexico

S.L. Ovando-Chacon Depto. de Química Y Bioquímica, Instituto Tecnológico de Tuxtla Gutiérrez, Tuxtla Gutiérrez, Chiapas, Mexico

F. Oviedo-Tolentino Facultad de Ingeniería, Universidad Autónoma de San Luis Potosí, Zona Universitaria Poniente, Av. Manuel Nava 8, San Luis Potosí, Mexico

J. Padilla Coba Faculty of Environmental Sciences, Universidad de la Costa, Barranquilla, Colombia

R. Peña Facultad de Ingeniería, Universidad Autónoma de San Luis Potosí, San Luis Potosí, Mexico

I. Pérez Reyes Facultad de Ciencias Químicas, Universidad Autónoma de Chihuahua, Chihuahua, Chih, Mexico

J. Pérez-Barrera Instituto de Energías Renovables, Universidad Nacional Autónoma de México, Temixco, Morelos, Mexico

M. Pliego-Díaz Instituto Tecnológico de Querétaro, Santiago de Querétaro, Qro, Mexico; Instituto Tecnológico de Querétaro. Ciencias Básicas. Av. Tecnológico S/N, Centro, Santiago de Querétaro, Mexico

J.T. Ponce-Palafox Universidad Autónoma de Nayarit, Tepic, Nayarit, Mexico

D. Porta Zepeda Facultad de Ciencias, UNAM, Delegación Coyoacán, Mexico D.F., Mexico

J.C. Prince-Avelino Depto. de Metal Mecánica Y Mecatrónica, Instituto Tecnológico de Veracruz, Veracruz, Mexico

H. Ramírez-León Instituto Mexicano del Petróleo, Mexico City, Mexico

J.M. Ramírez-Velasquez Physics Centre, Venezuelan Institute for Scientific Research (IVIC), Caracas, Venezuela; Departamento de Matemáticas, Cinvestav del I.P.N., Mexico, D.F., Mexico

G. Rangel Paredes Facultad de Ciencias, Departamento de Física, Universidad Nacional Autónoma de Mexico, Ciudad Universitaria, Delegación Coyoacán, Mexico D.F., Mexico

J.E. Rivera López Instituto Politécnico Nacional SEPI-ESIME. U.P. Azcapotzalco, Delegación Azcapotzalco, Mexico

J.N. Rivera Olvera Centro Conjunto de Investigación en Química Sustentable UAEM-UNAM, Carretera Toluca-Atlacomulco, Toluca, Estado de México, Mexico

P. Rodríguez-Aumente Departamento de Ingeniería Térmica y de Fluidos, Universidad Carlos III de Madrid, Leganés, Madrid, Spain

C. Rodríguez-Cuevas Faculty of Engineering, University of San Luis Potosí, San Luis Potosí, Mexico

A. Rodriguez-León Depto. de Metal Mecánica Y Mecatrónica, Instituto Tecnológico de Veracruz, Veracruz, Mexico

A. Rojano Coordinación de Riego y Drenaje, Instituto Mexicano de Tecnología del Agua, Jiutepec, Mor, Mexico

A. Rojas Instituto de Investigación en Ciencias Básicas Y Aplicadas, Universidad Autónoma del Estado de Morelos, Cuernavaca, Morelos, Mexico

R. Romero-Méndez Facultad de Ingeniería, Universidad Autónoma de San Luis Potosí, Zona Universitaria Poniente, Av. Manuel Nava 8, San Luis Potosí, Mexico

J. Rosales Instituto de Investigación en Ciencias Básicas Y Aplicadas, Universidad Autónoma del Estado de Morelos, Cuernavaca, Morelos, Mexico

A. Ruiz-Angulo Centro de Ciencias de la Atmósfera, Universidad Nacional Autónoma de México, Mexico, Mexico

G. Ruiz-Chavarría Facultad de Ciencias, Universidad Nacional Autónoma de México Ciudad Universitaria, Mexico, D.F., Mexico

L.G. Ruiz-Suárez Centro de Ciencias de la Atmósfera, UNAM, Circuito de la Investigación Científica s/n, Mexico, D.F., Mexico

E. Sandoval Hernández Natural and Exact Sciences Department CU-Valles, Universidad de Guadalajara, Ameca, Jalisco, Mexico

D.A. Serrano ESIME Zacatenco, Instituto Politécnico Nacional, Zacatenco, Mexico, D.F., Mexico

A. Servin-Martínez Depto. de Metal Mecánica Y Mecatrónica, Instituto Tecnológico de Veracruz, Veracruz, Mexico

R. Soto Facultad de Ciencias Físicas y Matemáticas, Departamento de Física, Universidad de Chile, Santiago, Chile

C. Stern Forgach Facultad de Ciencias, UNAM, Delegación Coyoacán, México D.F., México

F. Sánchez-Silva ESIME Zacatenco, Instituto Politécnico Nacional, Zacatenco, Mexico, D.F., Mexico

P. Tamayo ESIME Azcapotzalco, Instituto Politécnico Nacional, Santa Catarina, Mexico, D.F., Mexico

F. Torres-Bejarano Faculty of Environmental Sciences, Universidad de la Costa, Barranquilla, Colombia

A. Traslosheros Universidad Aeronáutica en Querétaro, Colón, Mexico

R.O. Vargas Aguilar Escuela Superior de Ingeniería Mecánica y Eléctrica, Azcapotzalco, Instituto Politécnico Nacional, Mexico, D.F., Mexico

F. Vázquez Centro de Investigación en Ciencias, Universidad Autónoma del Estado de Morelos, Cuernavaca, Morelos, Mexico

J.J. Villegas-León Facultad de Ingeniería, Universidad Autónoma de Baja California (UABC), Mexicali, BC, Mexico

G. Viramontes-Gamboa Faculty of Physics and Mathematics, Universidad Michoacana de San Nicolás de Hidalgo, Ciudad Universitaria, Morelia, Michoacán, Mexico

A. Zarazúa Cruz Facultad de Ciencias, UNAM, Ciudad Universitaria, Mexico D.F., Mexico

J. Zavala-Hidalgo Centro de Ciencias de la Atmósfera, Universidad Nacional Autónoma de México, Mexico, Mexico

Part I
Vortex and Circulation Phenomena

Numerical Study of the Cross Flow in a Non-isothermal Open Cavity

G.E. Ovando-Chacon, S.L. Ovando-Chacon, J.C. Prince-Avelino, A. Rodriguez-León and A. Servin-Martínez

Abstract In the present work, the laminar steady state fluid dynamics and heat transfer, in a two-dimensional open cavity with a cross flow due to a secondary jet injected at the top wall, are analyzed. The numerical study is carried out for a Reynolds number of 500 with different Richardson and Prandtl numbers. A hot plate is provided on the bottom of the cavity which generates the heating of the fluid. In order to investigate the effect of the length of the plate two different plate sizes are considered. The governing equations of continuity, momentum and energy for incompressible flow are solved by the finite element method combined with the splitting operator scheme. It is studied the streamlines and isotherms inside the cavity and it is analyzed the average Nusselt number, the average temperature and the outlet temperature as a function of the Richardson and Prandtl numbers. It is observed that the Prandtl and Richardson numbers play a major role in the thermal and fluid behavior of the flow inside the cavity with a cross flow. Moreover the results indicate that a secondary jet injected at the top wall enhances the average Nusselt number.

G.E. Ovando-Chacon (✉) · J.C. Prince-Avelino · A. Rodriguez-León · A. Servin-Martínez
Depto. de Metal Mecánica Y Mecatrónica, Instituto Tecnológico de Veracruz,
Calzada Miguel A. de Quevedo 2779, Col. Formando Hogar,
91860 Veracruz, Mexico
e-mail: geoc@itver.edu.mx

J.C. Prince-Avelino
e-mail: jcpa@itver.edu.mx

A. Rodriguez-León
e-mail: arleon@itver.edu.mx

A. Servin-Martínez
e-mail: alservinm@gmail.com

S.L. Ovando-Chacon
Depto. de Química Y Bioquímica, Instituto Tecnológico de Tuxtla Gutiérrez,
Carretera Panamericana Km. 1080, Tuxtla Gutiérrez, Chiapas, Mexico
e-mail: ovansandy@hotmail.com

1 Introduction

The numerical simulation of the flow in an open cavity with heat transfer is an important issue in many technological processes. Madadi et al. (2008) evaluated the optimal location of discrete heat source placed inside a ventilated cavity. Oztop et al. (2011) numerically examined the steady natural convection in an open cavity filled with porous media. Radhakrishnan et al. (2007) reported experimental and numerical investigation of mixed convection from a heat generating element in a ventilated cavity. Zhao et al. (2011) analyzed the characteristics of transition from laminar to chaotic mixed convection in a two-dimensional multiple ventilated cavity. Najam et al. (2002) presented the simulation of mixed convection in a T form cavity, heated with constant heat flux and ventilated from below with a vertical jet. Mamun et al. (2010) studied the effect of a heated hollow cylinder on mixed convection in a ventilated cavity. Mahmoudi et al. (2010) numerically examined the effect of the inlet and the outlet locations on the mixed convection flow and on the temperature field in a vented square cavity. Deng et al. (2004) investigated the laminar mixed convection in a two-dimensional displacement ventilated enclosure with discrete heat and contaminant sources. The main aim of this numerical investigation is to study the complex interaction of a cross flow with a perpendicular jet inside an open cavity in presence of a heating surface.

2 Problem Formulation

A sketch of the enclosure configuration studied is shown in Fig. 1. 2D numerical simulations are carried out inside an open square cavity ($H/W = 1$) with a cross flow due to a secondary jet injected at the top wall. The main fluid enters from the lower left side wall and leaves the cavity through the upper right side wall. The Reynolds number ($Re = U_mW/\nu$), based on the velocity of the main inlet flow U_m and the width W of the cavity, studied in this investigation is $Re = 500$ for different Richardson and Prandtl numbers. In order to induce the buoyancy effect, a hot plate is located on the bottom of the cavity which generates the heating of the fluid. Two different lengths W_p of the plate are considered. The main entrance and exit of the cavity are fixed to $h = 0.25\ W$, meanwhile the inlet of the jet on the top wall is fixed to $a = 0.05\ W$.

The governing equations for a non-isothermal incompressible steady state flow, in a two-dimensional domain Ω, are given as:

$$-\frac{1}{Re}\Delta\mathbf{u} + \mathbf{u}\cdot\nabla\mathbf{u} + \nabla p = RiTj \text{ in } \Omega, \tag{1}$$

$$\nabla\cdot\mathbf{u} = 0 \text{ in } \Omega, \tag{2}$$

Fig. 1 Geometry of the open cavity with a cross flow due to secondary jet injected at the top wall
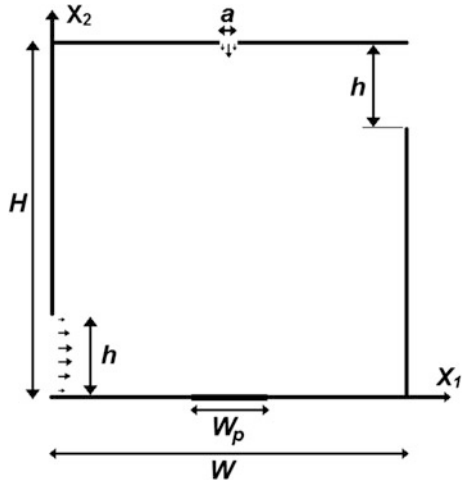
$$-\frac{1}{Pe}\Delta T + \mathbf{u}\cdot\nabla T = 0 \text{ in } \Omega, \tag{3}$$

In the above equations $\mathbf{u} = (u_1, u_2)$ is the velocity vector, being u_1 and u_2 the horizontal and vertical velocity components, respectively; ν is the kinematic viscosity, p is the pressure, T is the temperature and j is the vertical unitary vector. In the governing equations, the Richardson number, Reynolds number and Peclet number are defined as follow:

$$Ri = g\beta W (T_h - T_c)/U_m^2, \quad \text{Re} = U_w W/\nu, \quad Pe = \text{Re Pr}, \tag{4}$$

where g is the gravity, β is the compressibility coefficient, T_h is the hot temperature, T_c is the cold temperature. No slip boundary conditions ($u_1 = u_2 = 0$) were established in all the walls of the cavity and adiabatic walls ($\partial T/\partial n = 0$) were supposed except in the bottom wall where the heating takes places. The temperatures of the jet and main inlet flows are fixed to $T = T_c$, meanwhile the temperature of the isothermal heater plate is fixed to $T = T_h$. The non-dimensional values of this temperature were $T_c = 0$ and $T_h = 1$. The boundary conditions of the main inlet flow were $u_1 = U_m$, and $u_2 = 0$. On the outlet flow was imposed $\partial u/\partial n = 0$.

3 Numerical Solution of the Model and Results Validation

Numerical simulations are conducted for the laminar flow inside an open cavity for the Reynolds number of *500* with Richardson and Prandtl numbers ranging between *0.01* and *10*. A 2D geometry is used (see Fig. 1) and several types of meshing are included in order to obtain independent results from the numerical parameters. The governing equation are solved with the finite element method combined with the

operator splitting scheme, see Glowinski (2003). The convergence analysis is done for three different meshes with resolution of 25050, 27200 and 30080 elements. An analysis of the temperature profiles on the middle horizontal and vertical lines indicates that the largest difference of the results between the meshes of 25050 and 27200 is 8.5 %, while the maximum difference of the results between the meshes of 27200 and 30080 is 1.0 %. The analysis is also done for the velocity components, for all cases the worst relative error between the meshes of 27200 and 30080 is less than 1.0 %. The whole simulations presented in this paper are performed for a cavity with 30080 elements.

4   Results and Discussions

Figure 2 shows the streamlines, for $W_p = 0.10$. For the lowest Richardson number a strong jet is observed from the entrance to the exit of the cavity, above this diagonal jet three vortices are formed as a result of the boundary layer detachment from the surface driven by the fluid motion that crosses the cavity and its interaction with the flow of the secondary jet injected at the top wall, further a clockwise vortex is formed at the bottom left corner of the cavity. As the Richardson number is increased the strength of the diagonal stream decreases, for $Ri = 1.0$ and $Pr = 0.01$ only two vortices can be observed due to the circulation of the fluid injected at the top inlet. For the natural convection regime $Ri = 10$ with $Pr = 0.01$, a strong circular vortex is formed, which occupies the whole of the cavity. Increasing the Prandtl number to $Pr = 1.0$, it is observed that three vortices tend to form above the main stream, however when the Prandtl number is increased to $Pr = 10$ and natural convection regime dominates, these vortices merge to form only one vortex above of the main stream which moves from left to right and then rises toward the outlet of the cavity. For the lowest Richardson number, the velocity field remains without changes as the Prandtl number is increased, however as the Richardson and Prandtl numbers are increased different configuration of the streamlines are formed, as a result of the buoyancy effect.

Figure 3 shows the streamlines, for $W_p = 0.75$. For forced convection regime the distribution and number of vortices inside the cavity are independent of the length of the heating plate and the thermal properties of the fluid, see left panels of Figs. 2 and 3. For $Ri = 1.0$, the size and distribution of the vortices depend on the length of the heating plate, see middles vertical panels of Figs. 2 and 3. For $Ri = 10$, the number and size of the vortices tends to change with the variations of the length of the heating surface as the Prandtl number is increased. On both cases, $W_p = 0.10$ and 0.75, it can be observed that the secondary jet tends to mix totally with the main stream in the natural convection regime due to the buoyancy effect.

Figure 4 shows the isotherms, for $W_p = 0.10$. For all cases, it can be seen that the temperature contours are clustered around the heater, a hot temperature region tends to grow up toward the inside of the cavity due to the thermal plume rises above of the heater and the heat fluxes from this one to the interior part of the cavity

Fig. 2 Streamlines for $W_p = 0.10$. Top: $Pr = 0.01$. Middle: $Pr = 1.0$. Bottom: $Pr = 10.0$. Left: $Ri = 0.01$. Middle: $Ri = 1.0$. Right: $Ri = 10.0$

heating the fluid located at the neighborhood of the heat source. For the lowest Prandtl number the isotherms elongates toward the whole part of the cavity due to the thermal diffusion regime, however as Prandtl number is increased the contours tend to elongate from the heater toward the exit of the cavity due to the cooling of the fluid as a result of the flow motion that crosses the cavity.

Figure 5 shows the isotherms, for $W_p = 0.75$. Due to the increase in the length of the heating plate, the fluid inside the cavity remains hotter than the previous case. The contours tend to intensify as a result of the more energy injected. For low Richardson numbers the temperature contours are affected by the forced convection regime, however for the highest Richardson number the contours tend to follow the behavior of the streamlines, as the Prandtl number is increased, driven by the natural convection regime. For both lengths of the heating surface, a perturbation of the main isotherms at the central part of the top wall is observed due to the injection of cool fluid. For low Prandtl number the isotherms of the secondary jet are
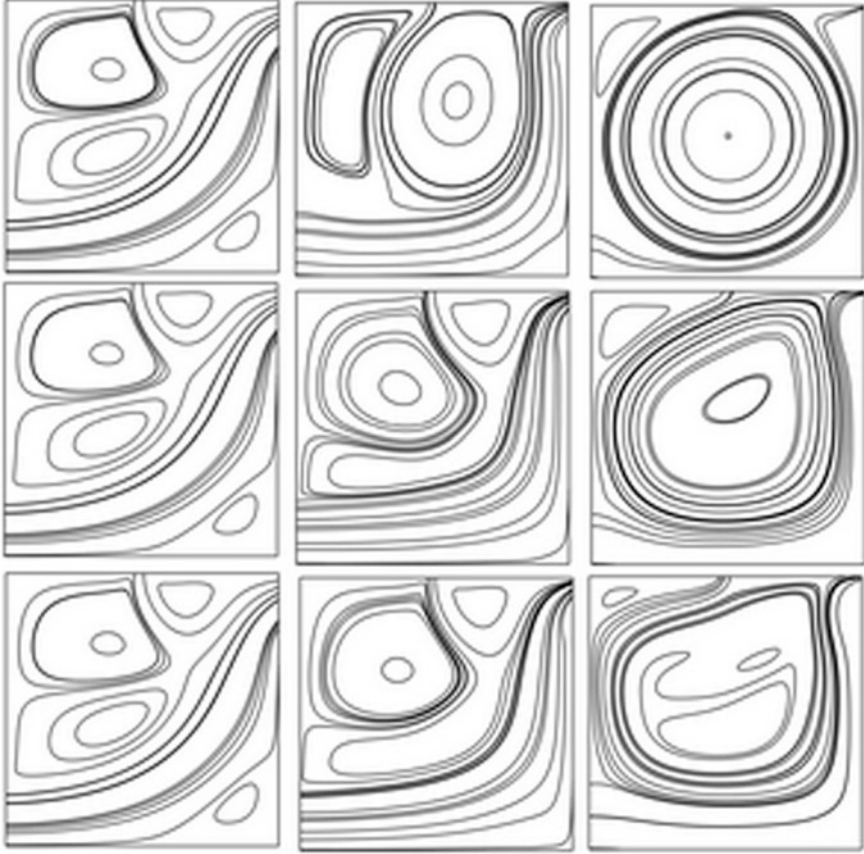
Fig. 3 Streamlines for $W_p = 0.75$. Top: $Pr = 0.01$. Middle: $Pr = 1.0$. Bottom: $Pr = 10.0$. Left: $Ri = 0.01$. Middle: $Ri = 1.0$. Right: $Ri = 10.0$

clustered at the neighborhood of the top entrance, however as the Prandtl number is increased the thermal contours of the secondary jet elongates interacting with the main contours. On the other hand, the temperature gradients increase as the Richardson and Prandtl numbers also increase. The highest temperatures are reached when natural convection and thermal diffusion occurs, meanwhile the lowest temperatures are reached when forced convection and momentum diffusion dominate.

Figure 6 shows the average Nusselt number as a function of the Richardson number for $W_p = 0.1$ (left) and $W_p = 0.75$ (right) with Prandtl numbers in the range of [0.01–10]. For the lowest length of the heater, the average Nusselt numbers are lower than the corresponding values of the highest length of the heater. This variation is increased as the Prandtl increases. Furthermore, for a given Richardson number the Nusselt number increases as the Prandtl number increases, this behavior
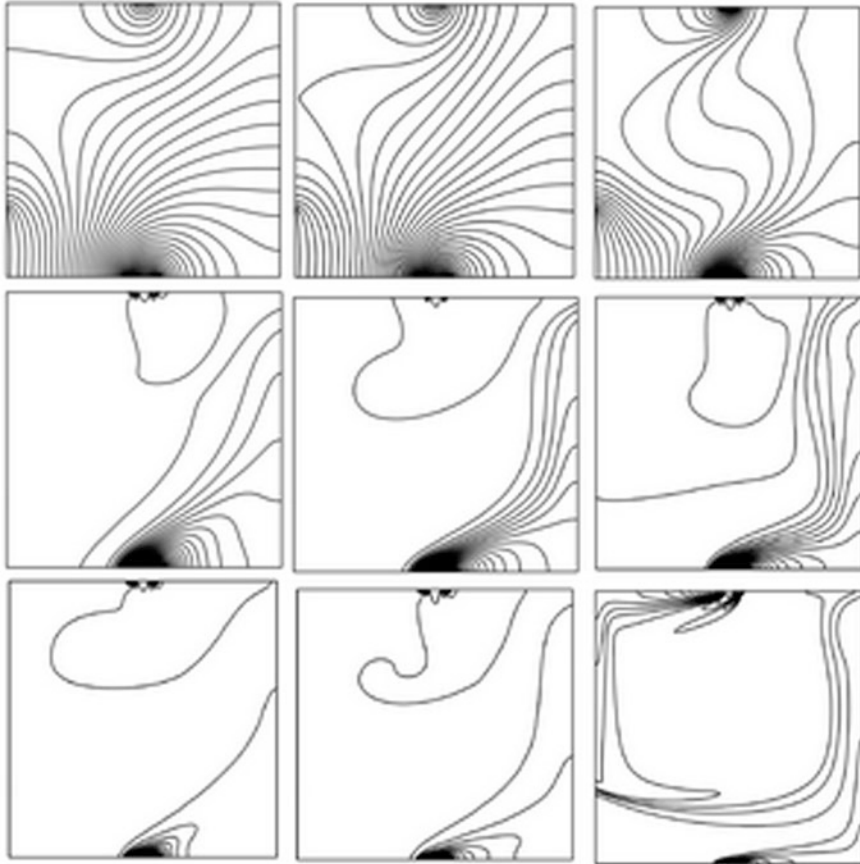
Fig. 4 Isotherms for $W_p = 0.10$. Top: $Pr = 0.01$. Middle: $Pr = 1.0$. Bottom: $Pr = 10.0$. Left: $Ri = 0.01$. Middle: $Ri = 1.0$. Right: $Ri = 10.0$

is observed for both lengths of the heater. This implies that the cooling of the cavity is enhanced when momentum dissipation is augmented. On the other hand, for a given Prandtl number the Nusselt number is increased as the Richardson number is increased, this variation is intensified as Prandtl number increases, this implies that natural convection regime enhances the heat transfer rate inside the cavity.

Figure 7 depicts the effect of the Richardson and Prandtl numbers on the average temperature inside the cavity, for $W_p = 0.1$ (left) and $Wp = 0.75$ (right). For $Ri \leq 1$, the average temperature of the fluid decreased slightly for $Pr = 0.1$, 1.0 and 10 when $W_p = 0.1$, this behavior is also observed when $W_p = 0.75$ for $Pr = 10$ and 1.0, beyond $Ri = 1$, the average temperature increased as the Richardson number increased. Keeping constant the Richardson number, the average temperature is increased as the Prandtl number decreases due to the fact that the thermal diffusivity
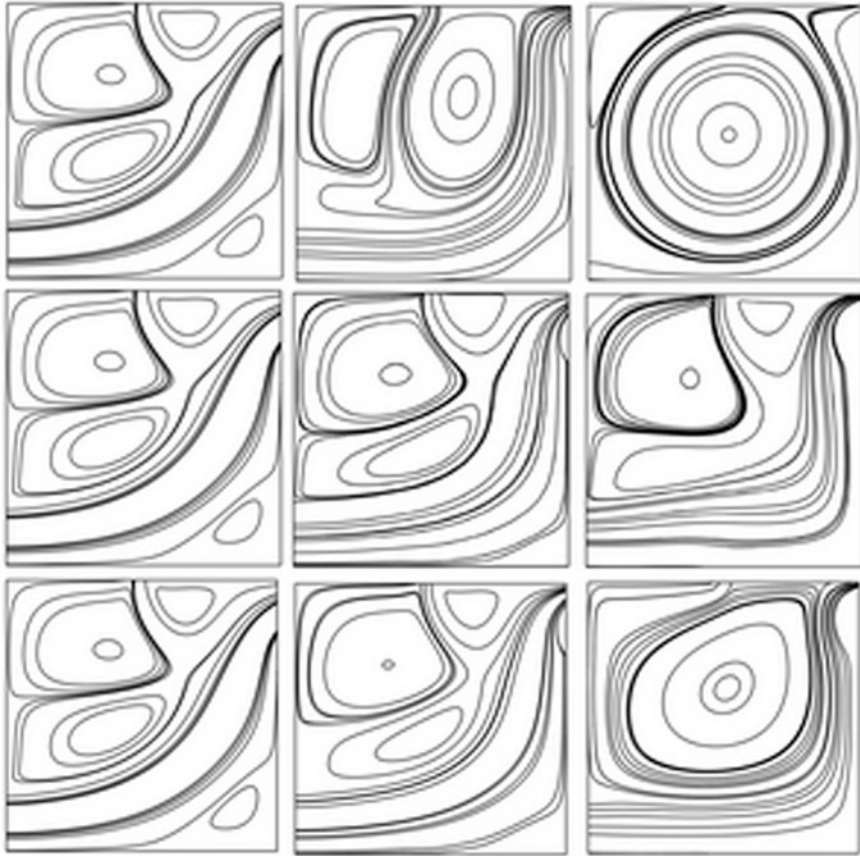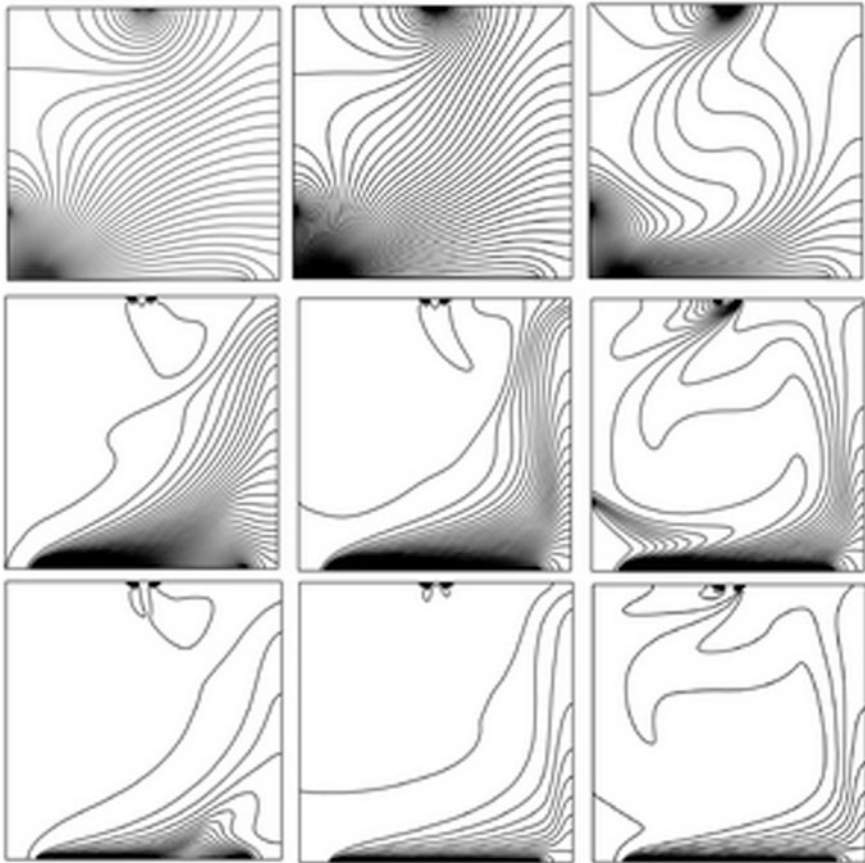
Fig. 5 Isotherms for $W_p = 0.75$. Top: $Pr = 0.01$. Middle: $Pr = 1.0$. Bottom: $Pr = 10.0$. Left: $Ri = 0.01$. Middle: $Ri = 1.0$. Right: $Ri = 10.0$
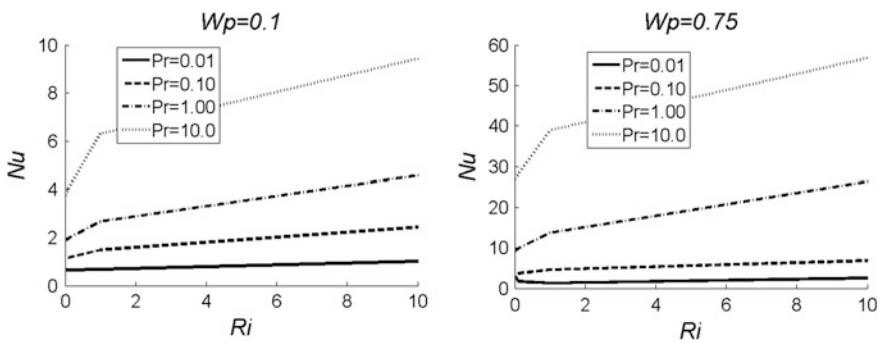
Fig. 6 Average Nusselt number as a function of the Richardson number for two different lengths of the heater with different Prandtl numbers
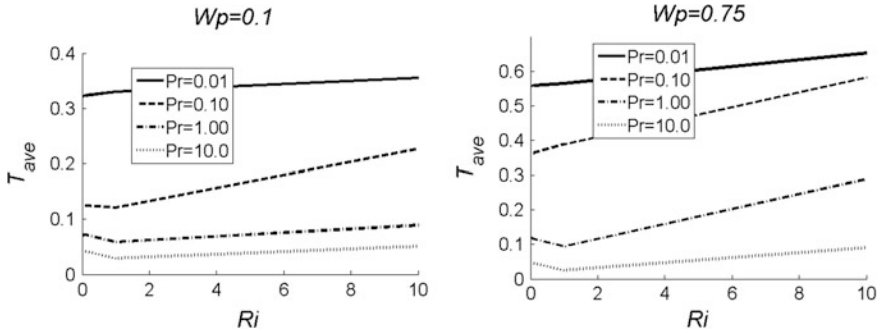
Fig. 7 Average temperature as a function of the Richardson number for two different lengths of the heater with different Prandtl numbers

plays a major role in the heat transfer process. The maximum value of the average temperature is *0.65* for $Ri = 10$, $Pr = 0.01$ and $W_p = 0.75$.

Figure 8 shows the outlet temperature of the fluid at the exit of the cavity is a function of the Richardson number for $W_p = 0.10$ (left) and $W_p = 0.75$ (right) with different Prandtl numbers. For $W_p = 0.10$ the outlet temperature of the fluid is lower than the corresponding values for $W_p = 0.75$. This variation is increased as the Prandtl number increases. Moreover, for a given Prandtl number the outlet temperature of the fluid is increased as the Richardson number is increased, this variation is intensified as Prandtl number increases, this implies that the buoyancy effect enhances the heat transfer rate inside the cavity. On the other hand, for a given Richardson number the outlet temperature of the fluid increases as the Prandtl number decreases, this behavior is observed for both lengths of the heater. This implies that the cooling of the cavity is enhanced when the viscous diffusion rate is augmented.
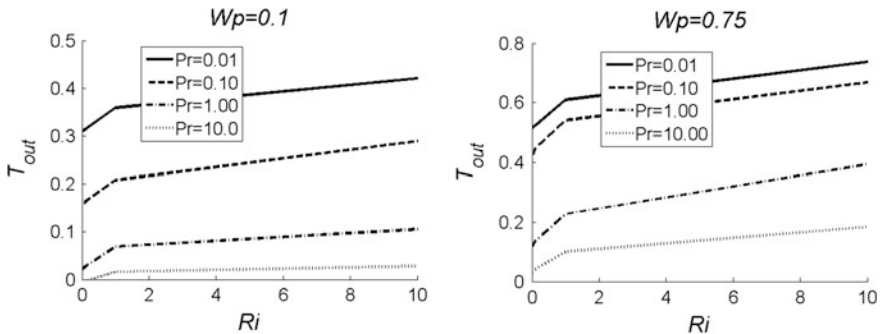
Fig. 8 Outlet temperature as a function of the Richardson number for two different lengths of the heater with different Prandtl numbers
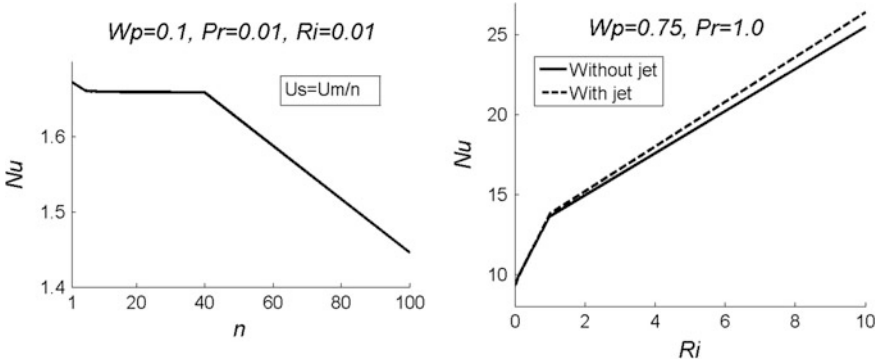
Fig. 9 *Left* Average Nusselt number as a function of the intensity of the secondary jet velocity. *Right* Average Nusselt number as a function of the Richardson number for the cases with jet and without jet

So far, all the results have been presented for the case when the inlet velocity of the secondary top jet equals the inlet velocity of the main stream ($U_s = U_m$), however, in order to understand the effect of the intensity of the secondary top jet velocity, left panel of Fig. 9 shows the average Nusselt number as a function of the intensity of the secondary jet velocity for $W_p = 0.1$, $Pr = 0.01$ and $Ri = 0.01$, observing that as the intensity of the top jet start to increase the average Nusselt number is enhanced rapidly until $n = 40$, then remains almost constant until $n = 2$, and finally increases when $n = 1$, this implies that the average Nusselt number increases as the velocity of the secondary jet increses. On the other hand, the right panel of Fig. 9 shows the effect of the top jet on the average Nusselt number for different Richardson numbers, observe that the secondary top jet tends to enhance the average Nusselt number, this enhancement is increased for the natural con-vection regimen and decreases in the forced convection regime.

5   Conclusions

In this work results of finite element simulation of the flow inside an open cavity with a cross flow due to a secondary jet injected at the top wall are presented. The analysis is carried out for the laminar regimen with different convection and dif-fusion regimes. The streamline patterns reveal that if the momentum force gener-ated by the fluid velocity at the main inlet aperture produces a movement of the inside fluid higher than the one produces by the buoyancy force, then forced convection will dominate the form of the vortex distribution. On the other hand, if the inlet velocities are slow, the buoyancy forces will determine the streamline patterns. The heat transfer rate inside the cavity is enhanced as the momentum dissipation and natural convection regimen are augmented. Increasing the velocity

of the secondary jet the average Nusselt number is enhanced. Furthermore, the average Nusselt number is increased when a secondary jet is applied at the top wall as the Richardson number is increased, due to the secondary jet produces a perturbation in the flow pattern promoting heat transfer inside the cavity.

References

Deng QH, Zhou J, Chi Mei, Shen YM (2004) Fluid, heat and contaminant transport structures of laminar double-diffusive mixed convection in a two-dimensional ventilated enclosure. Int J Heat Mass Transf 47:5257–5269

Glowinski R (2003) Numerical methods for fluids. part 3, In: Garlet PG Lions JL (eds.) Handbook of numerical analysis, vol IX. North-Holland, Amsterdam

Madadi RR, Balaji C (2008) Optimization of the location of multiple discrete heat sources in a ventilated cavity using artificial neural networks and micro genetic algorithm. Int J Heat Mass Transf 51:2299–2312

Mahmoudi AH, Shahi M, Talebi F (2010) Effect of inlet and outlet location on the mixed convective cooling inside the ventilated cavity subjected to an external nanofluid. Int Commun Heat Mass Transf 37:1158–1173

Mamun MAH, Rahman MM, Billah MM, Saidur R (2010) A numerical study on the effect of a heated hollow cylinder on mixed convection in a ventilated cavity. Int Commun Heat Mass Transf 37:1326–1334

Najam M, El Alami M, Hasnaoui M, Amahmid A (2002) Numerical study of mixed convection in a T form cavity submitted to constant heat flux and ventilated from below with a vertical jet. C. R. Mecanique 330:461–467

Oztop HF, Al-Salem K, Varol Y, Pop I (2011) Natural convection heat transfer in a partially opened cavity filled with porous media. Int J Heat Mass Transf 54:2253–2261

Radhakrishnan TV, Verma AK, Balaji C, Venkateshan SP (2007) An experimental and numerical investigation of mixed convection from a heat generating element in a ventilated cavity. Exp Thermal Fluid Sci 32:502–520

Zhao M, Yang M, Lu M, Yuwen Zhang (2011) Evolution to chaotic mixed convection in a multiple ventilated Cavity. Int J Therm Sci 50:2462–2472

Oscillations of a Flexible Plate Immersed in a Vortex Street

E. Sandoval Hernández and A. Cros

Abstract This experimental study deals with the oscillation of a flexible plate inside the von Kármán street. The flow velocities are much lower than the threshold above which the fluttering instability would develop. The flexible plate is fixed at its leading edge whereas its leading edge is free. The vortices are detected by tin oxide and the whole system is recorded by a videocamera. We find that the trailing edge of the plate oscillates with a small amplitude and with the same frequency as the incoming vortices. Moreover, the plate wavelength is more than twice the plate length. These results are different from the previous experiments of Allen and Smits (2001) performed with larger plates and at much higher Reynolds numbers. Alben (2010) theoretical study permits to explain these differences.

1 Introduction

A flexible plate can flutter spontaneously in a flow if the flow velocity is high enough. This flutter is due to the aeroelastic instability (Païdoussis 1998) whose mechanism is as follows. The flow generates infinitesimal pressure differences between the two sides of the plate, which provoke plate oscillations. When the flow velocities are lower than a velocity threshold, these oscillations are damped. Nevertheless, above a velocity threshold, the plate oscillations are amplified and the plate flutters with typical spatial shapes and temporal frequencies which depend upon the geometrical and elastic characteristics (Eloy et al. 2008; Michelin et al. 2008).

E. Sandoval Hernández
Natural and Exact Sciences Department CU-Valles, Universidad de Guadalajara,
Carretera Guadalajara—Ameca km. 45.5. C.P., 46600 Ameca, Jalisco, Mexico

A. Cros (✉)
Physics Department CUCEI, Universidad de Guadalajara,
Av. Revolución 1500. Col. Olímpica. C.P., 44430 Guadalajara, Jalisco, Mexico
e-mail: anne@astro.iam.udg.mx

The equation of movement which describes the transversal deflection $y(x, t)$ of the flexible plate in a uniform flow (where x is the axis parallel to the plate chord at rest, t is time and y is the coordinate transversal to the plate area at rest) depends upon the pressure difference Δp between the two faces of the plate. This term is difficult to estimate when it comes from a uniform flow around the plate. In this work a periodic term Δp is set via the von Kármán street.

This experimental study is performed as follows. First a vortex wake is generated behind a cylinder at low Reynolds numbers $(100 < Re < 150)$. Then the flexible plate is fixed at its leading edge out of the recirculation region which forms downstream the cylinder, that is at a distance greater than a few cylinder diameters downstream the cylinder. The flexible plate trailing edge is free. We measure the amplitude and the frequency of the free end of the plate as a function of the cylinder diameter and of the Reynolds number, for a fixed plate length. The deflection of the other points along the flexible plate can also be plotted as a function of time. Finally, we compare our results with two previous studies: the experimental work of Allen and Smits (2001) and Alben's (2010) theoretical study.

The paper is organized as follows. In Sect. 2, we present our experimental device. In Sect. 3, we show our results, which are analyzed and discussed in Sect. 4. Conclusion is written in Sect. 5.

2 Experimental Device

The flow is generated in a water channel thanks to a centrifugal pump and controlled via a triphasic frequency converter. Hence, flow velocity can be varied from $v = 0.8$ to 2.0 cm/s with a precision better than 2 %. A 10-cm-long cylindrical obstacle, of two different diameters $D = 5$ and 13 mm, is vertically fixed at the beginning of the test section as illustrated in Fig. 1a. The test section dimensions are $10 \times 10 \times 100$ cm^3. The flexible plate is cut from a transparent sheet protector and its elastic and geometrical characteristics are shown in Table 1.

The leading edge of the flexible plate is fixed to a thin metallic wire at the distance $s = 7$ cm downstream the cylinder center, as shown in Fig. 1b. This distance is chosen in such a way that the plate leading edge be outside the suction region behind the cylinder. Besides, the pinned limit condition leads to a natural first frequency in water equal to $f_I \approx 1.2$ Hz.

The visualizations are made by oxidizing a thin tin wire which passes through the flow perpendicularly to the cylinder. One of the extremes of the wire is connected to the negative pole of a power supply while the positive pole is connected to a copper electrode at the end of the test section (Taneda et al. 1977). This visualization method gives better results than the dye method because the vortices appear less deformed when passing near the flexible plate. A photo of the flow and the flexible plate is shown in Fig. 2.
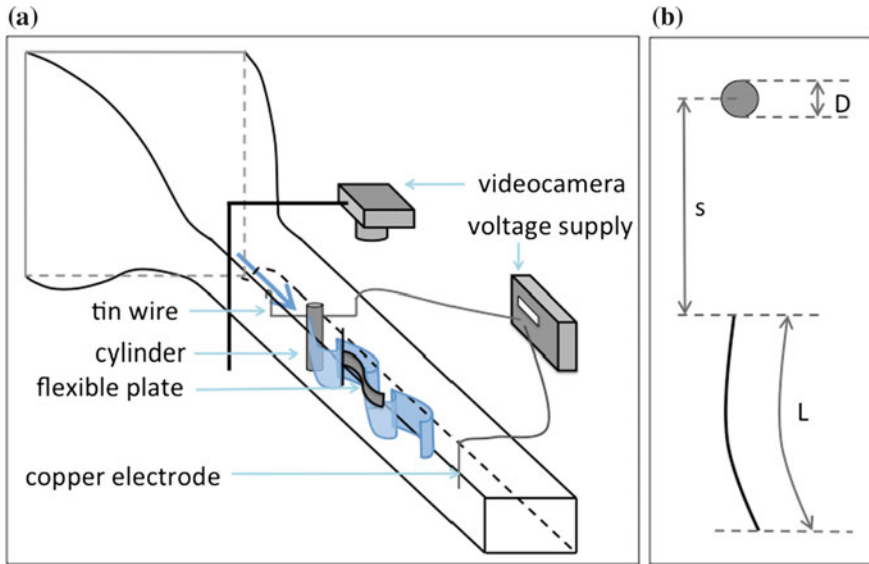
Fig. 1 a Experimental set-up. **b** Top view of the system cylinder—flexible plate with the specific distances: the plate length is $L = 6.5$ cm, the cylinder diameters are $D = 5$ and 13 mm, the distance between the plate leading edge and the cylinder center is $s = 7$ cm

Table 1 Geometrical and elastic characteristics of the flexible plate. L is the length, H the height, e the thickness, m_s the mass per unit of area, B the plate flexural rigidity

L (cm)	H (cm)	e (mm)	m_s (g/m^2)	B (N.m)
6.5	2	0.044	34	8.1×10^{-5}
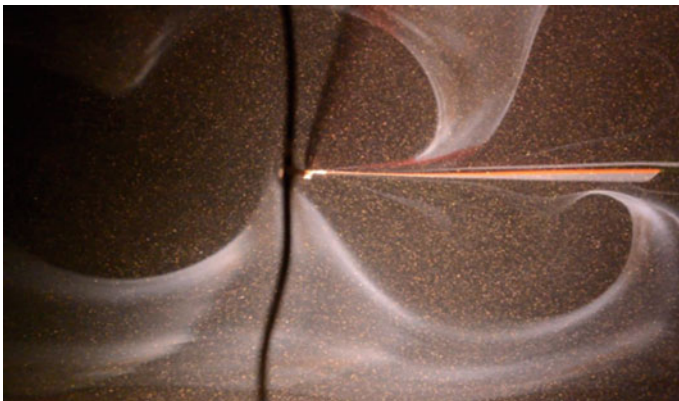
Fig. 2 Photo of the flow around the flexible plate visualized via the tin oxide. The flow goes from *left* to *right*. The cylinder is not shown in the photo. The *dark vertical line* comes from the support of the flexible plate axis. The vortices are delimited by the tin oxide so that they correspond to the dark regions of the flow

The system {vortices + flexible plate} is recorded thanks to a videocamera (Nikon D5200) placed above the system. The frame size is 1080 × 1800 pixels, so that the resolution equals to 10 pixels by millimeter.

3   Results

3.1   Influence of the Cylinder Diameter

First, we checked that the flexible plate does not oscillate when it is immersed in the uniform laminar flow generated by the water channel. No oscillation was observed for flow velocities between 0.8 and 2.0 cm/s.

Then, we placed a cylinder with a diameter $D = 5$ mm upstream from the plate. We could not detect any oscillation of the trailing edge of the flexible plate for the same velocity interval.

Finally, the von Kármán street was generated by a cylinder with a diameter $D = 13$ mm. The videocamera could detect a slight oscillation of the free end of the plate. In order to quantify the deflection $y(L, t)$, we performed spatiotemporal diagrams. From each picture of the video we extracted the column of pixels that passes through the free end of the plate. This column is put in the spatiotemporal diagram of Fig. 3 and the same process is repeated for all the pictures. In this way, the x-axis of Fig. 3 is time while the vertical axis represents the space. In the flow, the dark areas correspond to the vortices. It can be observed that the flexible plate oscillates with the same frequency as the von Kármán vortices.
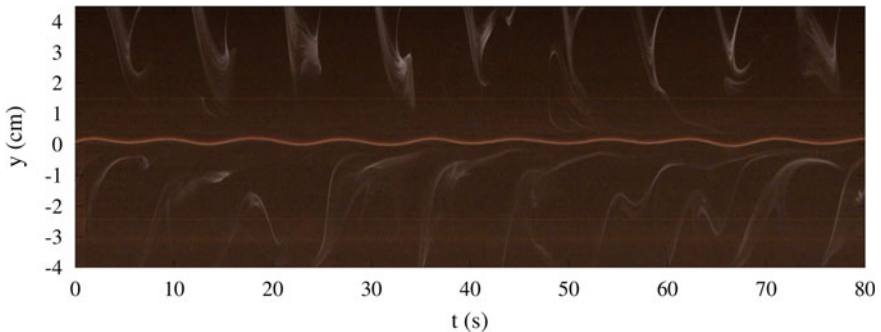
Fig. 3 Spatiotemporal diagram for the cylinder with diameter $D = 13$ mm and $Re = 113$
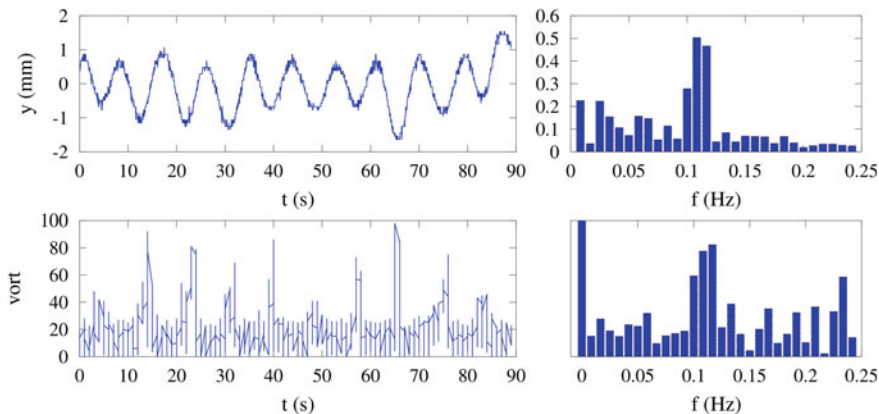
Fig. 4 *Left-hand top plot* temporal evolution of the trailing edge deflection of the plate for $Re = 113$. *Left-hand bottom plot* pixel values of the *horizontal line* ($y = 3.0$ cm) of the spatiotemporal diagram. *Right-hand plots* respective Fourier spectra

3.2 Influence of the Reynolds Number

We varied the flow velocity v in such a way that the Reynolds number calculated via the obstacle diameter $D = 13$ mm was $Re = [108, 143]$. Several spatiotemporal diagrams were performed and we extracted the trailing edge oscillation, as shown in the left-hand top plot of Fig. 4.

The left-hand bottom plot of Fig. 4 shows the pixel values of the line located at $y = 3.0$ cm in the spatiotemporal diagram. In this plot, the vortices correspond to low values of the pixels (dark areas) while the tin oxide correspond to clearer regions, that is, higher values of the pixels. The right-hand plots are the respective spectra of the left-hand plots. The spectra allow to determine the frequency of the plate and of the vortices for each Reynolds number. These two quantities are plotted in Fig. 5. The red points correspond to the plate trailing edge frequencies while the blue points (generally superimposed with the red points) correspond to the frequency of the von Kármán vortices in presence of the plate. The plain line represents the expected evolution of the vortices frequency as a function of the Reynolds number for the usual von Kármán street given by Fey et al. (1998). This plot means that the presence of the flexible plate does not influence the vortices frequency and that the plate is synchronized with the incoming vortices. Moreover, spatiotemporal diagrams performed at different coordinates of the plate (not shown here) allowed us to conclude that all the points along the plate oscillate with the same phase. That means that the plate wavelength λ is such that $L/\lambda < 0.5$.

Besides, the amplitude A of the plate trailing edge is shown in Fig. 6. It can be seen that A is very small, with a maximum of $A/L \approx 0.01$, equivalent to $A = 0.7$ mm and $A/D \approx 0.05$, at $Re = 140$. This amplitude is much lower than in the Allen and Smits (2001) experiments as discussed next.

Fig. 5 Evolution of the
frequencies f of the von
Kármán vortices (*blue*) and
the plate trailing edge (*red*) as
a function of Reynolds
number Re calculated via the
cylinder diameter. The *plain
line* represents the expected
frequency of the von Kármán
vortices without flexible plate
as a function of the Reynolds
number (Fey et al. 1998)
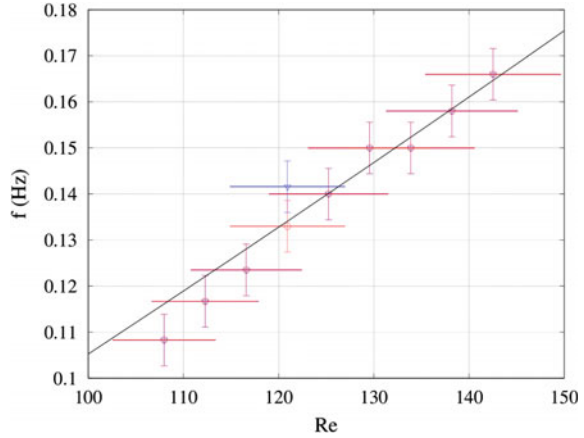
Fig. 6 Evolution of the
non-dimensional amplitude
A/L of the plate trailing edge
as a function of the Reynolds
number Re calculated on the
cylinder diameter
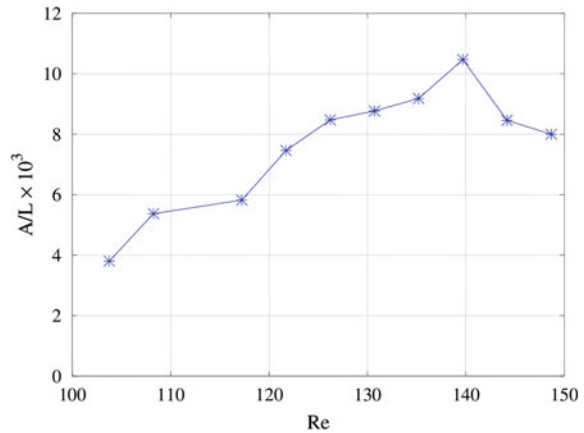
4 Analysis and Discussion

Allen and Smits (2001) performed the same kind of experiments with plates of
different characteristics. In order to compare their plates with ours, the geometrical
dimensions, m_s and B values of their plates are shown in Table 2. We also note that
the von Kármán street was generated in their experiments by planar bluff bodies
perpendicular to the flow ($D = 5.08$ and 3.81 cm), so that their Reynolds number
(calculated via D) varied between 5000 and 40000.

As it can be seen in Table 2, the dimensions and density of their plates are much
larger than our plate. As their plate thicknesses are greater too, their flexural
rigidities are also higher. The first difference between their observations and our
experiments is that their plates oscillate such that $L/\lambda = 1.5 - 2$, where λ is the plate

Table 2 Characteristics of the plates used by Allen and Smits (2001). L is the length, H the height, e the thickness, m_s the mass per unit of area, B the plates flexural rigidity

	L (cm)	H (cm)	e (mm)	m_s (g/m²)	B (N.m)
18 PVDF	45.7	7.62	0.70	1100	3.1×10^{-3}
24 PVDF	61.0	7.62	0.70	1100	3.2×10^{-3}
18 PU	45.7	7.62	0.60	980	6.1×10^{-4}
18 plastic	45.7	7.62	0.10	200	4.2×10^{-4}

wavelength. This difference can be explained by calculating the wavenumber k^* of the free oscillations of the flexible plate in vacuum. Alben (2010) defines two nondimensional numbers as:

$$R_1 = m_s / \rho L \qquad \text{and} \qquad R_2 = \frac{B}{\rho v^2 L^3} \left(\frac{l}{L} \right)^2 \tag{1}$$

where ρ is the air density, v the vortex translation velocity and l the vortices wavelength. Alben (2010) defines the nondimensional wavenumber as

$$\frac{k^*}{2\Pi} = \frac{1}{\sqrt{2\pi}} \left(\frac{R_1}{R_2} \right)^{1/4} \approx \frac{L}{\lambda}. \tag{2}$$

The order of magnitude of these quantities are shown in Table 3. The value of R_2 is much lower for Allen and Smits (2001) than in our experiment because both their flow velocity and their plate lengths are higher. That is why those authors could observe more than a wavelength along their plate length. It can be seen moreover that the theoretical values of $k^*/(2\Pi)$ correspond qualitatively to the observed experimental values L/λ.

Let note that the expression of k^* is also equivalent to the ratio $(\omega_v/\omega_p)^{1/2}$, where $\omega_v = 2\Pi v/l$ is the vortex frequency and $\omega_p = [B/(m_s \, L^4)]^{1/2}$ is a characteristic frequency of the plate. In our case, the vortex frequency ($\omega_v = 0.6 - 1$ rad/s, see Fig. 5) is much lower than the natural frequency of the plate ($\omega_p = 12$ rad/s). In this way, the plate wavelength λ/L is related to the ratio between the natural frequency of the plate and the frequency of the vortices.

The second difference is that Allen and Smits (2001) observed that their plates could reach an amplitude $A = 5D$. This value is much higher than our plate amplitude. Once again, this observation is consistent with the predictions of Alben (2010) who found that the higher R_1, the greater the amplitude.

Table 3 Order of magnitude of R_1, R_2 (Eq. 1) and $k^*/(2\Pi)$ (Eq. 2) in our experiment and in the Allen and Smits (2001) work

	R_1	R_2	$k^*/(2\Pi)$
This study	1×10^{-3}	50–100	0.02
Allen and Smits (2001)	$(0.9–4.8) \times 10^{-3}$	1×10^{-6}–3×10^{-3}	0.3–1.5

Finally, in the work of Allen and Smits (2001), when $Re < 10000$, the plates oscillate with a lower frequency than the incoming vortices. They lock on the von Kármán street frequency for high enough flow velocities. In our experiments, we saw that the plate oscillates with the same frequency as the von Kármán vortices for the whole Reynolds interval $Re = [108, 143]$. We think that this is possible thanks to the small oscillation amplitude.

5   Conclusion

In this experimental work, we studied the oscillation of a flexible plate inside von Kármán vortices. The plate has a length $L \approx l$, where l is the wavelength of the incoming vortices. The vortices are generated by a cylinder of diameter D in the interval $Re = [108, 143]$. When $D = 5$ mm, no oscillation is observed. When $D = 13$ mm, we observed that (i) the plate oscillates with the same frequency as the von Kármán vortices and that (ii) the maximum oscillation amplitude is A/D 0.05. Moreover, (iii) our plate oscillates with a wavelength higher than twice the plate length. These observations are different from the results of Allen and Smits (2001), who worked at much higher Reynolds numbers $Re = [5000, 40000]$ and with larger plates. These authors found that (i) their plates reach the same frequency as the von Kármán vortices for high enough Reynolds numbers and that (ii) their plates oscillate with amplitudes that reach $A = 5D$. Moreover, (iii) whereas all the points along our plate oscillate with the same phase, the plates of Allen and Smits (2001) oscillate with a wavelength λ such that $L/\lambda = 1.5 - 2$. These differences are well explained by two nondimensional numbers defined by Alben (2010) which are related to the pressure that the flow exerts on the plate and the mass inertia.

Finally, we comment that, while the objective of Allen and Smits (2001) was to harvest electrical energy from the piezoelectric plate, this kind of experiment is also important to understand how a passive fish can be propelled upstream when placed in von Kármán vortices, as shown by Beal et al. (2006).

References

Alben S (2010) Passive and active bodies in vortex-street wakes. J Fluid Mech 642:95–125
Allen JJ, Smits AJ (2001) Energy harvesting eel. J Fluids Struct 15(3):629–640
Beal DN, Hover FS, Triantafyllou MS, Liao JC, Lauder GV (2006) Passive propulsion in vortex wakes. J Fluid Mech 549:385–402
Eloy C, Lagrange R, Souilliez C, Schouveiler L (2008) Aeroelastic instability of cantilevered flexible plates. J Fluid Mech 611:97–106

Fey U, König M, Eckelmann H (1998) A new Strouhal-Reynolds-number relationship for the circular cylinder in the range $47 < Re < 2 \times 105$. Phys Fluids 10:1547–1549

Michelin S, Llewellyn Smith SG, Glover BJ (2008) Vortex shedding model of a flapping flag. J Fluid Mech 617:1–10

Païdoussis MP (1998) Fluid–structure interactions, slender structures and axial flow, vol 1. Academic, London, p 572

Taneda S, Honji H, Tatsuno M (1977) The electrolytic precipitation method of flow visualization. In: The International symposium on flow visualisation, pp 133–138

Experimental Study of a Vortex Generated at the Edge of a Channel with a Step

E.J. López-Sánchez, C.D. García-Molina, G. Ruiz-Chavarría and A. Medina

Abstract At the outlet of estuary-like systems, three vortices are formed: a dipole and a spanwise vortex. The spanwise vortex is formed due to the separation of the bottom boundary layer, just in front of the dipole. If a step occurs at the bottom in the channel output, a single vortex will be formed, the dipole becomes a part of a structure having a horseshoe shape. In a periodic driving flow, after a while this structure results in a dipole and a spanwise vortex. To study in laboratory this kind of vortices we made experiments in a system consisting of two domains connected by a channel in which the flow is induced by a periodic forcing. The channel layer depth is different with respect the depth in the two others domains. In order to investigate this system some measurements of velocity field using PIV were carried out in the vertical plane passing along the channel centerline. On the other hand, the detection of vortices composing the dipole was made with the synthetic Schlieren method. Vortices are low pressure regions, then they produce a deformation of the free surface which can be detected with this method. We observed that at the channel output a horseshoe vortex is formed by the flushing into the open domain. This structure remains for some time, after it decomposes in a dipole and a spanwise vortex. Finally all three vortices are destroyed.

1 Introduction

A large concentration of sand and other particles has been observed in front of coastal estuary-like systems (Albagnac et al. 2011), which may have many different interests, for instance in fishing or due to possible ship accidents. The aforesaid distribution is due to the presence of two counter rotating vortices. In the space between

E.J. López-Sánchez (✉) · C.D. García-Molina · G. Ruiz-Chavarría
Facultad de Ciencias, Universidad Nacional Autónoma de México
Ciudad Universitaria, 04510 Mexico, D.F., Mexico
e-mail: lsej@unam.mx

E.J. López-Sánchez · A. Medina
ESIME-Azcapotzalco, Instituto Politécnico Nacional, Av. de Las Granjas 682,
Azcapotzalco, Santa Catarina, 02250 Mexico, D.F., Mexico

vortices a flow like a jet is produced, then the flow can carry particles for long distances compared with the channel width (Wells and Heijst 2003; Ruiz-Chavarria and Lopez-Sanchez 2016). Some previous works have been devoted to this kind of flow. For instance Nicolau del Roure et al. (2009) performed experiments to study a pair of counter rotating vortices formed in periodic flows in the shallow water approximation. They measured, among others, the position of the vortices, the maximum vorticity, the circulation and the effective diameter. For this purpose they used PIV to determine the velocity field in the surface and they measured geometrical properties through visualization. An important result is that the dipole produced in the first period behaves differently with respect to the dipoles produced in subsequent cycles. If the vortices escape channel influence, finally they are destroyed. Nicolau del Roure et al. (2009) associate this destruction to the friction on the bottom. However there exist other mechanisms, such as the appearance of instabilities (Crow 1970; Billant et al. 1999).

Apart from the dipole, a spanwise vortex has been recently reported (Lacaze et al. 2010; Albagnac et al. 2011). Its properties have been investigated both numerically and experimentally. This vortex appears as a consequence of the bottom boundary layer detachment. Albagnac (2010) made a comprehensive study of this structure when it is produced by the motion of two vertical flaps. She found that its shape resembles a horseshoe. In a periodic forced flow the shape of the spanwise vortex evolves in time (Lopez-Sanchez 2013; Lopez-Sanchez and Ruiz-Chavarria 2015). The motivation of this work is that in a periodic forced flow an accumulation of particles occurs inside the channel (Lopez-Sanchez and Ruiz-Chavarria 2014; Villamil Sapien et al. 2015), then the depth becomes non uniform. On the other hand, this kind of systems can be found in some coastal lagoons, during the rainy season. In such case, rain leads to an increase of the water level in the lagoon eventually producing the connection with to the sea.

In order to evaluate the effects of a channel with a depth lower than the remaining domains we have performed the following experiment. First, we induce a periodic driving flow. Then, we put a slug into the channel to reduce the depth by 25 and 50 %. Finally properties of vortices are investigated.

This paper is organized as follows: In Sect. 2 we present the theoretical framework and the dimensionless parameters governing the flow. In Sect. 3 the experimental setup is shown. The results of the PIV and synthetic Schlieren measurements are presented. Finally, in Sect. 5 conclusions are drawn.

2 Theoretical Framework

As result of periodicity of tides, water flow through the channel at estuary-like systems is periodic. To mimic this behavior we produce in laboratory a sinusoidal flow. The procedure to generate a variable flow rate $Q(t)$ is to partially submerge a solid block into the water. The displaced volume is:

$$V(t) = l \times a \times h(t) \tag{1}$$

where l is the block length, a is the width and $h(t) = h_0 (1 - \cos(2\pi f t))$ is the instantaneous depth (the distance from free surface to the lower end of the block).

The flow rate is simply the time derivative of $V(t)$:

$$Q(t) = \frac{d V(t)}{d t} = 2\pi f \times l \times a \times h_0 \cos(2\pi f t) \tag{2}$$

Because water is incompressible and if we neglect changes in water level, $Q(t)$ is also the flow rate through the channel (Villamil Sapien et al. 2015). From the previous equation we found that the flow rate amplitude is:

$$Q_0 = 2\pi f \times l \times a \times h_0 \tag{3}$$

To determine the flow velocity into the channel we need to determine its cross area. This is $A = Hhn$, where H is the channel width, h is the layer depth in the two basins and n is the fraction of the water layer in the channel above the step. We have chosen two values of n, namely, $n = \frac{1}{2}$ and $n = \frac{3}{4}$. We can estimate the maximum velocity U in terms of the channel width H and the maximum flow rate Q_0 as

$$U = \frac{Q_0}{Hhn} \tag{4}$$

In this system two dimensionless numbers are relevant, the Strouhal and the Reynolds numbers. To define them we use the channel width H as the characteristic length, the representative velocity is that given in Eq. (4) and t is non dimensionalized with $\tau = H/U$. The Strouhal number is $S = \frac{U}{HT}$ while the Reynolds number is $Re = \frac{UH}{v}$. From these definitions, the dimensionless flow rate is:

$$Q^*(t^*) = Q_0^* \sin(2\pi S t^*) \tag{5}$$

From Eq. (4) the Reynolds number becomes:

$$Re = \frac{Q_0}{Hhn} \frac{H}{v} = \frac{Q_0}{hnv} \tag{6}$$

So, the Reynolds number does not depend on the channel width H.

On the other side, to calculate vorticity from velocity data, we use a second order centered finite differences schema, as follows:

$$\omega = \frac{\partial v}{\partial x} - \frac{\partial u}{\partial y} \approx \frac{v_{j+1} - v_{j-1}}{\Delta x} - \frac{u_{i+1} - u_{i-1}}{\Delta y} \tag{7}$$

Among other quantities we calculate vorticity and position of dipoles. To determine the position of vortices we use the idea of centroid. The last one is defined in terms of circulation. If we remember the definition of circulation (Dritschel 1986;

Landau and Liftshitz 1987), the vortex center (x_c, y_c) is:

$$\Gamma = \iint \omega \, dx \, dx \approx \sum \omega \, \Delta x \, \Delta y \tag{8}$$

$$x_c = \iint \frac{\omega \, x \, dx \, dy}{\Gamma} \tag{9}$$

$$y_c = \iint \frac{\omega \, y \, dx \, dy}{\Gamma} \tag{10}$$

To study the spanwise vortex we need to make a distinction between the vorticity created at the bottom and the vortex itself (even if vortex is fed by wall vorticity). Before the appearance of the spanwise vortex, velocity field in the vicinity of the bottom is essentially horizontal. However, when vortex is present the vertical component of velocity is not negligible. A quantity well suited to determine the formation of the vortex is the vertical kinetic energy density (Lacaze et al. 2010):

$$E = \int v^2 \, ds \tag{11}$$

where integration extends over a vertical plane. This energy density quantifies the vertical movements which are not associated with the bottom boundary layer. Therefore, this quantity distinguishes between the vortex vorticity and boundary layer vorticity. It should be noted that for calculating the energy density, the portion near the vertical wall of the step has not been considered.

3   Experimental Setup

As can be seen in Fig. 1, we performed our experiments in a tank which consists of two basins connected by a channel. In our system, both basins have the same depth h, but in an attempt to get a more realistic model of estuary-like systems, the channel depth represents a fraction of h. We filled the tank with water up to get a uniform water layer of $h = 5.0$ cm. We have put a slug in the channel which reduces layer depth to 25 and 50 % of h.

To have different values of S and Re we have chosen an unique driving period $T = 12.5$ s and three different channel widths, namely, $H = 0.026$ m, $H = 0.04$ m and $H = 0.05$ m. The periodic water flow was induced by partially submerging a block having the following dimensions: $l = 0.577$ m, $a = 0.0149$ m. Otherwise the amplitude of its vertical motion is $h_0 = 0.015$ m.

Measurements were conducted in two ways: the study of the horizontal vorticity was made by PIV (Raffel et al. 1997; Meunier and Leweke 2003). The velocity field was measured in the vertical plane of symmetry. For this purpose we seed the water with glass coated silver spheres ($r = 5\,\mu$m) and we produce a vertical sheet with a solid state laser having a power of 1.6 W and emitting light at 532 nm. The images

Fig. 1 Diagram of the
experimental setup
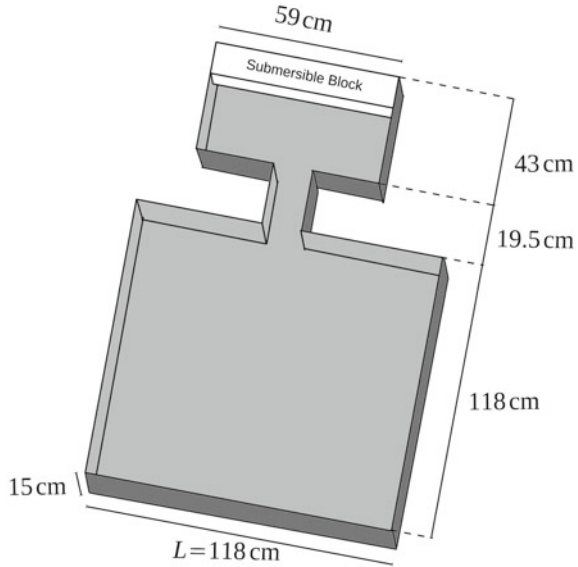
we acquired with a high speed camera at a rate of 250 fps and covering an area of
$0.10 \times 0.05\,\text{m}^2$. The resolution of camera is 720×576 pixels and factor conversion
between length and pixels is $\alpha = 4900\,\text{px/m}$ Because we need to cover the region
where vortex pass, the camera was put at two different locations. For those config-
urations we recorded two videos of three full periods each, these videos covered a
distance of 0.14 m from the channel output with an overlap of 0.06 m. The first video
covered from the channel output up to a distance of 0.10 m from it; and other one
covered the interval from 0.04 to 0.14 m from the channel output.

To obtain properties of vertical vorticity we determined the free surface topog-
raphy with the synthetic Schlieren method (Moisy et al. 2009). A vortex core is a
low pressure region, then when it attains a free surface, variations of the water level
are observed. As Synthetic Schlieren is a method for measuring the deformation in
the water surface (Moisy et al. 2009), this technique is appropriate to characterize
the formation and evolution of vortices attaining the free surface. To implement this
method a dot pattern was placed at the bottom of the recipient. At a distance of
0.95 m above the water surface, we placed a video camera to record a dot pattern
area of $L_1 \times L_2 = 0.206 \times 0.116\,\text{m}^2$. With this configuration, the distance between
the camera and the free surface is enough to avoid rays crossing (Moisy et al. 2009).
To record image we take videos with a full high defintion camera, JVC Everio HD,
modelGZ-HM845BE, at a rate 50 fps, with an image resolution of 1920×1080 pix-
els (Everio 2011). The factor conversion between length and pixels is 9300 pixel/m.
Later, we have extracted individual images using software ffmpeg and finally they
are processed with software DPIVsoft (Meunier et al. 2004).

4   Results

In this paper we present data of the velocity field in a vertical plane passing through the channel centerline. The images taken for PIV measurements have a resolution of 720×576 pixels and cover an area of $15.5\,\text{cm} \times 11.8\,\text{cm}$. Because the height of a frame is bigger than the water layer depth and also due to the size of the laser sheet, the frames were trimmed to a size of 400×260 pixels or 500×260. We have chosen cells of 32×32 pixels for the processing in the DPIV software.

On the other hand the evolution of the dipole was investigated with the synthetic Schlieren method. The images recorded have a size of 1920×1080 pixels and cover an area of $20.6\,\text{cm} \times 11.6\,\text{cm}^2$.

As we have mentioned above experiments were made for three different channel width: 2.6, 4 and 5 cm. In addition, two different layer depths into the channel were considered: $n = \frac{1}{2}$ and $n = \frac{3}{4}$. For the case $n = 1/2$; the transversal area of the channel is $A = 0.05 \times 0.03675 = 0.001225\,\text{m}^2$, and according to Eq. (4), $U = 0.106\,\text{m/s}$. For the case $n = 3/4$, the transversal area of the channel is $A = 0.05 \times 0.03675 = 0.0018375\,\text{m}^2$ and $U = 0.071\,\text{m/s}$. Given these quantities, the Reynolds and Strouhal numbers can be computed; these values are presented in the Table 1.

All the experimental configurations described in this article gave us similar results, so we have decided to present the most representative ones, the case with $n = 1/2$.

4.1   PIV Measurements

The fluid leaving the channel forms a single vortex. The two branches, which in other circumstances forms a dipole, now are connected near the bottom. The horizontal section of this structure initially is located near the step and after it moves and approaches the bottom. Later it goes away from the channel, the vortex is divided in a dipole and a clockwise vortex. Finally the latter is destroyed during the stage of negative flow rate at a distance of approximately of one time the channel width, whereas the dipole remains for more than one cycle.

Figure 2 shows a sequence of the velocity field in the symmetry plane for the $S = 0.0732$ (see Table 1). The horizontal section of vortex is produced just at the edge of the channel in the same manner as the two vertical branches, that is, because the

Table 1   Values of Reynolds and Strouhal numbers for all cases here studied

	$n = 1/2$, $Re = 2734$	$n = 3/4$, $Re = 1823$
$H = 0.05\,\text{m}$	$S = 0.0732$	$S = 0.1097$
$H = 0.04\,\text{m}$	$S = 0.0468$	$S = 0.0702$
$H = 0.026\,\text{m}$	$S = 0.0198$	$S = 0.0297$
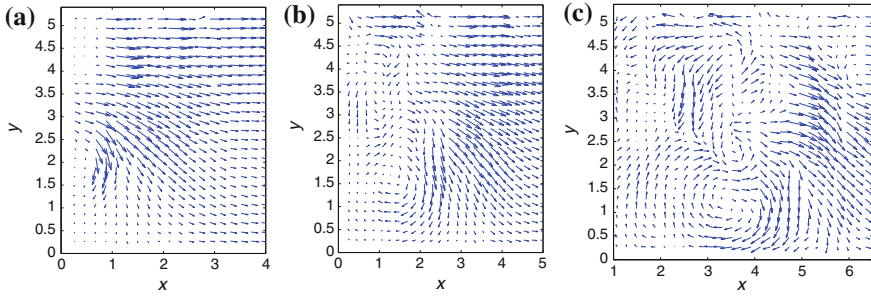
Fig. 2 Time evolution (as a function of the period T) of the velocity field in the vertical plane at the symmetry axis between 0 and 10 cm for $S = 0.0732$. **a** $t = 0.1143\,T$s. **b** $t = 0.2\,T$. **c** $t = 0.29\,T$
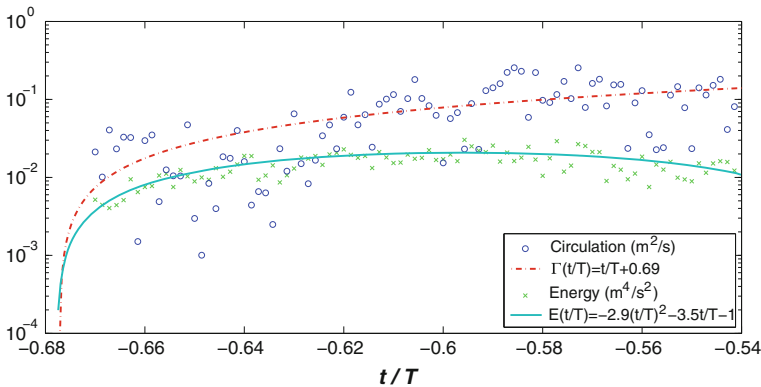
Fig. 3 Circulation and energy density at the vertical rectangular plane $x \in (0, 6)$ cm and $y \in (0, 2.5)$ cm, where the vortex is

boundary layer separation. According to our reference system, the vorticity is negative. In Fig. 2a the initial stage of the vortex formation can be observed. Figure 2b shows the vortex at a time close to that of maximum flow rate. Finally, in Fig. 2c we can see the transversal vortex at the bottom, and to a distance of $x \approx 3.5$ cm from the channel output. The size of vortex is larger than that shown in Fig. 2b.

In Fig. 3 we plot the circulation and the vertical kinetic energy versus time during the first half driving period. Initially circulation is zero because fluid is at rest. After it increases due to the addition of the vorticity created by the non slip condition in the channel's bottom. Circulation attains a local maximum and then decreases until the final dissipation of this section of the vortex. This reduction is related to the bottom friction and the fact that near the wall vorticity of opposite sign is created. On the other hand, the vertical energy density is an increasing function of time. It means that the vortex grows in size and also in intensity along the half period. The experimental data for Γ and E were fitted with a polynomial. In the first case we choose a cubic fit, whereas for E a quadratic one was made. Both curves are included, they are the dashed and the continuous lines respectively in the figure.
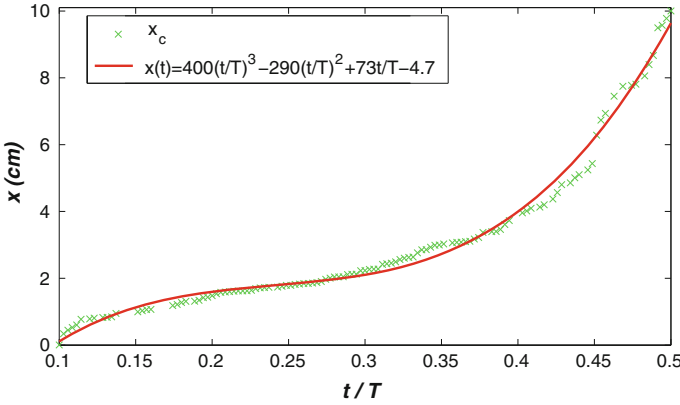
Fig. 4 Position of the horizontal section of vortex in the interval $x \in (0, 10)$ cm within a half period
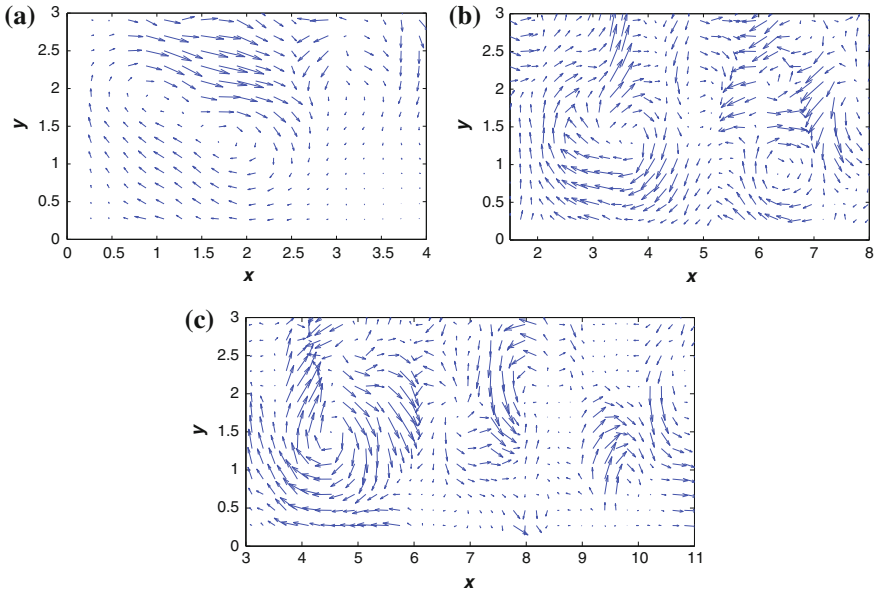
Fig. 5 Velocity field in the vertical plane at the symmetry axis during the second driving period. **a** At $t = 1.11\,T$ we observe an elongated vortex **b** $t = 1.23\,T$, two vortices are observed, one of them at $x \approx 3.5$ cm. $x \approx 6.5$ cm. **c** Velocity field at $t = 1.45\,T$

The vortex position was estimated based on the centroid calculation Eqs. (9) and (10). The center does not fall to the bottom completely (see Fig. 2c). At $t = 0.5\,T$ the vortex center is approximately to a distance of $h_{cent} \approx 1$ cm from the bottom. Based in data of centroids the distance traveled by the horizontal branch of the vortex is presented in Fig. 4. The data wera fitted with a cubic polynomial. Initially the speed

is small, $v \approx 0.3$ cm/s. After a while the vortex is accelerated and it reaches a velocity of $v \approx 3.5$ cm/s.

Figure 5 shows three snapshots of the velocity field over the second driving period. In Fig. 5a we see the velocity field at $t = 1.11\,T$. It is important to remark that flow properties are different when compared with the same stage at the first cycle. In particular the vortex now is elongated. The same behavior has been observed for other values of S an Re. After a while, at $t = 1.23\,T$, we can observe a velocity field indicating the presence of two vortices at $x \approx 3.5$ cm and $x \approx 6.5$ cm (see Fig. 5b). This behavior is presumably the result of the detachment of a fraction of the vorticity of the elongated vortex an to the bottom bounddary layer separation. Finally, in Fig. 5c both vortices have moved and they are at $x \approx 4.5$ and $x \approx 9.5$ respectively.

4.2 Dipole Properties

To study the dipole we use synthetic Schlieren method. The Fig. 6 shows the topography of the free surface at two different times. Vortex core in Fig. 6 coincides with free surface depression. The amplitude of depression is roughly proportional to vortex intensity. Figure 6a shows free surface deformation at $t = 0.5\,T$, that is, during the first cycle. While in Fig. 6b we show the free surface deformation at $t = 1.4\,T$, that is, in the subsequent period. Here we observe that at the first period, the depression amplitude is around a half of the depression amplitude for the successive cycles. Which is another expression that the vortex in the first cycle have differences with vortices produced in the subsequent cycles.

Figure 7 shows the deformation of the surface in two different cycles. In the first period Fig. 7a it can be observed a dipole leaving the channel. This dipole is the only one in the first cycle. In Fig. 7b we can observe the surface deformation at $t = 1.1\,T$. Apart of the main dipole created in each cycle (in Fig. 7b in the position $x = 4$ cm) we can see another depression at $x = 1$ cm, $y = -3$ cm corresponding to a secondary vortex formed after the main dipole.
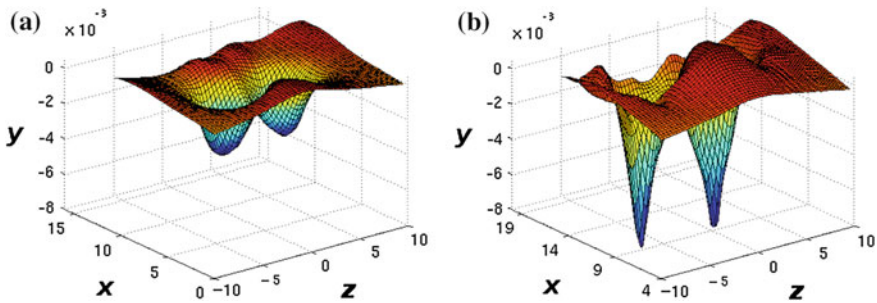
Fig. 6 Deformation of the water surface at two times. **a** $t = 0.5\,T$. **b** $t = 1.4\,T$

(a)

(b)
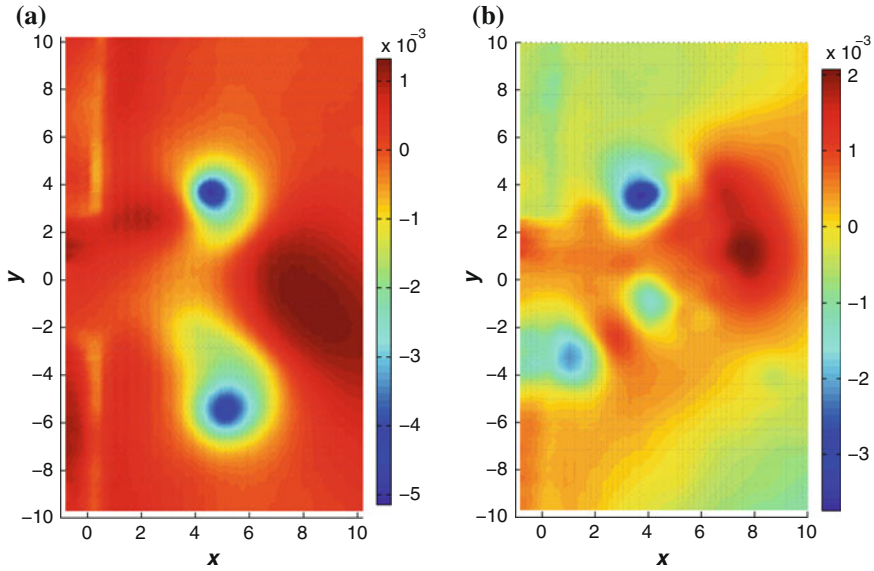
Fig. 7 Deformation of the water surface at two times. **a** $t = 0.23\,T$. **b** $t = 1.1\,T$
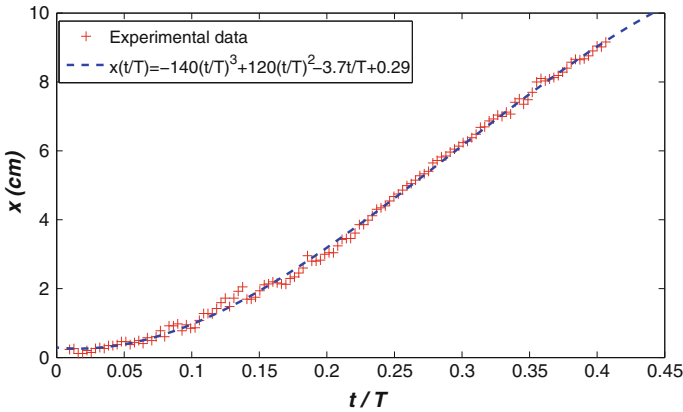
Fig. 8 Dipole displacement in function of t/T. These data was taken in an interval of $5\,s$. The displacement dipole velocity is $v_d \approx 0.8\,cm/s$

Finally in Fig. 8 we present the position x of the dipole as a function of time. In the same figure a cubic fit is also included. At the end the vortex moves approximately with constant speed. At $t = 0.4\,T$ the dipole is in $x = 9\,cm$, and its speed is $2.4\,cm/s$. By a linear regression, the mean dipole velocity in the range $t/T \in (0.1, 0.4)$ is $2\,cm/s$. According to data obtained with Schlieren method we observe that the dipole moves up to a distance of three times the channel width before its destruction.

5 Conclusions

In this paper we have presented some results of the flow between two basins connected by a channel. The channel and the basins have a different depth. The velocity field in a vertical plane and the deformation of the free surface were measured. These measurements provide information about vortices formed in front of the channel. First, the existence of an edge in the bottom at the channel output modifies the flow properties with respect of a system with constant depth. The adverse gradient pressure in the open domain leads to the formation of a horseshoe vortex. In other conditions only two counter rotating vortex are produced. In this case the two vortices are connected near the bottom, forming an unique structure. The further evolution is influenced by the bottom friction. For $t/T < 1/2$ the transverse section of the horseshoe vortex approaches the bottom. After the vortex splits in a dipole and a spanwise vortex. On the other side, during the stage of negative flow rate the streamwise vortex disseapears because the combined effect of bottom friction and the production of vorticity of opposite sign near the bottom.

As in the previous works in which bottom is constant (Lacaze et al. 2010; Albagnac 2010; Albagnac et al. 2011), a streamwise vortex appears in front of the dipole. It travels a distance of approximately three times the channel width before its destruction

References

Albagnac J (2010) Dynamique tridimensionnelle de dipoles tourbillonnaires en eau peu profonde. Thèse de doctorat, Université Paul Sabatier Toulouse III Institut de Mcanique des Fluides de Toulouse, France

Albagnac J, Lacaze L, Brancher P, Eiff O (2011) On the existence and evolution of a spanwise vortex in laminar shallow water dipoles. Phys Fluids 23:086601

Billant P, Brancher P, Chomaz JM (1999) Three dimensional stability of a vortex pair. Phys Fluids 11:2069-2077

Crow SC (1970) Stability theory for a pair of trailing vortices. AIAA J 8(12):2172

del Roure Nicolau F, Sokolofsky SA, Chang K (2009) Structure and evolution of tidal starting jet vortices at idealized barotropic inlets. J Geophys Res 114:C05024

Dritschel DG (1986) The nonlinear evolution of rotating configutations of uniform vorticity. J Fluid Mech 172:157–182

Everio JVC (2011) CAMCORDER Detailed User Guide. Victor Company of Japan website. http://manual3.jvckenwood.com/c1c/lyt2339-010sp/

Lacaze L, Brancher P, Eiff O, Labat L (2010) Experimental characterizat ion of the 3D dynamics of a laminar shallow vortex dipole. Exp Fluids 48:225–231

Landau LD, Liftshitz EM (1987) Fluid mechanics. Pergamon Press, Oxford, UK

Lopez-Sanchez E.J (2013) Vorticidad y transporte de partculas en un flujo peridico a la salida de un canal. PhD thesis. Facultad de Ciencias, UNAM, México

Lopez-Sanchez EJ, Ruiz-Chavarria G (2014) Transport of particles in a periodically forced flow. In: Experimental and computational fluid mechanics. Springer International Publishing, pp 271–278

Lopez-Sanchez EJ, Ruiz-Chavarria G (2015) Numerical simulation of the spanwise vortex in a periodic forced flow. submitted to: Experimental and computational fluid mechanics. Springer International Publishing

Meunier P, Leweke T (2003) Analysis and minimization of errors due to high gradients in Particle Image Velocimetry. Exp Fluids 35(5):408–421

Meunier P, Leweke T, Lebescond R, Van Aughem B, Wang C (2004) DPIVsoft. User guide. Institut de Recherche sur les Phnomnes Hors Equilibre. UMR 6594 CNRS / Universits Aix-Marseille I et II, Francia

Moisy F, Rabaud M, Salsac K (2009) A synthetic Schlieren method for the measurement of the topography of a liquid interface. Exp Fluids 46:10211036

Raffel M, Willert CE, Wereley ST, Kompenhans J (1997) Particle image velocimetry: a practical guide. Springer, Berlin

Ruiz-Chavarria G, Lopez-Sanchez EJ (2016) Formation of multiple dipoles in a periodic driving flow. submitted to: Phys. Fluids, AIP

Villamil Sapien P, Sánchez Calvo González I, Lopez-Sanchez EJ and Ruíz Chavarría G (2015) Erosion and deposition of particles in a periodic forced flow. In: Klapp J et al. (eds) Selected topics of computational and experimental fluid mechanics, environmental science and engineering. Springer International Publishing, pp 447–453

Wells MG, van Heijst G-JF (2003) A model of tidal flushing of an estuary by dipole formation. Dyn Atmos Oceans 37:223–244 (Elsevier)

Fluid Forces on a Flexible Circular Cylinder in Vortex-Induced Vibrations

C. Monreal-Jiménez, F. Oviedo-Tolentino, G.L. Gutiérrez-Urueta, R. Romero-Méndez and G. Mejía-Rodríguez

Abstract In this work fluid forces acting on a flexible circular cylinder in Vortex-Induced Vibrations (VIV) were studied. An experimental campaing was conducted at low mass-damping ratio ($m_{cil}^* \zeta = 0.126$) covering the entire lock-in region. The dynamic response of the cylinder was computed using the Particle Tracking Velocimetry technique on the cylinder free end tip. Drag and lift coefficients (C_D and C_L) were determined using the experimental data from the cylinder response in a spring-mass-damping model. Results show that C_L is one order of magnitude greater than C_D. Strong cylinder oscillations are associated with a flow pattern showing two vortex center lines corresponding mainly at the upper end of the initial region.

1 Introduction

The Vortex-Induced Vibration (VIV) is a problem present in a large number of engineering applications. VIV may be observed in oil pipelines, heat exchangers, high voltage lines, bridges and cooling towers, among others. The main consequence of having VIV in a structure is the failure that may occur due to fatigue.

The studies of VIV of circular cylinders may be classified according the cylinder boundary condition. In literature, the elastic, pivoted and flexible cylinders with one or two degrees of freedom are common models. In Vortex-Induced Vibrations literature, it is understood as rigid cylinder one that experiences displacements as a rigid body (cylinder oscillations are homogeneous along the cylinder span-wise). In other words, a rigid cylinder has the characteristic of not being deformed by the effect of external forces. On the other hand, flexible cylinders are those whose oscillations vary along the cylinder span-wise (from zero, at the cylinder base, to a maximum value, at the cylinder free end tip). That is to say that in a flexible cylinder,

C. Monreal-Jiménez (✉) · F. Oviedo-Tolentino · G.L. Gutiérrez-Urueta ·
R. Romero-Méndez · G. Mejía-Rodríguez
Facultad de Ingeniería, Universidad Autónoma de San Luis Potosí,
Zona Universitaria Poniente, Av. Manuel Nava 8, 78290 San Luis Potosí, Mexico
e-mail: cintiamj123@gmail.com

the external forces cause deformation. This deformation appears as an opposition to the external force and therefore, when the force is removed the cylinder returns to its original state. Generally, investigations using rigid cylinders are conducted under one degree of freedom (cross-flow direction), while flexible cylinders are allowed to oscillate in two directions (in-line and cross-flow). In this sense, a flexible cylinder was preferred to study the lift and drag forces on the structure.

Commonly, VIV investigations focus on the following parameters: mass-damping ratio, added mass, hysteretic behavior, blockage ratio, vortex shedding frequency, cylinder frequency, vortex shedding patterns and cylinder free-end paths. The main task is to relate the parameters above with the cylinder vibrational response (lock-in).

The amplitude responses of the cylinders are normally classified according their mass-damping ratio, $m^*\zeta$. Here the mass damping ratio represents the multiplication of two coefficients. The mass ratio, m^*, represents the ratio between the cylinder mass and the displaced fluid mass. And the damping ratio, ζ, measures the decay of the cylinder oscillations after undergoing a disturbance. Cylinders with high mass-damping ratio show two branches of amplitude response (initial and lower), often referred as the Feng-type response (Feng 1968). On the other hand, experimental studies at very low mass-damping ratio were conducted by Khalak and Williamson (1996, 1997a, b, 1999). In these cases, the lock-in shows three branches of amplitude response (initial, upper and lower). The branches are separated by discontinuous mode transitions. Oviedo et al. (2014) suggested to use the cylinder frequency response in order to correctly identify the branch formation in the lock-in.

The effect of the added mass in the lock-in region were studied by Vikestad et al. (2000) and Willden and Graham (2001); the results show a monotonic decrease of the added mass as the Reynolds number is increased. The variation of the added mass affects the cylinder vibrational response (amplitude and frequency) and the fluid forces acting on the cylinder. Fluid forces are directly related with the vortex wake pattern. Therefore changes in the lift and drag coefficients should be related with changes in the vortex wake patterns. In this way, the cylinder response can be understood in the three stages: initial, upper and lower branches.

Most of the numerical studies in VIV are able to compute the cylinder fluid forces in the lock-in region, like Prasanth and Mittal (2008) and Navrose and Mittal (2013). Experimentally, Khalak and Williamson (1996, 1997a, b, 1999) show the cylinder fluid forces using an accelerometer inserted in the cylinder. However, experimental studies in cylinder fluid forces in the lock-in region are scarce. In this study, cylinder fluid forces were calculated by using cylinder time traces and a mathematical model. The cylinder vibrational response was measured by means of non-intrusive technique (Particle Tracking Velocimetry, PTV).

2 Experimental Details

A sketch of the experimental model used to analyze the dynamic response is shown in Fig. 1. The model consists of a solid circular cylinder which is normally inserted

into a flat acrylic plate. The cylinder is a copper-zinc metallic alloy with an elastic modulus of 10.5×10^{10} Pa. The dimensions and mechanic properties of the cylinder are sufficient in order to study the entire lock-in region with the experimental equipment. The acrylic flat plate is 9 mm thick and was beveled in its inlet region to avoid unwanted disturbances to the main flow. For all the experiments, the cylinder was attached to this acrylic plate by means of interference fit to avoid any displacement relative to the flat plate.

The experiments were performed in a water tunnel with an operating range from 1 to 30 cm/s. The test section of the tunnel is 38.1 cm wide, 50.8 cm high and 150 cm long. Flow stabilizer system in the water tunnel provides a flow at the inlet section with a turbulence level less than 1 % RMS.

The cylinder free-end displacements were recorded using a high speed camera. The camera used is engineered with a specialized 1280×1024 CMOS image sensor, ultra high-speed electronics, memory, and image processing electronics. This camera allows up to 17,791 fps (frames per second) at 192×96 pixels resolution. An external lighting was used so the high-speed video camera could record properly. The lighting consisted of two 180-lumen rechargeable LED lanterns. The lanterns were facing each other, both pointing to the tip of the cylinder.

2.1 Dynamic Response

The cylinder dynamic response was determined processing the recorded images with the high speed camera. Each test includes a record of 20 s at a frame rate of 240 fps and 100 μs as exposure time. The recording settings give files with a total of 4800 images. The images were processed in Matlab using the PTV technique. It consists of giving a template figure of the interest region (in this case the tip of the cylinder, see Fig. 2) and then look for the new coordinates on the subsequent images. The "normxcorr2" Matlab function computes the normalized cross-correlation of two images, the result is a matrix that contains correlation coefficients. The maximum correlation coefficient is used as reference to trace the path of the tip of the cylin-

Fig. 1 Experimental model scheme
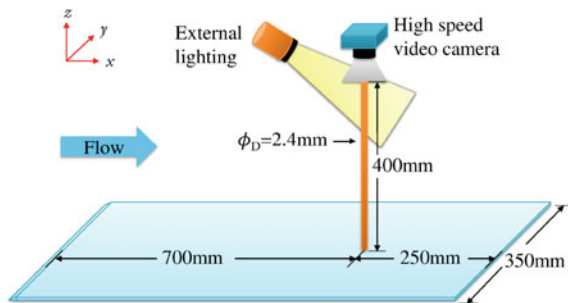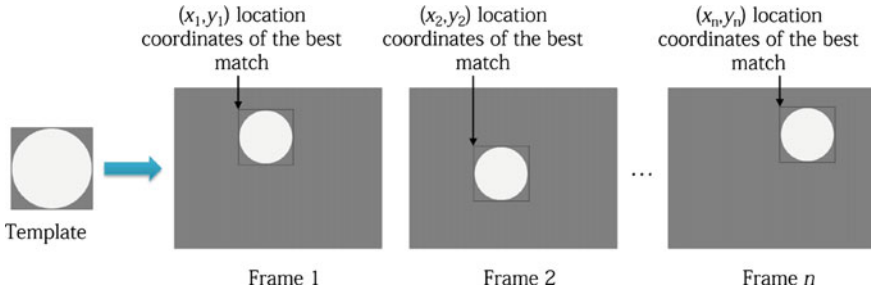
Fig. 2   PTV technique in the tip of the cylinder

der. This technique allows to determine the cylinder location over time in both axes separately.

The (x, y) coordinates can be processed by the discrete Fourier transform. The Fourier analysis converts time into frequency by decomposing a sequence of values into components of different frequencies. By doing this, the natural frequency of the system, f, can be known.

2.2   Hydrodynamic Response

For studying the hydrodynamics around the circular cylinder, the PIV technique was implemented. The scheme used to perform the experiments is shown in Fig. 3. In this technique the fluid was seeded with tracer particles with 14 μm diameter silver coated hollow glass spheres. The particles have the quality of being neutrally buoyant, this feature is important for a good fluid flow description. The seeded flow was then illuminated in a plane with high-power laser (2000 mW) and finally recorded with the high speed camera.

The motion of the seeding particles was used to calculate speed and direction (flow field) of the flow, see Fig. 4. In order to perform the PIV, the images were processed using the "PIVlab" software. The vorticity, ω, is defined as the curl of

Fig. 3   Experimental model
with the laser

Frame 1   Frame 2   Subframe 1-2   Velocity field
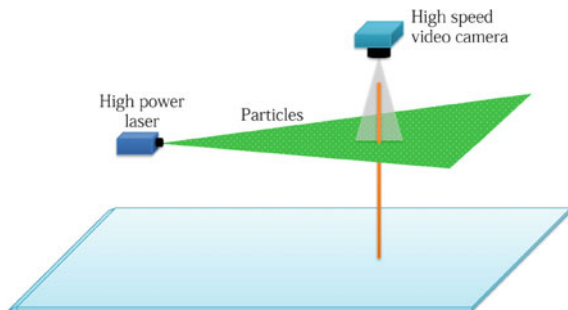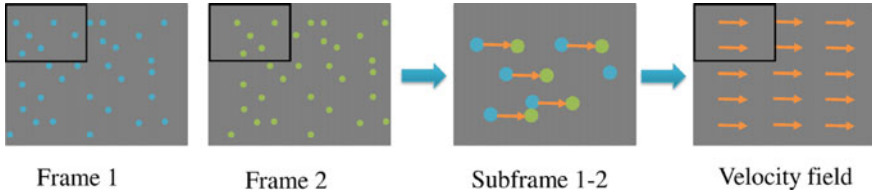
Fig. 4 PIV technique. The original images are separated in small sub-windows. In each window, a cross-correlation is performed using two consecutive frames. Using statistical methods, the average movement of the particles can be determined in that window, and hence, the velocity flow

the flow velocity vector, i.e. $\omega = \nabla \times \mathbf{u}$. In this case, from the PIV technique the flow field is known. The vorticity can be calculated by $[curlz, cav] = curl\,(X, Y, U, V)$ which computes the curl z-component and the angular velocity (in radians per second) of a 2-D vector field (U for the x-component, and V for the y-component of the flow velocity vector). Here X, and Y define the coordinates for U, and V respectively.

3 Mathematical Model

The study of vortex induced vibrations may be conducted in different ways, i.e., forced vibration and free vibration with one or two degrees of freedom. In this investigation, the experimental model, see Fig. 5, undergoes free vibration with two degrees of freedom. The equations of motion more frequently used to model vortex-induced vibrations in circular cylinders are shown in Eqs. (1) to (4).

$$m\ddot{y} + c\dot{y} + ky = F_y\,(t) \tag{1}$$

where:

$$F_y\,(t) = F_0 \sin\left(\omega\,t + \phi_y\right) \tag{2}$$

$$y\,(t) = A_y \sin(\omega\,t) \tag{3}$$

$$m\ddot{x} + c\dot{x} + kx = F_x\,(t) \tag{4}$$

where:

$$F_x\,(t) = F_0 \cos\left(\omega\,t + \phi_x\right) \tag{5}$$

$$x\,(t) = A_x \cos(\omega\,t + \theta) \tag{6}$$

In this case $\omega = 2\pi f$, m is the total punctual mass of the cylinder, c is the structural damping, k is the cylinder stiffness, F is the fluid force, f is the oscillation frequency of the cylinder, ϕ represents the phase angle between the fluid force and the body

Fig. 5 Theoretical model
scheme represented by a
mass-spring-damper system
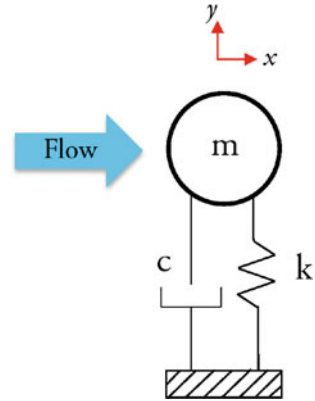
displacement, θ is the phase between the movement in the x and y axis, and A is the
amplitude of the cylinder.

4 Results

4.1 Cylinder Response

Experimental results illustrate that the lock-in region is formed by two or three
branches, depending of the mass-damping ratio value. Cylinders with high mass-
damping ratio show two branches of amplitude response while cylinders with low
mass damping-ratio show three branches of amplitude response. These branches
were delimited in Khalak and Williamson (1999) using the discontinuous mode tran-
sitions in the vibrational cylinder response. However, Oviedo et al. (2014) suggested
a branch delimitation by using the frequency response. The frequency response was
used in this work to identify the three branches formed.

Three specific cases of the cylinder vibrational response: initial, upper and lower
branch are shown in Fig. 6. This result shows the cross-flow cylinder oscillations
as the principal response. The vibrational amplitude in the cross-flow direction is
almost ten times bigger than the one in the in-line direction, $A_y \sim O(10) \cdot A_x$.

Data in Fig. 6 show an elliptical response as well. This suggests that the in-
line and cross-flow cylinder oscillations have the same frequency with a phase
angle between signals. Kheirkhah et al. (2012) associated the elliptical path with
a high structural coupling between vibrations in the cross-flow and in-line direc-
tion. Moreover, the initial response (Fig. 6a) shows a variable vibrational response
and a multi-frequential behavior in accordance with Prasanth and Mittal (2008) and
Blevins (1997).
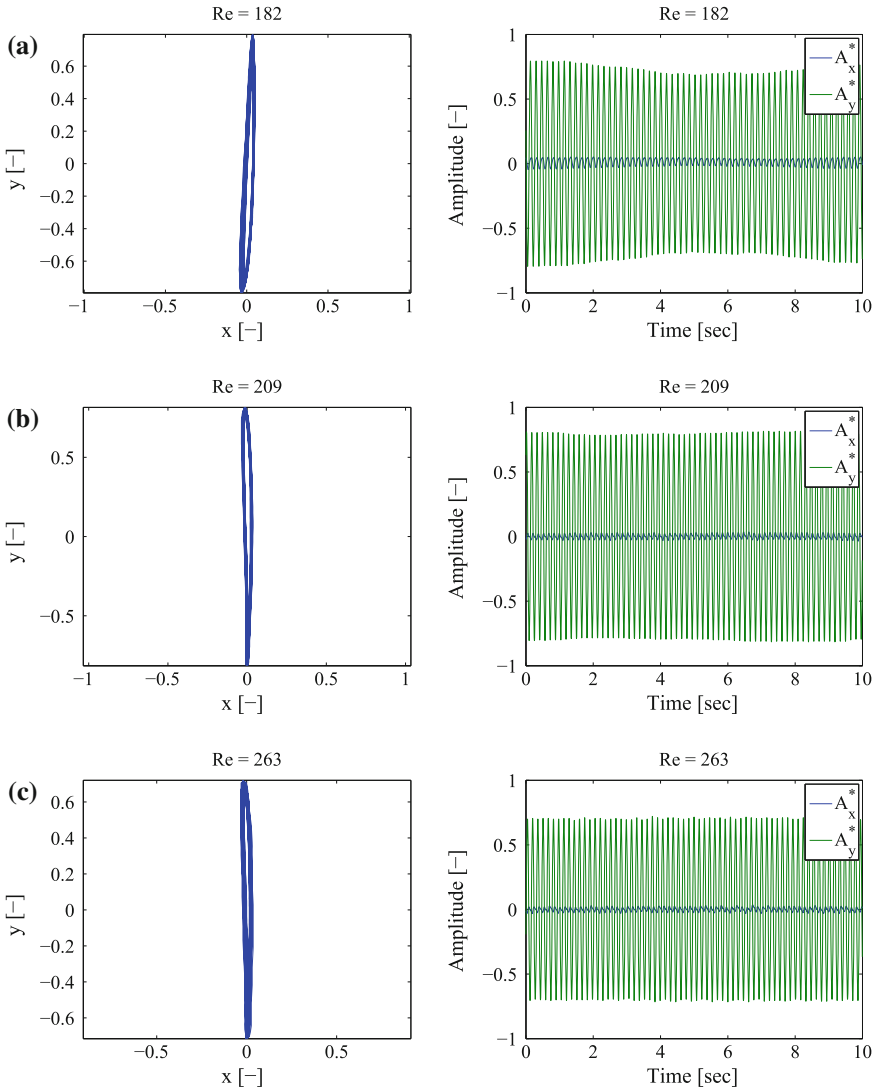
Fig. 6 In the *left* column the orbits of the free-end of the cylinder are shown. In the *right* column the cylinder displacements over time are shown in both axes, ○ *blue line* for the *x* axis and □ *green line* for the *y* axis. Both columns show the three branches of the lock-in region: **a** initial @ $Re = 182$ and $f = 5.95$, **b** upper @ $Re = 209$ and $f = 6.40$, and **c** lower @ $Re = 263$ and $f = 6.45$

The experimental data shown in Fig. 6 was used to fit Eqs. (3) and (6) for the y and x axis, respectively. These equations describe the dynamic response of the cylinder over time. From curve fitting, the amplitude and the phase angle can be determined. The frequency is known by using the Fourier transform. Despite its nature, in the initial branch Eq. (3) fitted the data with good accuracy, $R^2_{adj} = 0.93$. In the upper and lower branch the amplitude is practically constant and the model is even more accurate, $R^2_{adj} = 0.98$ and 0.99 respectively.

In the x axis, the motion is more chaotic and the model does not fit the data as well as in the y axis. A root mean square value was considered for the amplitude and used into the model, Eq. (6). Now that a model for the motion of the cylinder on each axis is known, the forces can be determined.

4.2   Drag and Lift Coefficients

The force usually used in the literature is the 'total fluid force', Eqs. (1) and (4). Instead, in this work, the 'vortex force' was used to obtain the C_D and C_L coefficients. As Lighthill showed in 1986, the 'total fluid force' can be decomposed into a 'potential force' given by the potential added mass and a 'vortex force' given by the dynamics of the so call, 'additional vorticity'. The term 'additional vorticity' means the entire vorticity in the flow field minus "the vorticity attached to the boundary in the form of a vortex sheet allowing exactly the tangential velocity (slip) associated with the potential flow", as Lighthill (1986) proposed.

$$F_{total} = F_{vortex} - F_{potential} \tag{7}$$

Thus the 'potential force' is given by:

$$F_{potential} = m' \ddot{y}(t) \tag{8}$$

where the m' coefficient refers to the added mass. Here the added mass is calculated from the natural frequency of the cylinder by: $\omega_n = \sqrt{k/(m + m')}$. The added mass is defined by Sumer and Fredsøe (1997) as the mass of the fluid around the body which is accelerated with the movement of the body due to the action of pressure.

Once the 'vortex force' is calculated for each experiment, the force coefficients can be known. For the transverse direction, we have:

$$C_L = \frac{F_{vortex, y}}{\frac{1}{2}\rho v_\infty^2 A} = \frac{\left(m + m'\right) \ddot{y} + c\dot{y} + ky}{\frac{1}{2}\rho v_\infty^2 A} \tag{9}$$

and for the longitudinal direction:

$$C_D = \frac{F_{vortex,x}}{\frac{1}{2}\rho v_\infty^2 A} = \frac{(m + m')\ddot{x} + c\dot{x} + kx}{\frac{1}{2}\rho v_\infty^2 A} \tag{10}$$

Here, the density of the fluid is given by ρ and v_∞ represents the velocity of the free stream. The choice of reference area will affect the numerical value of the coefficients. In this work the reference area was taken to be $A = 2\pi rL$, where r is the radius of the cylinder, and L is the length of the cylinder.

The actual values of the C_D and C_L are plotted in Fig. 7. From each experiment along the lock-in region, the RMS values for the force coefficients were obtained. These results are plotted in Fig. 8. In the initial branch, both coefficients rise up.

According to Sarpkaya (1978), the multi-frequential behavior in the initial branch dictates mass changes in the system. Vikestad et al. (2000) and Willden and Graham (2001) show that the added mass decreases monotonically as the reduced velocity is increased. Equations (9) and (10), show a relationship between the lift, drag coefficients and the added mass. Therefore, any oscillation in the added mass affects the lift and drag coefficients as shows Fig. 8.

From Fig. 8, it can be concluded that high oscillations in C_D and C_L occur in the initial branch. In the upper branch, the C_L starts to decline while the C_D drops dramatically. This difference is attributed to remarkable change in the vortex wake as will be shown in the hydrodynamic results. Finally in the lower branch the C_L has a less steep slope, whereas the C_D remains nearly constant.

4.3 Fluid Response

Figure 9 shows the flow tracers reveling the flow behavior. This effect can be achieved by increasing the camera exposure time. The flow behavior shows the classical von Kármán vortex street defined by Williamson and Roshko (1998) as two vortex shed per cycle. The flow behavior in the initial, upper and lower branches are shown in Fig. 10. The vortex wake follows the same definition as the 2 S classification in agreement with Navrose and Mittal (2013). The '2S' indicates two single vortices formed per cycle, one spinning in clockwise and other in the counter-clockwise direction. The main difference in flow behavior is in the vortex formation. As the cylinder response increases from the initial to the upper branch the vortex tends to convect away from the center line, i.e., starts with one vortex center-line and pass to two vortex center lines (see Fig. 9). After passing the upper branch the vortex wake shows again only one vortex center line (see Fig. 10b, c). Therefore, the two vortex center lines are associated with the high values in drag and lift coefficients in Fig. 8.

Traditionally the C_D has been associated with the vortex wake. For the laminar case, cylinders under cross-flow, the vortex wake is wider than the turbulent case. In the literature, measures of C_D show greater values for the laminar case than for the
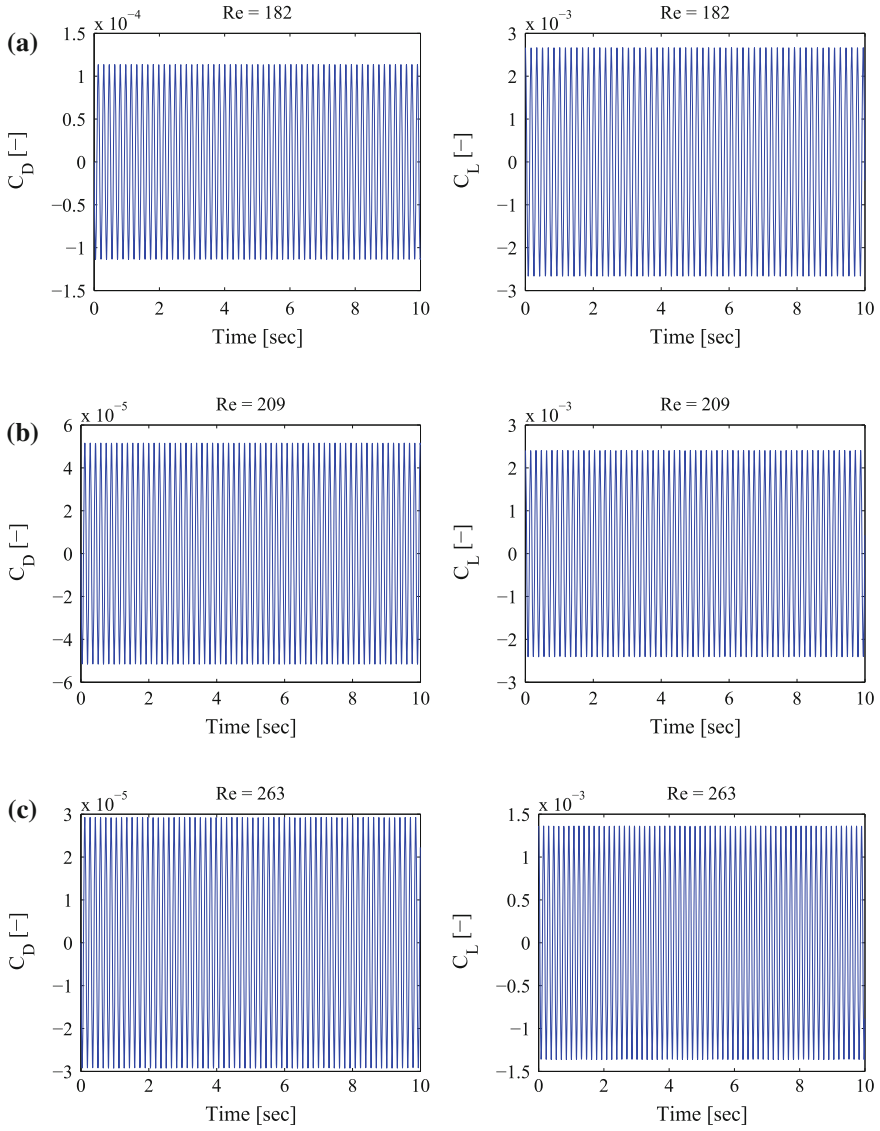
Fig. 7 Actual values varying over time of the C_D and C_L in the three branches of the lock-in region: **a** initial @ $Re = 182$, **b** upper at $Re = 209$ and **c** lower at $Re = 263$
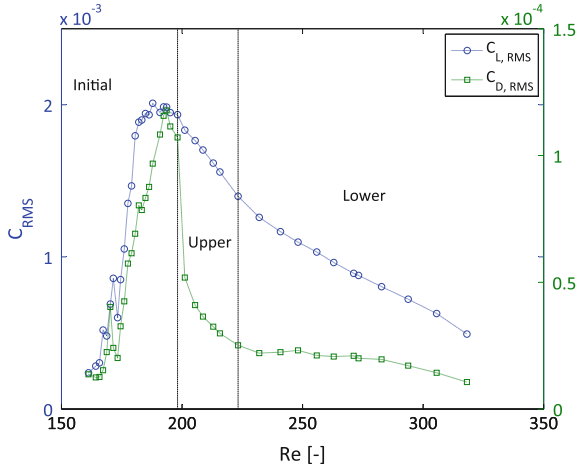
Fig. 8 Lift (○ *blue line*) and drag (□ *green line*) coefficients in the lock-in region in RMS values
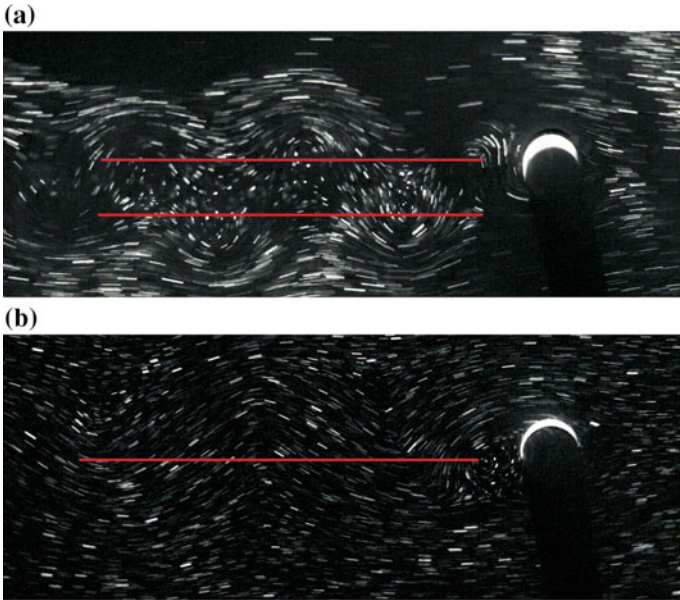
Fig. 9 Actual photos showing the flow behavior developed behind the flexible circular cylinder at $H/L = 0.80$. **a** Two vortex *center lines* @ $Re = 173$ in the initial branch, and **b** One vortex *center line* @ $Re = 223$ in the *lower* branch

turbulent case. Therefore, wider vortex wakes (two vortex center line) suggest higher values of C_D than narrower vortex wakes (one vortex center line). This behavior agrees with Figs. 8 and 10.

(a)

(b)

(c)
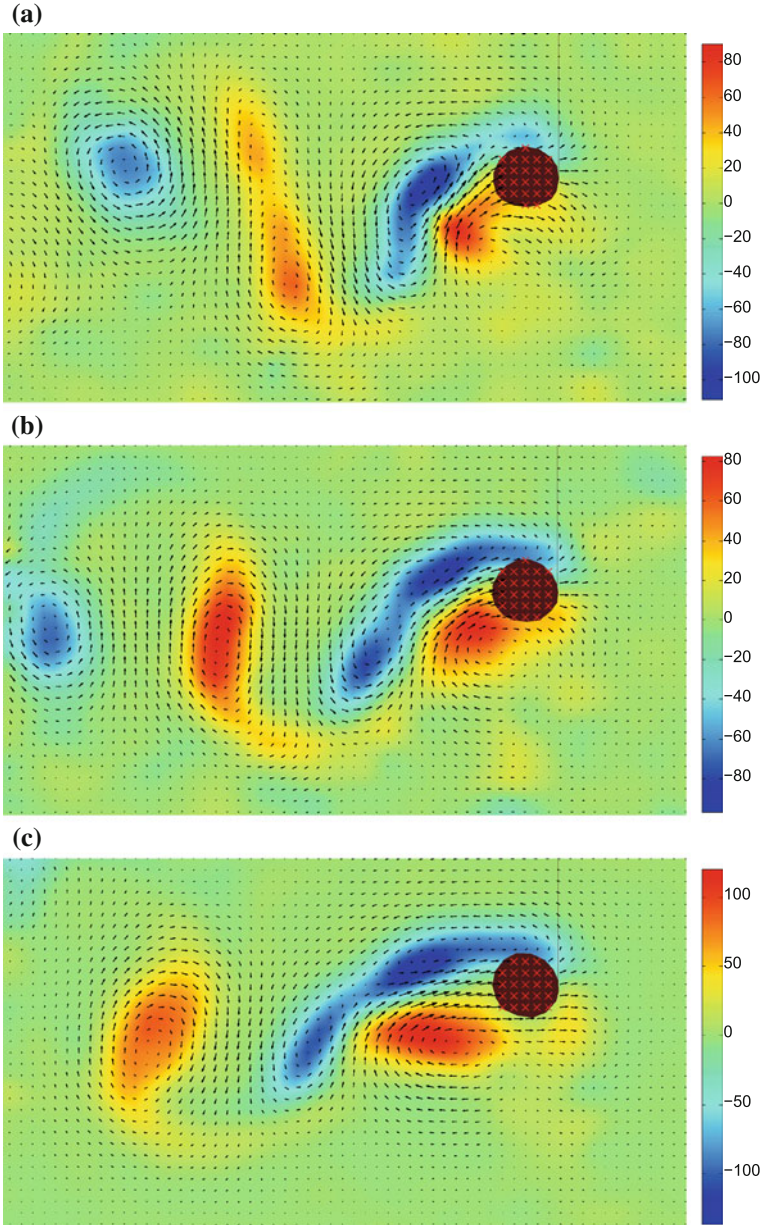
Fig. 10 Vortex shedding mode at $H/L = 0.80$ **a** $Re = 182$, **b** $Re = 209$ and **c** $Re = 263$. 2S vortex shedding mode for the three branches: **a** initial, **b** upper and **c** lower. The three images show the hydrodynamic response when the cylinder reaches its maximum amplitude in the transverse direction. Here the colormap represents the vorticity [1/s] and the arrows represent the flow velocity field obtained with the PIV technique

5 Conclusions

Results have been presented for a flexible circular cylinder in VIV with low mass-damping ratio ($m^*_{cil}\zeta = 0.126$) in the entire synchronization region. The fluid forces on the cylinder can be measured from the cylinder vibrational response and a spring-mass-damper model. The lift and drag coefficients show three distinguishable behavior which were delimited by the initial, upper and lower branch. This results are qualitatively similar to those found by Govardhan and Williamson (2000). The vibrational response of the cylinder in cross-flow direction is one order of magnitude greater than in the in-line direction. The rapid increase in the lift and drag coefficients is associated with a vortex wake transition from a configuration with one vortex center-line to a configuration with two vortex center-line. The oscillatory behavior of the lift and coefficients in the initial branch is associated with the added mass oscillations. In the lower branch the lift and drag coefficients show only a Reynolds number dependence. The vortex wake behavior in the entire lock-in region is basically the 2 S mode defined by Williamson and Roshko (1998).

References

Blevins RD (1997) Flow-induced vibration, vol 1. New York, Van Nostrand Reinhold Company, p 337

Feng CC (1968) The Measurements of Vortex-induced effects in flow past a stationary and oscillating circular and D-section Cylinders (M.S. thesis). University of British Columbia, Vancouver, BC, Canada

Govardhan R, Williamson CHK (2000) Modes of vortex formation and frequency response of a freely vibrating cylinder. J Fluid Mech 420:85–130

Khalak A, Williamson CHK (1996) Dynamics of a hydroelastic cylinder with very low mass and damping. J Fluids Struct 10:455–472

Khalak A, Williamson CHK (1997a) Fluid forces and dynamics of a hydroelastic structure with very low mass and damping. J Fluids Struct 11:973–982

Khalak A, Williamson CHK (1997b) Investigation of relative effects of mass and damping in vortex-induced vibration of a circular cylinder. J Wind Eng Ind Aerodyn 69:341–350

Khalak A, Williamson CHK (1999) Motions, forces and mode transitions in vortex-induced vibrations at low mass-damping. J Fluids Struct 13:813–851

Kheirkhah S, Yarusevych S, Narasimhan S (2012) Orbiting response in vortex-induced vibrations of a two-degree-of-freedom pivoted circular cylinder. J Fluids Struct 28:343–358

Lighthill J (1986) Fundamentals concerning wave loading on offshore structures. J Fluid Mech 173:667–681

Navrose M, Mittal S (2013) Free vibrations of a cylinder: 3-D computations at Re= 1000. J Fluids Struct 41:109–118

Oviedo-Tolentino F et al (2014) Vortex-induced vibration of a bottom fixed flexible circular beam. Ocean Eng 88:463–471

Prasanth TK, Mittal S (2008) Vortex-induced vibrations of a circular cylinder at low Reynolds numbers. J Fluid Mech 594:463–491

Sarpkaya T (1978) Fluid forces on oscillating cylinders. NASA STI/Recon Tech Rep 78:46523

Sumer BM, Fredsø J (1997) Hydrodynamics around cylindrical structures. Singapore: World Scientific

Vikestad K, Vandiver JK et al (2000) Added mass and oscillation frequency for a circular cylinder subjected to vortex-induced vibrations and external disturbance. J Fluids Struct 14:1071–1088

Willden RHJ, Graham JMR (2001) Numerical prediction of VIV on long flexible circular cylinders. J Fluids Struct 15:659–669

Williamson CHK, Roshko A (1988) Vortex formation in the wake of an oscillating cylinder. J Fluids Struct 2:355–381

Vortical Structures Generated Behind Flapping Foils with Different Aspect Ratios

B. Franco Llamas, E. Sandoval Hernández and A. Cros

Abstract Different vortical patterns are observed behind flapping foils in a uniform water flow. Previous studies have described these structures and delimited the parameter intervals for which each pattern develops. Generally, the two pertinent nondimensional numbers are the Strouhal number St_D, proportional to the foil oscillation frequency, and A_D, related to the foil oscillation amplitude. In this experimental study, we show that the value of the foil aspect ratio radically changes the transition diagram. More particularly, for the St_D and A_D values for which the reversed von Kármán street develops when the foil is "long", another pattern is generated when the foil is shorter.

1 Introduction

The reversed von Kármán street can be generated behind a flapping foil when both the flapping frequency f and amplitude A are high enough. Godoy-Diana et al. (2008) drew in the plane (St_D, A_D) the different patterns generated behind a foil of chord $L = 23$ mm and diameter $D = 5$ mm. $St_D = fD/v$ is the Strouhal number, where v is the flow velocity, and $A_D = 2A/D$ is the nondimensional peak-to-peak amplitude. Typically, for a fixed amplitude, the generated pattern evolves as follows. For low values of St_D, the "usual" von Kármán street (noted here as "vK") develops. When St_D is increased, the vortices align and the pattern is noted as "2S". Now, if the

B. Franco Llamas · A. Cros (✉)
Physics Department CUCEI, Universidad de Guadalajara, Av. Revolución 1500. Col. Olímpica. C.P., 44430 Guadalajara, Jalisco, Mexico
e-mail: anne@astro.iam.udg.mx

E. Sandoval Hernández
Natural and Exact Sciences Department CU-Valles, Universidad de Guadalajara, Carretera Guadalajara—Ameca km. 45.5. C.P., 46600 Ameca, Jalisco, Mexico

flapping amplitude is high enough, the reversed von Kármán street ("rvK") appears and the two counter-rotating vortices generate a jet behind the foil. This jet permits the fishes to propel themselves.

In Schnipper et al. (2009), performed the same kind of experiments in a flowing soap film. They used two different flapping foils with the same aspect ratio $L/D = 6$ (where $D = 1$ and 2 mm). Their transition diagram exhibits a great variety of structures as for example "2P", denoting the generation of 2 vortex pairs by flapping cycle. For lower values of the Strouhal number, the structures are more complex as up to 8P can appear.

In these two previous studies, the foil aspect ratio L/D is greater than 4 and the two transition diagrams qualitatively agree as the vK pattern is observed for low values of A_D and St_D while the rvK pattern develop for higher values of these two parameters.

The objective of the present work is to investigate if, when the vortices are generated behind a flapping foil with a low aspect ratio $L/D = 2$, the same patterns are observed in the same region of the diagram (St_D, A_D). We chose to work with a fixed, high enough amplitude $A_D = 2.5 \pm 0.1$, for which the rvK pattern is observed in the two previous works when $St_D > 0.1$.

This paper is organized as follows. In Sect. 2, we present our experimental device. In Sect. 3, we show our results, which are analyzed and discussed in Sect. 4. Conclusion is written in Sect. 5.

2 Experimental Device

The foils are submitted to an oscillation thanks to a slider-crank-like mechanism. The same device was described by Espinosa Ramírez and Cros (2014) and will be briefly described again here. The first pulley, noted (1) in Fig. 1, is connected to a motor and is performing complete rotations with a frequency that is fixed by a direct current motor. A connecting rod connects the pulley (1) to a second pulley (2) so that it oscillates between to limit angles $-\theta_0$ and θ_0. The foil axis corresponds to the pulley (2) axis. The complete experimental scheme is shown in Fig. 1.

In the water channel, a centrifugal pump, a honeycomb system and a convergent permit to generate a laminar, uniform flow in the test section as we checked by PIV (Particle Image Velocimetry). In this study, the flow is fixed to $v = 5.1$ cm/s so that the Reynolds number calculated with the foil diameter is $Re = 255$. This value allowed us to compare our results with those of Godoy-Diana et al. (2008).

Our experiments were performed with two steel foils of different aspect ratios described in Table 1. The foils span is constant and equal to 8 cm. We fixed the nondimensional amplitude to $A_D = 2.5 \pm 0.1$ by varying the radius of pulley (2) and the connecting rod length. Table 1 indicates also the value $2\theta_0$ of the foil angle as shown in Fig. 1. The ratio between the flapping amplitude and the channel width is 13 %.

Fig. 1 Experimental set-up. A laminar, uniform flow with velocity v, is generated in a water channel. The flapping foil is submitted to oscillations thanks to a slider-crank-like mechanism. The foil has a diameter D, peak-to-peak amplitude $2A$ and length L
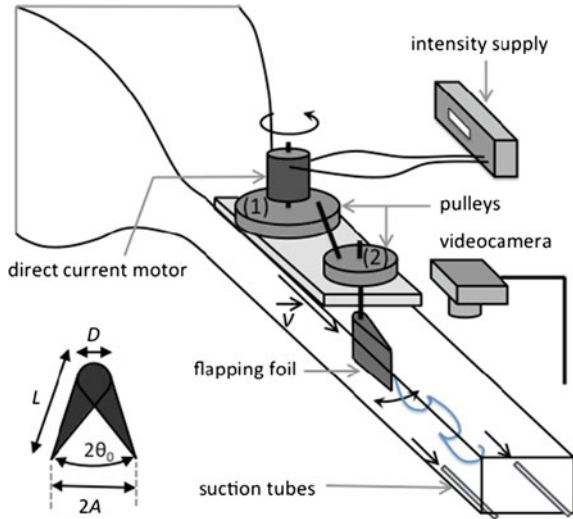
Table 1 Characteristics of the foils

D (mm)	L (mm)	$2\theta_0$ (°)	$2A$ (mm)	L/D
5	25	33	13	5
5	10	106	12	2

L is the chord, D the diameter, $2\theta_0$ the foil angle amplitude and $2A$ the oscillation amplitude in mm. L/D is the foil aspect ratio

The methodology is described as follows. The long foil ($L = 2.5$ cm) is fixed to the oscillation device and immersed inside the laminar flow. The flow velocity and the oscillation amplitude are fixed. The foil oscillation frequency is varied via the direct current motor from $f = 0.40$ to 2.20 Hz so that the Strouhal number $St_D = [0.04; 0.22]$. Fluorescein is injected via a thin needle a few millimeters upstream the foil leading edge. For each frequency a video is recorded and the pattern generated at the foil tip is identified. The same steps are repeated for the short foil.

3 Results

We first checked that we found the same results as in the two previous studies for the long foil with aspect ratio $L/D = 5$. Figure 1 shows the typical patterns generated for different Strouhal numbers: $St_D = 0.088; 0.098; 0.10$ and 0.12. The sequence of pictures shows how the typical von Kármán vortices (Fig. 2a) which develops for low frequency values, slowly evolves towards an aligned configuration (Fig. 2b) when the frequency is increased and then to the reversed von Kármán street (Fig. 2c) which gets turbulent and antisymmetric for higher frequency values
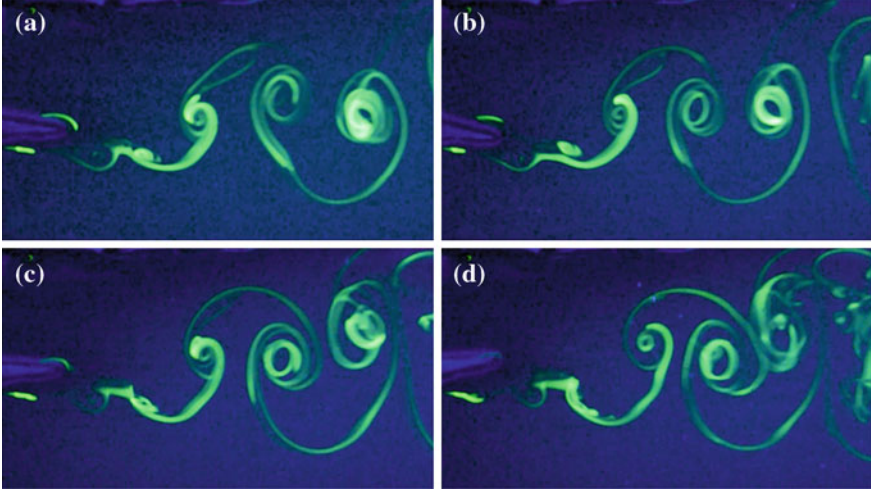
Fig. 2 Different patterns generated by the "long" flapping foil with aspect ratio $L/D = 5$. **a** Usual von Kármán street (vK), $f = 0.90$ Hz, $St_D = 0.088$. **b** Aligned vortices (2S), $f = 1.00$ Hz, $St_D = 0.098$. **c** Reversed von Kármán street (rvK), $f = 1.08$ Hz, $St_D = 0.10$. **d** Reversed anti-symmetric von Kármán street (rvKa), $f = 1.20$ Hz, $St_D = 0.12$

(rvKa pattern, Fig. 2d). This evolution is in qualitative agreement with the transition diagram of Godoy-Diana et al. (2008), who found that the rvKa pattern develops for $St_D > 0.20$ when $A_D = 2.0$. Schnipper et al. (2009) found that the threshold between vK and rvK patterns is $St_D = 0.11$. They also observed the 2P pattern in the interval $0.06 < St_D < 0.09$.

The patterns identified for the short foil ($L/D = 2$) are shown in Fig. 3. In this case, the maximum angle $2\theta_0$ of the foil is greater than the long foil angle (see Table 1), so that the vortical structures are ejected from the tip of the foil in a larger spanwise direction. Figure 3a shows the pattern which develops for the lowest frequency values ($St_D < 0.15$). For a better identification, a scheme of the generated structure was drawn in Fig. 3c, and corresponds to 2 pairs of counter-rotative vortices ejected by flapping cycle. They are similar to the 2P pattern of Schnipper et al. (2009), whereas in our case the vortices which are further from the center line are smaller.

Figure 3a shows a photo of the pattern that appears for higher frequency values for the short foil. Figure 3d shows more clearly that only three vortices per cycle are formed: a counter-rotating pair downwards and a single vortex upwards. This corresponds the P + S pattern, defined by Williamson and Roshko (1988). This structure appears in our experiment when $St_D > 0.15$.
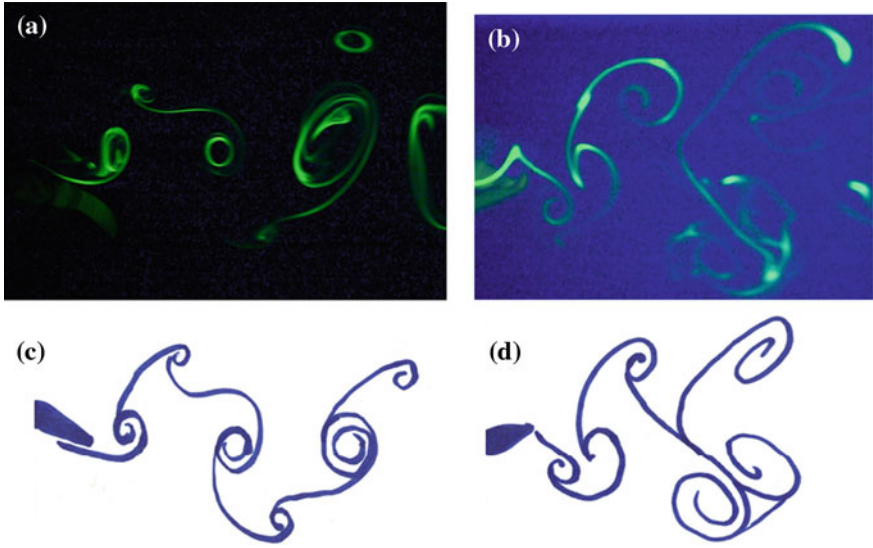
Fig. 3 Different patterns generated by the "short" flapping foil with aspect ratio $L/D = 2$. **a** 2P pattern, $f = 0.76$ Hz, $St_D = 0.075$. **b** P + S pattern, $f = 1.62$ Hz, $St_D = 0.160$. **c, d** Scheme of the dye lines of the top photos

4   Analysis and Discussion

All the observations reported for the two foils in the previous section are summarized in the transition diagram of Fig. 4. It shows that, whereas the nondimensional amplitude A_D is the same for our two experiments, the generated structures are different for the short and the long foils when their flapping frequency is varied.

Even though our results for the long foil can be compared to previous similar studies, our observations for short foils are new. The 2P and P + S patterns were identified by Williamson and Roshko (1988). These authors studied the structures
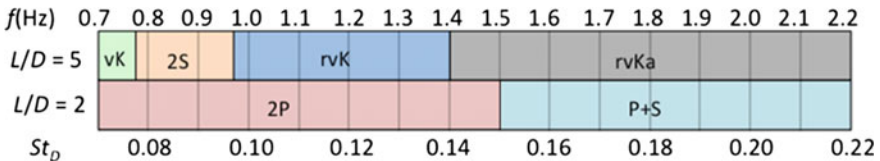
Fig. 4 Transition diagram for our two foils. The *top* axis represents the foil frequency f (Hz) while the *bottom* axis is the Strouhal number St_D. The top row shows the patterns generated downstream the long foil whereas the second row is for the short foil. The notations are as following: "vK" is the usual von Kármán street (Fig. 2a, "2S" stands for the aligned pattern (Fig. 2b, "rvK" is the reversed von Kármán street (Fig. 2c, "rvKa" represents the reversed and antisymmetric von Kármán street (Fig. 2d, "2P" are for 2 pairs by flapping cycle (Fig. 3a, c, "P + S" is shown in Fig. 3b, d

generated behind a cylinder of diameter D that oscillates transversally to the flow with amplitude A and frequency f. The 2P structure develops when their parameters values are $0.2 < A_D < 3.6$ and $0.125 < St_D < 0.25$. Besides, the region of existence of the P + S pattern belongs approximately to the region $1.6 < A_D < 4$ and $0.17 < St_D < 0.5$. In this last work, like in our study and the one of Schnipper et al. (2009), a general feature indicates that the lower the Strouhal number, the more numerous the vortices.

Finally, our observations showed that three nondimensional parameters determine which vortical structure is generated behind a flapping foil. In addition to the already used nondimensional numbers A_D and St_D, the current work shows that a third parameter has to be taken into account which is the foil aspect ratio L/D, where L is the foil span and D the diameter of the foil semi-circular leading edge.

5 Conclusion

In this experimental work, we identified the vortical structures that develop downstream a flapping foil in a uniform water flow. We used two foils with different aspect ratios, $L/D = 5$ and 2, where L is the foil chord and D the diameter of its semi-circular leading edge. The flapping frequency f was varied while the peak-to-peak amplitude $2A$ was constant for the two foils in such a way that $A_D = 2A/D = 2.5 \pm 0.1$. Hence, the shorter foil flaps with a greater angle than the long foil. The structures that form downstream the long flapping foil are the same as in the study performed by Godoy-Diana et al. (2008) and Schnipper et al. (2009) for the same amplitude. In these two works, the regions of existence of different patterns were delimited in the (A_D, St_D) space, where $St_D = fD/v$ is the Strouhal number, v the flow velocity. However, our shorter foil exhibits patterns that are different from the long foil in the same region of the (A_D, St_D) space. This means that the foil aspect ratio L/D is a third pertinent nondimensional parameter that delimits regions of existence of the patterns which develop behind flapping foils.

References

Espinosa Ramírez AC, Cros A (2014) Wake patterns behind a flapping foil. In: Klapp J, Medina A (eds) Experimental and computational fluid mechanics. Springer, p 473

Godoy-Diana R, Aider JL, Wesfreid JE (2008) Transitions in the wake of a flapping foil. Phys Rev E 77(1):016308

Schnipper T, Andersen A, Bohr T (2009) Vortex wakes of a flapping foil. J Fluid Mech 633:411–423

Williamson CHK, Roshko A (1988) Vortex formation in the wake of an oscillating cylinder. J Fluids Struct 2(4):355–381

Circulation Control: A Comparative Study of Experimental and Numerical Investigation

H. Carmona, A. Cházaro, A. Traslosheros, A. Iturbe and J. Hernández

Abstract Circulation Control is an aerodynamic method in which the Coanda effect is induced in specific sections of the airfoil, typically near the trailing edge on the suction side in such a way that, the aerodynamic properties of an airfoil are improved. Although the Coanda effect was discovered in the 1930s, research on Circulation Control can be tracked to the 1960s. The bases for Circulation Control technology are mainly empirical given by: the experiments performed in those days, the use of aerodynamic tools and the use of numerical methods. Since its discovery, this technology has not been used widely but nowadays it is thought that it is mature enough to be applied to the next generation aircrafts. As an example, the goal of some NASA Subsonic Fixed Wing projects such as the Cruise Efficient Short Take Off and Landing program (Couluris et al. 2010), is to apply this technology to design aircrafts that can take-off in much smaller distances than the typical airport runway. The key for the development of this technology is the understanding, simulation and control of the flowfield around the airfoil; for this purpose physical experiments are required for validation of numerical methods and such methods will be used then for design purposes. On the other hand, various numerical methods lead to different ranges of uncertainty in the flowfield simulation. This article presents a review of the state of the art on circulation control research, a comparative study of articles from the 1960s to 2014 of different physical experiments, numerical methods, simulations

H. Carmona (✉) · A. Cházaro · A. Traslosheros · A. Iturbe · J. Hernández
UNAQ, Colón, Mexico
e-mail: hugolfons@hotmail.com

A. Cházaro
e-mail: adriana.chazaro@unaq.edu.mx

A. Traslosheros
e-mail: altrami@hotmail.com

A. Iturbe
e-mail: aris.iturbe@unaq.edu.mx

J. Hernández
e-mail: jorge.hernandez@unaq.edu.mx

57

of the Coanda effect and Circulation Control and its results. Finally, the conclusion of the work is a complete vision of the usage of the analyzed techniques in future applications.

1 Introduction

Circulation Control (CC): Is an aerodynamic technology in which a high momentum jet inside an airfoil is tangentially impinged into a curved surface near the trailing edge (TE) in such manner that the jet remains attached to the curve and entrains air over the airfoil. Geometry: Typically, Circulation Control wings consist of an airfoil with an inner chamber that discharges the flow into a curved (Coanda) surface. This curved surface substitutes the typical sharp trailing edge, resulting in a curved surface that connects the top rear end to the bottom rear end of the airfoil. The slot is located in such way that the flow from the inner chamber is discharged tangentially over the Coanda surface. The exit slot is relatively narrow, common values range from 0.1 to 0.5 % of the airfoil chord length (Jones and Englar 2003). As an example for the prototypes tested in (Abramson 1977), the slots ratios are 0.0015, 0.0022 and 0.003; Fig. 1 shows a cross section of one of these prototypes. Some CC wings include a flap-like mechanism in which a sharp trailing edge rotates and a curved surface connects the exit slot to the TE; this is carried out to recover the typical aerodynamic shape when no pressurized air is used.

Aerodynamic effect: Pressurized air inside the chamber is discharged through the slot to the curved surface. In this process and as a result of the expansion and the high momentum the air increases its velocity and travels then downstream to the trailing edge attached to the curved surface. The attachment results from the static air pressure balance: the high momentum jet has lower static pressure than the
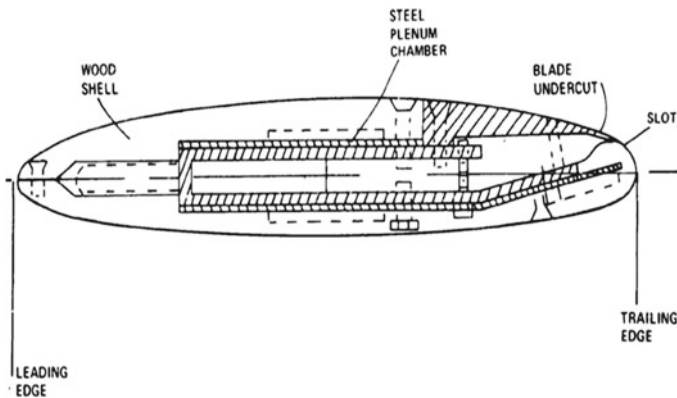
Fig. 1 CC airfoil used in Abramson Experiments (Abramson 1977)

atmospheric air resulting in the surrounding air pushing the jet against the curved wall. While the expanding air travels over the curved surface, the high momentum jet entrains air from the surroundings; thus, the air above the airfoil is energized and moved in the direction of the jet. Since the air over the rear portion of the airfoil is energized by the jet entrainment, the boundary layer will remain attached until the balance of jet and ambient static pressure separate the jet. Note that the point of jet separation will be a function of the jet momentum; this characteristic implies that the stagnation point can be moved over the curve and thus the effect is similar to changing the airfoil camber. If further blowing is employed, the streamlines over the airfoil not only will remain attached to the surface but they will also be deflected downwards; this effect is known as super-circulation region while the use of blowing to avoid BL separation is known as separation control (Jones and Englar 2003; Wang and Sun 2000; Allan et al. 2011; Economon and Milholen II 2008; Sellers et al. 2002; Anders et al. 2004; WernerspsSpatz et al. 2012; Jones 2005; Pepper et al. 1996; Dam et al. 2000).

Figure 2 from (Jones and Englar 2003) shows the separation control and super-circulation regions of GACC airfoil. Figure 3 shows CFD simulations where the separation point is moved around the Coanda surface as a result of jet momentum variation. It is clearly seen that plot d) of this figure corresponds to the super-circulation region as the streamlines are deflected downwards and the momentum coefficient of 0.06 is located in this region of Fig. 2.

As a result of the flow entrainment by the jet and the jet itself, very low static pressure is achieved at the rear portion of the airfoil as shown in the Pressure coefficient plot in Fig. 4 also from (Jones and Englar 2003). In this plot it is seen that the rear peak of low static pressure will lead to heavy nose-down moment coefficients. The effect is not only produced by a steady blown jet, but also by pulses of air that lead to high lift coefficients as well, but with reduced amounts of pressurized air.

Improvements and drawbacks in performance: Due to the high jet velocity and the low static pressure, especially near the trailing edge, very high lift coefficients are obtained with this technique. Lift coefficients as high as 8 have been reported in the experiments made by (Jones and Englar 2003). The lift produced by the airfoil

Fig. 2 Regions of Circulation Control from (Jones and Englar 2003)
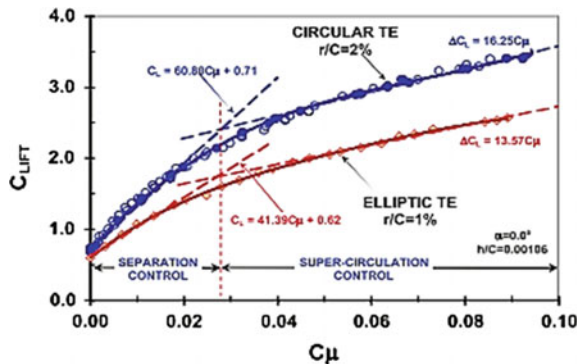
Fig. 3 CFD simulation for various jet momentum coefficients around a Coanda Surface (Jones and Englar 2003)
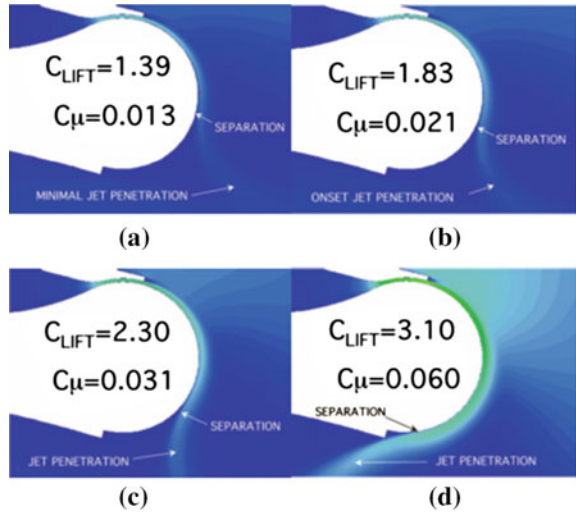
Fig. 4 Pressure distribution of GACC at a lift coefficient of 1.2 airfoil from (Jones and Englar 2003)
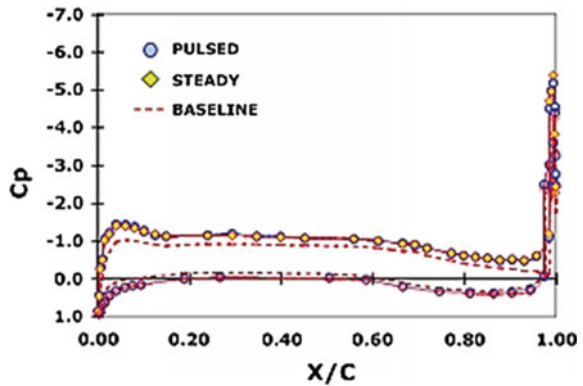
is related to the jet momentum and it is possible to regulate it with the use of valves. However the technology has some drawbacks; the lift increase comes with the cost of pressurized air, which is not easy to obtain in an aircraft. The engines are the natural candidates to provide pressurized air, another source would require a dedicated system. In the other hand, any mass flow obtained from the engine will reduce the available thrust. And even though the Coanda jets will provide thrust to the aircraft, it will not compensate the engine-taken thrust due to losses in the pressure distribution system. A dedicated system would add weight to the aircraft and the structure should be designed to support the thermal loads imposed by hot compressed air. Also, as implied by pressure distribution in Fig. 4, heavy nose-down moments must be taken into account in the aircraft stability and probably it will be required additional or larger stabilizing surfaces with its associated weight increase.

1.1 Benefits of the Technology

Take-off: Since the lift coefficient is directly related to aircraft performance, it is easy to see why this technology has been studied for over 65 years and pursued especially to use it in Air Force applications. Take-off, climb and landing performance require airfoils with maximum lift coefficients as high as possible. For instance, the stall speed, which defines the Take-Off and Landing distance, is a function of the Lift Coefficient as shown in Eq. 1.

$$V_{STALL} = \sqrt{\frac{2W_1}{\rho_\infty S C_{LMAX}}} \tag{1}$$

Any increase in the max-lift coefficient (C_{LMAX}) for a constant stall speed (V_{STALL}) could reduce the wing surface requirement (S) or increase the weight (payload) (W_1), for a given free stream air density ρ_∞. What is even more interesting is the stall speed reduction, which would be translated into drastically reduced Take-Off distances. An analysis by (Englar 2005) shows that, if CC technology was employed in a Boeing 737 airplane its take-off distance would be reduced to about 1/3 of conventional aircraft. Figure 5 extracted from (Anders et al. 2004) shows a relationship between lift coefficient and landing distance and the possibilities with Circulation Control technology.

Few mechanical components: Benefits of the technology not only involve performance benefits, but also reduced complexity of the high-lift devices. Typical high lift mechanical systems such as flaps or slats are composed by several parts that imply considerable weight, complexity and with them there are associated design, manufacturing and especially maintenance costs. Circulation control pneumatic technol-

Fig. 5 Effect of aerodynamic lift on landing distance (Anders et al. 2004)
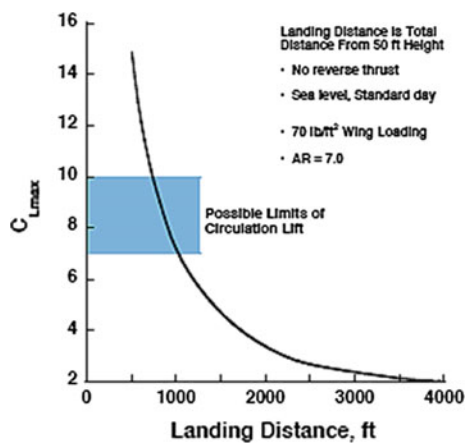
Fig. 6 GACC-Dual Radius from (Lee-Rausch et al. 2006)
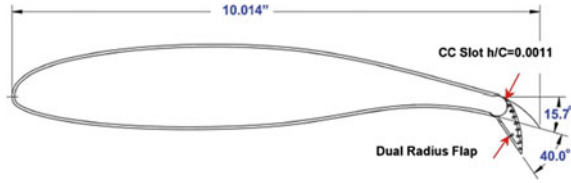
ogy instead, requires few components; in the same analysis (Englar 2005) suggests that the 15 lift devices of the Boeing 737 could be replaced by 3 circulation control devices.

Aircraft Optimization: The fact that the lift coefficient of a circulation control wing can be controlled by regulating the pressurized air flow allows a performance optimization of the wing according to the phase of the aircraft mission. In other words, the wing can be configured for take-off or cruise flight to change the max-lift coefficient and the C_L/C_d ratio. Although the rounded trailing edge of a typical circulation control wing is very thick for cruise flight; blowing small amounts of air improves the characteristics of the airfoil (reduction of C_d) when very low drag coefficient is required. Even a flap-like mechanism can reconfigure the airfoil to cruise flight as shown in the dual radius circulation concept airfoil from (Lee-Rausch et al. 2006) shown in Fig. 6.

Parameters involved in CC: For a circulation control wing the usual airfoil parameters describe the performance; this is the lift, drag and moment coefficients. The performance description also requires the momentum coefficient C_μ shown in (2), which is the employed jet momentum expressed in a non-dimensional form:

$$C_\mu = \frac{\dot{m} V_{JET}}{q_\infty S} \tag{2}$$

where $\dot{m}$ represents the mass flow of compressed air, V_{JET} represents the jet velocity, q_∞ represents the reference dynamic pressure and S the wing surface. The jet mass flow and the jet velocity are calculated with the following expressions:

$$\dot{m} = \rho_{JET} V_{JET} hw \tag{3}$$

$$V_{JET} = \left[\frac{2\gamma RT}{\gamma - 1} \left(1 - \left(\frac{\rho_\infty}{\rho_{0-PLNM}} \right)^{\frac{\gamma-1}{\gamma}} \right) \right]^{0.5} \tag{4}$$

where h and w are the height and the width of the exit slot, γ is the ratio of specific heats of the fluid (air), R is the gas constant of the air, P is the air pressure and ρ the air density. Sub-indexes ∞ stand for free stream conditions, 0 stands for total pressure, *JET* for the conditions in the jet and *PLNM* for the air conditions inside the plenum.

   Two important comments must be made about the main airfoil performance parameters. First: Lift, drag and moment coefficients are not only a function of the Reynolds number as in typical configurations but the C_μ has also an important effect on these numbers as shown in Fig. 7.

   Second, there are other derived parameters that give important information about the performance of the circulation control airfoils. The ratio of lift coefficient increment (extra lift compared with the unblown case) with the C_μ is defined in (Englar 2005) as the augmentation ratio and expresses the efficiency of the jet when generating lift. For the elliptical circulation control airfoil from (Englar et al. 2009) it is shown in Fig. 8 that the most efficient region is for C_μ of 0.1 approximately. Another derived parameter is the lift to drag coefficient ratio which is related to the aircraft range and endurance performance. In (Englar 2005) values reported for CC airfoils are even higher than the NACA 0012.

Fig. 7 Lift to Momentum coefficient from (Englar et al. 2009)
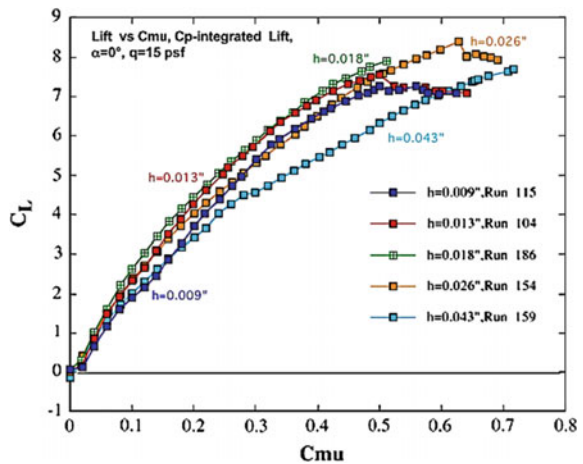
Fig. 8 Augmentation ratio for an elliptical Circulation Control from (Englar et al. 2009)
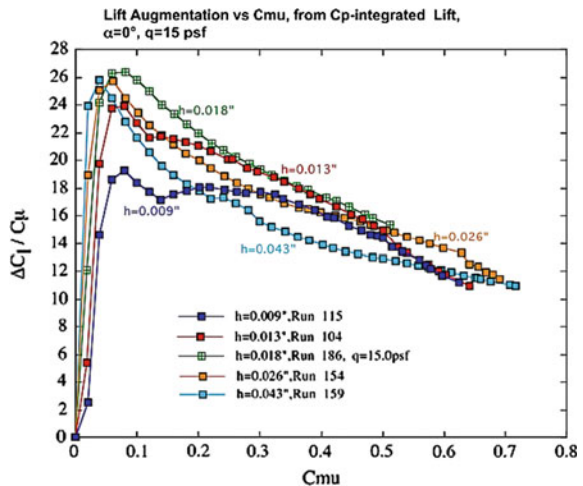
1.2   Why Circulation Control Technology Is Not Widely Used

Required energy: In the context of fixed wing aircrafts, the high lift requirement is needed mainly for the take-off and landing phases of the flight mission. At these phases the aircraft is flying at the lowest possible speed and is where the power requirement is greater. In order to fly at the lowest possible velocity the angle of attack of the aircraft wing must be as high as allowed by the stall-angle. Aircraft position induces a huge amount of drag (due to the high lift component directed backwards) which demands most of the engine power. Thus, if any amount of pressurized air is required from the engine, it would need a more powerful power-plant or an air reservoir, which would oversize the aircraft to be used only for this phase of the mission. With the already built large runways this is not a payoff improvement.

Moment coefficients: Related with the redesign of the general arrangement of existing aircrafts, the use of circulation control devices results in heavy nose-down moments as it was seen in previous section. This fact would require the modification of the stabilizing aerodynamic surfaces.

Accurate predictions: Circulation control technology involves complex aerodynamic phenomena that are still difficult to simulate and strong 3D effects complicate the task of experimental data reduction. Numerical simulations required for design are still very costly; Direct Numerical Simulations (DNS) and Large Eddy Simulations (LES) need considerable amounts of time (months). Reynolds Averaged Navier-Stokes (RANS) simulations are much faster but require careful selection of turbulence models and the results are not always acceptable. A conclusion of the 2004 NASA/ONR Circulation Control Workshop was that the lift of a CC airfoil is always over predicted by CFD codes at high rates of blowing but it was not clear why; it was attributed to grid detail, turbulence modeling and 3D effects that become dominant in the Wind Tunnel at high rates of *lift/blowing* (Jones 2005). Research by (Swanson et al. 2005) showed that Turbulence modeling plays an important role in the CC simulations and states that this is the major component in the success of numerical methods for CC. Table 1 from this reference a more recent investigation also from Swanson et all shows a comparison of lift coefficient prediction (RANS) vs. experimental data where 3 different turbulence models were used: Spalart-Allmaras (SA) which is a one-equation model for the kinematic eddy viscosity, Spalart-Allmaras with Rotation-Curvature (SARC) which is modification of the SA model that includes modifications for curvature effects, and the Shear Stress Transport model (SST) of Menter which is a two equations model for the turbulence kinetic energy and the specific dissipation rate (Swanson and Rumsey 2009). For low blowing rates it can be seen that the three turbulence model results are in agreement with the experimental data, which is not the case for high blowing rates.

Further numerical investigations seem to be in line with Swanson: 3D CFD RANS models simulating the Wind Tunnel walls indicate that the 3D effects do not explain the CFD over prediction of lift coefficient (Allan et al. 2011).
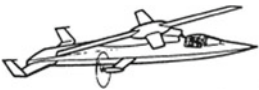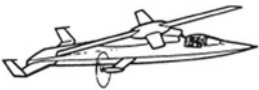
Recent interest on CC: Sect. 2 of this article shows some achievements in Circulation Control and it is seen that recent projects starting last decade and beyond rely on

Table 1 Comparison of numerical and experimental results (Swanson and Rumsey 2009)

Model	c_μ	Grid 5	$(c_L)_{exp}$	c_L	c_D
SA	0.030	Coarse	1.500	1.797	0.02735
	0.030	Medium		1.845	0.02516
	0.030	Fine		1.853	0.02450
SA	0.100	Coarse	3.575	4.109	0.05501
	0.100	Medium		4.421	0.05066
	0.100	Fine		4.480	0.04864
SARC	0.030	Coarse	1.500	1.627	0.02619
	0.030	Medium		1.671	0.02435
	0.030	Fine		1.707	0.02356
SARC	0.100	Coarse	3.575	3.512	0.04921
	0.100	Medium		3.769	0.04583
	0.100	Fine		3.826	0.04449
SARC	0.226	Coarse	5.452	5.833	0.10930
	0.226	Medium		6.359	0.11290
	0.226	Fine		6.546	0.11550
SST	0.030	Coarse	1.500	1.681	0.02572
	0.030	Medium		1.786	0.02458
	0.030	Fine		1.806	0.02469
SST	0.100	Coarse	3.575	4.098	0.05205
	0.100	Medium		4.423	0.05086
	0.100	Fine		4.432	0.05070
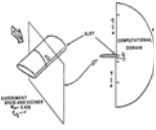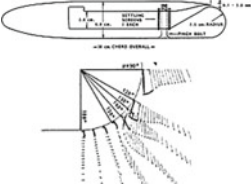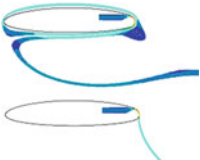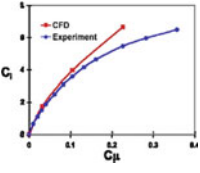
this technology to meet the design requirements. Personal Air Vehicles or Short Take Off and Landing Vehicles have been proposed and can hardly meet design requirements without CC (Moore 2006). In 2008 Hybrid Wing Body (HWB) aircrafts were announced relying on CC for high lift capability (Jones et al. 2008) and in 2012 and 2013 wind tunnel experiments of aircraft models with Circulation Control have been reported (Milholen et al. 2012). Also BAE-systems has built and flown in 2010 the UAV DEMON that uses Circulation Control wings for roll control and thrust vectoring (TRIMBLE 2010; Simon 2015). Finally, an overview by (Djojodihardjo and Thangarajah 2014) shows recent patents, from 2013 related to CC technology. From these examples and the future demand of STOL aircrafts (Coururis et al. 2010; Rodman and Wood 1986; Sun et al. 2008; Gologan et al. 2009) it is clear that CC technology is finding its place within the aerospace industry. To the day of elaboration of this article no reports have been found describing successful CC numerical predictions at high blowing rates and for different CC airfoils, however it is clear that the technology is mature enough for design purposes, at least for some Research Centers and Aircraft companies.

Table 2 Brief history of Circulation Control

Model image	References
	1934: Henri Coanda fills a patent describing a device for deflecting a stream of elastic fluid projected into an elastic fluid (Coanda 1936)
	1965: National Gas Turbine and Establishment (NGTE) in the UK researches on circular section profile with Circulation Control for rotor applications (Englar 2005)
	1968: NASA research with an elliptic Circulation Control airfoil for rotor applications (Englar 2005)
	1974: West Virgina University under contract with the Office of Naval Research (ONR) for design, fabrication and test of a Circulation Control demonstrator plane (Englar 2005)
	1975: Potential flow theory successfully predicts Circulation Control airfoil characteristics (Gibbs and Ness 1976)
	1976: Design Trade-offs for a X-wing VTOL (Englar 1998)
	1976: Design of full scale CC technology demonstrator based on Kaman XH2/CCR helicopter (Englar 1998)
	1977: Detailed wind tunnel investigation of a Circulation Control airfoil by (Abramson 1977) and Rodman (Rodman and Wood 1986)
	1979: Flight testing of the A-6/CC Wing demonstrator (Englar 1998)
	1981: Numerical optimization of Circulation Control Airfoils (Englar 1998)
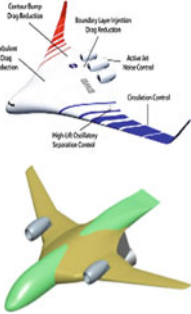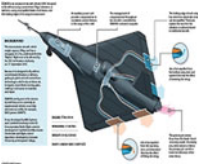
(continued)

Table 2 (continued)

Model image	References
	1986: NASA CC workshop, Navier-Stokes calculations and Turbulence modeling for the trailing edge of CC airfoil (Nielsen 1987)
	1986: Laser Doppler Velocimetry investigation by Lockheed Martin of a CC airfoil gathers Turbulence data for CFD development (Novak and Cornelius 1987)
	1987: X-wing test aircraft ready to fly but program was canceled that year (Linden and Biggers 1987) (Linden et al. 2013)
	1993: NASA and GTRI collaboration for CC research (Englar 1998)
	2002: US Naval Surface Warfare Center (NSWC) successfully simulates Coanda effect on airfoil intended for Submarine improved maneuverability (Slomski and Marino 2002)
	2004: NASA/ONR CC Workshop. It is realized that there are still challenges for the correct numerical simulation of CC airfoils, especially at high blowing rates (high momentum coefficient). At the same time it is also perceived that the CC technology is enough for applied engineering (Joslin 2004)
	2006: Personal Air Vehicle (PAV) sector of the NASA Vehicles Systems Program sets goals for PAVs development, including takeoff distances of less than 300 ft; Circulation Control being part of the key technologies (Moore 2006)

(continued)

Table 2 (continued)

Model image	References
	2008: Proposal of Hybrid Wing Body projects for future transportation that relies on CC (Jones et al. 2008)
	2010: BAE systems presents DEMON UAV that substitutes all moving components with blown actuators, including CC for roll-control and thrust vectoring (TRIMBLE 2010)
	2013–2015: Wind Tunnel Tests reported for HWB concepts (Jim 2015)
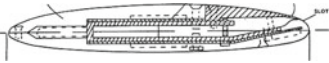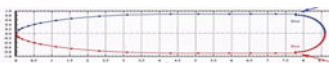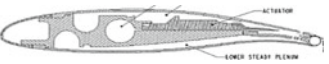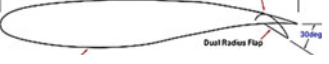
2 Evolution of Circulation Control Technology

Table 2 shows a timeline of Circulation Control, including some of the main achievements or projects related with the Circulation Control technology.

3 Comparison of Circulation Control Investigations

Experimental results: In the previous section it was shown that most of the investigations are based on a few number of Circulation Control airfoils. The airfoils employed are shown in Table 3. Inspection of this table shows that airfoils can be divided in two main groups: Airfoils with high thickness to chord ratios mainly intended for research of Circulation Control and CFD validations (airfoils 1, 2, 3 and 8) and those more slender intended for applications (airfoils 4, 5, 6, 7 and 9).

Table 3 Airfoils investigated in CC research

	Airfoil	References
1		Abramson (1977)
2		Englar et al. (2009)
3		Economon and Milholen II (2008)
4		Cagle and Jones (2002)
5		Lee-Rausch et al. (2006)
6		Lee-Rausch et al. (2006)
7		Alexander et al. (2005)
8		Franke and Harvell (1987)
9		Jones et al. (2008)

A detailed list of experimental investigations is shown in Table 4. including information concerning data availability, airfoil type, boundary conditions, maximum lift coefficient reported in each investigation and whether pulsed jets were used or not. Some research quality aspects such as wind tunnel boundary layer control are included. The results from some of these investigations have been used for CFD codes validations.

For instance, airfoils 1 and 2 have been extensively investigated at various blowing rates and at different facilities. Airfoil 1 from (Abramson 1977) has been tested at the David W. Taylor Naval Ship Research and Development Center (DTNSRDC, US) and at Stanford University (Rodman and Wood 1986); the results were used as benchmark for the 2004 NASA/ONR Circulation Control Workshop. Airfoil 2 has been tested at Georgia Tech Research Institute and at NASA Langley Research Center; the detailed results have been used for RANS and LES numerical investigations.

Maximum lift coefficient values as high as 8.5 listed in Table 4 along with Fig. 4 give an idea of the possibilities of Circulation Control technology over the reduc-

Table 4 Airfoils investigated in CC research

References	Jones and Englar (2003)	WernerspsSpatz et al. (2012)	Simon (2015)	Gologan et al. (2009)	Jones (2005)	Sellers et al. (2002)	Coululris et al. (2010)	Englar (2005)
Year	1977	1982	1986	1986	1988	2002	2003	2003
Airfoil								
Steady	x	x					x	
Pulsed						x	x	
Airfoil coord	x							
Pressure taps	x	x		x		x		x
Aero-balance						x		x
Interferometry		x			x			
Const. details	x					x		
Wall BL control	x							
Flow visual								
Dyn prssr	x		x	x		x		
Cm	x		x				x	x
Slot height	x		x	x				
Internal pressure	x	x	x					
Mass flow	x					x	x	
Max CL	4.8	1.7	4.8	3.5		3.5	8.5	1.7
CL vs Cm	x		x	x		x		
Cd	x		x	x				

(continued)

Table 4 (continued)

References	Jones and Englar (2003)	WernerspsSpatz et al. (2012)	Simon (2015)	Gologan et al. (2009)	Jones (2005)	Sellers et al. (2002)	Couluris et al. (2010)	Englar (2005)
DCL	x		x			x	x	
CL/CD								
Cp dist	x	x	x				x	x
Pulsed jet Freq						35	35	
References	Economon and Milholen II (2008)	Lee-Rausch et al. (2006)	WernerspsSpatz et al. (2012)	Jones and Joslin (2005)	Anders et al. (2004)	Jones et al. (2008)	Englar et al. (2009)	Swanson et al. (2005)
Year	2005	2005	2005	2006	2007	2009	2012	2013
Airfoil								
Steady			x		x	x	x	
Pulsed			x	x	x			
Airfoil coord			**					
Pressure taps	x		x	x	x	x		x
Aero-balance			x	x	x	x		
Interferometry				x			x	x
Const. details			x			x	x	x
Wall BL control			x		x		x	x
Flow visual							x	
Dyn prssr	x					x		
Cm	x		x	x		x		x
Slot height	x		x	x		x		x
Internal pressure	x					x	x	

(continued)

Table 4 (continued)

References	Economon and Milholen II (2008)	Lee-Rausch et al. (2006)	WernerspsSpatz et al. (2012)	Jones and Joslin (2005)	Anders et al. (2004)	Jones et al. (2008)	Englar et al. (2009)	Swanson et al. (2005)
Mass flow	x		x	x	x	x		
Max CL		0.4	3.2	3.7	3.8	8		3.4
CL vs Cm			x			x		
Cd			x			x		
DCL	x		x			x		
CL/CD			x					
Cp dist	x		x	x	x	x	x	x
Pulsed jet Freq			x		160			

Table 5 Numerical investigations of CC airfoils

References	Wang and Sun (2000)	Liu et al. (2001)	Liu et al. (2004)	McGowan and Gopalarathnam (2005)	Swanson et al. (2005)	Lee-Rausch et al. (2006)
Year	2000	2001	2004	2004	2006	2006
Airfoil						
Steady	x	x	x	x		
Pulsed		x	x			
Airfoil coord					***	
Code				6	1	2, 3, 1
2D		x	x			
3D						
Grid details		x	x	x		x
Domain extent [chords]				20	20	30
Points [$\times 10^5$]					0.70	
Cells [$\times 10^5$]				1.3		1.336
Pnts around airfoil					235470	
Pnts around coanda						
Y+					<1	<1
Mach		x	x	x	x	x
Free str. velocity		x	x			
Dynamic pressure		x	x			x
Reynolds		x	x	x	x	x
# Re [$\times 10^6$]		0.39				

(continued)

Table 5 (continued)

References	Wang and Sun (2000)	Liu et al. (2001)	Liu et al. (2004)	McGowan and Gopalarathnam (2005)	Swanson et al. (2005)	Lee-Rausch et al. (2006)
Cm		x		x	x	x
AoA		x		x	x	x
NPR						
Steady		x				x
Unsteady		x				
LES						
RANS				x	x	x
Turb model		a, b	a	b	b, c, d, e	b, d
Max CL	3.2	4	4.2	3.7		4.2
CL vs Cm	x	x	x	x	x	x
Cd					x	
CL/CD					x	
Cp dist.				x	x	x
Pulsed jet frequency		x				

References	Englar et al. (2009)	Swanson and Rumsey (2009)	Nishino et al. (2010)	Rumsey and Nishino (2011)	Allan et al. (2011)	Paschal and Neuhart (2012)
Year	2009	2009	2010	2011	2011	2012
Airfoil						
Steady	x	x		x		x

(continued)

Table 5 (continued)

References	Englar et al. (2009)	Swanson and Rumsey (2009)	Nishino et al. (2010)	Rumsey and Nishino (2011)	Allan et al. (2011)	Paschal and Neuhart (2012)
Pulsed						
Airfoil coord						
Code	4	1	5	2, 1, 5	4	4
2D	x			x	x	
3D			x	x	x	x
Grid details	x	x	x	x	x	
Domain extent [chords]		40	13.6		85	
Points [$\times 10^5$]	5		1160	1750	51420	
Cells [$\times 10^5$]				4.5		
Pnts around airfoil	1242	1185			1241	
Pnts around coanda	401	289	800	1600	401	
Y+	< 1	< 1				
Mach		x		x		
Free str. velocity	x		x	x		
Dynamic pressure	x					
Reynolds	x	x	x	x		
# Re [$\times 10^6$]			0.49	0.48		
Cm		x		x	x	
AoA	x	x			x	
NPR	x	x			x	x

(continued)

Table 5 (continued)

References	Englar et al. (2009)	Swanson and Rumsey (2009)	Nishino et al. (2010)	Rumsey and Nishino (2011)	Allan et al. (2011)	Paschal and Neuhart (2012)
Steady	x				x	x
Unsteady						
LES			x	x		
RANS	x	x		x	x	x
Turb model	d	b, c, d		f	d, b	
Max CL	8	5.45	1.36		2.68	
CL vs Cm	x	x				
Cd	x					
CL/CD	x					
Cp dist.	x			x	x	x
Pulsed jet frequency						

Code:1. CFL3D 2. FUN3D 3. TLNS3D 4. Overflow 5. CDP 6. Fluent

Turbulence Models: a. Baldwin Lomax b. Spallart-Almaraz (SA) c. SA with rotation curvature
d. Menter Shear Stress Transport e. EASM kw -Smagorinsky
g. SSTRC

tion of Take-off and landing distances. In the same manner, the use of pulsed jets has shown that similar lift coefficients can be obtained but with reduced amount of pressurized air.

Table 5 has a list of numerical investigations that result from the physical experiments shown in Table 4. The table indicates the available data as well as the type of the simulation. Most of the simulations are Reynolds-Average Navier Stokes (RANS) although a couple of Large Eddy Simulations are listed. The CFD simulations agree well with the experiments at low blowing rates. However, as the momentum coefficient increases, the correspondence between code and experimental data diverges resulting in lift over predictions.

It is still not clear why lift is over predicted as many details of the flowfield tend to agree including boundary layer separation point over the Coanda surface (Rumsey and Nishino 2011). It was suspected that strong 3D effects within wind tunnels at high blowing rates could lead to wrong 2D average - pressure readings, however 3D CFD models have shown that even with the 3D effects simulated, the lift is still over predicted (Liu et al. 2001). Table 5 also includes the CFD codes, details of the grid and turbulence models used. It must be mentioned that according to (Swanson et al. 2005), turbulence modeling is the major component in success of the numerical method for CC.

4　Conclusions

Circulation Control airfoils use tangential blowing jets that induce high momentum over the upper boundary layer of the trailing edge region of the airfoil, preventing boundary layer separation and leading to very high lift coefficients. Lift Coefficient values as high as 8.5 have been reported, indicating that use of this technology could dramatically reduce the take-off and landing distances of aircrafts equipped with Circulation Control wings. Circulation Control technology has been under development at least since 1965; numerous wind tunnel tests have been performed and have served as technology demonstrations as well as basis for the validation of numerical codes. Prediction of performance characteristics is well understood for low blowing rates but it is still a challenge for high momentum coefficients. This however, has not stopped the integration of this technology in aircraft design as there are already various projects of future transportation concepts that rely on this technology. Circulation Control is a key technology for future aircraft concepts intended for short take-off and landing distances.

References

Abramson J (1977) Two-dimensional subsonic wind tunnel evaluation of two related cambered 15-percent thick circulation control airfoils. Technical Report September 1977. Naval Ship Research and Development Center

Alexander MG, Anders SG, Johnson SK (2005) A wind tunnel experiment for trailing edge circulation control on a 6 % 2-D airfoil up to transonic mach numbers. In: Jones GS (ed) Proceedings of the 2004 NASA/ONR circulation control workshop. Langley Research Center, pp 407–434

Allan BG, Jones GS, Lin JC (2011) Reynolds-averaged Navier-Stokes simulation of a 2D circulation control wind tunnel experiment. In: 49th AIAA Aerospace sciences meeting including the new horizons forum and aerospace exposition, pp 1–16. AIAA

Anders SG, Sellers WL, Washb AE, Sellers WE, Illt, Washburn AE (2004) Active flow control activities at NASA langley. In: 2ND AIAA flow control conference, number July 2004. AIAA

Cagle CM, Jones GS (2002) A wind tunnel model to explore unsteady circulation control for general aviation applications. In: 22nd AIAA Aerodynamic measurement technology and ground testing conference, number June 2002. AIAA

Coanda H (1936) Device for deflecting a stream of elastic fluid projected into an elastic fluid

Couluris GJ, Signor DB, Phillips JD (2010) Cruise-efficient short takeoff and landing (CESTOL): potential impact on air traffic operations. Technical report. NASA

Djojodihardjo H, Thangarajah N (2014) Research, development and recent patents on aerodynamic surface circulation control—a critical review. Recent Patents Mech Eng 7(1):1–37. ISSN 22127976. doi:10.2174/2212797607666140204004542

Economon TD, Milholen II WE (2008) Parametric investigation of a 2-d circulation control geometry. Technical report, Configuration Aerodynamics Branch Research and Technology Directorate

Englar RJ (2005) Overview of circulation control pneumatic aerodynamics: blown force and moment augmentation and modification as applied primarily to fixed-wing aircraft. In: Jones GS (ed) Proceedings of the 2004 NASA/ONR circulation control workshop. Langley Research Center, pp 37–79. NASA

Englar RJ, Jones GS, Allan BG, Lin JC (2009) 2-D circulation control airfoil benchmark experiments intended for cfd code validation. In: 47th AIAA Aerospace sciences meeting including the new horizons forum and aerospace exposition, pp 1–27. AIAA

Englar RJ (1998) Continued development and application of circulation control pneumatic technology to advanced transport aircraft. Technical report, NASA Langley Research Center

Franke ME, Harvell JK (1987) Wind tunnel studies of circulation control elliptical airfoils. In: Nielsen JN (ed) Proceedings of the circulation-control workshop, pp 267–287. NASA

Gibbs EH, Ness N (1976) Analysis of circulation controlled airfoils. J Aircraft 13(2):158–160

Gologan C, Stagliano F, Schmitt D (2009) Impact of ESTOL capability on the mission fuel burn of regional jets. In: 9TH AIAA aviation technology, integration, and operations conference (ATIO), pp 1–19. AIAA

Jim B (2015) Amelia's innovations inspire unusual dedication. http://www.nasa.gov/topics/aeronautics/features/amelia.html

Jones GS, Englar RJ (2003) Advances in pneumatic-controlled high-lift systems through pulsed blowing. In: 21st AIAA Applied aerodynamics conference, pp 1–14. AIAA

Jones GS, Joslin Jones GS (2005) Proceedings of the 2004 NASA/ONR circulation control workshop, Part 1. In: Jones GS (ed) Proceedings of the 2004 NASA/ONR circulation control workshop. NASA Langley Research Center

Jones GS, Joslin RD (2004) Summary: 2004 NASA/ONR Circulation control workshop. In: Jones GS (ed) Proceedings of the 2004 NASA-ONR circulation control workshop, pp 1023–1050, Langley Research Center. NASA

Jones GS, Lin JC, Allan BG, Milholen WE (2008) Overview of CFD validation experiments for circulation control applications at NASA. In: 2008 International powered lift conference, pp 1–16

Jones GS (2005) Pneumatic flap performance for a 2D circulation control airfoil, steady & pulsed. In: Jones GS (ed) Proceedings of the 2004 NASA/ONR Circulation control workshop, pp 845–888. NASA Langley Research Center

Lee-Rausch EM, Vatsa VN, Rumsey CL (2006) Computational analysis of dual radius circulation control airfoils. In: 3rd AIAA flow control conference, pp 1–18. AIAA

Linden A, Biggers J (1987) X-Wing potential for navy applications. In: American Helicopter Society 41st annual forum. American Helicopter Society

Linden A, Rosen K, Wing WAX (2013) http://www.sikorskyarchives.com/X-WING.php

Liu Y, Sankar LN, Englar RJ, Ahuja KK, Gaeta R (2004) Computational evaluation of the steady and pulsed jet effects on the performance of a circulation control wing section. In: 42nd AIAA Aerospace sciences meeting and exhibit, pp 295–321. AIAA

Liu Y, Sankar L, Englar R, Ahuja K (2001) Numerical simulations of the steady and unsteady aerodynamic characteristics of a circulation control wing airfoil. In: 39th Aerospace sciences meeting and exhibit. AIAA

McGowan G, Gopalarathnam A (2005) CFD analysis of circulation control airfoils using Fluent. In: Proceedings of the 2004 NASA/ONR circulation control workshop, pp 813–843. NASA

Milholen W, Jones G, Chan D, Goodliff SL (2012) High-Reynolds number circulation control testing in the national transonic facility. In: 50TH AIAA AEROSPACE sciences meeting including the new horizons forum and aerospace exposition. AIAA

Moore MD (2006) NASA personal air transportation technologies. SAE Technical paper 2006-01-2413

Nielsen JN (1987) Proceedings of the circulation-control workshop. National Aeronautics and Space Administration

Nishino T, Hahn S, Shariff K (2010) Calculation of the turbulence characteristics of flow around a circulation control airfoil using LES. In: 48th AIAA Aerospace sciences meeting including the new horizons forum and aerospace exposition, pp 1–15. AIAA

Novak CJ, Cornelius KC (1987) Investigations of a circulation control airfoil flowfield using an advanced laser velocimeter. In: Proceedings of the circulation-control workshop, pp 71–98. NASA Ames Research Center

Paschal KB, Neuhart DH (2012) Circulation control model experimental database for CFD Validation. In: 50TH AIAA Aerospace sciences meeting, pp 1–10. AIAA

Pepper RS, van Dam CP, Gelhausen PA (1996) Design methodology for high-lift systems on subsonic transport aircraft

Rodman LC, Wood NJ (1986) Verification of performance results for a low-speed 15% elliptical circulation control airfoil. Technical Report. Department of Aeronautics and Astronautics, Stanford University

Rumsey CL, Nishino T (2011) Numerical study comparing RANS and LES approaches on a circulation control airfoil. Int J Heat Fluid Flow 32(5):847–864. ISSN 0142727X

Sellers WL, Jones GS, Moore MD (2002) Flow control research at NASA Langley in support of high-lift augmentation. In: 2002 Biennial international powered lift conference and exhibit. AIAA

Simon S (2015) Demon UAV—flying without flaps. http://www.baesystems.com

Slomski J, Marino T (2002) Navy successfully simulates effect that may improve low-speed maneuverability. J Art Fluent Softw Usres JA(153):1–4

Sun WC, Broichhausen K, Seifert J, Luftfahrt B (2008) EV. Promising future aircraft concept-estol. In: 26th Congress of the international council of the aeronautical sciences, pp 1–8. www.icas.org

Swanson RC, Rumsey CL, Anders SG (2005) Aspects of numerical simulation of circulation control airfoils. In: Proceedings of the 2004 NASA/ONR circulation control workshop, pp 227–273. NASA

Swanson RC, Rumsey CL (2009) Computation of circulation control airfoil flows. Comput Fluids 38(10):1925–1942, December 2009. ISSN 00457930. doi:10.1016/j.compfluid.2009.05.002

Trimble S (2010) British team proves flapless flight with Demon UAV, 2010. www.flightglobal. com/news/articles/pictures-amp-video-british-team-proves-flapless-flight-with-demon-347894/

van Dam CP, Paris JK, Vander Kam JC (2000) High-lift design methodology for subsonic civil transport aircraft

Wang C, Sun M (2000) Separation control on a thick airfoil with multiple slots blowing at small speeds. Acta Mechanica 143(3-4):215–227. ISSN 0001-5970. doi:10.1007/BF01170949, http://dx.doi.org/10.1007/BF01170949

Werner-Spatz C, Heinze W, Horst P, Radespiel R (2012) Multidisciplinary conceptual design for aircraft with circulation control high-lift systems. CEAS Aeronaut J 3(2-4):145–164. ISSN 1869-5582. doi:10.1007/s13272-012-0049-5

CFD RANS Simulation of 2D Circulation Control Airfoil

H. Carmona, A. Cházaro, A. Traslosheros, A. Iturbe and J. Hernández

Abstract In the present work, the Circulation Control technology applied to an airfoil with a discontinuous not-rounded surface is explored. First a numerical model is constructed and compared against a physically-tested and well known Circulation Control airfoil. Then the model is modified to analyze the airfoil with discontinuous not-rounded surfaces. This last numerical model suggests that, if enough jet momentum is applied, the Coanda effect can be induced in the airfoil with discontinuous not-rounded surfaces. The model also suggests that when the Coanda effect is induced, a small vortex is generated at the geometric discontinuities and the flow acts as if the geometry was in fact rounded.

1 Introduction

Circulation Control (CC) is an aerodynamic method in which a high speed jet is tangentially impinged into a Coanda surface near the trailing edge of an airfoil, resulting in improved lift if compared with typically unblown airfoils. Lift coefficients (C_l) as high as 8 have been reported with this technique (Robert 2005). The motivation of CC research is simple: as the maximum C_l defines aircraft take-off/landing distances (through stall velocity) and since high Cls can be obtained with CC, the technology has been a topic of interest for more than 65 years (Rumsey and Nishino 2011). In

H. Carmona (✉) · A. Cházaro · A. Traslosheros · A. Iturbe · J. Hernández
Universidad Aeronáutica en Querétaro, Colón, Mexico
e-mail: hugolfons@hotmail.com

A. Cházaro
e-mail: adriana.chazaro@unaq.edu.mx

A. Traslosheros
e-mail: altrami@hotmail.com

A. Iturbe
e-mail: aris.iturbe@unaq.edu.mx

J. Hernández
e-mail: jorge.hernandez@unaq.edu.mx

fact a study by Englar (2005) suggests that landing distance can be reduced about one third of the airport lengths required today.

CC improves airfoil performance by increasing the flow momentum over an airfoil. Due to a balance between jet centrifugal force and jet-low static pressure, the impinged jet remains attached to the Coanda surface changing continually its initial direction as it flows over the curvature. The high speed jet entrains the flowfield over the airfoil through viscous forces in a mixing layer region; this results in higher velocity, increased circulation around the airfoil and higher lift than those obtained in unblown airfoils. As the jet flows over the Coanda surface there is also a dissipation of the jet momentum leading to the Boundary Layer (BL) separation. The consequence of this effect is that the separation point can be controlled by increasing or decreasing the momentum, or in other words by changing the airfoil plenum pressure that defines the jet velocity. Since the separation point defines the circulation around an airfoil and the separation point can be controlled by changes in plenum pressure, then circulation around the airfoil (and lift) can be controlled independently on the angle of attack.

The performance of a CC airfoil can be expressed through the relation of jet momentum coefficient (C_μ) and the lift coefficient (C_l). The C_μ is defined in the Eq. 1, where $\dot{m}$ represents the mass flow of compressed air, v_j represents the jet velocity, q_∞ represents the reference dynamic pressure and S the wing surface.

$$C_\mu = \frac{\dot{m}v_j}{q_\infty S} \tag{1}$$

The performance can be divided into two main behaviors as shown by physical experiments in Robert (2005), Abramson (1977) separation-control and super-circulation, being the former more efficient with C_l-C_μ slope higher than the super-circulation region, Fig. 1.

In this context, the motivation of this work is the exploration of CC applied to airfoils with non-rounded surfaces. For this purpose first a numerical model of a reference CC airfoil (Abramson 1977) was defined and compared with the experimental results and second, the main characteristics of the numerical model are used for a CC airfoil with non-rounded trailing edge. Both airfoils are shown in Figs. 1 and 2 respectively. It must be mentioned that most (if not all) of the CC airfoils
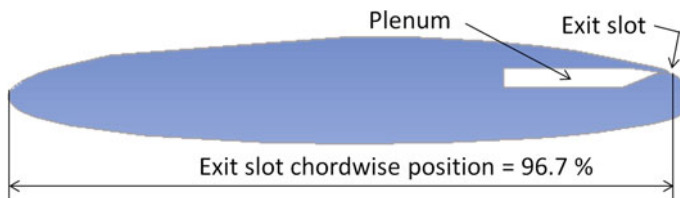
Fig. 1 CC NCCR airfoil tested in Abramson (1977)
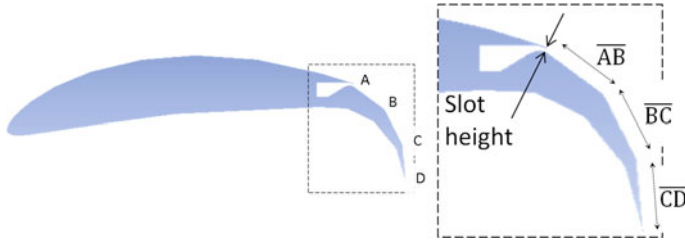
Fig. 2 CC airfoil with flat-discontinuous surfaces

Fig. 3 Coanda original device (Voedisch 1947)
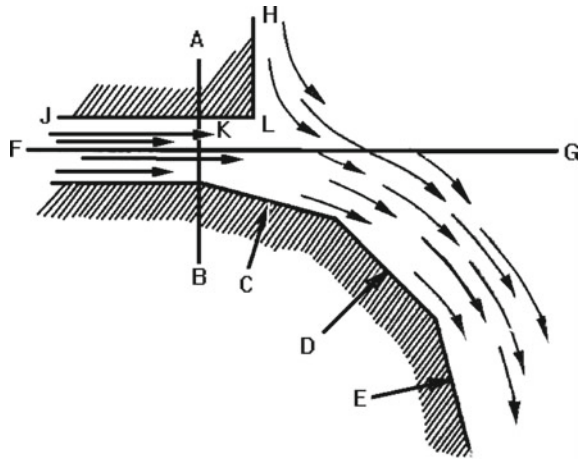
investigated incorporate a rounded trailing edge where the jet flows, and also that Coanda effect was in fact studied first with non-rounded surfaces as shown in Fig. 3 (Voedisch 1947).

2 NCCR-1015-7076N CC Airfoil

The airfoil used for this experiment is the NCCR 1510-7067N with a 15 % thickness to chord ratio, a chord of 20.34 cm and the slot being located at 19.6 cm from the leading edge; the tests were reported by Abramson (1977). The model consisted of a 38×51 cm section that was tested at the David Taylor Naval Ship R&D Center (DTNSRDC) and corrections for blockage and for wall boundary layer separation were made.

The experiments performed include three subtypes of the airfoil: slot to chord ratio airfoil of 0.0015, 0.0022 and 0.003. The report of the experiments include Momentum coefficient to airfoil internal duct pressure, slot height variation with

duct pressure, lift to momentum coefficient ratio and a plot of the pressure coefficient distribution around the airfoil among the main results. The airfoil with slot to chord ratio of 0.0015 was selected for the present analysis since more data was available for this configuration. Although the wind tunnel velocity was not explicitly mentioned by Abramson (1977), it is mentioned that the wind tunnel dynamic pressure runs were from 10 to 40psf and for Reynolds numbers from 0.375×10^6 to 0.52×10^6. With this data the wind tunnel velocity was estimated. Also the duct pressure within the airfoil was estimated along with the slot deformation due to the pressurization.

3   NCCR Numerical Model

Governing equations: The physical effects around CC airfoils involve strong viscous phenomena mainly produced by a mixed layer composed by the jet and the entrained air, for this reason the analysis cannot be performed with simple analytical methods such as potential flow theory; instead, the solution requires modeling of viscous forces which are considered in the Navier-Stokes (NS) equations; this set of equations includes the transport of momentum and the continuity equations (Peric and Ferziger 2002) can be seen in numerous textbooks such as Peric and Ferziger (2002), Fletcher (1998), Versteg and Malalasekera (1995).

Method of solution: there are various methods to solve the set of equations: Finite Differences, Finite Element, Finite Volume Method (FVM), Lattice-Boltzmann, etc. From these options the FVM was selected due to software availability.

Turbulence treatment: As the problem involves Re numbers above 3000, the problem includes turbulent regime.. This turbulence is incorporated in the set of NS equations by separating flow variables into time-average and instantaneous components (Reynolds decomposition) leading to Reynolds-Averaged Navier-Stokes equations (RANS, see Peric and Ferziger (2002), Sect. 9.4 for example). Due to this decomposition of flow variables, the required discretization and solution of equations can be processed with available desktop computers; In fact most of the numerical investigations on CC reviewed use this approximation (McGowan and Gopalarathnam 2004; Swanson et al. 2006; Lee-Rausch et al. 2006; Englar et al. 2009; Swanson and Rumsey 2009; Rumsey and Nishino 2011; Allan et al. 2011; Liu et al. 2004). Other options such as Direct Numerical and Large Eddy. Simulations (Rumsey and Nishino 2011; Nishino et al. 2010) require much more computing time and were discarded. The derivation of RANS however brings a closure problem since the decomposition introduces more variables than available equations and requires Turbulence Models. Such models are derived under specific flow conditions and its complexity varies according to the number of additional transport equations proposed for turbulence parameters.

Turbulence model: The Reynolds Stress Model was used in the numerical model. In this model the Reynolds Stresses are calculated by obtaining the second momentum equations; this is obtained means by multiplying the momentum equations by

the velocity components and then performing the Reynolds decomposition. In this process, 4 equations are obtained for the transport of Reynolds stresses (for 2D flows) and one additional equation for the transport of dissipation rate.

In the Reynolds stresses transport equations (see Fluent 2011, Sect. 4.9), the following terms are included: Turbulent Diffusion, Molecular Diffusion, Stress Production, Buoyancy Production, Pressure Strain, Dissipation, Production by System Rotation and User defined Source. From these, the Turbulent Diffusion, the Molecular Diffusion and the Dissipation terms require modeling. This model of turbulence is very complete and has the advantage that the turbulence is no longer considered isotropic as in other models. However, one disadvantage is that modeling the required terms that is a difficult task and compromises the accuracy. In general, the model is recommended for complex flows although its accuracy needs to be considered. Also, the model suffers from instability problems (Rumsey 2014).

Pressure-velocity coupling and solution algorithm: inspection of the transport equations of NS shows that the pressure cannot be directly solved since the term is not provided as a known condition for the whole domain and neither appears in the continuity equation. In compressible flows density and pressure are linked (state equation) and the problem can be solved by deriving an additional transport equation for the density (Peric and Ferziger 2002). In the case of the NCCR airfoil experiments however most of the flowfield is well below $M = 0.3$, is incompressible and there is not a strong link pressure-density, so a different method is required to solve the pressure field.

The SIMPLE (Fluent 2011) iterative algorithm was used initially. It starts with an initial guess of the pressure followed by solution of velocity components; with the velocity field defined, a correction to the pressure field is done with a correction equations derived from combining NS with continuity equations. The algorithm is repeated until the difference between the initial guess and the solution is small enough.

Convergence problems however were present. A different approach was implemented with the coupled method (Fluent 2011) where pressure and the velocity field are solved simultaneously in vector form. Problems arise at low Mach numbers due to high difference between velocity and sound speed; to overcome the problem a preconditioning technique is used. In this technique the time-derivative terms in the coupled vector equation are pre-multiplied to have terms with the same order of magnitude. Further explanation about the method can be found in Turkel et al. (1996).

Discretization scheme: In the FVM, RANS are solved for each control volume and the solution represents the value of the flow variables at the centroid of the element. To compute the effect of the variables on face elements, an interpolation scheme is required such as: First order, second order and QUICK. In this case the First Order method was selected for initial computations and then a quadratic upwind differencing (QUICK) scheme (Peric and Ferziger 2002; Fluent 2011) for final calculations.

Geometry: In the article Abramson (1977) the X-Y coordinates of the airfoil are provided. With them, the geometry is defined using CAD software. The dimensions of the airfoil were taken of those reported by Abramson.
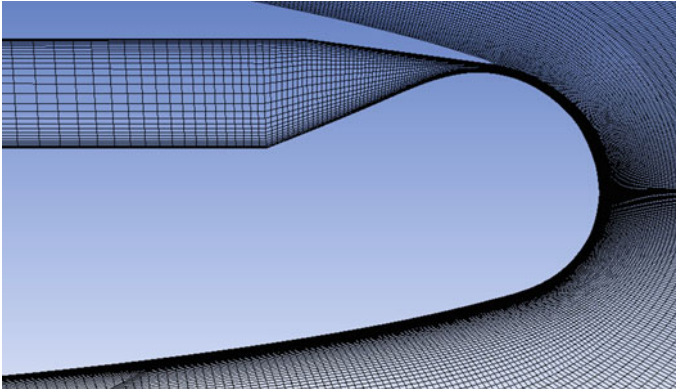
Fig. 4 Mesh around exit slot

Fluid domain discretization: A quadrilateral mesh was constructed around the CC airfoil being mapped for most of the domain. A difference between CC airfoils and typical airfoils is the jet and this implies that at some point the mesh of the discretization of the inner plenum gets together with the mesh of the discretization around the airfoil. At this intersection, the mesh contains a number of elements to discretize the domain around the airfoil plus a number of elements to discretize the plenum; if this pattern is combined around the airfoil a spiral mesh will be obtained. This case has been applied by Dennis et al. (1987) but in the present model a non-mapped section was used on the lower surface of the airfoil. With this discontinuity, the rest of the fluid domain was discretized with a mapped mesh. A final number of 5×10^5 elements were used for the discretization. In the Fig. 4 shows a detail of the mesh at the rear section including the intersection point of jet and freestream.

Boundary conditions: data from the physical experiments was obtained from Abramson (1977).

Corrections: It must be mentioned that pressurization deformation and angle of attack corrections were made. The pressurization of the plenum has the effect of increasing the slot height where the jet exits and defines in part the momentum of the jet since there is a considerable variation of flow exit area. At a blowing rate of $C\mu = 0.201$ and baseline slot to chord ratio of 0.0015 for example, the gap increases 14 % (based on tables provided in the article). The angle of attack correction is required due to the high lift coefficients and induced downwash (Abramson 1977).

Convergence criteria: In order to consider that the solution converged, the default settings for the convergence criteria were lowered one order of magnitude, being all the residuals set to 1×10^{-4} except those of the energy equations which were set to 1×10^{-7}. With these changes, the four significant digits of the lift coefficient did not change for over 1000 iterations. Table 1 shows a summary of the numerical model used for the analysis of the NCCR-1015-7076N CC airfoil.

Table 1 Summary of NCCR airfoil numerical model

Parameter	Data
Dimensionality	2D-Steady State
Governing eqs	Navier Stokes
Solution technique	Finite volume method
Turbulence treatment	Reynolds-Averaged Navier-Stokes (RANS)
Turbulence model	Reynolds Stresses Model (5 eq. Model)
Pressure-velocity algorithm	Coupled (preconditioning method for low speed flows)
Discretization scheme	QUICK
Geometry	Reproduced from data in article Abramson (1977)
Discretization	Hybrid mesh, 143786 elements
Boundary conditions	Obtained from Abramson (1977) report (the internal pressure is calculated)

4 NCCR Model Results

The blowing momentum coefficient in the numerical model was varied to match the points included in the reference report for the same slot to chord ratio (0.0015) and a constant angle of Attack of 0°. A plot of lift coefficient versus blowing momentum coefficient is included in Fig. 5 superimposed on the results reported by Abramson.

It can be observed that experimental and numerical simulation data are consistent at C_μ up to 0.04 (the differences are around 4 %), but above $C_\mu = 0.04$ the numerical model under-predicts the lift coefficient. Also it is seen that above $C_\mu = 0.04$ the mismatch between the numerical model and the experiment increases with blowing rate.

As expected there is high velocity due to the pressure ratio between plenum and freestream air, in consequence the static pressure around the Coanda surface is very low compared with the surrounding freestream (Fig. 6) causing this stream to push the jet against the Coanda surface and resulting in jet attachment.

Another consequence of the high velocity jet is the tangential force acting over the surrounding flowfield Fig. 7 shows contours of the strain rate where it is clearly seen a mixing layer between the jet and the flow over the airfoil. High values of strain rate indicate that the jet momentum is transmitted to the flow over the airfoils through tangential (viscous) forces. This entrainment increases the flowfield velocity over the airfoil which in turn results in higher lift as the difference between static pressure over and under the airfoil increases.
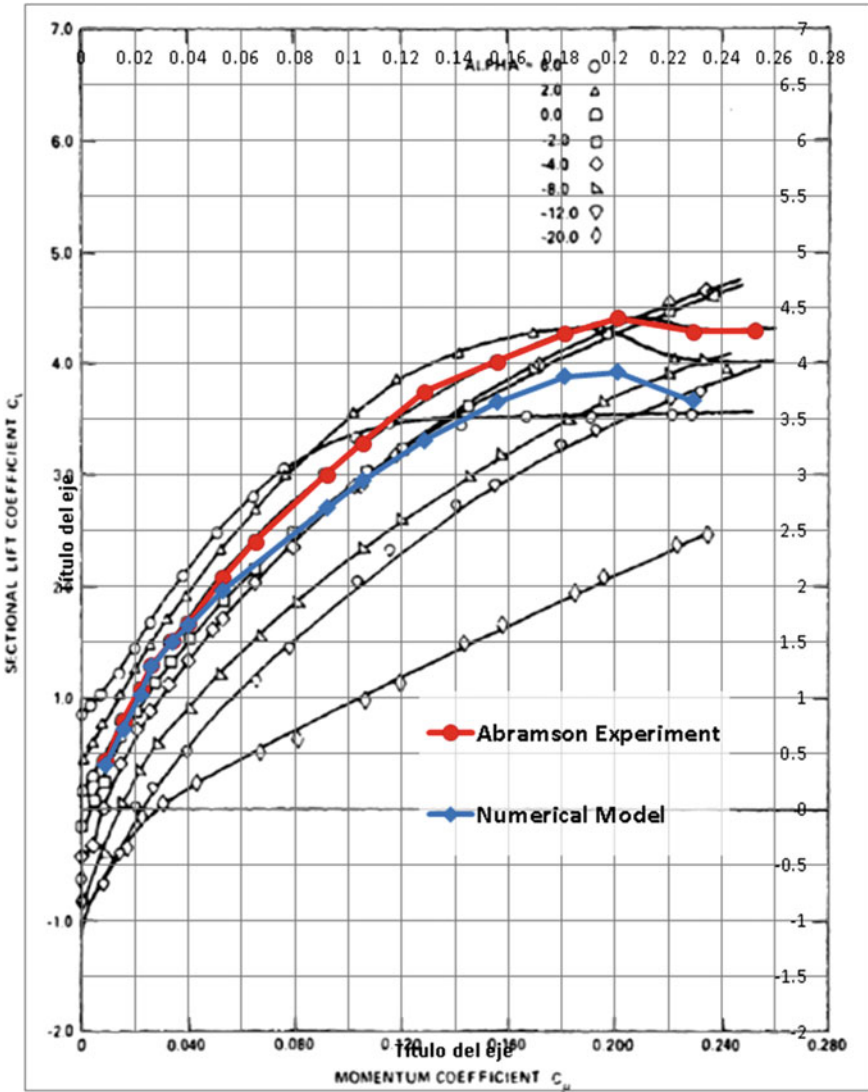
Fig. 5 *Cl* as a function of C_μ for a slot to chord ratio of 0.0015 and angle of attack of zero degrees. Numerical results (*blue*) superimposed on Abramson experimental results (*red*)

Contours of Static Pressure (pascal)

Jun 01, 2015
ANSYS Fluent 14.5 (2d, dp, pbns, RSM)
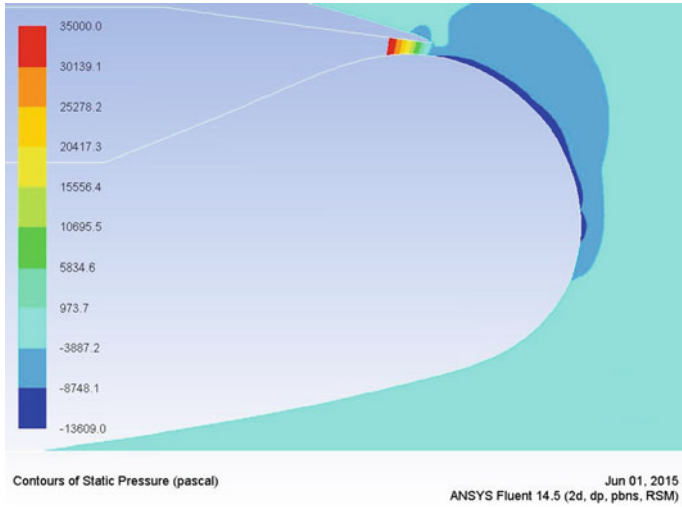
Fig. 6 Contours of static pressure [Pa] indicating a low values over the Coanda surface

Contours of Strain Rate (1/s)

May 29, 2015
ANSYS Fluent 14.5 (2d, dp, pbns, RSM)
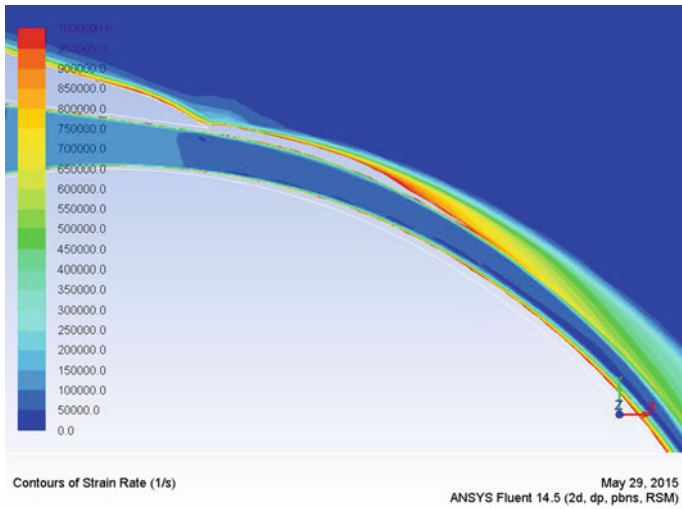
Fig. 7 Contours of strain rate [$1/s$]. A mixing layer is developed between the jet and the outer flow through which the jet entrains the outer flow by means of tangential forces

As explained in the previous section, the main difference between typical airfoils with a sharp trailing edge and CC airfoils is the separation point. In the former case the separation point is passively-controlled in the geometry itself while in the CC airfoils the separation point is affected in part also by the geometry but mainly it is controlled through the blowing rate.

Prediction of the separation point is fundamental for a successful numerical simulation and it is affected by the selection of the turbulence model in the case of RANS simulations (Swanson and Rumsey 2009). In the case of the present numerical model it is assumed that the prediction is accurate enough; there are three reasons to make this assumption: there is no record of jet separation point on the reference physical experiment to compare with, the difference between experimental and numerical lift coefficient (affected by separation point) is below 10 % and the numerical results correctly predict the trend in lift coefficient versus blowing momentum coefficient.

A mixing layer between the jet and the flow over the airfoil can be seen in Fig. 8 that shows contours of turbulent dissipation rate. This mixing layer is a source of turbulence and as a consequence there is energy dissipation. Also, energy from the jet is dissipated by viscous forces in the boundary layer over the Coanda surface. It can be seen that as the jet moves through the Coanda surface, the mixing layer thickness increases as well as the boundary layer resulting in increasing turbulence. In this way the jet momentum is continuously being dissipated as it moves over the surface until eventually there is no more momentum to counteract adverse pressure gradients and/or the momentum of the incoming flow under the airfoil leading to Boundary Layer (BL) separation.
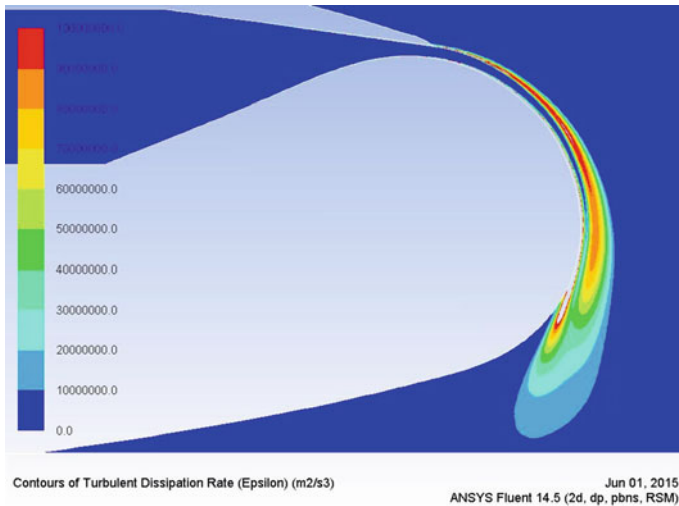
Fig. 8 Contours of turbulent dissipation rate $[m^2/s^3]$ around the NCCR Coanda surface

Fig. 9 Angle at which separation of BL takes place for the NCCR airfoil as blowing rate was increased. Slot to chord ratio = 0.0015 and angle of attack of zero degrees
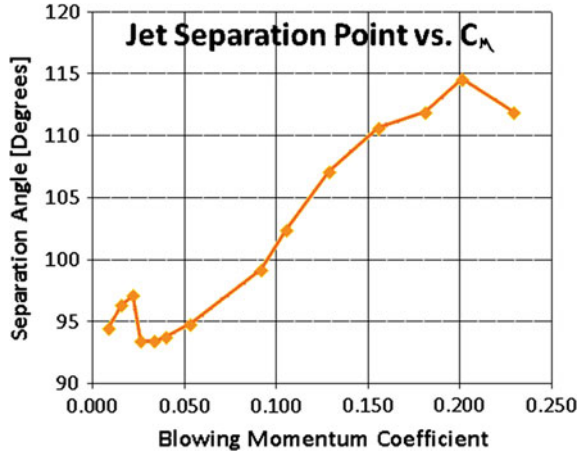
The separation point was defined by inspection of the Wall Shear Stress values equal to zero. Figure 9 shows the separation angle relative to the center of the Coanda surface as the blowing rate increases.

Inspection of the front point of stagnation shows that the leading edge can be stalled as mentioned in previous investigations (Englar et al. 2009; Robert 2005), Fig. 10 shows pathlines at the leading edge for the case $C_\mu = 0.201$.
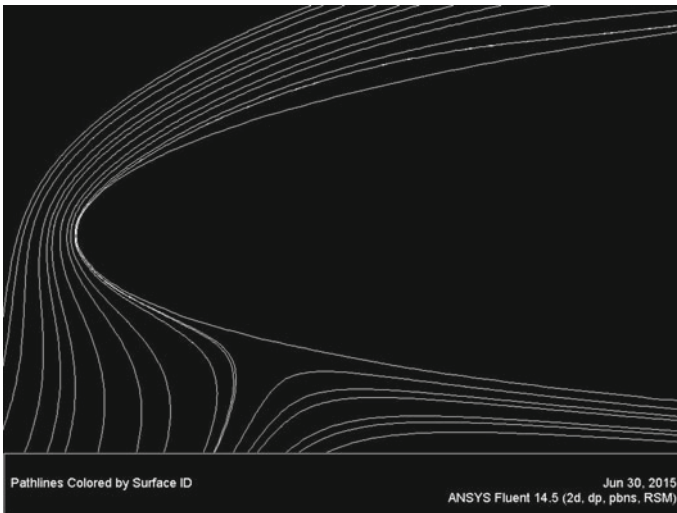
Fig. 10 Pathlines around NCCR leading edge indicating displacement of the front stagnation point to the low airfoil surface region at high blowing rate

5   Discontinuous Coanda Trailing Edge

A hypothetical CC airfoil was proposed. The main characteristic is that the trailing surface of the airfoil is formed by 3 flat segments between the jet exit slot and the sharp trailing edge (AB, BC and CD shown previously in 2) instead of the typical rounded Coanda surfaces of most CC airfoils. The exit slot was fixed at 76 % chord-wise position of the original airfoil with a slot height to chord ratio of 0.004; the chord for the original reference airfoil is 20.24 cm, the same of the NCCR airfoil. In addition a cambered airfoil was selected with a leading edge pointing downwards in order to delay leading edge stall. Another important characteristic of this hypothetical design is the variation of the airfoil exit angle; the exit angle was defined as the angle formed by the last trailing flat surface and the airfoil chord axis as shown in Fig. 11. The motivation for the analysis of this airfoil through a numerical model is to answer the question: Can the Coanda effect be induced in a series of flat surfaces without any rounding? It must be mentioned that the Coanda effect in fact was discovered by Henri Coanda not with a rounded surface but with a series of flat surfaces (Analytical investigation of the Coanda Effect) (Voedisch 1947) so positive results were expected a priori.

It is assumed that rounded surfaces are desired for improved efficiency, in fact it has been reported many times that the optimum region of operation for CC airfoils is with trailing edge radius to chord ratios of around 4 % (Jones et al. 2003). It is also assumed that if the Coanda effect can be induced, then this configuration would be a bottom low level in airfoil performance and any improvement by design and especially manufacture would improve CC characteristics.

Various exit angles were proposed to explore the behavior of the flow around such airfoil and can be seen in Fig. 11 where the numbers on it indicate the exit angle. The airfoil with an exit angle of 85° is shown complete on Fig. 2. It is realized that the C_μ is related to the power requirements and often associated to the main engines in the context of aircrafts. However high pressure reservoirs could store a limited but enough amount of compressed air that could induce CC for short periods of time and improve maneuverability. For this reason, the numerical cases were defined mostly in terms of internal pressure instead of momentum coefficient.

Fig. 11 Modified airfoil with 3 trailing flat surfaces and no rounding. Exit angles relative to chord from 25 to 85°
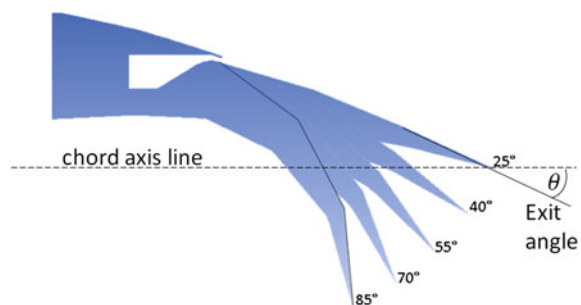
Table 2 A total of 20 performance points analyzed with numerical model

EE PP	EE PP	EE PP	EE PP
$25 - 7.1$Pa	$25 - 28$Pa	$25 - 52$Pa	$25 - 60$Pa
$40 - 7.1$Pa	$40 - 28$Pa	$40 - 52$Pa	$40 - 60$Pa
$55 - 7.1$Pa	$55 - 28$Pa	$55 - 52$Pa	$55 - 60$Pa
$70 - 7.1$Pa	$70 - 28$Pa	$70 - 52$Pa	$70 - 60$Pa
$85 - 7.1$Pa	$85 - 28$Pa	$85 - 52$Pa	$85 - 60$Pa

Each point is defined by airfoil exit angle and plenum internal pressure
Notes EE = exit angle and PP = Plenum pressure

It must be mentioned that the geometric model was parameterized in such way that the deflection of the flat surfaces is proportional in each hinging point and thus there is only one degree of freedom being this defined by the exit angle. The chord was defined as the same as that of the NCCR airfoil, the slot to chord ratio is 0.004 and the location of the exit slot is at 76 % of the original airfoil.

Numerical model: All of the characteristics of the NCCR numerical model described previously in the Table 1, except for the geometry and the mesh, were applied to the proposed airfoil. In a great extent of the computational domain, a mapped mesh was used just as in the NCCR numerical model. However the non-mapped mesh was larger in this case in order to allow automatic meshing for different exit angles. Boundary conditions were the same of the NCCR model with a zero angle of attack. The resulting inner pressures from the NCCR model were the same but as the slot exit ratio is different to that of the reference airfoil; the resulting C_μ is higher due to higher mass flow. A total of 20 points were analyzed by combining 5 exit angles from 25° to 85° and 4 plenum pressures from 7.1 to 60 KPa (Table 2).

6 Results

Effect of the discontinuous surface: Fig. 12 shows the lift coefficient plotted versus the exit angle with lines of constant plenum pressure. A first inspection makes evident that the higher the exit angle the higher the C_l, but also that the plenum internal pressure has a significant contribution. At an exit angle of 85° for example a difference of more than 3 C_l units are made by plenum pressure.

It is also seen that for low plenum pressures there is a drastic change in C_l as angle increases. In the case of 85° with 7.1 KPa point, the drastic decrease in lift is caused by stall of the trailing edge. Inspection of the turbulence intensity contours show that for low pressures (Fig. 14, left column) the boundary layer is separated and a thick wake developed. With further examination of contours of turbulent dissipation rates for the highest exit angle and lowest plenum pressure (Fig. 13) it is seen that the separation point takes place in the first of the surface discontinuities.
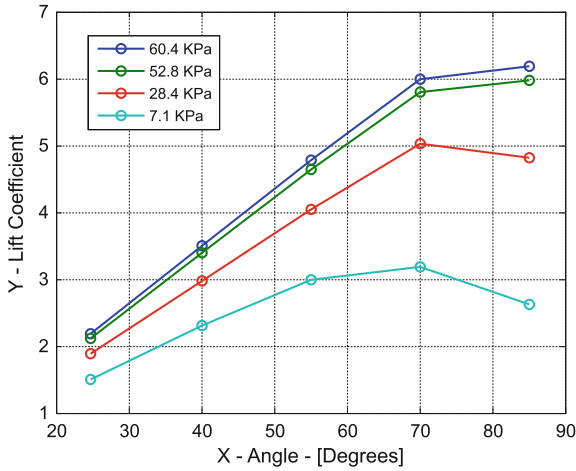
Fig. 12 Lift coefficient as a function of airfoil exit angle with lines of constant plenum internal pressure
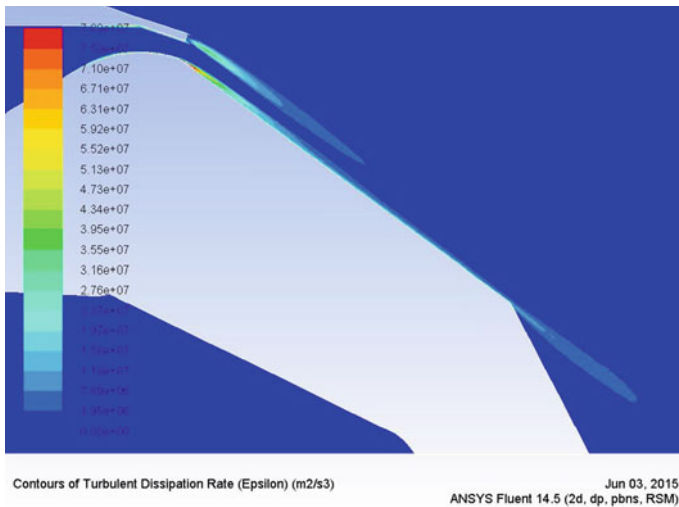
Fig. 13 Contours of Turbulent Dissipation Rate [m^2/s^3] for an exit angle of 85° and internal pressure of 7.1 KPa

These data confirms the expected behavior of the jet tendency to separate from the surface at geometric discontinuities. But it also confirms that if the jet has enough momentum, it can remain attached downstream of such geometric discontinuities.

Jet attachment in discontinuous surface: Fig. 15a–c shows the pathlines around the trailing surface of the modified airfoil at an exit angle of 85° and for internal
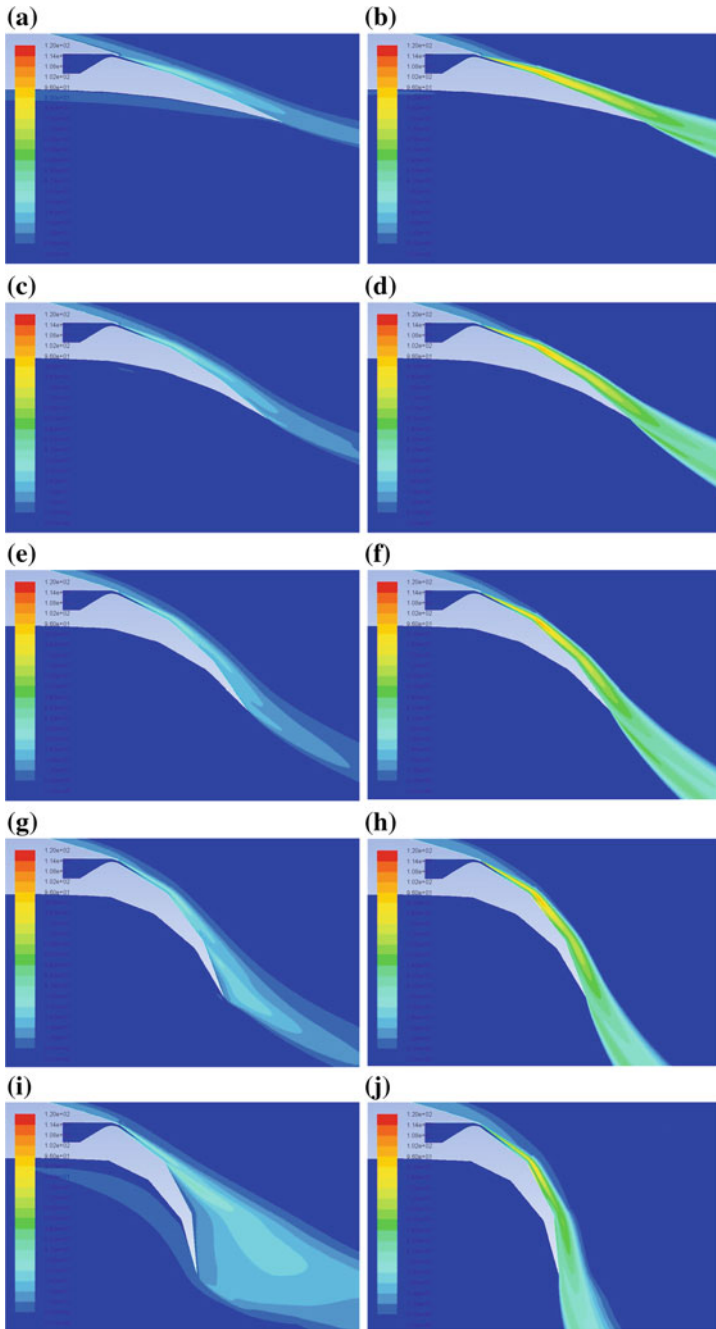
Fig. 14 Contours of Turbulence intensity in the range of 0–120; Cases of constant pressure of 7.1 KPa and 60 KPa for *left* and *right* columns respectively

Fig. 15 Figures **a**–**c** show the pathlines around trailing surface for modified airfoil with exit angle of 85° and plenum pressures of 7.1, 28 and 52 KPa respectively, details of (**c**) can be observed in (**d**)
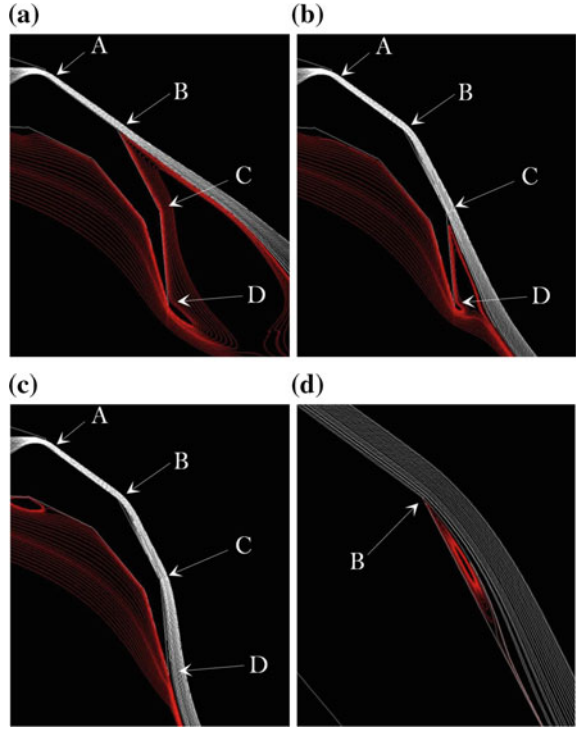
pressures of 7.1, 28 and 52 KPa respectively. The sources of red pathlines are under the airfoil and white pathlines sources are inside the plenum.

These figures show that jet separation occurs at the geometric discontinuous points B and C for internal pressure of 7.1 and 28 KPa respectively. In Fig. 15c the jet is attached to the third and last trailing surface. Figure 15d shows a trapped vortex between airfoil surface and jet, starting at point B in Fig. 15c.

These numerical results suggest that as the internal pressure and jet momentum are increased, jet attachment can be obtained even with not rounded surface.

Further inspection of the results indicates that the detached jet from point *B* in Fig. 15a entrains air under the jet and a vortex is formed between the jet and the segments *BC* and *CD*. In Fig. 15b the vortex is formed between the jet and the segment *CD* and for Fig. 15c the jet remains attached to the three segments.

These results suggest that as the jet momentum and entrainment increase the vortex strength also increases until the static pressure, reduced by the vortex, is low enough to cause reattachment.

It is interesting to note that for the case of the jet attached to three segments with an internal pressure of 52 KPa (Fig. 15c), a small vortex is kept trapped between the jet and the surface, starting just at the discontinuity as shown in Fig. 15d with red pathlines. Inspection of this figure indicates that the small vortex acts as if the geometry was in fact rounded.

Fig. 16 Distribution of pressure coefficient over trailing surface for an exit angle of 85° and plenum pressure of 7.1, 28 and 52 KPa respectively
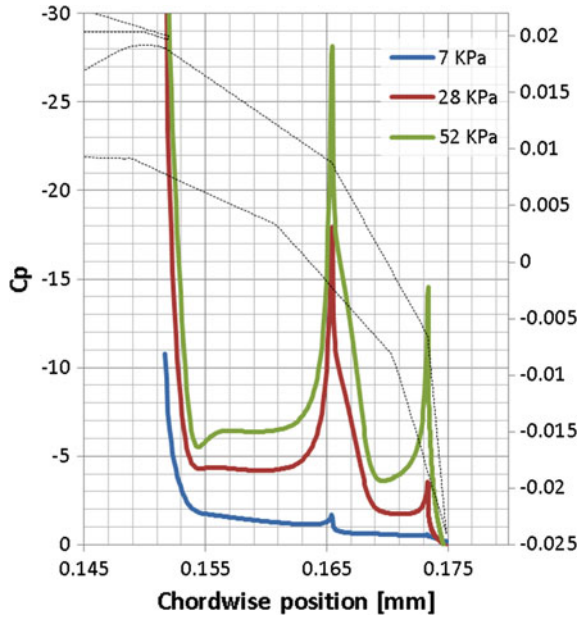
Figure 16 shows the distribution of pressure coefficient over the trailing surface of the airfoils for the same cases of Fig. 15a–c. This figure support the fact that increased plenum pressure (higher momentum) reduces the static pressure over the trailing surface which in turn contributes to higher lift. It also shows that peaks of low static pressure take place at the geometric discontinuities where the jet has a tendency to separate.

Separation control and super circulation: As a function of the plenum internal pressure, two different behaviors of the lift coefficient are shown in Fig. 12. When the exit angle is 70, either, the lift decreases due to trailing edge stall or, the lift continues increasing but with a lower C_l-C_μ slope. It is assumed that the super-circulation region is responsible for this last effect.

This means that there is a given amount of jet momentum required to avoid the boundary layer separation to deflect the jet in a given direction (and in consequence increase the lift due to jet deflection). Any additional increase in momentum will not deflect the jet further down due to the sharp trailing edge. Instead, additional momentum will entrain more air over the upper surface of the airfoil leading to higher velocities and a moderate increase in lift. These regions of CC operation can be seen in the experiments by Abramson in 5 for the lowest angle of attack with the NCCR airfoil there is a localized region of about $C_\mu = 0.025$ in which the slope changes. For higher angles of attack the limit of the separation-control region fades with the effect of lift reduction due to the displacement of the front stagnation point displaced to the lower airfoil surface as can be seen in 10.

Maximum lift coefficient at minimum C_μ: There are several combinations of exit angle and pressure that would define a fixed lift coefficient which could be achieved if

Fig. 17 Intersection of
planes of constant lift with
fitted surface of C_l versus
exit angle versus C_μ
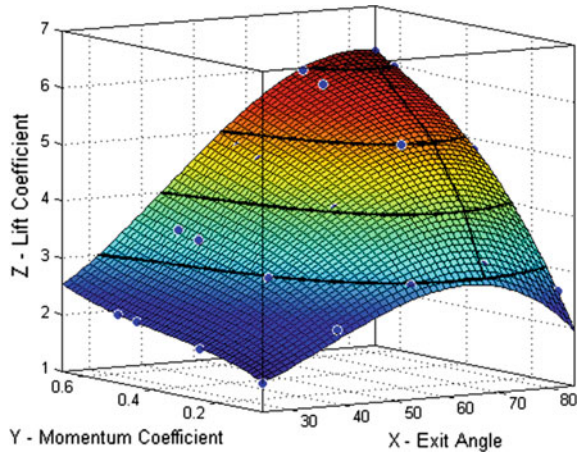
the maximum pressure allows the airfoil to operate in the super-circulation region. As
is shown in Fig. 15a–c, in a CC airfoil the rear exit angle and the plenum pressure can
be varied independently to generate such combinations. To find the best compromise
for these variables, first a polynomial surface was fitted to the set of points analyzed
before and then it was intersected with surfaces of constant lift. This intersection
results in a function that defines the combinations of exit angle and pressure for
a required lift. Minimizing the function then provides the minimum pressure for a
given lift. This procedure is represented by Fig. 17 showing lines of constant lift of
4, 5 and 6, and another line connecting the points of minimum C_μ.

CC performance: Fig. 18 shows C_l as a function of C_μ with lines of constant
exit angles solved with the numerical model. An additional set of points is included
where the values correspond to the minimized C_μ for constant values of lift. For the
values of minimum C_μ, the C_l-C_μ slope results in 8.27, a low value as expected given
that the trailing surface is not rounded and the slot to chord ratio and slot chordwise
position are not in the optimum range. For reference, the C_l-C_μ slope for the NCCR
airfoil is about 35.7 in the separation-control region and 11.5 in the super-circulation
region.

7   Future Work

Physical experiments: Further investigation of the effect of geometry changes or
change in operation is desirable such as the effect of increasing roundness at the
intersection of the flat surfaces, or the effect of pulsed jets on the airfoil. However, the
numerical model should be validated first. A physical test is being planned at UNAQ
with 3D printing technology considered for fast prototyping and a laser Doppler

Fig. 18 C_l as a function of C_μ for lines of constant exit angle, and additional line indicating points of minimum C_μ for angle-pressure combinations. The angles at which minimum C_μ was achieved is indicated next to the points
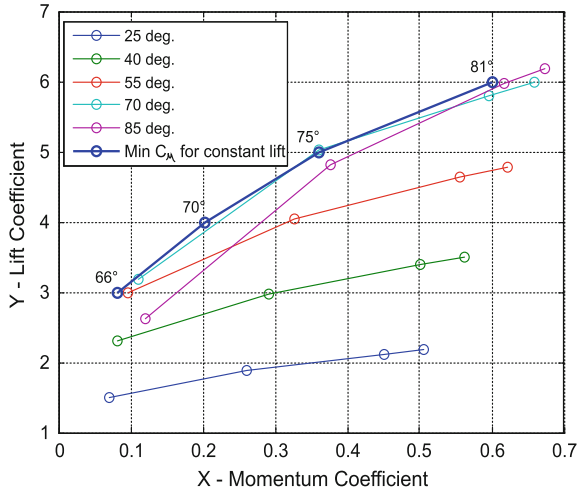
anemometry. It must be mentioned however that so far the reduced tolerances are a challenge for 3D printers and other manufacture processes are also considered.

Numerical simulations: Further investigation showing a more detailed study of the Coanda effect with more appropriated turbulence considerations already identified, including additional study of the boundaries between stalled airfoil, circulation-control and super-circulation.

The work on the discontinuous surface airfoil is based on a numerical model taken from the model of a NCCR rounded trailing edge airfoil and it has been assumed that the same model could describe both airfoils; but, given the sensitivity of turbulence models to different conditions, flatness and roundness in this case, this assumption is not necessarily true and should be investigated.

Also, the numerical models described in this document are based on RANS equations where turbulence effects are simplified by Reynolds decomposition. On the other hand it is accepted that NS equations describe Newtonian-fluid motion and in fact predict turbulence. A much more realistic but computational-demanding analysis including full turbulence effects can be performed with a Direct Numerical Simulation which is planned at UNAQ.

8 Conclusions

Numerical and experimental results for the NCCR-1015-7076N airfoil were compared resulting in that the CFD numerical model successfully predicts the trend of C_l versus C_μ with an acceptable precision for low blowing rates and reasonably precision for high blowing rates. The mixing layer acts as a region where momentum is transferred from the jet to the surrounding flow through tangential forces but inspec-

tion of the numerical solution also suggests that the mixing layer acts as region of high energy dissipation. Inspection of turbulence dissipation results show that the turbulent mixing layer reaches the turbulent boundary layer before the separation point, or in other words, the mixing layer contributes to the jet momentum dissipation that leads to an eventual jet separation. The numerical results of the second airfoil that includes 3 flat discontinuous surfaces indicate that even though the trailing surface is not rounded, the Coanda effect can be induced and high lift obtained if enough jet momentum is provided. These results also show that when the jet is fully attached, a vortex appears between the jet and the trailing surface and acts as if there were no geometry discontinuities and the surface was in fact rounded. Finally, by analyzing different combinations of exit angle and plenum pressure, it was found the combination that minimized the momentum coefficient for constant values of lift.

References

Abramson J (1977) Two-dimensional subsonic wind tunnel evaluation of two related cambered 15-percent thick circulation control airfoils (Sept 1977)

AllanBG, Jones GS, Lin JC (2011) Reynolds-averaged Navier-Stokes simulation of a 2D circulation control wind tunnel experiment, pp 1–16

Englar RJ (2005) Overview of circulation control pneumatic aerodynamics: blown force and moment augmentation and modification as applied primarily to fixed-wing aircraft. In: Langley Research Center, Jones GS (ed), Proceedings of the 2004 NASA/ONR circulation control workshop, pp 37–79

Englar RJ, Jones GS, Allan BG, Lin JC (2009) 2-D circulation control airfoil benchmark experiments intended for CFD code validation. AIAA Paper (January):1–27

Fletcher CAJ (1998) Computational techniques for fluid dynamics 1, 2nd edn. Springer

Fluent A (2011) Ansys fluent theory guide, vol. 15317

Jespersen DC, Pulliam TH, Barth TJ (1987) Navier-Stokes computations for circulation control airfoils. In: Proceedings of the circulation-control workshop, pp 135–163

Jones GS, Englar RJ (2003) Advances in pneumatic-controlled high-lift systems through pulsed blowing. AIAA Paper, pp 1–14

Lee-Rausch EM, Vatsa VN, Rumsey CL (2006) Computational analysis of dual radius circulation control airfoils. AIAA Paper, pp 1–18

Liu Y, Sankar LN, Englar RJ, Ahuja KK, Gaeta R (2004) Computational evaluation of the steady and pulsed jet effects on the performance of a circulation control wing section. AIAA paper, pp 295–321

McGowan G, Gopalarathnam A (2004) CFD analysis of a circulation control airfoil using fluent. .../ONR Circulation Control..., pp 813–843

Nishino T, Hahn S, Shariff K (2010) Calculation of the turbulence characteristics of flow around a circulation control airfoil using LES. AIAA Paper (January 2010):1–15

Peric M, Ferziger JH (2002) Computational methods for fluid dynamics, 3rd edn. Springer

Rumsey CL, Nishino T (2011) Numerical study comparing RANS and LES approaches on a circulation control airfoil. Int J Heat Fluid Flow 32(5):847–864

Rumsey CL (2014) Turbulence modeling resource. https://www.turbmodels.larc.nasa.gov

Swanson RC, Rumsey CL, Anders SG (2006) Aspects of numerical simulation of circulation control airfoils. American Institute of Aeronautics, Reston, VA, pp 227–273

Swanson RC, Rumsey CL (2009) Computation of circulation control airfoil flows. Comput Fluids 38(10):1925–1942

Turkel E, Vasta VN, Radespiel R (1996) Preconditioning methods for low-speed flows

Versteg HK, Malalasekera W (1995) An introduction to computational fluid dynamics

Voedisch A Jr (1947) Analytical investigation of the coanda effect

Calibration of a Background Oriented Schlieren (BOS)

A. Aguayo Ortiz, H. Cardoso Sakamoto, C. Echeverría Arjonilla,
D. Porta Zepeda, C. Stern Forgach and G. Monsivais Galindo

Abstract A Background Oriented Schlieren (BOS) experiment was designed to measure density gradients in a transparent medium. The BOS technique presented here consists on a comparison between a reference image of a dot matrix and another image of the same matrix behind the flow of a transparent gas. The presence of the flow induces changes in the refractive index, so the dots in the matrix appear displaced in the second image. The displacement of each dot is determined through a cross-correlation algorithm between both images. From the displacement, the changes in the refractive index can be determined, which in turn are related to the density by the Gladstone-Dale equation. In the experiment described in this paper, two different gases with known properties were used for the calibration.

A. Aguayo Ortiz (✉) · H. Cardoso Sakamoto · C. Echeverría Arjonilla ·
D. Porta Zepeda · C. Stern Forgach
Facultad de Ciencias, UNAM, Av. Universidad 3000, Circuito Exterior S/N,
C.P., 04510 Delegación Coyoacán, D.F., Mexico
e-mail: aaguayoo92@gmail.com

H. Cardoso Sakamoto
e-mail: jehcs55@gmail.com

C. Echeverría Arjonilla
e-mail: carlosea1982@gmail.com

D. Porta Zepeda
e-mail: alviond@gmail.com

C. Stern Forgach
e-mail: catalina@ciencias.unam.mx

G. Monsivais Galindo
Instituto de Física, UNAM, Av. Universidad 3000, Circuito Exterior S/N,
C.P., 04510 Delegación Coyoacán, D.F., Mexico
e-mail: monsi@fisica.unam.mx

1 Introduction

In fluid dynamics, the use of non-intrusive techniques to measure properties such as the density and the viscosity is important. The two main visualization techniques based on the change in the local refractive index of the flow, are schlieren and shadowgraph, that are extensively used for qualitative results. BOS takes advantage of the images obtained with those techniques to quantify the density field.

Ota et al. (2011, 2012), Venkatakrishnan and Meier (2004), Venkatakrishnan et al. (2010), van Hinsberg and Rösgen (2014) and Elsing (2003) used BOS, but obtained only relative values of the density because the Gladstone-Dale constant is still unknown in many cases due to its complex calculation and measurement. Furthermore, Tipnis et al. (2013), Clem et al. (2013), Lee et al. (2013), Venkatakrishnan et al. (2010) and Elsing (2003) use BOS in particular phenomena such as the study of a supersonic rectangular free-jet, shockwaves and a Prandtl-Meyer expansion fan. A drawback is the lack of comparison between the obtained density field and a known phenomenon.

For this reason, the main objective of this work was to test the technique using a gas with known parameters (density, refractive index and the Gladstone-Dale coefficient), and compare them with the experimental results. Once validated, the implemented BOS technique will be applied to specific experiments where the change of local density cannot be measured directly.

2 Theoretical Framework

For dielectric media, a relationship between the refractive index and the density can be obtained from the analysis of the polarization of the medium due to an external electric field. This expression is known as the Lorenz-Lorentz equation:

$$\frac{n^2 - 1}{n^2 + 2} = K\rho \tag{1}$$

where n is the refractive index of the medium, ρ its density, and K is a constant that depends on the number of molecules and the mean polarizability.

If the gas under study is diatomic, translucent and its refractive index is close to one, the Lorentz-Lorenz can be linearized and the Gladstone-Dale equation is obtained:

$$n - 1 = K_{G-D}\rho \tag{2}$$

with

$$K_{G-D}(\lambda) = 2.2244 \times 10^{-4} \times \left(1 + \left[6.7132 \times \frac{10^{-8}}{\lambda}\right]^2\right)$$

K_{G-D} is the Gladstone-Dale coefficient (Hartberger 2011). In standard conditions, this coefficient has a value of 0.229 cm^3/g for CO_2, when light of 532 nm is used. For other gases, it may vary roughly between 0.1 and 1.5 (Settles 2001; Kawahara et al. 2006).

2.1 Shadowgraph

The simplest shadowgraph array (Fig. 1) consists of a point light source and a screen. The rays emerging from the source pass through the medium of interest, usually called the schlieren object, where there is a density gradient; and are deflected an angle ε. They arrive at the screen with a displacement Δa with respect to its original reaching point. This technique gives the second derivative of the refractive index $\frac{\partial^2 n}{\partial x^2}$ (Settles 2001).

2.2 Schlieren

Schlieren arrays are more complicated (Fig. 2). A first lens collimates a beam leaving a point source; then a second lens refocuses it to an image of the point source. A knife is placed at the focus of the second lens to improve the contrast of the image, and thus detect small changes of the refractive index $\left(\frac{\partial n}{\partial x}\right)$ (Settles 2001).

Fig. 1 Diagram of the direct shadowgraph method in its simplest form (Settles 2001)
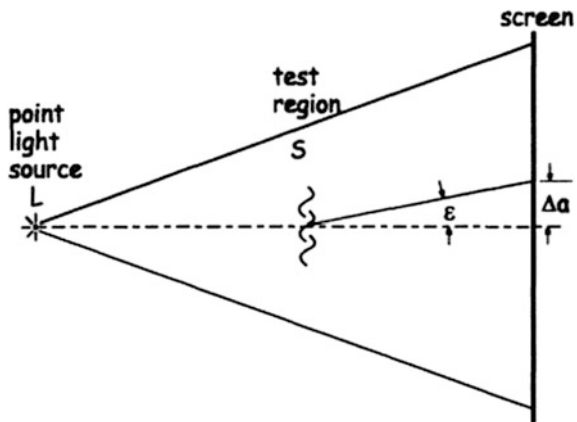
Fig. 2 Diagram of a simple schlieren system with a point light source (Settles 2001)
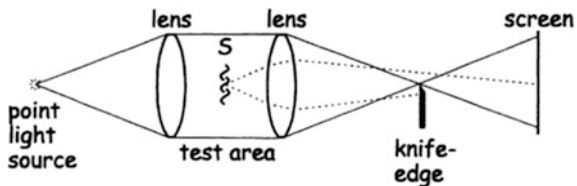
2.3 Background Oriented Schlieren

If we consider a light beam passing through a dot pattern (background), each dot will project a shadow on a screen far away. If a medium with different density is set in between the background and the screen, the rays will suffer a refraction of an angle ε and the shadows will have an apparent displacement Δy (Fig. 3) with respect to their original trajectory given by: Settles (2001), Elsing (2003)

$$\Delta y = M Z_D \varepsilon_i \tag{3}$$

where M is the optical magnification, Z_D the distance between the background and the schlieren object and ε_i the deflecting angles where the i subindex refers to the direction, are considered small so that Δy is perpendicular to the optical axis (Ota et al. 2011; Richard and Raffel 2001; Raffel 2015; Elsing 2003). These angles can be expressed as a function of the changes of the refractive index:

$$\varepsilon_i = \frac{1}{n_0} \int_{Z_D - z_0}^{Z_D + z_0} \frac{\partial n}{\partial x_i} dz \tag{4}$$

with i = 1, 2, then $\varepsilon_1 = \varepsilon_x$ y $\varepsilon_2 = \varepsilon_y$, n_0 the ambient refractive index, and the integration limits represent the schlieren object's borders along the optical axis (Vinnichenko et al. 2011; Raffel 2015; Elsing 2003; Iffa et al. 2010).

Due to the small angle hypothesis, the change of n along the schlieren object may be considered as a constant, so Eq. (4) can be written as:

$$\varepsilon_i = \frac{1}{n_0} \frac{\partial n}{\partial x_i} h \tag{5}$$
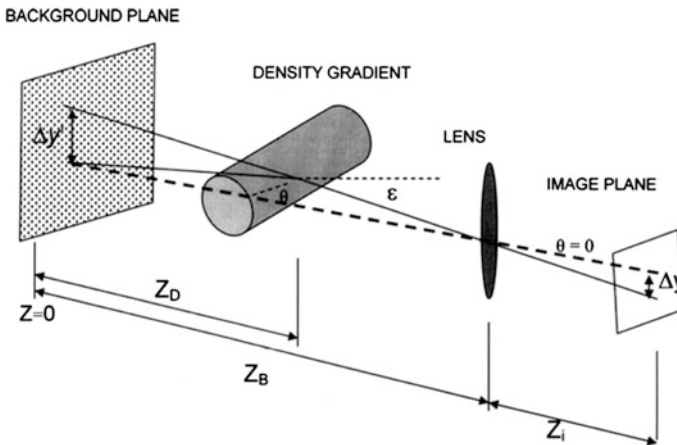
Fig. 3 BOS experimental set-up (Venkatakrishnan and Meier 2004)

where h (Vinnichenko et al. 2011) is the schlieren object's width. Substituting in Eq. (3), for each component, gives a system of differential equations for the refractive index.

$$
\begin{cases}
\frac{\partial n}{\partial x} = \frac{n_0 \xi_x}{M Z_D h} \\[2ex]
\frac{\partial n}{\partial y} = \frac{n_0 \xi_y}{M Z_D h}
\end{cases}
\tag{6}
$$

where $\xi = (\xi_x, \xi_y)$ is the apparent displacement vector measured for each dot or set of dots on the background. The usual form of the integration of this system, as presented by Vinnichenko et al. (2011), Raffel (2015), Tipnis et al. (2013) and Lee et al. (2013), comes from taking the derivative of each one with respect to the corresponding component and adding them. The result is a Poisson Equation, which can be solved numerically

$$
\frac{\partial^2 n}{\partial x^2} + \frac{\partial^2 n}{\partial y^2} = \frac{n_0}{M Z_D h} \left[\frac{\partial \xi_x}{\partial x} + \frac{\partial \xi_y}{\partial y} \right]
\tag{7}
$$

with the Gladstone-Dale equation, (7) can be written in terms of the density:

$$
\frac{\partial^2 \rho}{\partial x^2} + \frac{\partial^2 \rho}{\partial y^2} = \frac{1}{K_{G-D}} \frac{n_0}{M Z_D h} \left[\frac{\partial \xi_x}{\partial x} + \frac{\partial \xi_y}{\partial y} \right]
\tag{8}
$$

3 Experimental Set-Up

To calibrate the BOS technique, a Schlieren arrangement of parallel beams was set up with a white LED of 100 Watts as the light source and a High-Speed Camera Miro M-310 (Fig. 4). Two different gases with known parameters were used: CO_2 and Acetylene (C_2H_2).
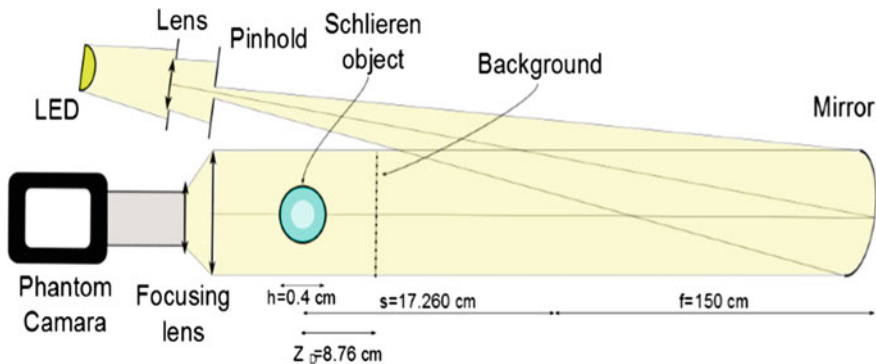
Fig. 4 Schlieren parallel beams arrangement

The environmental conditions in the laboratory are shown in Table 1:

The dominant wavelength of the LED, which is at 546 nm (green), was determined with a spectrophotometer. Figure 5 shows the spectrum.

A random dot pattern was used (Fig. 6):

Table 1 Environmental conditions

Refractive index	$n_{air} = 1.0002921$
Density	$\rho_{air} = 1.204 \, kg/m^3$
Temperature	20 °C
Pressure in Mexico City	0.765 atm
Humidity	40 %
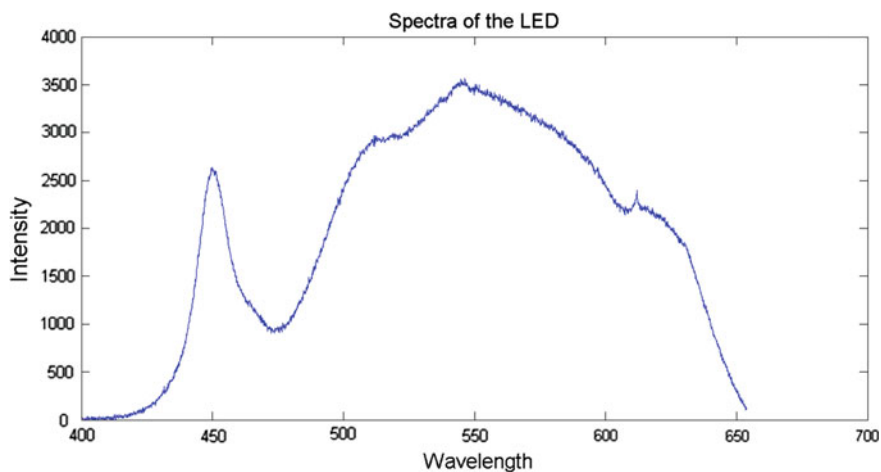
Fig. 5 Spectra of the LED
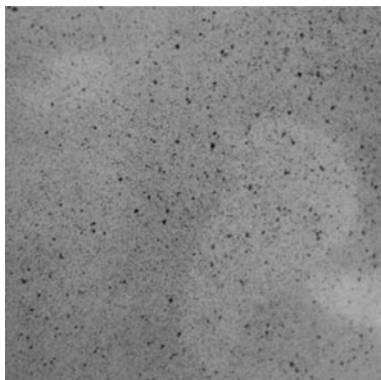
Fig. 6 Dot pattern

Two pictures of the background were taken with stationary air first, and then with another gas moving very slowly. The exposure time was 274.96 μs. Both images were processed dividing them into a 64 × 64 uniform pixel mesh. A computational algorithm was created to determine the vector displacement field, from it the changes in the index of refraction and when possible, the density.

4 BOS Algorithm

The important information of the phenomenon under study is obtained by comparing the two images. Each one can be represented as matrix where the numeric values are related either to a color or to a scale of gray. This is done by a computational algorithm of the next cross-correlation equation:

$$C(m,n) = \sum_i \sum_j PIP_1(i,j)PIP_2(i-m,j-n) \tag{9}$$

where PIP_1 and PIP_2 are the first and second images, respectively (Huang et al. 1997; Vinnichenko et al. 2011) (Fig. 7).

The cross-correlation compares pixel by pixel the two images. The maximum corresponds to the most probable displacement, and generates a corresponding vector in each interrogation area of the image. On certain applications, values like brightness can vary from one interrogation spot to another depending on the conditions under which the image was taken. It is then important to normalize the cross-correlation as shown by Eq. 10 (Huang et al. 1997, 2007).

Fig. 7 Diagram of the cross-correlation (Huang et al. 1997)
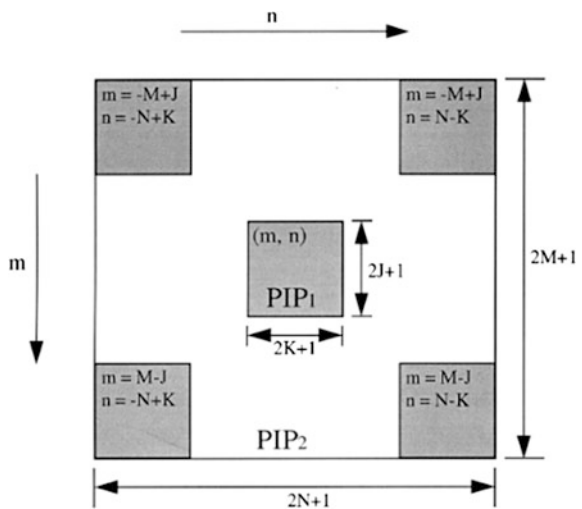
$$C'(m,n) = \frac{C(m,n)}{\left\{ \sum_{i,j} PIP_1^2(i,j) \sum_{i,j} PIP_2^2(i,j) \right\}^{1/2}} \tag{10}$$

Equation (9) yields an error of ± 0.5 pixel. In order to reduce this error it is important to locate the maximum of the correlation with the best possible accuracy. The algorithm uses a Gaussian method for curve fitting. Furthermore, the maxima of the correlations take the shape of a Gaussian distribution (Huang et al. 1997).

$$x = x_0 + \frac{logC(x_0-1,y_0) - logC(x_0+1,y_0)}{\{2[logC(x_0-1,y_0) + logC(x_0+1,y_0)] - 2logC(x_0,y_0)\}} \tag{11}$$

$$y = y_0 + \frac{logC(x_0,y_0-1) - logC(x_0,y_0+1)}{\{2[logC(x_0,y_0-1) + logC(x_0,y_0+1)] - 2logC(x_0,y_0)\}} \tag{12}$$

where (x_0, y_0) is a peak of the cross-correlation function $C(m,n)$.

The algorithm was applied to both images in order to obtain a displacement vector field (Fig. 8); the areas with no displacement were removed. The accuracy of the vector field increases as the interrogation area is reduced, so a refinement of the algorithm was made using an overlap of the interrogation areas.

- Dirichlet conditions in the boundaries parallel to the flow

$$\rho_0 = \rho_{air}$$

Fig. 8 Displacement vector field of a test with CO_2. The last part of the algorithm solves the Poisson equation numerically. Four boundary conditions were assumed (Vinnichenko et al. 2011; Venkatakrishnan and Meier 2004 and Tipnis et al. 2013)
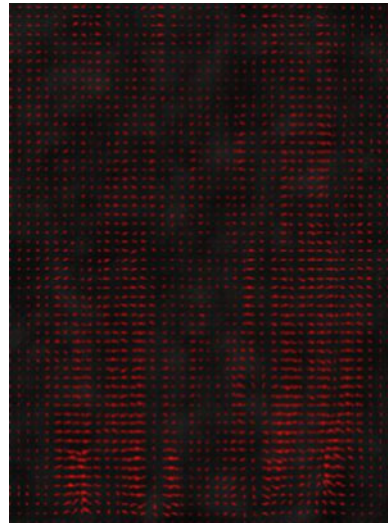
- Newmann conditions in the boundary perpendicular to the flow

$$\frac{\partial \rho}{\partial x} = 0$$

5 Results

The values measured near the flow entrance using the present technique are presented in Fig. 9:

- n = 1.00041
- $\rho = 1.74$ kg/m^3

Given the prevailing wavelength of the LED and the temperature of the laboratory, the used Gladstone-Dale constant for CO_2 was 2.275×10^{-4} m^3/kg (Huang et al. 1997).

For acetylene (C_2H_2) the results of the present technique are presented in Fig. 9. In this case, a Gladstone-Dale constant for the laboratory conditions was not found, therefore only the refractive index was measured, again near the flow entrance (red zones) (Fig. 10). The value obtained is

- n = 1.00055.
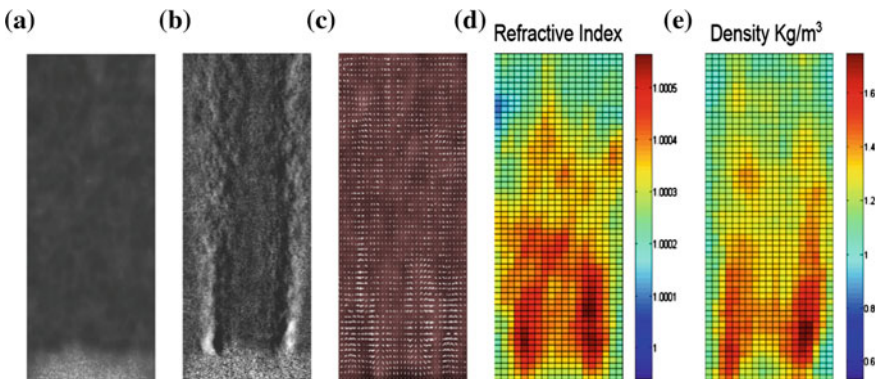
Fig. 9 a Reference pattern. **b** Gas. **c** Displacements vector field. **d** Refractive index. **e** Density
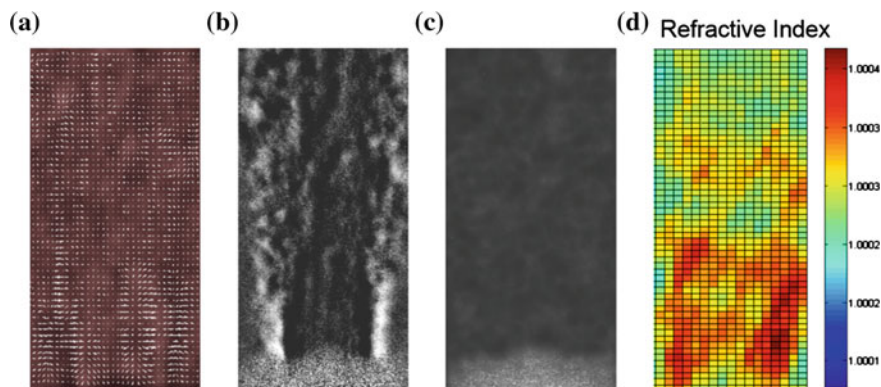
Fig. 10 **a** Displacements vector field. **b** Gas. **c** Reference pattern. **d** Refractive index

Table 2 Comparison of the density between value reported in literature and the result obtained in this work (www.chemicalbook.com/)

	Literature (kg/m^3)	BOS algorithm (kg/m^3)	Relative error (%)
CO_2	1.74	1.87	6.9

Table 3 Comparison of the refractive index between value reported in literature and the result obtained in this work (http://refractiveindex.info/)

	Literature	BOS algorithm	Relative error (%)
CO_2	1.00041	1.00046	0.005
C_2H_2	1.00055	1.00051	0.004

6 Analysis

A comparison between the experimental and expected values was made (Tables 2 and 3).

7 Conclusions

A BOS technique was implemented to measure the refractive index of two transparent gases: CO_2 and C_2H_2. When possible, this value was used to obtain the density through the Gladstone-Dale equation. The gases were introduced into stationary air. Near the entrance of the flow, the measured index of refraction for CO_2 is 1.00041 with an error of 0.005 %. The corresponding value for the density is

$1.74 \, \text{kg}/\text{m}^3$ with an error of $6.9\,\%$. For C_2H_2 the measured refractive index was 1.00055 with an error of 0.004%. No Gladstone-Dale constant was found for the laboratory conditions so the value density could not be determined. The experimental values were very close to those that appear in the literature, so the implemented BOS technique was validated.

As the distance from the tube increased, values of density and refractive index decreased as expected, due to the diffusion of the gas in air.

The technique can be applied to study supersonic flows where changes in the density are important and difficult to measure.

References

Atcheson B et al (2007) Imaging and 3D tomographic reconstruction of time-varying, inhomogeneous refractive index fields, UBC-C

Clem M, Brown C, Fagan A (2013) Background oriented Schlieren implementation in a jet-surface interaction test. In: 51st AIAA Aerospace sciences meeting

Elsing G (2003) Density measurements by means of schlieren methods, TUDelft

Hartberger JE (2011) Background oriented schlieren pattern optimization. Air Force Institute of Technology, Wright-Patterson Air Force Base, Ohio, USA

Huang H, Dabiri D, Gharib M (1997) On errors of digital particle image velocimetry. Meas Sci Technol 8(12):1427–1440

Iffa E, Aziz A, Malik A (2010) Concentration measurement of injected gaseous fuel using quantitative schlieren and optical tomography. J Eur Opt Soc:10029

Lee J, Kim N, Min K (2013) Measurement of spray characteristics using the background-oriented schlieren technique. Meas Sci Technol 24:025303

Merzkirch W (1987) Flow visualization. Edit. Academic, USA. Capítulo 3, pp 116–123

Nobuyuki K, Eiji T, Kenji O, Kazuhiro G (2006) Unburned gas temperature measurement in an SI engine using fiber-optic laser interferometry. Technical Papers and Articles, Yamaha Motor Technical Review, M&D

Ota M, Hamada K, Kato H, Maeno K (2011) Computed-tomographic density measurement of supersonic flow field by colored-grid background oriented schlieren (CGBOS) technique. Meas Sci Technol 22:104011

Ota M, Kato H, Maeno K (2012) Improvements of special resolution of corlored-grid background oriented schlieren (CGBOS) technique by introducing telecentric optical system and reconstruction of density field. In: 15th International symposium on flow visualization

Raffel M (2015) Background-oriented schlieren (BOS) techniques. Exp Fluids 56:60

Richard H, Raffel M (2001) Principle and applications of the background oriented schlieren (BOS) method. Meas Sci Technol 12:1576–1585

Settles GS (2001) Schlieren and shadowgraph techniques; visualizing phenomena in transparent media. Springer, USA, pp 26–37

Tipnis T, Finnis M, Knowles K, Bray D (2013) Density measurements for rectangular free jets using background-oriented schlieren. Aeronaut J 117(1194):771–784

van Hinsberg N, Rösgen T (2014) Density measurements using near-field background-oriented Schlieren. Exp Fluids 55:1720

Venkatakrishnan I, Meier G (2004) Density measurements using the background oriented schlieren technique. Exp Fluids 37:237–247

Venkatakrishnan L, Wiley A, Kumar R (2010) Density field measurements of a supersonic impinging jet wth microjet control. In: 48th AIAA Aerospace sciences meeting

Vinnichenko N, Znamenskaya I, Glazyrin F, Uvarov A (2011) Study of background oriented schlieren method accuracy by menas of synthetic images analysis. Faculty of Physics, Moscow State University, Moscow

Measurement of the Density Inside a Supersonic Jet Using the Background Oriented Schlieren (BOS) Technique

D. Porta, C. Echeverría, A. Aguayo, J.E. Hiroki Cardoso and C. Stern

Abstract Shock waves are usually modeled as sharp discontinuities in pressure, density and temperature. A Background Oriented Schlieren (BOS) system was set-up to determine the actual widths of the density gradients in these regions of a supersonic jet. The technique consists on a comparison between a reference image of a dot matrix and another image of the same matrix deformed by the flow of a transparent gas. The apparent displacement of the dots in the second image, due to changes in the index of refraction, can be related to changes in the density. The flow is generated when compressed air passes through a straight nozzle with a diameter of 4 mm. Density measurements along the centerline are presented for three Mach numbers: 2.79, 1.89 and 1.79.

1 Introduction

1.1 Previous Work

Background Oriented Schlieren (BOS) is a relatively new technique, (Meier 1999), that has proven its effectiveness to determine changes in the local density of

D. Porta (✉) · C. Echeverría · A. Aguayo · J.E.H. Cardoso · C. Stern
Facultad de Ciencias, UNAM, Av. Universidad 3000, Circuito Exterior S/N Delegación Coyoacán, C.P. 04510 Ciudad Universitaria, D.F., Mexico
e-mail: alviond@gmail.com

C. Echeverría
e-mail: carlosea1982@gmail.com

A. Aguayo
e-mail: aaguayoo92@gmail.com

J.E.H. Cardoso
e-mail: jehcs55@gmail.com

C. Stern
e-mail: catalina@ciencias.unam.mx

phenomena in transparent compressible flows like shock waves Venkatakrishnan (2004). Goldhahn and Seume (2007) made a tomographic reconstruction from BOS applied to two parallel supersonic jets on a sub-expanded regime. Clem et al. (2012) compared the results obtained with BOS to shadowgraphs of a supersonic flow in the range of $1 < M < 1.7$ produced by a convergent divergent nozzle. He obtained the shock pattern and associated it with screech, identifying 8 states. Tipnis (2013) obtained a good correlation between his BOS results and his simulation of a supersonic jet.

1.2 Description of the Technique

The BOS technique allows the quantification of local changes of density in a transparent medium. It consists in the digital comparison of two photographs of the same background, a dot matrix. The first image is obtained in the absence and the second in the presence of the flow. The apparent displacement of the background is produced by changes in the refractive index due to an axisymmetric supersonic jet, Fig. 1.

Displacements are determined by a cross-correlation, with the same software used in PIV (Particle Image Velocimetry). The displacements can be related to the change in refractive index. Finally, the Gladstone Dale equation relates the refractive index with the density.
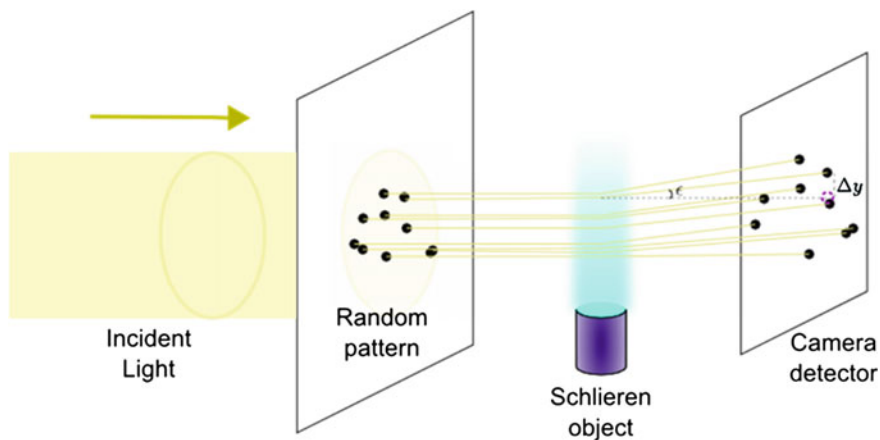
Fig. 1 Apparent displacement of the background due to local changes in the density produced by the schlieren object

2   Theoretical Background

For a diatomic gas, with refractive index close to one, we can use the Gladstone-Dale equation, which relates the density of the medium with the refractive index:

$$n - 1 = K_{G-D}\rho \tag{1}$$

where n is the refractive index of the medium of incidence, ρ is its density and K_{G-D} is the Gladstone-Dale coefficient which depends on the medium and the wavelength of the light.

When a beam of light passes through a matrix of dots (background), each of the dots will cast a shadow. If a different medium, called schlieren object, is placed between the matrix and the screen or camera, the light rays deviate an angle ε, and the shadows of the dots in the matrix have an apparent shift Δy that can be written as (Raffel 2015)

$$\Delta y = M Z_D \varepsilon_i \tag{2}$$

where M is the magnification of the optical arrangement, and Z_D is the distance from the schlieren object to the background and ε_i are the deflecting angles, where the i subindex refer to the angle direction. Under the assumption that deflection angles are small, and occur in the direction perpendicular to the optical axis (x and y), they can be expressed in terms of changes in the refractive index by the following equation (Raffel 2015; Venkatakrishnan 2004; Vinnichenko 2011):

$$\varepsilon_{x_i} = \frac{1}{n_0} \int\limits_{Z_D - z_0}^{Z_D + z_0} \frac{\partial n}{\partial x_i} dz \tag{3}$$

where n_0 is the refractive index of the surroundings, and the integration limits represent the boundaries along the optical axis of the schlieren object.

Under the assumption of small angles, Eq. (3) can be re written as (Vinnichenko 2011):

$$\varepsilon_i = \frac{1}{n_0} \frac{\partial n}{\partial x_i} h \tag{4}$$

where h is the width of the schlieren object. Substituting Eq. (4) in (2), a differential equation for the refractive index in each direction is obtained:

$$\begin{cases} \dfrac{\partial n}{\partial x} = \dfrac{n_0 \xi_x}{M Z_D h} \\[2mm] \dfrac{\partial n}{\partial y} = \dfrac{n_0 \xi_y}{M Z_D h} \end{cases} \tag{5}$$

where $\xi = (\xi_x, \xi_y)$ is the apparent displacement vector calculated for each point or set of points in the background. The usual way to integrate these equations, as shown by Vinnichenko (2011), Raffel (2015), Tipnis (2013) and Lee (2013), among others, is to derive both equations with respect to the corresponding variable and to add them. This results in a Poisson equation that is solved by a successive over-relaxation method:

$$\frac{\partial^2 n}{\partial^2 x} + \frac{\partial^2 n}{\partial^2 y} = \frac{n_0}{MZ_D h}\left[\frac{\partial \xi_x}{\partial x} + \frac{\partial \xi_y}{\partial y}\right] \tag{6}$$

Substituting the index of refraction by the density using the Gladstone-Dale equation, Poisson equation for the density is obtained:

$$\frac{\partial^2 \rho}{\partial^2 x} + \frac{\partial^2 \rho}{\partial^2 y} = \frac{1}{K_{G-D}}\frac{n_0}{MZ_D h}\left[\frac{\partial \xi_x}{\partial x} + \frac{\partial \xi_y}{\partial y}\right] \tag{7}$$

3 Supersonic Jet

As air flows through a straight nozzle, it can be accelerated to speeds (u) greater than the speed of sound (c). The dimensionless parameter used to characterize this phenomenon is the Mach number (M), defined as the ratio between the velocity of the object and the speed of sound.

Compressibility effects are significant from $M \sim 0.7$. A flow is considered supersonic when $1 \leq M < 5$. Supersonic flows are very complex, they are compressible and turbulent. An apparently stationary shock structure appears close to M = 1, with abrupt changes in density and pressure. They are usually represented as oblique lines.

The Mach number of a supersonic flow can be determined through Eq. 8 (Chapman 2000), that relates M with the complementary angle of the first shock wave with the nozzle as shown in Fig. 2.

$$M = \sqrt{1 + \cot^2\alpha} \tag{8}$$

4 Experimental Procedure

The experimental device used is shown in Fig. 3. The light source is a 100 Watts white LED (cree® Xlamp®cXa3050), which is collimated and sent to a first surface spherical mirror with a diameter of 15 cm. From the mirror parallel rays leave. The background matrix and the supersonic flow are placed in this region. The light is then captured by a focusing lens that directs the light into a fast camera (Phantom Miro M310) with another lens (Infinity CENTRIMAX K1). The system has a magnification of 0.6.
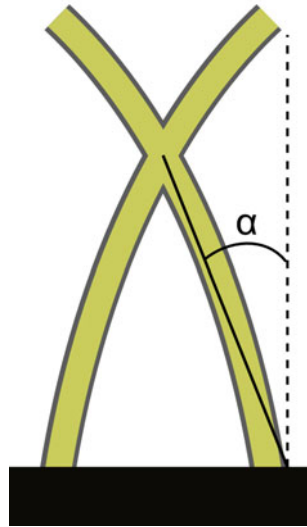
Fig. 2 Schematic of the angle used to determine the Mach number
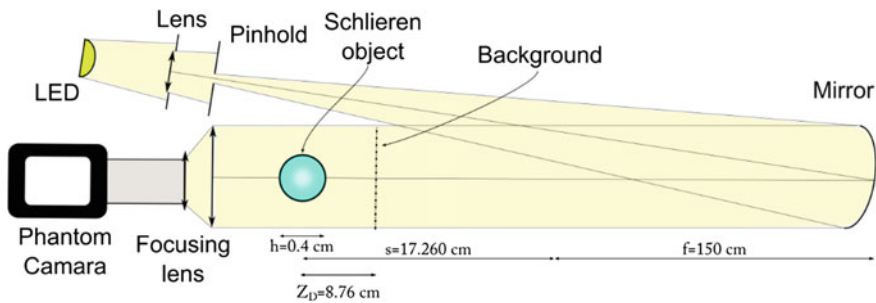
Fig. 3 Experimental setup

The supersonic flow is produced with a straight nozzle with a diameter of 4 mm. Experiments were performed at an altitude of 2290 m above sea level at a room temperature of 20 °C and relative humidity of 30 %.

The supersonic jet was recorded at 5435 fps with an exposure time of 80 ms and a resolution of 768 by 768 pixels.

5 Experimental Results

The three frames shown in Fig. 4 were chosen for analysis. The angle of the shock was measured from the frames using ImageJ software. Mach numbers 2.79, 1.89 and 1.79 were calculated with Eq. 8.
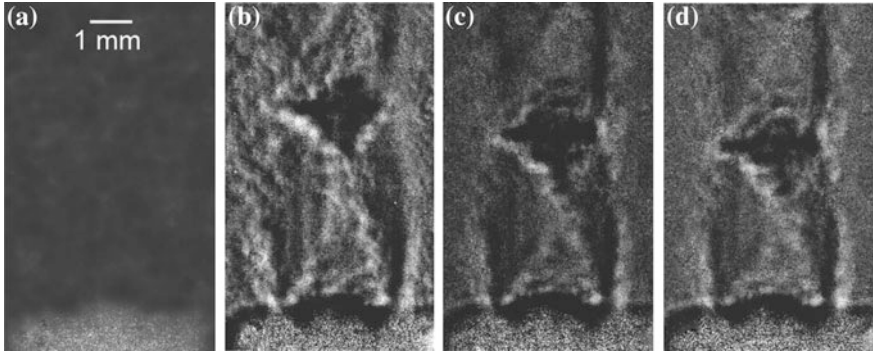
Fig. 4 Background with supersonic jet. **a** Original image, **b** M = 2.78, **c** M = 1.89 and **d** M = 1.79

Software was developed based on the work of Huang (1997). The technique was calibrated (Aguayo et al. 2014) for local changes in density. The apparent displacement was obtained using cross-correlation between the frames with a schlieren object and without it. The analysis was performed with interrogation areas of 64 by 64 pixels and 8 pixels refinement. The results are shown in Fig. 5.

Once the displacement vector field is determined, the results are used to obtain a Poisson equation for the index of refraction. To solve Eq. 6, inhomogeneous
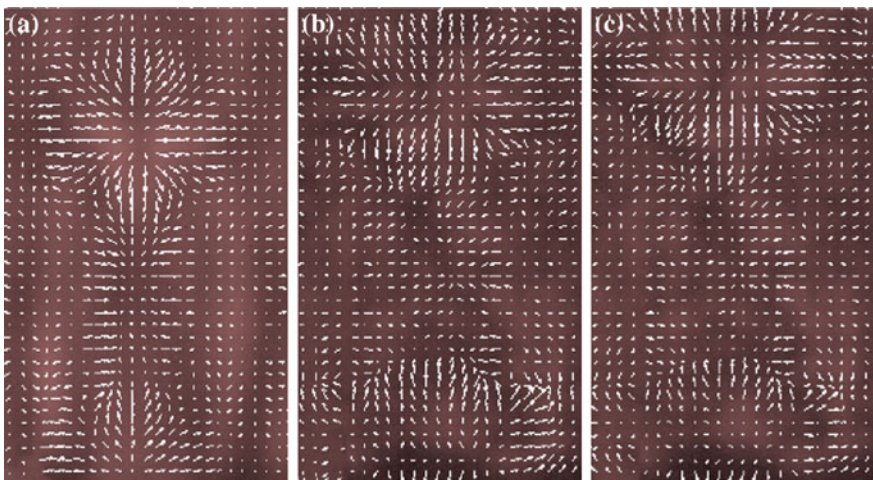
Fig. 5 Displacement field of the jet at three different Mach numbers. **a** M = 2.78, **b** M = 1.89, **c** 1.79 obtained from the images shown in Fig. 4
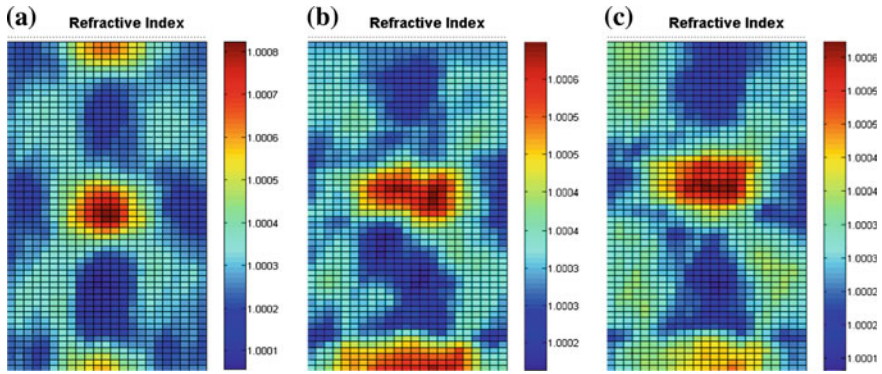
Fig. 6 Results obtained by solving the Poisson equation for the refractive index for each of the displacement fields. **a** M = 2.78, **b** M = 1.89, **c** M = 1.79

Dirichlet conditions were used in the eastern and western border, and Newmann boundary conditions in the northern and southern borders (Aguayo et al. 2014). The results are shown in Fig. 6.

With these results the density field is obtained through the Gladstone-Dale Eq. (1) for the supersonic flow. For air, the Gladstone-Dale constant is $K_{G-D} = 2.2649 \times 10^{-4}$ m^3/Kg. The results are shown in Fig. 7.

It may be noted in Fig. 6 that the greatest value of the refractive index corresponds to M = 2.78 and the smallest to M = 1.79. The same applies to the density.
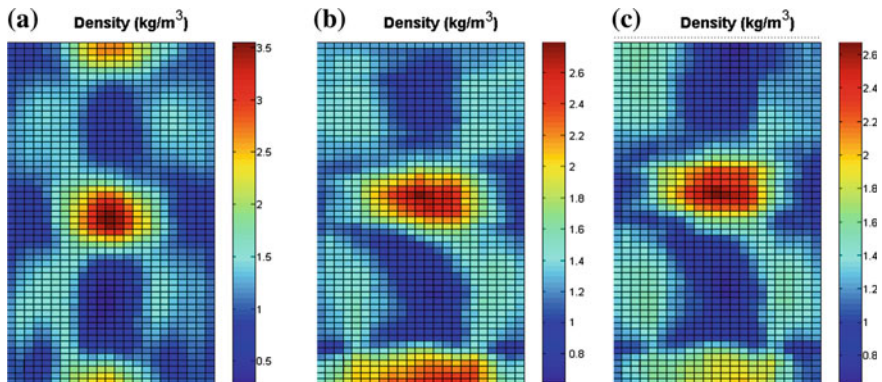
Fig. 7 Results obtained by solving the Poisson equation and use Gladstone-Dale equation for the density for each of the displacement fields. **a** M = 2.78, **b** M = 1.89, **c** M = 1.79
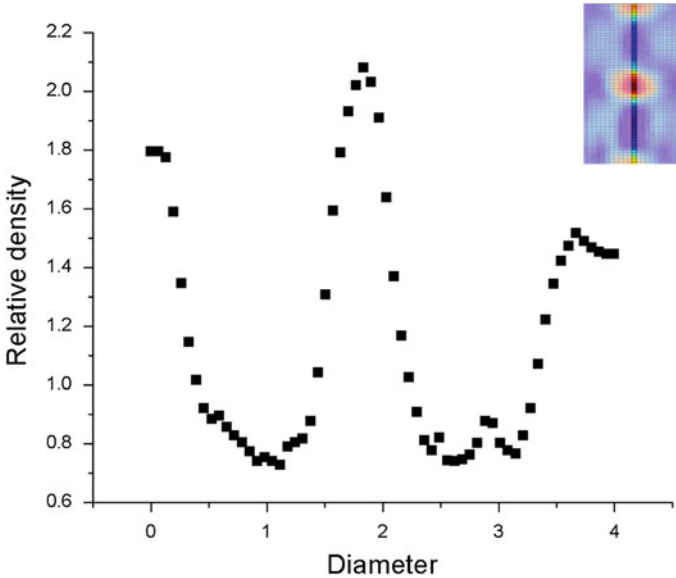
Fig. 8 Plot of density versus position along the centerline of a supersonic jet with M = 2.79

These results are consistent with shadowgraph images of the same supersonic flow. As could be expected from the linear relationship between the index of refraction and the density, their scalar fields are similar.

Figure 8 shows the density values along the centerline of the flow.

As can be observed in Fig. 8, the density at the exit is greater than that of the stagnant air, then decays below the atmospheric value and rises again to a maximum value. It keeps oscillating along the shock pattern.

An important result of this experiment is that density changes do not occur abruptly but through a certain thickness (3.4 mm). That is, shock waves have a finite width.

Figure 9 shows that the behavior of the three supersonic flows is similar. As the Mach number diminishes, the maximum value of the density is lower and it is reached at a shorter distance from the nozzle.
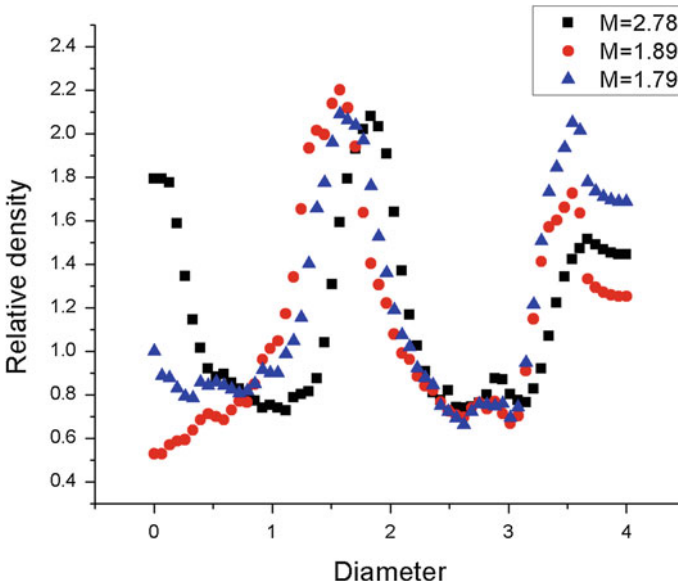
Fig. 9 Plot of density versus position along the centerline for three flows with supersonic Mach numbers of 2.78, 1.89 and 1.79 respectively

6 Conclusions

The experiment presented in this papers shows that BOS is a nonintrusive technique that can detect and quantify changes in the local densities, in flows where this measurement would be otherwise impossible. Thus, the apparent displacements, the refractive index and the density inside an axisymmetric supersonic jet were measured successfully. The results are consistent with the behavior found by Tipnis (2013). However, the geometry of the nozzle and the Mach numbers are different, so the numerical values cannot be compared. The technique has given new results that combined with other techniques used for the local velocity can give new insight of the behavior of supersonic flow, in particular close to the shock structure. In particular, the behavior of a fluid particle in this region is not understood.

Future work includes a more profound analysis of the boundary conditions used to solve the Poisson equation. The assumption that the bottom boundary condition is $\frac{\partial \rho}{\partial X} = 0$ should be investigated more carefully.

Also, a refinement of the background matrix should be done, to reduce the uncertainty in the measurement of the displacements. The exposure times should be evaluated.

The great advantage of BOS over other techniques like PIV and LDA, is that it is completely non-intrusive.

Absolute values of the local densities instead of ratios could be determined, since the technique was calibrated in previous experiments.

References

Aguayo A, Cardoso H, Echeverría C, Porta D, Stern C (2014). Calibration of a background oriented schlieren (BOS). Personal communication

Chapman CJ (2000) High speed flow. Cambridge University Press, Cambridge

Goldhahn E, Seume J (2007) The background oriented Schlieren technique: sensitivity, accuracy, resolution and application to a three-dimensional density field. Exp Fluids 43:241–249

Huang H, Dabiri D, Gharib M (1997) On errors of digital particle image velocimetry. Meas Sci Technol 8(12):1427–1440

Lee J, Kim N, Min K (2013) Measurement of spray characteristics using the background-oriented Schlieren technique. Meas Sci Technol 24:025303

Meier GEA (1999) Patente: Hintergrund-Schlierenverfahren. Deutsche Patentanmeldung DE 19942856:A1

Michelle C, Khairul Z, Amy F (2012) Background oriented Schlieren applied to study shock spacing in a screeching circular jet. In: 50th AIAA Aerospace sciences meeting including the new horizons forum and aerospace exposition, 9–12 Jan 2012, Nashville Tennessee

Raffel M (2015) Background-oriented Schlieren (BOS) techniques. Exp Fluids 56:60

Tipnis T, Finnis M, Knowles K, Bray D (2013) Density measurements for rectangular free jets using background-oriented Schlieren. Aeronaut J 117(1194):771–784

Venkatakrishnan L, Meier GEA (2004) Density measurements using the background oriented Schlieren technique. Exp Fluids 37:237–247

Vinnichenko N, Znamenskaya I, Glazyrin F, Uvarov A (2011) Study of background oriented schlieren method accuracy by means of synthetic images analysis. Faculty of Physics, Moscow State University, Moscow

Part II
Environmental Applications

Experimental Evaluation of Specific Components Working in an Environmentally Friendly Cooling System

G. Gutierrez Urueta, F. Oviedo, R. Peña, P. Rodríguez-Aumente, C. Monreal and J. Arellano

Abstract Solar cooling is an interesting application regarding the use of renewable energy to activate climatization systems. Thermally driven chillers (absorption or desorption systems) use the solar energy to provide heat to the generator of an absorption chiller. In this work, an experimental facility, designed for testing innovative components of a simple effect absorption cooling system, is presented. The study is focused on performance analysis of evaporators and its influence on the overall performance of the machine. Experimental results indicate the detection of some operational difficulties. Due to the particular design of the machine, which contains two evaporators, the distribution of refrigerant mass flow rate is not symmetrical in some cases. Therefore, one of the evaporators could be not operating. This situation explains the decrease of cooling power when it is supposed to have an increasing tendency, according to the thermal power supplied to the generator of the machine.

G. Gutierrez Urueta (✉) · F. Oviedo · R. Peña · C. Monreal · J. Arellano
Facultad de Ingeniería, Universidad Autónoma de San Luis Potosí, Dr. Manuel
Nava # 8, Zona Universitaria Poniente, C.P., 78290 San Luis Potosí, Mexico
e-mail: geydy.gutierrez@uaslp.mx

F. Oviedo
e-mail: francisco.oviedo@uaslp.mx

R. Peña
e-mail: rafael.pena@uaslp.mx

C. Monreal
e-mail: cintiamj123@gmail.com

J. Arellano
e-mail: carlos.arellano@uaslp.mx

P. Rodríguez-Aumente
Departamento de Ingeniería Térmica y de Fluidos, Universidad Carlos III de Madrid,
Av. Universidad 30, C.P., 28911 Leganés, Madrid, Spain
e-mail: aument@ing.uc3m.es

Nomenclature

COP	Coefficient of performance
h	Enthalpy (kJ kg^{-1})
K	Loss coefficient
LiBr	Lithium bromide
$\dot{m}$	Mass flow rate (kg h^{-1})
P	Absolute pressure (mbar)
PHE	Plate heat exchanger
$\dot{Q}$	Thermal power (kW)
t	Temperature, external (°C)
T	Temperature, internal (°C)
u	Velocity (ms^{-1})
x	Quality

Subscripts

A	Absorber
C	Condenser
ch	Chilled
E	Evaporator
f	Friction
exp	Experimental
G	Generator
i	Inlet
l	Liquid
o	Outlet
r	Recirculated
ref	Refrigerant
set	Established value
t	Tube
v	Vapour
V	At valve conditions
w	Water

Greek letter

η	Efficiency
ρ	Density

1 Introduction

Absorption technology consists of using heat, instead of electricity, to activate a cycle and produce cooling or heating. The electricity consumption due to the existence of a pump in the cycle is very low in comparison with the one needed to activate a compressor in a conventional system. This offers the possibility of avoiding polluting emissions to atmosphere and increasing sustainability.

Solar cooling is an interesting application of the use of renewable energy to activate climatization systems. The heat obtained from solar energy is utilized in the generator to operate in a single effect cycle. The growing importance of solar energy systems makes absorption systems an alternative for use in summer for air conditioning.

With the objective of improving the absorption in a chiller, the adiabatic process is being investigated. It consists on dispersing the solution inside an adiabatic chamber. The resulting heat is extracted downstream using a compact heat exchanger. Thus, the mass and heat transfer processes that occurs simultaneously in conventional absorbers, are split in separated apparatus when the adiabatic absorption is used. The works developed by Gutierrez-Urueta et al. (2006, 2011), Venegas et al. (2004, 2005), Arzos et al. (2005), Warnakulasuriya and Worek (2006), Elperin et al. (2007) and Wang et al. (2007) summarizes state of the art, including experimental and theoretical studies concerning adiabatic absorption.

Interpretation of experimental data must incorporate the particular features, in both design and operation, of the facility here presented. Once the overall performance of the machine is defined, it is necessary to carry out the particular detailed analysis of each component in order to explain their effects on the overall performance obtained. In this paper, the analysis is focused on the evaporators.

2 Experimental Set Up

The diagram of the experimental facility is presented in Fig. 1. It consists of a single-effect water-lithium bromide absorption cooling system. The test facility design incorporates compact plate heat exchangers (PHEs), due to the well-known benefits regarding high heat transfer capacity in a reduced volume.

The absorption process takes place in an adiabatic chamber and the heat is extracted in an external PHE (subcooler). Because the solution absorbs less vapor as its temperature is higher, it is necessary to recirculate part of the solution ($\dot{m}_r$) to the absorber after it has been cooled in the PHE. A pump is used to achieve this recirculation and also to carry the weak solution to the generator. Both the solution coming from the generator $\dot{m}_{strong}$ and the re-circulated solution $\dot{m}_r$ flow inside the absorber as free falling drops. The objective of placing two evaporators is having a larger heat exchange area available and to guarantee the symmetry in the supply of vapour to the absorption vessel. Nevertheless, distribution problems in the
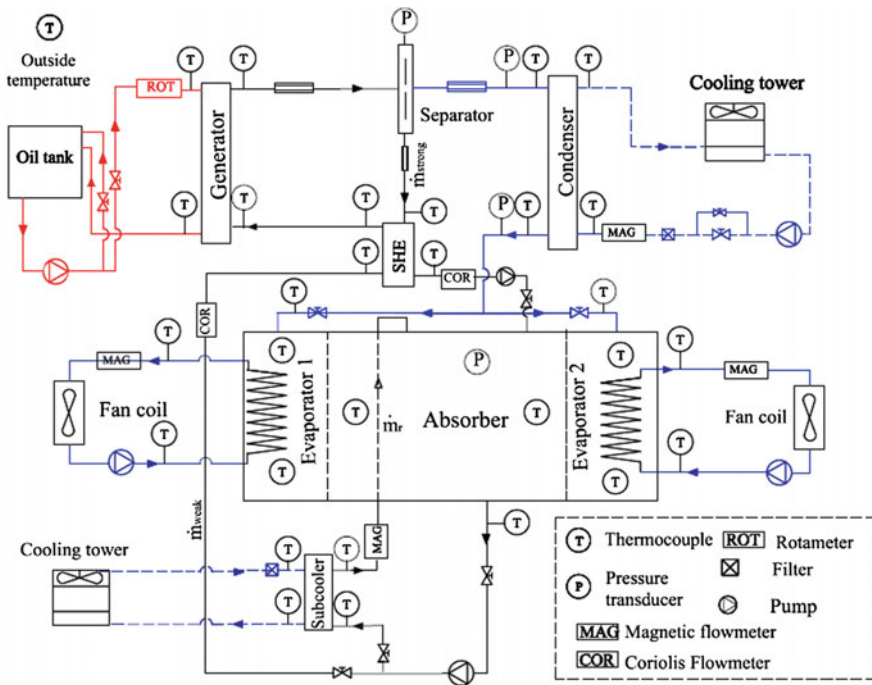
Fig. 1 Diagram of the experimental facility

refrigerant flow were detected; which is discussed in next sections. The experimental setup configuration, the data acquisition system and the experimental procedure were described in detail in previous works (Gutiérrez-Urueta 2006, 2011). The facility is highly instrumented, such that individual component performance can be evaluated.

Data of temperature, pressure and mass flow rates in every component were recorded in intervals of 0.5 s in order to accurately determine steady state periods. The experimental setup was configured to allow determining the coefficient of performance (*COP*) and thermal powers exchanged in the different components.

3 Evaporators Performance and Refrigerant Mass Flow Rate Distribution

In a previous work (Gutierrez-Urueta et al. 2011) the drastic fall in the cooling capacity at high generation temperatures was observed (Fig. 2). The experimental data corresponding to this figure was obtained through the control and variation of external fluid temperature at the generator, t_{set}, and fixing the weak solution mass flow rate, $\dot{m}_{weak}$. Due to the obvious dependence of the performance and the
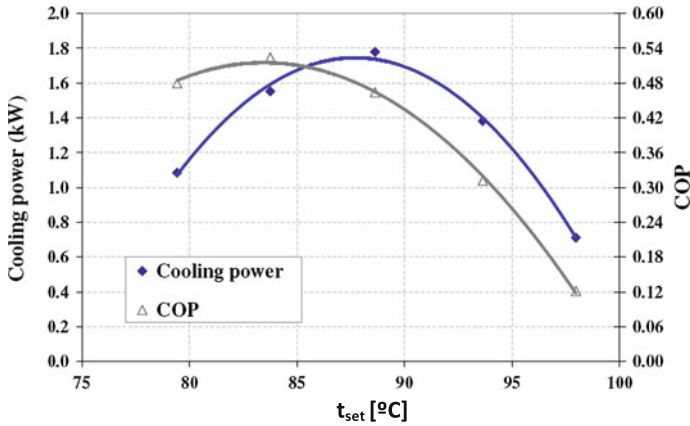
Fig. 2 Influence of hot fluid temperature on cooling power and coefficient of performance at weak solution mass flow rate $\dot{m}_{weak} = 230\,kg/h$

cooling capacity obtained, the experimental results suggest that the evaporation process could not be completed. For this reason, the present study considers the evaporators as the principal component to be analyzed. In the following, the evaporators' efficiency and refrigerant mass flow rate distribution to the evaporators will be estimated and discussed.

For all the evaluation parameters described next and for the thermo-physical and transport properties calculations, the software Engineering Equation Solver (EES) was used.

3.1 Evaporators Efficiency

An energy balance in the evaporators allows the calculation of the maximum cooling capacity, as follows:

$$\dot{Q}_{E,ref} = \dot{m}_{ref} \cdot (h_{E,i} - h_{E,o}) \tag{1}$$

The inlet evaporator enthalpy $h_{E,i}$ was obtained from the enthalpy corresponding to the liquid water at condenser outlet, Eq. (2), assuming that isenthalpic processes take place in the expansion valve. The vapor enthalpy at the evaporator outlet $h_{E,o}$ was calculated considering that vapor is saturated, Eq. (3).

$$h_{iE,in} = f(T_{C,o}, P_{C,o}) \tag{2}$$

$$h_{E,o} = f(P_E, x = 1) \tag{3}$$

Equation (1) gives the cooling capacity that would be obtained if the entire refrigerant evaporated. In order to measure the quantity of evaporated refrigerant, and therefore the performance of evaporators, $\dot{Q}_{E,\,ref}$ is compared with the cooling capacity calculated through an energy balance on the external flow:

$$\dot{Q}_{E,\,\exp} = \dot{m}_{chw} \cdot C_w \cdot (t_{chw,\,i} - t_{chw,\,o}) \qquad (4)$$

The fraction of refrigerant evaporated, named from now on efficiency of evaporators, is then obtained by dividing Eqs. (4) and (1):

$$\eta_E = \frac{\dot{Q}_{E,\,\exp}}{\dot{Q}_{E,\,ref}} \qquad (5)$$

The corresponding COP_{ref} is calculated using Eq. (6) therefore allowing the comparison of maximum and experimental values:

$$COP_{ref} = \frac{\dot{Q}_{E,\,ref}}{\dot{Q}_{G,\,\exp}} \qquad (6)$$

$$\dot{Q}_{G,\,\exp} = \dot{m}_{oil} \cdot C_{oil} \cdot (t_{oil,\,i} - t_{oil,\,o}) \qquad (7)$$

These parameters allow expressing the behavior of the evaporators, because their variation with operating conditions of the machine is significant, as discussed below.

3.2 Refrigerant Mass Flow Rate Distribution

Estimation of the quantity of refrigerant going to each evaporator, $\dot{m}_1$ and $\dot{m}_2$, is important for the evaluation of their individual performance due to its strong influence over the resulting global performance of the system.

Ideally, the refrigerant mass flow rate distribution is expected to be symmetrical. But in practice this is not the case, due to the different opening of expansion valves, or different length and height of both connecting pipes. Temperatures at the end of the process, after the expansion valves, will also be different as a consequence of the different pressure drop in each stream.

Figure 3 represents the diagram of the refrigerant distribution system in the machine under study. The boundary of control volume goes from the condenser outlet to the inlet of evaporators. The expansion valves corresponding to each evaporator are represented as V_1 and V_2. The other valves (d_1 and d_2) represent the expansion process taking place inside the evaporators, in the orifices of distribution tubes. E_1 and E_2 represent the refrigerant conditions at the state of the evaporation process.

Fig. 3 Diagram of refrigerant mass flow rate distribution from condenser (c) to evaporators (E_1 and E_2)
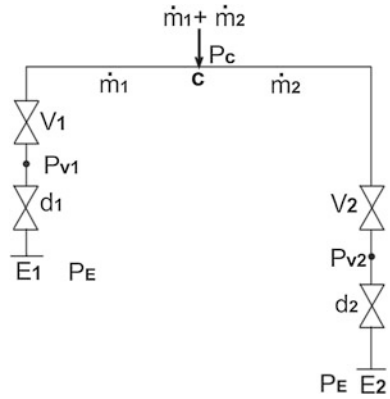
In the following, the analysis of the system is developed with the aim to determine the specific quantity of refrigerant going to each evaporator.

High and low pressures, as well as temperatures after the expansion valves T_{V1} and T_{V2} are known from the experimental data. The following data are therefore known: P_C, P_{V1}, P_{V2}, P_E, h_C.

The unknown data are: $\dot{m}_1$, $\dot{m}_2$, ρ_{V1}, ρ_{V2}, ΔP_{fd1}, ΔP_{fd2}. The last two terms represent the pressure drop due to the expansion of refrigerant in the evaporators inlet (subscript d), corresponding to each valve. Figure 4 represents the Temperature-Entropy diagram of the process. This diagram aims to show the difference of output conditions (quality) of the refrigerant flow going to each evaporator. In most cases, the temperature of each flow is different, as seen in next section.

Knowing that $\Delta P_{fv} = K \cdot \frac{1}{2} \cdot \rho \cdot (u)^2 = K \cdot \frac{1}{2} \cdot \rho \cdot \left(\frac{\dot{m}}{\rho A_t}\right)^2$

We obtain:

$$\dot{m} = A_{effective} \cdot \sqrt{2 \cdot \rho \cdot \Delta P_{fv}} \tag{8}$$

$$P_{V1} - P_E = \Delta P_{fd1} \tag{9}$$

Fig. 4 Diagram Temperature—Entropy for the refrigerant distribution system
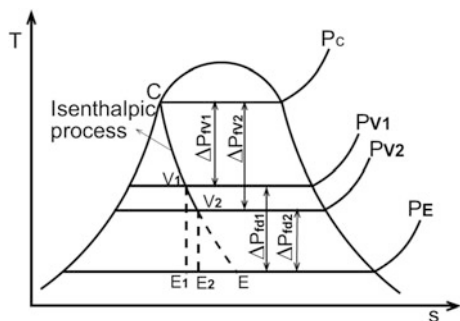
$$P_{V2} - P_E = \Delta P_{fd2} \tag{10}$$

P_{V1} and P_{V2} are the saturation pressures corresponding to T_{V1} and T_{V2}, respectively.

The two phase flow densities ρ_{V1} and ρ_{V2} can be estimated from h_C and T_{V1}, T_{V2}.

From (8) and assuming that $A_{ed2} = A_{ed1} = A_{de}$.

$$\dot{m}_1 = A_{de} \cdot \sqrt{2 \cdot \rho_{V1} \cdot \Delta P_{fd1}} \tag{11}$$

$$\dot{m}_2 = A_{de} \cdot \sqrt{2 \cdot \rho_{V2} \cdot \Delta P_{fd2}} \tag{12}$$

Combining (11) and (12):

$$\frac{\dot{m}_1}{\dot{m}_2} = \sqrt{\frac{\rho_{V1}}{\rho_{V2}} \cdot \frac{\Delta P_{fd1}}{\Delta P_{fd2}}} \tag{13}$$

$$\dot{m}_{ref} = \dot{m}_1 + \dot{m}_2 \tag{14}$$

Solving the equation system defined by Eqs. (9), (10), (13) and (14), the refrigerant mass flow rate distribution is estimated.

4 Results and Discussions

Results of the equation system previously explained allow the calculation of the quantity of refrigerant mass flow rate, $\dot{m}_{ref}$, received by each evaporator. Figure 5 illustrates this distribution for the different experiments carried out. This figure is an illustrative example to have an idea about the distribution of the refrigerant and the corresponding inlet generator temperature ($t_{Gi} = t_{set}$) along the whole experimental campaign. In those experiments in which the distribution is more equitable, the cooling power associated is higher. Besides, it has been detected that the distribution of $\dot{m}_{ref}$ ($\dot{m}_1$ and $\dot{m}_2$) is not symmetrical in some cases, and therefore one of the evaporators could be not operating. This situation also explains why $\dot{Q}_{E,\,exp}$ slopes down when it is supposed to have an increasing tendency; i.e., when $t_{G,i}$ rises.

Figures 6 and 7 illustrate the quantity of refrigerant going to each evaporator versus t_{Gi} and the total $\dot{Q}_{E,\,exp}$ obtained, for several fixed values of solution mass flow rate $\dot{m}_{weak}$ and $\dot{m}_r$.

Figures 8 and 9 show the global performance parameters (evaporators efficiency η_E, cooling power and COP) obtained for a specific operation condition as a function of t_{Gi}. The cases plotted correspond to experimental data obtained for
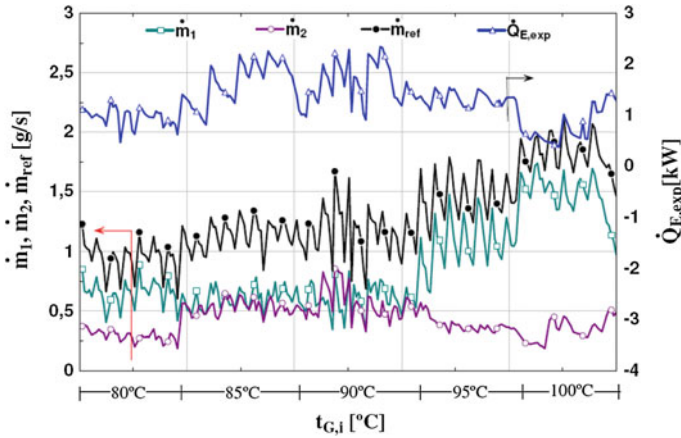
Fig. 5 Refrigerant distribution for different experiments
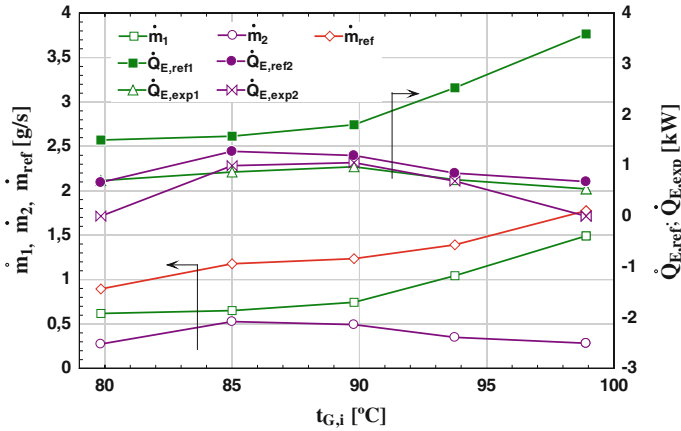
Fig. 6 Refrigerant distribution and corresponding experimental and maximum cooling capacity for each evaporator versus t_{Gi}. $\dot{m}_{weak} = 230 \, \text{kg/h}$

$\dot{m}_{weak}$ fixed to 230 and 300 kg/h. It can be noticed that, in general, $\dot{Q}_{ref}$ (expected cooling capacity) increases when t_{Gi} increases. This behavior was found similar for all values of $\dot{m}_{weak}$.

The difference between an ideal value, $\dot{Q}_{E, ref}$, and the one obtained, $\dot{Q}_{E, \, exp}$, is a clear evidence of the loss in the evaporators performance, which is also shown for each case plotted. The average loss in cooling capacity due to overflow obtained for the whole set of experimental points corresponds to 49 %. This low performance is a consequence of the current layout, where the excess of refrigerant is not recirculated to the evaporators and therefore it goes to the solution reservoir inside the absorber. This behavior is similar to the one in the evaporator of some conventional
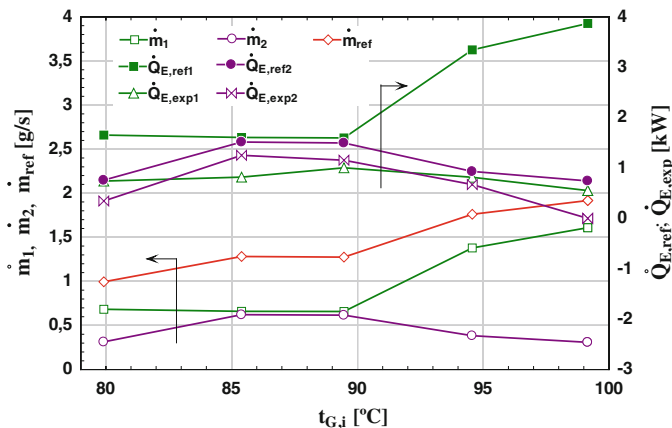
Fig. 7 Refrigerant distribution and corresponding experimental and maximum cooling capacity for each evaporator versus t_{Gi}. $\dot{m}_{weak} = 300 \, \text{kg/h}$
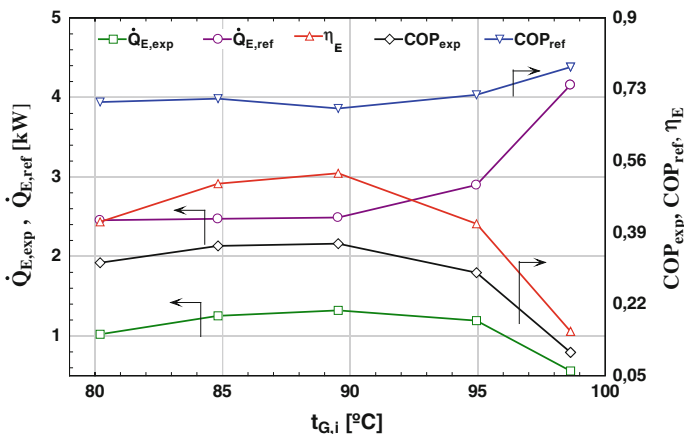
Fig. 8 Evaporators efficiency and corresponding experimental and maximum cooling capacity and COP for each evaporator versus t_{Gi}. $\dot{m}_{weak} = 230 \, \text{kg/h}$ and a fixed $\dot{m}_r$

absorption chillers such as Yazaki WFC-10 (Albers and Ziegler 2005) under specific operation conditions.

Corresponding values of COP_{ref} and COP_{exp} show the same behavior described for the cooling capacity. An appreciable difference is observed between expected and experimental values.

In Fig. 9 it can be noticed that experimental cooling power is almost constant over the complete range of $\dot{Q}_{E,ref}$. In most cases, $\dot{Q}_{E,\,exp}$ do not reach the expected or maximum value, $\dot{Q}_{E,ref}$.

Fig. 9 Experimental versus maximum cooling capacities
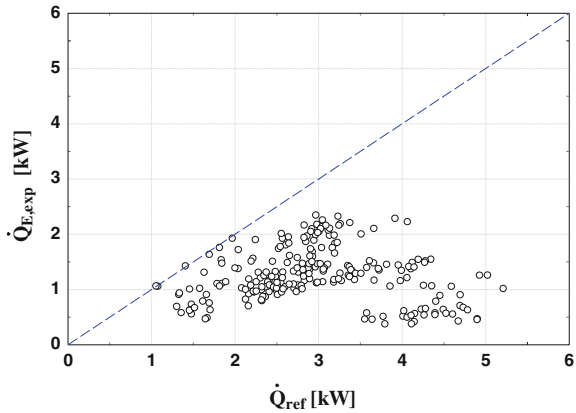
This shows clearly that the drop system used for the spreading of the refrigerant on the fin tubes is not working as expected. Therefore, the spreading system must be improved in order to obtain a cooling capacity closer to the ideal one.

The above mentioned fact (one of the evaporator runs dry) is noticeable when we observe that the individual cooling capacity, estimated through chilled water temperatures and mass flow rates, is close to cero.

5   Conclusions

An environmentally friendly cooling system, based on the absorption technology was presented. An analysis of the evaporators system was developed with the aim to estimate their efficiency η_E and the quantity of refrigerant mass flow rate received by each evaporator. It has been detected that the distribution of $\dot{m}_{ref}$ is not symmetrical in some cases, leading to a partial or defective functioning of one evaporator. This explains why the cooling capacity slopes down when it is supposed to have an increasing tendency. The average η_E obtained for the totality of experimental points was 50 %. This low performance is a consequence of being unable to evaporate all the condensed water. Liquid accumulation leads to overflow of refrigerant out of the evaporators. This shows clearly that the drop system used for the spreading of the refrigerant on the fin tubes is not working as expected and it must be improved in order to obtain a cooling capacity closer to the ideal one.

References

Albers J, Ziegler F (2005) Improved control strategies for solar assisted cooling systems with absorption chillers using a thermosyphon generator. In: Proceedings of the international solar air conditioning, Kloster Banz, Germany, 16–17 Oct 2005

Arzoz D, Rodriguez P, Izquierdo M (2005) Experimental study on the adiabatic absorption of water vapor into LiBr–H2O solutions. Appl Therm Eng 25(5–6):797–811

Elperin T, Fominykh A, Orenbakh Z (2007) Coupled heat and mass transfer during nonisothermal absorption by falling droplet with internal circulation. Int J Refrig 30(2):274–281

Gutiérrez G, Venegas M, Rodríguez P, Izquierdo M, Lecuona A (2006) Experimental characterization of a single stage LiBr-H2O absorption test rig. In: Proceedings ECOS, vol 3, Crete, Greece, 12–14 July 2006, pp 1331–1316

Gutiérrez-Urueta G, Rodríguez P, Ziegler F, Lecuona A, Rodríguez-Hidalgo MC (2011) Experimental performances of a LiBr-water absorption facility equipped with adiabatic absorber. Int J Refrig 34(8):1749–1759

Venegas M, Izquierdo M, Rodríguez P, Lecuona A (2004) Heat and mass transfer during absorption of ammonia vapour by LiNO3–NH3 solution droplets. Int J Heat Mass Transf 47(12–13):2653–2667

Venegas M, Rodríguez P, Lecuona A, Izquierdo M (2005) Spray absorbers in absorption systems using lithium nitrate–ammonia solution. Int J Refrig 28(4):554–564

Wang L, Chen GM, Wang Q, Zhong M (2007) Thermodynamic performance analysis of gas-fired air-cooled adiabatic absorption refrigeration systems. Appl Therm Eng 27(8–9):1642–1652

Warnakulasuriya FSK, Worek WM (2006) Adiabatic water absorption properties of an aqueous absorbent at very low pressures in a spray absorber. Int J Heat Mass Transf 49(9–10): 1592–1602

Rainfall Series Fractality in the Baja California State

A. López-Lambraño, C. Fuentes, A. López-Ramos, M. Pliego-Díaz and M. López-L

Abstract A fractal analysis of rainfall events registered in Baja California was carried out. Rainfall data from 92 climatological stations distributed along the studied region with at least 30 years of records were used. By studying rainfall series patterns, Hurst exponent values were obtained. The rescaled range method (R/S), box-counting method and the Multifractal Detrended Fluctuation Analysis (MF-DFA) were used, having as a result the Hurst exponent values for different time scales (entire record, 25, 10, and 5 years scales). Data showed that the daily rainfall series tended to present a persistent pattern. The analysis from the Hurst

A. López-Lambraño (✉)
Facultad de Ingeniería, Universidad Autónoma de Baja California (UABC),
Km. 103 Carretera Tijuana—Ensenada, C.P. 22860 Mexicali, BC, Mexico
e-mail: altoti@gmail.com; alopezl@hidrusmx.com
URL: http://www.hidrusmx.com

A. López-Lambraño
HIDRUS S.A. de C.V., Querétaro, Mexico

C. Fuentes
Instituto Mexicano de Tecnología del Agua, Paseo Cuauhnahuac 8532,
Progreso, 62550 Jiutepec, Morelos, Mexico
e-mail: cbfuentesr@gmail.com

A. López-Ramos
Escuela de Ingenierías y Arquitectura, Facultad de Ingeniería Civil,
Universidad Pontificia Bolivariana-Seccional Montería, Km. 8 vía a Cereté,
Montería, Córdoba, Colombia
e-mail: alopezramos@hotmail.com

M. Pliego-Díaz
Instituto Tecnológico de Querétaro, Ciencias Básicas. Av. Tecnológico S/N,
Centro, 76000 Santiago de Querétaro, Qro, Mexico
e-mail: maxehekatl@yahoo.com.mx

M. López-L
Universidad del Norte, Km. 5 Vía Puerto Colombia, Barranquilla, Colombia
e-mail: mlambrano@uninorte.edu.com

139

exponent on the previously mentioned time scales showed that, at a lesser time scale, their values increase; thus, the series tended to present a stronger persistent behavior.

1   Introduction

Rainfall is a random variable that evolves in time and space (Kandelhardt et al. 2003; Xu et al. 2015; Brunsell 2010; Gires et al. 2014; Millan et al. 2011; Pinel et al. 2014); therefore it can be analyzed spatially and temporally, allowing to comprehend the climatological behavior of a region based on its basic characteristics such as magnitude, duration and frequency.

Time series analysis studies a variable, in order to comprehend its evolution through time (Hoang et al. 2012); for which stochastic methods and fractal methods have been applied. Stochastic methods make predictions and obtain a relationship with other variables (Akbari and Friedel 2014; Caballero et al. 2002; Nunes et al. 2011); however, these methods present a disadvantage: a random variable, in this case rainfall, cannot be analyzed at different scales (Haui-Hsien et al. 2013; Svanidze 1980); therefore, fractal methods have been applied to analyze rainfall time series at multiple scales and dimensions (Lovejoy et al. 1987; Fluegeman and Snow 1989; Gallant et al. 1994; Lovejoy and Mandelbrot 1985; Lovejoy et al. 2012; Pinel et al. 2014; Schepers et al. 1992; Selvam 2010; Sivakumar 2000; Venugopal et al. 1999; Rangarajan and Sant 2004).

Mandelbrot (1967) introduced the concept of fractal in terms of self-similar statistics, stating that the shape of an object does not define its size; and established fractals as objects that possess a similar appearance when observed at different scales.

While determining the self similarity characteristics and the spatial-temporal fluctuations at multiple scales for rainfall time series, several methodologies have been applied; such as: rescaled range (R/S) (Hurst 1951, 1956; Mandelbrot 1972), box-counting method (Lovejoy et al. 1987; Breslin and Belward 1999), Multifractal Detrended Fluctuation Analysis (MF-DFA) (Movahed 2006), wavelet method (Velasquez et al. 2013), power spectrum method (Valdes-Cepeda et al. 2003), Higuchi method (Kalauzi et al. 2009), Detrended Fluctuation Analysis (DFA) (Yuval and Broday 2010), Fractal-Multifractal method (Huai-Hsien et al. 2013), Hurst-Kolmogorov method (Koutsoyiannis et al. 2011), Fractionally Integrated Flux (FIF) (Verrier et al. 2010), Fractal Brownian Surface (Tao and Barros 2010) and the fractal correlation dimension (D2) (Capecchi et al. 2012). Due to the application of the previous methods, it has been found that rainfall possesses fractal properties (Venugopal et al. 1999; Amaro et al. 2004; Beran 1994; Oñate 1997; Peters et al. 2002; Schertzer et al. 2010; Turcotte 1994; Lanza and Gallant 2006; Hubert and Carbonnel 1990); however the distribution of rainfall drops do not have these properties (Malinowki et al. 1993; Lovejoy and Schertzer 1987, 1990, 2006; Hentschel and Procaccia 1984; Lombardo et al. 2012).

Fractal behavior of rainfall time series has a relationship with altitude, such that at higher altitude a stronger antipersistent behavior occurs (Velasquez et al. 2013). A high frequency of zero values in the rainfall time series is an important factor to consider, as it can influence the fractal parameters obtained (Gires et al. 2012; Lopez-Lambraño 2012; Verrier et al. 2010).

The aim of this research is to analyze the fractal behavior of rainfall events in Baja California, Mexico, with the purpose of find a relation with climatological distribution, altitude above sea level, average temperature and average annual rainfall. So as to achieve this, 92 climatological stations with at least 30 years of records were analyzed; subsequently, using the Hurst exponents, a spatial and temporal analysis was carried out with the object of compare it with the previously mentioned variables. The expected results will allow to find a relation that enables to conduct climate change analysis in the studied zone.

2 Theory

2.1 Rescalated Range Method (R/S)

The original scheme proposed by Hurst (1951, 1956) proceeds with the following steps: the input data (daily rainfall) are taken as the difference between the rainfalls on two consecutive days:

$$I_i' = I_i - I_{i+1} \tag{1}$$

where I_i is the total rain amount on day i. The mean value of the difference over a period τ is:

$$\langle I' \rangle_\tau = \frac{1}{\tau} \sum_{i=1}^{\tau} I_i' \tag{2}$$

Now let $X(i, \tau)$ be the difference between I_i' and $\langle I' \rangle_\tau$ defined as

$$X(i, \tau) = \sum_{u=1}^{i} \left[I_u' - \langle I' \rangle_\tau \right] \tag{3}$$

Finally, the variable R and the standard variation S are given by

$$R(\tau) = \max_{1 \le i \le \tau} X(i, \tau) - \min_{1 \le i \le \tau} X(i, \tau) \tag{4}$$

$$S(\tau) = \left\{ \frac{1}{\tau} \sum_{i=1}^{\tau} \left[I'_i - \langle I' \rangle_\tau \right]^2 \right\}^{1/2} \tag{5}$$

We therefore obtain, for each value of the scale τ, an R/S number which follows a power law. If we take logarithms on both sides, we obtain the Hurst exponent value H as the value of the slope:

$$\log(R/S) \sim H \log(\tau) \tag{6}$$

2.2 Box-Counting Method

According to Peñate et al. (2013), the box counting method is based on dividing the space of observation (the time interval T) into n non-overlapping segments of characteristic size s, such that $s = T/n$ for $n = 2, 3, 4, \ldots$, and computing the number $N(s)$ of intervals of length s occupied by events. If the distribution of events has a fractal structure, then the relationship $N(s) = Cs^D$ prevails. The fractal or box-counting dimension D_f is estimated from the slope D of the regression line of $\log(N(s))$ versus $\log(s)$. This parameter, $D_f = |D|$, describes the strength of the events and can measure the phenomenon's nature since it quantifies the scale-invariant clustering of the time series. Clustering increases when D approaches 0. Hence, the smaller fractal dimensions correspond to clusters formed by events that occur sparsely. If D is close to 1, the events are randomly spaced in time. To sum up, the box-counting method uses boxes to cover an object to find the fractal dimension. The signal is partitioned into boxes of various sizes and the amount of non-empty squares is counted. A log-log plot of the number of boxes versus the size of the boxes is done. The box dimension is defined by the exponent D_b in the relation:

$$N(s) \approx \frac{1}{s^{D_b}} \tag{7}$$

where $N(s)$ is the number of boxes with linear size, s needed to cover the set of points distributed on a bidimensional plane. A number of boxes, proportional to a $1/s$, are needed to cover the set of points on a line; proportional to $1/s^2$, to cover a set of points on a plane, etcetera.

In theory, for each box size, the grid should be configured in such a way that the minimum number of boxes is occupied. This can be achieved by rotating the grid for each box size in 90° and plotting the minimum value of $N(d)$.

The Hurst exponent value can be calculated from the following expression:

$$D_b = 2 - H \tag{8}$$

where H is the Hurst exponent value.

2.3 Multifractal Detrended Fluctuation Analysis

According to Yuval and Broday (2010) and Movahed et al. (2006), the modified multifractal DFA (MF-DFA) procedure consists of five steps. Suppose that x_k is a series of length N, and that this series is of compact support, i.e. $x_k = 0$ for an insignificant fraction of the values only.

Step 1—Determine the profile:

$$Y(i) = \sum_{k=1}^{i} [x_k - \langle x \rangle], \qquad i = 1, \ldots, N. \tag{9}$$

Subtraction of the mean $\langle x \rangle$ is not compulsory, since it would be eliminated by the later detrending in the third step.

Step 2—Divide the profile $Y(i)$ into $N_s = \mathrm{int}(N/s)$ non-overlapping segments of equal lengths s since the length N of the series is often not a multiple of the timescale s considered, a short part at the end of the profile may remain. In order to disregard this part of the series, the same procedure is repeated starting from the opposite end. Thereby, $2N_s$ segments are obtained altogether.

Step 3—Calculate the local trend for each of the $2N_s$ segments by a least squares fit of the series. Then determine the variance:

$$F^2(s, v) = \frac{1}{s} \sum_{i=1}^{s} \{Y[(v-1)s + i] - y_v(i)\}^2 \tag{10}$$

For each segment $v, v = 1, \ldots, N_s$, and:

$$F^2(s, v) = \frac{1}{s} \sum_{i=1}^{s} \{Y[N - (v - N_s)s + i] - y_v(i)\}^2 \tag{11}$$

For $v = N_s + 1, \ldots, 2N_S$. Here $y_V(i)$ is the fitting polynomial in segment v. Linear, quadratic, cubic or higher order polynomials can be used in the fitting procedure. Since the detrending of the time series is done by the subtraction of the polynomial fits from the profile, different order DFA differ in their capability of eliminating trends in the series.

Step 4—Average over all segments to obtain the qth-order fluctuation function, defined as

$$F_q(s) = \left\{ \frac{1}{2N_S} \sum_{v=1}^{2N_S} \left[F^2(s,v) \right]^{q/2} \right\}^{1/q} \tag{12}$$

Where, in general, the index variable q can take any real value except zero. For $q = 2$, the standard DFA procedure is retrieved. Generally we are interested in how the generalized q dependent fluctuation functions $F_q(s)$ depend on timescale s for different values of q. Hence, we must repeat steps 2, 3 and 4 for several timescales s. It is apparent that $F_q(s)$ will increase while increasing s. Of course $F_q(s)$ depends on the DFA order m. By construction, $F_q(s)$ is only defined for $s \geq m + 2$.

Step 5—Determine the scaling behavior of the fluctuation functions by analyzing log-log plots of $F_q(s)$ versus s for each value of q. If the series x_i are long range power law correlated, $F_q(s)$ increases, for large values of s, as a power law,

$$F_q(s) \sim s^{h(q)} \tag{13}$$

In general, the exponent $h(q)$ may depend on q. The exponent $h(2)$ is identical to the well-known Hurst exponent.

3   Methodology

The research takes place in Baja California, Mexico, comprised between the coordinates (32.713N, 114.723O), (32.527N, 117.141O), (28.095N, 115.364O), and (27.994N, 112.799O).

For the purpose of this research, data from 92 climatological stations distributed along the studied region with at least 30 years of rainfall records were analyzed.

In order to obtain the previously mentioned data, the use of two climatological systems was required: Rapid Climatological Information Extractor (ERIC III) and the National Climatological Database (Clicom); both of them give availability to daily national climate data.

In order to expand the panorama of this research, it has been chosen to utilize a series of time scales classified in the following scenarios:

(a) Hurst exponent value H calculated from the analysis of a time scale equally in duration to the total time series (n = Entire record duration)
(b) Hurst exponent value H calculated from the analysis of 25 years long time (n = 25 years).
(c) Hurst exponent value H calculated from the analysis of 10 years long time (n = 10 years).

(d) Hurst exponent value H calculated from the analysis of 5 years long time (n = 5 years).

After calculating these values, an average value, obtained from the three previously mentioned methods (Rescaled range (R/S) using Eq. (6), box-counting method using Eq. (7) and MF-DFA using Eq. (13), is calculated for each time scale. The results obtained from same time scales are averaged.

4 Results and Discussions

Given the importance to assess the fractal behavior of the daily rainfall series, and to analyze the variability of the Hurst exponent at different time scales, an analysis was carried out considering the previously mentioned time scales which correspond to: the Hurst exponent values H resulting from the analysis of the entire record for rainfall daily events, as well for the different time scales (25, 10, and 5 years long).

From Table 1, Hurst values behavior for daily rainfall events, at different time scales were reported. While analyzing the data, two mainly behaviors can be noticed for each of the time series in the analyzed variable: anti-persistent and persistent behavior. Both of these behaviors will be discussed below.

According to Table 1, the stations Presa Rodriguez, San Vicente, Tijuana, Valle de las Palmas, Presa Emilio Lopez Zamora, and Santo Tomas, which are located in the northeast region of Baja California, presented Hurst exponent values as follows: 0.45, 0.48, 0.49, 0.48. 0.47 y 0.47 respectively, i.e. they are anti-persistent in time. This means that rainfall events, which take place in this region, present a high probability of showing a positive increasing behavior, followed by a negative increasing behavior in its record values and vice versa.

According to Malamud and Turcotte (1999), an anti-persistent time series will have a stationary behavior in time; due to the increases and decreases that compensate themselves, statistical moments are independent from the time series. Rehman (2009) establishes that, in the case of rainfall, an anti-persistent behavior indicates a lesser dependency in accordance with previously stated values.

Nevertheless, when the rainfall series in the previously mentioned stations were analyzed in 25 years long scales, the Hurst values were reported as follows: 0.62, 0.65, 0.62, 0.63, 0.64 y 0.62, respectively. These values indicate a persistent behavior in time, meaning that, if the rainfall series registers a positive increase, it is more likely that a positive increase will follow. This implies that each rainfall event has a degree of occurrence over future events or in its long-term behavioral memory.

Continuing with the analysis of the previously mentioned stations, and considering the 10 and 5 years long time scales, increases in the Hurst values are noticeable once again and continuing with a persistent behavior throughout time. It can be found that the Hurst exponent increases while establishing shorter time scales.

Table 1 Averaged Hurst exponent results for climatological stations in Baja California for all time scales for daily rainfall events

#	Climatological station	Elevation above sea level (meters)	Average annual rainfall (mm/year)	Average annual temperature (°C)	Average Hurst exponent for the different time scales			
					Entire record	25 years	10 years	5 years
2001	Agua caliente	400	272.7	12.68	0.51	0.60	0.66	0.68
2002	Bahía de los ángeles	4	63.77	21.98	0.65	0.74	0.79	0.81
2003	Bataquez	23	69.33	20.02	0.61	0.74	0.78	0.82
2004	Ignacio Zaragoza	540	294.04	12.21	0.54	0.62	0.69	0.73
2005	Boquilla santa rosa de l	250	260.9	13.22	0.54	0.64	0.64	0.65
2006	Chapala	660	115.15	19.59	0.57	0.70	0.71	0.75
2008	Colonia guerrero	30	156	15.34	0.53	0.61	0.67	0.71
2009	Colonia Juárez	17	57.13	19.01	0.61	0.68	0.78	0.79
2011	Delta	12	46.65	19.76	0.65	0.72	0.77	0.80
2012	Ejido j. María Morelos	20	62.74	15.53	0.65	0.77	0.79	0.85
2014	El álamo	1115	265.7	13.66	0.52	0.60	0.66	0.72
2015	El arco	288	102.75	17.62	0.59	0.74	0.78	0.86
2016	El barril	50	81.31	24.12	0.61	0.76	0.78	0.85
2019	El compadre	1110	293.43	18.84	0.58	0.63	0.68	0.69
2020	El mayor	15	56.16	17.74	0.69	0.80	0.83	0.89
2021	El Pinal	1320	453.8	9.22	0.55	0.64	0.70	0.78
2022	El rosario	40	168.59	16.78	0.59	0.72	0.76	0.81
2023	El socorro	26	106.08	17.11	0.59	0.79	0.80	0.84
2024	El testerazo	380	240.57	11.72	0.65	0.72	0.76	0.76
2027	Isla cedros	3	62.72	19.74	0.71	0.81	0.84	0.87
2029	La providencia	40	257.24	13.93	0.57	0.72	0.73	0.78
2030	La puerta	480	326.51	13.56	0.51	0.64	0.69	0.70
2031	La rumorosa	1232	137.99	14.7	0.60	0.73	0.73	0.79
2032	Las escobas	30	132.73	15.03	0.51	0.70	0.75	0.80
2033	Mexicali (DGE)	3	72.98	18.8	0.57	0.75	0.76	0.81
2034	Mexicali (SMN)	3	95.18	20.24	0.60	0.72	0.77	0.88
2035	Ojos negros	680	222.32	12.73	0.50	0.61	0.66	0.69
2036	Olivares mexicanos	340	279.9	14.46	0.53	0.68	0.70	0.76
2037	Presa Morelos	40	61.4	17.83	0.61	0.66	0.74	0.82
2038	Presa Rodríguez	120	208.46	14.63	0.45	0.62	0.65	0.70
2039	Punta prieta	325	89.93	16.47	0.57	0.74	0.76	0.84
2040	Rancho alegre	120	120.32	15.83	0.59	0.75	0.75	0.82
2041	Nuevo rosarito	20	110.32	16.84	0.58	0.74	0.75	0.79
2043	San Agustín	552	111.09	17.13	0.57	0.75	0.76	0.81

(continued)

Table 1 (continued)

#	Climatological station	Elevation above sea level (meters)	Average annual rainfall (mm/year)	Average annual temperature (°C)	Average Hurst exponent for the different time scales			
					Entire record	25 years	10 years	5 years
2044	San Borja	445	104.9	18.03	0.57	0.73	0.76	0.85
2045	San Carlos	164	263.3	15.19	0.55	0.68	0.69	0.75
2046	San Felipe	10	64.9	22.5	0.66	0.84	0.86	0.94
2049	San Juan de Dios del norte	1280	362.9	12.09	0.52	0.58	0.61	0.65
2050	San Juan de Dios del sur	480	92.7	16.7	0.69	0.73	0.76	0.80
2051	San Luis baja california	440	124.9	17.82	0.62	0.81	0.83	0.89
2053	San miguel	60	187.8	19.44	0.62	0.70	0.71	0.77
2055	San Telmo	110	211.7	13.8	0.55	0.65	0.73	0.76
2056	San Vicente	1150	248.7	13.21	0.48	0.65	0.73	0.74
2057	Santa Catarina norte	317	137.6	14.53	0.51	0.60	0.62	0.66
2058	Santa Catarina sur	410	128.2	16.38	0.54	0.71	0.73	0.79
2059	Santa Clara	980	265.3	18.84	0.58	0.69	0.73	0.80
2060	Santa Cruz	400	105.4	15.57	0.52	0.63	0.66	0.71
2061	Santa Gertrudis	28	160.6	18.06	0.62	0.72	0.75	0.84
2063	Santa María del mar	250	211.5	14.95	0.54	0.71	0.73	0.79
2064	Santo domingo	180	259.14	14.06	0.58	0.72	0.74	0.79
2065	Santo tomas	20	215.6	16.43	0.47	0.62	0.65	0.67
2068	Tijuana	280	206.9	15.22	0.49	0.62	0.66	0.72
2069	Valle de las palmas	242	291.19	12.74	0.48	0.63	0.69	0.72
2070	Valle redondo	740	204.72	15.01	0.54	0.60	0.61	0.65
2071	Colonia valle de la trinidad	43	250.99	10.59	0.51	0.59	0.62	0.67
2072	Presa Emilio López Zamora	710	264.08	14.58	0.47	0.64	0.66	0.69
2079	El alamar	517	135.6	12.8	0.54	0.63	0.68	0.69
2084	El progreso	495	132.9	17.64	0.60	0.73	0.76	0.83
2085	San Regis	860	214.48	17.97	0.59	0.73	0.73	0.78
2086	Ejido Jacume	1000	263.6	13.24	0.58	0.67	0.72	0.74
2088	Ejido héroes de la Independencia	180	187.2	14.08	0.61	0.71	0.72	0.75
2089	Ejido Emilio López Zamora	170	269.9	14	0.68	0.75	0.75	0.78
2091	Ejido Ignacio López Ray	968	214.2	11.88	0.55	0.67	0.69	0.74

Table 1 (continued)

#	Climatological station	Elevation above sea level (meters)	Average annual rainfall (mm/year)	Average annual temperature (°C)	Average Hurst exponent for the different time scales			
					Entire record	25 years	10 years	5 years
2092	Ejido san Matías	780	231.18	15.95	0.56	0.63	0.67	0.73
2093	Ejido valle de la trinidad	210	209.38	11.6	0.57	0.71	0.74	0.79
2096	La calentura	460	71.5	14.27	0.59	0.69	0.72	0.77
2099	Rancho los algodones	50	46.12	19.3	0.74	0.78	0.80	0.87
2101	El centinela	16	36.32	20.7	0.81	0.88	0.90	0.93
2102	La ventana	8	202.84	21.3	0.71	0.88	0.88	0.92
2104	El Ciprés	50	202.02	15.25	0.59	0.70	0.72	0.74
2106	Maneadero	600	120.7	15.28	0.57	0.69	0.73	0.73
2107	Percebu	4	40.7	19.12	0.78	0.87	0.90	0.92
2108	Punta banda	15	260.6	15.13	0.59	0.70	0.72	0.76
2109	Santa Rosalita	8	136.02	16.64	0.69	0.78	0.82	0.87
2110	Guayaquil	530	123.5	17	0.65	0.72	0.77	0.80
2111	Ejido nueva baja california	17	134.9	14.13	0.62	0.72	0.74	0.77
2114	Ejido Carmen Serdán	560	231.8	11.57	0.62	0.72	0.74	0.77
2118	Valle san Rafael	721	218.4	12.45	0.54	0.66	0.69	0.71
2120	Ejido México	75	176.9	13.61	0.64	0.71	0.75	0.78
2121	El hongo	960	286.35	12.55	0.52	0.61	0.63	0.67
2124	El carrizo ii	300	231.88	13.59	0.53	0.63	0.65	0.68
2137	Colonia mariana	9	57.61	19.4	0.65	0.75	0.78	0.82
2139	Colonia Rodríguez	17	36.8	18	0.73	0.82	0.88	0.90
2140	Colonia Zaragoza	8	65.16	12.43	0.86	0.82	0.88	0.94
2141	Compuerta Benassini	20	55.11	17.9	0.63	0.75	0.80	0.84
2144	Ensenada blanca	10	89.07	19.7	0.69	0.75	0.82	0.84
2145	Rancho Williams	29	63.05	20.57	0.61	0.73	0.77	0.83
2146	Colonia san pedro mártir	416	106.3	16.19	0.60	0.74	0.75	0.81
2151	Agua de chale	5	53.12	22.59	0.68	0.82	0.83	0.88
2152	Ejido j. María del pino	1380	273.6	8.7	0.62	0.72	0.74	0.75
2153	Ejido Uruapan	195	288.55	13.9	0.61	0.70	0.72	0.75
2154	Colonia zacatecas	12	52.12	18.46	0.71	0.80	0.81	0.87

Anti-persistent series kept a positive increase tendency with minor negative increases; thus, while considering shorter periods of times (25, 10, 5 years), it is reasonable that series starts to behave in a more persistent manner. This is due to the fact that, the shorter the considered time scale is, the greater the possibility to analyze a time period with a predominant behavior that, in this case, is a persistent behavior; this could explain the increase in the Hurst values in the analyzed rainfall series.

Continuing the analysis on the other 86 remaining stations and considering the established time scales, increases in the Hurst values are noticeable, keeping a persistent behavior tendency since the values are greater than 0.5.

This means that rainfall series is not stationary and that moments are time scale dependent. The presence of persistency is an indicator that, not only what takes place in the present influence the near future, it will also influence long term future.

5   Conclusions

Even though three methods (Multifractal Detrended Fluctuation Analysis, box-counting method, and rescalated range (R/S)) were utilized to calculate the Hurst exponent for each analyzed scale time, it is difficult to determine which of these methods is the most efficient; however, the rescalated range method has been reported as the most used method.

Registered daily rainfall series throughout Baja California can be characterized by using the Hurst exponent, having as a result a tendency to present a persistent behavior. Thus, when a positive increase is registered, it is more likely that the following increase will be positive as well.

The existence of dependency between the rainfall and temperature climate variables in relation with altitude can be noticed. Regions with an altitude near to sea level tend to register the highest temperature values, as well as the lowest rainfall annual average. It can be established that a proportional inverse relation between altitude and temperature exists, as well as a proportional direct relation between altitude and rainfall.

Taking into account the Hurst exponent used in this research, a proportional inverse relation with altitude and rainfall can be noticed; in regions that are close to sea level, high values can be reported; on the other hand, regions where the average annual rainfall is high, the analysis showed low values for the Hurst exponent. It can be confirmed that the Hurst exponent depends in the climatological conditions and physiographic characteristics in a specific region.

Taking into account shorter time scales (25, 10, 5 years long in this research), it can be found that the series' persistency is stronger. The greater the number of considered scale times to analyze rainfall series, the greater the possibility to understand its behavior and tendencies.

Finally, it can be confirmed that fractal theory provides information that allows to analyze the occurrence of a climatological variable, such as rainfall (in the case

for this research). This provides a useful tool to study and mitigate climate change in a given region.

It is recommended to use multifractal theory in future researches, having as a main purpose the chance to study the scale invariability from a mathematical perspective and to describe the climatic variables behavior with potential laws which are characterized by its exponents.

References

Akbari A, Friedel M (2014) Forecasting conditional climate-change using a hybrid approach. Environ Modell Softw 52:83–97

Amaro IR, Demey JR, Macchiavelli R (2004) Aplicación del análisis R/S de Hurst para estudiar las propiedades fractales de la precipitación en Venezuela. Interciencia 29:617–620

Beran J (1994) Statistics for long-memory processes. Monographs on statistics and probability 61. Chapman & Hall, New York

Breslin MC, Belward JA (1999) Fractal dimensions for rainfall time series. Math Comput Simul 48:437–446

Brunsell N (2010) Amultiscale information theory approach to assess spatial–temporal variability of daily precipitation. J Hydrol 385:165–172

Caballero R, Jewson S, Brix A (2002) Long memory in surface air temperature: detection, modeling, and application to weather derivative valuation. Clim Res 21:127–140

Capecchi V, Crisci A, Melani S, Morabito M, Politi P (2012) Fractal characterization of rain-gauge networks and precipitations: an application in Central Italy. Atmos Ocean Phys 107:541–546

Fluegeman RH Jr, Snow RS (1989) Fractal analysis of long-range paleoclimatic data: oxygen isotope record of pacific core V28-239. PAGEOPH 131:307–313

Gallant JC, Moore ID, Hutchinson MF, Gessler P (1994) Estimating fractal dimension of profiles: a comparison of methods. Math Geol 26:455–481

Gires A, Tchiguirinskaia I, Schertezer D, Lovejoy S (2012) Influence of the zero rainfall on the assessment of the multifractal parameters. Adv Water Resour 45:13–25

Gires A, Tchiguirinskaia I, Schertzer D, Schellart A, Berne A, Lovejoy S (2014) Influence of small scale rainfall variability on standard comparison tools between radar and rain gauge data. Atmos Res 138:125–138

Hentschel HG, Procaccia I (1984) Relative diffusion in turbulent media: the fractal dimension of clouds. Phys Rev A 29:1461–1470

Hoang CT, Tchiguirinskaia I, SchertzerD Arnaud P, Lavabre J, Lovejoy S (2012) Assessing the high frequency quality of long rainfall series. J Hydrol 438–439:39–51

Huai-Hsien H, Puente CE, Cortis A, Fernández JL (2013) An effective inversion strategy for fractal–multifractal encoding of a storm in Boston. J Hydrol 496:205–216

Hubert P, Carbonnel JP (1990) Fractal characterization of intertropical precipitations variability and anisotropy. Non-Linear Variab Geophys 3:209–213

Hurst HE (1951) Long-term storage capacity of reservoirs. Trans Am Soc Civil Eng 116:770–880

Hurst HE (1956) Methods of using long-term storage in reservoirs. Proc Inst Civil Eng 1:516–543

Kalauzi A, Cukic M, Millan H, Bonafoni S, Biondi R (2009) Comparison of fractal dimension oscillations and trends of rainfall data from Pastaza Province, Ecuador and Veneto, Italy. Atmos Res 93:673–679

Kantelhardt JW, Rybski D, Zschiegner SA, Braun P, Koscielny-Bunde E, Livina V, Havlin S, Bunde A (2003) Multifractality of river runoff and precipitation: comparison of fluctuation analysis and wavelet methods. Phys A 330:240–245

Koutsoyiannis D, Paschalis A, Theodoratos N (2011) Two-dimensional Hurst-Kolmogorov process and its application to rainfall fields. J Hydrol 398:91–100

Lanza LG, Gallant J (2006) Fractals and similarity approaches in hydrology. Encycl Hydrol Sci 123–133

Lombardo V, Volpi E, Koutsoyiannis D (2012) Rainfall downscaling in time: theoretical and empirical comparison between multifractal and Hurst-Kolmogorov discrete random cascades. Hydrol Sci J 57:1052–1066

López Lambraño AA (2012) Tesis de Doctorado en Facultad de Ingeniería, Universidad Autónoma de Querétaro

Lovejoy S, Mandelbrot B (1985) Fractal properties of rain and a fractal model. Tellus 37A:209–232

Lovejoy S, Pinel J, Schertzer D (2012) The global space–time cascade structure of precipitation: satellites, gridded gauges and reanalyses. Adv Wat Resour 45:37–50

Lovejoy S, Schertzer D, Tsonis AA (1987) Functional box-counting and multiple elliptical dimensions in rain. Science 235:1036–1038

Lovejoy S, Schertzer D (1990) Multifractals, universality classes and satellite and radar measurements of cloud and rain fields. J Geophys Res 95:2021–2034

Lovejoy S, Schertzer D (2006) Multifractals, cloud radiances and rain. J Hydrol 322:59–88

Malamud BD, Turcotte DL (1999) Self-affine time series: measures of weak and strong persistence. J Stat Plan Inf 80:173–196

Malinowski SR, Lecrerc MY, Baumgardner D (1993) Fractal analysis of high-resolution cloud droplet measurements. J Atmos Sci 397–413

Mandelbrot BB (1972) Statistical methodology for nonperiodic cycles: from the covariance to R/S analysis. Ann Econ Soc Meas 1(3):259–290

Mandelbrot BB (1967) How long is the coast of Britain? Statistical self-similarity and fractional dimension. Science 156:636–638

Millan H, Rodriguez J, Ghanbarian-Alavijeh B, Biondi R, Llerena G (2011) Temporal complexity of daily precipitation records from different atmospheric environments: chaotic and Lévy stable parameters. Atmos Res 101:879–892

Movahed S, Jafari G, Ghasemi F, Rahvar S, Rahimi M (2006) Multifractal detrended fluctuation analysis of sunspot time series. J Stat Mech-Theory E P02003:1–17

Nunes S, Romani L, Avila A, TrainaJr C, de Sousa EPM, Traina AJM (2011) Fractal-based analysis to identify trend changes in multiple climate time series. J Inf Data Manag 2:51–57

Oñate JJ (1997) Fractal analysis of climatic data: annual precipitation records in Spain. Theoret Appl Climatol 56(1–2):83–87

Peñate I, Martín-González JM, Rodríguez G, Cianca A (2013) Scaling properties of rainfall and desert dust in the Canary Islands. Nonlinear Process Geophys 20:1079–1094

Peters O, Hertlein C, Christensen K (2002) A complexity view of rainfall. Phys Rev Lett 88:1–4

Pinel J, Lovejoy S, Schertzer D (2014) The horizontal space–time scaling and cascade structure of the atmosphere and satellite radiances. Atmos Res 140–141:95–114

Rangarajan G, Sant D (2004) Fractal dimensional analysis of Indian climatic dynamics. Chaos Solitons Fractals 19:285–291

Rehman S (2009) Study of Saudi Arabian climatic conditions using Hurst. Chaos Solitons Fractals 39:499–509

Schepers HE, van Beek JHGM, Bassingthwaighte JB (1992) Four methods to estimate the fractal dimension from self-affine signals. IEEE Eng Med Biol 11:57–64

Schertzer D, Tchiguirinskaia I, Lovejoy S, Hubert P (2010) No monsters, no miracles: in nonlinear sciences hydrology is not an outlier! Hydrol Sci J—Journal des Sciences Hydrologiques 55:965–979

Schertzer D, Lovejoy S (1987) Physical modeling and analysis of rain and clouds by anisotropic scaling multiplicative processes. J Geophys Res 92:9693–9714

Selvam AM (2010) Universal inverse power law distribution for fractal fluctuations in dynamical systems: applications for predictability of inter—annual variability of Indian and USA region rainfall. Cornell University Library, pp 1–28

Sivakumar B (2000) A preliminary investigation on the scaling behavior of rainfall observed in two different climates. Hydrol Sci J 45:203–219

Svanidze GG (1980) Mathematical modeling of hydrologic series. Water Resources Publications, USA, pp 847–848

Tao K, Barros A (2010) Using fractal downscaling of satellite precipitation products for hydrometeorological applications. J Atmos Ocean Technol 27:409–427

Turcotte D (1994) Fractal theory and estimation of extreme floods. J Res Nail Inst Stand Technol 99:377–389

Valdez-Cepeda R, Hernandez-Ramirez D, Mendoza B, Valdes-Galicia J, Maravilla D (2003) Fractality of monthly extreme minimum temperature. Fractals 11:137–144

Velásquez MA, Medina G, Sánchez I, Oleschko K, Ruiz JA, Korvin G (2013) Spatial variability of the hurst exponent for the daily scale rainfall series in the State of Zacatecas, Mexico. Am Meteorol Soc 52:2771–2780

Venugopal V, Foufola-Georgiuo E, Sapozhnikov V (1999) Evidence of dynamic scaling in space-time rainfall. J Geophys Res 104:31599–31610

Verrier S, de Montera L, Barthès L, Mallet C (2010) Multifractal analysis of African monsoon rain fields, taking into account the zero rain-rate problem. J Hydrol 389:111–120

Xu J, Chen Y, Li W, Liu Z, Tang J, Wei C (2015) Understanding temporal and spatial complexity of precipitation distribution in Xinjiang, China. Theor Appl Climatol 1–13

Yuval, Broday DM (2010) Studying the time scale dependence of environmental variables predictability using fractal analysis. Environ Sci Technol 44:4629–4634

Hydrodynamic Modeling for the Sustainable Management of the Guájaro Hydrosystem, Colombia

F. Torres-Bejarano, J. Padilla Coba, H. Ramírez-León, C. Rodríguez-Cuevas and R. Cantero-Rodelo

Abstract The Guájaro reservoir is the most important water body located at the north of Colombia. It is supplied by an artificial channel (*Canal del Dique*) through a two floodgates system. As a result of excess nutrients and other pollution loads from the drainage basin in recent decades, the Guájaro reservoir suffers eutrophication and other pollution problems; however it still continues being exploited. For this reason, it is necessary to regulate the hydraulic structures that supply this water body, as they play an important role in managing levels, and these in turn for water supply and environmental purposes. The present work is carried out as a sustainability management alternative of the reservoir. The implementation of a two-dimensional hydrodynamic model and its calibration is achieved using time series of the free surface levels, and comparing the measured velocities and those estimated by the model for two different climatic periods, to assist the operation of the *Canal del Dique-Guájaro* hydrosystem. The corresponding comparisons showed a good behavior between measured and simulated data. Based on the

F. Torres-Bejarano (✉) · J. Padilla Coba · R. Cantero-Rodelo
Faculty of Environmental Sciences, Universidad de la Costa,
Barranquilla, Colombia
e-mail: ftorres4@cuc.edu.co

J. Padilla Coba
e-mail: jpadilla15@cuc.edu.co

R. Cantero-Rodelo
e-mail: rcantero@cuc.edu.co

H. Ramírez-León
Instituto Mexicano del Petróleo, Mexico City, Mexico
e-mail: hrleon@imp.mx

C. Rodríguez-Cuevas
Faculty of Engineering, University of San Luis Potosí,
San Luis Potosí, Mexico
e-mail: clemente.rodriguez@uaslp.mx

quantitative results of the Nash-Sutcliffe reliability method, the results are considered quite satisfactory for estimating and predicting the amount of water flowing in and out of the reservoir through the channel reservoir hydrosystem.

1 Introduction

Currently, a widespread concern in relation to global environmental degradation is going on. Phenomena such as global warming, caused mainly by industrial development and unsustainable population growth, make it necessary to have tools that help us understand these phenomena and evaluate scenarios in case of emergency events, in order to make effective accurate and realistic decisions (Torres-Bejarano et al. 2013).

When solving problems related to water resources, both a spatial representation of the system and the understanding of such problems are needed. In this regard, the hydrodynamic models can represent the characteristics and behavior of system relations, supported on the associated predictive analytics capabilities, which are most useful in the planning and management of complex problems in aquatic resources. The Integrated Water Resources Management (IWRM) nowadays is a prerequisite for environmental preservation and economic development. However, the implementation of proposed actions is significantly hampered due to insufficient necessary data, and the lack of interactions between hydrological and ecological components (Dimitriou and Zacharias 2006). According to McIntosh et al. (2007), a variety of software and modeling technologies are emerging in the form of "support tools" to better handle the problems of use of scientific knowledge in environmental research and planning activities. These technologies are motivated by legitimate concerns about the inefficiency of conventional research methods and of ensuring that science can be effective and easily transferred to management applications, particularly with regard to water resources.

Therefore, the objective of this work is to implement a hydrodynamic numerical model to contribute to the sustainable management of water resources in the Guájaro reservoir, Colombia, considering primarily the management of water levels.

For that reason, the model Environmental Fluid Dynamics Code (EFDC) was chosen for its friendliness to the pre-processing of data and its processing capacity, high performance computing and numerical robustness, plus, it has been applied and successfully implemented in several case studies worldwide. In the last two decades, it has become one of the most used and technically defensible hydrodynamic models in the world. It has been applied in more than 100 water bodies and for environmental water resource management (Kim et al. 1998; Moustafa and Hamrik 2000; Ji et al. 2001; Park et al. 2005; Luo and Li 2009).

2 Materials and Methods

The methodology used in this work includes the implementation of the numerical model EFDC Explorer 7.1 (commercial distribution) version for simulations of hydrodynamic variables in the Guájaro reservoir; the model calibration using a statistical method to evaluate the model's predictive capacity (Molnar 2011); and an indicator of goodness-of-fit as the Nash-Sutcliffe efficiency coefficient (Nash and Sutcliffe 1970).

Within the procedures carried out are: measurements of reservoir hydrodynamics using an Acoustic Doppler Current Profiler (ADCP), with a frequency range of 600 kHz which continuously recorded the magnitude and direction of water velocities. Depths were determined with a bathymetric Sounder Garmin GPSMAP 441S. For hydrometeorology, data from monitoring stations from the Institute of Hydrology, Meteorology and Environmental Studies of Colombia (IDEAM for its acronym in Spanish) were used. From Repelon (code 29035200) and El Limon (code 29035120) stations, located at Latitude: 10.5, Longitude: −75.116667, and Latitude: 10.416667, Longitude: −75.066667, respectively, wind velocity, wind direction, humidity, temperature and precipitation parameters were obtained.

2.1 Model Description

The EFDC Model was originally developed at the Virginia Institute of Marine Science and later sponsored by the US Environmental Protection Agency (USEPA). The EFDC model is a fully dynamic 2D and 3D tool, adaptable to the necessary characteristics of water bodies studies (Hamrick 1992). It is a hydrodynamic and water quality model that can be applied to any surface water body, including lakes and rivers. The characteristics of physical, chemical and ecological processes can be simulated by numerical functions. The EFDC was developed with a structure characterized by a model built with cells of finite elements; the possibility of wetting and drying in the contour processing; allowing exchange of heat with the atmosphere; and simulation of water quality (Wang et al. 2013). It is a package of multi-dimensional hydrodynamic modeling, capable of simulating a diverse range of environmental and transport problems. The model solves 3-D vertically hydro-static, free surface, turbulent averaged equations of momentum for a variable density fluid.

The EFDC is a comprehensive and flexible tool designed for the EFDC modelling system, which was optimized by Dynamic Solutions-International (DSI), who developed a user interface that makes friendly the model implementation, from the data pre-processing to the results post-processing.

The model solves the momentum equations, (1) and (2), the continuity Eq. (3), the state Eq. (4), the transport equations for salinity and temperature (5) and (6),

and the turbulence intensity and the longitudinal turbulence scale, Eqs. (7) and (8). The model uses the sigma coordinate on the vertical and Cartesian or curvilinear orthogonal coordinates in the horizontal axes:

$$\partial_t(Hmu) + \partial_x(m_yHuu) + \partial_y(m_xHvu) + \partial_z(mwu) - (mf + v\partial_xm_y - u\partial_xm_x)Hv$$
$$= -m_yH\partial_x(g\varsigma + \rho) - m_y(\partial_xh - z\partial_xH)\partial_yp + \partial_z(mH^{-1}A_v\partial_vu) + Q_u \tag{1}$$

$$\partial_t(mHv) + \partial_x(m_yHuv) + \partial_y(m_xHvv) + \partial_z(mwv) + (mf + v\partial_xm_y - u\partial_xm_x)Hu$$
$$= -m_xH\partial_y(g\varsigma + \rho) - m_x(\partial_yh - z\partial_yH)\partial_zp + \partial_z(mH^{-1}A_v\partial_zv) + Q_v \tag{2}$$

$$\partial_t(m\varsigma) + \partial_x(m_yHu) + \partial_y(m_xHv) + \partial_z(mw) = 0 \tag{3}$$

$$\rho(P,T,S) = \frac{\rho_0}{\left(1 - \frac{P}{k_P}\right)} \tag{4}$$

$$\partial_t(mHS) + \partial_x(m_yHuS) + \partial_y(m_xHvS) + \partial_z(mwS) = \partial_z(mH^{-1}A_b\partial_zS) + Q_s \tag{5}$$

$$\partial_t(mHT) + \partial_x(m_yHuT) + \partial_y(m_xHvT) + \partial_z(mwT) = \partial_z(mH^{-1}A_b\partial_zT) + Q_T \tag{6}$$

$$\partial_t(mHq^2) + \partial_x(m_yHuq^2) + \partial_y(m_xHvq^2) + \partial_z(mwq^2) = \partial_z(mH^{-1}A_v\partial_zq^2) + Q_p$$
$$+ 2mH^{-1}A_v(\partial_zu)^2 + (\partial_zv)^2 + mgE_1E_2lA_b\partial_zb - 2mH(B_1l)^{-1}q^3 \tag{7}$$

$$\partial_t(mHq^2l) + \partial_x(m_yHuq^2l) + \partial_y(m_xHvq^2l) + \partial_z(mwq^2l) = \partial_z(mH^{-1}A_v\partial_zq^2l)$$
$$+ Q_l + mH^{-1}E_1A_v\left[(\partial_zu)^2 + (\partial_zv)^2\right] + mgE_1E_3lA_b\partial_zb - mHB_l^{-1}q^3\left[1 + E_2(kL)^2l^3\right] \tag{8}$$

where the u and v terms are the velocity components at the horizontal curvilinear-orthogonal coordinates (x and y); m_x and m_y are the square roots of the diagonal components; $H = h + \zeta$ is the sum of the depth below the free surface displacement relative to the undisturbed physical vertical coordinate origin, $z^* = 0$; p is the physical pressure in excess of the reference density; f is the Coriolis parameter; A_v and A_b, are the terms of the vertical turbulent diffusion and vertical diffusion or eddy viscosity; Q_u and Q_v, representing the additional forces or sources and sinks including: turbulent diffusion and horizontal pulse, vegetation resistance and Reynolds stress wave; ρ represents the density; T and S, temperature and salinity, respectively; Q_S and Q_T, include the dissemination of horizontal scale of sub-mesh, and thermal sources and sinks, respectively; q is the diffusion of turbulent intensity; l is the turbulent length scale; and E_1, E_2, E_3, B_1 are empirical constants.
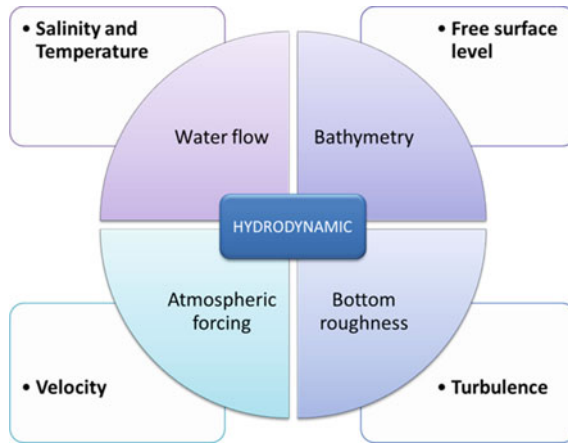
Fig. 1 Structure of the EFDC hydrodynamic model

Figure 1 shows the structure that uses the EFDC model for hydrodynamic surface water.

2.2 Model Calibration

The purpose of the model calibration is to reproduce the mass water movement for known conditions by varying the physical parameters within rationally suitable values (Palacio et al. 2010). To calibrate the model, a total time of 15 days were simulated for two scenarios. The elevations and the corresponding area to the maximum level for that period were used; also outflows and inflows for dry and rainy season, respectively, were determined. To verify the goodness of fit, the root mean square error (RMSE) and the Nash-Sutcliffe efficiency coefficient (Ceff) were used. The error in the model predictions is quantified in terms of units of the calculated variable by RMSE which is expressed in Eq. (9), followed by the efficiency coefficient using Eq. (10).

$$RMSE = \sqrt{\frac{\sum_{i=1}^{n}(O_i - p_i)^2}{N}} \qquad (9)$$

$$Ceff = \frac{\sum_{i=1}^{n}(O_i - p_i)^2}{\sum_{i=1}^{n}(O_i - \bar{O}_i)^2} \qquad (10)$$

where O_i and p_i are the reservoir levels; N is the number of samples in the time series; and $\bar{O}_i$ is the value of the time average reservoir levels.

Validation involves assessing the predictive ability of the model. This means checking the model results with observed data and adjusting the parameters until

the results are within acceptable limits of accuracy. The parameter adjusted in this work was the flow rate flowing in/out through the floodgates system.

2.3   Data Requirement

To configure and implement the model, a dataset was required to specify the boundary conditions or model inputs, thus allowing the corresponding simulations to validate the model for the study area. All data obtained by sampling or measuring equipment were processed and digitized in shape files and displayed in thematic maps, according to the projection WGS (Word Geodetic System) 1984 18N. The ADCP measures were processed and filtered; then the required values and their averages in the water column were extracted. It should be stressed that it was necessary to obtain digitized contours of the reservoir for the sampling dates; satellite images of those dates were obtained from the US Geological Survey, http://glovis.usgs.gov/.

Bathymetry. Depth information was obtained from measurement campaigns carried out on July 18th, 19th and 20th of 2013 for the dry season and October 27th, 28th and 29th for the rainy season of the same year. Figure 2 shows graphically the
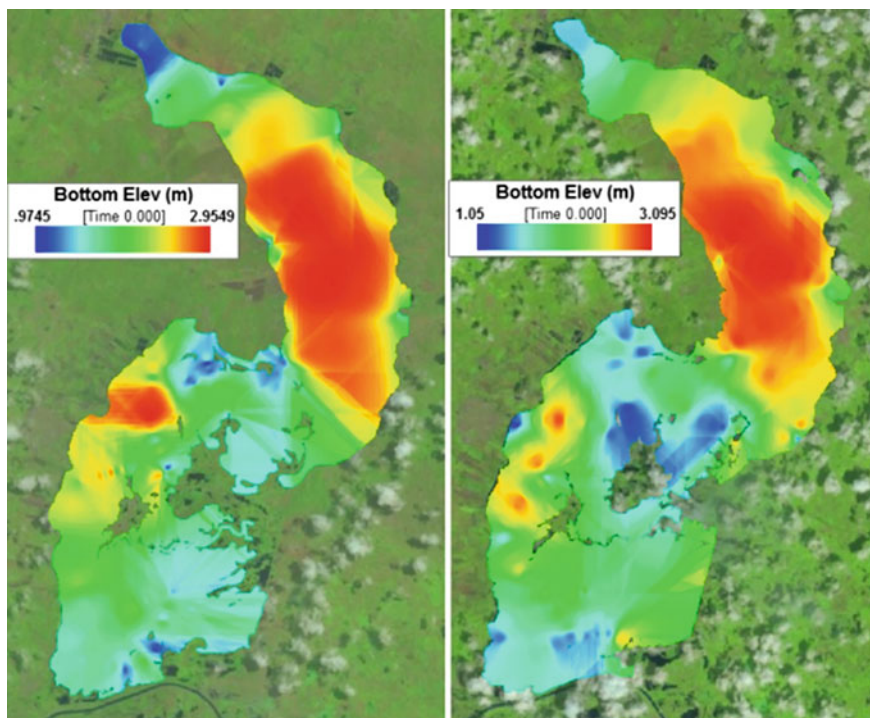
Fig. 2   Bathymetry of Guájaro reservoir; dry season (*left*), rainy season (*right*)
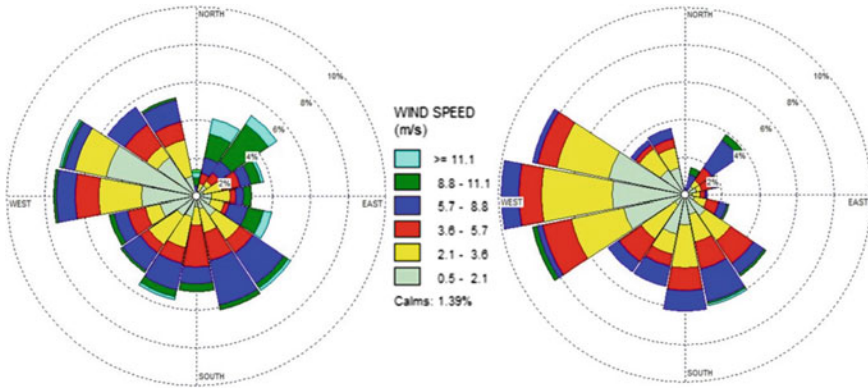
Fig. 3 Wind rose: dry season (*left*); rainy season (*right*)

range of depths of the reservoir in the two selected periods, where the bathymetry covered an area of approximately 12,500 Ha.

Water levels. The corresponding reservoir levels were extracted from the daily measurements records implemented by the environmental authority at the region, The Autonomous Corporation of Atlantic Department (CRA for its acronym in Spanish). These data were compared with the time series calculated by the numerical model, as shown below in Figs. 6 and 8.

Winds. The free surface wind effects were also considered; their magnitudes and directions were obtained from an IDEAM meteorological station, located in the study area (Fig. 3).

3   Model Adaptation

3.1   Study Zone Description

The Guájaro reservoir is considered a strategic ecoregion, located at north Colombia (Fig. 4) at 10°42′ N and 75°6′ W, a few km from the Caribbean Sea. This water body covers an area of 16,000 Ha, a volume of 400 Mm^3; it drains 12,000 Ha by an irrigation district, and has two sets of floodgates that communicate with the *Canal del Dique* channel; these allow the control of the reservoir levels (Uninorte 2009). Today the floodgates have an operation protocol that establishes the actions required according to the hydrological season presented.

Fig. 4 Study zone location
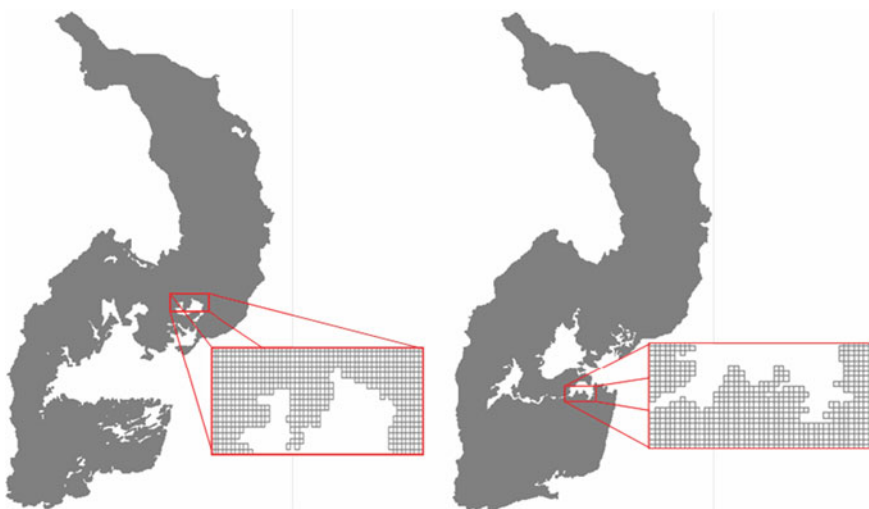
Fig. 5 Computational grid for dry season (*left*) and rainy season (*right*)

3.2 Computational Grid Configuration

A mesh with $\Delta X = \Delta Y = 30$ m was used, for the dry season 320 elements in the horizontal direction and 600 in the vertical direction, for a total of 201,736 elements, of which 84,589 are active cells; and for the rainy season 334 elements in the horizontal and 600 direction in the vertical direction, for a total of 201,736 elements with 84,594 active cells (Fig. 5). The time step used in each simulation was 2 s, generating results every 2 h.
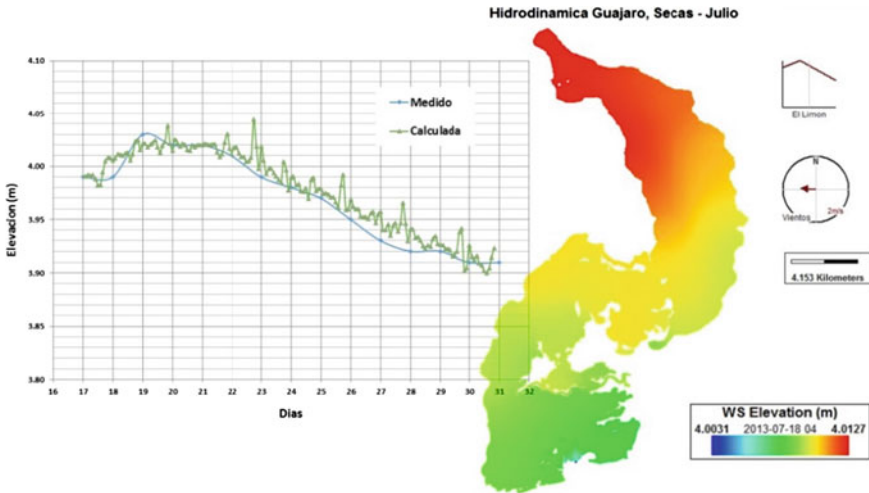
Fig. 6 Behavior of measured and simulated reservoir levels for dry season

4 Results and Discussion

4.1 Dry Season Simulation

The climatological measurements reported for this period show that the Guájaro reservoir reached a maximum level of 4.03 m, and according to the water balance, a minimum level of 3.91 m. Figure 6 shows the variation of the reservoir levels. Likewise, the behavior of reservoir levels obtained with the applied numerical model is illustrated.

Regarding the water body hydrodynamics, the depth averaged velocities were compared with those obtained by the numerical model. This comparison of measured and calculated velocity vectors is shown in Fig. 7.

4.2 Rainy Season Simulation

The measured free surface levels corresponding to the simulated period show that the Guájaro reservoir was 4.08 m above the sea level, and according to the floodgates operations the reservoir reached a maximum level of 4.16 m above the sea level. Likewise, the numerically calculated level behavior is illustrated in Fig. 8.

Figure 9 shows the measured and calculated velocity vectors for the rainy season. For this period, a good correspondence between those measured and calculated is also found.
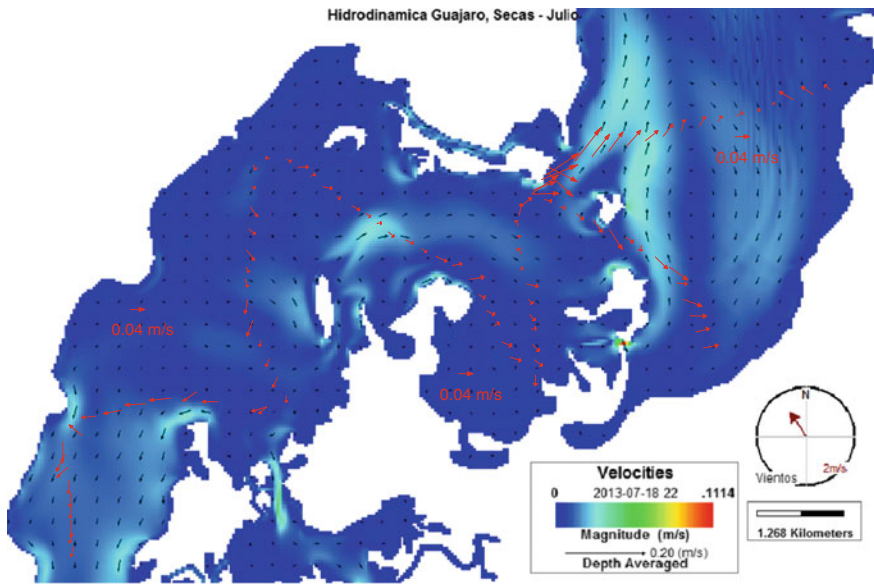
Fig. 7 Measured (*red*) and simulated (*black*) velocity vectors for dry season
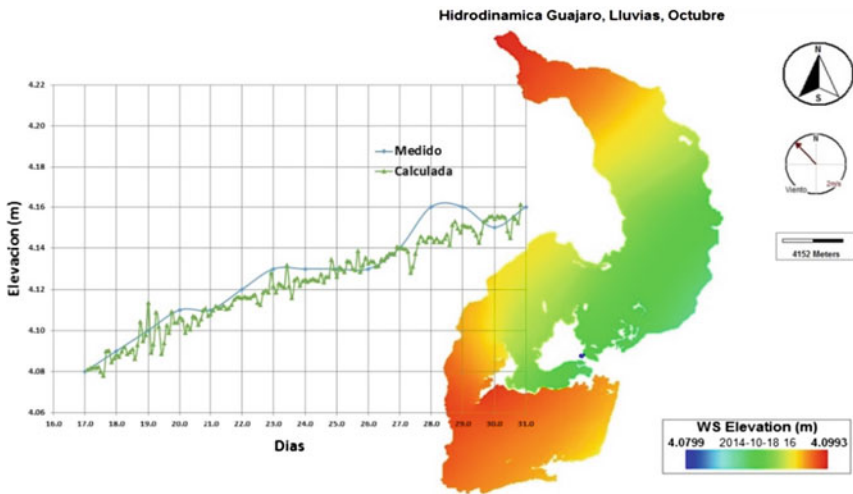
Fig. 8 Behavior of measured and simulated reservoir levels for rainy season
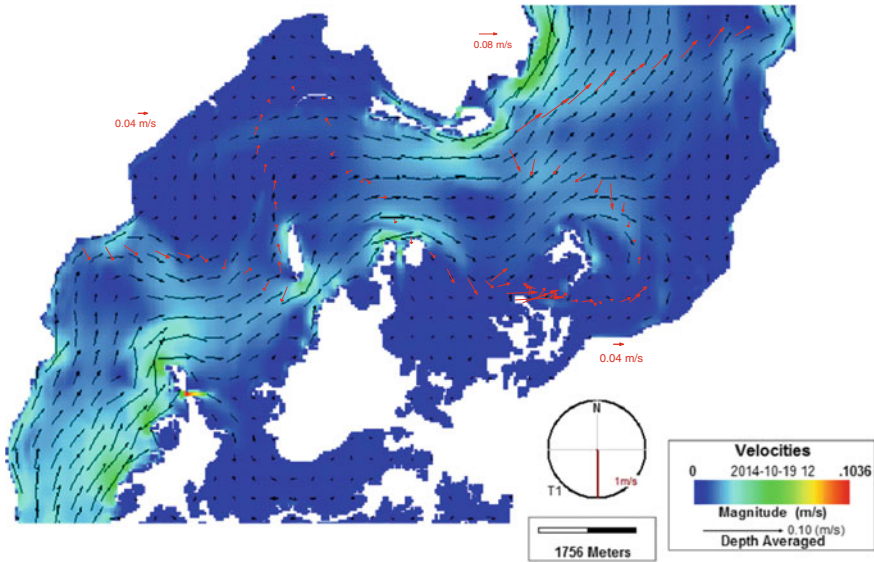
Fig. 9 Measured (*red*) and simulated (*black*) velocity vectors for rainy season

4.3 Calibration Results

In this work, to calibrate the EFDC model, theoretical flows were initially estimated using the difference in water levels and the reservoir surface for each corresponding level. With these values, sequential tests have been conducted by modifying this hydraulic parameter.

As early mentioned, the model results were evaluated using the RMSE y *Ceff* statistical method, to prove if predicted (simulated) water levels results were consistent with the observed values; for dry season (Fig. 6) RMSE = 0.016 and *Ceff* = 0.87263, for rain season (Fig. 8) RMSE = 0.018 and *Ceff* = 0.92709. This show an excellent adjustment and correlation between simulated and field observed, which means, the model results are consistent with the measurements.

The modeling results show, in general, a good agreement with the measurements. The model reproduces quite well the main features of the water movement forced by wind in the Guajaro reservoir. In addition, the results indicate that input and output tributaries (watershed streams, agricultural areas, etc.) play a less important role in the hydrodynamic behavior of the reservoir, while the wind strongly affects velocity fields and circulation patterns.

5 Conclusions

This work shows the EFDC model calibration and validation process for the Guájaro reservoir. This process was carried out comparing the measurements for the two seasons with the calculated or simulated values. The goodness of fit estimators *Ceff* and *RMSE* allow to better estimate the model's capacity to simulate scenarios.

The model has been applied to study the flow exchange through the hydraulic structures (floodgates) that control the water levels of this reservoir; their operation allows the exchange of water within the Canal del Dique-Guájaro hydrosystem. Minimum water levels occur in the dry season, requiring actions to counter the water volume deficit; whereas water levels rise in the rainy season, likewise requiring actions to control the excess volume and levels. Accordingly, the selected model was calibrated and validated for both seasons, proving its ability to simulate and represent the hydrodynamic behavior for these climatic periods.

Given the results obtained in the hydrodynamic calibration and validation processes, this model can be implemented to estimate the possible levels in a water body, considering the climatic factor of occurrence. Finally, the hydrodynamic numerical modeling proves to be an important and useful contribution in the integrated water management and decision making.

References

Dimitriou E, Zacharias I (2006) Quantifying the rainfall-water level fluctuation process in a geologically complex Lake catchment. Environ Monit Assess 119(1–3):491–506

Hamrick JM (1992) A three-dimensional environmental fluid dynamics computer code: theoretical and computational aspects. The College of William and Mary, Virginia Institute of Marine Science, p 317, Special report

Ji ZG, Morton MR, Hamrick JM (2001) Wetting and drying simulation of estuarine processes. Estuar Coast Shelf Sci 53:683–700

Kim SC, Wright DL, Maa JPY, Shen J (1998) Morphodynamic responses to extratropical meteorological forcing on the inner shelf of the middle atlantic bight: wind wave, currents, and suspended sediment transport. In: Spaulding ML, Blumberg AF (eds) Estuarine and coastal modeling V. ASCE, New York, pp 456–466

Luo F, Li RJ (2009) 3D water environment simulation for North Jiangsu offshore sea based on EFDC. J Water Resour Protect 1:41–47

McIntosh BS, Seaton RAF, Jeffrey P (2007) Tools to think with? Towards understanding the use of computer-based support tools in policy relevant research. Environ Model Softw 22:640–648. doi:10.1016/j.envsoft.2005.12.015

Molnar P (2011) Calibration. Watershed modelling. Institute of Environmental Engineering, Chair of Hydrology and Water Resources Management, ETH Zürich, Switzerland

Moustafa MZ, Hamrick JM (2000) Calibration of the wetland hydrodynamic model to the everglades nutrient removal project. Water Qual Ecosyst Model 1:141–167

Nash JE, Sutcliffe JV (1970) River flow forecasting through conceptual models, part I: a discussion of principles. J Hydrol 10:282–290

Palacio C, García F, García U (2010) Calibración de un Modelo Hidrodinámico 2D para la Bahía de Cartagena. DYNA 164(77):152–166

Park K, Jung HS, Kim HS, Ahn SM (2005) Three-dimensional hydrodynamic eutrophication model (HEM-3D): application to Kwang-Yang Bay, Korea. Marine Environ Res 60:171–193

Torres-Bejarano F, Ramirez H, Denzer R, Frysinger S, Hell T, Schlobinski S (2013) Linking numerical water quality models in an environmental information system for integrated environmental assessments. J Environ Protect 4:126–137

Uninorte (Universidad del Norte) (2009) Guajaro reservoir: hydraulic and environmental assessment of current conditions, pp 3–4

Wang Y, Jiang Y, Liao P, Gao X, Huang H, Wang X, Song X, Lei (2013) 3-D hydro-environmental simulation of Miyun reservoir, Beijing. J Hydro-environ Res Engl 1–13 (in press)

Numerical Modeling of Hydrodynamics in the Agua Brava Lagoon, Located in Nayarit, Mexico

H. Barrios-Piña, H. Ramírez-León, A. Cuevas-Otero, F. Torres-Bejarano and J.T. Ponce-Palafox

Abstract In this paper a study of the hydrodynamics of the Agua Brava lagoon system is performed by numerical modeling. The importance of studying this lagoon system lies with aquaculture activities carried out by shrimp farms. The π-HYDRO model is used for the numerical simulations of hydrodynamics and temperature and salinity dispersion. The boundary conditions regarding ocean properties were generated with the HYCOM ocean model, whereas tides were calculated from the tidal predictions of the MAR V1.0. A hydrological study was also performed to calculate the freshwater contributions and take them into account in the numerical simulations. The scenarios analyzed are the dry and wet seasons particularly for 2013. For the case of the dry season, a slight influence of hydrological contributions to the dynamics of the lagoon is observed, where the effects of the tidal flow are predominant. For the wet scenario, the effects of both tidal and hydrological flow drive the motion within the lagoon, especially being predominant the hydrological flow due to the river discharges in the near region to the shrimp farms.

H. Barrios-Piña (✉)
Tecnológico de Monterrey, Guadalajara, Jalisco, Mexico
e-mail: hector.barrios@itesm.mx

H. Ramírez-León
Instituto Mexicano del Petróleo, Mexico City, Mexico
e-mail: hrleon@imp.mx

A. Cuevas-Otero
DEPFI-UNAM, Mexico City, Mexico
e-mail: abraham.esiaz@gmail.com

F. Torres-Bejarano
Faculty of Environmental Sciences, Universidad de la Costa,
Barranquilla, Colombia
e-mail: ftorres4@cuc.edu.co

J.T. Ponce-Palafox
Universidad Autónoma de Nayarit, Tepic, Nayarit, Mexico
e-mail: jesus.ponce@usa.net

1   Introduction

The Agua Brava lagoon is a particularly complex system that signifies an economic, political and social importance for the region. As much of the Mexican coastal systems, the Agua Brava lagoon has been affected by anthropogenic activities and by effects related with the climate global change. The well-known problem of the Cuautla channel is proof of this statement.

The Agua Brava lagoon has a direct interaction with the ocean through the Cuautla channel (the inlet) while being highly influenced by the hydrological and geohydrological components. This causes the lagoon to suffer some alterations due to concentrations of substances dragged by the hydrological flow. The Agua Brava lagoon is characterized by aquaculture activities of shrimp farms located at the landward margin, which are particularly affected by the hydrological flow contamination.

Moreover, the hydrologic balance of the lagoon is drastically altered during the wet season by the occurrence of hurricanes, which cause changes in the physico-chemical and ecological properties.

In this work, a study of the hydrodynamics of the Agua Brava lagoon system by numerical simulations is shown. The π-HYDRO model is used to characterize the flow. This model has been validated and applied in many studies for different coastal zones of Mexico (Ramírez-León et al. 2005a, b, 2010; Rodríguez et al. 2005; Barrios-Piña et al. 2014). Because of the strong influence of the ocean on the lagoon hydrodynamics through the Cuautla channel, the sea properties to be imposed as boundary conditions in the numerical simulations were obtained from the global ocean predictions of the HYCOM model. These conditions were ocean currents, temperature and salinity. For the hydrologic balance, the contribution of the main streams discharging into the lagoon was also considered. A bibliographical compilation of meteorological information from different data bases was completed to determine predominant wind speeds and directions. Astronomical tides were obtained from the application MAR V1.0 developed by the Centro de Investigación Científica y de Educación Superior de Ensenada (CICESE 2015).

The numerical simulations were carried out under two different scenarios: dry and wet seasons. These scenarios were defined based on a hydro-meteorological study of the region. Some visor points distributed near the shrimp farms were fixed to visualize the behavior of currents, temperature and salinity predicted by the numerical model.

2   Case Study

The Agua Brava lagoon is part of the hydrological region RH11B and is delimited by the Acaponeta watershed which is divided into several sub-basins and surface runoffs. The discharge of the Acaponeta River is the largest, where the maximum

occurs during autumn with a monthly average of 505.2 million cubic meters (INEGI 1990).

The Agua-Brava lagoon is also part of a water system known as the Teacapán-Agua Brava lagoon system located in the coastal plain of Nayarit State at the geographical coordinates Lat 22°04′–22°35′N and Long 105°20′–105°50′W. Nayarit is the 23rd state of Mexico regarding territorial extension, and includes the Marias, Marietas and Isabel islands.

The lagoon system is connected to the Pacific Ocean by the Teacapán inlet and the Cuautla channel. The Teacapán inlet is located northwest of the lagoon system in the Municipality of Acaponeta, Nayarit, and is 1,660 m wide with depths from 3 to 9 m. The bottom is predominantly sandy. The artificial channel called Palmar de Cuautla was built in 1976 about 40 km south of the Teacapán inlet. Before the opening of the Palmar de Cuautla channel, the ocean entrance through the Teacapán inlet was restricted to the Teacapán estuary to near the Acaponeta River discharge. After dredging the Palmar de Cuautla artificial channel, the entire lagoon system has undergone an important forcing from tides because of an uncontrolled and gradual growth of the artificial channel (Fig. 1). The Agua-Brava lagoon is a shallow water body with maximal depths of 16 m only observed in the Cuautla channel. The rest of the lagoon shows depths between 1 and 3 m.

Figure 2 shows the study domain considered in the present work for the numerical simulations, where the Cuautla channel is observed at the north and the zone of shrimp farms at the southeast. The red arrows indicate the discharges of the five rivers which drain in the Agua Brava lagoon.
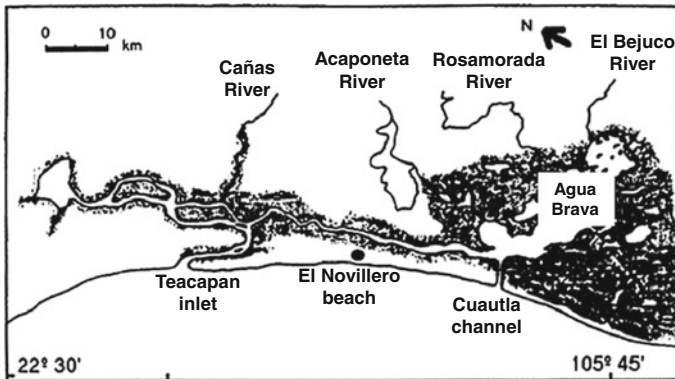
Fig. 1 The Teacapán-Agua Brava lagoon system

Fig. 2 Study domain

3   The π-HYDRO Model

3.1   Governing Equations

The system of equations used to describe the velocity fields and the free surface variations are the shallow water equations, given by:

$$\frac{\partial U}{\partial t} + U\frac{\partial U}{\partial x} + V\frac{\partial U}{\partial y} = -\frac{\rho g}{\rho_0}\frac{\partial \eta}{\partial x} + \frac{\partial}{\partial x}\left(2\nu_E\frac{\partial U}{\partial x}\right) \\ + \frac{\partial}{\partial y}\left[\nu_E\left(\frac{\partial U}{\partial y} + \frac{\partial U}{\partial x}\right)\right], \tag{1}$$

$$\frac{\partial V}{\partial t} + U\frac{\partial V}{\partial x} + V\frac{\partial V}{\partial y} = -\frac{\rho g}{\rho_0}\frac{\partial \eta}{\partial y} + \frac{\partial}{\partial y}\left(2\nu_E\frac{\partial V}{\partial y}\right) \\ + \frac{\partial}{\partial x}\left[\nu_E\left(\frac{\partial U}{\partial y} + \frac{\partial V}{\partial x}\right)\right], \tag{2}$$

where t is the time (in s), U, V and W are the time-averaged velocity components (in m/s), in the x-, y- and z-directions, respectively, ρ is the water density (in kg/m^3), η is the free surface elevation (in m) and ν_E is the kinematic eddy viscosity (in m^2/s) which is defined as $\nu_E = \nu_t + \nu$, where ν_t is the turbulent viscosity and ν is the kinematic viscosity. The turbulent viscosity coefficient ν_t is computed through a mixing-length model of Stansby (2003) and ν is set as the water kinematic viscosity

under standard conditions. Integrating the continuity equation over the water depth and using a kinematic condition at the free surface yields the following free surface equation:

$$\frac{\partial \eta}{\partial t} + \frac{\partial}{\partial x}\left(\int_{-h}^{\eta} U dz\right) + \frac{\partial}{\partial y}\left(\int_{-h}^{\eta} V dz\right) = 0, \tag{3}$$

where the water depth $h(x, y)$ and the free surface elevation $\eta(x, y)$ are measured from a reference level or from the undisturbed water surface.

A state equation is used to compute density variations and is defined as (UNESCO 1981):

$$\rho(P, T, S) = \frac{\rho_0}{\left(1 - \frac{P}{k_P}\right)}, \tag{4}$$

where k_P is a coefficient function of pressure, temperature and salinity. The formulation to compute the value of k_P can be found in UNESCO (1981). The transport equations to compute the temperature and salinity fields are:

$$\frac{\partial T}{\partial t} + U\frac{\partial T}{\partial x} + V\frac{\partial T}{\partial y} = \frac{\partial}{\partial x}\left(K\frac{\partial T}{\partial x}\right) + \frac{\partial}{\partial y}\left(K\frac{\partial T}{\partial y}\right), \tag{5}$$

$$\frac{\partial S}{\partial t} + U\frac{\partial S}{\partial x} + V\frac{\partial S}{\partial y} = \frac{\partial}{\partial x}\left(K\frac{\partial S}{\partial x}\right) + \frac{\partial}{\partial y}\left(K\frac{\partial S}{\partial y}\right), \tag{6}$$

where T and S are time-averaged. The diffusion coefficient K (in m^2/s) is considered function of the turbulent viscosity as $K = \nu_t/\text{Pr}$, where the Prandtl number is $\text{Pr} = 0.9$.

3.2 Numerical Approach

The numerical model is based on a second-order finite difference formulation. A spatial mesh which consists of rectangular cells with horizontal size spaces Δx and Δy, and height Δz, is used. Scalars as density, pressure, temperature and salinity are located at the middle of cells and velocity components are shifted at the middle of cell sides.

Time accuracy is also second-order and the solution method is an adaptation of the semi-implicit Eulerian-Lagrangian scheme proposed in Casulli (1990) and Casulli and Cheng (1992). This method solves the advection and diffusion terms

differently. The solution of the advection terms given by a Lagrangian formulation through the characteristics method and the diffusion terms are computed by an Eulerian formulation through the Adams-Bashforth scheme.

4 Description of the Seasonal Scenarios Under Study

According to the region and based on the period of time during which the shrimp farms are empty (from December to February), only two seasons were considered in this study: dry season from March to April, and wet season from September to October. The year under analysis was 2013. The hydrological flow regime of the lagoon is mainly driven by five rivers: Acaponeta, San Francisco, Rosamorada, Bejuco and San Pedrito. The annual hydrological flow peaks occur between September and October when the lagoon undergoes a strong interaction of both forcing from river discharges and forcing from tides. This condition is characteristic of the wet season and causes an important mixing of freshwater of the river discharges and saltwater of the sea, where salinity concentrations can vary from a limnic state (<0.5 psu) to a hypersaline state (>40 psu). On the other hand, the dry season is characterized by minimal freshwater discharges occurring during a typical year, and the hydrologic balance is mainly given by the interchange ocean-lagoon. Under this condition, the lagoon becomes temporarily hypersaline.

The average monthly discharges of the five rivers were calculated by the rational method for the dry and wet conditions. These discharges were imposed in the numerical simulations as boundary conditions and the flow rates are shown in Sects. 5.2 and 5.3.

The climate of the region is Aw: humid subtropical, according to the Köppen classification (Instituto de Ciencias del Mar y Limnología 2011). The average temperature is 25 °C, the average precipitation is about 1,660 mm and the predominant winds comes from the northeast in winter and from the southwest in summer. The annual average wind speed is of 3.17 m/s in 2013, according to the Sistema Estatal de Monitoreo Agro-Climático de Nayarit of the Instituto Nacional de Investigaciones Forestales, Agrícolas y Pecuarias (INIFAP).

To determine the ocean hydrodynamics and the seawater properties such as temperature and salinity, the real-time assimilated data of the HYCOM ocean model were created for each scenario under study. This allows us to define the appropriate boundary conditions at the Cuautla channel for the numerical simulations. In addition, the corresponding astronomical tide was obtained from the MAR V1.0 application of the CICESE. Since the MAR V1.0 does not report tides of the study zone, tides of Mazatlán, Sinaloa, and San Blas, Nayarit were pondered to generate the tide to be imposed in the Cuautla channel (Fig. 3). The tide is mixed of a semidiurnal predominance.

(a)

(b)
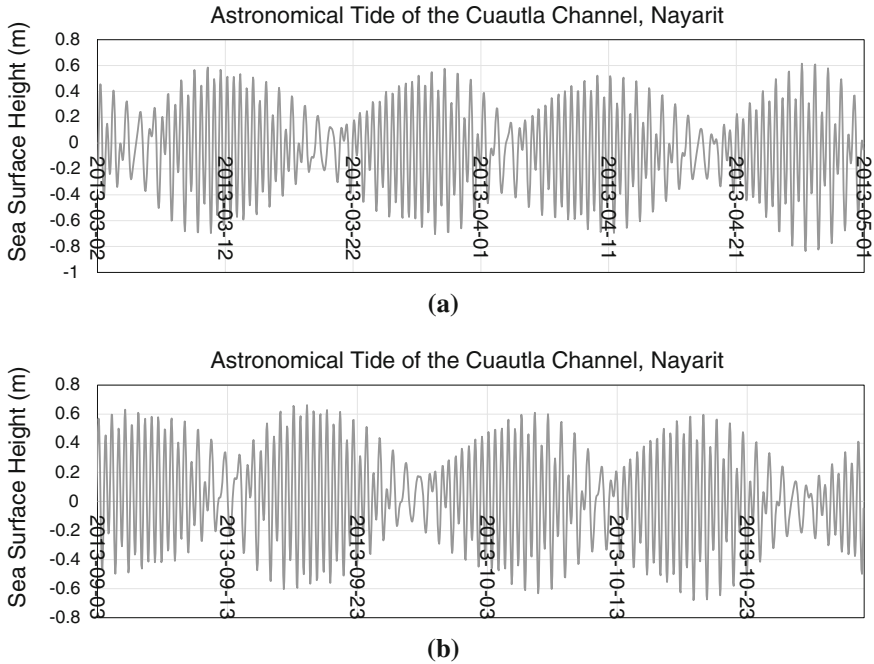
Fig. 3 Astronomical tide calculated in the coast of Agua Brava **a** Dry season; **b** wet season

5 Results and Discussion

5.1 Implementation of the Numerical Model

The mesh used in this study is shown in Fig. 4, which is bi-dimensional and consists of 388 × 340 rectangular cells of space sizes of $\Delta x = \Delta y = 80$ m. The numerical simulations were completed with a time step Δt of 1 s.

To observe the evolution of the hydrodynamic variables, particularly near the shrimp farms of the Agua Brava lagoon, four visors were distributed in some strategic points where the flow velocity components U and V, the free surface elevation, temperature and salinity were stored (Fig. 5).

5.2 Dry Season

As mentioned above, the ocean properties generated with the HYCOM ocean model and the astronomical tide of Fig. 3a were imposed at the Cuautla channel. The initial conditions for the numerical simulations of the dry season were: zero flow velocity, uniform seawater temperature and salinity of 23.0 °C and 34.7 psu,

Fig. 4 Numerical mesh used
for numerical simulations
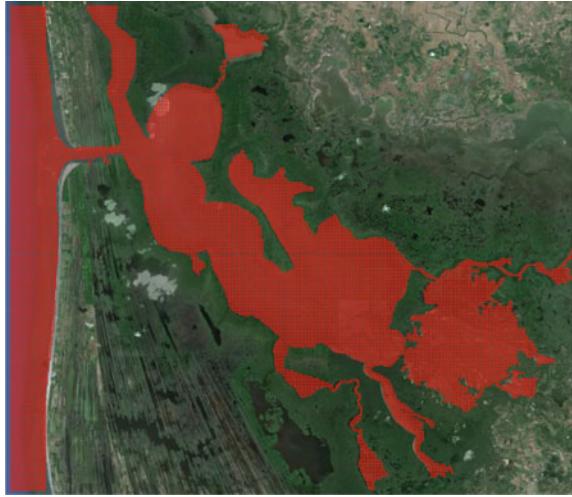
Fig. 5 Visor points located
near the shrimp farms of the
Agua Brava lagoon

respectively; and uniform lagoon water temperature and salinity of 31.3 °C and
34 psu, respectively. Table 1 shows the boundary conditions regarding the dis-
charges of the rivers.

The calculated hydrodynamic, temperature and salinity fields of the lagoon
system are shown in Fig. 6, where the contours are instantaneous fields taken from
the flow evolution. The maximal flow velocities occur within the Cuautla channel
and stagnation zones are observed in the landward margin of the lagoon, near the
shrimp farms. Some recirculating regions are visible with the aid of the streamlines.
The temperature fields as well as the salinity fields show the influence area of the
river discharges.

Table 1 Hydrological conditions considered for the numerical simulations in dry season

River	Discharge (m³/s)		Temperature (°C)		Salinity (ups)	
	March	April	March	April	March	April
Acaponeta	41.5	11.3	34.0	34.0	1.0	1.0
San Francisco	15.7	5.3	34.0	34.0	1.0	1.0
Bejuco-Rosa Morada	35.5	13.8	29.9	29.9	1.0	1.0
San Pedrito	2.9	1.7	38.5	38.5	1.6	1.6

Flow velocity *r* in m/s and streamlines

Temperature in °C

Salinity in psu
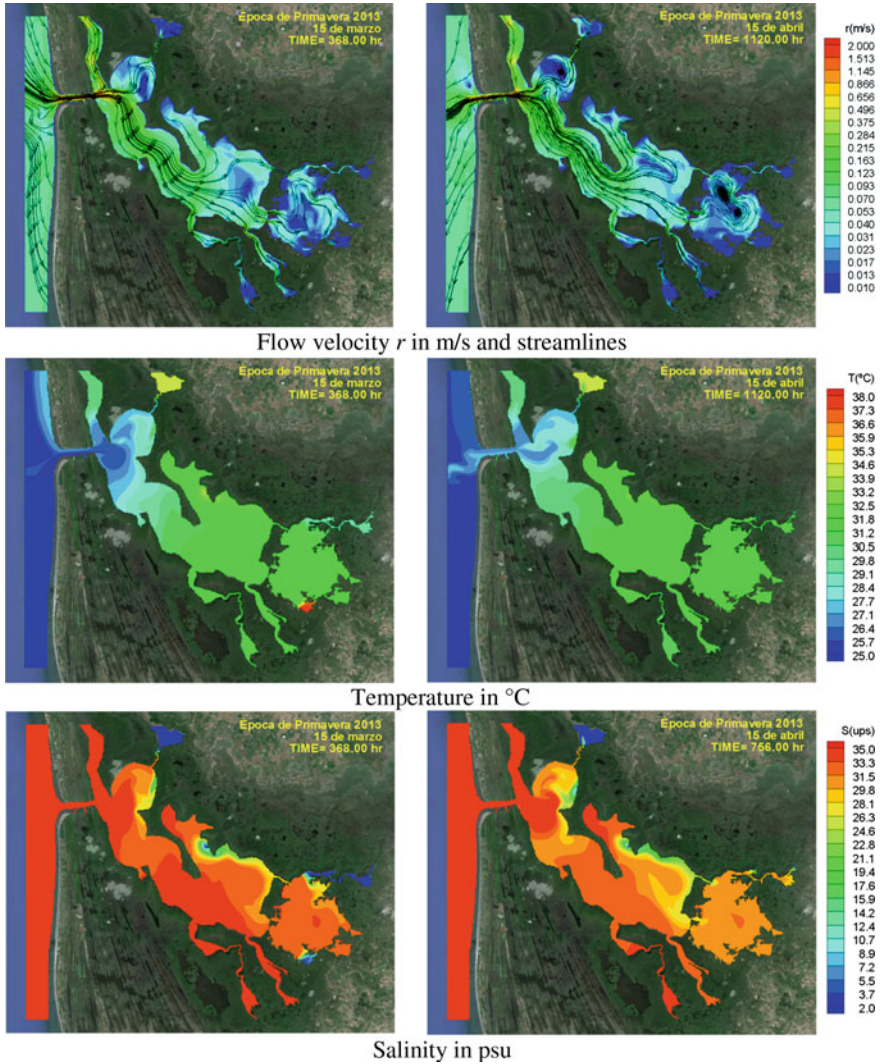
Fig. 6 Flow velocity, temperature and salinity fields of the dry season in Agua Brava lagoon
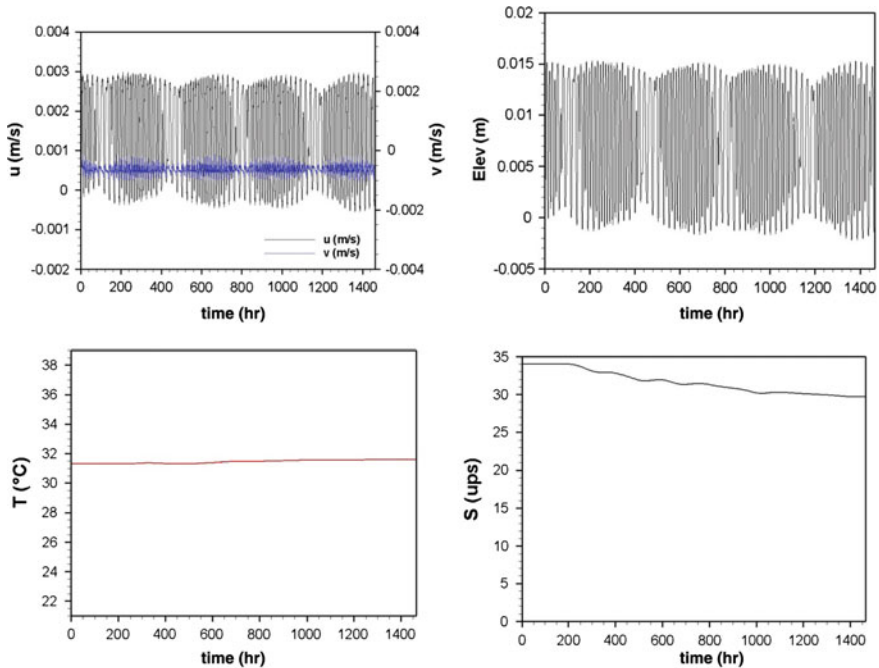
Fig. 7 Evolution of *U* and *V* velocity components, free surface elevation, temperature and salinity, for the dry season in visor 4

For simplicity, only the variables stored in the visor 4 are discussed. Figure 7 shows the evolution of flow velocity components *U* and *V*, free surface elevation, temperature and salinity. The behavior of the velocity components and the free surface elevation exhibits an influence of the ocean because the signals keep the frequency of the astronomical tide imposed at the Cuautla channel. An effect of hydrological flow is perceived through the curve of salinity which shows a slight decrease. The temperature shows no significant variations.

5.3   Wet Season

As well as for the case of dry conditions, the ocean properties of the HYCOM model and the astronomical tide of Fig. 3b were imposed at the Cuautla channel. The initial conditions for the numerical simulations of the wet season were: zero flow velocity, uniform seawater temperature and salinity of 31.5 °C and 34.4 psu, respectively; and uniform lagoon water temperature and salinity of 22.7 °C and 21 psu, respectively. Table 2 shows the hydrological boundary conditions imposed.

Table 2 Hydrological conditions considered for the numerical simulations in wet season

River	Discharge (m³/s)		Temperature (°C)		Salinity (ups)	
	September	October	September	October	September	October
Acaponeta	3,464.6	991.5	21.6	21.6	1.0	1.0
San Francisco	856.1	236.2	21.5	21.5	1.0	1.0
Bejuco-Rosa Morada	2,628.9	611.1	25.4	25.4	1.0	1.0
San Pedrito	92.9	28.73	21.5	21.5	1.6	1.6

Flow velocity r in m/s and streamlines

Temperature in °C

Salinity in psu
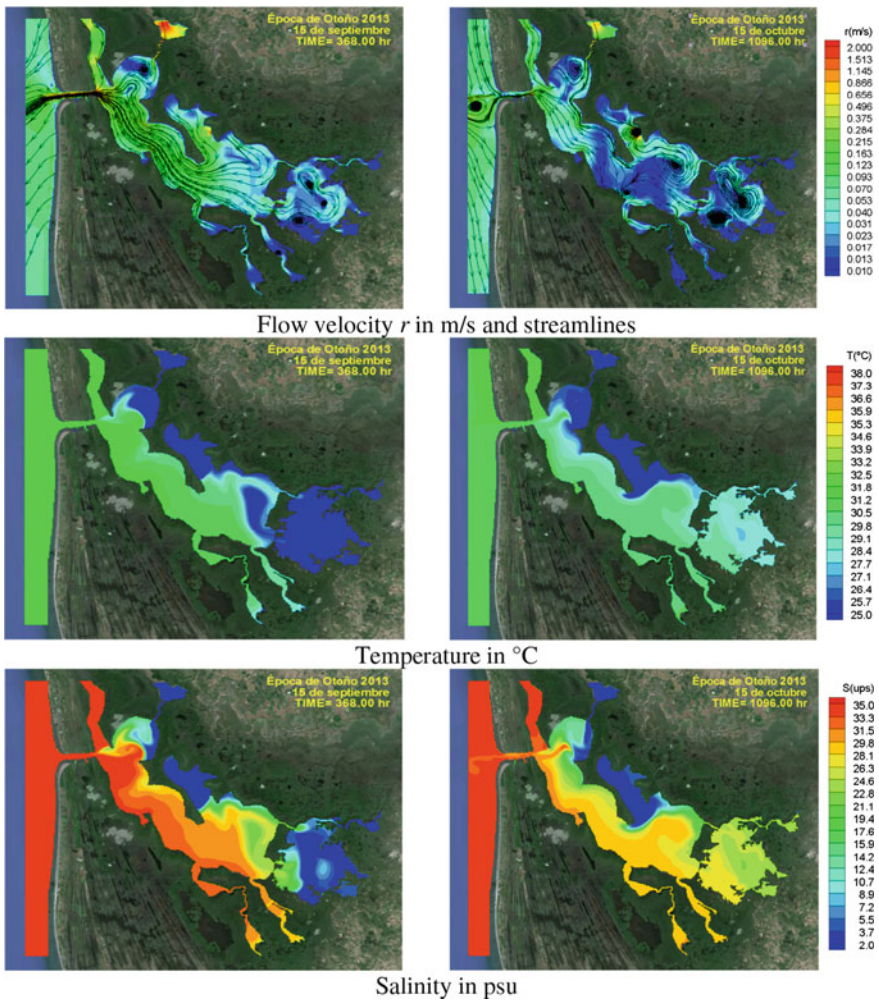
Fig. 8 Flow velocity, temperature and salinity fields of the wet season in Agua Brava lagoon

The calculated hydrodynamic, temperature and salinity fields of the lagoon system are shown in Fig. 8, where the patterns are instantaneous fields taken from the flow evolution. Important flow velocities occur within the Cuautla channel as observed for the dry scenario; however, high velocity values are also denoted in regions near the river discharges. Stagnation zones are still observed in the landward margin of the lagoon, near the shrimp farms. From the streamline patterns, more recirculating flow zones appear within the lagoon compared with the dry season case. The influence of the hydrological discharges is also observed through the thermal and salt dispersions given in the entire lagoon surface.

To compare against the case under dry conditions, Fig. 9 also shows the signals of variables calculated in the visor 4. The behavior of the variables in this case exhibits not only the influence of tide but also the influence of hydrological flow. The distortion observed in the signal of the velocity components and the free surface elevation, at about 350 h of simulation time, is due to effects of hydrological flow transported to the zone where the visor 4 is located. The salinity curve denotes a significant decrease of salt concentration in this point, which confirms the presence of freshwater discharged from the rivers. The temperature does not show significant changes, but it can be relative to the initial and boundary values imposed on each river discharge.
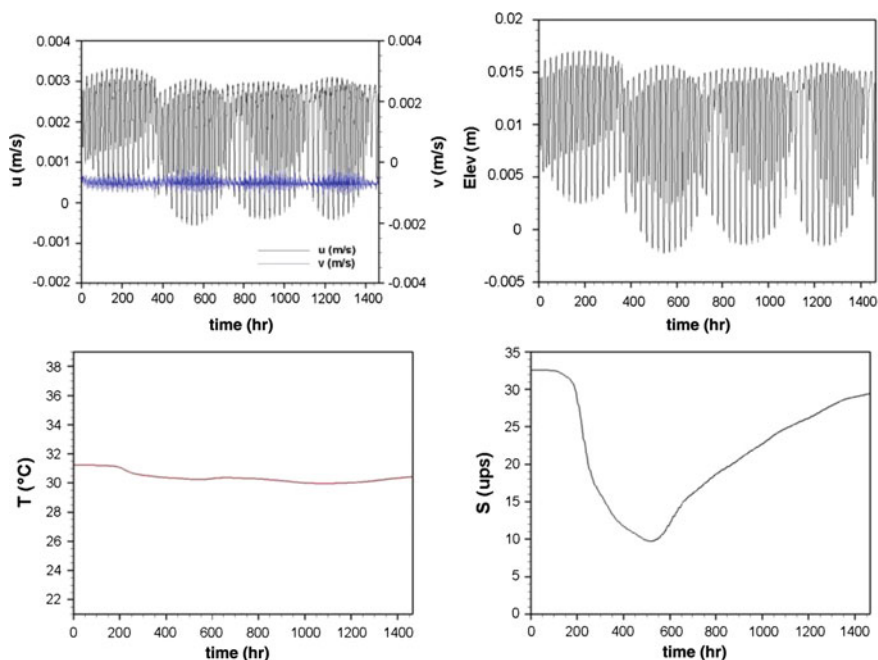
Fig. 9 Evolution of U and V velocity components, free surface elevation, temperature and salinity, for the wet season in visor 4

6   Conclusions

A numerical model for hydrodynamics of the Agua Brava lagoon was implemented and used in this work: an interface was developed with the HYCOM model to generate the properties of the coastal region of Nayarit, Mexico. This is necessary because of the permanent communication existing between the Agua Brava lagoon and the ocean through the Cuautla channel. Simulations for the dry and wet seasons of 2013 were carried out. The hydrologic contribution of the main rivers that reach the lagoon system was considered, the Acaponeta River being the most important. Many visors were distributed in the region near the shrimp farms to monitor the results of the simulations and to observe the impact of tidal and/or hydrological flow on the region near the shrimp farms. From the results, for the dry season a slight influence of hydrological contributions to the dynamics of the lagoon is observed, where the effects of the tidal flow are predominant. For the wet scenario, the effects of both the tidal flow and the hydrological flow drive the motion within the lagoon, especially being predominant the hydrological flow due to the river discharges in the region near the shrimp farms. More recirculating flow zones were observed in the lagoon for the case of wet season, which can be induced by the river discharges.

References

Barrios-Piña H, Ramírez-León H, Rodríguez-Cuevas C, Couder-Castañeda C (2014) Multilayer numerical modeling of flows through vegetation using a mixing-length turbulence model. Water 6:2084–2103

Casulli V (1990) Semi-implicit finite difference methods for the two-dimensional shallow water equations. J Comput Phys 86:56–74

Casulli V, Cheng R (1992) Semi-implicit finite difference methods for three-dimensional shallow water flow. Int J Numer Meth Fluids 15:629–648

CICESE (2015) Programa MAR V1.0. http://predmar.cicese.mx/programa/

INEGI (1990) Clima y precipitación del estado de Nayarit. Instituto Nacional de Estadística, Geografía e Informática. México

Instituto de Ciencias del Mar y Limnología (2011) Vulnerabilidad de las zonas costeras del Pacífico Mexicano (Sinaloa-Nayarit) ante el cambio climático. Programa de Investigación sobre el cambio climático. México D.F

Ramírez-León H, Barrios-Piña H, Rodríguez-Cuevas C, Couder-Castañeda C (2005a) Baroclinic mathematical modeling of fresh water plumes in the interaction river-sea. Int J Numer Anal Model 2:1–14

Ramírez-León H, Rodríguez-Cuevas C, Herrera Díaz E (2005b) Multilayer hydrodynamic model and their application to sediment transport in estuaries. In: Special issue Shanghai conference, current trends in high performance computing and its applications, pp 59–70. Springer, Berlin, Germany

Ramírez-León H, Couder-Castañeda C, Herrera-Díaz IE, Barrios-Piña H (2010) Modelación numérica de la descarga térmica de la Central Nucleoeléctrica de Laguna Verde. Rev Int Mét Num Cálc Dis Ing 15:185–211

Rodríguez C, Serre E, Rey C, Ramírez H (2005) A numerical model for shallow-water flows: dynamics of the eddy shedding. Wseas Trans. Environ Dev 1:280–287

Stansby PK (2003) A mixing-length model for shallow turbulent wakes. J Fluid Mech 495:369–384

UNESCO (1981) Background papers and supporting data on the international equation of state of seawater 1980. UNESCO Tech Pap Mar Sci 38:192

Hydraulic, Hydrodynamic and Environmental Design of an Offshore Outfall for the Campeche Sound Marine Region

A. Cuevas-Otero, H. Ramírez-León and H. Barrios-Piña

Abstract This work focuses on the integral design of an offshore outfall as an alternative to the proper disposal of produced water generated by the oil industry in the Campeche Sound Marine Region. In recent years, the volume of extracted oil has increased and therefore produced water has grown in the same way. This effluent consists of high levels of salinity, temperature and some pollutants related to hydrocarbons. For this reason it cannot be exploited by the oil industry and the only way for managing it is to dispose of it to the sea. Through the implementation of hydrodynamic and water quality numerical models, it was possible to simulate the trajectory and pollutant levels of the effluent when it is transported by the currents outside the outfall. The results showed consistency according to values stipulated by regulations about water disposal.

1 Introduction

The Campeche Sound Marine Region (CSMR) is a zone where industrial production generated by oil extraction plays an important role for the stability of the Mexican economy.

Mature fields located in this region currently have the highest hydrocarbons production in Mexico and a great variety of components which derive from them.

A. Cuevas-Otero (✉)
SEPI-ESIA, IPN, Mexico City, Mexico
e-mail: abraham.esiaz@gmail.com

H. Ramírez-León
Instituto Mexicano del Petróleo, Mexico City, Mexico
e-mail: hrleon@imp.mx

H. Barrios-Piña
Tecnológico de Monterrey, Guadalajara, Mexico
e-mail: hector.barrios@itesm.mx

The process of oil extraction and separation that takes place at the different production centres constantly generates large volumes of produced water and its management represents a big problem for the oil industry. Furthermore, the water pollution problem in many different water bodies is a phenomenon related to the development of industrial processes and increasing marine transportation; all of these issues have significantly increased in recent years (Ramírez-León and Cuevas-Otero 2013).

The referred significant increase in production of produced water related to hydrocarbons has become an important concern for the oil industry given the impact that produced water could cause to the environment and subsea infrastructure.

Currently, hydrodynamic and water quality modeling in conjunction with an accurate hydraulic design represent a reliable option to analyse the viability to implement offshore outfalls as an alternative for managing produce water in the CSMR and avoid increasing levels of ocean pollution.

In this work, a CORMIX model, approved by the Environmental Protection Agency (EPA), was implemented to carry out the hydraulic and hydrodynamic design; later, a π-HYDRO model was used to characterize the flow and π-WQ and π-TOXIC models were adapted to simulate the pollutant dispersion. π Models are supported with CFD techniques and allow us to perform simulations in near field with sufficient accuracy. Given the high range of salinity and temperature characteristic of the produced water, a state equation proposed by Dessouky-Ettouney (2002) was adapted to the hydrodynamic model. The results obtained showed consistency according to values stipulated by regulations related to produced water disposal.

2   Materials and Methods

2.1   Offshore Outfall Description

An outfall consists of submerged pipes that transport industrial and sewage from a treatment plant to an offshore injection zone. The injection site must be previously studied to know the dispersal patterns as a function of the metocean variables which determine the trajectory and pollutants dispersion. There are two possible options when an offshore outfall is designed, the first one consisting of a single jet made by a riser. According to studies reported in the literature, in this case the effluent results in lowered dilutions. The second option consists of a multiport diffuser which is used mostly when the density of the wastewater is higher than the receiving water and high dilution is considered most convenient when the effluent comes into contact with the receiving water body.

2.2 Produced Water Management

Current levels of oil production reach around 2.6 million barrels per day, or over 400,000 m³/d. Products of the exploitation of oil fields consist of a varying mixture of crude oil, gas and water. On average, produced waters represent 20 % water per volume of extracted oil, giving a value of approximately 80,000 m³/d. Produced water is a fluid associated to hydrocarbons in the reservoir, generated during underground extraction of oil. It contains salts and several pollutants, and is considered a waste product which may cause damage to the environment and the existing subsea infrastructure. Offshore disposal of produced water is a new activity in Mexico and therefore there are no appropriate regulations for its management. For this reason standards from Canada and the United States have been consulted to know the maximum allowable limits for each pollutant contained in the produced water.

2.3 Data Requirement

Two databases of metocean information were analysed to obtain the initial and boundary conditions to implement in the numerical models for the hydrodynamic and pollutant dispersion. The first one consists of data such as wind, currents, salinity and temperature measured by the metocean buoy CS2-tamil (Fig. 1),
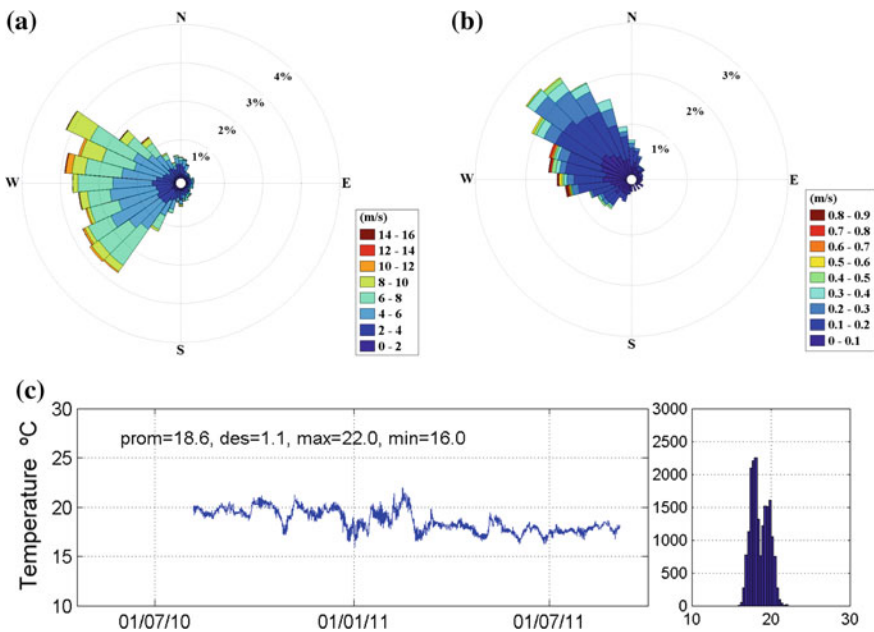
Fig. 1 Metocean variables used for simulations. **a** Wind rose for dry season, **b** magnitude of currents to 42 m deep, **c** temperature values at the end of 2010 and the beginning of 2011

located in the CSMR, and the second one corresponds to measurements made by the Justo Sierra UNAM oceanographic vessel; the measured variables were used to generate global metocean parameters for dry, rainy and cold front seasons in the south region of the Gulf of Mexico (Salas de León et al. 2005). The results of both databases were complemented with simulations generated by the HYCOM ocean model (http://www.hycom.org) to get high accuracy defining initial and boundary conditions for the simulations carried out in this work.

2.4 Numerical Models Description

The CORMIX model (http://www.cormix.info/) was used for the complete design of the riser-feeder-diffuser system; in particular, diffuser design consisted of analysing various options to find the optimal design consisting of 47 nozzles duckbill termination, as described below. Subsequently π models (http://www.pimas-consultores.com) were implemented to simulate the offshore outfall effluent discharge; the first one was the π-HYDRO model, which was used to characterize physical variables such as temperature, salinity and density. The second was the π-WQ model and the third the π-TOXIC model, used to characterize chemical and toxic variables respectively.

2.4.1 π-HYDRO Model Description

Governing equations. The hydrodynamic model π-HYDRO is based on the Reynolds-Averaged Navier-Stokes equations for shallow water flows. These equations describe the velocity fields and the free surface variations (Eqs. 1, 2, 3 and 4, respectively).

$$
\frac{\partial U}{\partial t} + U\frac{\partial U}{\partial x} + V\frac{\partial U}{\partial y} + W\frac{\partial U}{\partial z} = -\frac{\rho g}{\rho_0}\frac{\partial \eta}{\partial x} - \frac{g}{\rho_0}\int_z^\eta \frac{\partial \rho'}{\partial x}dz - \frac{1}{\rho_0}\frac{\partial P_{atm}}{\partial x}
$$
$$
+ \frac{\partial}{\partial x}\left(2\nu_E\frac{\partial U}{\partial x}\right) + \frac{\partial}{\partial y}\left[\nu_E\left(\frac{\partial U}{\partial y} + \frac{\partial V}{\partial y}\right)\right] + \frac{\partial}{\partial z}\left(\nu_E\frac{\partial U}{\partial z}\right) + fV
$$
(1)

$$
\frac{\partial V}{\partial t} + U\frac{\partial V}{\partial x} + V\frac{\partial V}{\partial y} + W\frac{\partial V}{\partial z} = -\frac{\rho g}{\rho_0}\frac{\partial \eta}{\partial y} - \frac{g}{\rho_0}\int_z^\eta \frac{\partial \rho'}{\partial y}dz - \frac{1}{\rho_0}\frac{\partial P_{atm}}{\partial y}
$$
$$
+ \frac{\partial}{\partial y}\left(2\nu_E\frac{\partial V}{\partial y}\right) + \frac{\partial}{\partial x}\left[\nu_E\left(\frac{\partial U}{\partial y} + \frac{\partial V}{\partial x}\right)\right] + \frac{\partial}{\partial z}\left(\nu_E\frac{\partial V}{\partial z}\right) - fU
$$
(2)

$$
\frac{\partial W}{\partial z} = -\left(\frac{\partial U}{\partial x} + \frac{\partial V}{\partial y}\right)
$$
(3)

where t is the time (in s), U, V and W are the time-averaged velocity components (in m/s), in the x-, y- and z-directions, respectively, ρ is the water density (in kg/m^3), η is the free surface elevation (in m) and ν_E is the kinematic eddy viscosity (in m^2/s) which consists of turbulent and molecular components, such that $\nu_E = \nu_t + \nu$.

Integrating the continuity equation over the water depth and using a kinematic condition at the free surface yields the following free surface equation:

$$\frac{\partial \eta}{\partial t} = -\frac{\partial}{\partial x}\left(\int_{-h}^{\eta} U dz\right) - \frac{\partial}{\partial y}\left(\int_{-h}^{\eta} V dz\right) \tag{4}$$

where the water depth $h(x,y)$ (in m) and the free surface elevation $\eta(x,y)$ (in m) are measured from a reference level or from the undisturbed water surface.

The model solves salinity and temperature variations by implementing the transport equations (Eqs. 5 and 6, respectively).

$$\begin{aligned} &\frac{\partial T}{\partial t} + U\frac{\partial T}{\partial x} + V\frac{\partial T}{\partial y} + W\frac{\partial T}{\partial z} \\ &\qquad = \frac{\partial}{\partial x}\left(K_{Tx}\frac{\partial T}{\partial x}\right) + \frac{\partial}{\partial y}\left(K_{Ty}\frac{\partial T}{\partial y}\right) + \frac{\partial}{\partial z}\left(K_{Tz}\frac{\partial T}{\partial z}\right) \end{aligned} \tag{5}$$

$$\begin{aligned} &\frac{\partial S}{\partial t} + U\frac{\partial S}{\partial x} + V\frac{\partial S}{\partial y} + W\frac{\partial S}{\partial z} \\ &\qquad = \frac{\partial}{\partial x}\left(K_{Sx}\frac{\partial S}{\partial x}\right) + \frac{\partial}{\partial y}\left(K_{Sy}\frac{\partial S}{\partial y}\right) + \frac{\partial}{\partial z}\left(K_{Sz}\frac{\partial S}{\partial z}\right) \end{aligned} \tag{6}$$

where T is the temperature (°C) and S is the salinity (psu); K_{Ti} and K_{Si} are the thermal and the salt diffusion coefficients (in m^2/s), and they are evaluated in terms of the Prandtl number as: $K_{Ti} = \nu_t/\text{Pr}$ and $K_{Si} = \nu_t/\text{Pr}$, respectively. In both cases Pr = 0.9.

The density is solved from the state equation proposed by Dessouky-Ettouney (2002), which is in function of temperature, salinity and pressure fields (Eq. 7).

$$\rho(S,T,P) = \frac{\rho_0}{\left(1 - \frac{P}{k_p}\right)} \tag{7}$$

where ρ_0 is the reference density (in kg/m^3) and k_p is a constant coefficient.

Turbulence modeling. The simple mixing-length model for turbulence presented by Stansby (2003) has been implemented in the current numerical model. The defining characteristic of this model is that the horizontal mixing length is explicitly made a multiple of the vertical mixing within a general three-dimensional eddy-viscosity formulation. This means that the horizontal mixing length and associated strain rates determine the magnitude of the eddy-viscosity, which

determines the degree of vertical mixing. The turbulent viscosity coefficient ν_t is then computed through the following mixing-length model:

$$\nu_t = \left\{ l_h^4 \left[2\left(\frac{\partial U}{\partial x}\right)^2 + 2\left(\frac{\partial V}{\partial y}\right)^2 + \left(\frac{\partial V}{\partial x} + \frac{\partial U}{\partial y}\right)^2 \right] + l_l^4 \left[\left(\frac{\partial U}{\partial z}\right)^2 + \left(\frac{\partial V}{\partial z}\right)^2 \right] \right\}^{1/2} \quad (8)$$

where the vertical length scale $l_v = k(z - z_b)$ for $(z - z_b)/\delta < \lambda/k$ and $l_v = \lambda\delta$ for $\lambda/k < (z - z_b)/\delta < 1$; k is the von Karman constant, typically 0.41; $(z - z_b)$ is the distance from the wall; δ is the boundary-layer thickness; and λ is a constant, typically 0.09. In the case of shallow water flows, due to the steady current, the boundary-layer thickness may be assumed to be equal to the water depth h. The horizontal length scale is usually different from the vertical length scale, and the simplest assumption is directly proportionally defined by $l_h = \beta l_v$. The constant β must be determined experimentally. For parallel (or near-parallel) flow cases, eddy viscosity reverts to its standard boundary-layer form. With $l_h = l_v$, it reverts to its correct mathematical three dimensional form (with negligible vertical velocity).

2.4.2   π Water Quality Models

The water quality models π-WQ and π-TOXIC solve the transport equation, which consists of the advection, diffusion and reaction terms as:

$$\frac{\partial C}{\partial t} + U\frac{\partial C}{\partial x} + V\frac{\partial C}{\partial y} + W\frac{\partial C}{\partial z}$$
$$= \frac{\partial}{\partial x}\left(K_{Cx}\frac{\partial C}{\partial x}\right) + \frac{\partial}{\partial y}\left(K_{Cy}\frac{\partial C}{\partial y}\right) + \frac{\partial}{\partial z}\left(K_{Cz}\frac{\partial C}{\partial z}\right) \pm \Gamma c \quad (9)$$

where C (in g/mL) is a generic variable which represents the concentration of any substance or pollutant. The π-WQ model is used to solve physico-chemical and eutrophication variables and π-TOXIC model for toxic variables. The turbulent diffusion coefficients K_{Ci} are solved in terms of the turbulent viscosity. The reaction term Γc is particular of each pollutant or substance and needs to be solved simultaneously by means of a one ordinary differential equation (ODE) or a system of ODE's (Torres-Bejarano 2009).

2.4.3   Numerical Solution of π Models

The numerical model is based on a second-order finite difference formulation. A spatial mesh which consists of rectangular cells with horizontal sizes Δx and Δy, and height Δz is used. Scalars are located at the center of cells and velocity

components are shifted at the middle of cell sides (staggered cell). Each cell is denoted at its center with indices i, j and k (Fig. 2), and the vertical grid can be defined as uniform or variable layers as shown in Fig. 3. The time accuracy is also second-order and the solution method is an adaptation of the semi-implicit Eulerian-Lagrangian scheme proposed by Casulli and Cheng (1992). This method treats the advection and diffusion terms differently. The solution of the advection terms is given by a Lagrangian formulation through the characteristic method and the solution of the diffusion terms is obtained by an Eulerian formulation through the Adams-Bashforth scheme (Ramirez-León et al. 2005; Couder et al. 2008).
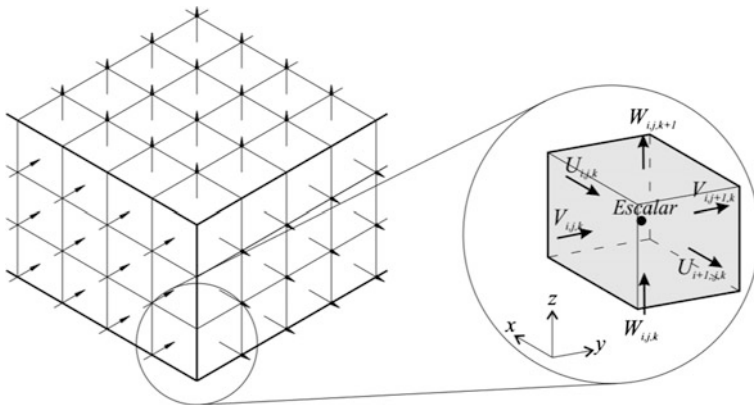
Fig. 2 Position of variables in the numerical cells
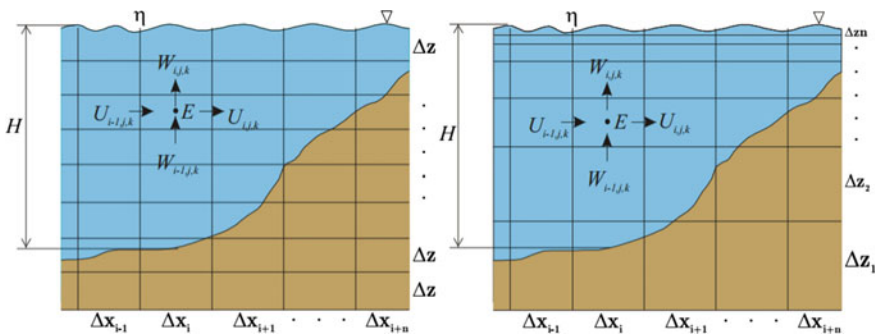
Fig. 3 Vertical options of the π-HYDRO model: on the *left*, constant layers; on the *right*, variable layers

3 Offshore Outfall Designs

In this work the design of an offshore outfall for the oil industry was carried out because of the large quantities of produced water generated in the CSMR that need to be disposed of into the sea according with the regulations. A review of design parameters and the operation of the proposed outfall were made to guarantee an optimal dilution of the effluent.

3.1 Environmental Review and Design Parameters

The CSMR presents a great variation in sea salinity, temperature and density, current patterns and meteorological parameters. In this work, dry season was considered as the main climatic scenario because salinity and temperature increase due to the absence of rains and slow currents, which results in a critical scenario for the pollutants dispersion. Figure 4 shows the salinity and temperature gradients from water surface to the bottom.

3.2 Riser-Feeder-Diffuser

The outfall is integrated by a riser, a feeder and a multiport diffuser, which work together to dispose of produced water to the sea (Fig. 5).

For optimal functioning of an outfall, hydraulic and hydrodynamic studies are necessary; the hydraulic study provides velocity and volume flux variables for each nozzle of the multiport diffuser. These variables are required as initial and boundary conditions to make the hydrodynamic and pollutant dispersion.

The primary objective of the multiport diffuser is to reduce pollutants to safe levels that have minimal toxic effects on marine environment (Abessi 2014). The multiport diffuser designed measures 60 m, it consists of forty-seven ports; the port
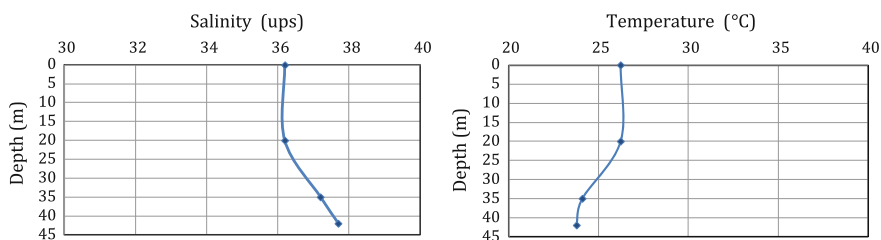
Fig. 4 Vertical structure for dry season: salinity (*left*); temperature (*right*)
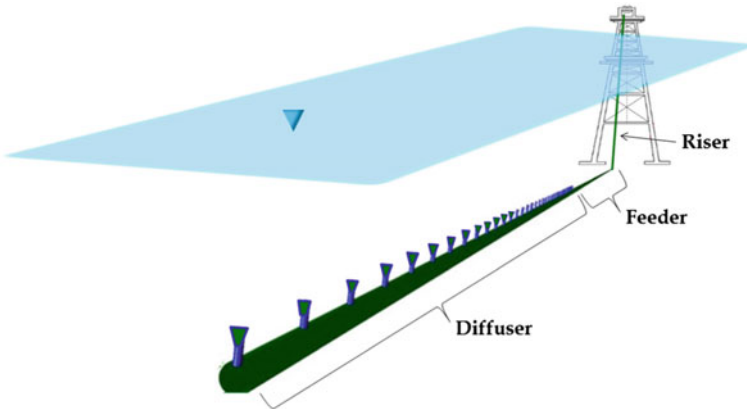
Fig. 5 Components of an offshore outfall

Table 1 Boundary and initial conditions—dry season

Parameter	Value
Discharge characteristics	
Discharge salinity	135 psu
Discharge temperature	40 °C
Number of ports	47
Port diameter	0.05 m
Environment properties	
Sea salinity	37.59 psu
Sea temperature	23.40 °C
Currents direction	W
Intensity of bottom currents	0.029 m/s
Wind intensity	2.5 m/s

spacing in this case is 1.1 m between each other and the shape of the port is duckbill because of the high dilution achieved with this type of nozzle.

In Table 1 boundary and initial conditions for the simulations are presented. First, the discharge characteristics such as salinity, temperature and velocity are shown and secondly the environment properties such as salinity, temperature, currents and wind intensity are given.

3.3 Hydraulic Analysis

When designing an offshore outfall, hydraulics and hydrodynamics parameters are essential to know the inner workings of the system and predict changes in salinity and temperature in the environment.

The high velocities at the nozzles in contact with the environment can quickly reduce levels of potential contaminants to safe levels. Also, an important hydraulic parameter that must be taken into account is the densimetric Froud number, salt-water intrusion can be avoided by keeping this consideration (Wilkinson 1988), which must satisfy the following relation given in Eq. 10:

$$F_p = \frac{V_p}{\sqrt{g' D_p}} > 1 \tag{10}$$

where V_p denotes the port exit velocity (in m/s); D_p the port diameter (in m); $g' = g\Delta\rho/\rho$ is the reduced gravity, which considers the density difference ($\Delta\rho$) at the port orifice between the effluent and the ambient water. This condition can be achieved by designing either small enough port diameters or using variable area orifices.

Hydraulic design was carried out using CORMIX model; Fig. 6 shows the results for each port and jet velocity from the multiport diffuser where the lowest velocity equal to 1.5 m/s was reached at the end of the diffuser (nozzle 1) and the highest velocity equal to 2.7 m/s was reached at the beginning of the diffuser (nozzle 47).

In the same way, Fig. 7 shows the volume flux distribution along the forty-seven nozzles located over the diffuser. The total pressure required to guarantee the optimal functioning of the outfall is 7.048 kg/cm^2, which was calculated from the free water surface at the location of the riser to the last nozzle located at the end of the diffuser.
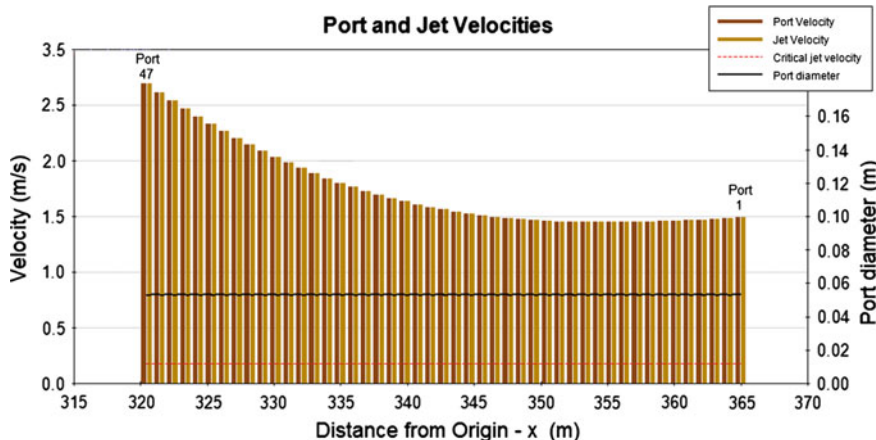
Fig. 6 Port and jet velocities in each nozzle
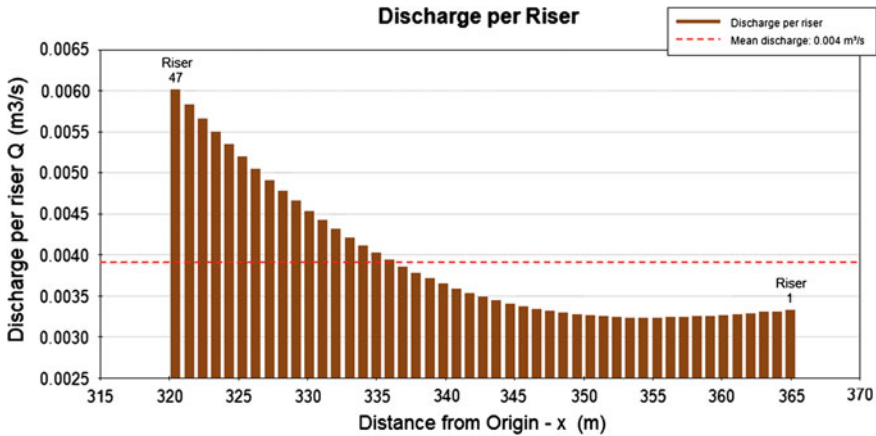
Fig. 7 Volume flux distribution in each nozzle

4   Results and Discussion

This section shows the results of the temperature and salinity plume dispersions obtained with the π-HYDRO model. The Total Petroleum Hydrocarbons (TPH) and Hydrogen Sulphide (H_2S) dispersions computed with the π-WQ and π-TOXIC models are also described; according to some studies, these pollutants present high concentration levels when produced water is separated from the oil.

Temperature and salinity dispersion. In Fig. 8 the plume characterizes the salinity and temperature dispersion generated by the diffuser, where the thermo-dynamics stratification plays an important role to avoid the plume reaches the free water surface. The initial salinity was reduced in about 75 % when the effluent got in contact with the environment as shown on the left side of Fig. 8. On the other hand, the temperature decreased about 40 % as shown on the right side of Fig. 8 in the x-z and y-z planes respectively.

Pollutants dispersion. In this section results from numerical simulations for pollutants such as TPH and H_2S are presented and discussed. In Fig. 9, 3D, x-y and x-z visualizations are shown for the plume dispersion, where dry season obtained the highest concentrations compared with rainy and cold-front seasons.

Discussion. The results of hydrodynamic and water quality modeling yield lower concentration levels compared to the initial values pollutants had before the numerical simulations. Physical components of produced water such as salinity reduced about three times their initial concentration; otherwise, the temperature decreased about 40 %. TPH and H_2S, as part of chemical and toxic pollutants, reduced significantly their initial concentration in several orders of magnitude. The contaminant plume in all cases indicates local impact around the diffuser.

3D visualization

planes x-z

planes y-z
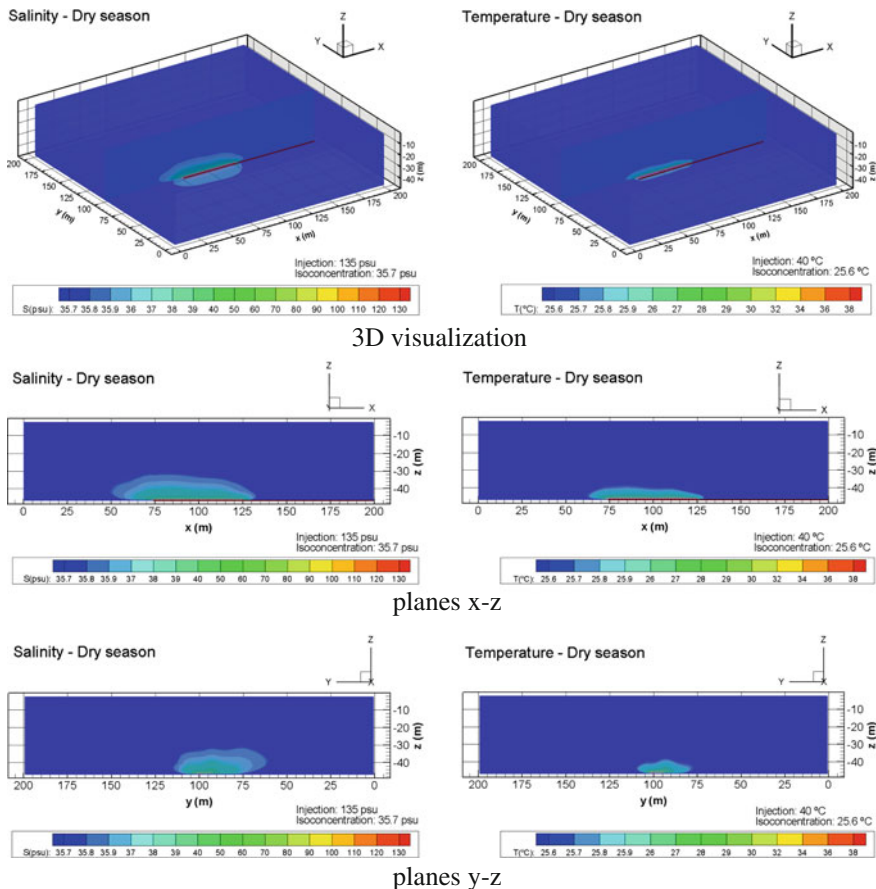
Fig. 8 Plume dispersion: salinity (*left*); temperature (*right*)

5 Conclusions

This study serves as a guide for the design of offshore outfalls to reduce physical and chemical concentrations of this kind of effluents, since the results for all the pollutants modelled showed lower levels. Furthermore, numerical modeling and hydraulic design confirmed to be adequate tools to make an integral analysis for this kind of problematic and provide enough accuracy in the results.

3D visualization

Planes x-z

Planes y-z
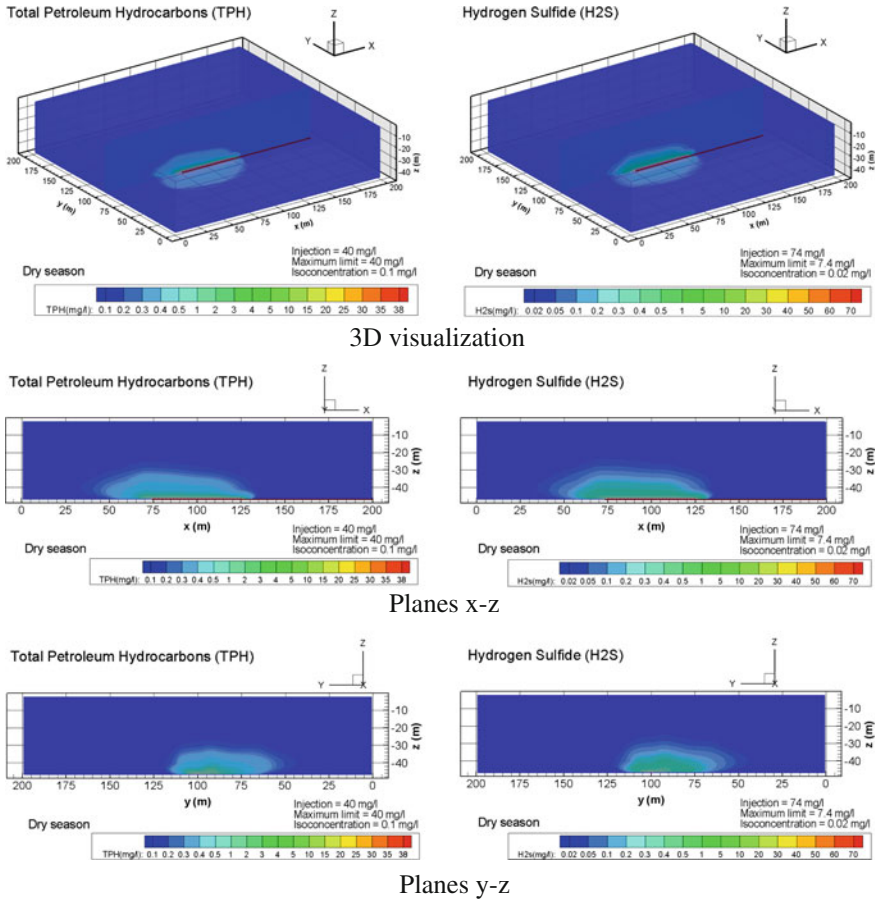
Fig. 9 Plume dispersion: TPH (*left*); H$_2$S (*right*)

References

Abessi O, Roberts PJW (2014) Multiport diffusers for dense discharges. American Society of Civil Engineers, United States

Bleninger T (2006) Couple 3D hydrodynamic models for submarine outfalls: environmental hydraulic design and control of multiport diffusers. PhD, Institute for Hydromechanics, University of Karlsruhe, Germany

Bleninger T, Lipari G, Jirka GH (2002) Design and optimization program for internal diffuser hydraulics. In: Proceedings of international conference marine waste water discharges, Istanbul, Turkey

Casulli V, Cheng RT (1992) Semi-implicit difference methods for three dimensional shallow water flow. Int J Numer Meth Fluids 15:629–648

CNA (2004) Manual para el diseño de emisores submarinos, Mexico

Couder C, Ramírez H, Herrera E (2008) Numeric Optimization of the hydrodynamic model YAXUM/3D. Capítulo 342 Del Libro numerical modeling of coupled phenomena in science and engineering-practical uses and examples. Publicado por Springer Verlag

El-Dessouky HT, Ettouney HM (2002) Fundamentals of salt water desalination. ELSERVIER Science B. V., The Netherlands

Ramírez-León H, Barrios-Piña H, Rodríguez-Cuevas C, Couder-Castañeda C (2005) Baroclinic mathematical modelling of fresh water plumes in the interaction river-sea. Int J Numer Anal Model 2:1–14

Ramírez-León H, Cuevas-Otero A (2013) Estudio para la selección del difusor marino para el centro de proceso Akal-J. Instituto Mexicano del Petróleo, Mexico

Salas DA et al (2005) Simulación numérica de la circulación oceánica de la Región Marina de la Sonda de Campeche. Instituto de Ciencias del Mar y Limnología, UNAM, Mexico

Soto AL (2009) PEMEX y la salud ambiental de la Sonda de Campeche. Instituto Mexicano del Petróleo, Mexico

Stansby PK (2003) A mixing-length model for shallow turbulent wakes. J Fluid Mech 495:369–384 (Cambridge University Press, United Kingdom)

Torres-Bejarano FM (2009) Desarrollo de un sistema de información ambiental para el estudio integral de ecosistemas acuáticos vinculados a la industria petrolera. PhD, Instituto Mexicano del Petróleo, Mexico

Wilkinson DL (1988) Avoidance of seawater intrusion into ports of ocean outfalls. J Hydraul Eng 114(2)

Numerical Air Quality Forecast Modeling System: Mexico Case Study

A.R. Garcia, B.E. Mar-Morales and L.G. Ruiz-Suárez

Abstract Air pollution has effects on ecosystems, infrastructure and human health, and therefore it is important to develop pollution exposure reduction. Large cities, like Mexico Megacity, have high pollution concentration episodes, even though an air quality monitoring network can measure and issue alarms when high level of air pollutants concentrations are reached, the population is exposed to harmful air pollutants before being aware of it. Air quality forecast information can reduce exposure to air pollution high concentrations for sensitive and general public. This work describes an operative air quality forecast modeling (AQFM) system. The modeling domain covers Mexico country, it uses a meteorology-chemistry coupled model in a high performance computing hardware, the AQFM forecasts primary (carbon monoxide CO, sulfur dioxide SO_2) and secondary (ozone O_3) air pollutants, and the time span is for up to 42 h starting at 12Z. Model results are given in terms of pollutant concentration distribution images, which are displayed in a web site. System like this can be applied for regional or urban areas in order to advice and to reduce pollution exposure.

Keywords Forecast · Air quality · Numerical modeling · Emissions inventory · Ozone · Mexico

1 Introduction

The World Health Organization (2011) estimates that 3.7 million premature deaths are due to air pollution, which also has negative effects on materials, plants, animals and climate. Pollutant concentrations depend on emissions, atmospheric chemistry

A.R. Garcia (✉) · B.E. Mar-Morales · L.G. Ruiz-Suárez
Centro de Ciencias de la Atmósfera, UNAM,
Circuito de la Investigación Cientìfica s/n, 04510 Mexico, D.F., Mexico
e-mail: agustin@atmosfera.unam.mx
URL: http://www.atmosfera.unam.mx

195

and weather conditions. In order to understand the pollution phenomenon it is required to have information about emissions, meteorological conditions and chemical interaction among different compounds in the atmosphere. On the one hand, a vast amount of data is required and, on the other hand, the air quality modeling simulation uses a considerable amount of computer resources and high-performance computing is required in order to obtain results in a reasonable time. In this work a description of the emissions, the coupled weather-air chemistry model, the air quality forecast modeling (AQFM) system setup and visualization products are described in the method section. Examples of the products are presented in Sect. 3, while the discussion of the results along with the conclusions and future developments are given in Sect. 4.

2 Method

The complexity of air pollution and its forecast involves the use of different information data sets to produce the forecast. It is required to incorporate topography elevation, land use, soil properties, pollutant emission, solar radiation and weather variables in order to compute the atmospheric photochemistry and air pollutant dispersion. With all this input it is possible to obtain the regional air quality. The following sections describe the input information and the model used to obtain the air quality forecast.

2.1 Emissions Inventory

Air pollutants are emitted from different human activities. In an atmospheric chemistry model, it is necessary to have, for each source, its spatial, temporal and chemical distribution allocated in a gridded mesh. The Mexican National Emissions Inventory 2008 (sub-sistema del Inventario 2016) was used to produce a model ready emissions inventory. Figure 1 presents in general terms the procedure. The first step was to map each emissions category with its corresponding U.S. Environmental Protection Agency (EPA) source classification code (SCC) (US EPA http://www.epa.gov/ttn/chief/net/2011inventory.html). Geospatial information from land use (INEGI 2007–2010), population density (INEGI 2010a, b) and roads and highways from (INEGI 2011) were used in order to allocate spatially the emissions in the mesh. The temporal emissions allocation was performed by using the SCC data (US EPA http://www.epa.gov/ttnchie1/emch/temporal/). EPA emissions speciation (US EPA http://www.epa.gov/ttnchie1/emch/speciation/) based on SCC was used in order to disaggregate volatile organic compounds (VOC) and PM2.5 particles into individual chemical species components. In order to perform this procedure a set of fortran programs was developed and the product of those programs is the emissions inventory in netcdf format file (Unidata http://www.unidata.ucar.edu) that can be read by the WRF-chem model.
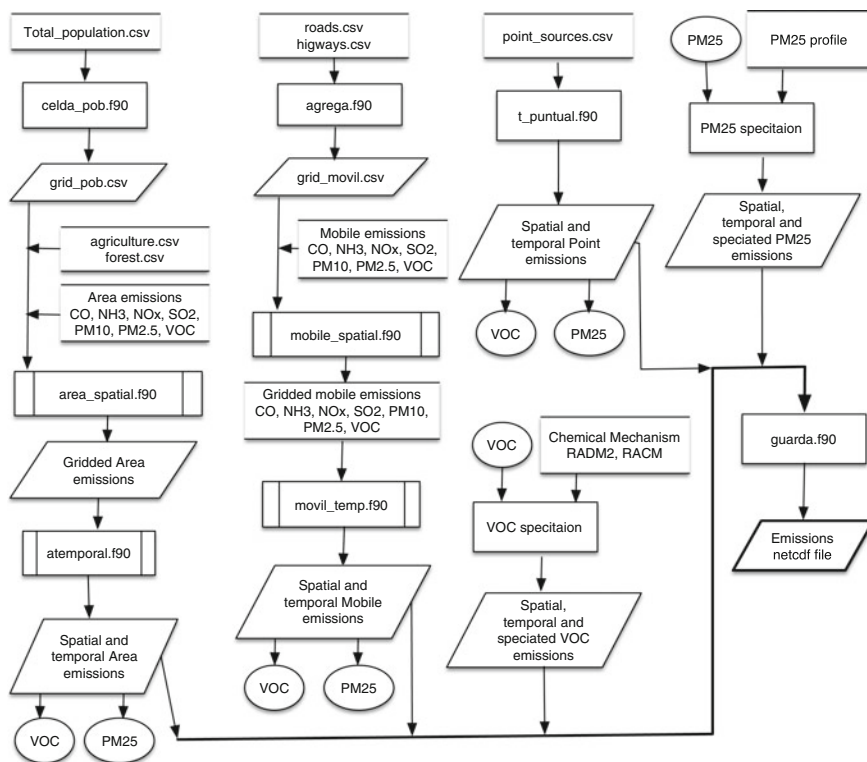
Fig. 1 Conversion of area, mobile and point emissions into model emissions. Spatial distribution, temporal allocation and chemical categories were added to the original emissions

2.2 Air Quality Model

A coupled meteorology-transport-chemistry model, i.e., the Weather Research and Forecasting/Chemistry (WRF-chem) is used to estimate the air quality in the domain. A fully description of the model can be found in Grell et al. (2005), Fast et al. (2006) and Peckham et al. (2011). This model was developed for use in parallel computer.

The domain used for the air quality forecast system considers a grid of 147 per 104 cells, each one of 24 per 24 km and 30 vertical levels. The following parametrizations were used: microphysics single moment 5-class scheme ($mp\_physics = 4$), Longwave Radiation Rapid Radiative Transfer Model RRTM ($ra\_lw\_physics = 1$), short wave radiation Goddard scheme ($ra\_sw\_physics = 2$), surface layer ETA similarity ($sf\_sfclay\_physics = 2$), land surface rapid update cycle land surface model ($sf\_surface\_physics = 3$), planetary boundary layer Mello-Yamada-Janjic scheme ($bl\_pbl\_physics = 2$), cumulus parametrization Grell 3D ($cu\_physics = 5$), the chemical mechanism RADM2 and MADE/SORGAM aerosols ($chem\_opt = 2$) module.

All these schemes and modules are described in detail in the WRF-chem user's guide (WRF-Chem 2014).

The run configuration of the WRF-chem model was compiled and executed using the message passing interface mpich2 (MPI 2016) for distributed-memory applications in 28 AMD cores.

2.3 Air Quality Forecast System

The air quality forecast is performed by using a set of c-shell scripts. The main control script (`ejecuta.csh`) is described. This script starts after the downloading the meteorological information from the Global Forecast System (National Centers for Environmental Prediction 2016). In `do_wps.csh` a file name list.input is configured to start the forecast from current day 12Z and 42 h after, it prepares the input files for the vertical interpolation performed by `do_real.csh` script. The meteorological and the atmospheric chemistry is computed for the selected area and time period by using `do_wrf.csh` script. The post processing uses an ARW post utility and a GrADS script (GrADS 2016) to generate all the figures in jpg format and after that it the `sube_fig.csh` script upload the files in the Air Quality Forecast web page server. A scheme of this procedure is shown in Fig. 2. An additional step is the
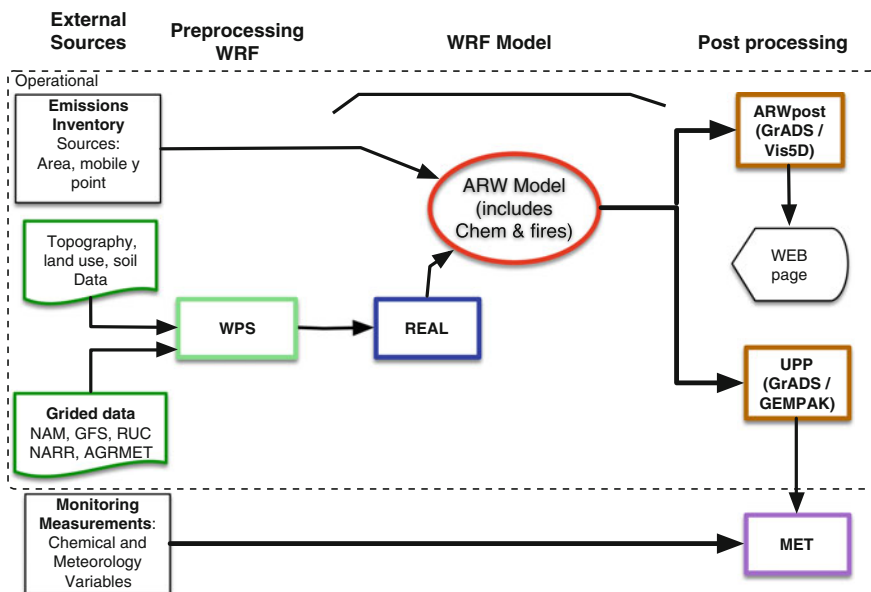
Fig. 2 Forecast system scheme

model evaluation using the Unified Post Processing code (UPP) (NCEP 2016) which is used to compare model results against observations.

A web page (http://www.atmosfera.unam.mx/procca/principal.php) displays the results of the real-time forecast. Ozone concentration figures are for central Mexico, Guanajuato, Chiuahua, Guadalajara and Monterrey-Saltillo, and in the case of particles $PM_{2.5}$ only for central Mexico.

3 Results

The domain considered is displayed in Fig. 3. It covers the south part of US, Mexico and Central America.

Figure 4 presents the distributed emissions for carbon monoxide. There are 252 images produced for the web page. Figure 5 shows a sample of the web page. Meteorological information was downloaded at 00:05 am and the final images were uploaded by 3:50 am. Current illustrations display ozone concentrations (ppb). In future work, an air quality atmospheric index can be applied for public use. The total time employed to perform only the air quality forecast was 180 min.
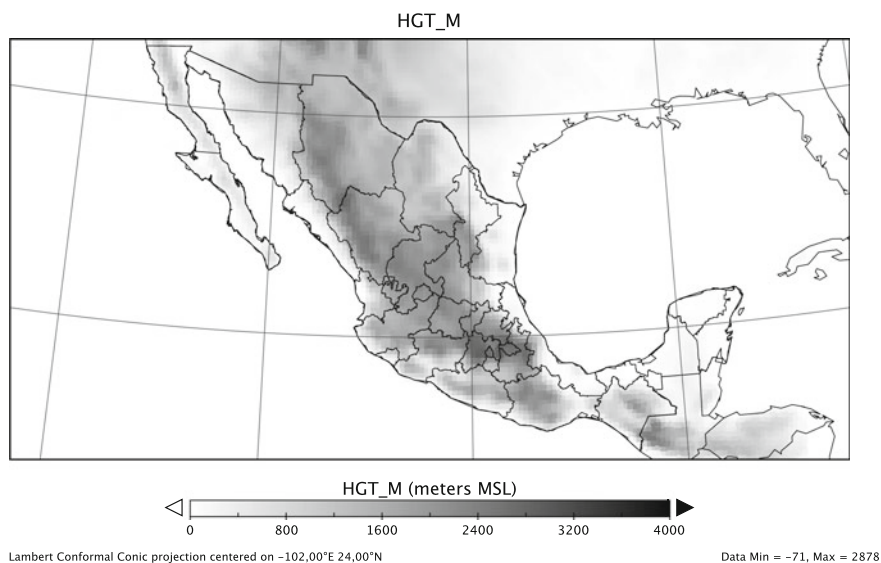
Fig. 3 Forecast domain used, *shaded* areas is topography elevation (m.a.s.l.)

CO emissions

E_CO (mol km^–2 hr^–1)

Lambert Conformal Conic projection centered on –102,00°E 24,00°N   Data Min = 0, Max = 3154
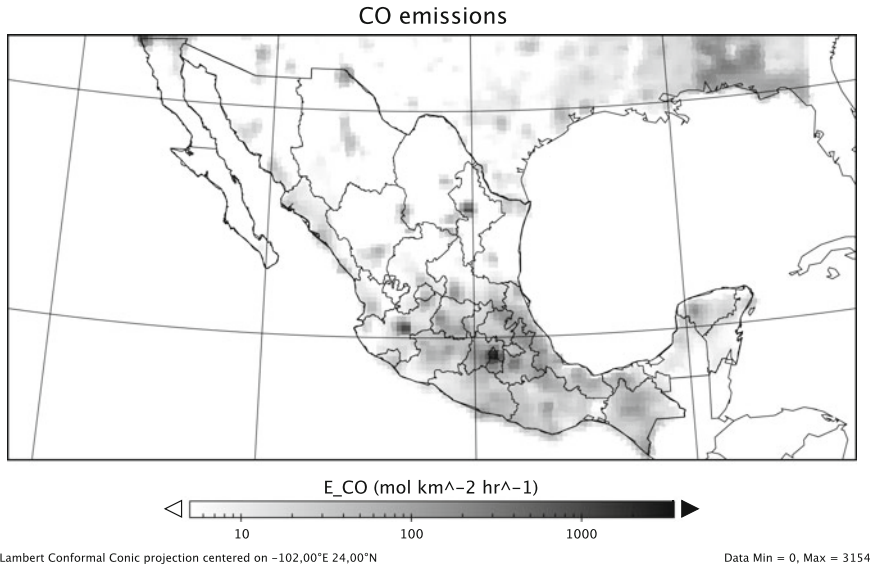
Fig. 4 Carbon monoxide (CO) emissions obtained by the conversion procedure
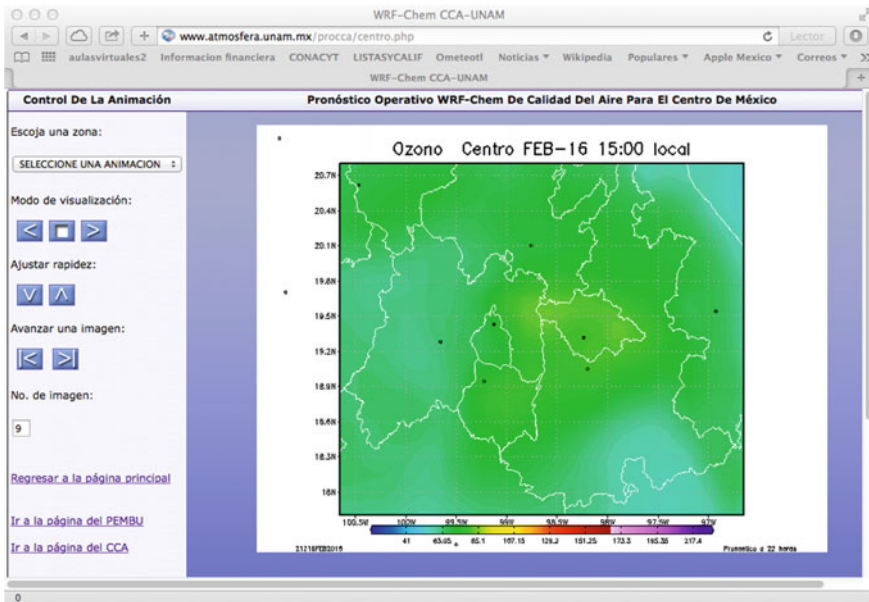
Fig. 5 Ozone distribution concentrations in central Mexico

4 Summary and Conclusions

An air quality forecast system using a coupled meteorology-chemistry model was presented. A description of the Emissions Inventory Module to convert national emission into model ready emissions was presented. This module can be applied to obtain spatial and temporal distribution as well as the chemical categories for RADM, SAPRC and RACM chemical mechanisms. The procedure to generate the air quality forecast was described. For the air quality computations the WRF-chem model was setup and the physics and the cumulus options used were described.

Currently a real-time, operational air quality forecast is running for Mexico and produces a 42 h forecast for primary and secondary pollutants. From the pollutant distribution it is possible to observe that higher concentrations are allocated near large cities, such as Mexico Megacity. However, a quantitative evaluation is required. The parallel capability of the WRF-chem code made it suitable for use in systems with a large number of processors in order to reduce forecast calculation time. A general description of the web page was presented.

This system is operational and can be applied for regional or urban areas.

5 Future Work

In terms of the hardware, the use of a computer with a large number of processors will help increasing the model grid resolution and reducing the computational time. A further future activity is to evaluate the model performance against meteorology and air quality measured data. A web page can be improved using an air quality index such as IMECA in order to give a more simple information about how polluted is a site.

References

Fast JD, Gustafson WI Jr, Easter RC, Zaveri RA, Barnard JC, Chapman EG, Grell GA (2006) Evolution of ozone, particulates, and aerosol direct forcing in an urban area using a new fully-coupled meteorology, chemistry, and aerosol model. J Geophys Res 111:D21305
Grell GA, Peckham SE, Schmitz R, McKeen SA, Frost G, Skamarock WC, Eder B (2005) Fully coupled 'online' chemistry in the WRF model. Atmos Environ 39:6957–6976
Grid Analysis and Display System (GrADS). http://iges.org/grads/
INEGI Conjunto de Datos Vectoriales de Uso del Suelo y Vegetación Serie IV (2007–2010), escala 1:250 000. http://www.inegi.org.mx

INEGI Marco Geoestadístico Nacional (2010a) versión 5.0A (Censo de Población y Vivienda 2010). http://www.inegi.org.mx

INEGI Censo de Población y Vivienda (2010b) Principales resultados por área Geoestadística Básica (AGEB) y manzana urbana. http://www.inegi.org.mx

INEGI (2011) Conjunto de Datos Vectoriales de Carreteras y Vialidades Urbanas Edición 1.0 (distribución por Entidad Federativa) Topografía. 1. http://www.inegi.org.mx/geo/contenidos/topografia/vectoriales_carreteras.aspx

Message Passing Interface (MPI) standard (MPI-1, MPI-2 and MPI-3). http://www.mpich.org

National Centers for Environmental Prediction. http://www.emc.ncep.noaa.gov/index.php?branch=GFS

NCEP Unified Post Processor. http://www.dtcenter.org/wrf-nmm/users/overview/upp_overview.php

Peckham S, Grell GA, McKeen SA, Barth M, Pfister G, Wiedinmyer C, Fast JD, Gustafson WI, Zaveri R, Easter RC, Barnard J, Chapman E, Hewson M, Schmitz R, Salzmann M, Freitas S (2011) WRF-chem Version 3.3 User's Guide. NOAA Technical Memo. p 98

Sub-sistema del Inventario Nacional de Emisiones a la Atmósfera de México. http://sinea.semarnat.gob.mx/sinea.php

Unidata. NetCDF libraries and source code. http://www.unidata.ucar.edu

US EPA Source Classification Codes for the 2011 National Emissions Inventory. http://www.epa.gov/ttn/chief/net/2011inventory.html

US EPA Emissions Modeling Clearinghouse Temporal Allocation. http://www.epa.gov/ttnchie1/emch/temporal/

US EPA Emissions Modeling Clearinghouse Speciation. http://www.epa.gov/ttnchie1/emch/speciation/

World Health Organization (2011) Burden disease. http://www.who.int/gho/phe/outdoor_air_pollution/burden/en/

WRF-Chem Version 3.6 User's Guide (2014) http://ruc.noaa.gov/wrf/WG11/Users_guide.pdf

Internal Wave Observations in the Petacalco Canyon, México

A. Ruiz-Angulo and J. Zavala-Hidalgo

Abstract This study presents the observation of large amplitude internal wave activity, of the order of 50 m, near the head of the Petacalco submarine canyon located in the Mexican Pacific. The waves propagate with periods similar to the M_2 tide component and the observations show that the rates of change of temperature reached up to 10 °C/hr. The presence of submarine canyons enhances turbulent mixing locally. The slopes of the canyon's wall trap the waves as they propagate up-canyon. Based on linear wave theory, along the axis slope of the Petacalco canyon there are regions where the critical refraction is reached, suggesting that there are regions favorable for wave breakage. This process enhances mixing of cold water masses with shelf hot water. Through this mechanism, the mixed waters remain near the surface for longer periods of time, resulting in an alternative process to upwelling. Additionally, it is suggested that this process may be very important in the region since the winds there are very weak and do not support wind driven upwelling transport for most of the year.

1 Introduction

The continental shelves are regions where primary production is enhanced; the water masses from the adjacent oceanic regions, full of nutrients, are upwelled onto the shelf. Although there are several mechanisms responsible for the enrichment of shelf waters, their characterization in different locations is not yet well known. Besides the pure wind-driven upwelling due to Ekman transport near coastal regions, the presence of canyons enhances the upwelling of deep water (Allen and Hickey 2010; Allen and de Madron 2009; Hickey 1997). The interaction of the alongshore flow with the canyon generates a quasi-stationary eddy, resulting in a net upwelling of deep water over one side of the canyon. Thus, one of the important effects of coastal subma-

A. Ruiz-Angulo (✉) · J. Zavala-Hidalgo
Centro de Ciencias de la Atmósfera, Universidad Nacional Autónoma de México,
Mexico, Mexico
e-mail: angel@atmosfera.unam.mx

rine canyons is that deep water from adjacent oceanic regions, rich in nutrients, is brought up onto the shelf enhancing the primary production to the benefit of fisheries (Hickey and Banas 2008; Allen et al. 2001).

In addition to the mechanisms presented so far, internal tides or internal waves bring nutrients to the shallow regions, contributing to phytoplankton blooms (Pineda 1991; Nash et al. 2012). Internal waves are generated by the interaction of the barotropic tide with the bottom topography (Bell 1975; Wunsch 1975; St. Laurent and Garrett 2002), and are radiated through the interior of the ocean as low mode internal waves (Kunze et al. 2011; Rainville and Pinkel 2006). The internal tides usually radiate with the same frequency as the barotropic tide that generated them (Hall and Carter 2011; Nash et al. 2012; Gregg et al. 2003; Kunze and Smith 2004). However, their propagation frecuency, ω, is bounded by the Coriolis frequency, f, and the buoyancy frequency, N, determined by the fluid stratification, i.e. $f < \omega < N$. Thus, through the entire ocean the lunar semidiurnal tide, M_2, is dominant; spanning all latitudes less than 75.4° (St. Laurent and Garrett 2002).

As the waves approach the coast, the slope changes, affecting the propagation of internal waves. From linear wave theory, for a given internal wave propagating at a frequency ω, it is possible to characterize the interaction between a wave ray-path (characteristic) slope and the topographic slope using the steepness parameter, α, given by:

$$\alpha = \frac{s_{slope}}{s_{wave}} = \frac{\partial H/\partial x}{[(\omega^2 - f^2)/(N^2 - \omega^2)]^{1/2}}. \tag{1}$$

where $\partial H/\partial x$ is the topographic slope, i.e. the change of H along the direction x, ω is the frequency of the internal wave, f is the Coriolis parameter, and N is the average buoyancy frequency. This parameter defines two regimes of reflection: supercritical, $\alpha > 1$, the internal waves continue their displacement toward deeper water, and subcritical, $\alpha < 1$, where internal waves are reflected towards shallower waters. In the limit, for values of $\alpha \sim 1$, there is a singularity in Eq. (1), which is interpreted as the critical slope where the internal waves break, enhancing locally turbulent mixing (St. Laurent and Garrett 2002; Carter and Gregg 2002; Nash et al. 2004; Kunze and Smith 2004; Hall and Carter 2011).

Submarine canyons on the continental shelves are a common topographic structure in the Ocean (Allen and de Madron 2009; Hickey 1995). Along the Mexican Pacific coastline, there are several submarine canyons (Ramírez-Herrera and Urrutia-Fucugauchi 1999); however, there are very few studies on the dynamics of these canyons. In particular, the Petacalco submarine canyon has been studied mainly from the geological point of view by Reimnitz and Gutierrez-Estrada (1969), Reimnitz (1971), Reimnitz et al. (1976). In terms of oceanic processes, Marshall (1975) found in the Petacalco canyon that currents flow periodically up and down canyon, sometimes synchronized with the tide, remarking as well that canyons act as amplifiers of oceanic activity. More recently, Rodriguez-Valencia (2004) suggested the possible

relation of the submarine canyon with the locally high levels of primary productivity. Submarine canyons in both, deep (Thurnherr et al. 2005) and shallow waters have been identified as hot spots for turbulent mixing, several studies have proposed them as amplifiers of oceanic activity (Marshall 1975). This turbulent mixing enhancement has been quantified for several canyons (e.g. Monterey canyon, La Jolla canyon).

In this manuscript observations of internal waves in the Petacalco Canyon are described and their dynamics characteristics analyzed. Section 2 deals with a description of the area and the observations that were carried out, Sect. 3 describes the observation of the internal waves and a discussion of this observations is given in Sect. 4.

2 Survey Region and Measurements

The head of the Petacalco submarine canyon is located in the Petacalco Bay, on the Mexican Pacific Ocean (See Fig. 1). Canyon spans up to 110 km offshore, reaching the Mesoamerican Trench at 4600 m depth (Reimnitz and Gutierrez-Estrada 1969; Rodriguez-Valencia 2004).

This study was carried out in the near shoreline region, up to 8 Km offshore. Within the studied region, the canyon rim depth is about 20 m and the maximum local depth is about 400 m at the bottom of the canyon.

During September 2010, an expedition including simultaneous CTD (Conductivity Temperature Depth) survey, moored current profilers and thermistor arrays measurements were carried out. Figure 1 shows the survey area with the detailed bathymetry (Osorio-Tai 2010) and the corresponding location of the instruments. The moored instruments were deployed for a period of 3 days; the two thermistor arrays, A1 and A2, were deployed approximately at the 60 m isobath, just below the canyon rim on the south west side of the canyon axis. On each array, 12 HOBO temperature sensors were attached every 5 m, and 6 HOBO temperature-pressure sensors every 10 m. The temperature and pressure data was sampled every 60 s. The CTD survey was carried out in two days, the CTD stations are shown in Fig. 1 as the solid black dots.

The two current profilers were placed on each side of the canyon axis at approximately 20 m depth, which is about the depth of the canyon rim isobath. The current profiler ($C1$), an awac with 600 kHz, was placed in a relatively flat area, rather far from the region where the steep gradients of the canyon walls begin. The second current profiler ($C2$), an aquadropp 600 kHz, was placed right at the beginning of the slope of the canyon wall. In addition to those instruments, long time series of currents outside the Petacalco bay have been taken almost continuously from 2008 to 2010.
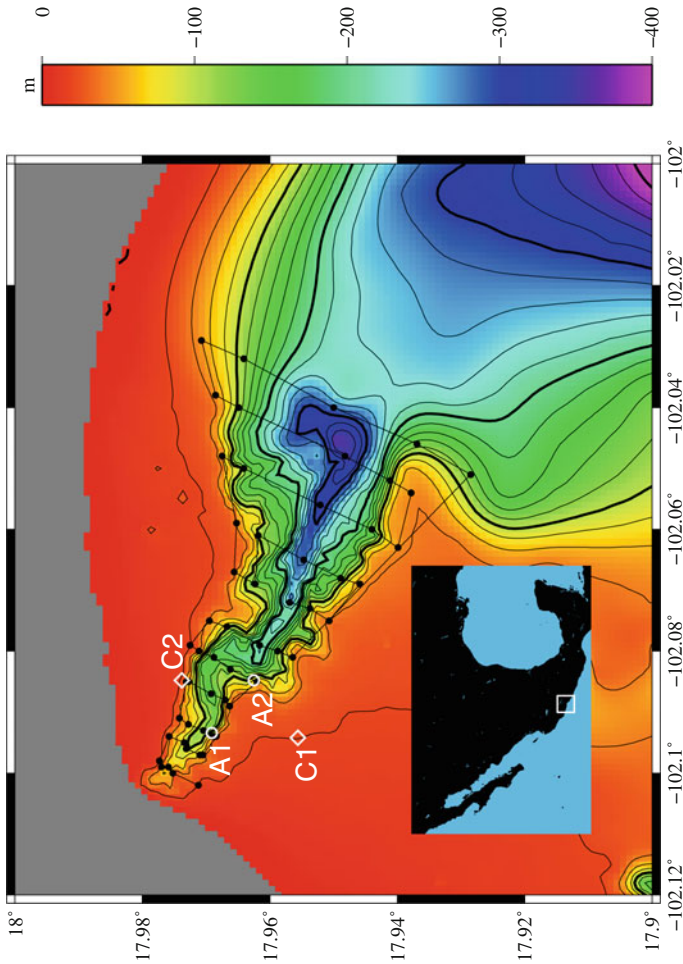
Fig. 1 Detailed bathymetric chart and instruments positions of the surveyed area during the September 2010 expedition in Petacalco. The *color contour lines* show the bathymetry in meters. The location of the deployed thermistor arrays, *A1* and *A2*, and the current profilers, *C1* (awac) and *C2* (aqua)

3 Observations

On the studied region, CTD observations show cold water tongues at the head of the canyon (Fig. 2) suggesting that cold water from deeper regions was being pushed towards the canyon and spilled over the canyon rim. This scenario was also observed in previous surveys, which inspired the detailed survey presented on this paper, showing large amplitude variations of temperature close to the canyon's head. Those variations are due to the presence of internal waves with associated large isotherms
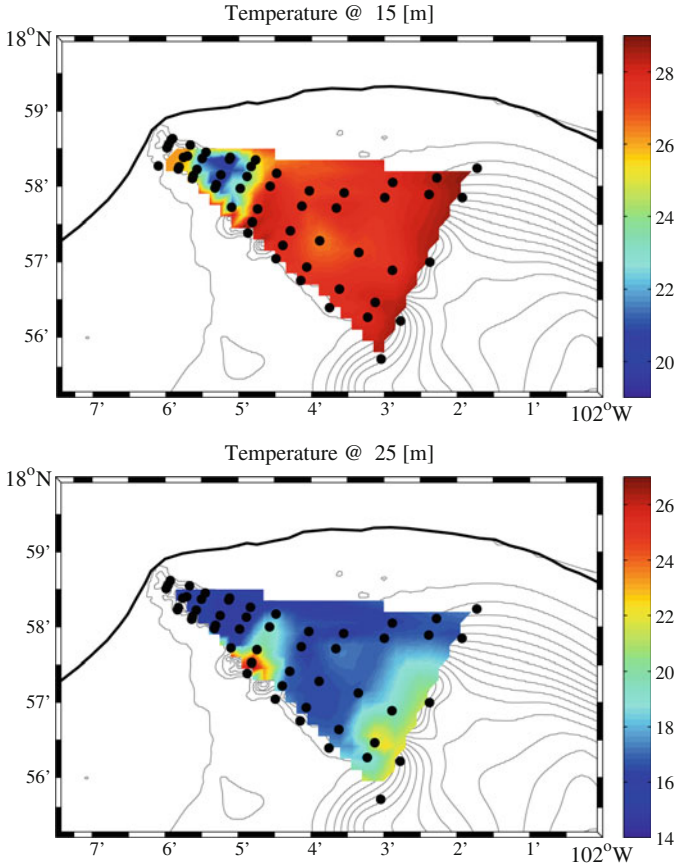
Fig. 2 Temperature contours obtained from CTD at 15 m (*upper panel*) and 25 m (*lower panel*) depth. The CTD measurements were carried out during 10–11 of September 2010

displacements. An example of these temperature anomalies is shown in Fig. 2, corresponding to the detailed survey measurements carried out during 10–11 of September 2010.

3.1 Hydrographic Data

The recorded temperature time series from the thermistor arrays, *A*1 and *A*2, are shown in Fig. 3. The corresponding depths were estimated after performing a linear regression from the data of the pressure sensors placed on each moored array.
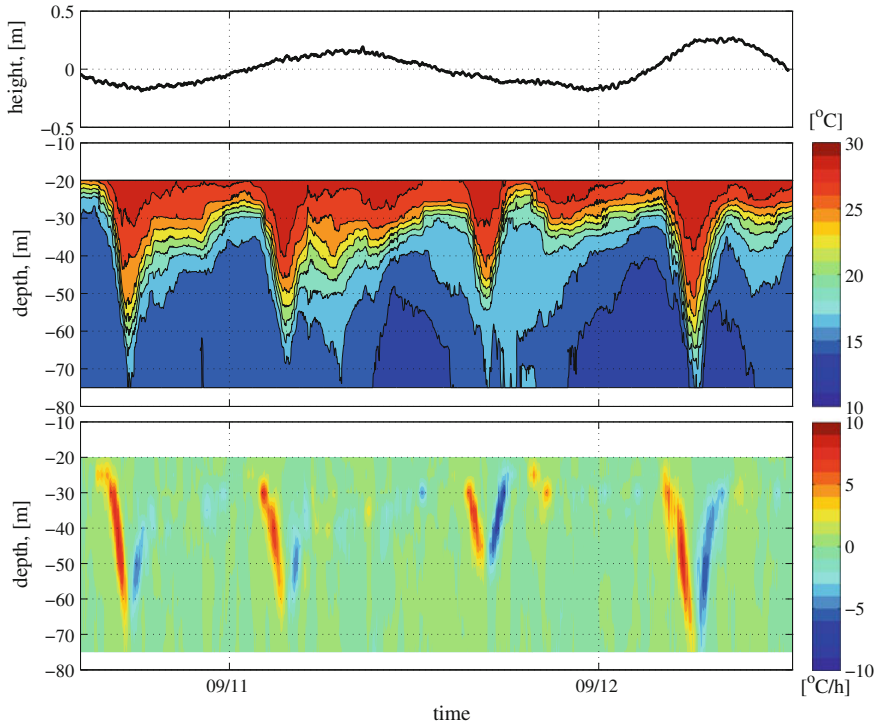
Fig. 3 Time series of the moored array A1 (see Fig. 1 for location). (*Upper*) Barotropic tide estimated from the pressure sensor on the current profiler C1, (*middle*) Temperature vertical distribution time series, °C, and the temperature rate of change (*lower*), dT/dt °C/h

The displacement of the isotherms during this survey is remarkable for the two moored arrays. The maximum displacements are observed on the water masses below the 20 m depth. For example, from the array A1, the 12 °C isotherm contour is displaced from about 80 m depth to about 40 m depth over a period of about 12 h. For the same array, the warmer contours are displaced down a similar distance reaching the maximum displacement with a semidiurnal frequency. The same pattern is observed on both arrays. The experiments were conducted during neap tides when the barotropic tide behaved mainly diurnal, without a clear agreement with the observed internal waves.

The rate of change of the isotherms with respect of time is as remarkable as the temperature amplitude oscillations. This rate reaches 10 [°C/h] when the warmer isotherms are plunging down, the rate of the colder isotherms is lower and not as steep as the warmer ones. There is a relaxation period between the maximum events when the depth of the isotherms becomes rather stable. During this period, the flow re-stratifies until the next internal wave arrival modifies this state of relative equilibrium.

Fig. 4 Bathymetric profile along the axis of the Petacalco canyon (*upper panel*) and the steepness parameter, *α* (*lower panel*) estimated along the axis. This parameter was estimated based on the internal waves frequency *M*2 and the average buoyancy frequency from the CTD survey on the canyon axis, only values of N below 40 m were used
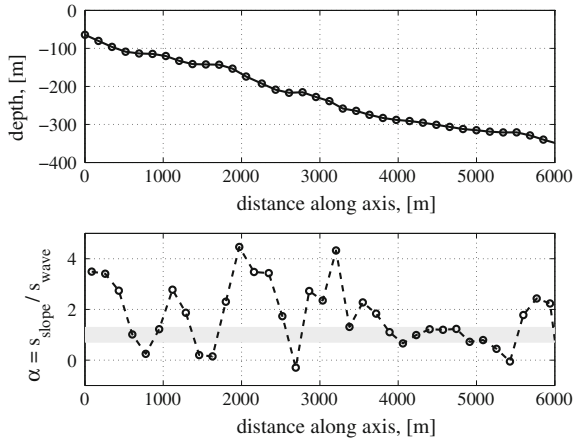
The CTD survey was carried out over two days, with a total of 55 stations. The stations were visited over periods with relatively small changes on the displacements of the isotherms, in the absence of low-mode internal wave activity. The CTD data was mainly used to estimate the local values of buoyancy frequency, *N*.

Along the canyon axis, internal waves are expected to travel and then they break when the critical slope is reached (Carter and Gregg 2002; Hall and Carter 2011; St. Laurent and Garrett 2002). Figure 4 shows in the upper panel the topographic profile along the axis of the canyon; and in the lower panel, shows the steepness parameter Eq. (1), *α* for internal waves with a semidurnal frequency, *M*2, and an average buoyancy frequency, estimated from the CTD survey. Only values of *N* below 40 m were used.

The interaction of the internal waves and a slope is determined by the steepness parameter, the case of $\alpha \sim 1$ corresponds to the critical reflection and it is interpreted as breaking of internal waves. Thus, as shown in the lower panel of Fig. 4, those regions are the most probable ones where turbulence is enhanced by this mechanism and occurs at several locations along the canyon axis. This mechanism could be responsible of producing enough mixing of deep oceanic waters with continental shelf waters, increasing the abundance of nutrients in the surrounding region.

3.2 Currents

The long time series currents records obtained from the ADCP (Acoustic Doppler Current Profiler) current meter placed outside de Petacalco bay, at 20 m depth, was used to obtain the main tidal constituents. The tides are mixed: *M*2, *K*1, are the main components. The *M*2 amplitude is very large compared to the rest and the tidal analysis carried out with *t_tide* (Pawlowicz et al. 2002) shows a very large Signal to Noise Ratio, SNR, for the *M*2 component. The temperature sensor on the current
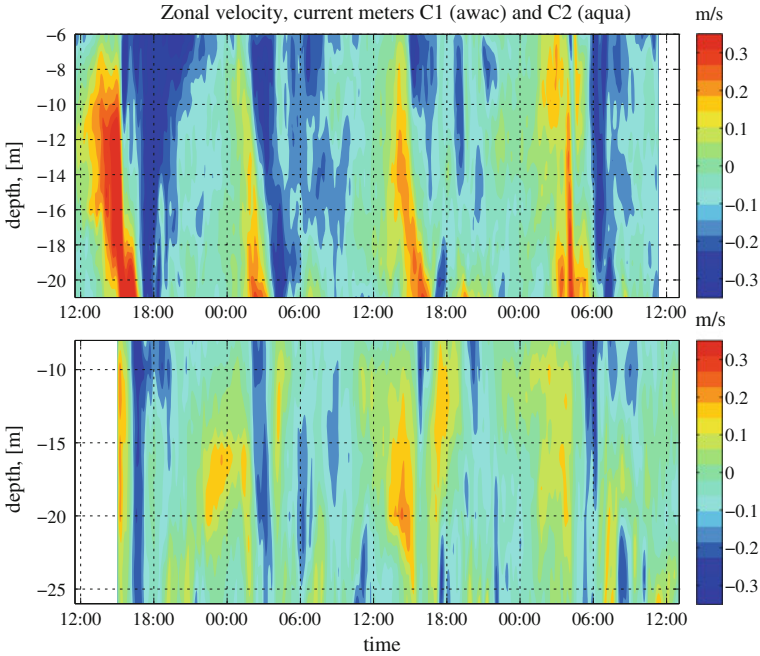
Fig. 5 Zonal velocity time series from the current meters C1 (*upper panel*) and C2 (*lower panel*). The velocities are in [m/s] previously low pass filtered (see Fig. 1 for location)

meter also shows an *M*2 variation; however, during summer periods, the water warms up drastically deepening the mixed layer. This reduces the internal wave signature at that particular depth (20 m), as the mixed layer gets shallower, the internal tide signature reappears.

The current meters placed on both sides of the canyon axis, C1 (awac) and C2 (aqua), show (Fig. 5) on both, zonal and meridional velocities, periodic variations in the direction of the flow attributed to internal waves. The observed periods of those time series match the ones in the thermistor arrays signals, roughly 12 h (see Fig. 3). Additionally, there is no significant lag between the two current meters, and with the moored arrays A1 and A2 at that particular depth. The current meter C1 was placed on a relatively flat region, far from the steep slopes of the canyon walls; whereas, C2 was placed very close to the canyon wall, showing a noisier signal related to higher turbulence levels near the canyon. The limited resources for this particular experiment did not allow us to place the current meters along the axis of the canyon, which would have been desirable to observe the propagation of the internal waves along the canyon axis.

4   Discussion

Although the observations for this study cover a very short period of time and many more observations have to be done in the area to quantify the contribution of this canyon to the nutrient-rich waters in the region, it can be expected that this mechanism has a strong seasonal and inter-annual variability. It is known that downwelling coastal trapped waves travel across the area between June and August and that during *El Niño* (*La Niña*) the mixed layer in the area becomes deeper (shallower) changing the availability of nutrients in the region (Zamudio et al. 2006). How this processes are reflected in the Petacalco Canyon are questions that have to be investigated.

The observations presented in this paper support the idea that submarine canyons along the continental shelf act as a guide path for internal waves, the walls of the canyons usually have the right slopes (supercritical) to trap the waves focusing them towards the canyon heads (Marshall 1975; Gordon and Marshall 1976; Kunze et al. 2002; Carter and Gregg 2002. The observations from the moored arrays show the presence of internal wave activity, those waves are expected to travel upcanyon (Shepard et al. 1974; Wunsch 1969) along the canyons axis. As the waves propagate upslope, they reach regions near the critical slope (see Fig. 4). For this particular survey, internal waves traveling at a semidiurnal frequency have several possible locations for breaking, which will result on a local enhancement of turbulent mixing of subsurface waters, rich in nutrients, with the continental shelf waters. In previous studies, it has been suggested that the internal waves bring nutrients to the surface as they push oceanic waters onto the shelf, which produces phytoplankton blooms (Pineda 1991). The internal waves are a source of energy to bring nutrient-rich waters onto the photic zone, and they are particularly important in this region, since along the Mexican Pacific shoreline, particularly in this region, there is not a strong coastal upwelling due to a strong Ekman transport as is observed in other regions on the western coasts. For example, the strong upwelling signatures on the western coast of the United States and Baja California Peninsula (Amador et al. 2006; Romero-Centeno et al. 2007).

Thus, internal waves and their interaction with coastal canyons, enhancing turbulent mixing, are good candidates for local nutrient blooming events, responsible of the high productivity levels in the region.

The Petaclaco submarine canyon belongs to a group of canyons, which perhaps, all together, have a significant contribution to the enrichment of nutrients on the region. However, there is an incomplete detailed bathymetry of those canyons and very few hydrographic and current data. Thus, a complete estimate of the relevance of this particular group of canyons is not yet possible. The observations in this study suggest that internal waves are important in this region and they should be studied in more detail in the forecoming years.

References

Allen SE, Durrieu de Madron X (2009) A review of the role of submarine canyons in deep-ocean exchange with the shelf. Ocean Sci 5:607–620

Allen SE, Hickey BM (2010) Dynamics of advection-driven upwelling over a shelf break submarine canyon. J Geophys Res 115(C8):08

Allen SE, Vindeirinho C, Thomson RE, Foreman MGG, Mackas DL (2001) Physical and biological processes over a submarine canyon during an upwelling event. Can J Fish Aquat Sci 58(4):671–684

Amador JA, Alfaro EJ, Lizano OG, Magaña VO (2006) Atmospheric forcing of the eastern tropical pacific: a review. Prog Oceanogr 69(2–4):101–142. ISSN 0079-6611. doi:10.1016/j.pocean.2006.03.007

Bell TH (1975) Topographically generated internal wavesin the open ocean. J Geophys Res 80(3)

Carter Glenn S, Gregg Michael C (2002) Intense, variable mixing near the head of monterey submarine canyon. J Phys Oceanogr 32(11):3145–3165

Gordon RL, Marshall NF (1976) Submarine canyons: Internal wave traps? Geophys Res Lett 3(10)

Gregg Michael C, Sanford Thomas B, Winkel David P (2003) Reduced mixing from the breaking of internal waves in equatorial waters. Nature 422(6931):513–515

Hall RA, Carter GS (2011) Internal tides in monterey submarine canyon. J Phys Oceanogr 41(1):186–204

Hickey BM (1995) Coastal submarine canyons. Topographic effects in the ocean, 'Aha Hulika'a, proceedings of the Hawaiian Winter Workshop (1376)

Hickey BM (1997) The response of a steep-sided, narrow canyon to time-variable wind forcing. J Phys Oceanogr 27(5):697–726

Hickey BM, Banas NS (2008) Why is the northern end of the california current system so productive? Oceanography 21(SPL.ISS. 4):90–107

Kunze E, Smith SGL (V) The role of small-scale topography in turbulent mixing of the global ocean. Oceanography 17(1)

Kunze E, Rosenfeld LK, Carter GS, Gregg MC (2002) Internal waves in monterey submarine canyon. J Phys Oceanogr 32(6):1890–1913

Kunze E, MacKay C, McPhee-Shaw EE, Morrice K, Girton JB, Terker SR (2011) Turbulent mixing and exchange with interior waters on sloping boundaries. J Phys Oceanogr 42(6):910–927

Marshall N (1975) The measurement and analysis of water motion in submarine canyons. IEEE Ocean 351–356

Nash JD, Shroyer EL, Kelly SM, Inall ME, Levine MD, Duda TF, Jones NL, Musgrave RC (2012) Are any coastal internal tides predictable? Oceanography 25(2):80–95

Nash JD, Kunze E, Toole JM, Schmitt RW (2004) Internal tide reflection and turbulent mixing on the continental slope. J Phys Oceanogr 34(5):1117–1134

Osorio-Tai ME (2010) Modelo batimétrico de la bahía de petacalco. Undergraduate Thesis

Pawlowicz R, Beardsley B, Lentz S (2002) Classical tidal harmonic analysis including error estimates in MATLAB using t_tide. Comput Geosci 28(8):929 – 937. ISSN 0098-3004. doi:10.1016/S0098-3004(02)00013-4

Pineda Jesus (1991) Predictable upwelling and the shoreward transport of planktonic larvae by internal tidal bores. Science 253(5019):548–549

Rainville L, Pinkel R (2006) Propagation of low-mode internal waves through the ocean. J Phys Oceanogr 36(6):1220–1236

Ramírez-Herrera MT, Urrutia-Fucugauchi J (1999) Morphotectonic zones along the coast of the pacific continental margin, southern mexico. Geomorphology 28(3–4):237–250

Reimnitz Erk (1971) Surf-beat origin for pulsating bottom currents in the rio balsas submarine canyon, mexico. Geol Soc Am Bull 82(1):81–90. doi:10.1130/0016-7606(1971)82[81:SOFPBC]2.0.CO;2

Reimnitz E, Gutierrez-Estrada M (1969) Rapid changes in the head of the rio balsas submarine canyon system, mexico. Marine Geology

Reimnitz Erk, Toimil Lawrence J, Shepard Francis P, Gutiérrez-Estrada Mario (1976) Possible rip current origin for bottom ripple zones, to 30 m depth. Geology 4(7):395–400. doi:10.1130/0091-7613(1976)4<395:PRCOFB>2.0.CO;2

Rodriguez-Valencia JA (2004) Respuesta de los poliquetos bentónicos a la variabilidad ambiental y condiciones el niño en bahía petacalco (guerrero, méxico). Ciencias Marinas 30:515–526

Romero-Centeno R, Zavala-Hidalgo J, Raga GB (2007) Midsummer gap winds and low-level circulation over the eastern tropical pacific. J Clim 20:3768. doi:10.1175/JCLI4220.1

Shepard FP, Marshall NF, McLoughlin PA (1974) "Internal waves" advancing along submarine canyons. Science 183(4121):195–198

St. Laurent L, Garrett C (2002) The role of internal tides in mixing the deep ocean. J Phys Oceanogr 32(10):2882–2899

Thurnherr AM, St. Laurent LC, Speer KG, Toole JM, Ledwell JR (2005) Mixing associated with sills in a canyon on the midocean ridge flank*. J Phys Oceanogr 35(8):1370–1381

Wunsch Carl (1969) Progressive internal waves on slopes. J Fluid Mech 35(01):131–144

Wunsch C (1975) Internal tides in the ocean. Rev Geophys 13(1):167–182. ISSN 1944-9208. doi:10.1029/RG013i001p00167

Zamudio L, Hurlburt HE, Metzger EJ, Morey SL, O'Brien JJ, Tilburg C, Zavala-Hidalgo J (2006) Interannual variability of tehuantepec eddies. J Geophys Res Oceans 111(C5):n/a–n/a, 2006. ISSN 2156-2202. doi:10.1029/2005JC003182

Part III
Fluid–Structure Interaction

Stochastic Simulation for Couette Flow of Dilute Polymer Solutions Using Hookean Dumbbells

A. Gómez López, I. Pérez Reyes, A. López Villa and R.O. Vargas Aguilar

Abstract This paper presents a stochastic simulation technique to the classic problem of the flow between parallel plates (Couette) for Newtonian and viscoelastic fluids. From the Cauchy equation, the total stress tensor splits up into two contributions, the viscous and polymeric (elastic) terms. An implicit finite difference scheme is used to solve the momentum equation (macro) and an explicit second order scheme is employed for the polymer (stochastic) contribution. The influence of important parameters such as the number of Hookean dumbbells, the Weissenberg number and the solvent/polymer viscosity ratio in both the velocity and shear stress tensor fields are analyzed.

A. Gómez López
Facultad de Ingeniería, Universidad Nacional Autónoma de México,
04510 México, DF, Mexico
e-mail: aldo009.gl@gmail.com

I. Pérez Reyes
Facultad de Ciencias Químicas, Universidad Autónoma de Chihuahua,
Circuito Universitario s/n, Paseos de Chihuahua,
Chihuahua, Chih, Mexico
e-mail: ildebrando3@gmail.com

A. López Villa
Instituto Politécnico Nacional SEPI-ESIME, U.P. Azcapotzalco,
Mexico, D.F., Mexico
e-mail: abelvilla77@hotmail.com

R.O. Vargas Aguilar (✉)
Escuela Superior de Ingeniería Mecánica y Eléctrica, Azcapotzalco,
Instituto Politécnico Nacional, Avenida de Las Granjas No. 682, Colonia Santa Catarina,
Delegación, Azcapotzalco, 02250 Mexico, D.F., Mexico
e-mail: rvargasa@ipn.mx

1 Introduction

The fluid rheological constitutive models can be built mainly in two levels of description: continuum mechanics and kinetic theory (Bird et al. 1987a). The continuum mechanics develops macroscopic equations of state (known as constitutive equations) derived from empirical or macroscopic principles (Bird et al. 1987b). The kinetic theory of fluid dynamics studies from a simple description of chains formed by springs and bars the molecular dynamics. Statistical mechanics provides a partial differential equation known as diffusion equation or Fokker-Planck equation for the probability density of microstructural quantities (Owens 2002).

The development of greater computational resources has allowed us to gradually use more accurate description levels by coupling both perspectives using Brownian simulation models. These address the problem of describing the behavior of a system composed of many particles to understand the dependence between the deformation of the particles and their resulting effect on flow properties (Öttinger 1997).

The micro-macro approach allows for greater flexibility in the kinetic theory models that can be used in numerical simulations since they do not require the existence of an equivalent or approximate closed-form constitutive equation. Furthermore, effects such as polydispersity and hydrodynamic interactions can be easily incorporated into these models since it is the motion of individual polymer molecules that is simulated (Phillips 2005).

It is possible to simulate the behavior of a viscoelastic fluid from a fluid analysis of the polymer in terms of beads and springs using the Fokker-Planck equation (Lozinski 2003) and to solve this equation using a stochastic technique. The idea of using stochastic dynamics simulations to determine the polymer contribution comes from the work of Laso and (Öttinger 1993), CONNFFESSIT's technique (Calculation of Non-Newtonian Flow: Finite Element and Stochastic Simulation Technique). The original CONNFFESSIT method suffered from several shortcomings including the necessity to determine the trajectories of a large number of model polymer molecules and the possible generation of nonsmooth stresses. Variance reduction may be used to reduce the statistical error in a stochastic simulation without increasing the
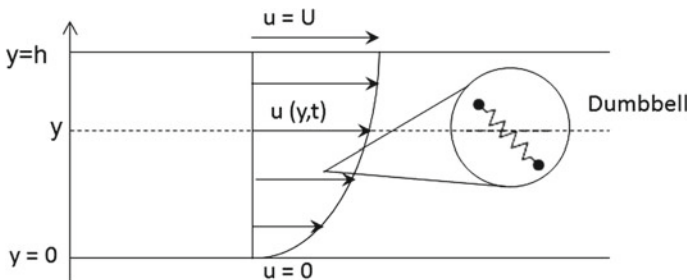
Fig. 1 Simple shear flow between flat plates

number of trajectories that need to be simulated (Öttinger 1995). The method of Brownian fields is applied to overcome the problem of having to track individual particles. This method is based on the evolution of a number of continuous Brownian configuration fields (Hulsen 1997), which are spatially smooth, resulting in an ideal method for smooth problems.

In this work a technique for performing stochastic simulations based on the concept of Brownian configuration fields is presented along with the start-up of plane Couette flow as shown in Fig. 1. The conservation equation is decoupled from the stochastic differential equation that governs the evolution of the configuration fields. The momentum equation is solved using an ADI scheme (Anderson 1995) and for the polymeric part a Brownian configuration field method is used, which is based on Hookean dumbbells.

2   Conservation Equations

The equations for conservation of mass and momentum that govern the isothermal incompressible flow of a viscoelastic fluid are

$$\nabla \cdot \underline{V} = 0, \tag{1}$$

$$\rho(\frac{\partial \underline{V}}{\partial t} + \underline{V} \cdot \nabla \underline{V}) = -\nabla P + \nabla \cdot \underline{\underline{T}}, \tag{2}$$

where ρ, $\underline{V}$, $\nabla \cdot$, P and $\underline{\underline{T}}$ are the density, the velocity vector, the divergence operator, the pressure and the stress tensor, respectively. For viscoelastic fluids, it is useful to decompose the stress tensor $\underline{\underline{T}}$ into a polymeric contribution ($\underline{\underline{\tau}}$) and a viscous contribution ($\underline{\underline{\tau}}_s$), according to:

$$\underline{\underline{T}} = \underline{\underline{\tau}} + \underline{\underline{\tau}}_s = \underline{\underline{\tau}} + 2\mu\underline{\underline{d}}, \tag{3}$$

where μ is the solvent viscosity and $\underline{\underline{d}}$ is the rate of deformation tensor, given by

$$\underline{\underline{d}} = \frac{1}{2}(\nabla \underline{V} + (\nabla \underline{V})^T). \tag{4}$$

With this decomposition the momentum Eq. (2) becomes

$$\rho(\frac{\partial \underline{V}}{\partial t} + \underline{V} \cdot \nabla \underline{V}) = -\nabla P + \mu\nabla^2 \underline{V} + \nabla \cdot \underline{\underline{\tau}}. \tag{5}$$

The polymeric contribution to the extra-stress tensor can be calculated using either a constitutive equation or stochastic simulations. This model can be derived either from continuum mechanics considerations, for example the Oldroyd B model which is not considered in this work, or from an equivalent microscopic description of the polymer dynamics in terms of an ensemble of Hookean dumbbells, as used in this work.

3 Kinetic Model

For the kinetic approximation, the polymeric molecules are modeled as dumbbells composed of beds joined by a Hookean spring as shown in Fig. 2. In this model, each bead undergoes four basic forces; the force of the spring, the force of the hydrodynamic drag, the Brownian force and any external forces like those induced by magnetic fields (Hulsen 1997).

We derive an equation for the conformation of the dumbbells using the Fokker-Planck equation (Öttinger 1996; Lozinski 2003) and using an stochastic scheme to solve it, this equation is:

$$dQ(t) = \left(-\underline{V}(x,t) \cdot \nabla \underline{Q}(x,t) + \underline{\underline{\kappa}}(x,t) \cdot \underline{Q}(x,t) - \frac{1}{2\lambda} F(\underline{Q}) \right) dt + \sqrt{\frac{1}{\lambda}} d\underline{W}(t), \quad (6)$$

where $\underline{Q}$ is the vector of conformations, $\underline{\underline{\kappa}}(x,t)$ is the transposed matrix of the velocity gradient, λ is the relaxation time, $\underline{W}(t)$ is a Wiener process which carries the stochastic part of the equation (Gard 1988) and $F(\underline{Q})$ is the force of the spring, $F(\underline{Q}) = H\underline{Q}$ for a Hookean model, where H is the spring constant. In this scheme the polymer viscosity depends on the number of dumbbells in the system, the Boltzmann constant, the temperature of the system and the relaxation time, $\eta_p = nkT\lambda$. The relaxation time of the system depends on H, and ζ the friction coefficient, $\lambda = \zeta/4H$ (Hulsen 1997).

Local values of the polymeric tensor, $\underline{\underline{\tau}}(\underline{X}, t)$, are determined from Kramers equation in the form:

Fig. 2 Dumbbell model
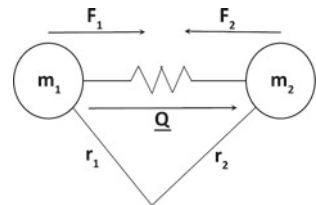
$$\underline{\underline{\tau}}(\underline{X}, t) = \frac{\eta_p}{\lambda}(-\underline{\underline{I}} + (\lim_{N_f \to \infty} \sum_{j=1}^{N_f} \underline{Q}_j \otimes \underline{Q}_j)), \tag{7}$$

where N_f defines the number of trajectories used:

$$\lim_{N_f \to \infty} \sum_{j=1}^{N_f} \underline{Q}_j \otimes \underline{Q}_j = \underline{\underline{I}} \tag{8}$$

For practical use, the above sum has to be truncated using a finite number of trajectories. For N_f large enough, according to the central limit theorem, the statistical error of the extra effort is proportional to $1/\sqrt{N_f}$, which means that numerical convergence towards noise-free solution is of the order of $O(1/\sqrt{N_f})$. This means that the equation for the polymeric effort must be resolved many times, typically for $N_f = O(10^3)$ (Öttinger 1996) and the Kramers expression for the polymeric contribution to the extra-stress tensor becomes

$$\underline{\underline{\tau}} = \frac{\eta_p}{\lambda}(-\underline{\underline{I}} + \langle \underline{Q} \otimes F(\underline{Q}) \rangle), \tag{9}$$

where the symbol $\otimes$ denotes the outer product of two vectors and the angular brackets denote the ensemble average over configuration space.

4 Dimensionless Equations

In this work, all equations are written in dimensionless form. This is motivated by the need to construct a general algorithm that can be used to simulate a large class of constitutive models. Using a characteristic length L and a characteristic velocity U, the dimensionless time is defined by L/U, the pressure and the extra stress tensor by $\eta_t U/L$, where η_t is the total viscosity $\eta_t = \mu + \eta_p$, while a quadratic characteristic length for the kinetic conformations is given by, $Q_c^2 = kT/H$. If we define the Reynolds number (Re), the Weissenberg number (We) and the viscosity ratio (β) are defined by

$$Re = \frac{\rho U L}{\eta}, \quad We = \frac{\lambda U}{L}, \quad \beta = \frac{\mu}{\eta_T} = \frac{\mu}{\mu + \eta_p}. \tag{10}$$

Then the system of non-dimensional equations for the Hooke model is

$$Re\left(\frac{\partial \underline{V}^*}{\partial t^*} + \underline{V}^* \cdot \nabla \underline{V}^*\right) = -\nabla P^* + \beta \nabla^2 \underline{V}^* + \nabla \cdot \underline{\underline{\tau}}^*, \tag{11}$$

$$d(\underline{Q}^*) = (-\underline{V}^* \cdot \nabla \underline{Q}^* + \underline{\underline{\kappa}}^* \cdot \underline{Q}^* - \frac{1}{2We} F(\underline{Q}^*))dt + \sqrt{\frac{1}{We}} d\underline{W}(t^*), \quad (12)$$

$$\underline{\underline{\tau}}^* = -\frac{1-\beta}{We}(\langle \underline{Q}^* \underline{Q}^* \rangle - \underline{\underline{I}}). \quad (13)$$

5 Boundary Conditions

The main direction of the velocity vector is a function of the direction y^* and time, $u^* = u^*(y^*, t^*)$. The initial condition and boundary conditions for the velocity are

$$u^*(y^*, 0) = 0, \quad u^*(0, t^*) = 0, \quad u^*(1, t^*) = 1. \quad (14)$$

6 Numerical Discretization

An Alternating Direction Implicit (ADI) method is used for the numerical discretization, while all partial differential equations are discretized using a finite difference scheme and solved using the Thomas algorithm (Anderson 1995). All first-order derivatives are discretized as $\frac{\partial u}{\partial x} = \frac{u_{i+1,j} - u_{i-1,j}}{2\Delta_x}$ and second-order derivatives as $\frac{\partial^2 u}{\partial x^2} = \frac{u_{i+1,j} - 2u_{i,j} + u_{i-1,j}}{\Delta_x^2}$.

Fig. 3 Numerical and analytical solution of velocity as a function of time for the points $y = (h/4, h/2, 3h/4)$
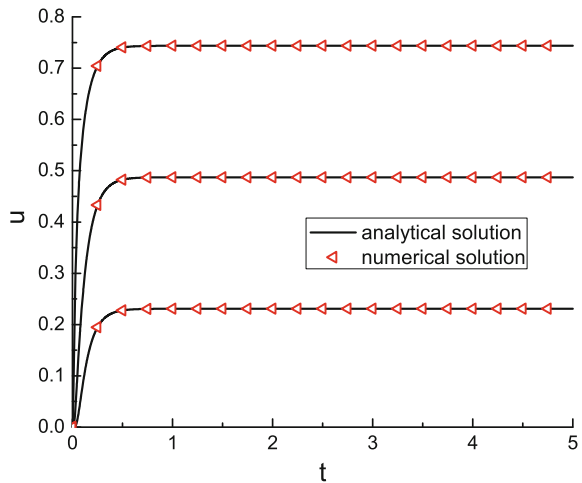
7 Validation

The code is validated by comparing the results of the Newtonian case to the analytical solution (Munson 2002):

$$u(y,t) = \frac{U}{h}y + \sum_{r=1}^{\infty} \frac{2U}{r\pi} cos(r\pi)e^{-(\frac{r^2\pi^2\mu t}{h^2\rho})} sen(\frac{r\pi y}{h}), \qquad (15)$$

where the properties of the fluid are: $\rho = 1$, $\mu = 1$, the upper plate velocity is $U = 1$, the distance between plates $h = 1$ and the time step $\Delta t = 0.001$. The comparison of the velocity for three different positions ($y = (h/4, h/2, 3h/4)$) is presented in Fig. 3, where the numerical solutions are seen to match the analytical one given by Eq. 15.

8 Results

A comparison between Hooke and Newtonian models at three different points between the two plates using the following parameters: $We = 1$, $Re = 1$, $Nf = 200$, $\beta = 1/9$, and $\Delta t^* = 0.001$ is presented in Fig. 4. The Newtonian model achieves a stationary state faster than the Hookean model as expected, the Hookean model presents an overshoot in the velocity evolution and a retarded motion to reach the steady-state due to elastic forces.

The evolution of the velocity field for the Newtonian and Hookean fluids is displayed in Fig. 5. For the Newtonian fluid the linear profile is reached almost instantaneously, while for the Hookean fluid the linear profile is lost in the transitory-state

Fig. 4 Velocity evolution of the Newtonian and Hookean fluids at different points across the channel $We = 1$, $Re = 1$, $\beta = 1/9$, $N_f = 1000$ and $\Delta t^* = 0.001$
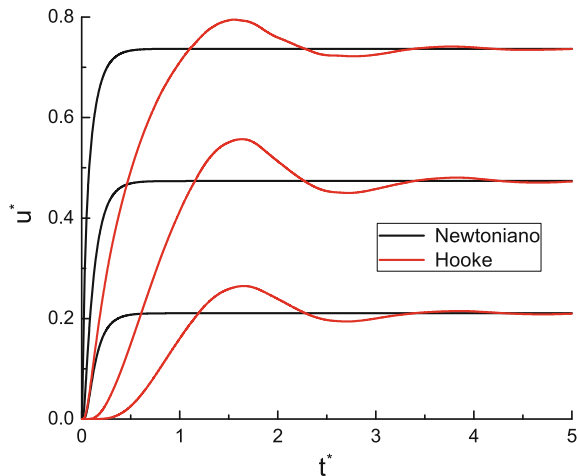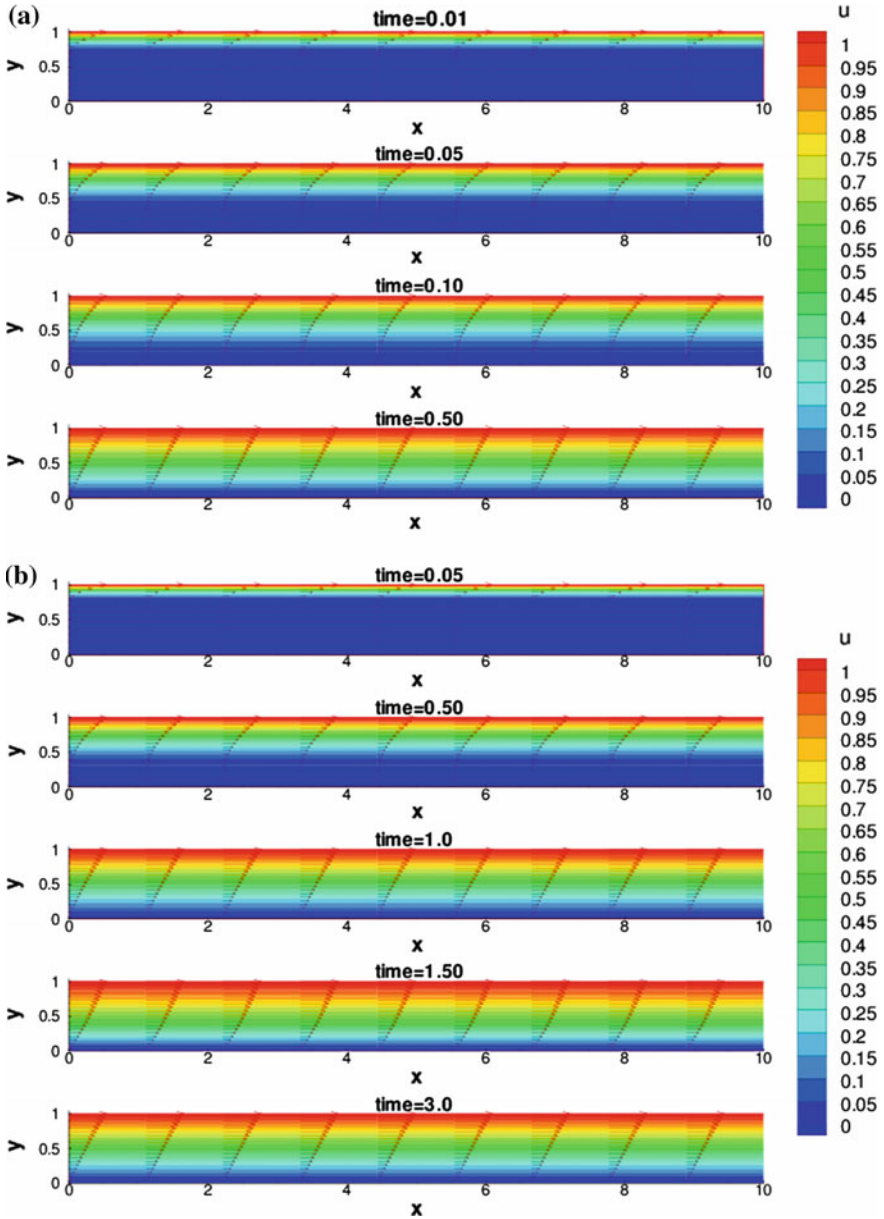
Fig. 5 Velocity evolution field for **a** Newtonian fluid and **b** Hookean fluid, with: $We = 1$, $Re = 1$, $\beta = 1/9$, $N_f = 1000$ and $\Delta t^* = 0.001$
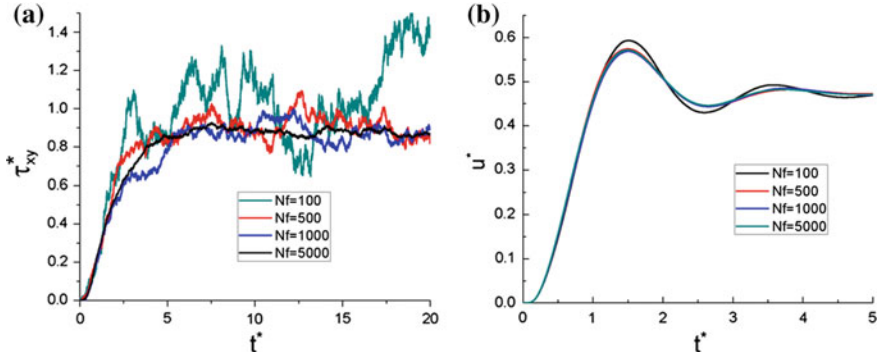
Fig. 6 **a** Polymeric stress τ_{xy} and **b** velocity evolution as a function of dimensionless time t^* for different values of N_f with: $We = 1$, $Re = 1$, $\beta = 1/9$ and $\Delta t^* = 0.001$ at $y^* = 1/2$

Fig. 7 Evolution of velocity, u, for different values of β, with $We = 1$, $Re = 1$, $\Delta t^* = 0.001$, $N_f = 1000$, in the point $y^* = 1/2$
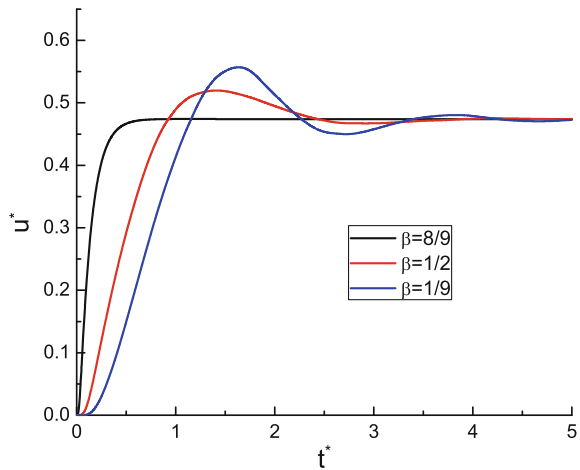
and recovered at the steady-state. In addition, the retarded motion is associated to the elastic contribution.

8.1 Number of Trajectories N_f

The polymeric stress contribution to the total stress is highly dependent on the number of trajectories (N_f) used. It can be noticed that, increasing N_f reduces the level of noise on the stress. The Brownian configuration fields technique uses a variance reduction method so that the polymeric stress is well approximated with N_f=5000 as shown in Fig. 6.
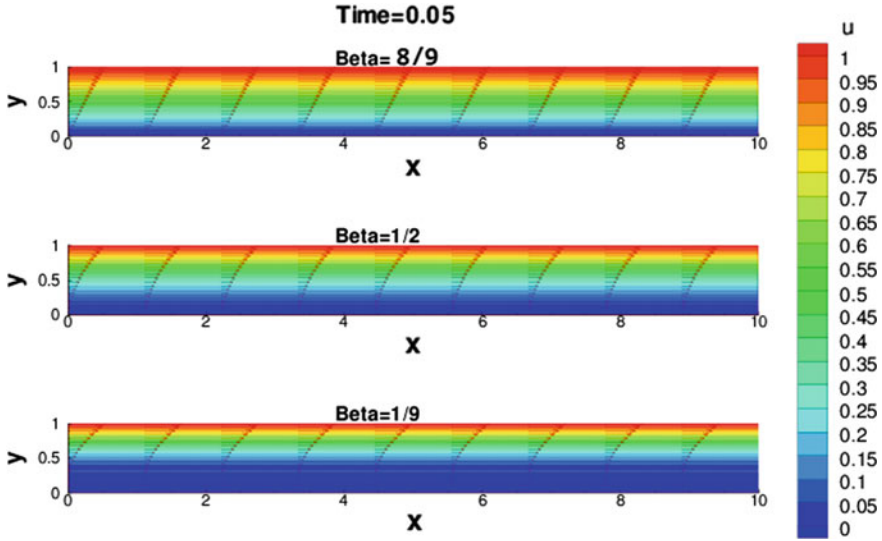
Fig. 8 Velocity profiles for different values of β, with $We = 1$, $Re = 1$, $\Delta t^* = 0.001$, $N_f = 1000$

8.2 β Effects

The viscoelastic behavior is strongly dependent on the viscosity ratio β. When $\beta \to 1$ the Newtonian case is recovered and when $\beta \to 0$ the maximum polymeric contribution is obtained and the fluid composition behaves as an elastic solid. In Fig. 7 the velocity evolution is shown. The overshoot is reduced as β increases. On the other hand, the velocity profile presents a retarded motion as shown in Fig. 8. Also, in Fig. 8 different velocity profiles for different values of β are presented.

8.3 We Effects

One of the most important parameters used for viscoelastic fluids is the Weissenberg number (*We*). It relates the fluid relaxation time to the shear rate. Figure 9 presents the effects of *We* on the velocity evolution as a function of the dimensionless time at a single point with $Re = 1$, $N_f = 1000$, $\beta = 1/9$ and $\Delta t^* = 0.001$. Figure 9 shows that increasing the elastic forces causes a retardation and reduction of the overshoot of the velocity evolution.

Fig. 9 Evolution of velocity, $u(1/2, t^*)$ for different values of We, with, $Re = 1$, $\beta = 1/9$, $\Delta t^* = 0.001$, $N_f = 500$, in the point $y^* = 1/2$
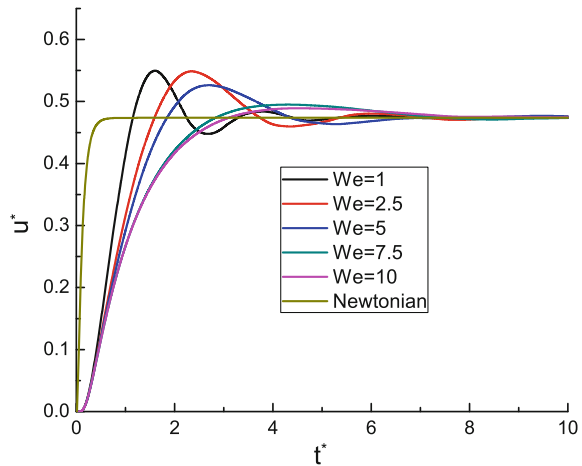
9 Conclusions

In the presented research work, a stochastic simulation technique for Couette flow of dilute polymer solutions using Hookean dumbbells is implemented. The code is validated comparing the analytical and numerical solution of the Newtonian case. The Brownian Configuration Fields method is used including the elastic force for Hookean dumbbells. The viscoelastic effects on the velocity evolution are analyzed depending on the variation of the viscosity ratio, number of trajectories and Weissenberg number. The elastic effects are presented in the transitory-state. These effects cause an overshoot and the retardation motion in the velocity evolution. This uncouple method is sufficiently flexible to allow the use of other kinetic models like, for example, the FENE or FENE-P methods, where a more realistic behavior can be obtained.

References

Anderson Jr JD (1995) Computational fluid dynamics, the basics with applications. McGraw-Hill

Bird RB, Curtiss CF, Armstrong RC, Hassager O (1987a) Dynamics of polymer liquids, vol 1, 2nd edn. Wiley, New York

Bird RB, Curtiss CF, Armstrong RC, Hassager O (1987b) Dynamics of polymer liquids, vol 2, 2nd edn. Kinetic Theory. Wiley, New York

Gard TC (1998) Introductions to Stochastic differential equations. Marcel Dekker Monographs ans Texbooks in Pure and Applied Methematics, vol 114

Lozinski A, Chauvière C (2003) A fast solver for fokker-planck equation applied to viscoelastic flows calculations: 2d fene model. J Comput Phys 189(2):607625

Melchior M, Öttinger HC (1996) Variance reduced simulations of polymer dynamics. J Chem Phys 105:3316-3331

Melchior M, Ottinger H-C (1995) Variance reduced simulations of stochastic differential equations. J Chem Phys 103:9506–9509

Munson BR, Young DF, Okiishi TH (2002) Fundamentals of fluid mechanics. Wiley

Öttinger HC (1996) Stochastic processes in polymeric fluids: tools and examples for developing simulation algorithms. Springer

Öttinger HC, Laso M (1993) Calculation of viscoelastic ow using molecular models: the CON-NFFESSIT approach. J Non-Newtonian Fluid Mech 47:1-20

Öttinger HC, van den Brule BHAA, Hulsen MA (1997) Brownian configuration fields and variance reduced CONNFFESSIT. J Non-Newtonian Fluid Mech 70:255261 64

Owens RG, Phillips TN (2002) Computational rheology. Imperial College Press

Phillips TN, Smith KD (2005) A spectral element approach to the simulation of viscoelastic flows using brownian configuration fields. J Non-Newtonian Fluid Mech. 138(2):98–110

van Heel APG, Hulsen MA, van den Brule BHAA (1997) Simulation of viscoelastic flows using brownian configuration fields. J Non-Newtonian Fluid Mech 70:79101

Two-Dimensional Motion of a Viscoelastic Membrane in an Incompressible Fluid: Applications to the Cochlear Mechanics

Y.N. Domínguez-del Ángel, M. Núñez-López,
J.G. González-Santos and A. López-Villa

Abstract In this work we present the two-dimensional motion of a viscoelastic membrane immersed in incompressible inviscid and viscous fluids. The motion of the fluid is modelled by two-dimensional Navier-Stokes equations, and a constitutive equation is considered for the membrane which captures along with the fluid equations the essential features of the vibrations of the fluid. By using the Fourier transform, the linearized equations are reduced to a functional equation for membrane displacement which is solved analytically and the inverse transform is evaluated asymptotically. Results obtained show some of the basic known characteristics of cochlear mechanics.

1 Introduction

This work focuses on the interaction between an incompressible viscous fluid and a viscoelastic membrane immersed in the fluid. The aim of this study is to gain insight into the dynamical phenomena that occur in a fluid-filled rectangular system

Y.N. Domínguez-del Ángel
Posgrado en Ciencias Naturales e Ingeniería, Universidad Autónoma Metropolitana,
Cuajimalpa Av. Vasco de Quiroga 4871, Col. Santa Fe Cuajimalpa,
Cuajimalpa de Morelos, 05300 Mexico, D.F., Mexico

M. Núñez-López (✉)
Departamento de Matemáticas Aplicadas y Sistemas, DMAS, Universidad Autónoma
Metropolitana, Cuajimalpa Av. Vasco de Quiroga 4871, Col. Santa Fe Cuajimalpa,
Cuajimalpa de Morelos, 05300 Mexico, D.F., Mexico
maynunlop@gmail.com

J.G. González-Santos
Escuela Superior de Física y Matemáticas ESFM-IPN, Av. Luis Enrique Erro S/N,
Unidad Profesional Adolfo López Mateos, Zacatenco, Gustavo A. Madero,
07738 Mexico, D.F., Mexico

A. López-Villa
Instituto Politécnico Nacional SEPI-ESIME, U.P. Azcapotzalco,
Mexico, D.F., Mexico

separated by the membrane into two channels (upper and lower compartments) by considering a two-dimensional model. The purpose is to investigate the basic features of the membrane response when it interacts with the fluid flow. In this sense, previous investigations have been carried out in order to obtain physical insight of the cochlea, which is located in the inner ear and is the main sensory organ in the process of hearing. Numerous mathematical models of the cochlea have helped to improve our understanding of the cochlear mechanics. However, despite much effort to simulate the activity in the cochlea, the situation is still far from satisfactory because the cochlear mechanics problem is too complex. Despite powerful computers and sophisticated codes currently available to construct more detailed computational models of the cochlea, it is still of great interest to derive closed solutions whenever possible in order to gain insight into the most basic physical properties of the membrane response. Reviews of important aspects of the cochlear anatomy and physiology are available, see Givelberg and Bunn (2003), Pozrikidis (2007), and Chhan et al. (2014). The problem of the cochlear mechanics is seen as a problem of the interaction of fluid flow and a viscoelastic membrane (basilar membrane). The model equations are basically the same as discussed in Leveque et al. (1985, 1988). However, several points still need to be clarified, in particular, those concerning the approximations used to make the mathematical treatment feasible. To this end, the model equations are solved to obtain improved solutions and more quantitative comparisons. Indeed, an extension to this model is currently being studied.

According to previous investigations, for the cochlear mechanics problem, it seems sufficient to employ a two-dimensional model to study the principal effects of the membrane if fluid motion in the perpendicular direction to the membrane is more important that the influence in the z-direction see Fig. 1. The motion of the fluid in each compartment is assumed to be governed by the Navier-Stokes equations of a viscous incompressible fluid

$$\rho \frac{\partial \mathbf{u}}{\partial t} + \rho \left(\mathbf{u} \cdot \nabla \right) \mathbf{u} = -\nabla p + \mu \nabla^2 \mathbf{u}, \tag{1}$$

and the continuity equation

$$\nabla \cdot \mathbf{u} = 0, \tag{2}$$

where $\mathbf{u} = (u(x, y, t), v(x, y, t))$ is the fluid velocity, $p(x, y, t)$ is the fluid pressure, ρ is the fluid density, and μ is the fluid viscosity. The pressure distribution p on both sides of the membrane is the pressure measured with respect to some reference pressure, such as the atmospheric.

For the viscoelastic membrane, which is represented by a line, it is assumed that neighboring points along the length of the membrane have no elastic coupling between them. Thus, it is assumed that the membrane is rigid in the x-direction and that its displacement $y = h(x, t)$ is determined completely by the pressure difference between the two channels. Each point of the membrane is treated as a second-order system with mass, damping, and stiffness that vary along the length of the

membrane. When $h(x, t)$ is positive in the positive y-direction, the equation of motion for the membrane is specified by

$$\left[p(x, h(x, t), t) \right] = m(x) \frac{\partial^2 h(x, t)}{\partial t^2} + r(x) \frac{\partial h(x, t)}{\partial t} + s(x) h(x, t) \, , \qquad (3)$$

where $m(x)$, $r(x)$ and $k(x)$ are mass, damping coefficient, and stiffness of the membrane per unit area. The pressure difference across the membrane is $\left[p(x, h(x, t), t) \right] = p_2(x, h(x, t), t) - p_1(x, h(x, t), t)$, where p_1 and p_2 denote the pressure in the upper and lower channel, respectively.

2   The Model Equations

The coupled system of partial differential equations, Eqs. (1–3), contains several difficulties for its study. One of them comes from the fact that the fluid domain is moving and unknown. There is an unknown function $h(x, t)$ in the boundary conditions which makes it a very difficult free-boundary problem. A significant simplification can be obtained if we assume that the system is externally forced by small perturbations such that the displacements of the membrane are small, when compared to the height a, see Fig. 1 (for the basilar membrane $h(x, t)$ is of the order of nanometers and $a \approx 10^{-3}$ m). Then, the driving force of the membrane has a leading-order term which corresponds to the transmembrane pressure $[p]$ evaluated at $y = 0$. Thus, the left-hand side of Eq. (3) is evaluated at $y = 0$ rather than at $y = h(x, t)$. In this model, the membrane mass is neglected on the observation that the density of the fluid plays an important role, i.e., the fluid provides inertia to the system. On the other hand, the damping coefficient and stiffness of the membrane have an exponential dependence on position with a decay coefficient λ in the direction of increasing x. For the basilar membrane, experiments by von Békésy (1960) indicate that the exponential dependence of stiffness on position is $\lambda^{-1} = 0.7$ cm. This way the viscoelastic membrane is modeled as

$$\left[p(x, 0, t) \right] = p(x, 0-, t) - p(x, 0+, t) = s_0 e^{-\lambda x} \left(h(x, t) + \beta \frac{\partial h(x, t)}{\partial t} \right) . \qquad (4)$$

The notation with subscripts is not used, so that $p(x, 0+, t)$ and $p(x, 0-, t)$ are the values of the pressure on both sides of the membrane. Here, the parameter s_0 is a stiffness constant and β is a time constant than determines if the system possesses a passive or active mechanism. The driving forces and the resulting responses are taken to be so small that the nonlinear convective term in Eq. (1) can be neglected, when compared to the unsteady term.

For reasons of simplicity and to get a better analytical understanding of the behavior of the membrane, the viscoelastic membrane and the fluid are assumed to be
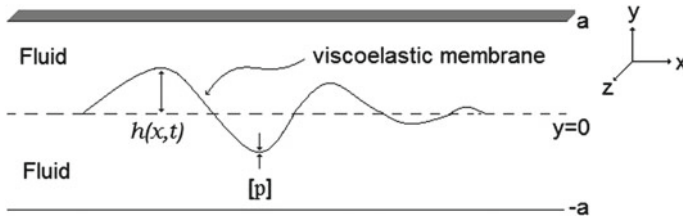
Fig. 1 Longitudinal cross-section of the two-dimensional model

contained in an infinite strip $(-\infty, \infty) \times (-a, a)$ in the xy space. It still remains to consider other boundary conditions.

Since the fluid is incompressible, the vertical component of the velocity is continuous across the membrane, so that

$$v(x, 0\pm, t) = \frac{\partial h(x, t)}{\partial t}. \qquad (5)$$

It is assumed that the fluid is bounded by rigid walls at $y = \pm a$. That is, the vertical component of velocity at $y = \pm a$ must be zero:

$$v(x, y = \pm a, t) = 0, \quad \forall x, t. \qquad (6)$$

The last boundary condition has to do with the way the system is driven. The method of solution applied to this problem does not require this condition. Yet, the membrane is acting as a transmission medium that carries bounded waves from one end to another, in the direction in which x increases, as if there is a source of vibration at $x = -\infty$ whose time-dependence is $e^{i\omega t}$.

At this point we may look for a solution to the linear system. For a phenomenological understanding of the problem, first we analyze the case when the fluid is inviscid, and then the case when it is viscous.

3 Reduction to a Functional Equation for Membrane Displacement

This section shows that by using the Fourier transform the membrane response should satisfy a functional equation in the frequency domain. It is assumed that solution representing the steady state response of the membrane has the same frequency that externals excitation.

3.1 Case I. Inviscid Fluid

Here, we neglect the fluid viscosity. Therefore, the coupled system of partial differential equations to be solved is

$$\frac{\partial u}{\partial x} + \frac{\partial v}{\partial y} = 0 \,, \tag{7}$$

$$\frac{\partial u}{\partial t} + \frac{1}{\rho}\frac{\partial p}{\partial x} = 0 \,, \tag{8}$$

$$\frac{\partial v}{\partial t} + \frac{1}{\rho}\frac{\partial p}{\partial y} = 0 \,, \tag{9}$$

with the boundary conditions:

$$p(x,0-,t) - p(x,0+,t) = s_0 e^{-\lambda x}\left(h + \beta\frac{\partial h}{\partial t}\right)(x,t) \,, \tag{10}$$

$$u(x,0\pm,t) \neq 0 \,, \tag{11}$$

$$v(x,y = \pm a,t) = 0 \,, \tag{12}$$

$$v(x,0\pm,t) = \frac{\partial h(x,t)}{\partial t} \,. \tag{13}$$

Equation (11) indicates that the no-slip condition on the viscoelastic membrane is relaxed due to the inviscid nature of the flow. We take into account only harmonic vibrations of the source with frequency f and assume time-periodic solutions of the form

$$\begin{pmatrix} u \\ v \\ p \end{pmatrix}(x,y,t) = \begin{pmatrix} U \\ V \\ P \end{pmatrix}(x,y)e^{-2\pi v x}e^{i\omega t} \,, \tag{14}$$

$$h(x,t) = H(x)e^{-2\pi v x}e^{i\omega t} \,, \tag{15}$$

where $\omega = 2\pi f$ is the angular frequency. After replacing the solutions (14) and (15) in Eqs. (7–13), we transform the x-variable by means of the Fourier transform. Then, we have three ODEs

$$\rho i\omega\hat{U}(\zeta,y) + 2\pi i(\zeta + i2v)\hat{P}(\zeta,y) = 0 \,, \tag{16}$$

$$\rho i\omega\hat{V}(\zeta,y) + \frac{d}{dy}\hat{P}(\zeta,y) = 0 \,, \tag{17}$$

$$2\pi i(\zeta + i2v)\hat{U}(\zeta,y) + \frac{d}{dy}\hat{V}(\zeta,y) = 0 \,, \tag{18}$$

with the boundary conditions

$$\left[\hat{P}(\zeta)\right] = \hat{P}(\zeta, 0+) - \hat{P}(\zeta, 0-) = -s_0(1 + i\omega\beta)\hat{H}(\zeta - \frac{\lambda i}{2\pi}), \qquad (19)$$

$$\hat{U}(\zeta, 0\pm) \neq 0, \qquad (20)$$

$$\hat{V}(\zeta, y = \pm a) = 0, \qquad (21)$$

$$\hat{V}(\zeta, 0\pm) = i\omega\hat{H}(\zeta). \qquad (22)$$

We shall use the notation $\hat{f}(\cdot)$ or $\mathscr{F}\{f(\cdot)\}$ to denote the Fourier transform of function $f(\cdot)$. Note that we used the fact that

$$\hat{P}(\zeta, y) = \int_{-\infty}^{\infty} P(x, y)e^{-2\pi\nu x}e^{-2\pi i\xi x}dx = \int_{-\infty}^{\infty} P(x, y)e^{-2\pi i(\xi - i\nu)x}dx,$$

and similarly for $\hat{U}(\zeta, y)$, $\hat{V}(\zeta, y)$, and $\hat{H}(\zeta)$; where $\zeta = \xi - i\nu$. In deriving equation (19) we have used

$$\hat{H}(\zeta - \frac{\lambda i}{2\pi}) = \int_{-\infty}^{\infty} H(x)e^{-\lambda x}e^{-2\pi i(\xi - i\nu)x}dx = \int_{-\infty}^{\infty} H(x)e^{-2\pi i(\xi - i(\nu + \lambda/2\pi))x}dx.$$

As we are interested in the displacement of the membrane we proceed to the solution of this boundary value problem as follows. Equation (18) is used to remove $\hat{U}(\zeta, y)$ from Eq. (16) and the resulting equation is used to eliminate $\hat{P}$ from Eq. (17). Thus, the resulting ODE for $\hat{V}$

$$\frac{\partial^2 \hat{V}(\zeta, y)}{\partial y^2} - 4\pi^2(\zeta + i2\nu)^2\hat{V}(\zeta, y) = 0$$

can be solved with the boundary conditions at $y \pm a$ and continuity of $\hat{V}$, $\hat{V}(\zeta, 0+) = \hat{V}(\zeta, 0-)$, at $y = 0$. It is found that the solution is

$$\hat{V}(\zeta, y) = A \sinh(2\pi(\zeta + i2\nu)|y|) - A \tanh(2\pi a(\zeta + i2\nu)) \cosh(2\pi(\zeta + i2\nu)y),$$

where the coefficient $A(\zeta)$ is not yet determined. From Eqs. (16) and (18) it follows that

$$\hat{P}(\zeta, y) = -\frac{\rho\omega i}{4\pi^2(\zeta + i2\nu)^2} \frac{d}{dy}\hat{V}(\zeta, y) \Rightarrow \left[\hat{P}(\zeta, y)\right] = -\frac{\rho\omega i}{4\pi^2(\zeta + i2\nu)^2} \left[\hat{V}_y(\zeta, y)\right],$$

where $\left[\hat{V}_y(\zeta, y)\right] = (\hat{V}_y(\zeta, y+) - \hat{V}_y(\zeta, y-))$, where we have used the relation $\frac{d|y|}{dy} =$ sgn(y). By evaluating at $y = 0$ we obtain $A = (\pi i(\zeta + i2\nu)/\rho\omega)\left[\hat{P}(\zeta)\right]$ and from Eq. (22) we obtain that $[\hat{P}(\zeta)] = -\rho\omega^2 \{\pi(\zeta + i2\nu)\tanh(2\pi a(\zeta + i2\nu))\}^{-1}\hat{H}(\zeta)$. From these results and Eq. (19), we obtain the following functional equation for $\hat{H}$:

$$\hat{H}(\zeta) = \frac{\pi s_0(1 + i\omega\beta)}{\rho\omega^2}(\zeta + i2\nu)\tanh(2\pi a(\zeta + i2\nu))\hat{H}(\zeta - \frac{\lambda i}{2\pi}). \qquad (23)$$

Note that a special case of the functional equation (23) arises when $a \to \infty$, i.e., the infinite strip occupies the entire xy plane:

$$\hat{H}(\zeta) = \frac{\pi s_0 (1 + i\omega\beta)}{\rho\omega^2} (\zeta + i2\nu)\mathrm{sgn}(\mathrm{Re}[\zeta])\hat{H}(\zeta - \frac{\lambda i}{2\pi}). \tag{24}$$

The functional equations (23) and (24) determine the wave propagation along the membrane for each particular case. To solve them we consider the case when $\nu = 0$. When $\nu \neq 0$, we must consider the fact that if $\hat{P}(\xi)$, $\hat{U}(\xi)$, $\hat{V}(\xi)$ and $\hat{H}(\xi)$, are well defined, then these functions can be extended to analytic functions in the complex plane. However, althrough $\nu = 0$, it is assumed that $e^{-\lambda x} H(x)$ has a Fourier transform which extend the definition of $\hat{H}$ to a function $\hat{H}(\zeta)$ defined in $\Omega = \{\zeta := \xi + i\eta \mid -\lambda/2\pi \leq \eta \leq 0 \& -\infty < \xi < \infty\}$ and which is analytic in the interior of Ω. But the Fourier transform of the function $e^{-\lambda x} H(x)$ may not be well defined because $e^{-\lambda x}$ grows too rapidly when $x \to -\infty$. There is no problem if $H(x)$ has compact support or is rapidly attenuated (of exponential type), or satisfies any other condition, such that $\mathscr{F}\left\{e^{-\lambda x} H(x)\right\}$ is well defined. We will need to make use of the theory of generalized functions (distribution theory) to find a solution corresponding to the fluid dynamics problem presented here. We only provide concise important results and basic definitions (see the Appendix). The theory of distributions can be found in Griffel (2002), Strichartz (1994), and Zemanian (1965).

Equations (23) and (24) can be simplified by noting that when $\nu \to 0$ gives, respectively:

$$\hat{H}(\xi) = \alpha\xi\tanh(2\pi\xi a)\hat{H}(\xi - \frac{\lambda i}{2\pi}), \tag{25}$$

$$\hat{H}(\xi) = \alpha|\xi|\hat{H}(\xi - i\frac{\lambda}{2\pi}), \tag{26}$$

where $\alpha = \pi s_0(1 + i\omega\beta)/\rho\omega^2$. The first indication that the width of the strip $2a$ has little effect on the membrane response because $|\xi| \approx \xi\tanh(2\pi\xi a)$, except near the origin. This seems to indicate that in order to investigate the effect of fluid viscosity on the membrane response is justified by assuming $a = \infty$.

3.2 Case II. Viscous Fluid

The viscous term in the linear Navier-Stokes equations is now retained. We look for solutions of the same form as those given by Eqs. (14) and (15), but with $\nu = 0$. By using the Fourier transform we obtain the system of equations in the frequency domain:

$$i\omega\rho\hat{U} + 2\pi i\xi\hat{P} = \mu\left(-4\pi^2\xi^2\hat{U} + \frac{d^2\hat{U}}{dy^2}\right), \tag{27}$$

$$i\omega\rho\hat{V} + \frac{d\hat{P}}{dy} = \mu\left(-4\pi^2\xi^2\hat{V} + \frac{d^2\hat{V}}{dy^2}\right), \tag{28}$$

$$2\pi i\xi\hat{U} + \frac{d\hat{V}}{dy} = 0, \tag{29}$$

with the boundary conditions at $y = 0$,

$$\left[\hat{P}(\xi)\right] = -s_0(1 + i\omega\beta)\hat{H}(\xi - \frac{\lambda i}{2\pi}), \tag{30}$$

$$\hat{U}(\xi, y = 0\pm) = 0, \tag{31}$$

$$\hat{V}(\xi, y = 0\pm) = i\omega\hat{H}(\xi). \tag{32}$$

We also need the conditions $\hat{U}(\xi, y \to \pm\infty) \to 0$ y $\hat{V}(\xi, y \to \pm\infty) \to 0$.

Here we use Eq. (29) to remove $\hat{U}(\xi, y)$ from Eq. (27) and the resulting equation is used to eliminate $\hat{P}$ from Eq. (28). Thus, the problem is reduced to a ordinary differential equation of $\hat{V}$

$$\left(\frac{d^2}{dy^2} - \left(4\pi^2\xi^2 + \frac{i\omega\rho}{\mu}\right)\right)\left(\frac{d^2}{dy^2} - 4\pi^2\xi^2\right)\hat{V}(\xi, y) = 0. \tag{33}$$

Since the solution $\hat{V} \to 0$ as $|y| \to \infty$, then

$$\hat{V}(\xi, y) = \begin{cases} C_1^+ e^{-\sigma_1 y} + D_1^+ e^{-\sigma_2 y}, & y > 0 \\ C_1^- e^{+\sigma_1 y} + D_1^- e^{+\sigma_2 y}, & y < 0 \end{cases} \tag{34}$$

where $\sigma_1 = \sqrt{4\pi^2\xi^2 + i\omega\rho/\mu}$ and $\sigma_2 = \sqrt{4\pi^2\xi^2} = 2\pi|\xi|$. The coefficients $C_1^\pm(\xi)$ and $D_1^\pm(\xi)$ are determined using the following boundary conditions:

$$\hat{V}_y(\xi, 0+) = 0, \quad \hat{V}_y(\xi, 0-) = 0, \quad \hat{V}(\xi, 0+) = \hat{V}(\xi, 0-), \quad \left[\hat{V}_{yyy}(\xi, 0)\right] = \frac{4\pi^2\xi^2}{\mu}[\hat{P}(\xi)].$$

The first two conditions are obtained from Eqs. (29) and (31). The third condition is the continuity of $\hat{V}$ at $y = 0$, Eq. (32). The last condition can be found from Eqs. (27) and (29) by evaluating V at $y = \pm0$. It is found that $C_1^+ = C_1^-$ and $D_1^+ = D_1^-$, where $C_1^+ = -(2\pi^2\xi^2/i\omega\rho\sigma_1)[\hat{P}(\xi)]$ and $D_1^+ = (2\pi^2\xi^2/i\omega\rho\sigma_2)[\hat{P}(\xi)]$. Therefore, Eq. (34) can be expressed as

$$\hat{V}(\xi, y) = -\left(\frac{e^{-\sigma_1|y|}}{\sigma_1} - \frac{e^{-\sigma_2|y|}}{\sigma_2}\right)\frac{2\pi^2\xi^2}{i\omega\rho}\left[\hat{P}(\xi)\right]$$
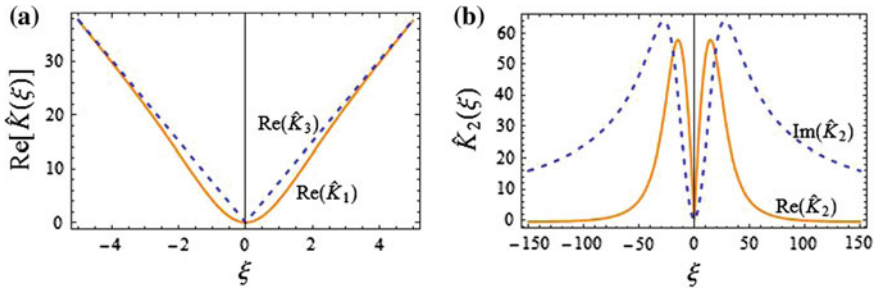
Fig. 2 **a** The real parts of $\hat{K}_1(\xi)$ and $\hat{K}_3(\xi)$. The imaginary parts look similar but proportional to $\omega\beta$. For $|\xi| > 2/\pi a$, $\hat{K}_1 \cong \hat{K}_3$. **b** The real and imaginary parts of $\hat{K}_2(\xi)$. The parameters are $s_0 = 6 \times 10^5 [\text{g/cm}^2\text{s}^2], \rho = 1.0 [\text{g/cm}^3], \beta = 10^{-4}[\text{s}], a = 0.1[\text{cm}], \mu = 0.02[\text{g/cm·s}], \omega = 500[\text{s}^{-1}]$

which together with Eq. (32) gives we have the equation for $\hat{H}$ in terms of $[\hat{P}]$ which in turn can be combined with Eq. (30) to give us the functional equation

$$\hat{H}(\xi) = \alpha|\xi|\left(1 - \frac{1}{\sqrt{1 + iv\xi^{-2}}}\right)\hat{H}(\xi - i\frac{\lambda}{2\pi}). \tag{35}$$

where $v = \omega\rho/4\pi^2\mu$. Note that $v \to \infty$ when $\mu \to 0$ and Eq. (35) tends to Eq. (26). Equations (25), (26), and (35) can be grouped together in a generalize functional relation of the form $\hat{H}(\xi) = \hat{K}(\xi)\hat{H}(\xi - \lambda i/2\pi)$. For simplicity we define

$$\hat{K}_1(\xi) = \alpha\xi\tanh(2\pi\xi a), \quad \hat{K}_2(\xi) = \alpha|\xi|\left(1 - \frac{1}{\sqrt{1 + iv\xi^{-2}}}\right), \quad \hat{K}_3(\xi) = \alpha|\xi|.$$

We can observe that for small values of ξ^2, $\hat{K}_2(\xi) \cong \hat{K}_3(\xi)$, i.e., the viscosity does not influence the low spatial frequencies. For large values of ξ^2, $\hat{K}_2(\xi)$ behaves like $|\xi|^{-1}$ because of the non-zero viscosity, see Fig. 2.

In the following section, for each particular case, we seek a solution $\hat{H}(\zeta : \xi + i\eta)$, which is analytic for $-\lambda/2\pi < \eta < 0$ and which approaches boundary values satisfying $\hat{H}(\xi) = \hat{K}_i(\xi)\hat{H}(\xi - i\lambda/2\pi)$, with $i = 1, 2, 3$. The general solution technique was discussed by Leveque et al. and we must be able to compute the Fourier transform of several functions that do not exist in the classical sense. Fourier Transforms of some distributions are developed in the Appendix.

4 The Membrane Response in the Frequency Domain

Here the solution technique for $\hat{H}(\xi) = \hat{K}(\xi)\hat{H}(\xi - i\lambda/2\pi)$ is described briefly. Set $\hat{h}(\xi) = \ln\hat{H}(\xi)$ and $\hat{k}(\xi) = \ln\hat{K}(\xi)$. Then,

$$\hat{h}(\xi) = \hat{k}(\xi) + \hat{h}(\xi - \lambda i/2\pi). \tag{36}$$

If $\hat{h}(\zeta)$ is analytic in $\overset{\circ}{\Omega}$ then the inverse Fourier transform of equation (36) gives $h(x) = k(x) + e^{-\lambda x}h(x)$ and which can be solved for $h(x)$; $h(x) = k(x)(1 - e^{-\lambda x})^{-1}$. Thus, $\hat{h}(\xi)$ can be calculated to obtain $\hat{H}(\xi) = e^{\hat{h}(\xi)}$. The main problem is that some functions do not have a Fourier transform in the classical sense, while we need to determine the Fourier transform for such functions.

4.1   Solution of the Functional Equation $\hat{H}(\xi) = \hat{K}_3(\xi)\hat{H}(\xi - i\lambda/2\pi)$

We begin by finding the function $\hat{H}(\xi)$ which satisfies the functional equation $\hat{H}(\xi) = \hat{K}_3(\xi)\hat{H}(\xi - i\lambda/2\pi)$. According to the solution technique,

$$\hat{k}_3(\xi) = \ln \alpha + \ln |\xi| - 2\pi i U(\xi)$$

where the last term arises from $\lim_{a \to \infty} \lim_{\nu \to 0-} \ln \{\alpha(\zeta + i2\nu) \tanh(2\pi a(\zeta + i2\nu))\}$, by considering a more general case, see Eq. (23), as noted by Leveque et al. Note that $\hat{k}_3(\xi)$ is a function of slow growth, then the inverse Fourier transform exists as a tempered distribution generated by $k_3(x) = (\ln \alpha - \gamma - \ln 2\pi - \pi i)\,\delta(x) + 1/x - 1/2|x|$. However, this distribution cannot be obtained from a locally integrable function because $k_3(x)$ has a singularity at $x = 0$. Functions with nonintegrable singularities define singular distributions, which may also be tempered distributions, by Hadamard's finite part of the divergent integral, see Griffel (2002) and Zemanian (1965). We are now ready to calculate the Fourier transform of $h(x)$ but we must first obtain an expression for $\hat{h}(\zeta)$. Thus, we proceed calculating the Fourier transform of $h_\eta(x) = k_3(x)g_\eta(x)$, where $g_\eta = e^{2\pi\eta x}/(1 - e^{-\lambda x})$. We set

$$h_\eta(x) = \theta\delta(x)g_\eta(x) + \left(\frac{1}{x} - \frac{1}{2\,|x|}\right) g_\eta(x),$$

where $\theta = (\ln \alpha - i\pi - \ln 2\pi - \gamma)$, and calculate the Fourier transform of the two terms.

To calculate the Fourier transform of $\delta(x)g_\eta(x)$ we use the expansion

$$\frac{e^{2\pi(\eta - i\xi)x}}{1 - e^{-\lambda x}} = \frac{1}{\lambda x} + \left(\frac{1}{2} + \frac{2\pi}{\lambda}(\eta - i\xi)\right) + \tilde{f}(x),$$

where $\tilde{f}(x) = O(x)$ as $x \to 0$, $x\delta'(x) = -\delta(x)$, $\int_{-\infty}^{\infty} \delta'(x)dx = 0$, and $\int_{-\infty}^{\infty} \delta(x)\tilde{f}(x)dx = 0$.

We do not have a formula for the Fourier transform of $I_\eta(x) = (1/x - 1/2|x|)g_\eta(x)$. Thus, we proceed to find an approximation to this function considering that $g_\eta(x)$ decays exponentially as $|x| \to \infty$ for $-\lambda/2\pi < \eta < 0$:

$$I_\eta(x) = \begin{cases} O\left(e^{2\pi\eta x}\right) & \text{if} \quad x \to +\infty \\ O\left(e^{(2\pi\eta+\lambda)x}\right) & \text{if} \quad x \to -\infty \end{cases},$$

and near the origin $g_\eta \approx 1/\lambda x + (1/2 + 2\pi\eta/\lambda)$. The main idea is to find a function $G_\eta(x)$ such that $I_\eta(x) = I_\eta(x) - G_\eta(x) + G_\eta(x) \approx G_\eta$, i.e., $f_\eta(x) = I_\eta(x) - G_\eta(x)$ contributes little to $I_\eta(x)$. We decompose $I_\eta(x)$ as

$$I_\eta(x) = \left(\frac{1}{x} - \frac{1}{2|x|}\right)\left\{U(x)e^{2\pi\eta x} - U(-x)e^{(\lambda+2\pi\eta)x} + e^{-\lambda|x|}\left(\frac{1}{\lambda x} + \frac{1}{2} + \frac{2\pi\eta}{\lambda}\right)\right\} + f_\eta(x),$$

where

$$f_\eta(x) = \left(\frac{1}{x} - \frac{1}{2|x|}\right)\left\{g_\eta(x) - U(x)e^{2\pi\eta x} + U(-x)e^{(\lambda+2\pi\eta)x} - e^{-\lambda|x|}\left(\frac{1}{\lambda x} + \frac{1}{2} + \frac{2\pi\eta}{\lambda}\right)\right\}.$$

Note that $f_\eta(x)$ has a classical Fourier transform for each value of η because $f_\eta(x) \in L_1(\mathbf{R})$. One can verify numerically the behavior of $\hat{f}_\eta(\xi)$. The real and imaginary parts are shown in Fig. 3a, b, respectively, for $\eta = 0$.
Using

$$\mathscr{F}\left\{\theta\left(\frac{e^{2\pi\eta x}}{1 - e^{-\lambda x}}\right)\delta(x)\right\} = \theta\left(\frac{1}{2} + \frac{2\pi}{\lambda}(\eta - i\xi)\right),$$

$$\mathscr{F}\left\{\left(\frac{1}{x} - \frac{1}{2|x|}\right)U(x)e^{2\pi\eta x}\right\} = -\frac{\gamma}{2} - \frac{1}{2}\ln 2\pi - \frac{1}{2}\ln(-\eta + i\xi),$$

$$\mathscr{F}\left\{-\left(\frac{1}{x} - \frac{1}{2|x|}\right)U(-x)e^{(\lambda+2\pi\eta)x}\right\} = -\frac{3}{2}\gamma - \frac{3}{2}\ln 2\pi - \frac{3}{2}\ln\left(\frac{2\pi\eta + \lambda}{2\pi} - i\xi\right),$$

$$\mathscr{F}\left\{\left(\frac{1}{x} - \frac{1}{2|x|}\right)\left(\frac{1}{\lambda x} + \frac{1}{2} + \frac{2\pi\eta}{\lambda}\right)e^{-\lambda|x|}\right\} = -\frac{2i(\lambda + 2\pi(\eta - i\xi))}{\lambda}\tan^{-1}\left(\frac{2\pi\xi}{\lambda}\right) - 2$$

$$+ \frac{2i\pi\xi}{\lambda} + \left(\frac{5}{4} + \frac{\pi(\eta - i\xi)}{\lambda}\right)\ln\left(4\pi^2\left[\xi^2 + \left(\frac{\lambda}{2\pi}\right)^2\right]\right) + \gamma\left(\frac{5}{2} + \frac{2\pi}{\lambda}(\eta - i\xi)\right),$$

we have that

$$\hat{h}(\xi + i\eta) = (\ln\alpha - i\pi)\left(\frac{1}{2} + \frac{2\pi}{\lambda}(\eta - i\xi)\right) - \frac{1}{2}\ln(-\eta + i\xi) - \frac{3}{2}\ln\left(\frac{2\pi\eta + \lambda}{2\pi} - i\xi\right)$$

$$+ \left(\frac{5}{4} + \frac{\pi(\eta - i\xi)}{\lambda}\right)\ln\left(\xi^2 + \left(\frac{\lambda}{2\pi}\right)^2\right) - \left(2i + \frac{4\pi}{\lambda}(\xi + i\eta)\right)\tan^{-1}\left(\frac{2\pi\xi}{\lambda}\right)$$

$$+ \frac{2i\pi\xi}{\lambda} - 2 + \int_{-\infty}^{\infty} f_\eta(x)e^{-2\pi i\xi x}dx, \tag{37}$$
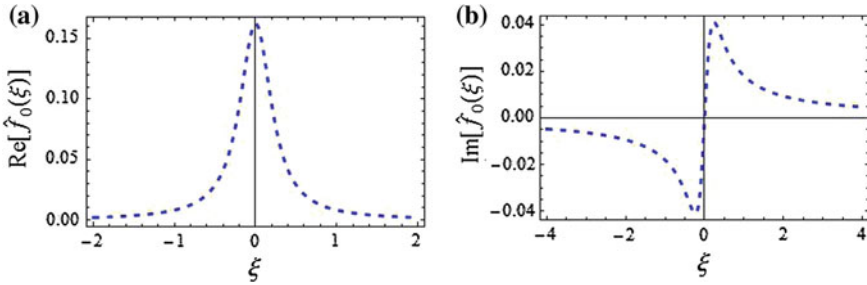
Fig. 3 Behavior of $\hat{f}_0(\xi)$ obtained by numerically transforming $f_0(x)$. **a** The real part of $\hat{f}_0(\xi)$, Re[$\hat{f}_0(\xi)$]. **b** The imaginary part of $\hat{f}_0(\xi)$, Im[$\hat{f}_0(\xi)$]

where $\hat{h}_\eta(\xi) = \hat{h}(\xi + i\eta)$. According to the solution technique, $\hat{h}(\zeta)$ is the desired function which leads to a solution for $\hat{H}(\zeta)$ throughout $\bar{\Omega}$. It is the unique solution up to an arbitrary additive constant. The solution on the real axis can be obtained by $\hat{H}(\xi) = \lim_{\eta \to 0} \hat{H}(\xi + i\eta)$. From now on we denote the solution for this particular case as $\hat{H}_3(\xi)$ because it corresponds to the solution when we consider $\hat{K}_3(x)$. Thus, we have

$$
\hat{H}_3(\xi) = AExp\left\{ \frac{2\pi\xi}{\lambda}\left(\tan^{-1}\omega\beta - \pi - 2\tan^{-1}\left(\frac{2\pi\xi}{\lambda}\right)\right) + \frac{1}{2}\ln\left(\frac{\left(\frac{\lambda}{2\pi}\right)^2 + \xi^2}{|\xi|}\right) \right.
$$
$$
\left. + i\left(2\pi\xi x_0 - \frac{1}{4}\pi\,\mathrm{sgn}(\xi) - \frac{1}{2}\tan^{-1}\left(\frac{2\pi\xi}{\lambda}\right) + \frac{2\pi\xi}{\lambda} - \frac{\xi\pi}{\lambda}\ln\left(\left(\frac{\lambda}{2\pi}\right)^2 + \xi^2\right)\right)\right\},
$$
$$
\tag{38}
$$

where $A = A'e^{-x_0\left(\frac{\lambda}{2} + \frac{2}{x_0}\right) + i\frac{1}{2}\left(\tan^{-1}\omega\beta - \pi\right)}$ with A' being an arbitrary constant. It has been taken into account the change of variable $x_0 = -\frac{1}{\lambda}\ln\left(\frac{\pi s_0}{\rho\omega^2}\sqrt{1 + \omega^2\beta^2}\right)$ and the fact that $\ln\alpha = \ln\left(\frac{\pi s_0}{\rho\omega^2}\sqrt{1 + \omega^2\beta^2}\right) + i\tan^{-1}\omega\beta$. Also, it has been assumed that $e^{\hat{f}_0(\xi)}$ is close to unity because $\hat{f}_0(\xi) \approx 0$, as was is shown in Fig. 3.

4.2 Solution to the Functional Equation $\hat{H}(\xi) = \hat{K}_1(\xi)\hat{H}(\xi - i\lambda/2\pi)$

For this case of study, $\hat{k}_1(\xi) = \ln\alpha + \ln|\xi| - 2\pi iU(\xi) + \ln|\tanh(2\pi a\xi)|$. Following the same procedure as above we find that

$$\hat{h}(\xi + i\eta) = (\ln \alpha - i\pi)\left(\frac{1}{2} + \frac{2\pi}{\lambda}(\eta - i\xi)\right) - \frac{1}{2}\ln(-\eta + i\xi) - \frac{3}{2}\ln\left(\frac{2\pi\eta + \lambda}{2\pi} - i\xi\right)$$

$$+ \left(\frac{5}{4} + \frac{\pi(\eta - i\xi)}{\lambda}\right)\ln\left(\xi^2 + \left(\frac{\lambda}{2\pi}\right)^2\right) - \left(2i + \frac{4\pi}{\lambda}(\xi + i\eta)\right)\tan^{-1}\left(\frac{2\pi\xi}{\lambda}\right)$$

$$- 2 + \frac{2i\pi\xi}{\lambda} + \int_{-\infty}^{\infty} f_\eta(x)e^{-2\pi i\xi x}dx + \left(\frac{1}{2} + \frac{2\pi\eta}{\lambda}\right)\ln|\tanh(2\pi a\xi)|$$

$$+ \mathscr{F}\left\{-\frac{1}{2\lambda x^2}\tanh\left(\frac{\pi x}{4a}\right)\right\} + \mathscr{F}\left\{-\frac{1}{2x}\tanh\left(\frac{\pi x}{4a}\right)\tilde{g}_\eta(x)\right\} ,$$

which differs from Eq. (37) in the last three terms. Thus, $\hat{H}(\varsigma) = e^{\hat{h}(\varsigma)+cte}$ satisfies the functional equation $\hat{H}(\xi) = \hat{K}_1(\xi)\hat{H}(\xi - i\lambda/2\pi)$ and $\hat{H}(\xi) = \lim_{\eta \to 0}\hat{H}(\xi + i\eta)$, and from now on we denote it by $\hat{H}_1(\xi)$, so that

$$\hat{H}_1(\xi) = Ae^{\hat{j}_0(\xi)}Exp\left\{\frac{2\pi\xi}{\lambda}\left(\tan^{-1}\omega\beta - \pi - 2\tan^{-1}\left(\frac{2\pi\xi}{\lambda}\right)\right) + \frac{1}{2}\ln\left(\left(\frac{\lambda}{2\pi}\right)^2 + \xi^2\right)\right.$$

$$+ i\left(2\pi\xi x_0 - \frac{1}{4}\pi\mathrm{sgn}(\xi) - \frac{1}{2}\tan^{-1}\left(\frac{2\pi\xi}{\lambda}\right) + \frac{2\pi\xi}{\lambda} - \frac{\xi\pi}{\lambda}\ln\left(\left(\frac{\lambda}{2\pi}\right)^2 + \xi^2\right)\right)$$

$$\left. + \frac{1}{2}\ln\left(\frac{\tanh(2\pi a\xi)}{\xi}\right)\right\} , \tag{39}$$

where $A = A'e^{-x_0\left(\frac{\lambda}{2} + 2\pi\eta + \frac{2}{x_0}\right) + i\left(\frac{1}{2} + \frac{2\pi\eta}{\lambda}\right)(\tan^{-1}\omega\beta - \pi)}$ and

$$\hat{j}_0(\xi) = \hat{f}_0(\xi) + \mathscr{F}\left\{-\frac{1}{2\lambda x^2}\tanh\left(\frac{\pi x}{4a}\right)\right\} + \mathscr{F}\left\{-\frac{1}{2x}\tanh\left(\frac{\pi x}{4a}\right)\tilde{f}_0(x)\right\} .$$

We set $F_1(x) = -\frac{1}{2\lambda x^2}\tanh\left(\frac{\pi x}{4a}\right)$ and $F_2(x) = -\frac{1}{2x}\tanh\left(\frac{\pi x}{4a}\right)\tilde{f}_0(x)$ in order to investigate the contribution of these to $\hat{H}_1(\xi)$. The Fourier transform of $F_1(x)$ can be obtained by the convolution theorem

$$\mathscr{F}\left\{-\frac{1}{2\lambda x^2}\tanh\left(\frac{\pi x}{4a}\right)\right\} = \mathscr{F}\left\{\frac{1}{\lambda x}\right\} * \mathscr{F}\left\{-\frac{1}{2x}\tanh\left(\frac{\pi x}{4a}\right)\right\}$$

$$= -\frac{i\pi}{\lambda}\ln|\tanh(2\pi a\xi)| * \mathrm{sgn}(\xi) = \frac{i\pi}{\lambda}\int_{-\xi}^{\xi}\ln|\tanh(2\pi a\eta)|\, d\eta .$$

The above integral $I_1(\xi) = \int_{-\xi}^{\xi}\ln|\tanh(2\pi a\eta)|\, d\eta$ can be solved analytically, $I_1(\xi) = (\ln(\tanh 2\pi a\xi)\ln(1 + \tanh 2\pi a\xi))/2a\pi + \big(\mathrm{Li}_2(1 - \tanh 2\pi a\xi) + \mathrm{Li}_2(-\tanh 2\pi a\xi)\big)/2a\pi - 1/12a\pi$, where $\mathrm{Li}_2(z) = -\int_0^z \frac{\ln(1-z)}{z}dz = \int_0^z \frac{dz}{z}\int_0^z \frac{dx}{1-z} = \frac{z}{1^2} + \frac{z^2}{2^2} + \frac{z^3}{3^2} + \cdots$ is the dilogarithm function. $I_1(\xi)$ is almost constant except near the origin, $\lim_{\xi \to \infty} I_1(\xi) = -\frac{\pi}{8a}$ and $\lim_{\xi \to -\infty} I_1(\xi) = +\frac{\pi}{8a}$. Also, when $a \to \infty$, $\hat{F}_1(\xi)$ contributes little to $\hat{j}_0(\xi)$ for large values of $|\xi|$ as $\lim_{a \to \infty}\lim_{\xi \to \pm\infty}\hat{F}_1(\xi) = 0$. To compute $\hat{F}_2(\xi)$ we note that
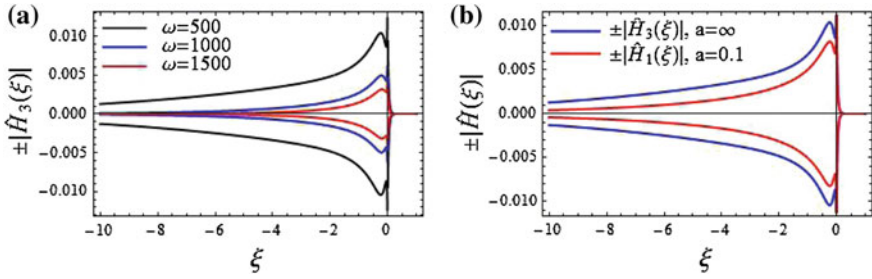
Fig. 4 **a** The envelopes $\pm|\hat{H}_3(\xi)|$ with three different values of ω. **b** The envelopes $\pm|\hat{H}_1(\xi)|$ and $\pm|\hat{H}_3(\xi)|$ are compared for $\omega = 500$

$\mathscr{F}\left\{\tanh\left(\frac{\pi x}{4a}\right)\right\} = i2a\left(\tanh\left(2\pi a\xi\right) - \coth\left(2\pi a\xi\right)\right) = -i4a/\sinh(2\pi a\xi)$ and $\mathscr{F}\{x^n\} = (-1)^n(2\pi i)^{-n}\delta^{(n)}(\xi)$. Then, assuming that $\tilde{f}_0(x)$ is decomposed into power series of x, we have

$$\hat{F}_2(\xi) = i\frac{\lambda 4a}{4 \cdot 3!}\frac{1}{\sinh(2\pi a\xi)} - i\frac{\lambda^3 4a}{12 \cdot 5!}\frac{1}{\sinh(2\pi a\xi)} * \frac{\delta^{(2)}(\xi)}{2^2\pi^2} + \cdots .$$

Ignoring the term $\hat{\tilde{f}}_0(\xi)$, we find the following expression for $\hat{\tilde{j}}_0(\xi)$:

$$\hat{\tilde{j}}_0(\xi) \approx \frac{i}{2a\lambda}\left(\ln(\tanh 2\pi a\xi)\ln(1 + \tanh 2\pi a\xi) + \text{Li}_2(1 - \tanh 2\pi a\xi) + \text{Li}_2(-\tanh 2\pi a\xi)\right)$$

$$- i\frac{\pi^2}{12a\lambda} + i\frac{\lambda 4a}{4 \cdot 3!}\frac{1}{\sinh(2\pi a\xi)} - i\frac{\lambda^3 4a^3}{12 \cdot 5!}\left(\frac{\coth^2(2\pi a\xi)}{\sinh(2\pi a\xi)} + \frac{1}{\sinh^3(2\pi a\xi)}\right) + \cdots$$

The function $\hat{\tilde{j}}_0(\xi)$ has a singularity at $\xi = 0$ and consequently also Eqs. (38) and (39) have a similar singular behavior at $\xi = 0$. However, both are oscillating functions that decay as $\xi \to \pm\infty$. In Fig. 4a we have plotted $\pm|\hat{H}_3(\xi)|$ with different values of ω. A comparison between $\pm|\hat{H}_1(\xi)|$ and $\pm|\hat{H}_3(\xi)|$ is shown in Fig. 4b. In both cases the envelope has a peak location at ξ_{max} which it seems independent of ω but not its amplitude. The envelope shows qualitatively the same shape for the cases presented: the envelope rises gradually to a prominent peak and beyond the peak is attenuated rapidly; without taking into account the singularity at $\xi = 0$ that arises because to the solution technique.

4.3 Solution to the Functional Equation $\hat{H}(\xi) = \hat{K}_2(\xi)\hat{H}(\xi - i\lambda/2\pi)$

The solution to this important case is denoted by $\hat{H}_2(\xi)$ which we assume to have the form $\hat{H}_2(\varsigma) = \hat{M}(\varsigma)\hat{H}_3(\varsigma)$. This reduces the problem to solve only the functional

equation $\hat{M}(\xi) = \left(1 - 1/\sqrt{1 + iv/\xi^2}\right)\hat{M}(\xi - \frac{\lambda i}{2\pi})$. We proceed as in the previous cases. We set $\hat{m}(\xi) = \ln \hat{M}(\xi)$ and $\hat{k}(\xi) = \ln\left(1 - 1/\sqrt{1 + iv/\xi^2}\right)$. Thus, we seek the Fourier transform $m(x) = k(x)(1 - e^{-\lambda x})^{-1}$ to obtain $\hat{M}(\xi) = e^{\hat{m}(\xi)}$. The function $\hat{k}(\xi)$ grows logarithmically as $\xi \to \infty$ so its Fourier transform exists as a tempered distribution. To calculate $\hat{m}(\xi)$ we decompose the function $(1 - e^{-\lambda x})^{-1}$ into power series and use the convolution theorem:

$$\hat{m}(\xi) = \frac{1}{\lambda}\hat{k}(\xi) * \mathscr{F}\{1/x\} + \frac{1}{2}\hat{k}(\xi) + \hat{k}(\xi) * \mathscr{F}\{\tilde{f}_0\}.$$

Note that $\hat{k}(\xi)$ is an even function and therefore

$$\mathscr{F}\left\{\frac{k(x)}{x}\right\} = -i\pi\hat{k}(\xi) * \mathrm{sgn}(\xi) = -i\pi \int_{-\infty}^{\infty} \hat{k}(\eta)\mathrm{sgn}(\xi - \eta)d\eta$$

$$= -i\pi\left\{\int_{-\infty}^{-\xi} \hat{k}(\eta)d\eta - \int_{-\xi}^{0}\hat{k}(\eta)d\eta - \int_{0}^{\xi}\hat{k}(\eta)d\eta - \int_{\xi}^{\infty}\hat{k}(\eta)d\eta\right\}$$

$$= i\pi \int_{-\xi}^{\xi}\hat{k}(\eta)d\eta = 2i\pi \int_{0}^{\xi}\hat{k}(\eta)d\eta.$$

Note that for ξ near the origin and v large we can approximate $\hat{k}(\xi)$ by $\frac{|\xi|}{\sqrt{2v}}(-1 + i) + \frac{i}{2}\left(\xi/\sqrt{v}\right)^2 + \mathcal{O}\left(\left(\xi/\sqrt{v}\right)^3\right)$. Thus, $\int_0^\xi \hat{k}(\eta)d\eta \approx \frac{(-1+i)}{\sqrt{2v}}\int_0^\xi |\eta|\,d\eta = \frac{(-1+i)}{\sqrt{2v}}\left(\frac{1}{2}\xi^2\right)$ and therefore

$$\hat{m}(\xi) \approx \frac{2\pi\xi}{\lambda}\left(-\frac{\xi}{2\sqrt{2v}} - \frac{\lambda}{4\pi\sqrt{2v}}\right) + \frac{2\pi i\xi}{\lambda}\left(-\frac{\xi}{2\sqrt{2v}} + \frac{\lambda}{4\pi\sqrt{2v}}\right) + \hat{k}(\xi) * \hat{\tilde{f}}_0(\xi).$$

The final term $\hat{k}(\xi) * \hat{\tilde{f}}_0(\xi)$ has been investigated as follows. It is necessary to know the behavior of derivatives $\hat{k}^{(n)}(\xi)$ with n odd, as $\mathscr{F}\{x^n\} = (-1)^n(2\pi i)^{-n}\delta^{(n)}(\xi)$. But the coefficients of $\mathscr{F}\{x^n\}$ and $\tilde{f}_0(x)$ tend to zero rapidly, so it appears sufficient to consider only $\hat{k}^{(1)}$ and $\hat{k}^{(3)}$ to gain some insight into the contribution of $\hat{k}(\xi) * \hat{\tilde{f}}_0(\xi)$ to $\hat{m}(\xi)$. In Fig. 5, $\hat{k}^{(1)}$ and $\hat{k}^{(3)}$ are plotted and we conclude that $\hat{k}(\xi) * \hat{\tilde{f}}_0(\xi)$ contributes little to $\hat{m}(\xi)$.

Then we conclude that $\hat{M}(\xi) \approx Exp\left\{\frac{2\pi\xi}{\lambda}\left(-\frac{\xi}{2\sqrt{2v}} - \frac{\lambda}{4\pi\sqrt{2v}} - \frac{i\xi}{2\sqrt{2v}} + \frac{i\lambda}{4\pi\sqrt{2v}}\right)\right\}$ and the solution for the functional equation $\hat{H}(\xi) = \hat{K}_2(\xi)\hat{H}(\xi - i\lambda/2\pi)$ is
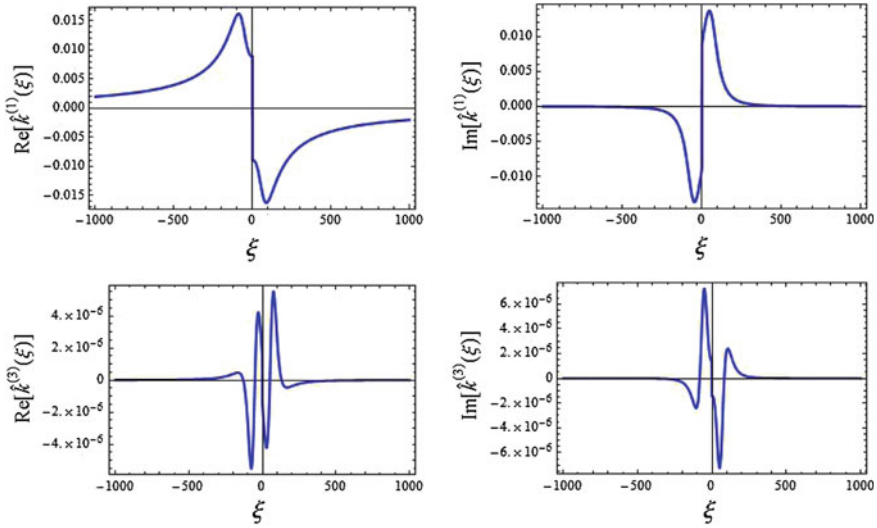
Fig. 5 Behavior of the first and third derivative of $\hat{k}(\xi)$. The real and imaginary parts of $\hat{k}^{(1)}(\xi)$ are nearly constants to zero except near the origin. Similarly for $\hat{k}^{(3)}(\xi)$. The values are $\rho = 1.0[g/cm^3]$, $\mu = 0.02[g/cm \cdot s]$ and $\omega = 500[s^{-1}]$

$$\hat{H}_2(\xi) = A Exp \left\{ \frac{2\pi\xi}{\lambda} \left(\tan^{-1} \omega\beta - \pi - 2\tan^{-1}\left(\frac{2\pi\xi}{\lambda}\right) \right) + \frac{1}{2} \ln\left(\frac{\left(\frac{\lambda}{2\pi}\right)^2 + \xi^2}{|\xi|} \right) \right.$$

$$\left. + i\left(2\pi\xi x_0 - \frac{1}{4}\pi \, sgn(\xi) - \frac{1}{2}\tan^{-1}\left(\frac{2\pi\xi}{\lambda}\right) + \frac{2\pi\xi}{\lambda} - \frac{\xi\pi}{\lambda}\ln\left(\left(\frac{\lambda}{2\pi}\right)^2 + \xi^2\right) \right) \right\}$$

$$\times Exp\left\{ \frac{2\pi\xi}{\lambda}\left(-\frac{\xi}{2\sqrt{2\upsilon}} - \frac{\lambda}{4\pi\sqrt{2\upsilon}} \right) + \frac{2\pi i\xi}{\lambda}\left(-\frac{\xi}{2\sqrt{2\upsilon}} + \frac{\lambda}{4\pi\sqrt{2\upsilon}} \right) \right\}. \qquad (40)$$

where $A = A' e^{-x_0\left(\frac{\lambda}{2} + \frac{2}{x_0}\right) + i\frac{1}{2}\left(\tan^{-1}\omega\beta - \pi\right)}$. Similarly to $\hat{H}_1(\xi)$ and $\hat{H}_3(\xi)$, $\hat{H}_2(\xi)$ has a singularity at $\xi = 0$ but decays exponentially as $|\xi| \to \infty$. Also, the envelope has a peak and its amplitude depends on ω, see Fig. 6a. The decay toward the left of the peak in $+|\hat{H}_2(\xi)|$ is faster that in $+|\hat{H}_3(\xi)|$, see Fig. 6b. The functions $\hat{H}_i(\xi)$, with $i = 1, 2, 3$, are nearly zero for $\xi > 0$ and are dominated by negative spatial frequencies, which means that the wave propagates to the right.

In the next section we want to find an expression for $H_i(x)$. However, it is difficult to compute $H_i(x) = \int_{-\infty}^{\infty} \hat{H}_i(\xi)e^{2\pi ix\xi}d\xi$ Instead we calculate an approximation to these function by using the method of stationary phase.
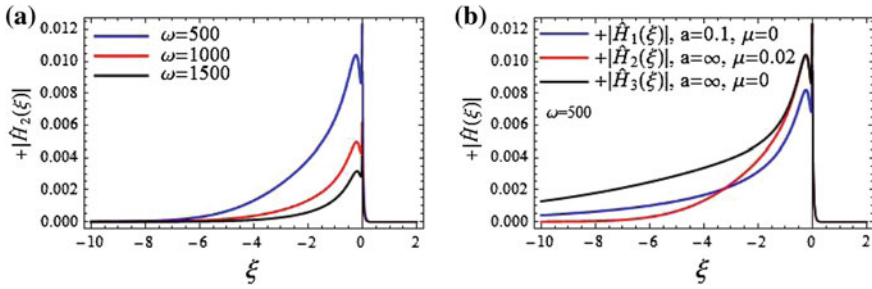
Fig. 6 **a** Behavior of $+|\hat{H}_2(\xi)|$ for different values of ω. **b** A comparison of $+|\hat{H}_1(\xi)|$, $+|\hat{H}_2(\xi)|$, and $+|\hat{H}_3(\xi)|$ for $\omega = 500$. The values are $\rho = 1.0[\text{g/cm}^3]$, $\beta = 10^{-4}[\text{s}]$, $s_0 = 1[\text{g/cm}^2\text{s}^2]$, $\lambda = 0.7^{-1}[\text{cm}^{-1}]$, $A' = 1$

5 Results

We approximate $\hat{H}_3(\xi)$, Eq. (38), for negative values of ξ away from the origin:

$$\hat{H}_3(\xi) \approx AU(-\xi)\, Exp\left\{\frac{2\pi\xi}{\lambda}\tan^{-1}\omega\beta + \frac{1}{2}\ln|\xi| + \frac{i2\pi\xi}{\lambda}\left(\lambda x_0 + 1 - \ln|\xi|\right)\right\}.$$

We now seek the integral

$$H_3(x) = \int_{-\infty}^{\infty} \hat{H}_3(\xi)e^{2\pi ix\xi}d\xi \approx \int_{-\infty}^{\infty} A\, U(-\xi)\, Exp\left\{\frac{2\pi\xi}{\lambda}\tan^{-1}\omega\beta + \frac{1}{2}\ln|\xi|\right\}e^{2\pi i\varphi(\xi)}d\xi,$$

where $\varphi(\xi) = \xi\left(x + x_0 + \frac{1}{\lambda} - \frac{1}{\lambda}\ln|\xi|\right)$. Hence, according to the method of stationary phase, the leading term in the asymptotic expansion of the above integral comes from the neighborhood of the point $\bar{\xi} = -e^{\lambda(x+x_0)}$, where $\varphi'(\bar{\xi}) = 0$. Then, we obtain

$$H_3(x) \approx AExp\left\{\frac{2\pi\bar{\xi}}{\lambda}\tan^{-1}\omega\beta + \frac{1}{2}\ln|\bar{\xi}|\right\}e^{2\pi i\varphi(\bar{\xi})}\int_{-\infty}^{\infty}e^{-i\pi(\xi-\bar{\xi})^2/\lambda\bar{\xi}}d\xi.$$

We use the fact that $\int_{-\infty}^{\infty}e^{-i\pi(\xi-\bar{\xi})^2/\lambda\bar{\xi}}d\xi = \sqrt{-\lambda\bar{\xi}}e^{i\pi/4}$. Thus, finally we get

$$H_3(x) \approx A\sqrt{\lambda}e^{i\pi/4}Exp\left\{-\frac{2\pi}{\lambda}e^{\lambda(x+x_0)}\left(\tan^{-1}\omega\beta + i\right) + \lambda(x + x_0)\right\}. \tag{41}$$

The solution $h(x, t) = \text{Re}\left(H(x)e^{i\omega t}\right)$ is a traveling wave with a stationary envelope. In Fig. 7 we have plotted the real part of $H_3(x)$ with different values of ω which is sufficient to infer features of the membrane response.

Although the membrane is infinitely long, excitation thereof occurs only in a finite interval along the longitudinal axis, henceforth to be called motion's region. The wave propagating along the membrane shows a maximum response (locus of
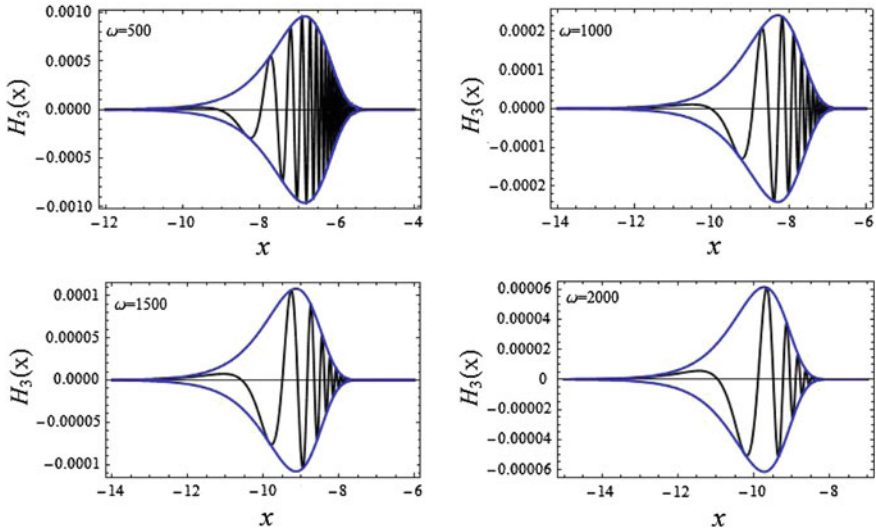
Fig. 7 In each case, for a different value of ω, the real part of $H_3(x)$ and the envelopes $\pm|H_3(x)|$ are shown. After the peak the spatial frequency increases with increasing x but the oscillations decrease with increasing ω. The values are $\rho = 1.0[\text{g/cm}^3]$, $\beta = 10^{-4}[\text{s}]$, $s_0 = 1[\text{g/cm}^2\text{s}^2]$, $\lambda = 0.7^{-1}[\text{cm}^{-1}]$, and $A' = 1$

resonance) and it is seen that the wavelength $\lambda(x)$ along the motion region decreases monotonically. To the left of the locus of resonance there is a traveling wave with location-dependent propagation velocity and beyond the locus of resonance the wave is rapidly attenuated. The region of maximum response, known as the region of resonance, is where the effects of interaction between fluid and membrane are more important. The term *resonance* is suggestive, however, it must be noted that the membrane model has zero mass

The envelope of the wave has the same shape regardless of ω: it rises gradually to show a maximum response (a peak) at x_{max} and beyond the peak it is rapidly attenuated. The location of the peak is determined by maximizing $|H_3(x)|$ with respect to x, which corresponds to maximizing the real part of the function $\chi(x) = -\frac{2\pi}{\lambda}e^{\lambda(x+x_0)}\left(\tan^{-1}\omega\beta + i\right) + \lambda(x + x_0)$. We find $x_{max} \approx \frac{1}{\lambda}\ln\left(\frac{\lambda}{2\pi\tan^{-1}\omega\beta}\right) - x_0$, where x_0 is given as above. The peak location moves to the left depending logarithmically on the stimulus frequency and the amplitude of the envelope decreases with increasing ω, see Fig. 8a. The approximation of $H_3(x)$ is valid near the vicinity of the peak for small values of $\omega\beta$ This way x_{max} is large enough and $\bar{\xi}$ is sufficiently far from the origin.

For fixed ω, changes of ρ and s_0 cause changes in the location of the peak and the amplitude of the envelope, see Fig. 8b. Yet, the solution $H_3(x)$ retains an arbitrary constant which should also be determined.

We proceed in the same way to get an approximation to $H_1(x)$ and $H_2(x)$. $\hat{H}_j(\xi)$, $j = 1, 2$, is approximated for negative values of ξ far away from the origin and so
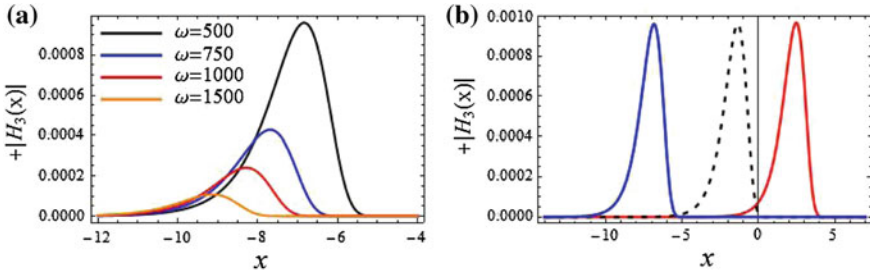
Fig. 8 **a** x_{max} moves to the left as $\omega = 2\pi f$ increases with increasing f from 20 Hz to 20 KHz. The values are $\rho = 1.0[\text{g/cm}^3]$, $\beta = 10^{-4}[\text{s}^{-1}]$, $s_0 = 1[\text{g/cm}^2\text{s}^2]$, $\lambda = 0.7^{-1}[\text{cm}^{-1}]$, $A' = 1$. **b** Behavior of $|H_3(x)|$ changing parameter s_0 and A'. The *blue line* is for $s_0 = 1[\text{g/cm}^2\text{s}^2]$ and $A' = 1$. The *dashed line* is for $s_0 = 2500[\text{g/cm}^2\text{s}^2]$ and $A' = 0.02$. The *red line* is for $s_0 = 6 \times 10^5[\text{g/cm}^2\text{s}^2]$ and $A' = 0.0013$
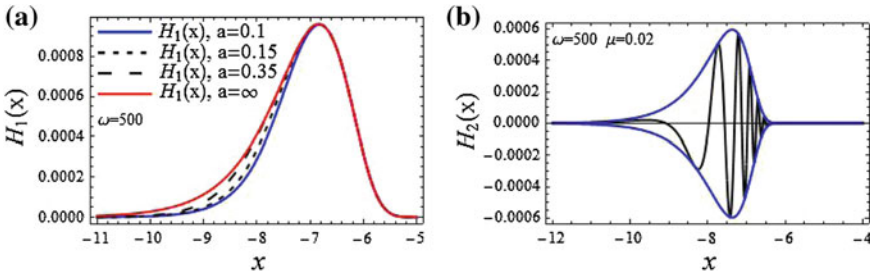
Fig. 9 **a** The magnitude of the envelope to the left of the peak is not dramatically influenced by the presence of the finite height a. **b** The real part of $|H_2(x)|$ Eq. (43). The values of the parameters are $\rho = 1.0[\text{g/cm}^3]$, $s_0 = 1.0[\text{g/cm}^2\text{s}^2]$, $\lambda = 0.7^{-1}[\text{cm}^{-1}]$, and $A' = 1$

we calculate the integral $H_j(x) = \int_{-\infty}^{\infty} \hat{H}_j(\xi)e^{2\pi i x\xi}d\xi$ using the method of stationary phase. Thus,

$$H_1(x) \approx A\sqrt{\lambda}e^{i\pi/4(1+\pi/2a\lambda)} Exp \left\{ -\frac{2\pi}{\lambda} e^{\lambda(x+x_0)} \left(\tan^{-1}\omega\beta + i \right) + \lambda(x + x_0) \right.$$
$$\left. + \frac{1}{2}\ln\left(\tanh(2\pi a e^{\lambda(x+x_0)})\right) \right\}, \tag{42}$$

and for the case of a viscous fluid, we have

$$H_2(x) \approx A\sqrt{\lambda}e^{i\pi/4} Exp \left\{ -\frac{2\pi}{\lambda} e^{\lambda(x+x_0)} \left(\tan^{-1}\omega\beta + i + \frac{e^{\lambda(x+x_0)}}{2\sqrt{2v}} - \frac{\lambda}{4\pi\sqrt{2v}} \right) + \lambda(x + x_0) \right\}. \tag{43}$$

Effect of a on the asymptotic solution (42) is seen in Fig. 9a. The decay of $H_1(x)$ to the left of the peak is much more gradual than that of $H_3(x)$ ($H_1(x)$ with $a = \infty$).
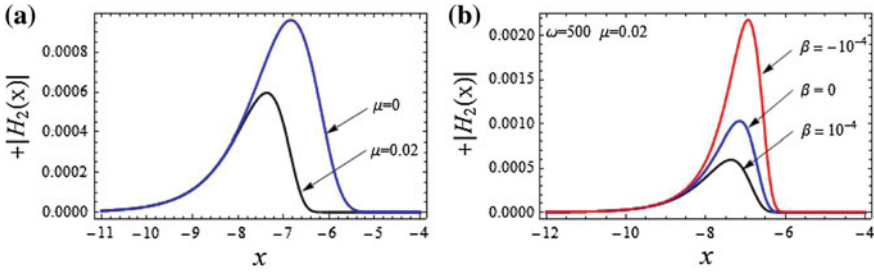
Fig. 10 **a** The viscous effects of the fluid shows that the peak moves to the left slightly. The amplitude of the envelope decreases, and the region of the resonance is less broad. **b** Behavior of $+|H_2(x)|$ considering a negative membrane friction, a positive friction, and a null friction. The values of the parameters are $\rho = 1.0[g/cm^3]$, $s_0 = 1.0[g/cm^2s^2]$, $\lambda = 0.7^{-1}[cm^{-1}]$, and $A' = 1$

However, the location of the peak does not change. In this way, it is clear that the value of a has little effect on the membrane response.

The viscous effects of the fluid are noted in Figs. 9b and 10. First, if the parameters are fixed, the real part of $H_2(x)$ shows less oscillations than $H_1(x)$ and $H_3(x)$, compared to Figs. 8 and 9b for $\omega = 500$. In any case, the envelope has the same shape. The location of the peak is moved and the amplitude of the envelope decreases, see Fig. 10a. The positions of the peaks for different stimulus frequencies are distributed logarithmically along the membrane. The location of the peak $x_{\mu max}$ is determined by maximizing the function

$$\chi_\mu(x) = -\frac{2\pi}{\lambda}\tan^{-1}\omega\beta\,e^{\lambda(x+x_0)} - \frac{\pi}{\lambda\sqrt{2\upsilon}}e^{2\lambda(x+x_0)} + \frac{1}{2\sqrt{2\upsilon}}e^{\lambda(x+x_0)} + \lambda(x+x_0)$$

$$\approx -\frac{2\pi}{\lambda}\tan^{-1}\omega\beta\,e^{\lambda(x+x_0)} - \frac{\pi}{\lambda\sqrt{2\upsilon}}e^{2\lambda(x+x_0)} + \lambda(x+x_0)\,.$$

We find that $x_{\mu max} = \frac{1}{\lambda}\ln\theta_1 - x_0$, where $\theta_1 = \frac{1}{2\kappa_\mu}\left(-\kappa_\beta + \sqrt{\kappa_\beta^2 + 4\kappa_\mu}\right)$, $\kappa_\mu = \frac{2\pi}{\lambda\sqrt{2\upsilon}}$, and $\kappa_\beta = \frac{2\pi}{\lambda}\tan^{-1}\omega\beta$. This case has the property that β can take a value of zero and still get a bounded solution. Moreover, it is possible to obtain a bounded solution even if $\beta < 0$. The consideration of a negative friction for the membrane ($\beta < 0$) can be interpreted as an amplification mechanism operating within the system. The injection of mechanical energy into the membrane dramatically boosts its motion around the peak, see Fig. 10b, as if the mechanical amplifier could be causing changes on the stiffness of the membrane.

In the two-dimensional model of an inviscid fluid in which a is finite, according to the wavelength $\lambda(x)$, the motion region into membrane can be divided into two parts, at least for $\omega\beta$ small: one in which wavelength is much greater than the depth a of the fluid and the other one considering the opposite. With waves of the first type, the use of one-dimensional models, also known as the long wave models (shallow-water

approximation), could be justified assuming that, when the membrane moves, the fluid displaced can only move in the longitudinal direction. These results are true if the depth of the fluid is very small compared to the wavelength. But this approximation fails where the spatial frequency increases and the wavelength becomes much less than the depth a of the fluid, i.e., where short waves dominate. It is therefore necessary to consider the fluid flow in two dimensions (deep-water approximation). In summary, part of the wave behaves as a one-dimensional wave and part as a two-dimensional wave. On the other hand, the extreme simplification with a infinite shows that the value of a is irrelevant to study the membrane response, supporting the existence of short waves in the membrane. However, in the two-dimensional model of a viscous fluid, the analysis shows that the wave on the membrane resemble shallow water waves.

6 Conclusions

The two-dimensional linear model considered here studies the problem of the interaction between a fluid and a membrane during stimulation of a single frequency. Using the Fourier transform, for the motion of the membrane an analytic solution in the frequency domain is obtained and the inverse Fourier transform is evaluated asymptotically by the method of the stationary phase. The analysis supports the propagation of a traveling wave on the membrane moving from left to right with a stationary envelope. The envelope of the propagating wave shows a maximum response, the so-called peak of the envelope, which designates the transition from propagation to attenuation. The location of the peak moves to the left depending logarithmically on the stimulus frequency and the peak amplitude decreases as ω increases. The wavelength of the wave propagating along the membrane decreases monotonically. Our analysis shows that the wave on the membrane resemble shallow water waves.

The form of the solution and the direction of wave propagation are due to the stiffness of the membrane and a friction mechanism (negative or positive) associated with the membrane and/or fluid viscosity, rather than to the location and manner in which the system is externally excited. At least a mechanism of energy dissipation in the system is necessary in order to find a bounded solution. The conclusions can be extrapolated to the problem of the cochlear mechanics since the analysis shows how the human cochlea works.

Appendix

A continuous linear functional $f \in \mathscr{D}'$ on the space $\mathscr{D}$ of C^{∞} test functions having compact support is called a distribution, or generalized function. The image of the test function ϕ under f is denoted by $\langle f, \phi \rangle$. Every locally integrable function f there corresponds to a distribution f defined by

$$\langle f, \phi \rangle = \int_{-\infty}^{\infty} f(x)\phi(x)dx, \quad for \quad \phi(x) \in \mathscr{D}.$$

The distribution f is said to be generated by the function f. For any distribution f, the functional $f' : \phi \longmapsto -\langle f, \phi' \rangle$ is a distribution. The derivative of a distribution f is also a distribution f' defined by $\langle f', \phi \rangle = -\langle f, \phi' \rangle$ for all $\phi \in \mathscr{D}$. A C^{∞} function $\phi(x)$ is of class $\mathscr{S}(\mathbf{R})$ if

$$x^n \phi^r(x) \to 0 \quad \text{as} \quad x \to \pm\infty \quad \text{for all} \quad n, r \geq 0.$$

$\mathscr{S}$ is called the Schwartz class and its elements are called test functions too. A distribution of slow growth (tempered distribution) is a continuous linear functional on the space $\mathscr{S}$. The space of all distributions of slow growth is denoted by $\mathscr{S}'$. $\mathscr{D}$ is a subspace of $\mathscr{S}$, but the distributions of slow growth comprise a proper subspace of $\mathscr{D}$, $\mathscr{D} \subset \mathscr{S} \subset \mathscr{S}' \subset \mathscr{D}'$. If $f(x)$ satisfies the condition $\lim_{|x|\to\infty} |x|^{-N} f(x) = 0$ for some integer N, then $f(x)$ is said to be of slow growth. If f is locally integrable and of slow growth, then f defines a tempered distribution given by

$$\langle f, \phi \rangle = \int_{-\infty}^{\infty} f(x)\phi(x)dx, \quad for \quad \phi(x) \in \mathscr{S}.$$

Distributions that can be generated through the above expression are called regular distributions. Distributions that are not regular are called singular distributions. If f is a tempered distribution, then the functional $\hat{f} : \phi \longmapsto \langle f, \hat{\phi} \rangle$ is a tempered distribution.

Definition 1 (*Generalized Fourier Transform*) If f is a tempered distribution, its Fourier transform is the tempered distribution $\hat{f}$ defined by $\langle \hat{f}, \phi \rangle = \langle f, \hat{\phi} \rangle$ for all $\phi \in \mathscr{S}$.

The inverse Fourier transform of a tempered distribution is also a tempered distribution defined by $\langle \mathscr{F}^{-1}\{f\}, \phi \rangle = \langle f, \mathscr{F}^{-1}\{\phi\} \rangle$ for all $\phi \in \mathscr{S}$. We now calculate the generalized Fourier transforms of some functions.

Example 1 Consider the Dirac delta function $\delta(x)$ (unsuitably called fuction). To calculate $\mathscr{F}\left\{\delta^{(k)}(x-a)\right\}$ we proceed as follows.

$$\left\langle \mathscr{F}\left\{\delta^{(k)}(x-a)\right\}, \phi(\xi)\right\rangle = \left\langle \delta^{(k)}(x-a), \mathscr{F}\{\phi\}\right\rangle = (-1)^k \left\langle \delta(x-a), (\mathscr{F}\{\phi\})^{(k)}\right\rangle$$

$$= (-1)^k \left\langle \delta(x-a), \mathscr{F}\left\{(-2\pi i\xi)^k \phi(\xi)\right\}\right\rangle$$

$$= (-1)^k \int_{-\infty}^{\infty} (-2\pi i\xi)^k \phi(\xi) e^{-2\pi i a\xi} d\xi$$

$$= \left\langle (2\pi i\xi)^k e^{-2\pi i a\xi}, \phi(\xi)\right\rangle$$

Hence $\mathscr{F}\left\{\delta^{(k)}(x-a)\right\} = (2\pi i\xi)^k e^{-2\pi i a\xi}$.

Example 2 Let f be the distribution generated by the function $f(x) = \ln|x|$. Note that $\lim\limits_{\varepsilon \to 0} \frac{(1-|x|^{-\varepsilon})}{\varepsilon} = \ln|x|$. Then

$$\langle \mathscr{F}\{\ln|x|\}, \phi(\xi)\rangle = \int_{-\infty}^{\infty} \ln|x|\, \mathscr{F}\{\phi(\xi)\}\, dx = \int_{-\infty}^{\infty} \ln|x| \left\{\int_{-\infty}^{\infty} \phi(\xi) e^{-2\pi i x\xi} d\xi\right\} dx$$

$$= \int_{-\infty}^{\infty} \phi(\xi) \left\{\int_{-\infty}^{\infty} \lim_{\varepsilon \to 0} \frac{\left(1 - |x|^{-\varepsilon}\right)}{\varepsilon} e^{-2\pi i x\xi} dx\right\} d\xi$$

$$= \int_{-\infty}^{\infty} \phi(\xi) \lim_{\varepsilon \to 0} \left\{\frac{1}{\varepsilon} \left[\int_{-\infty}^{\infty} e^{-2\pi i x\xi} dx - \int_{-\infty}^{\infty} |x|^{-\varepsilon} e^{-2\pi i x\xi} dx\right]\right\} d\xi$$

$$= \int_{-\infty}^{\infty} \phi(\xi) \lim_{\varepsilon \to 0} \left\{\frac{1}{\varepsilon} \left[\delta(\xi) - \Gamma(1-\varepsilon) \sin(\frac{\varepsilon\pi}{2}) 2^\varepsilon \pi^{(-1+\varepsilon)} |\xi|^{(-1+\varepsilon)}\right]\right\} d\xi,$$

$$= \left\langle -\frac{1}{2} |\xi|^{-1} - (\gamma + \ln 2\pi)\, \delta(\xi), \phi(\xi)\right\rangle,$$

by considering that $\Gamma(1-\varepsilon) \sin(\frac{\varepsilon\pi}{2}) 2^\varepsilon \pi^{(-1+\varepsilon)} = \frac{\varepsilon}{2} + \left(\frac{\gamma}{2} + \frac{\ln 2\pi}{2}\right) \varepsilon^2 + O(\varepsilon^3)$, $\lim\limits_{\varepsilon \to 0}$ $|\xi|^{\varepsilon-1} = 2\delta(\xi)$, and $\lim\limits_{\varepsilon \to 0} \left\{|\xi|^{(-1+\varepsilon)} - 2\varepsilon^{-1}\delta(\xi)\right\} = |\xi|^{-1}$.

Example 3 We consider the unit step function defined by

$$U(\xi) = \frac{1 + \operatorname{sgn}(\xi)}{2} = \begin{cases} 1 & \text{si} \quad \xi \geq 0 \\ 0 & \text{si} \quad \xi < 0 \end{cases}.$$

We have

$$\left\langle \mathscr{F}^{-1}\{U(\xi)\}, \phi(x)\right\rangle = \left\langle U(\xi), \mathscr{F}^{-1}\{\phi(x)\}\right\rangle = \int_{-\infty}^{\infty} U(\xi) \left\{\int_{-\infty}^{\infty} \phi(x) e^{2\pi i x\xi} dx\right\} d\xi$$

$$= \int_{-\infty}^{\infty} \phi(x) \left\{\int_{-\infty}^{\infty} U(\xi) e^{2\pi i x\xi} d\xi\right\} dx$$

$$= \int_{-\infty}^{\infty} \phi(x) \left\{\frac{1}{2} \int_{-\infty}^{\infty} (1 + \operatorname{sgn}(\xi)) e^{2\pi i x\xi} d\xi\right\} dx$$

$$= \int_{-\infty}^{\infty} \phi(x) \frac{1}{2} \left(\delta(x) + \frac{i}{\pi x}\right) dx = \left\langle \frac{1}{2} \left(\delta(x) + \frac{i}{\pi x}\right), \phi(x)\right\rangle.$$

Hence, $\mathscr{F}^{-1}\{U(\xi)\} = \frac{1}{2} \left(\delta(x) + \frac{i}{\pi x}\right)$.

References

David C, Charles T, Katherine A (2014) Two-dimensional analysis of fluid motion in the cochlea resulting from compressional bone conduction. J Sound Vib 333:1067–1078

Givelberg E, Julian B (2003) A comprehensive three-dimensional model of the cochlea. J Comput Phys 191:377–391

Griffel DH (2002) Applied functional analysis. Dover, 2a Ed

Leveque RJ, Peskin CS, Lax PD (1985) Solution of a two-dimensional Cochlea model using transform techniques. SIAM J Appl Math 45(3):450–464

Leveque RJ, Peskin CS, Lax PD (1988) Solution of a two-dimensional Cochlea model with fluid viscosity. SIAM J Appl Math 48(1):191–213

Pozrikidis C (2007) Boundary-integral modeling of cochlear hydrodynamics. J Fluids Struct 24:336–365

Strichartz RS (1994) A guide to distribution theory and fourier transforms. CRC Press, Boca Raton

von Békésy G (1960) Experiments in hearing. McGraw-Hill, New York

Zemanian AH (1965) Distribution theory and transform analysis: an introduction to generalized functions with applications. McGraw-Hill

Electromagnetically Driven Flow Between Concentric Spheres: Experiments and Simulations

A. Figueroa, J.A. Rojas, J. Rosales and F. Vázquez

Abstract The rotational flow continuously driven by electromagnetic forcing of an electrolytic fluid in the gap of a concentric spheres set-up is studied experimentally and theoretically. The driving Lorentz force is generated by the interaction of a dc electric current radially injected and the dipolar magnetic field produced by a permanent magnet (0.38 T). Laminar velocity profiles in the equatorial plane were obtained with particle image velocimetry. Steady-state and time-dependent flows were explored for injected currents ranging from 1 to 500 mA. A full three-dimensional numerical model that introduces the dipolar magnetic field and the radial dependency of the applied current was developed. A simple analytical solution for the azimuthal velocity was obtained. The theoretical models reproduce the main characteristic behaviour of the electromagnetically forced flow.

1 Introduction

Magnetized spherical Couette flow has been widely studied during recent years through theoretical analysis (Kleeorin et al. 1997; Starchenko 1998; Bühler 2009), complex laboratory experiments (Nataf et al. 2008; Zimmerman et al. 2014), and numerical simulations (Dormy et al. 1998; Gissinger et al. 2011; Figueroa et al. 2013). This flow is the simplification of related phenomena in astrophysical and planetary science. The spherical geometry is also important in geophysical flows, which provide insights into climatology, geology and meteorology. In most studies the driving force of the flow is mechanical, that is, by imposing differential rotation

A. Figueroa (✉) · F. Vázquez
Centro de Investigación en Ciencias, Universidad Autónoma del Estado de Morelos,
Av. Universidad No. 1001, Col. Chamilpa,
62209 Cuernavaca, Morelos, Mexico
e-mail: alfil@uaem.mx

J.A. Rojas · J. Rosales
Instituto de Investigación en Ciencias Básicas Y Aplicadas, Universidad
Autónoma del Estado de Morelos, Av. Universidad No. 1001, Col. Chamilpa,
62209 Cuernavaca, Morelos, Mexico

between the spherical shells. A few other studies take into account other body forces such as buoyancy (Jung and Tanahashi 2008). In a dielectric fluid, by establishing a.c. voltage differences between the spheres, the central polarization force can also drive the flow (Amara and Hegseth 2002). Electromagnetic forcing is a common experimental method to produce stirring in electrically conducting fluids. The idea is to produce a rotational Lorentz force by the injection of electric currents in fluids exposed to a steady external magnetic field. Owing to the high electrical conductivity of liquid metals and the strong magnetic field intensities reached through electromagnets or superconducting magnets, the Hartmann number, which estimates the ratio of magnetic to viscous forces, can be very high. Under these conditions, magnetohydrodynamic (MHD) effects can significantly change the purely hydrodynamical problem.

In previous work, the possibility of driving a flow electromagnetically rather than mechanically was suggested. Hollerbach et al. (2013) performed a numerical simulation of the Earth's inner/outer core radius ratio of 0.35, considering solid body rotation and high Hartmann number, as well as the injection of electric current in a wide ring-shaped electrode around the equator of the outer sphere with a predominantly imposed axial magnetic field. Electromagnetically driven flows allow greater flexibility, in terms of which body forces are to be imposed, whereas in Couette flows one can only vary the amplitude of the differential rotation.

The objective of the present contribution is twofold. In the first place, considering the idea of the electromagnetic forcing, we propose a simple experimental device with the flexibility in terms of the spatial structure of the forcing, keeping some basic aspects of the flow in planetary interiors. As a first approach, we consider an electrolyte as the working fluid. The low electrical conductivity of electrolytes compared with that of liquid metals and the small magnetic field intensities produced by permanent magnets result in low Hartmann number flows. Secondly, the work is aimed at an experimental-theoretical analysis of the flow in a spherical annulus generated by the interaction of a steady electric current with a dipolar magnetic field. We take advantage of the transparency of the electrolyte to explore the inner flow structure through particle image velocimetry (PIV) measurements in equatorial planes.

2 Experimental Procedure

The experiment was developed in a concentric spheres set-up, see Fig. 1. The spheres are made of glass. The diameter of the outer and the inner sphere is $a = 21$ and $b = 7$ cm, respectively. The inner sphere is held by an 11 mm-diameter glass shaft. This sphere is composed of two watertight glued hemispherical shells. The gap between the spheres is filled with a weak electrolytic solution of sodium bicarbonate ($NaHCO_3$) at 8.6 % by weight. The mass density, kinematic viscosity and electrical conductivity of the electrolyte are $\rho = 1.09 \times 10^3$ Kg/m^3, $\nu = 10^{-6}$ m^2/s, and $\sigma = 6.36$ S/m, respectively. The electric current is injected through two copper rings (of width 0.5 cm). The rings were located externally and internally on the equator of

Fig. 1 Sketch of the experimental device, not drawn to scale. The spherical coordinate system we use is shown. Both spheres are set to rest. An electrolytic solution fills the gap between the *outer* and the *inner spheres* of radii a and b, respectively. The *inner sphere* encloses a permanent magnet, which produces the imposed dipolar magnetic $\mathbf{B}^0$. The radially electrical current $\mathbf{j}^0$ is injected through two cooper rings located at the equators of the *spheres*, whereas the main direction of the Lorentz force is denoted by $\mathbf{F}^0$
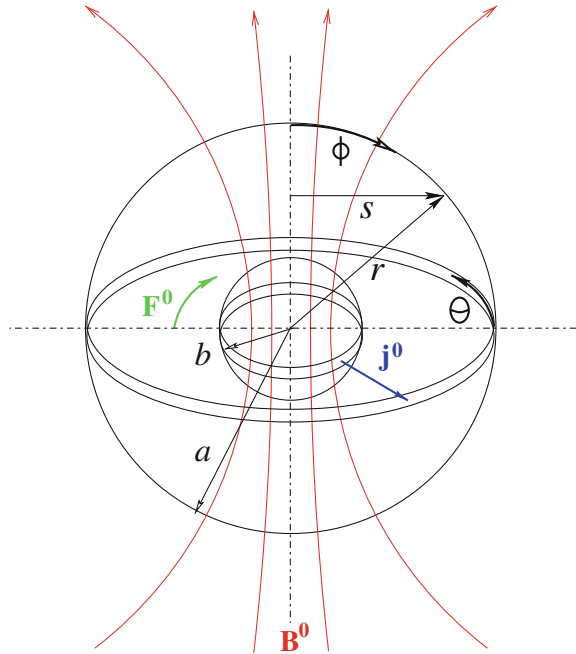
the smaller and bigger sphere, respectively. The dipolar magnetic field is generated by a rectangular parallelepiped Neodymium magnet with a side length of 50.8 mm, height of 25.4 mm and maximum strength of 0.38 T. The magnet is placed in the geometrical center of the inner sphere, the longer surfaces of the magnet are perpendicular to the **r** vector when pointing parallel to north and south directions. The direct current injected through the pair of electrodes interacts with the non-uniform magnetic field distribution generating a rotational Lorentz force that sets the fluid into motion. The direct electric current is obtained from a BK PRECISION 1696 DC regulated power supply. The amplitude of the injected current was kept fixed at 50 mA. With this value, laminar flow was explored. As the electrolyte is a transparent medium, experimental velocity fields were obtained with Particle Image Velocimetry (PIV). A continuous laser 5 mW Bright Red (635 nm) Laser Module (Coherent Lasiris SNF Alignment and Structured Light Module) was placed in order to create a light plane parallel to the equator of the spheres. The light sheet was placed 1 cm beneath the equatorial plane and parallel to it, in order to avoid the electrodes. The concentric spheres set-up was placed inside a rectangular container partially filled with water, the latter with the aim of reducing the aberration of the light sheet with the surface of the outer sphere. Avoiding the transient flow, flow images were extracted from video captured with a Nikon D80 camera with a AF micro-nikkor 60 mm f/2.8 D lens. The camera sat on a holder 30 cm below the experimental set-up. The actual area of the captured image was 14 cm × 8 cm. The images had 1280 × 720 pixels resolution. The PIVlab software was used to perform the analysis; we used interrogation

areas of 16×16 pixels with $50\,\%$ overlap in the horizontal and vertical directions, and vector validation. These conditions gave us a spatial resolution of $0.11 \times 0.11\,\text{mm}^2$. The time interval between photos was 41.66 ms. Images were masked for the PIV analysis in order to perform the analysis only on the flow zone. The error in the velocity data was obtained by adjusting a normal distribution to the data at sample points.

3 Mathematical Model

Flows driven by Lorentz forces created by the interaction of injected electric currents with applied magnetic fields in weak electrolytic solutions have been successfully modelled by neglecting induced effects for quasi-two-dimensional (Figueroa et al. 2009, 2014) and three-dimensional models (Figueroa et al. 2011). This means that currents induced by the motion of the fluid in the magnetic field, as well as Lorentz forces produced by these currents, can be completely disregarded. In this case, the flow is governed by the continuity equation and the Navier-Stokes equation with the Lorentz force term. In dimensionless terms the governing equations read

$$\nabla \cdot \mathbf{u} = 0, \tag{1}$$

$$\frac{\partial \mathbf{u}}{\partial t} + (\mathbf{u} \cdot \nabla)\mathbf{u} = -\nabla p + \nabla^2 \mathbf{u} + Re_* \, \mathbf{j}^0 \times \mathbf{B}^0, \tag{2}$$

where $\mathbf{u}$ stands for the velocity vector, normalized by $u_0 = \nu/d$, ν and d being the kinematic viscosity of the fluid and the characteristic length, namely, the gap between spheres $d = a - b$. The pressure field is denoted by p, normalized by ρu_0^2, where ρ is the density of the fluid. Coordinates are normalized by d. In turn, time t is normalized by u_0/d. The last term on the right-hand side of Eq. (2) represents the Lorentz force created by the non-uniform magnetic field distribution $\mathbf{B}^0(r, \theta, \phi)$ normalized by the amplitude of the magnetic field at the equator of the inner sphere $B^0 = 0.065$ T, and the applied electric current in the r-direction, namely, j_r^0 which is normalized by the current amplitude j^0. The parameter $Re_* = U_0 d/\nu$ stands for the Reynolds number based on the velocity of the fluid due to the electromagnetic force. The characteristic bulk velocity $U_0 = j^0 B^0 d^2/\rho\nu$, is obtained from a balance between viscous and Lorentz forces (Figueroa et al. 2009). Note that Re_* does not coincide with the experimental Reynolds number based on the maximum velocity ($Re = u_\theta d/\nu$). The system of Eqs. (1), (2) is fully determined provided the injected current $\mathbf{j}^0$ and the applied magnetic field $\mathbf{B}^0$ are known. In dimensionless terms, the applied magnetic field is denoted as

$$\mathbf{B}^0 = \frac{b^3}{r^3}(2\cos\phi\,\hat{r} + \sin\phi\,\hat{\phi}). \tag{3}$$

where ϕ is the colatitude, $\hat{r}$ and $\hat{\phi}$ are the unitary vectors in the radial and orthoradial directions and b is the dimensionless radius of the inner sphere. The expression for the current density comes from assuming that the electric current I is constant in the r-direction and that the normalizing value j^0 is the reference value for

$$j^0 = \frac{I}{\int b^2 \sin \phi d\phi d\theta}, \tag{4}$$

where the integral represents the area perpendicular to I. The integration limits for θ are 0 (zero) and 2π, whereas the values for ϕ can be obtained according to the width of the copper rings. Thus, the electric current density is given as

$$\mathbf{j}^0 = \frac{b^2}{r^2} \, \hat{r}. \tag{5}$$

The system of Eqs. (1) and (2) along with the expressions for the magnetic field and the current density given by Eqs. (3) and (5), respectively, conform a closed system for solving the electromagnetically driven flow in the gap between the spheres.

3.1 Analytical Solution

Let us first address the problem in a very simplified way that allows us to obtain an analytic solution. The main Lorentz force points to the θ-direction, thus the velocity components in the r and ϕ directions are neglected. Considering a low Reynolds number approximation, the flow is axisymmetric, thus there is no dependence in the θ direction. By focusing on the symmetry plane $\phi = \pi/2$, the u_θ component is only dependent on the r-direction. We also consider the steady state and no pressure gradient established in the θ-direction. Equations (1) and (2) reduce to

$$\frac{d^2 u_\theta}{dr^2} + \frac{2}{r} \frac{du_\theta}{dr} - \frac{u_\theta}{r^2} = Re_* \frac{b^5}{r^5}. \tag{6}$$

The term on the right-hand side of Eq. (6) corresponds to the applied Lorentz force. We must note that the electromagnetic dependence in the r-direction decays as r^{-5}. The solution of Eq. (6) that satisfies no-slip conditions takes the form

$$u_\theta(r) = Re_* \, b^5 \frac{\frac{b^{\sqrt{5}} - a^{\sqrt{5}}}{r^3} + r^{\left(\frac{\sqrt{5}-1}{2}\right)} (a^c - b^c) + r^{\left(\frac{-\sqrt{5}-1}{2}\right)} \left(b^c a^{\sqrt{5}} - b^{\sqrt{5}} a^c\right)}{5 \left(b^{\sqrt{5}} - a^{\sqrt{5}}\right)}, \tag{7}$$

where the constant c is defined as $c = (\sqrt{5} - 5)/2$. As convective terms are disregarded, we must note that Eq. (7) is only valid for the creeping flow regime.

3.2 Numerical Solution

As it will be shown in the next section, Eq. (7) approximates the velocity profiles only in the equatorial plane. However, this analytical solution is helpful for the physical understanding of the flow. In fact, a simple analytical solution that includes advective effects is not available. In general, advective effects may promote the three-dimensionality of the flow and therefore, an accurate modelling requires a three-dimensional (3D) numerical approach. In order to get the complete velocity field at different locations of the flow region, the system of Eqs. (1) and (2) were solved numerically in a volume corresponding to the dimensions of the experimental set-up. A finite difference method based on the procedure described in Griebel et al. (1998) and Cuevas et al. (2006) was adapted to a spherical coordinate system including electromagnetic forces. The numerical code has been successfully compared with experimental results where the flow is promoted by the rotation of the inner sphere (Wimmer 1976). The calculation of the Lorentz force term in Eq. (2) requires the full 3D magnetic field distribution of the permanent magnet. It was verified that expression (3) reproduces the magnetic field used in the experiment. Numerical solutions consider no-slip conditions on the spheres. A spatial resolution of $90 \times 60 \times 90$ cells was used in calculations with a time step of 2×10^{-6}. In the experiment, the inner sphere is held by a glass shaft, which was not included in the numerical model.

4 Results

In this section, we present numerical calculations and provide a comparison with analytical and experimental results. The general feature of the flow is observed in Fig. 2, were the velocity vector fields are shown. The resulting interaction between the injected current and the dipolar magnetic field, namely the Lorentz force, points mainly to the negative θ-direction. The flow develops a transient regime after which
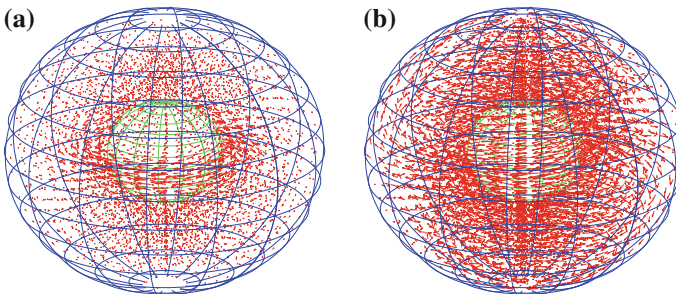
Fig. 2 Velocity field between the gap of the spheres. **a** $I = 1$ mA. **b** $I = 500$ mA. For the velocity scale, see Figs. 3 and 4. Numerical calculations

a circular motion is established. For small electric currents ($I \approx 1$ mA) convective effects are small, see Fig. 2a, the flow is mostly in the azimuthal direction with negligible motion in the radial and orthoradial directions. In fact, a doughnut-shaped recirculation is observed around the equator of the inner sphere. The flow is predominantly governed by diffusion so that the flow pattern is symmetric with respect to the ϕ-axis and does not depend on the azimuthal coordinate. In the case of high electric current, see Fig. 2b, convective effects mostly dominate and the recirculation is elongated in the radial and orthoradial directions filling the whole gap between the spheres and displaying a full three-dimensional motion.

The solutions are governed by one dimensionless number, namely, the Reynolds number. Based on the maximum velocity and the gap between spheres, the Reynolds numbers of the flow varied from 50, for injected currents of 1 mA, to 2340, for 500 mA. The Reynolds number determines the level of fluctuations. Flow instabilities are observed departing from the inner sphere's equator zone from $Re = 1340$ ($I = 200$ mA). These instabilities should be addressed in a future work. In turn, the Hartmann number $Ha = B_e d \sqrt{\sigma / \rho \nu}$, based on the maximum magnetic field strength B_e at the equators of the spheres, varied from 0.065 T in the inner sphere to 0.003 T in the outer sphere. As Ha is lower than unity, no inductive effects have been considered.

The general features of the velocity field are more clearly observed in Figs. 3, 4 and 5. Figures 3 and 4 display the magnitude of the time-averaged azimuthal velocity as a function of the position for equatorial and meridional planes, respectively. For low electric currents ($I = 1$ mA), two distinct regions show up in the map of mean azimuthal velocity for low electric current: an inner vorticity region, where the angular velocity predominately varies with radius r, see Fig. 3a, and a zero velocity region close to the outer surface. The boundary of the doughnut shaped vortex around the equator of the inner sphere can be easily seen in Fig. 4a. In the case of high electric currents, the low velocity zones are restricted to the no-slip boundaries at both surfaces and the polar zones. In both cases the maximum angular velocity is located in the equatorial plane. Owing to the no-slip condition at both surfaces, the highest
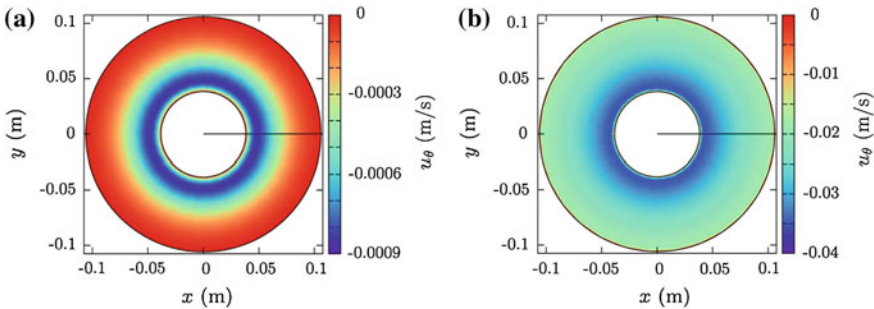
Fig. 3 Equatorial plane of the velocity field. Azimuthal velocity component u_θ isovalues. **a** $I = 1$ mA. Note the zone of rotation near the *inner sphere*. **b** $I = 500$ mA. Note that the rotation zone covers the full gap. Numerical calculations
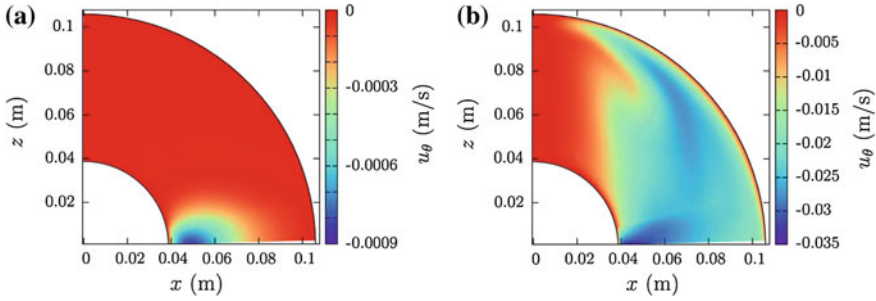
Fig. 4 Meridional slice of the velocity field. Azimuthal velocity component u_θ isovalues. **a** $I = 1$ mA. Note that the zone of rotation is a small portion around the *inner sphere's* equator. **b** $I = 500$ mA. Note that the rotation in the polar zone is null. Numerical calculations
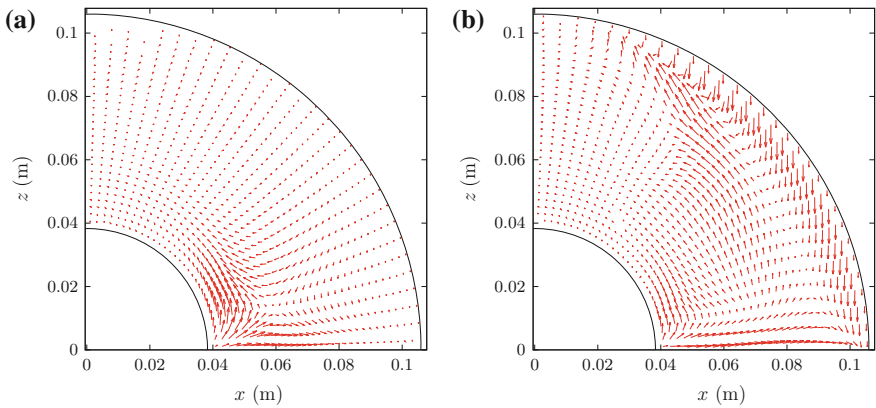
Fig. 5 Poloidal velocity field vector for **a** $I = 1$ mA and **b** $I = 500$ mA. Numerical calculations

velocities are located in the gap, in the neighbourhood of the inner sphere where the intensities of the current density and the magnetic field are strong, see Figs. 3b and 4b.

Figure 5 shows the time-averaged poloidal velocity vector field in the meridional plane. As stated previously, at low electric currents the radial and orthoradial velocity components are two orders of magnitude smaller than the azimuthal component. However, for large currents, the three components have the same order. Moreover, the vector field displays a circulation for large electric currents, see Fig. 5b.

In order to double-check our numerical code, we compare the velocity field of our simulation with the obtained analytical solution Eq. (7). Considering no-slip conditions on the spheres and keeping the low Reynolds number regime, $Re_* = 1$, two case scenarios were numerically simulated: equatorial ring electrodes and conducting shells. Figure 6 compares the radial profile of the azimuthal velocity in the equatorial plane of the one-dimensional analytical solution, and the three-dimensional numerical solution. Considering the ring electrodes (blue line), the numerical solu-

Fig. 6 Radial profiles of azimuthal velocity in the equatorial plane for different simulations and the analytic solution Eq. (7) with $Re_* = 1$. *Blue line* electric current is injected through the equatorial cooper rings. *Red line* electric current is injected through electric conductive spheres. Numerical and theoretical calculations
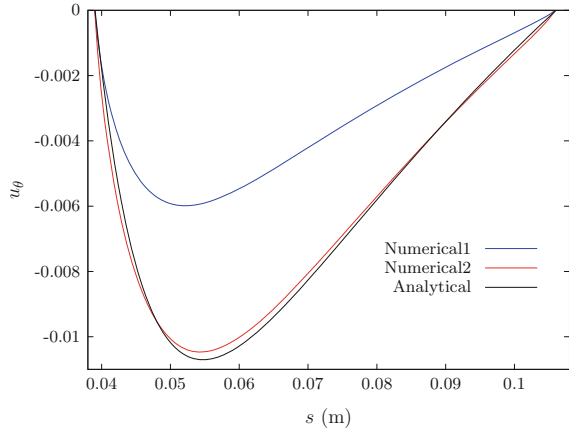
tion exhibits a lower azimuthal velocity. However, if we consider that both spheres are electric conductive, contrary to the experiment where they are insulators, in this case (red line) the numerical solution agrees very well. That is, our analytic solution models the case of conducting shells. Experimentally, the case of conducting shells was avoided since the shells shut the visual access to the fluid and PIV measurements can not be performed.

The profiles of the azimuthal velocity component as a function of the radius for different electric currents are presented in Fig. 7a. These profiles are obtained in the equatorial plane. For low currents, diffusive effects dominate and boundary layers cover the full gap (red line). Whereas the electric current is increased, convective effects arise and the boundary layer zones decrease, and the velocity profile becomes planar in the gap between boundary layers. The maximum velocity location depends on the boundary layer width, as convective effects are higher, the location of the max-
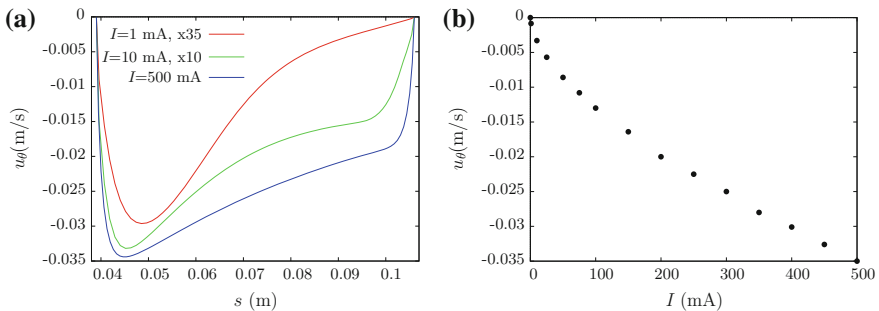
Fig. 7 **a** Radial profiles of azimuthal velocity in the equatorial plane for different electrical currents. For clarity in the visualization, the *red* and *green lines* are scaled up by a factor of 35 and 10, respectively. **b** Value of the maximum azimuthal component velocity (u_θ) as a function of the applied current I. Each symbol corresponds to an individual numerical calculation

Fig. 8 Experimental radial profile of azimuthal velocity 1 cm beneath the equatorial plane for $I = 50$ mA. The *continuous line* shows the numerical simulation for $I = 50$ mA
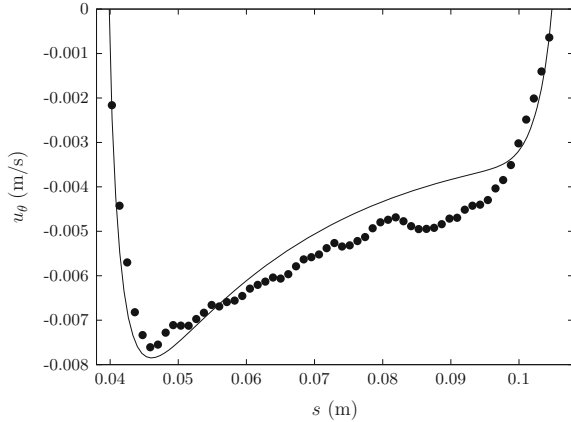
imum velocity approaches the inner sphere equator. Figure 7b displays the maximum velocity as a function of the applied current. The numerical observations fit the curve $u_\theta = -8 \times 10^{-14} I^5 + 5 \times 10^{-11} I^4 - 2 \times 10^{-8} I^3 + 3 \times 10^{-6} I^2$. It is worth noting that, for high electric currents the velocity profile is similar to the case of super rotation for the magnetohydrodynamic case when the flow driving is the rotation of the inner sphere (Figueroa et al. 2013).

Finally, Fig. 8 compares the radial profile of the azimuthal velocity in the equatorial plane computed with the numerical code and an experimental observation obtained with the PIV technique for $I = 50$ mA ($Re = 335$). The numerical solution agrees very well. The solution exhibits a slightly lower azimuthal velocity in the gap between the two boundary layers. The relative error is smaller than 18 %. These results indicate that the full three-dimensional model is able to reproduce the electromagnetically forced flow in the concentric spheres set-up.

5 Concluding Remarks

The flow generated in the gap of a concentric spheres set-up by a Lorentz force produced by the interaction of a dipolar magnetic field and an imposed radial electric current has been studied with theoretical and experimental tools. The simple experimental setting allows optical access to the flow and could be used to study a variety of complex fluid dynamics phenomena, such as mixing of fluids. We propose a relatively simple theoretical model that correctly captures the radial dependence of the main velocity component, namely, the azimuthal velocity.

A full three-dimensional numerical model was built. Numerical simulations were compared with available experimental results and the theoretical model. The dipolar magnetic field is modelled analytically and fitted accurately to reproduce the experimental field. Assuming that the electric current I is constant, the electric current

density in the radial direction goes as r^{-2}. In general, a good quantitative comparison is found between numerical and experimental results.

The three-dimensional picture of the flow structure was reconstructed. For small injected currents, a quite axisymmetric equatorial recirculation formed mainly by diffusive momentum transport was found. As the current is increased, convective effects are manifested by the elongation of the recirculation with the displacement of the point of maximum velocity towards the inner sphere's equator. For currents above $I = 200$ mA ($Re = 1340$) the flow becomes three-dimensional and time dependent. Instabilities of the inner boundary layer are observed for $I > 200$ ($Re > 1340$). The Reynolds numbers of the flow varied from 50, for injected currents of 1 mA, to 2340, for 500 mA. The very small values of Ha in the present experiment ($O(10^{-1})$) lead to negligible induced effects and to the predominance of viscous and imposed non-uniform Lorentz force.

Although there exist several experimental studies on MHD in concentric spheres, the detailed experimental exploration and modelling of continuously stirred electrolytic solutions by electromagnetic forces have, to the best of our knowledge, not been previously considered.

References

Amara K, Hegseth J (2002) Convection in a spherical capacitor. J Fluid Mech 450:297–316

Bühler L (2009) On the origin of super-rotating layers in magnetohydrodynamic flows. Theor Comput Fluid Dyn 23:491–507

Cuevas S, Smolentsev S, Abdou M (2006) On the flow past a magnetic obstacle. J Fluid Mech 553:227–252

Dormy E, Cardin P, Jault D (1998) MHD flow in a slightly differentially rotating spherical shell, with conducting inner core, in a dipolar magnetic field. Earth Planet Sci Lett 160:15–30

Figueroa A, Demiaux F, Cuevas S, Ramos E (2009) Electrically driven vortices in a weak dipolar magnetic field in a shallow electrolytic layer. J Fluid Mech 641:245–261

Figueroa A, Cuevas S, Ramos E (2011) Electromagnetically driven oscillatory shallow layer flow. Phys Fluids 23:013601

Figueroa A, Schaeffer N, Nataf H-C, Schmitt D (2013) Modes and instabilities in magnetized spherical Couette flow. J Fluid Mech 716:445–469

Figueroa A, Meunier P, Cuevas S, Villermaux E, Ramos E (2014) Chaotic advection at large Péclet number: electromagnetically driven experiments, numerical simulations, and theoretical predictions. Phys Fluids 26:013601

Gissinger C, Ji H, Goodman J (2011) Instabilities in magnetized spherical Couette flow. Phys Rev E 84:026308

Griebel M, Dornseifer T, Neunhoeffer T (1998) Numerical simulation in fluid dynamics. SIAM, New York

Hollerbach R, Wei X, Noir J, Jackson A (2013) Electromagnetically driven zonal flows in a rapidly rotating spherical shell. J Fluid Mech 725:428–445

Jung C-H, Tanahashi T (2008) Natural convection between concentric spheres in electromagnetic fields. J Mech Sci Technol 22:1202–1212

Kleeorin N, Rogachevskii I, Ruzmaikin A, Soward AM, Starchenko S (1997) Axisymmetric flow between differentially rotating spheres in a dipole magnetic field. J Fluid Mech 344:213

Nataf H-C, Alboussiere T, Brito D, Cardin P, Gagniere N, Jault D, Schmitt D (2008) Rapidly rotating spherical Couette flow in a dipolar magnetic field : an experimental study of the mean axisymmetric flow. Phys Earth Planet Inter 170:60

Starchenko SV (1998) Magnetohydrodynamic flow between insulating shells rotating in strong potential field. Phys Fluids 10:2412–2420

Wimmer M (1976) Experiments on a viscous fluid flow between concentric rotating spheres. J Fluid Mech 78:317–335

Zimmerman DS, Triana SA, Nataf H-C, Lathrop DP (2014) A turbulent, high magnetic Reynolds number experimental model of earth's core. J Geophys Res Solid Earth 119:4538–4557

Vibration of a Water Drop in a Hydrophobic Medium

G. Rangel Paredes, D. Porta Zepeda, C. Echeverría Arjonilla and C. Stern Forgach

Abstract The behavior of a water drop on a hydrophobic substrate subject to vertical vibrations is described. The dynamics of the surface passes through different phases: harmonic, geometric and chaotic (Flores Galicia et al.). To characterize the motion in terms of quantifiable variables, the height at different points on the surface was measured as a function of time. A Fourier analysis of the signal was made to determine the frequency response to changes in the forcing.

1 Introduction

A sessile drop on a hydrophobic substrate acquires a spherical or slightly ellipsoidal form for volumes smaller than 5 ml. When the drop is subjected to vertical vibrations, the geometry of its surface can be studied with a high speed camera and has been classified (Galicia et al. 2015; Noblin et al. 2009) in three phases:

a. Harmonic, at small frequencies the drop expands and contracts periodically
b. Geometric, as the frequency is increased, the surface shows oscillating polygonal figures
c. Chaotic, the surface oscillates in an irregular fashion

G. Rangel Paredes (✉)
Facultad de Ciencias, Departamento de Física, Universidad Nacional Autónoma de Mexico, Ciudad Universitaria, Av. Universidad 3000 Circuito Exterior S/N, C.P. 04510 Delegación Coyoacán, Mexico D.F., Mexico
e-mail: ghiordu-pardas@hotmail.com

D. Porta Zepeda · C. Echeverría Arjonilla · C. Stern Forgach
Facultad de Ciencias, UNAM, Av. Universidad 3000 Circuito Exterior S/N, C.P. 04510 Delegación Coyoacán, Mexico D.F., Mexico
e-mail: alviond@gmail.com

C. Echeverría Arjonilla
e-mail: carlosea1982@gmail.com

C. Stern Forgach
e-mail: catalina@ciencias.unam.mx
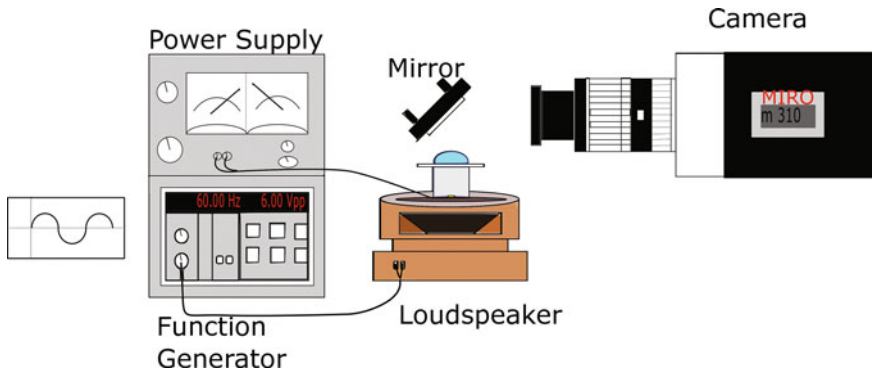
Fig. 1 Experimental set-up

For certain critical values of the forcing frequency, the drop breaks and small droplets are ejected from its surface. As the frequency is still increased, the drop recovers the geometric phase, probably due to loss of mass.

2 Experimental Set-up

The set-up consists of a function generator connected to a loudspeaker with a microscope slide on the top. The slide is treated with a hydrophobic substrate (Never wet), except for a small circle where a (1 ± 0.10) ml drop is placed. The angle of contact of the drop at rest is $(125.3 \pm 0.05)°$. The motion is filmed with a high speed camera Phantom Miro M310 at 4000 frames per second. The frames were analyzed using the CINE Viewer software (Fig. 1).

Five forcing frequencies were selected 15, 24, 33, 42 and 60 Hz. For each one, the amplitude of the voltage of the function generator was varied in the ranges of 1–10, 1–10, 1–4, 1–2 and 1–9 V, respectively.

To analyze the deformation, the displacement of five points on the surface of the drop was followed as a function of time. From a side view of the drop, X0 corresponds to the center and X4 to the last point where the drop touches the substrate. The distance along the x-axis was divided in four parts, thus defining X1, X2 and X3 (Fig. 2). The displacements along the y-axis were determined every five frames, which corresponds to 1.25 ms. The drop is considered symmetric so only half of it was measured.

3 Results

Figures 3, 4, 5, 6, 7 and 8 show the heights as a function of time and their respective Fourier transforms.
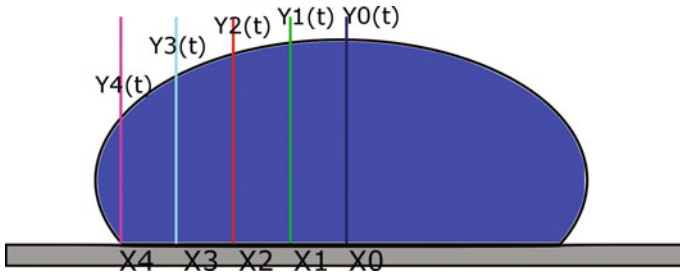
Fig. 2 Schematic of the points on the surface of the drop whose displacement was followed as a function of time
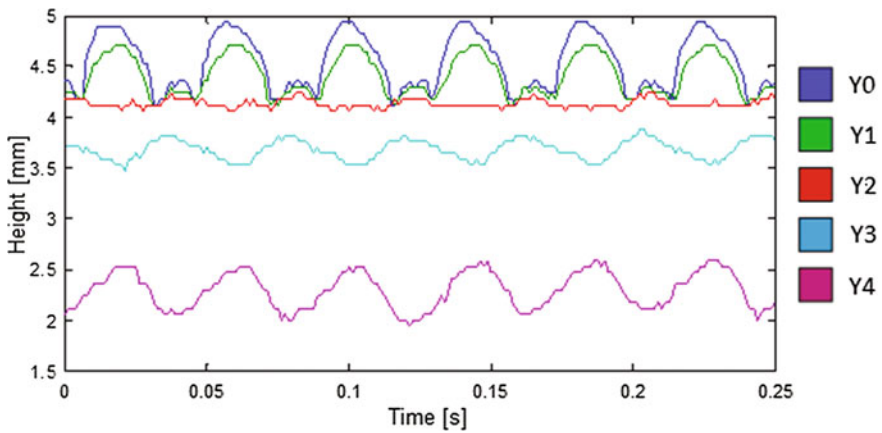
Fig. 3 Variations in height of five points on the surface of the drop as a function of time for a forcing frequency of 24 Hz and an amplitude of oscillation of the plate of 0.0882 mm (Harmonic phase)

The motion corresponds to a harmonic phase at which the drop oscillates as a whole. It is interesting to note that for this frequency, point (X2, Y2) corresponds to a node; there is no displacement and consequently no frequency. The frequency in all other points corresponds to the forcing frequency, the highest amplitudes are in the center of the drop.

The motion corresponds to a geometric phase. Even though the frequency is high, the amplitude of oscillation is small. In this case, several frequencies appear in the spectrum. However, the highest amplitude corresponds to the forcing frequency and at the center of the drop, for point (X0, Y0). At the other points, the next highest peak corresponds to 12 Hz, a fifth of the forcing frequency. At points 0, 1 and 2 a frequency of 8 Hz seems important but it disappears on the side points 3 and 4.
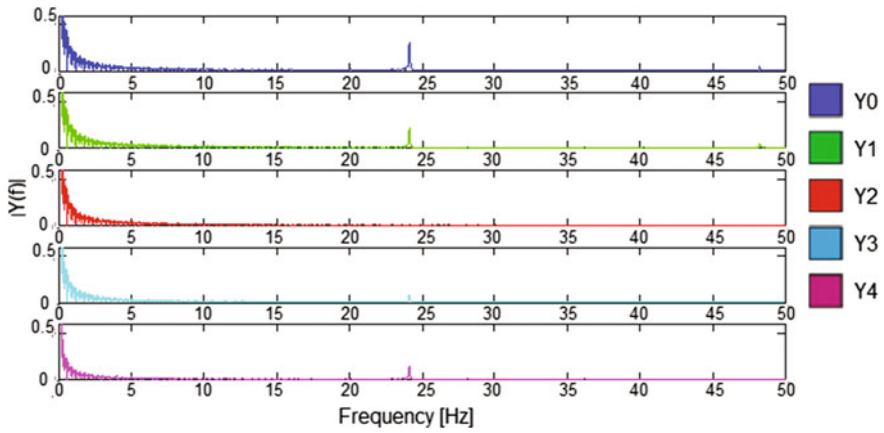
Fig. 4 Frequency spectrum of the signals shown in Fig. 3
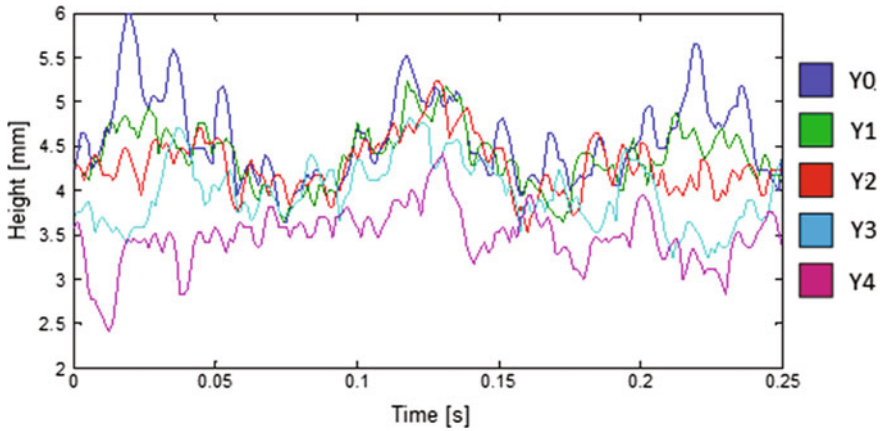
Fig. 5 Height as a function of time for a forcing frequency of 60 Hz and an amplitude of oscillation of the plate of 0.1389 mm (Geometric phase)

The motion corresponds to a chaotic phase. The frequency of oscillation is low but the amplitude is high. Peaks at 33 Hz, the forcing frequency and 16.5 Hz appears in the five spectra. The amplitude of the latter is quite small at point X5. From the video the motion seems chaotic as the displacements of the five points are out of phase. However the spectrum does not show a chaotic behavior.
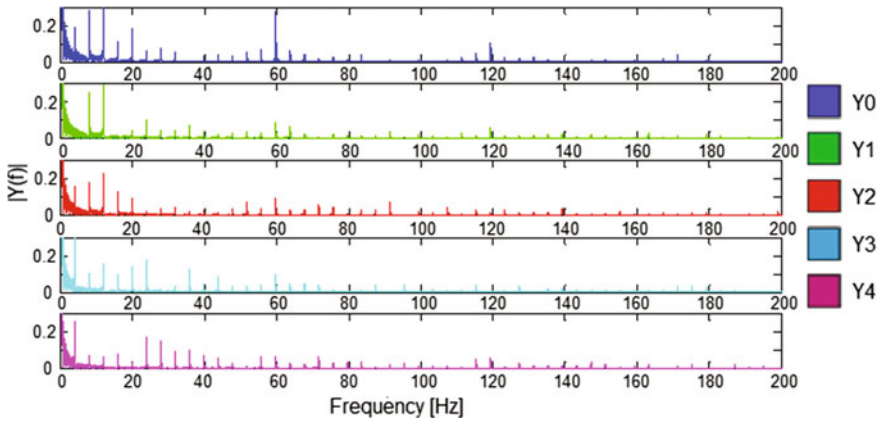
Fig. 6 Frequency spectrum of the signals shown in Fig. 5
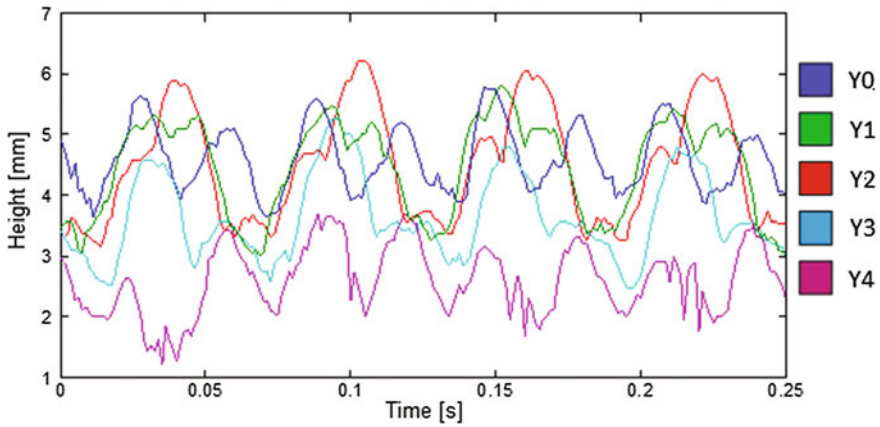
Fig. 7 Displacement of five points on the surface of the drop as a function of time for a forcing frequency of 33 Hz and an amplitude of oscillation of the plate of 0.2632 mm (Chaotic phase)

4 Analysis and Discussion

The frequency f_0 and the displacement x_{-0} of the loudspeaker are related through the acceleration A_0 of the excitation:

$$A_0 = \omega^2 x_0 = (2\pi f_0)^2 x_0 \tag{1}$$
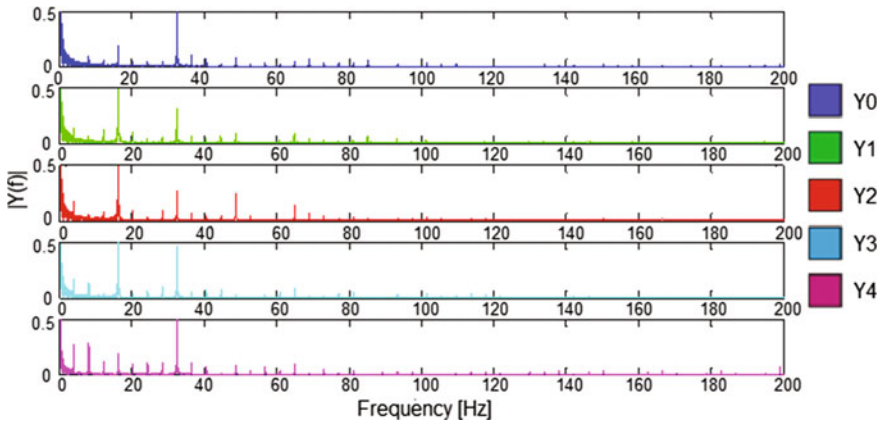
Fig. 8 Frequency spectrum of the signals shown in Fig. 7
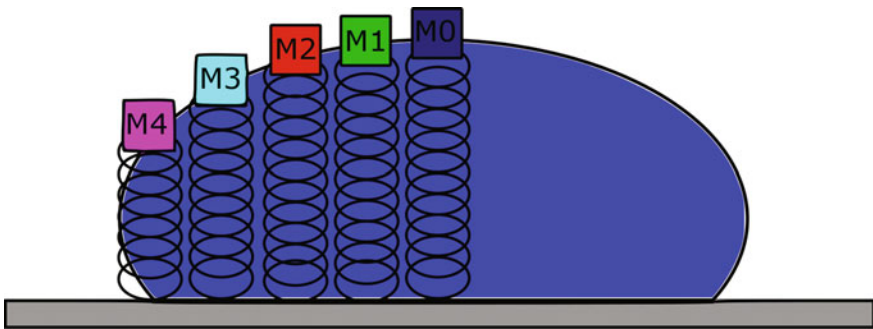
Fig. 9 Model of the oscillating motion using *five springs*

The amplitude of the displacement is defined as

$$\eta_0 = \frac{(Y_{max} - Y_{min})}{2},$$

(2)

where Y_{max} is the largest height and Y_{min}, the smallest at each X location.

4.1 Harmonic Phase

As was explained in Sect. 3, in the harmonic phase, four points respond exactly at the forcing frequency, and one point corresponds to a node. The motion of the surface of the drop can then be modelled as a series of springs that do not interact with each other.

Spring Model

The motion of the drop can be modelled with springs that follow Hooke's law (Fig. 9).

In this case, the displacement η can be described with the equation for simple harmonic motion.

$$\ddot{\eta} + \omega_0^2 \eta = 0 \tag{3}$$

then

$$\eta(t) = \eta_0 \cos(\omega_0 t), \tag{4}$$

where η_0 is the amplitude and $\omega_0 = 2\pi f_0$.

For the forcing frequencies 15.00 ± 0.45 and 24.00 ± 0.72 Hz, the drop is in the harmonic phase.

$$\eta(t) = \eta_0 \cos(30\pi t) \tag{5}$$

$$\eta(t) = \eta_0 \cos(48\pi t) \tag{6}$$

Figure 10 shows the measured values of the amplitude.
From Eq. (4)

$$\omega_0^2 = \frac{k}{m}, \tag{7}$$

where k can be considered a fictional spring constant and m its mass (Figs. 11 and 12).

Considering the value of the surface tension at ambient temperature, k can be considered

$$k = 7.275 \times 10^{-4} \; \frac{N}{m}$$

so

$$m = \frac{k}{\omega_0^2}. \tag{8}$$

A different mass is obtained for each frequency: $m_1 = 8.19 \times 10^{-8}$ kg, $m_2 = 3.20 \times 10^{-8}$ kg. The real mass of the drop cannot change with the oscillation, but this virtual or added mass is related to the acceleration.
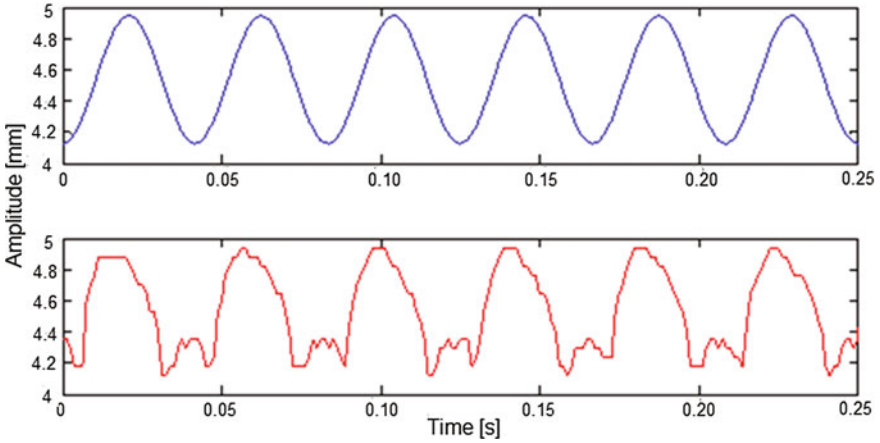
Fig. 10 Comparison between the model (*blue*) and the measured (*red*) time series. The acceleration of the excitation is 2.0064 ± 0.4118 m/s^2 for Y0(t)
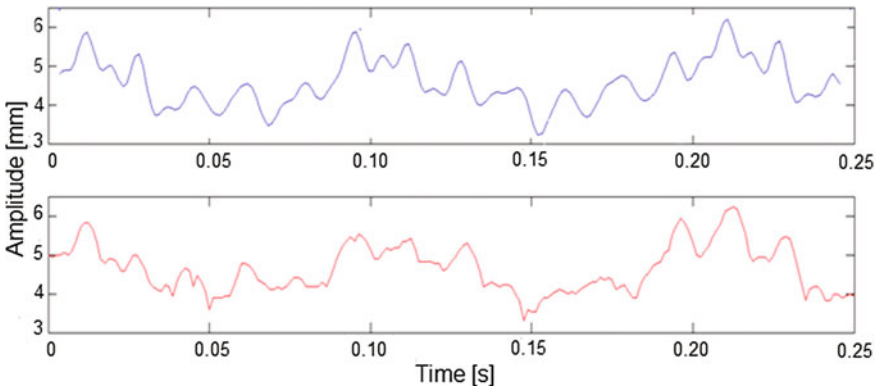
Fig. 11 Comparison between the model (*blue*) and the experimental data (*red*) for 60 Hz and an acceleration of 23.6918 ± 0.2262 m/s^2

From the previous values, an additional force can be calculated

$$F = -kx = -\left(7.275 \times 10^{-4} \frac{\text{N}}{\text{m}}\right)\eta_0 \cos(\omega_0 t). \tag{9}$$

Of course the model is valid only when there is only one frequency. The adjustment for the other two phases would require a model with more frequencies.
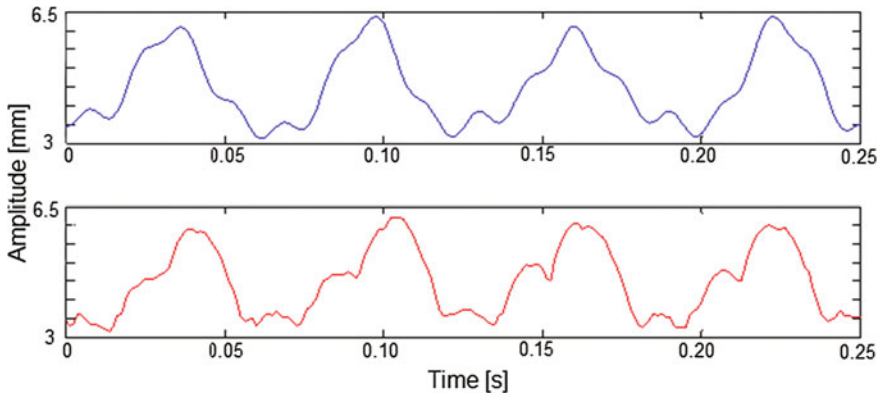
Fig. 12 Comparison between the model (*blue*) and the experimental data (*red*) for 33 Hz and an acceleration of 11.3138 ± 0.1080 m/s^2

4.2 Geometric Phase

In the experiments mentioned in this paper, the geometric phase appears for a forcing frequency of 60 Hz. The drop responds with the forcing frequency and several of its harmonics and subharmonics, and other frequencies that are linear combinations of the previous ones.

From the frequency spectra, the displacement can be calculated by

$$\eta(t) = \sum_{n=1}^{m} \eta_n \cos(n\omega_0 t) + \sum_{i=1}^{j} \eta_i \cos(\omega_i t), \tag{10}$$

where ω_0 is the forcing frequency and ω_i are the frequencies that correspond to linear combinations of the harmonics and subharmonics.

The amplitude of the subharmonics increases with the amplitude of the forcing frequency, and the amplitude of the other frequencies diminishes.

For example, for an acceleration of 23.6918 ± 0.2262 m/s^2 at Y0 (Fig. 7), the subharmonics increase and many of the other frequencies disappear, so (10) becomes

$$\begin{aligned}
\eta(t) = {}& \eta_5 \cos(2\pi(5)t) + \eta_9 \cos(2\pi(9)t) + \eta_{12} \cos(2\pi(12)t))t \\
& + \eta_{20} \cos(2\pi(20)t + \eta_{24} \cos(2\pi(24)t + \eta_{15} \cos(2\pi(15 \\
& + \eta_{60} \cos(2\pi(60)t + \eta_{120} \cos(2\pi(120)
\end{aligned}$$

4.3 Chaotic Phase

The phase is called chaotic because the video shows an irregular motion of the surface. However, each point has a periodic oscillation, out of phase with respect to the others. In the Fourier transform of the experimental data, new frequencies not related to the forcing frequency can be observed. So the behavior can also be described with (10).

For an acceleration of excitation of 3138 ± 0.1080 m/s^2 in Y1:

$$\eta(t) = \eta_1 \cos(2\pi(16.50)t) + \eta_2 \cos(2\pi(33.00)t) + \eta_4 \cos(2\pi(66.00)t)$$
$$+ \eta_I \cos(2\pi(21.88)t).$$

Three principal frequencies appear in the spectrum, and another one that does not seem to be related to the forcing frequency.

The frequencies 34.28 ± 1.97 and 21.88 ± 1.76 Hz appeared on the surface of the drop during the chaotic phase, for the forcing frequencies of 33.00 ± 0.99 y 42.00 ± 1.26 Hz), at different points and with different amplitudes of displacement. Their origin is still not understood.

5 Conclusions and Future Work

- The behavior of the height as a function of time was determined for several points at the surface of the drop as well as for several frequencies and amplitudes of the forcing frequency.
- The morphological characteristics come from the superficial waves that are generated as a response to the forcing.
- Each phase shows a characteristic frequency behavior.
- Internal currents have also been observed inserting dye inside the drop; in some cases they induce mixing. The relationship between the superficial waves and the internal currents, and their impact in the morphology of each phase will be studied in future work.
- Equation 10 will be used to model the oscillation at other points in the surface, for other forcing frequencies.

References

Galicia FF, Velázquez FGH, Paredes GR, Zepeda DP, Arjonilla CE, Forgach CS (2015) Dynamic behavior of a drop on a vertically oscillating surface. In: Ruíz-Chavarría K, Ovando M, Villa L, Sigalotti (eds) Selected topics of computational and experimental fluid mechanics, pp 261–270. Springer Environmental Science and Engineering

Noblin X, Buguin A, Brochard-Wyart F (2009) Vibrations of sessile drops. Eur Phys J Spec Top 166:7–10

Analysis of an Annular MHD Stirrer for Microfluidic Applications

J. Pérez-Barrera, A. Ortiz and S. Cuevas

Abstract An annular magnetohydrodynamic (MHD) device that may be used for the stirring of electrically conducting fluids in microfluidic applications is analyzed theoretically. A thin fluid layer is contained in the gap between two coaxial conducting cylinders connected to a potential difference under a uniform axial magnetic field. The imposed radial electric current that circulates in the fluid layer interacts with the magnetic field to produce an azimuthal Lorentz force that drives the fluid. A quasi-two-dimensional model that considers a linear friction due to the boundary layer attached to the insulating bottom wall is implemented and analytical solutions for the azimuthal flow are obtained for two different cases. The first case corresponds to a high conductivity fluid (a liquid metal) where the electric potential is coupled to the fluid velocity. The second case considers a low conductivity fluid (an electrolyte) where the electric potential is uncoupled from the fluid motion. The effect of slip boundary conditions at the walls of inner and outer cylinders, as well as the space between them, is explored.

1 Introduction

The use of electromagnetic forces to control and manipulate electrically conducting fluids in microfluidic devices has observed an increased interest in past years (Bau et al. 2003; Qian and Bau 2009). In fact, different procedures such as pumping, stirring, and mixing of fluids at micro scales can be suitably carried out by nonintrusive mechanisms provided by electromagnetic interactions. For instance, magnetohydrodynamic (MHD) pumps have proven to be useful even for the transport of

J. Pérez-Barrera · S. Cuevas (✉)
Instituto de Energías Renovables, Universidad Nacional Autónoma de México,
A.P. 34, 62580 Temixco, Morelos, Mexico
e-mail: scg@ier.unam.mx

A. Ortiz
Facultad de Ingeniería, Universidad Autónoma de Baja California,
Blvd. Unidad Universitaria, Benito Juárez S/N., B.C. 21280 Mexicali, Mexico

low conductivity liquids such as biological fluids (Kang and Choi 2011; Rivero and Cuevas 2012; Escandón et al. 2014). Further, it has been demonstrated that mixing of fluids can be properly accomplished using electromagnetic forces and, with a properly designed MHD stirrer, chaotic advection can substantially enhance mixing efficiency (Yi et al. 2002).

An interesting configuration for the mixing of fluids at micro scales is provided by an annular channel which uses an electromagnetic force to drive a conducting fluid in azimuthal motion (West et al. 2003; Gleeson et al. 2004; Gleeson 2005). In this channel, the fluid is confined in the gap between two coaxial electrically conducting cylinders, limited by an insulating bottom wall and an upper free surface. The channel is placed under a uniform magnetic field parallel to the cylinder's axis, produced by a permanent magnet or a magnetic solenoid. When an electric potential difference is applied between the coaxial cylinders, a radial electric current density circulates in the fluid. The interaction of the radial current with the axial magnetic field originates an azimuthal Lorentz force that drives the fluid. It has to be mentioned that the interest in MHD flows in the annular configuration is not restricted to microfluidics. In fact, liquid metal flows in annular ducts have also been studied to test the flow stability and duct flow behavior under strong uniform magnetic fields, avoiding the difficulty of considering the entrance region to the magnetic field that is present in rectilinear ducts (Moresco and Alboussière 2004; Zhao and Zikanov 2012; Mikhailovich et al. 2012). The instability of electrolytic flows has also been explored using annular configurations (Qin and Bau 2012; Pérez-Barrera et al. 2015).

The present contribution is aimed at searching analytical solutions for electromagnetically driven flows in annular channels. Although in some cases analytical treatments require highly idealized assumptions, conditions imposed in this work are closer to realistic microfluidic flows. Most analytical solutions reported in the literature for electromagnetically driven flows in annular configuration assume that coaxial cylinders are infinite (see, for instance, Qin and Bau 2012; Gleeson et al. 2004; Digilov 2007; Zhao et al. 2011). In this work, we use a quasi-two-dimensional (Q2D) model based on an averaging procedure in the normal direction that considers the presence of the bottom wall which originates either the Hartmann friction for high conductivity fluids (Sommeria 1988; Andreev et al. 2001) or pure viscous friction effects for low conductivity fluids (Satijn et al. 2001). In addition, given the relevance that slippage may have at microfluidic scale, generalized Navier slip boundary conditions are considered at the lateral walls which mainly determine the dynamic flow behavior (Rivero and Cuevas 2012; Smolentsev 2009). According to the electrical conductivity of the working fluid, two different cases are treated. The first case corresponds to a liquid metal flow where induction effects cannot be neglected and the equation of motion and that for the electric potential are coupled. In the second case, a solution is sought for a low conductivity fluid such as an electrolyte where induction effects are negligible. This implies that the electric potential is uncoupled from the fluid velocity and, therefore, can be determined independently from the equation of motion.
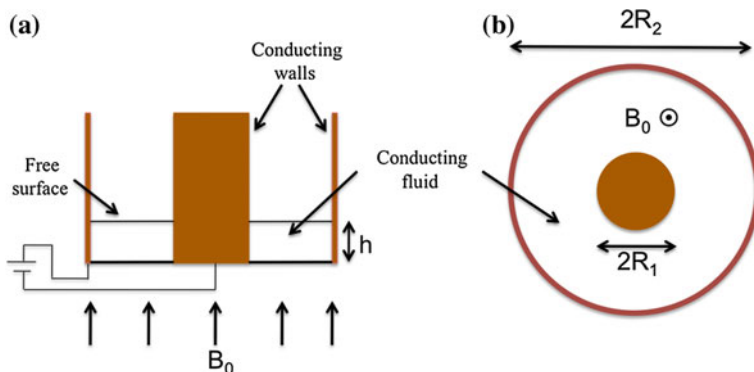
Fig. 1 Sketch of the analyzed annular MHD stirrer. **a** Side view. **b** Top view

2 Formulation

Figure 1 shows a sketch of the annular MHD stirrer (Pérez-Barrera et al. 2015). A thin layer of conducting fluid with thickness h lies in the gap between the inner and outer cylinders of radius R_1 and R_2, respectively, which are assumed to be perfect conductors. The bottom wall of the annular container is electrically insulated. An electric potential difference $\Delta\phi = \phi_2 - \phi_1$ is applied between the walls of the inner (ϕ_1) and outer (ϕ_2) cylinders so that a DC current can circulate radially in the fluid layer. The current interacts with a uniform applied magnetic field of strength B_0 parallel to the cylinder's axis and, therefore, a Lorentz force is produced in the azimuthal direction. Let us now summarize the governing MHD equations that must be solved to determine the flow in this device.

For the majority of MHD flows in laboratory or industrial applications using electrolytes or liquid metals, the magnetic field induced by the motion of the fluid is much smaller than the applied magnetic field. This condition, known as the low magnetic Reynolds number approximation, is expressed in the form $R_m \ll 1$, where the dimensionless parameter $R_m = \mu_o \sigma U L$ is the magnetic Reynolds number. Here, σ is the electrical conductivity of the fluid and μ_o the magnetic permeability of the vacuum, while U and L are characteristic velocity and length scales. Under this approximation, the basic equations that govern an MHD flow can be expressed as (Müller and Bühler 2001)

$$\nabla \cdot \mathbf{u} = 0, \tag{1}$$

$$\frac{\partial \mathbf{u}}{\partial t} + (\mathbf{u} \cdot \nabla)\mathbf{u} = -\frac{1}{\rho}\nabla p + \nu\nabla^2\mathbf{u} + \frac{1}{\rho}\mathbf{j} \times \mathbf{B}, \tag{2}$$

$$\mathbf{j} = \sigma(-\nabla\phi + \mathbf{u} \times \mathbf{B}), \tag{3}$$

$$\nabla^2\phi = \nabla \cdot (\mathbf{u} \times \mathbf{B}), \tag{4}$$

where $\mathbf{u}$, p, $\mathbf{B}$, $\mathbf{j}$, and ϕ are the velocity, pressure, applied magnetic field, electric current density, and electric potential, respectively, while ρ and ν are the mass density and kinematic viscosity of the fluid, respectively. Equations (1) and (2) are the continuity and Navier-Stokes equations, respectively. In turn, Eqs. (3) and (4) are the Ohm's law and the equation for the electrical potential that manifest the charge conservation.

2.1 Quasi-Two-Dimensional Approximation

Different physical mechanisms may promote the quasi-two-dimensionalization of flows, for instance, the force of gravity in a stratified flow, the Coriolis force in a rotating homogeneous fluid or the surface tension in a soap film. A strong magnetic field acting transversally to insulating walls that confine an MHD flow may also lead to the suppression of wall-normal motions. Quasi-two-dimensional (Q2D) flows also occur when a significant geometrical confinement is imposed, as in motions generated in shallow fluid layers, as may occur in microfluidic applications. This condition is satisfied when the relevant length scale in the plane of flow is much larger than the thickness of the fluid layer. The Q2D approach assumes that the transport of momentum in the normal direction is mainly diffusive and involves an averaging procedure where the governing equations are integrated in the normal direction (or along the lines of force when a magnetic field is present) within the thickness of the fluid layer. In this way, the problem is formulated in terms of core variables, while the effect of the boundary layer attached to the bottom wall is included through an additional linear term in the momentum equation accounting for the wall friction. In liquid metal flows under strong magnetic fields Hartmann boundary layers must be considered (Sommeria 1988; Andreev et al. 2001), while in flows of low conductivity fluids (i.e., electrolytes) with or without magnetic fields, the viscous boundary layer is the relevant one (Satijn et al. 2001).

In this work, we apply the Q2D approach and look for steady laminar azimuthal solutions, that is $\mathbf{u} = u_\theta(r)\hat{\mathbf{e}}_\theta$, where u_θ and $\hat{\mathbf{e}}_\theta$ are the velocity component and the unit vector in the azimuthal direction. In dimensionless form, the governing Eqs. (1)–(4) expressed in cylindrical coordinates take the following form when the Q2D approach is considered

$$\frac{u_\theta^2}{r + \alpha} = \frac{dp}{dr}, \tag{5}$$

$$\frac{d^2 u_\theta}{dr^2} + \frac{1}{r + \alpha}\frac{du_\theta}{dr} - \frac{u_\theta}{(r + \alpha)^2} - \frac{Ha}{\varepsilon}u_\theta - j_r = 0, \tag{6}$$

$$j_r = -\frac{d\phi}{dr} + Ha^2 u_\theta, \tag{7}$$

$$\frac{1}{r+\alpha}\frac{d}{dr}\left((r+\alpha)\frac{d\phi}{dr}\right) = \frac{Ha^2}{r+\alpha}\frac{d}{dr}\left((r+\alpha)u_\theta\right), \tag{8}$$

where u_θ, and the pressure, p, are normalized by $u_0 = \sigma B_0 \Delta\phi R/\rho\nu$ and ρu_0^2, respectively, with $R = R_2 - R_1$. In turn, the magnetic field is normalized by B_0 while the current density, j_r, is normalized by $\sigma\Delta\phi/R$. The dimensionless radial coordinate, r, and electric potential, ϕ, are defined as $r = (r' - R_1)/R = r'/R - \alpha$ and $\phi = (\phi' - \phi_1)/\Delta\phi$, where $\alpha = R_1/R$, r' and ϕ' being the dimensional radial coordinate and electric potential, respectively. The Hartmann number is defined as

$$Ha = B_0 R\sqrt{\frac{\sigma}{\rho\nu}}, \tag{9}$$

which estimates the strength of magnetic forces compared with viscous forces. The fourth term in Eq. (6) is the linear friction that results from the averaging procedure and considers the effect of Hartmann layers in the bottom wall (Sommeria 1988; Andreev et al. 2001), where $\varepsilon = h/R$ is the aspect ratio. In the following sections, we find solutions to the system of equations (5)–(8) considering slip boundary conditions in the cases of liquid metal and electrolyte flows.

3 Solution for Liquid Metal Flow

We first proceed to obtain solutions for the case of a liquid metal flow. Integrating Eq. (8) once we obtain

$$\frac{d\phi}{dr} = Ha^2 u_\theta + \frac{C}{r+\alpha}, \tag{10}$$

where C is an integration constant. If Eq. (10) is substituted into Eq. (7) and the result is then inserted into Eq. (6), it yields

$$\frac{d^2 u_\theta}{dr^2} + \frac{1}{r+\alpha}\frac{du_\theta}{dr} - \left(\beta^2 + \frac{1}{(r+\alpha)^2}\right)u_\theta = -\frac{C}{r+\alpha}, \tag{11}$$

where $\beta^2 = Ha/\varepsilon$. Equation (11) is a non-homogeneous Bessel equation and has to satisfy the general slip boundary conditions at the inner and outer cylinder's walls, that is,

$$u_\theta(0) = l_s\left(\frac{du_\theta}{dr} - \frac{u_\theta}{r+\alpha}\right)\Bigg|_{r=0} = l_s(r+\alpha)\frac{d}{dr}\left(\frac{u_\theta}{r+\alpha}\right)\Bigg|_{r=0}, \tag{12}$$

$$u_\theta(1) = -l_s\left(\frac{du_\theta}{dr} - \frac{u_\theta}{r+\alpha}\right)\Bigg|_{r=1} = -l_s(r+\alpha)\frac{d}{dr}\left(\frac{u_\theta}{r+\alpha}\right)\Bigg|_{r=1}, \tag{13}$$

where $l_s = L_s/R$ is the dimensionless slip length. The general solution of Eq. (11) can be expressed as

$$u_\theta(r) = C_1 J_1(-i\beta [r + \alpha]) + C_2 Y_1(-i\beta [r + \alpha]) + \frac{C}{\beta^2} \frac{1}{r + \alpha}, \qquad (14)$$

where J_1 and Y_1 are the Bessel's functions of order one of the first and second kind, respectively. As usually, only the real part has to be taken into account for physical interpretations. Constants C_1 and C_2 are obtained from the slip boundary conditions (12) and (13) in the form $C_1 = CA_1$ and $C_2 = CA_2$, where

$$A_1 = \frac{1}{\gamma\beta^2} \left(\frac{A(BY_1^{1+\alpha} - i\beta l_s(1 + \alpha)Y_0^{1+\alpha})}{\alpha} - \frac{B(AY_1^\alpha + i\beta l_s\alpha Y_0^\alpha)}{1 + \alpha} \right), \qquad (15)$$

$$A_2 = -\frac{1}{\gamma\beta^2} \left(\frac{A(BJ_1^{1+\alpha} - i\beta l_s(1 + \alpha)J_0^{1+\alpha})}{\alpha} - \frac{B(AJ_1^\alpha + i\beta l_s\alpha J_0^\alpha)}{1 + \alpha} \right), \qquad (16)$$

and

$$\gamma = \left(BJ_1^{1+\alpha} - i\beta l_s(1 + \alpha)J_0^{1+\alpha}\right) \left(AY_1^\alpha + i\beta l_s\alpha Y_0^\alpha\right)$$
$$- \left(AJ_1^\alpha + i\beta l_s\alpha J_0^\alpha\right) \left(BY_1^{1+\alpha} - i\beta l_s(1 + \alpha)Y_0^{1+\alpha}\right), \qquad (17)$$

$$A = \alpha + 2l_s, \quad B = 1 + \alpha - 2l_s. \qquad (18)$$

Here, the superscripts α and $1 + \alpha$ mean that the corresponding Bessel functions are evaluated at $-i\beta\alpha$ and $-i\beta(1 + \alpha)$, respectively. In addition, constant C is obtained by integrating Eq. (10) and applying the boundary conditions of the electric potential:

$$\phi(0) = 0, \quad \phi(1) = 1, \qquad (19)$$

therefore

$$\phi(r) = C \ln |r + \alpha| + \frac{Ha^2}{i\beta} C_1 J_0(-i\beta [r + \alpha]) + \frac{Ha^2}{i\beta} C_2 Y_0(-i\beta [r + \alpha]) + D, \quad (20)$$

where

$$C = \frac{1}{\left(1 + \dfrac{Ha^2}{\beta^2}\right) \ln |\kappa| + \dfrac{Ha^2}{i\beta} \left[A_1 \left(J_0^{1+\alpha} - J_0^\alpha\right) + A_2 \left(Y_0^{1+\alpha} - Y_0^\alpha\right)\right]}, \qquad (21)$$
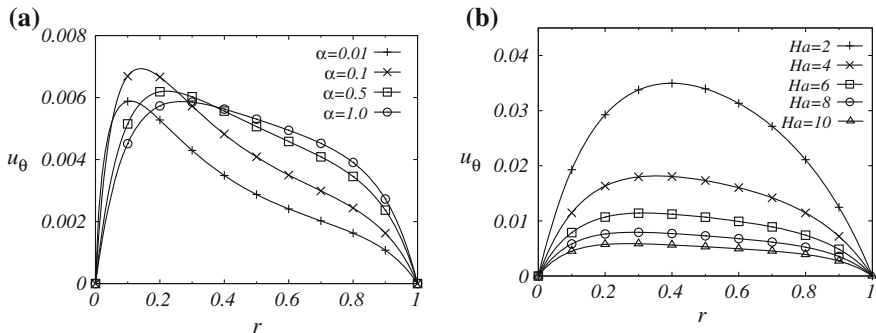
Fig. 2 **a** Velocity profile as a function of the radial coordinate for different values of the α parameter. $Ha = 10$, $l_s = 0$, $\varepsilon = 0.1$. **b** Velocity profile as a function of the radial coordinate for different values of the Hartmann number. $\alpha = 0.5$, $l_s = 0$, $\varepsilon = 0.1$

$$D = -\frac{\left(1 + \frac{Ha^2}{\beta^2}\right) \ln|\alpha| + \frac{Ha^2}{i\beta}\left[A_1 J_0^\alpha + A_2 Y_0^\alpha\right]}{\left(1 + \frac{Ha^2}{\beta^2}\right) \ln|\kappa| + \frac{Ha^2}{i\beta}\left[A_1 \left(J_0^{1+\alpha} - J_0^\alpha\right) + A_2 \left(Y_0^{1+\alpha} - Y_0^\alpha\right)\right]}, \quad (22)$$

the constant κ being defined as $\kappa = R_2/R_1 = 1 + 1/\alpha$. Figure 2 shows the azimuthal velocity profile as a function of the radial coordinate for the case of non-slip boundary conditions ($l_s = 0$). In all analyzed cases, a very thin fluid layer is assumed ($\varepsilon = 0.1$) which implies that Hartmann friction is strong and velocity magnitude is much smaller than in the case of cylinders of infinite length ($\varepsilon \to \infty$). Velocity profiles in Fig. 2a that correspond to $Ha = 10$, display a marked asymmetry as the α parameter, that characterizes the gap between concentric cylinders, is varied from 0.01 to 1 (the gap is reduced as α increases). The velocity does not present a monotonous behavior with α. First, it increases as α grows, reaching a maximum for $\alpha = 0.1$, and then decreases for higher values. Figure 2b shows the velocity profile as the Hartmann number is increased, for the case $\alpha = 0.5$, that is when the radius of the outer cylinder is three times that of the inner cylinder. For $Ha = 2$ a parabolic-like profile is obtained and, as Ha increases, the profile is flattened and the velocity decreases as a consequence of magnetic braking effects.

The effect of slip boundary conditions on the velocity profile is clearly shown in Fig. 3a where u_θ is plotted as a function of the radial coordinate for $Ha = 10$, $\varepsilon = 0.1$, $\alpha = 0.5$ and different values of the dimensionless slip length parameter, l_s. Higher velocities are found close to the inner cylinder and a drastic increase in the slip velocity at the walls is observed as l_s varies from 0 to 100, where the latter value could be considered as perfect slip ($l_s \to \infty$). Note, however, that the core flow remains mostly unchanged, independently of the l_s parameter. The effect of slip at the boundaries can also be assessed by calculating the volumetric flow rate, Q, in the gap between the cylinders. By direct integration of the velocity profile, we get

(a)

(b)
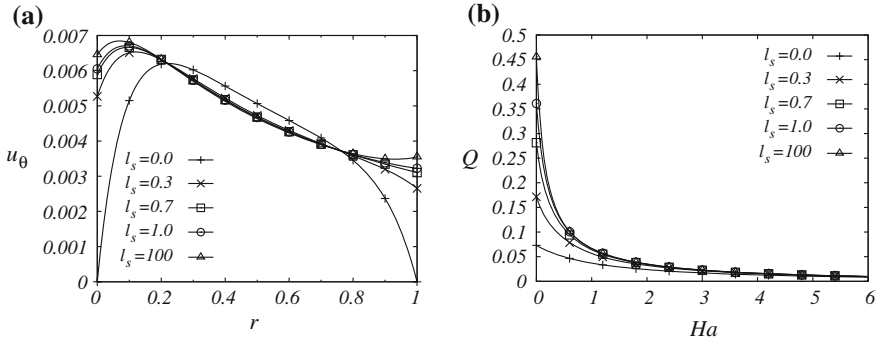
Fig. 3 **a** Velocity profile for liquid metal flow as a function of the radial coordinate for different values of the dimensionless slip length parameter. $Ha = 10$, $\alpha = 0.5$, $\varepsilon = 0.1$. **b** Liquid metal flow rate for different values of the dimensionless slip length parameter as a function of Ha. $\varepsilon = 0.1$, $\alpha = 0.5$

(a)

(b)
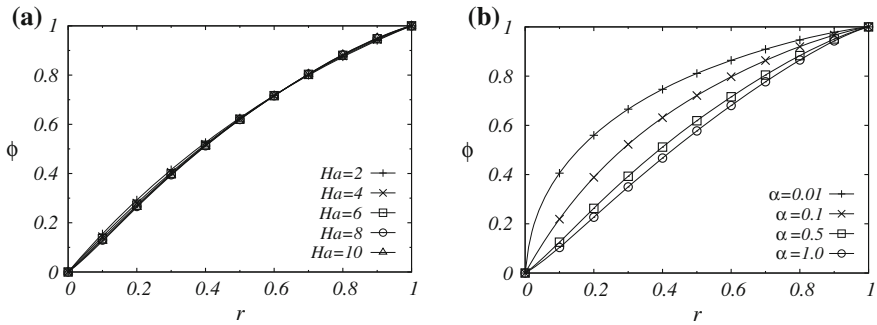
Fig. 4 Liquid metal flow. **a** Electric potential for the liquid metal flow as a function of radial coordinate for different values of the Hartmann number. $\alpha = 0.5$, $l_s = 0$, $\varepsilon = 0.1$. **b** Electric potential for the liquid metal flow as a function of radial coordinate for different values of the geometrical parameter α. $Ha = 10$, $\varepsilon = 0.1$, $l_s = 0$

$$Q = -\frac{iC_1}{\beta}\left[J_0(-i\beta\,[1+\alpha]) - J_0(-i\beta\alpha)\right] - \frac{iC_2}{\beta}\left[Y_0(-i\beta\,[1+\alpha]) - Y_0(-i\beta\alpha)\right]$$
$$+ \frac{C}{\beta^2}\ln|\kappa|. \tag{23}$$

Figure 3b shows the flow rate as a function of the Hartmann number for different values of the slip parameter. For $Ha < 1$, a substantial increase of Q is observed as l_s varies from 0 to 100, while for higher Hartmann number the reduction of Q is approximately the same for all l_s values. Figure 4a, b show the electric potential for the liquid metal flow (Eq. 20) as a function of the radial coordinate for different values of Ha and α, respectively. From Fig. 4a it is clear that the variation of the Hartmann number does not affect the electric potential distribution, while Fig. 4b shows that

this quantity is modified by the separation between the concentric cylinders (electrodes). This behavior has a consequence on the electric current distribution and, hence, on the Lorentz force.

4 Solution for Electrolytic Flow

It can be shown that for fluids of low electrical conductivity such as electrolytes, induction effects are negligible and fluid velocity is uncoupled from the electromagnetic equations (Figueroa et al. 2009). Also, in electrolytes under moderate magnetic fields the Hartmann number is very small ($Ha \ll 1$). In this case, the Poisson equation for the electric potential (4) reduces to a Laplace equation and the solution for ϕ is expressed as

$$\phi(r) = \ln\left(\frac{r+\alpha}{\alpha}\right) \Big/ \ln|\kappa|.$$

In fact, this solution can be obtained from Eq. (20) in the limit $Ha \to 0$. This implies that the applied radial current is proportional to $1/(r+\alpha)$. Under these conditions, Eq. (6) reduces to

$$\frac{d^2 u_\theta}{dr^2} + \frac{1}{r+\alpha}\frac{du_\theta}{dr} - \left(\frac{1}{(r+\alpha)^2} + \frac{1}{\varepsilon Re}\right)u_\theta = -\frac{1}{\ln|\kappa|}\frac{1}{r+\alpha}. \tag{24}$$

which is again a non-homogeneous Bessel equation. In this case, the linear friction term that appears in the Q2D approach due to the existence of a viscous boundary layer in the bottom wall takes the form $-u_\theta/\varepsilon Re$ (Satijn et al. 2001), where the Reynolds number is given by $Re = u_0 R/\nu$. The solution of Eq. (24) under slip boundary conditions (12) and (13), can be expressed as

$$u_\theta(r) = C_3 J_1(-i\beta[r+\alpha]) + C_4 Y_1(-i\beta[r+\alpha]) + \frac{1}{\beta^2 \ln|\kappa|}\frac{1}{r+\alpha}, \tag{25}$$

where $\beta^2 = 1/(\varepsilon Re)$. The constants C_3 and C_4 take the form

$$C_3 = \frac{1}{\gamma\beta^2\ln|\kappa|}\left(\frac{A(BY_1^{1+\alpha} - i\beta l_s(1+\alpha)Y_0^{1+\alpha})}{\alpha} - \frac{B(AY_1^\alpha + i\beta l_s\alpha Y_0^\alpha)}{1+\alpha}\right), \tag{26}$$

$$C_4 = -\frac{1}{\gamma\beta^2\ln|\kappa|}\left(\frac{A(BJ_1^{1+\alpha} - i\beta l_s(1+\alpha)J_0^{1+\alpha})}{\alpha} - \frac{B(AJ_1^\alpha + i\beta l_s\alpha J_0^\alpha)}{1+\alpha}\right), \tag{27}$$

where γ, A and B are given by Eqs. (17) and (18). Figure 5 shows the velocity profiles for the electrolytic flow as a function of the radial coordinate for $Re = 0.1$ and $\varepsilon = 0.1$. In Fig. 5a profiles are displayed for different values of the α parameter, assuming

(a)

(b)
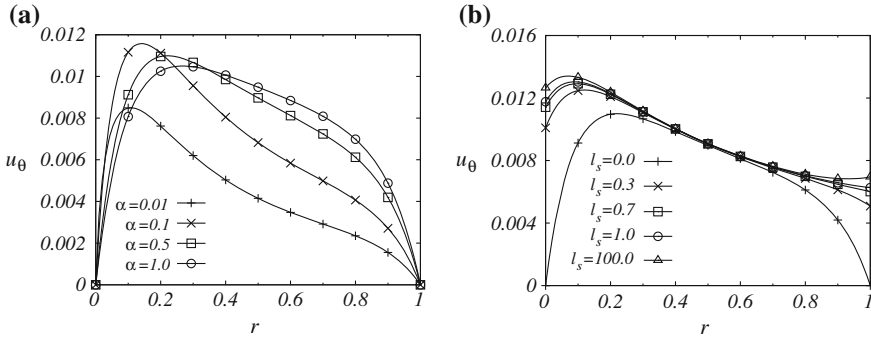
Fig. 5 **a** Velocity profile for electrolytic flow as a function of the radial coordinate for different values of the α parameter. $Re = 0.1$, $\varepsilon = 0.1$, $l_s = 0$. **b** Velocity profile for electrolytic flow as a function of the radial coordinate for different values of the dimensionless slip length parameter. $Re = 0.1$, $\varepsilon = 0.1$, $\alpha = 0.5$

(a)

(b)
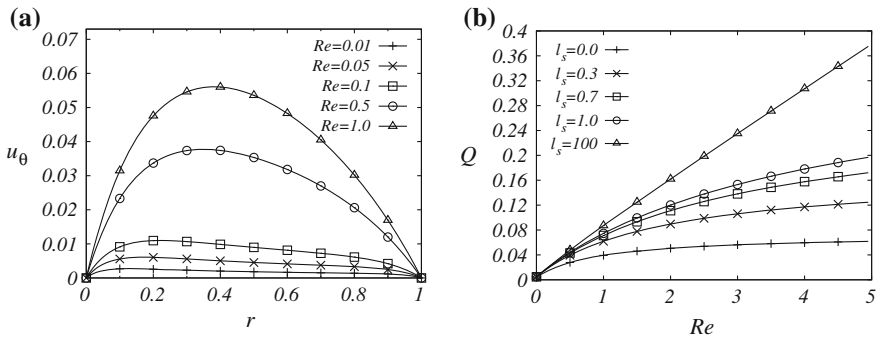
Fig. 6 **a** Velocity profile for electrolytic flow as a function of the radial coordinate for different Reynolds numbers. $\alpha = 0.5$, $\varepsilon = 0.1$, $l_s = 0$. **b** Electrolyte flow rate as a function of Re for different values of the dimensionless slip length parameter. $\varepsilon = 0.1$, $\alpha = 0.5$

the non-slip condition ($l_s = 0$). There is a resemblance with profiles obtained for the liquid metal flow (see Fig. 2a), but in this case the magnitude of the velocity is almost 50 % higher than for the liquid metal. This can be explained since the Hartmann friction is stronger than the viscous friction. Also, as in the liquid metal flow, the geometrical confinement has a pronounced effect on the asymmetry of the profile, the smaller the value of α (thick gap conditions) the stronger the asymmetry. Figure 5b shows the profiles for different values of the dimensionless slip length and $\alpha = 0.5$. Again, the profiles are similar to the ones obtained in the liquid metal case but the velocities are almost 50 % higher.

Figure 6a shows the velocity profile as a function of the radial coordinate for Reynolds numbers varying from 0.01 to 1, assuming non-slip conditions ($l_s = 0$) and $\alpha = 0.5$. The velocity increases as Re grows while the profile presents a more parabolic shape, although maximum velocity values are still closer to the inner cylinder.

In Fig. 6b the volumetric flow rate is displayed as a function of the Reynolds number for values of the dimensionless slip parameter ranging from 0 to 100. By integrating the velocity profile in the gap between the cylinders, the explicit form of the flow rate reads

$$Q = -i\frac{C_3}{\beta}\left[J_0(-i\beta\,[1+\alpha]) - J_0(-i\beta\alpha)\right] - i\frac{C_4}{\beta}\left[Y_0(-i\beta\,[1+\alpha]) - Y_0(-i\beta\alpha)\right]$$
$$+ \frac{1}{\beta^2}. \tag{28}$$

In spite of the viscous friction at the bottom, the flow rate grows with Re while, as expected, a substantial gain is also observed as the parameter l_s increases. It is observed that for $l_s \to \infty$, the flow rate grows linearly with Re, reaching a saturation value, as occurs also in other situations (Rivero and Cuevas 2012).

4.1 Electrolytic Flow Between Infinite Cylinders

As mentioned previously, most analytical solutions reported in the literature for the flow in the annular MHD configuration assume that cylinders are infinitely long. In this approximation, the friction produced by Hartmann or viscous boundary layers is absent. It is interesting to obtain solutions in this idealized situation under slip boundary conditions and explore some asymptotic limits. The equation of motion when the cylinders are infinite is obtained from Eq. (24) by taking the limit $\varepsilon \to \infty$, that is,

$$\frac{d^2u_\theta}{dr^2} + \frac{1}{r+\alpha}\frac{du_\theta}{dr} - \frac{u_\theta}{(r+\alpha)^2} = -\frac{1}{\ln|\kappa|}\frac{1}{r+\alpha}. \tag{29}$$

The solution of Eq. (29) under slip boundary conditions (12) and (13) is given by

$$u_\theta = -\frac{1}{2\ln|\kappa|}\left[(r+\alpha)\ln(r+\alpha) + C_5(r+\alpha) + \frac{C_6}{r+\alpha}\right], \tag{30}$$

where

$$C_5 = \frac{1}{F}\left\{2(1+2\alpha)l_s^2 + \left[2\ln(\alpha+1)^{(\alpha+1)^3}\alpha^{\alpha^3} - \alpha(\alpha+1)(2\alpha+1)\right]l_s\right.$$
$$\left. + \ln\left[\frac{(\alpha+1)^{\alpha(\alpha+1)^3}}{\alpha^{\alpha^3(\alpha+1)}}\right]\right\},$$

$$C_6 = \frac{\alpha^2}{F}\left\{(2\alpha+1)(\alpha+1)^2l_s + \alpha(\alpha+1)^3\ln\frac{\alpha}{\alpha+1}\right\},$$

with $F = (2\alpha + 1)\left[2(\alpha^2 + \alpha + 1)l_s + \alpha(\alpha + 1)\right]$. In the limit $l_s \to 0$, the functional form of solution (30) is the same of previously reported analytical solutions for non-negligible Hartmann number (Digilov 2007; Zhao et al. 2011).

We now modify the geometry of the stirrer with the purpose of understanding the flow behavior when the gap between the conducting cylinders is very large or very small. For instance, let us first consider that the radius of inner cylinder is very small so that it becomes a wire compared to the exterior cylinder. This situation corresponds to the limit $\alpha \to 0$. If Eq. (29) is expressed in the form

$$(r + \alpha)^2 \frac{d^2 u_\theta}{dr^2} + (r + \alpha) \frac{du_\theta}{dr} - u_\theta = -\frac{r + \alpha}{\ln |\kappa|}, \tag{31}$$

and the velocity is expanded in terms of the small parameter α, that is,

$$u_\theta = u_0 + \alpha u_1 + \alpha^2 u_2 + \cdots,$$

at order zero in α we get the equation

$$r^2 \frac{d^2 u_0}{dr^2} + r \frac{du_0}{dr} - u_0 = -\frac{r}{\ln |\kappa|}$$

whose solutions when slip boundary conditions (12) and (13) are applied, is found to be

$$u_0 = -\frac{1}{2 \ln |\kappa|} r \left[\ln(r) - l_s\right]. \tag{32}$$

This is an asymmetric profile with the maximum velocity located at $r = e^{l_s - 1}$. Notice that the slippage is approximately zero at the inner cylinder due to the very small slippage surface.

Let us now consider that the gap between the cylinders is very small (thin gap approximation). For this purpose, we chose a small parameter $\delta = \alpha^{-1}$ and, therefore, $R \ll R_1$ implies $\delta \to 0$. In terms of δ, Eq. (29) can be expressed in the form

$$(1 + \delta r) \frac{d^2 u_\theta}{dr^2} + \delta \frac{du_\theta}{dr} - \frac{\delta^2 u_\theta}{1 + \delta r} = -\frac{\delta}{(1 + \delta r) \ln |\kappa|}. \tag{33}$$

If we use the expansion

$$u_\theta = \delta u_0 + \delta^2 u_1 + \cdots$$

and collect terms of order δ we get

$$\frac{d^2 u_0}{dr^2} = -\frac{1}{\ln |\kappa|}.$$

The solution of this equation with slip boundary conditions (12) and (13) reduces to a parabolic profile

$$u_0 = -\frac{1}{2\ln|\kappa|}\left[r^2 - r - l_s\right], \tag{34}$$

where the maximum velocity is located at $r = 0.5$. Note that both the thin and thick gap approximations lead to symmetric and non-symmetric velocity profiles, respectively, as occurs in the Q2D solutions where the bottom friction exists.

5 Conclusions

In this paper, analytical solutions were provided for the azimuthal flow of a conducting fluid in an annular MHD stirrer that has been proposed for microfluidic applications (West et al. 2003; Gleeson et al. 2004; Gleeson 2005). The flow is driven by an azimuthal Lorentz force created by the interaction of an imposed radial current and an applied axial magnetic field. The cases of a highly conducting fluid (a liquid metal) and a poorly conducting fluid (an electrolyte) were considered. Unlike analytical solutions available in the literature where the conducting concentric cylinders are assumed to be infinitely long, MHD flows have been explored here using a Q2D model that introduces a linear friction term that accounts for the existence of boundary layers (either Hartman or viscous layers) attached to the bottom wall. The bottom friction has a drastic effect in the flow behavior, reducing considerably the magnitudes of the velocity and flow rate. In addition, slip boundary conditions were considered at the lateral walls (conducting cylinders) and it was verified that the maximum velocity and flow rate increase as the slip length parameter grows. Further, it was found that the gap between the cylinders has a strong influence in the shape of the velocity profile: the larger the gap, the more asymmetric the profile. This behavior is also found in asymptotic limits calculated for an idealized solution with infinitely long cylinders. The solutions presented here can be used as the starting point for microfluidic mixing studies, either with liquid metals or electrolytes, similarly to those performed with a more idealized solution (Gleeson et al. 2004; Gleeson 2005).

References

Andreev O, Haberstroh Ch, Thess A (2001) Magnetohydrodynamics 37:151–160
Bau HH, Zhu J, Qian S, Xiang Y (2003) Sens Actuators B 88:205–216
Digilov Y (2007) Am J Phys 75:361–367

Escandón J, Santiago F, Bautista O, Méndez F (2014) Int J Therm Sci 86:246–257

Figueroa A, Demieaux F, Cuevas S, Ramos E (2009) J Fluid Mech 641:245–261

Gleeson JP, Roche OM, West J, Gelb A (2004) SIAM J Appl Math 64:1294–1310

Gleeson JP (2005) Phys Fluids 17:100614

Kang HJ, Choi B (2011) Sens Actuators A: Phys 165:439–445

Mikhailovich B, Shapiro A, Sukoriansky S, Zilberman I (2012) Magnetohydrodynamics 48:43–50

Moresco P, Alboussière T (2004) J Fluid Mech 504:167–181

Müller U (2001) Bühler L Magnetofluiddynamics in channels and containers. Springer, Berlin

Pérez-Barrera J, Pérez-Espinoza JE, Ortiz A, Ramos E, Cuevas S (2015) Magnetohydrodynamics 51:203–213

Qian S, Bau HH (2009) Mech Res Commun 36:10–21

Qin M, Bau HH (2012) Phys Fluids 23:037101

Rivero M, Cuevas S (2012) Sens Actuators B 166–167:884–892

Satijn MP, Cense AW, Verzicco R, Clercx HJH, Van Heijst GJF (2001) Phys Fluids 13:1932–1945

Smolentsev S (2009) Theo Comput Fluid Dyn 23:557–570

Sommeria J (1988) J Fluid Mech 189:553–569

West J, Gleeson JP, Alderman J, Collins JK, Berney H (2003) Sens Actuators B 96:190–199

Yi M, Qian S, Bau HH (2002) J Fluid Mech 468:153–177

Zhao Y, Zikanov O, Krasnov D (2011) Phys Fluids 23:084103

Zhao Y, Zikanov O (2012) J Fluid Mech 692:288–316

Trajectories of Water and Sand Jets

D.A. Serrano, F. Sánchez-Silva, J. Klapp, P. Tamayo, A. Medina and G. Domínguez

Abstract In this paper we introduce a correlation for the trajectories of sand jets, of a non-cohesive granular material, emerging from vertical sidewall orifices of diameter D and wall thickness w. A contrast with water jet in similar configurations has been performed. We found that the theoretical trajectories agree well with the experimental ones.

D.A. Serrano (✉) · F. Sánchez-Silva
ESIME Zacatenco, Instituto Politécnico Nacional, Avenida Luis Enrique Erro S/N, 07738
Zacatenco, Mexico, D.F., Mexico
e-mail: arman2390@hotmail.com

F. Sánchez-Silva
e-mail: fsanchezs@ipn.mx

P. Tamayo · A. Medina
ESIME Azcapotzalco, Instituto Politécnico Nacional, Av. de las Granjas 682, 02250 Santa
Catarina, Mexico, D.F., Mexico
e-mail: ptamayom@ipn.mx

A. Medina
e-mail: amedinao@ipn.mx

J. Klapp
Departamento de Física, Instituto Nacional de Investigaciones Nucleares, La Marquesa,
52750 Ocoyoacac, Estado de México, Mexico
e-mail: jaime.klapp@inin.gob.com

J. Klapp
ABACUS-Centro de Matemáticas Aplicadas y Cómputo de Alto Rendimiento,
CINVESTAV-IPN, La Marquesa, 52740 Ocoyoacac, Estado de México, Mexico

G. Domínguez
Instituto Mexicano Del Petróleo, Eje Central Norte Lazaro Cardenas No 152, Col. San
Bartolo Atepehuacán, 07730 Del. Gustavo A. Madero, Mexico, D.F., Mexico
e-mail: gdzacari@imp.mx

1 Introduction

Leonardo da Vinci (1452–1519), performed experimental studies of the output water force through orifices, demonstrating that the water force changes according to the location of the orifices drilled on a wall container at different heights, his results are presented in the Codex of Madrid I, (Da Vinci 1480). In addition, he showed that the water jet attains a larger distance, when the orifice is in the lowest part of the container; due to this discovery, Leonardo was capable of considering the transformation of the implicit energy in the phenomenon and had the intuition about the conservation of the total energy (Levi 1986).

It is surprisingly common to find a drawing like the one shown in Fig. 1a, included in textbooks for hydrostatic pressure explanation. This drawing represents the water jets emerging of three orifices perforated on a container wall filled with water, opened to the atmosphere. Leonardo's intention was to demonstrate that the hydrostatic pressure increases with the depth, which is a correct idea. However, the drawing experimental results shown in Fig. 1a, were widely studied and questioned by Gorazd (2011), he performed the same experiments, and observed a different result from Leonardo's prediction, actually at present this topic is still a problem under study. But in fact the predictions proposed by Leonardo are correct, for the case when the orifice is in the lowest part of the container, the water jet attains bigger distances (Planinšič 2011).

Figure 1b shows that Leonardo performed experiments, using a container filled with water, there are perforations on the lateral wall and bottom of the container, he added different nozzles to the orifices, to observe weather the exit water force is a function of the orifice position in the container lower part or the height on his walls. Leonardo observed that the force is the same; it does not depend on the position of the orifices when they are located in the bottom of the container. On the contrary, for the orifices on the container sidewall, the one located in the lower part, emerges with a bigger force, due to the higher hydrostatic pressure in this point.

In Fig. 1c, Leonardo da Vinci questioned about; "What water will come out with the greatest violence, that from nozzle a, b, or c?" The right panel depicts an experiment designed to test whether the weight of water in the container bottom varies from one point to another. The "violence" of water discharged from the different nozzles was compared with a scale suspended whose plates were stroked by the jets of water. Since the plates are represented in equilibrium, Leonardo seems to have realized that the water weight in the container bottom does not change from point to point. In the experiment shown in the central panel, Leonardo tested whether the force exerted by the water on a point at the bottom depends on the volume of the container (Cavagnero et al. 2014).

Leonardo's observations show that he has anticipated Evangelista Torricelli (1608–1647) and Daniel Bernoulli (1700–1782) by admitting that a vertical stream rises to the same level of the free surface of still water that produces it. Torricelli's theorem is a fluid dynamics theorem that relates the speed of a jet outgoing through an orifice on a container wall, under the action of gravity force (Torricelli 1641).
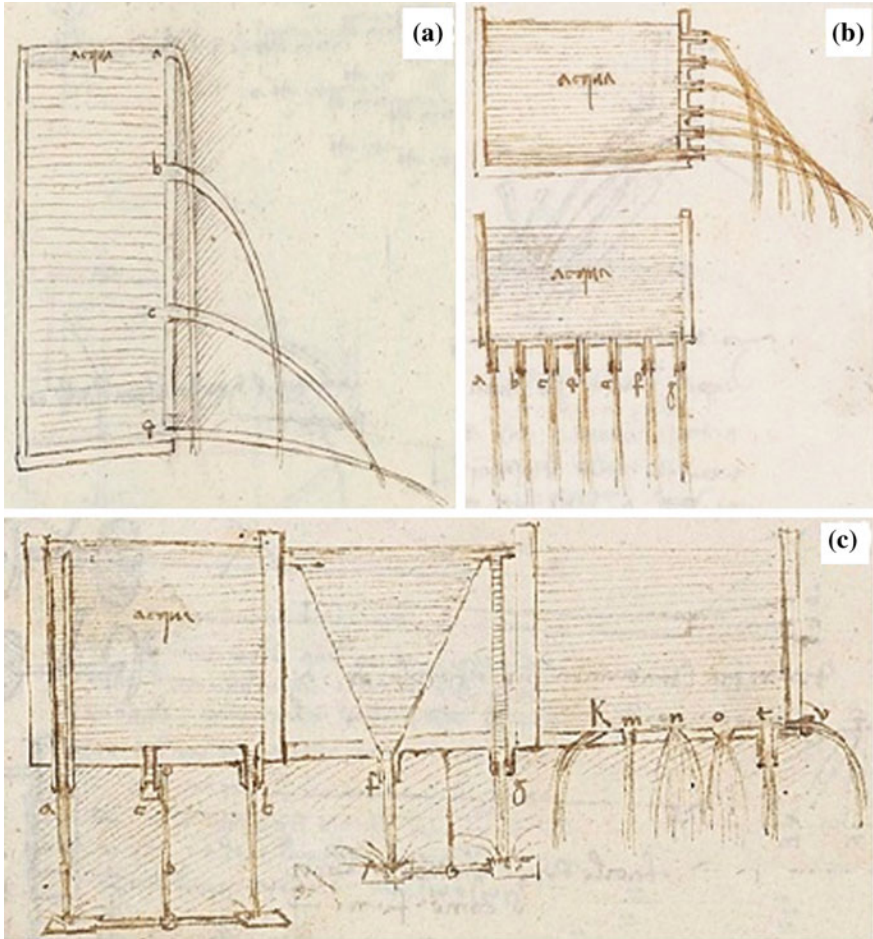
Fig. 1 Codex of Madrid I, Leonardo da Vinci performs experiments to demonstrate that: **a** the energy of the water changes according to the discharge orifice height, **b** the force of every jet in the horizontal plane is the same and **c** The weight of the water does not change from a point another

The output liquid speed through an orifice located in a container bottom is the same as the one a body acquires (in this case a drop of water) falling freely in a vacuum from a height, h, being the height of the fluid column, i.e., $v = \sqrt{2gh}$, where g is the acceleration due to gravity. Torricelli's law shows that the pressure increases when the orifice is in the lowest point of the container, producing a water jet with greater extension than the one at the top of the container.

For the experiment, at the beginning all three orifices are blocked, and then the tube is filled with water. Once the container is filled, we proceed to unlock the orifices. The jets have a static charge depending on the position they have on the wall, the exit fluid speed is higher as the orifice is located in the lower part of the
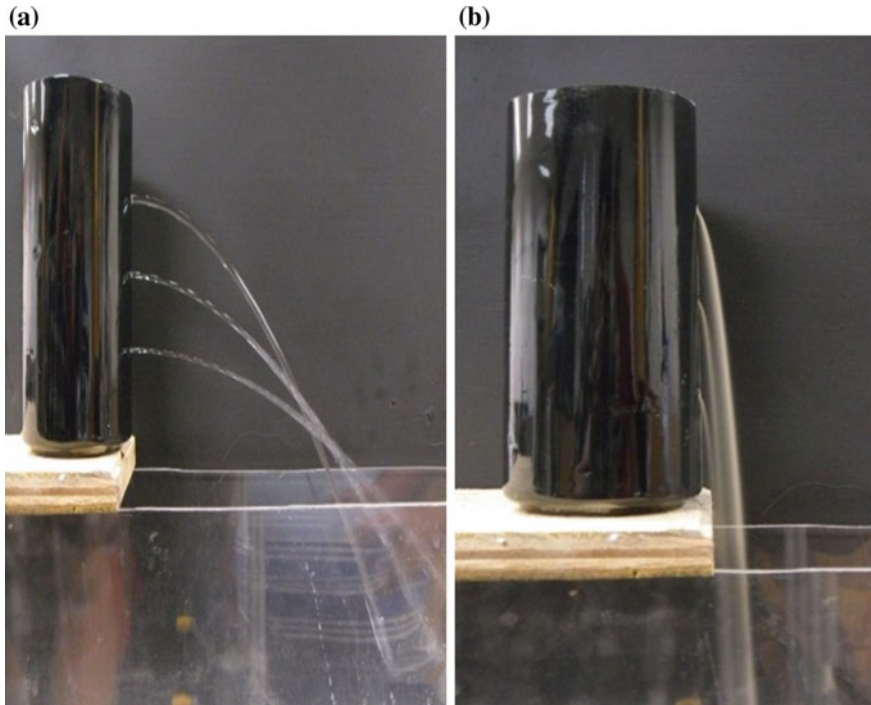
Fig. 2 Spouting can jets: liquid and non-cohesive dry sand

tube, (Fig. 2a). However, when the container is filled with dry sand and is drilled with three orifices of the same diameter, D, located as shown in Fig. 2b, the sand exit speed is the same and therefore the sand jet shape is similar in each orifice (Fig. 2b). The difference between the discharge of a container filled with dry sand and the discharge of other filled with water is that the mass flow rate, in the first case, does not depend on the orifice position, h.

The explanation most frequently used for this independence it based on the effect of the container walls geometry (Medina et al. 2013), when $\alpha > \theta_r$ the system will produce an outflow, α is the natural angle of the container wall, which can be defined as $\alpha = arctan(D/w)$ and θ_r it is the rest angle of the granular material. The sand output stream must be stopped when $\theta_r > \alpha$. Therefore a critical condition for the sand outflow is when, $\theta_r = \alpha$, the mass flow rate is proportional to $(\alpha - \theta_r)$, therefore; $\dot{m} \sim (\alpha - \theta_r)$. This is the first indication that the sand jets must be very different respect the water jets, on the other hand, the wall thickness, w, greatly affects the intensity and shape of sand jets, but this is not the case for water. In both cases, the competition between the frictional forces, the gravity force and the pressure affect the sand jet properties (Medina et al. 2013).

In this paper a discussion about the form of jets of water and sand when they outcome from the bottom of the container is presented. First, there is a brief review

about the trajectories followed by water jets due to gravity when a container with sidewalls is used. Then, a theoretical development for the description of sand jets is presented and finally there is a theoretical development for the sand jet trajectories, when the container is inclined.

2 Shape of the Water Jets and Sand in Horizontal Walls

The non-cohesive dry granular materials, exhibit a behaviour that crosses the boundaries between the different states of matter. They can behave as solid, liquid or gas. In certain situations, the granular materials show features that remember the instabilities encountered in fluids, as the Faraday instability, the presence of Taylor vortices, or the Kelvin-Helmholtz instability (Melo et al. 1995; Garcimartin et al. 2002). The experimental study of instabilities of jets emerging from the bottom orifices of containers full of water or metal powder was performed by Khamontoff (1890), as shown in Fig. 3. The study of the similarities and differences between the behaviour of a liquid and a granular flow is of great importance for the understanding the subtle properties of granular flows (Boudet et al. 2007).
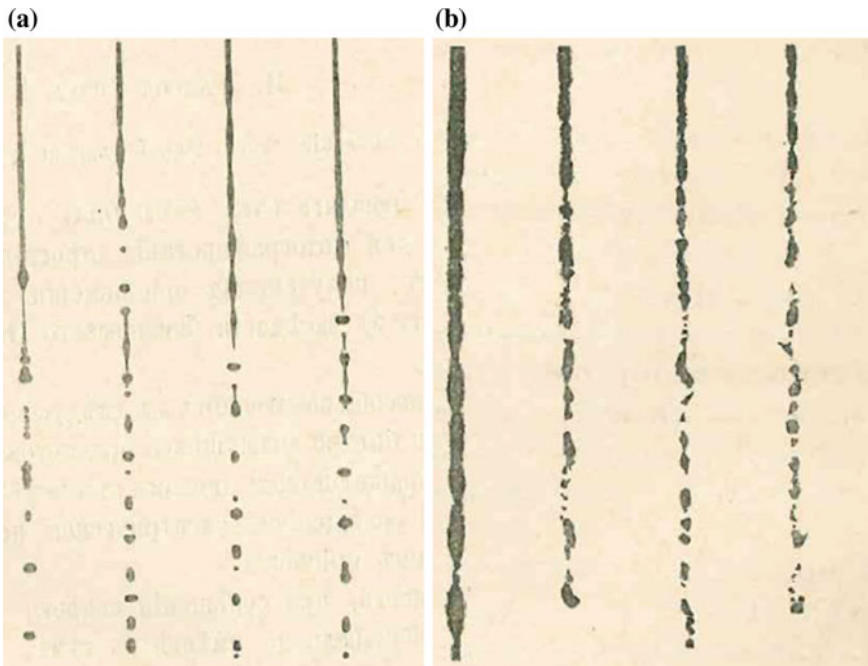
Fig. 3 From the bottom of the container: **a** water, and **b** metal powder

Fig. 4 Water jet emerging
from the *horizontal* walls of
the container
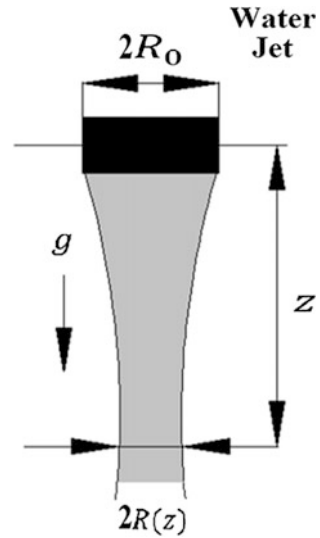
The simplest analysis about the way a water jet falls freely from the hopper by
gravity, is shown in Fig. 4, it follows the application of Bernoulli's equation (the
energy equation) for a water jet, in which viscosity effects and the surface tension
(the pressure varying with the jet radius) are disregarded (Middleman 1995).

The continuity equation $v_i A_i = v_s A_s$, relates the speed, v, and the cross section
area, A, in two different places of the water jet (subscripts "i" and "s" refer
respectively to the lower and upper parts of the water jet). The water emerges from
the orifice as shown in Fig. 4, it falls freely, since the nozzle exit, and its speed,
$V(z)$ increases with the distance, z, being, $V^2(O)$, the output velocity of the water
jet, it follows that

$$V(z) = \sqrt{2gz + V^2(O)} \tag{1}$$

The diameter $2R(z)$, shows the water jet dimensions during the water jet fall, as
the jet is reduced, for different diameters of funnel, we can observe that the shape of
the water jet changes as follows (Middleman 1995)

$$\frac{2R(z)}{2R_0} = \left(1 + \frac{2gz}{U_0^2}\right)^{-1/4} \tag{2}$$

Equation (2) shows how the shape of the water jet changes, once the radius R_0
and the height z, are adjusted by the diameter of the funnel. The equation is used for
water jets falling from the bottom of a container (Middleman 1995).

It is possible to characterize experimentally the fall of a sand jet by using the
same scheme given in Fig. 4. Due to the jet diameter reduction, the funnel formed

has different radius, and the shape of the jet of granular material goes as follows (Boudet et al. 2007)

$$\frac{R(z)}{R_0} \sim \left(\frac{z}{R_0}\right)^{-1/6} \tag{3}$$

Equation (3) gives the jet shape of granular material, resulting in a universal equation once the radius $R(z)$ and the height z are adjusted by the radius of the funnel. This scaling is valid if the height z, is greater than the diameter of the funnel. The equation is used for sand jets falling from a conical hopper or orifices in horizontal walls but none theoretical model supports such a formula (Boudet et al. 2007).

3 Shape of the Water Jets from Holes on Vertical Sidewalls

Lets first study the phenomenon closely related to the trajectories of the water jets. Since the beginning, the researchers found that the distance reached by the water jet increases with the depth at which the container orifice was drilled, as shown in Fig. 5. The drawing shows a container with water at a constant level, H, water jets emerging from three orifices drilled at levels of $h = \frac{1}{4} H$, $\frac{1}{2} H$ and $\frac{3}{4} H$. The intention was to demonstrate that the hydrostatic pressure influences the distance reached by the water jets (Banks 1998).

When conducting experiments about the water jet trajectories, researchers found that in the absence of air resistance, the trajectory of a basketball, for example, and the curve of a water jet are the same; both are parables. Instead, let's look at some

Fig. 5 Water jets from orifices on a *vertical* wall
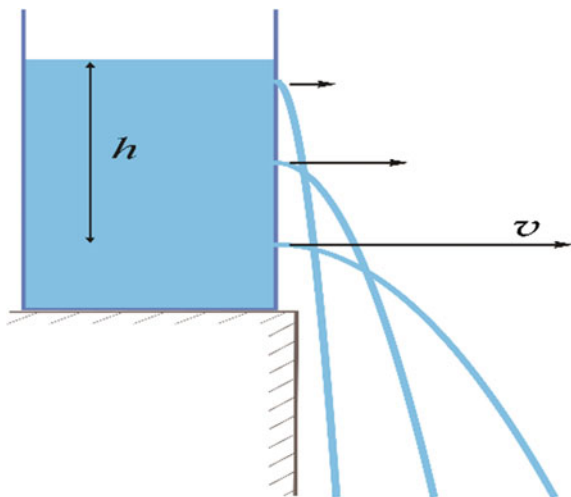
aspects of water jets and fountains. As before, it is assumed that the effects of air resistance can be ignored, that is, the water jet is in a vacuum medium (Banks 1998). Therefore it can be analyzed using the same equation for the trajectory of a projectile Eq. (5).

$$y = (tan\,\alpha)x - \left(\frac{g}{2U_0^2}\right)(sec^2\alpha)x^2 \qquad (4)$$

where U_0 is the initial velocity of the jet emerging from the hole.

In the above equation, it can be used the dimensionless parameters

$$\zeta = \frac{y}{h}$$

$$\eta = \frac{x}{h}$$

In Eq. (4), α is the exit angle, which may be positive or negative depending on the outlet orifice of the water jet (Lopac 2015), g is the gravity acceleration and x, is the trajectory followed by the water jet. Using the dimensionless parameters above presented ζ and η, and including the definition of the Froude number ($Fr = 2U_0^2/ hg$), the dimensionless resulting equation is

$$\zeta = \eta(tan\alpha) - \left(\frac{\eta^2}{Fr}\right)(sec^2\alpha) \qquad (5)$$

4 Shape of Sand Jets in Vertical Walls

As shown in Fig. 6, the container has a wall angle α, which depends on the wall thickness w. Figure 6a shows schematically a container with vertical sidewalls, on one of them there is an exit orifice of diameter, D, through which the granular
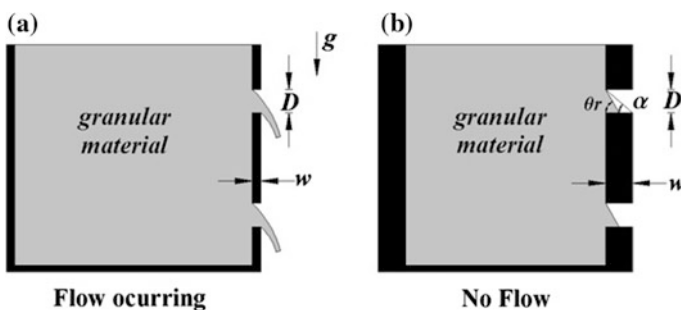
Fig. 6 Schematic side outlet of a vertical wall container in view

material flows. Figure 6b, also shows that there is a natural angle of the wall, α, which can be defined as; $\alpha = atan(D/w)$, reported in previous studies (Medina et al. 2013). The same figure also shows that there is no flow of granular material when the wall thickness is large enough, the material remains there until it reaches its angle of repose, θ_r, therefore, an outflow will occur only if $\alpha > \theta r$, as also has been noted by Woodcock and Mason (1987).

The actual study considers a dry non-cohesive granular material; sand density is much higher than the density of air, $\rho \gg \rho_a$, the output of the sand jet is a function of the angle of repose of the granular material and not of the container wall angle. Under these hypotheses, the Eqs. (6) and (7) of the momentum of Newton in both directions, are the same as in a linear approximation, so then they can be written as follows.

$$\frac{d^2x}{dt^2} = 0 \tag{6}$$

$$\frac{d^2y}{dt^2} = g \tag{7}$$

In these equations, t is the time and (x, y) are the coordinates of any point on the trajectory of the granular stream. Equations (6) and (7) represent an initial value problem, with the following conditions for an initial time $t = 0$.

$$\begin{aligned} x &= 0; & u_x &= U_0 cos\theta_r \\ y &= 0; & v_y &= U_0 sin\theta_r \end{aligned} \tag{8}$$

where U_0, is the initial velocity of the sand jet at the origin $(x = 0, y = 0)$. Using the initial conditions of the sand jet in the equations of momentum of Newton, and establishing the mass flow rate emerging from the container vertical wall $\dot{m} = c\dot{m}_0(\alpha - \theta_r)$, where the mass flow rate is equal to $\dot{m}_0 = \rho g^{1/2} D^{5/2}$ (Medina et al. 2013), the output speed of the mass flow rate is

$$U_0 = \frac{\dot{m}}{\rho A} \tag{9}$$

In the above equation A is the area of the circular orifice outlet of granular material $A = \pi D^2/4$, then the output speed is

$$U_0 = \frac{4c}{\pi} \sqrt{gD}(\alpha - \theta_r) \tag{10}$$

By using the initial conditions (8) and Eq. (10), in the momentum Eqs. (6) and (7), the trajectory for the sand jet is obtained as

$$y = \frac{\pi^2}{32c^2(\alpha - \theta_r)^2} \left(sec^2\theta_r \right) \left(\frac{x}{\sqrt{D}} \right)^2 + x \tan \theta_r \qquad (11)$$

where c, is a constant of the material properties. By doing the dimensionless analysis and considering the following dimensionless variables for the sand jet trajectories equation,

$$\psi = \frac{y}{D}, \quad \chi = \frac{x}{D},$$

once the above dimensionless variables are replaced in the Eq. (11), the equation for the trajectories of the sand jet of the path of blasting is obtained

$$\psi = \frac{\pi^2}{32c^2(\alpha - \theta_r)^2} \left(sec^2\theta_r \right) \chi^2 + \chi \tan \theta_r \qquad (12)$$

In previous studies about the estimation of the mass flow rate of granular material through vertical walls, (Medina et al. 2013), constructed a rectangular container with vertical walls of different thickness and outlet orifice diameter size. They observed that the output of granular material (beach sand) can be affected by the wall thickness and size of the orifice, as shown in Fig. 7.
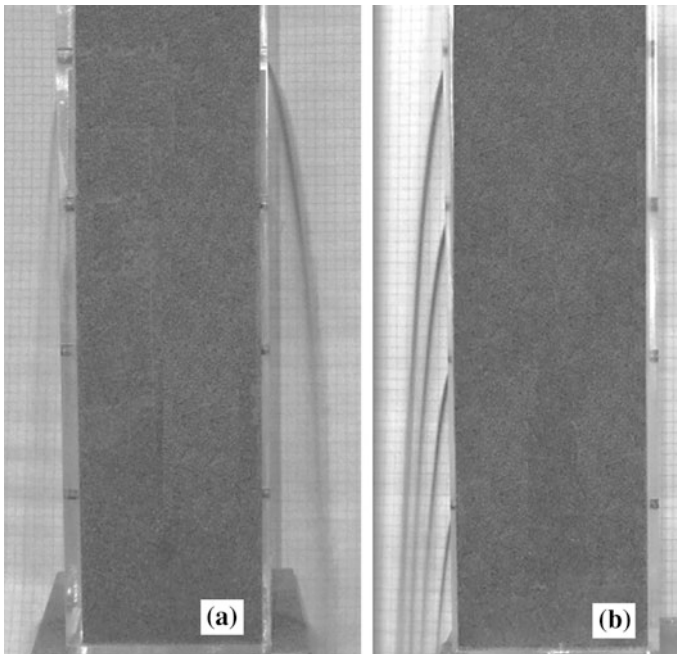
Fig. 7 Trajectory of the sand jet affected by the wall thickness and the diameter size of the orifice

By plotting Eq. (11), we can analyze the sand jets trajectories, considering the following cases:

(a) wall thickness very small (almost zero) $w = 0.01$ cm, for orifice diameters $D = 0.2, 0.25, 0.5$ and 0.6 cm.
(b) different wall thickness, $w = 0.3, 0.4, 0.6$ and 0.9 cm, the outlet orifice diameter was kept constant $D = 1$ cm.
(c) different orifice diameters, $D = 1.0, 0.8, 0.7$ and 0.5 cm the wall thickness was kept constant $w = 0.6$ cm.

In the plot of Fig. 8a, the wall thickness is very small, $w = 0.01$ cm, with the orifice diameter $D = 0.2$ cm, there is a decrement of the sand jet and a shorter extension range. If the diameter is $D = 0.6$ cm, there is an increment in sand jet and the jet is also wider, as shown in Fig. 2b, when the wall thickness is very small the shape and extension of the sand jet is a function of the exit orifice diameter.

In the plot of Fig. 8b, the orifice diameter on the wall container is constant of, $D = 1$ cm, for the wall thickness $w = 0.9$ cm, the sand jet comes out with a reduction and a shorter extension range, as shown in Fig. 7a, left sidewall of the container. For the wall thickness $w = 0.3$ cm, the sand jet comes out with greater intensity and longer extension range, as shown in Fig. 8b, left sidewall of the container, the wall thickness affects the intensity and extension of the sand jet.

The plot in Fig. 8c considers a constant wall thickness $w = 0.6$ cm, and varying the diameters of the outlet orifice. For the diameter $D = 1$ cm, the sand jet attains a longer extent than the jet for diameter $D = 0.6$ cm, as seen in Fig. 7b, left side of the sand container. The sand jet emerges with the same intensity, but when the orifice diameter is bigger the extent is larger.
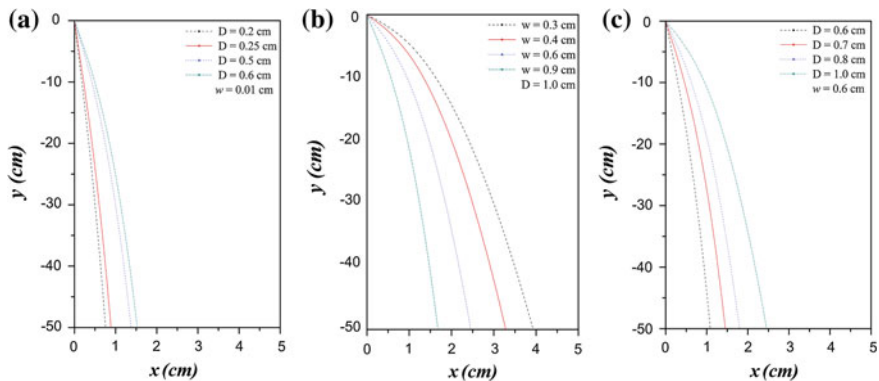
Fig. 8 Trajectory of the sand jets, **a** for different orifice diameters and a wall thickness $w = 0.01$ cm, **b** for different wall thickness and $D = 1.0$ cm and **c** for different orifice diameters and a wall thickness $w = 0.6$ cm

5   Conclusions

In this paper, the trajectories of water and sand jets were analysed for different situations but mainly for orifices on vertical sidewalls. The sand jet trajectories and their extension are represented well using Eq. (11). In previous work to estimate the mass flow rate of granular material through vertical walls of a silo, we note that the intensity and extension of the sand jet can be affected by the wall thickness and the orifice diameter in the jet outlet, as shown in three cases carefully discussed. To our knowledge this kind of studies, for these specific regimes, are for the first time discussed in the specialized technical literature.

References

Banks R (1998) Towing icebergs, falling dominoes and other adventures in applied mathematics. Princeton University Press, Princeton

Boudet JF, Amarouchene Y, Bonnier B, Kellay H (2007) The granular jump. J Fluid Mech 572:413–431

Cavagnero P, Revelli R (2014) The weight of water. Phys Today 67:41–46

Da Vinci L (1480) Codex Madrid I, Biblioteca Nacional de España. http://leonardo.bne.es/index.html

Garcimartin, A, Maza D, Ilquimiche JL, Zuriguel I (2002) Convective motion in a vibrated granular layer. Phys Rev E 65:031303-1–031303-5

Khamontoff N (1890) Application of photography to the study of the structure of trickles of fluid and dry materials. J Russ Physico-Chem Soc Saint Petersburg 22:281–284

Levi E (1986) El agua según la ciencia Evolución de la hidráulica. Series del Instituto de Ingeniería UNAM, Mexico

Lopac V (2015) Water jets from bottles, buckets, barrels, and vases with holes. Phys Teacher 53:169–173

Medina A, Serrano DA, Gutiérrez GJ (2013) On the mass flow rate from silos with lateral exit holes. Rev Mex Fis 59:287–291

Melo F, Umbanhowar P, Swinney HL (1995) Hexagons, kinks, and disorder in oscillated granular layers. Phys Rev Lett 75:3838–3841

Middleman S (1995) Modeling axisymmetric flows, dynamics of films, jets, and drops. Academic Press, San Diego

Planinšič G, Ucke C, Viennot L (2011) MUSE group (More Understanding with Simple Experiments) in the Physics Education Division (PED) of the European Physical Society (EPS). http://education.epsdivisions.org/muse/

Torricelli E (1641) Opera Geometrica. https://archive.org/details/operageometrica44900torrgoog

Woodcooks CR, Mason JS (1987) Bulk solids handling, an introduction to the practice and technology. Chapman and Hall, New York

Coupling of P-B Equation with Stokes System: Formation of Rayleigh Jets

L.B. Gamboa and M.A. Fontelos

Abstract In this paper we study the evolution of charged droplets for ionic solutions using a model described by Poisson-Boltzmann equation coupled with Stokes system. One of our main motivations is to describe the so-called Rayleigh jets studied in the laboratory and present in the functioning of technological devices as Electrospray, Mass Spectrometer, inkjet printers, etc. We show how the finite electrical conductivity and the presence of Debye layers in the electrolytic solutions induce the formation of these Rayleigh jets. We further estimate the main characteristics of the jet, such as speed and size.

1 Introduction

Rayleigh jets appear from charged droplets once the charge overcomes some critical value. In the case of a perfectly conducting liquid, the critical charge Q is such that the Rayleigh feasibility ratio X, defined as

$$X = \frac{Q^2}{32\gamma\pi^2\varepsilon_0 R_0^3}, \tag{1}$$

is larger than 1 (cf. Rayleigh 1882). In (1), γ is the surface tension coefficient, R_0 is the radius of the drop and ε_0 is the dielectric constant outside the drop (assuming for simplicity that the relative permittivity is $\varepsilon_r = 1$).

L.B. Gamboa (✉)
Universidad Autónoma de Yucatán Periférico Norte, Tablaje Cat. 13615,
Chuburná Hidalgo Inn, Mérida, Yucatán, Mexico
e-mail: lgamboa@correo.uady.mx

M.A. Fontelos
Campus de Cantoblanco, Instituto de Ciencias Matemáticas
(CSIC—UAM—UC3M—UCM), C/Nicolás Cabrera, 13-15, 28049 Madrid, Spain
e-mail: marco.fontelos@icmat.es

When the drop's charge is overcritical, the drop deforms into a prolate spheroid (cf. Duft et al. 2003; Beauchamp and Grimm 2003, 2005 for experimental results and Fontelos et al. 2008; Betelú et al. 2006 for numerical simulations) and conical tips tend to develop at the regions of maximum curvature. When the fluid is a perfect conductor and is modeled under Stokes approximation, it was shown in Beauchamp and Grimm (2003, 2005), that conical tips develop in finite time. Nevertheless, in the experimental observations, very fast and thin jets are produced from the conical tips (see Fig. 1). This is a fact that cannot be reproduced in the aforementioned papers under the Stokes and perfect conductor assumptions. For perfect and non-viscous fluids, jets have been reported recently in Garzon et al. (2014) where they use the level set techniques (cf. Sethian 1999). Nevertheless, for very small drops (of the order of $100\,\mu$m or smaller), Reynolds number can be very small (of the order of 10^{-4} or smaller), so that it seems necessary to investigate formation of jets under Stokes approximation. Our hypothesis is that it is the finite electric conductivity and the presence of Debye layers in electrolytic solutions what induces the production of Rayleigh jets. The first effect, finite conductivity, implies that electric charges do not move infinitely fast inside the liquid medium. The second effect, finiteness of Debye layer, implies that positive and negative charges do not balance exactly inside the drop so that the liquid is electrically neutral at the bulk of the fluid. Instead, they form a thin layer (the so-called Debye layer) where there is a nonzero net charge.

We will show that the hypothesis sketched above does indeed lie at the heart of the formation of Rayleigh jets and will be used to compute the jet's main characteristics such as velocity and size. Our results will also be used to discuss Rayleigh jet's features dependence on temperature and ion concentration.

D. Duft et al., Rayleigh jets from levitated microdroplets, *Nature, vol. 421, 9 January 2003, pg. 128.*
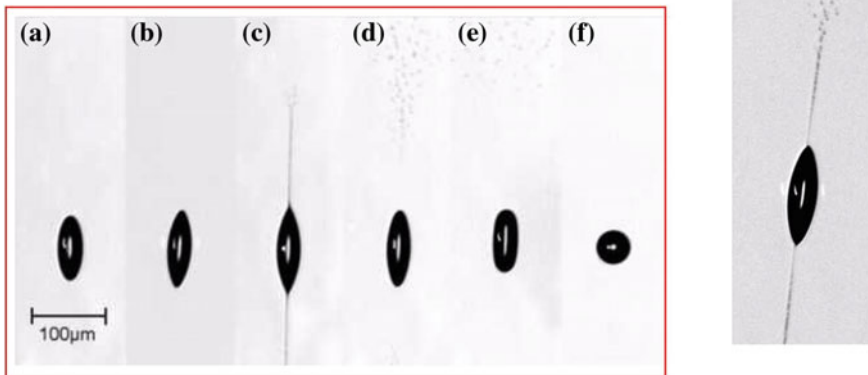
Fig. 1 Formation of Rayleigh jets as observed in Duft et al. (2003). After the jet is formed in (*c*) the drop loses an important part of its charge and relaxes to *spherical* shape

2 Physical Setting and Formulation

2.1 Introduction

In microfluidics, relevant physical dimensions are sufficiently large in comparison to atomic scales that it is permissible to treat the fluid as if it were a continuum.

We will consider masses of fluid at a very small length scale implying $Re \ll 1$ so that fluid inertia can either be neglected, or treated as a small perturbation. We arrive then to Stokes flow equations:

$$-\nabla p + \mu \Delta \mathbf{v} + \mathbf{F}_e = 0, \tag{2}$$

which is often referred to as slow, creeping or highly viscous flow.

The working fluid in microfluidic systems is normally water which contains ions of both signs due to dissociated water molecules or other ionic components: acids, salts, and molecules with dissociable charged groups. Normally, a volume element of such a fluid considered infinitesimal in the continuum view point still contains a sufficiently large number of ions of either sign for statistical fluctuations to be unimportant for the fluid element to be considered charge neutral. Therefore, the net algebraic transfer of momentum due to any ambient electric field is also zero (even though a non-zero electric current may exist in the fluid due to the ordered motion of these ions). Electrokinetic effects arise when this balance of positive and negative charges is disturbed due to external factors. In the macroscopic description, the drop consists of a viscous incompressible fluid containing ions, which are electrically charged and produce stresses on the fluid through the so-called Maxwell stress tensor:

$$\tau_{ij} = E_i E_j - \frac{1}{2}\delta_{ij} \left| \mathbf{E} \right|^2 ,$$

where $\mathbf{E} = -\nabla V$. Then $\mathbf{F}_e$ is the divergence of the Maxwell stress tensor τ:

$$F_i = \tau_{ij,j},$$

using Einstein notation for brevity in the formulas. We can write

$$F_i = (E_i E_j - \frac{1}{2}E_k E_k \delta_{ij})_{,j} = E_{i,j}E_j + E_{j,j}E_i - E_k E_{k,i} = V_{ij}V_i + \rho E_i - V_k V_{ki} = \rho E_i.$$

Therefore the fluid in the so called Debye Layer, experienced an electric force with volume density $\mathbf{F}_e = \rho\mathbf{E}$ with ρ the electric charge density and $\mathbf{E} = -\nabla V$ the local electric field with V the electric potential.

2.2   The Model

Let us consider now a droplet $\Omega(t)$ of a viscous incompressible fluid containing ions electrically charged, the droplet is suspended in a dielectric and also incompressible viscous fluid $\Omega^*(t) \setminus \overline{\Omega(t)}$, which is in contact with electrodes to zero potential, and which we would like to take infinite. In this case, the boundary $\partial\Omega(t)$ will move with the flow, so we have to take into account also the exterior fluid dynamics.

The mathematical formulation corresponding to the model for the electric potential V in $\Omega^*(t)$ that consists of an electrolytic droplet $\Omega(t)$ surrounded by a dielectric fluid $\Omega^*(t) \setminus \overline{\Omega(t)}$, is the Poisson-Boltzmann equation (Fontelos and Gamboa 2012)

$$\Delta V(\mathbf{x},t) = \frac{M(\mathbf{x},t)}{\int_\Omega e^{V/\varepsilon} d\mathbf{x}} e^{V/\varepsilon} - \frac{N(\mathbf{x},t)}{\int_\Omega e^{-V/\varepsilon} d\mathbf{x}} e^{-V/\varepsilon} \text{ in } \Omega^*(t), \tag{3}$$

$$V(\mathbf{x},t) \longrightarrow O\left(|\mathbf{x}|^{-1}\right) \text{ on } \partial\Omega^*(t),$$

with

$$M(\mathbf{x},t) = \begin{cases} M & \mathbf{x} \in \Omega(t) \\ 0 & \mathbf{x} \in \Omega^*(t) \setminus \Omega(t) \end{cases} \quad \text{and } N(\mathbf{x}) = \begin{cases} N & \mathbf{x} \in \Omega(t) \\ 0 & \mathbf{x} \in \Omega^*(t) \setminus \Omega(t), \end{cases}$$

comes from a nondimensional physical problem. The parameter

$$\varepsilon = \frac{\varepsilon_0 \varepsilon_r k_b T l}{(ez)^2},$$

k_b is the Boltzmann constant, T the absolute temperature, e the charge of the electron and z the valence of the ionic species, l is a characteristic length associated to $\Omega(t)$, is inversely proportional to ion mobilities. For the sake of simplicity, we are considering a binary ionic solution such as Na^+ and Cl^- produced from the dissociation of $NaCl$. In order to simplify the presentation, we will use for the electric problem the Lorentz-Heaviside units, so that $\varepsilon_0 = 1$.

We had assumed that the droplet contains a net amount of electric charge Q, so if we denote σ the surface charge density in the droplet $\Omega(t)$, we know that $\sigma(\mathbf{x},t) = -\left.\frac{\partial V}{\partial \mathbf{n}}\right|_{\partial\Omega(t)}$ and satisfies

$$\int_{\partial\Omega(t)} \sigma(\mathbf{x},t) \, dS(\mathbf{x}) = Q. \tag{4}$$

Q constant in time because of the charge conservation law.

Then the model governing the liquid flow in the droplet $\Omega(t)$ and in the exterior fluid is the Stokes system including the electric body force per unit volume $\rho\mathbf{E} = -\rho\nabla V$ in the momentum equation for the droplet:

$$-\nabla p^{(1)}(\mathbf{x},t) + \mu_1 \Delta \mathbf{v}^{(1)}(\mathbf{x},t) + \rho(\mathbf{x},t) \mathbf{E}(\mathbf{x},t) = 0 \, \mathbf{x} \in \Omega(t), \tag{5}$$

Fig. 2 Two fluids interacting

interface $\partial\Omega\,(t)$
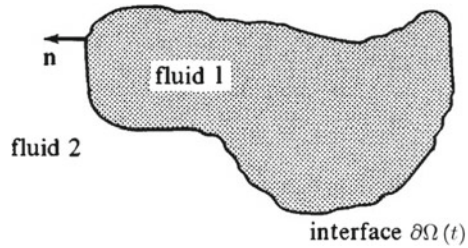
$$-\nabla p^{(2)}\,(\mathbf{x},t) + \mu_2 \Delta \mathbf{v}^{(2)}\,(\mathbf{x},t) = 0 \ \mathbf{x} \in \Omega^*\,(t)\,\backslash\overline{\Omega\,(t)}, \tag{6}$$

$$\nabla \cdot \mathbf{v}^{(k)}\,(\mathbf{x},t) = 0 \ \mathbf{x} \notin \partial\Omega\,(t)\,, k = 1, 2, \tag{7}$$

where $\mathbf{v}^{(k)}$ is the velocity field, $p^{(k)}$ is the pressure, μ_k the viscosity for $k = 1, 2$ the respective inner and outer viscosities (Fig. 2).

The normal component of the velocity has to be continuous across the boundary:

$$\mathbf{v}^{(1)} \cdot \mathbf{n} = \mathbf{v}^{(2)} \cdot \mathbf{n} \equiv \mathbf{v} \cdot \mathbf{n} \text{ on } \partial\Omega\,(t)\,,$$

The dependence on t comes from the motion of the boundary $\partial\Omega\,(t)$ given by the equation

$$\frac{d\mathbf{x}}{dt} \cdot \mathbf{n} = \mathbf{v}\,(\mathbf{x},t) \cdot \mathbf{n}, \tag{8}$$

with $\mathbf{n}$ exterior to $\Omega\,(t)$, expressing the fact that the surface of the drop moves in the direction of its normal, following the normal component of the velocity field. Note that the tangential velocity does not change the geometry of $\partial\Omega\,(t)$ but only redistributes its points.

2.3 Boundary Conditions

To describe a flow in the presence of an interface we must consider the flow on each side of the interface separately, and then require proper matching conditions for the velocity.

The traction vector depends linearly on the normal vector

$$f_j\,(\mathbf{x}, \mathbf{n}) = T_{ij}\,(\mathbf{x})\,n_i, \tag{9}$$

where T_{ij} is the Cauchy stress tensor.

We had assumed that our viscous fluids are Newtonian and incompressible, so the stress tensor T_{ij} is related to the pressure p and to the rate-of-deformation tensor by the linear constitutive equation

$$T_{ij}^{(k)} = -\delta_{ij}p^{(k)} + \mu_k \left(\frac{\partial v_i^{(k)}}{\partial x_j} + \frac{\partial v_j^{(k)}}{\partial x_i} \right) \qquad k = 1, 2,$$

expressing the effects of the forces acting in a fluid: pressure, and viscous friction or viscosity.

2.3.1 Traction Jump Across a Fluid Interface

The hydrodynamic traction undergoes a discontinuity defined as

$$\Delta \mathbf{f} = \mathbf{f}^{(2)} - \mathbf{f}^{(1)} = \left(\mathbf{T}^{(2)} - \mathbf{T}^{(1)} \right) \mathbf{n} = 2\gamma \mathscr{H} \mathbf{n}, \tag{10}$$

where $\mathbf{f}^{(2)} = \mathbf{T}^{(2)} \cdot \mathbf{n}$ is the traction exerted on the surface of the drop due to the exterior fluid and $\mathbf{f}^{(1)} = \mathbf{T}^{(1)} \cdot \mathbf{n}$ is the traction exerted on the surface due to the drop. The surface tension γ is constant, $\mathscr{H} = \frac{\mathscr{H}_1 + \mathscr{H}_2}{2}$ is the mean curvature of the interface.

Tangential effects only redistribute the points in the boundary, that is why are unimportant in this case. We will also assume that the flow vanishes at infinity.

In the next section we will transform the problem (5)–(8) containing the bulk force $\rho \mathbf{E}$, with boundary condition (10) into a problem without external bulk forces where condition (10) is modified to include electrokinetic stresses.

2.4 Coupling Poisson-Boltzmann and Stokes

Let us take t fixed, the charge density inside the droplet $\Omega(t)$ is

$$\rho(\mathbf{x},t) = -\Delta V(\mathbf{x},t) = \frac{N}{\int_{\Omega(t)} e^{-V/\varepsilon} d\mathbf{x}} e^{-V/\varepsilon} - \frac{M}{\int_{\Omega(t)} e^{V/\varepsilon} d\mathbf{x}} e^{V/\varepsilon}.$$

Denote

$$f(V(\mathbf{x},t)) = \frac{N}{\int_{\Omega(t)} e^{-V/\varepsilon} d\mathbf{x}} e^{-V/\varepsilon} - \frac{M}{\int_{\Omega(t)} e^{V/\varepsilon} d\mathbf{x}} e^{V/\varepsilon},$$

then

$$\rho \mathbf{E} = -f(V) \nabla V.$$

If we take the real function with real values F defined as:

$$F(x) = -\varepsilon \frac{N}{\int_{\Omega(t)} e^{-V/\varepsilon} d\mathbf{x}} e^{-x/\varepsilon} - \varepsilon \frac{M}{\int_{\Omega(t)} e^{V/\varepsilon} d\mathbf{x}} e^{x/\varepsilon},$$

we have

$$\frac{dF}{dx}(V(\mathbf{x},t)) = \frac{N}{\int_{\Omega(t)} e^{-V/\varepsilon} d\mathbf{x}} e^{-V/\varepsilon} - \frac{M}{\int_{\Omega(t)} e^{V/\varepsilon} d\mathbf{x}} e^{V/\varepsilon} = \rho(\mathbf{x},t).$$

By the chain rule applied to $F \circ V : \Omega(t) \longrightarrow \mathbb{R}$,

$$\nabla(F \circ V(\mathbf{x},t)) = \frac{dF}{dx}(V(\mathbf{x},t)) \nabla V(\mathbf{x},t),$$
$$= \rho \nabla V = -\rho \mathbf{E},$$

then the Eq. (5) can be rewritten as

$$-\nabla\left(p^{(1)} + F \circ V\right) + \mu_1 \Delta \mathbf{v}^{(1)} = 0 \quad \mathbf{x} \in \Omega(t). \tag{11}$$

Let us denote

$$P^{(1)} = p^{(1)} + F \circ V, \tag{12}$$

and

$$P^{(2)} = p^{(2)}, \tag{13}$$

we have

$$-\nabla P^{(2)} + \mu_2 \Delta \mathbf{v}^{(2)} = 0 \quad \mathbf{x} \in \Omega^*(t) \setminus \overline{\Omega(t)}. \tag{14}$$

The boundary conditions on the free boundary $\partial \Omega(t)$ in terms of the new pressure (12) becomes

$$\left[-\left(P^{(2)} - P^{(1)}\right)\delta_{ij} + \mu_2\left(\frac{\partial v_i^{(2)}}{\partial x_j} + \frac{\partial v_i^{(2)}}{\partial x_i}\right) - \mu_1\left(\frac{\partial v_i^{(1)}}{\partial x_j} + \frac{\partial v_i^{(1)}}{\partial x_i}\right)\right] n_j = 2\mathscr{H} n_i + (F \circ V) n_i.$$

The Eqs. (11) and (14) state that the pressure, viscous, and body forces, balance at any instant in time even though the flow may be unsteady. The instantaneous structure of the flow depends solely on the present boundary configuration and boundary conditions, and is independent of the history of motion. The history of motion enters the problem only by determining the current location of the boundaries. Therefore we will work with the steady state problem and, as we will see, we can use recursivity and the evolution formula (8) to obtain an approximate solution in an evolved domain. We will consider then the steady state problem and drop off the dependence on time:

$$\Omega_1 = \Omega(t).$$

We want to work with an infinite ambient fluid, therefore we will assume

$$\Omega_2 = \mathbb{R}^3 \backslash \overline{\Omega(t)}.$$

Finally, the system that models our problem is:

$$-\nabla P^{(k)}(\mathbf{x}) + \mu_k \Delta \mathbf{v}^{(k)}(\mathbf{x}) = 0, \, \mathbf{x} \in \Omega_k, \tag{15}$$

$$\nabla \cdot \mathbf{v}^{(k)} = 0, \, \mathbf{x} \in \Omega_k, \tag{16}$$

$$\left(\mathbf{T}^{(2)} - \mathbf{T}^{(1)} \right) \mathbf{n} = (2\mathcal{H} + (F \circ V)) \mathbf{n} \text{ on } \partial \Omega_1, \tag{17}$$

$$\mathbf{v} \longrightarrow \mathbf{0} \text{ as } |\mathbf{x}| \longrightarrow \infty. \tag{18}$$

2.5   The Asymptotic Boundary Conditions for $\varepsilon \ll 1$

The potential in the boundary layer inside Ω_1 can be written in the form (Fontelos and Gamboa 2012)

$$V = C + u^* + \overline{u},$$

with $\overline{u}$ solution of

$$\Delta \overline{u} = \mu \left(e^{\overline{u}/\varepsilon} - e^{-\overline{u}/\varepsilon} \right) \text{ in } \Omega_1,$$

C a constant associated to the perfect conductor problem and to (4),

$$\mu = \sqrt{\frac{MN}{\int_{\Omega_1} e^{(V-C)/\varepsilon} \int_{\Omega_1} e^{-(V-C)/\varepsilon}}} \text{ and } u^* = \varepsilon \ln \sqrt{\frac{N \int_{\Omega_1} e^{(V-C)/\varepsilon}}{M \int_{\Omega_1} e^{-(V-C)/\varepsilon}}} = \varepsilon c^*.$$

Then, it easily follows

$$F(V(\mathbf{x})) = -\varepsilon \mu \left[e^{\overline{u}/\varepsilon} + e^{-\overline{u}/\varepsilon} \right] = -2\varepsilon \mu \cosh \left(\frac{\overline{u}}{\varepsilon} \right). \tag{19}$$

We already have (Fontelos and Gamboa 2012) that

$$\overline{u}(\mathbf{x}) = \varepsilon \left(2\zeta \left(\frac{\xi(\mathbf{x})}{\delta} \right) \log \tanh \left(\frac{\sqrt{2} (\varepsilon \mu)^{1/2}}{|\sigma(x_S)|} \right) \left[\frac{\sigma(x_S)}{2} \frac{\xi(\mathbf{x})}{\varepsilon} + 1 \right] \right) + \varepsilon u_1(\mathbf{x})$$

$$= \varepsilon u_0(\mathbf{x}) + \varepsilon u_1(\mathbf{x}),$$

with

$$u_0(\mathbf{x}) = 2\zeta\left(\frac{\xi(\mathbf{x})}{\delta}\right)\log\tanh\left(\frac{\sqrt{2}\,(\varepsilon\mu)^{1/2}}{|\sigma(x_S)|}\right)\left[\frac{\sigma(x_S)}{2}\frac{\xi(\mathbf{x})}{\varepsilon}+1\right],$$

$\sigma(x_S) \simeq -\frac{\partial V}{\partial \mathbf{n}}$ in $\partial\Omega_1$, σ is approximately the surface charge density of the potential for the perfect conductor, in fact it is the surface charge density for the perfect conductor in $x_S = \eta(\mathbf{x}) \in \partial\Omega_1$ plus corrections. η, ξ are associated to a parametrization of the boundary layer and ζ is a cut-off function. Let us remind that $u_1(\mathbf{x})$

$$u_1(x_S) = \frac{\varepsilon^{1/2}}{2}\frac{\sqrt{2/\mu}\,\mathscr{H}(x_S)\sinh\left(\frac{2\sqrt{2}(\varepsilon\mu)^{1/2}}{|\sigma(x_S)|}\right)}{\cosh^4\left[\left(\frac{\sqrt{2}(\varepsilon\mu)^{1/2}}{|\sigma(x_S)|}\right)\right]+\sinh^4\left[\left(\frac{\sqrt{2}(\varepsilon\mu)^{1/2}}{|\sigma(x_S)|}\right)\right]}. \tag{20}$$

$\mathscr{H}(\mathbf{x})$ is the curvature of the level surface of the distance function that contains the point $\mathbf{x}$. In the limit when $\mathbf{x} \longrightarrow \partial\Omega_1$, that curvature tends to the mean curvature of the interface at x_S.

Therefore in $\partial\Omega_1$

$$F(V(x_S)) = -\frac{\sigma(x_S)^2}{2} - \frac{2}{3}\mu\varepsilon + \mathscr{H}(x_S)\left|\sigma(x_S)\right|\varepsilon + O(\varepsilon^2). \tag{21}$$

Assuming $\mu \ll 1$ we can redefine the pressure to drop off $-\frac{2}{3}\mu\varepsilon$ and we have:

$$F(V(x_S)) = -\frac{\sigma(x_S)^2}{2} + \mathscr{H}(x_S)\left|\sigma(x_S)\right|\varepsilon + O(\varepsilon^2). \tag{22}$$

The surface charge density for the electrolyte, i.e. $-\frac{\partial V}{\partial \mathbf{n}}(x_S)$, $x_S \in \partial\Omega_1$ results approximately the function $\sigma(x_S)$:

$$\sigma(x_S) = \sigma_0(x_S) + \varepsilon\sigma_1(x_S) + O(\varepsilon^2),$$

σ_0 the charge density for the perfect conductor and σ_1 is the correction given by the Lemma 3.2 in Fontelos and Gamboa (2012) and it is:

$$\sigma_1(x_S) = -\frac{2\int_{\partial\Omega}\mathscr{N}(\ln(\sigma_0))}{Q}\sigma_0(x_S) + 2\mathscr{N}(\ln(\sigma_0)) + O(\varepsilon),$$

$\mathscr{N}$ the Dirichlet to Neumann operator restricted to $\partial\Omega_1$.

Therefore

$$F(V(x_S)) = -\frac{\sigma_0(x_S)^2}{2} - \varepsilon\sigma_0(x_S)\sigma_1(x_S) + \mathscr{H}(x_S)\sigma_0(x_S)\varepsilon + O(\varepsilon^2). \tag{23}$$

3 The Boundary Integral Equation for a Harmonic Function

3.1 Introduction

We are interested now in calculating the boundary condition:

$$F(V) = -\frac{\sigma_0(x_S)^2}{2} - \varepsilon\sigma_0(x_S)\sigma_1(x_S) + \mathcal{H}(x_S)\sigma_0(x_S)\varepsilon + O(\varepsilon^2),$$

where $\sigma_0(x_S)$ is the surface charge density for the perfect conductor and

$$\sigma_1(x_S) = -2\frac{\int_{\partial\Omega}\mathcal{N}(\ln(\sigma_0))}{Q}\sigma_0(x_S) + 2\mathcal{N}(\ln(\sigma_0)) + O(\varepsilon),$$

with Q the net amount of electric charge, $\mathcal{N}$ the Dirichlet to Neumann operator restricted to $\partial\Omega_1$. The functions $\sigma_0(x_S)$ and $\mathcal{N}(\ln(\sigma_0))$ are related to the Laplace equation in Ω_2.

Strictly speaking, the domain depends on time because it is evolved by the velocity field and pressure, so we have a free boundary problem, but as we said before, we can fix a time t and deal with the steady state problem because we can use recursivity and an evolution formula depending on velocity to obtain the solution in the new domain $\Omega(t + \Delta t)$. Let us consider

$$\Delta u(\mathbf{x}) = 0 \text{ in } \Omega_2, \tag{24}$$
$$u(\mathbf{x})|_{\partial\Omega_1} = u_0(\mathbf{x}),$$
$$u(\mathbf{x}) \longrightarrow O(|\mathbf{x}|^{-1}) \text{ for } |\mathbf{x}| \longrightarrow \infty.$$

Last problem is related with $F(V)$ in the following sense: if we take $u_0(\mathbf{x}) = C$ for an appropriate constant C we have $\sigma_0(\mathbf{x}) = -\frac{\partial u}{\partial\mathbf{n}}\Big|_{\partial\Omega_1}$ and if $u_0(\mathbf{x}) = \ln(\sigma_0(\mathbf{x}))$ then $\mathcal{N}(\ln(\sigma_0)) = \frac{\partial u}{\partial\mathbf{n}}\Big|_{\partial\Omega_1}$, so let us establish first an integral formula for the harmonic function in (24).

3.2 The Axisymmetric Boundary Integral Equation

When $\mathbf{x}_0 \in \partial\Omega_1$

$$u(\mathbf{x}_0) = -\int_{\partial\Omega_1} G(\mathbf{x}, \mathbf{x}_0)\frac{\partial u}{\partial\mathbf{n}}(\mathbf{x})\,dS(\mathbf{x}) + \int_{\partial\Omega_1}[u(\mathbf{x}) - u(\mathbf{x}_0)]\frac{\partial G(\mathbf{x}, \mathbf{x}_0)}{\partial\mathbf{n}}\,dS(\mathbf{x}),$$

is a known integral formulation (c.f. Pozrikidis 2009) to the solution of (24), where
G is a suitable Green's function. For an axisymmetric surface the potential becomes

$$
\begin{aligned}
u\left(\mathbf{x}_0\right) = & -\int_a^b G^{Ax}\left(r, z, r_0, z_0\right) \frac{\partial u}{\partial n}(r, z) \, r(z) \sqrt{1+r'(z)^2} \, dz \\
& + \int_a^b \left[u(\mathbf{x}) - u\left(\mathbf{x}_0\right)\right] \frac{\partial G^{Ax}}{\partial n}\left(r, z, r_0, z_0\right) r(z) \sqrt{1+r'(z)^2} \, dz \\
= & -\frac{1}{\pi} \int_a^b \frac{F(k)}{\sqrt{\left(z-z_0\right)^2 + \left(r+r_0\right)^2}} \frac{\partial u}{\partial n}(r, z) \, r(z) \sqrt{1+r'(z)^2} \, dz \\
& + \frac{1}{2\pi} \int_a^b \left[u(\mathbf{x}) - u\left(\mathbf{x}_0\right)\right] \Bigg(-\frac{F(k)}{\sqrt{\left(z-z_0\right)^2 + \left(r+r_0\right)^2}} \\
& + \frac{E(k)\left[\left(z-z_0\right)^2 + 2\left(z-z_0\right) r(z) r'(z) + \left(r_0-r\right)\left(r_0+r\right)\right]}{\sqrt{\left(z-z_0\right)^2 + \left(r+r_0\right)^2}\left(\left(z-z_0\right)^2 + \left(r-r_0\right)^2\right)} \Bigg) dz.
\end{aligned}
$$

This is an expression to the potential in terms of $F(k)$ and $E(k)$, complete elliptic
integrals of the first and second kind respectively. We will use these expressions
later in the Boundary Elements Method (BEM) for obtaining local approximations
to $F(V)$.

We already have an integral equation for the boundary condition, next we will use
a similar representation for the velocity field in the Stokes flow.

4 The Boundary Integral Formulation for Stokes System

4.1 Introduction

In the construction of the model it is used two equations for the velocity and pressure
on either side of the interface, and one expression for the interfacial boundary condi-
tion in terms of the surface charge density σ_0, the curvature $\mathscr{H}$, and a correction σ_1;
we already have a boundary integral equation for calculating the boundary condi-
tions, now we will use a boundary integral representation for obtaining the velocity,
that finally will allow us to study the evolution of our droplet in terms of ε and the
amount of charge when we combine the integral representations with a numerical
method.

4.2   Integral Equation

We have used a boundary integral representation to the flow in a similar way as we did for Laplace equation but using an appropriate Green's function to this case.

 We are interested in finding the velocity field at the interface between the droplet and the surrounding fluid, because the evolution of the droplet is determined by the normal projection of this velocity field. Therefore let us start determining the velocity at the interior of the droplet, then at the exterior fluid and finally we will find an expression valid at the interface.

 From Pozrikidis (1992) we have

$$v_j\left(\mathbf{x}_0\right) = \frac{-1}{4\pi\left(\mu_1 + \mu_2\right)} \int_{\partial\Omega_1} \mathbb{G}_{ij}\left(\mathbf{x},\mathbf{x}_0\right) \Delta f_i\left(\mathbf{x}\right) dS \tag{25}$$

$$+ \frac{\mu_2 - \mu_1}{4\pi\left(\mu_1 + \mu_2\right)} \int_{\partial\Omega_1}^{PV} v_i\left(\mathbf{x}\right) \mathbb{T}_{ijk}\left(\mathbf{x},\mathbf{x}_0\right) n_k\left(\mathbf{x}\right) dS\left(\mathbf{x}\right),$$

with **n** exterior to Ω_1 and

$$\mathbb{G}_{ij}(\mathbf{x},\mathbf{x}_0) = \frac{\delta_{ij}}{\left|\mathbf{x} - \mathbf{x}_0\right|} + \frac{(x_i - x_{0,i})(x_j - x_{0,j})}{\left|\mathbf{x} - \mathbf{x}_0\right|^3},$$

$$\mathbb{T}_{ijk}(\mathbf{x},\mathbf{x}_0) = -6\frac{(x_i - x_{0,i})(x_j - x_{0,j})(x_k - x_{0,k})}{\left|\mathbf{x} - \mathbf{x}_0\right|^5},$$

for $i, j, k \in \{1, 2, 3\}$, where

$$\Delta f_i\left(\mathbf{x}\right) = (2\mathscr{H}\left(\mathbf{x}\right) + F\left(V\right))n_i \tag{26}$$

$$= \left(2\mathscr{H}\left(\mathbf{x}\right) - \frac{\sigma_0\left(\mathbf{x}\right)^2}{2} - \varepsilon\sigma_0\left(\mathbf{x}\right)\sigma_1\left(\mathbf{x}\right) + \mathscr{H}\left(\mathbf{x}\right)\sigma_0\left(\mathbf{x}\right)\varepsilon\right)n_i,$$

corresponding to the boundary condition (17). The Eq. (25) is the integral equation for the velocity at the interface $\partial\Omega_1$ that will be used to determine the evolution of the droplet together with the boundary conditions (26).

5   Numerical Implementation

We will use a numerical method, the Boundary Element Method (BEM) to approximate the functions involved in the boundary condition and also to approximate the velocity field **v**. We will start with Laplace problem for obtaining $F\left(V\right)$, then we will approximate the solutions for the Stokes system, and finally we will use the evolution

formula to study the behaviour of $\partial\Omega\left(t\right)$, the evolving boundary of the drop, in terms of t, ε, and the total charge Q.

5.1 Obtaining σ_0

In the axisymmetric equation

$$\Delta u\left(\mathbf{x},0\right) = 0 \text{ in } \mathbb{R}^3\backslash\overline{\Omega\left(0\right)},$$
$$u\left(\mathbf{x},0\right)|_{\partial\Omega} = u_0\left(\mathbf{x},0\right),$$
$$u\left(\mathbf{x},0\right) \longrightarrow O\left(|\mathbf{x}|^{-1}\right) \text{ for } |\mathbf{x}| \longrightarrow \infty,$$

we assume $u_0 = C$ for a suitable constant associated with the total charge in the droplet, the integral equation is:

$$C = -\frac{1}{\pi}\int_a^b \frac{F\left(k\right)}{\sqrt{\left(z-z_0\right)^2 + \left(r+r_0\right)^2}}\frac{\partial u}{\partial n}\left(r,z\right)r\left(z\right)\sqrt{1+r'\left(z\right)^2}dz,$$

which implies

$$C \simeq -\sum_{j=1}^{n-1}\left(\frac{\partial u}{\partial \mathbf{n}}\right)_j\int_{z_j}^{z_{j+1}} \frac{F\left(k\left(r\left(z\right),z,r_i^M,z_i^M\right)\right)}{\sqrt{\left(z-z_i^M\right)^2 + \left(r+r_i^M\right)^2}}\sqrt{1+r'\left(z\right)^2}r\left(z\right)dz,$$

for $i = 1,\ldots,n-1$. Inverting numerically as in Fontelos et al. (2008) and taking care with the subinterval that contains the pole (refining properly on it), we obtain an approximation to

$$\sigma_0\left(x_S\right) = -\left.\frac{\partial u}{\partial n}\left(r,z\right)\right|_{\partial\Omega(0)},$$

in the middle points (r_i^M, z_i^M) of each element. For the integration we used the trapezoidal rule, for the calculation of the inverse the GMRES method (an iterative gradient method for the solution of linear systems) and for approximations of the derivative, central differences.

5.2 Obtaining $\mathcal{N}\left(\ln\left(\sigma_0\right)\right)$

If now we assume that the boundary condition $u_0\left(\mathbf{x},0\right) = \ln\left(\sigma_0\left(r,z\right)\right)$ in $\partial\Omega\left(0\right)$, we will have:

$$\ln\left(\sigma_0\left(r_0,z_0\right)\right) = -\frac{1}{\pi}\int_a^b \frac{F\left(k\right)}{\sqrt{\left(z-z_0\right)^2+\left(r+r_0\right)^2}}\frac{\partial u}{\partial n}\left(r,z\right)r\left(z\right)\sqrt{1+r'\left(z\right)^2}dz$$

$$+\frac{1}{2\pi}\int_a^b \ln\left(\frac{\sigma_0\left(r,z\right)}{\sigma_0\left(r_0,z_0\right)}\right)\left(\frac{-F\left(k\right)}{\sqrt{\left(z-z_0\right)^2+\left(r+r_0\right)^2}}\right.$$

$$\left.+\frac{E\left(k\right)\left[\left(z-z_0\right)^2+2\left(z-z_0\right)r\left(z\right)r'\left(z\right)+\left(r_0-r\right)\left(r_0+r\right)\right]}{\sqrt{\left(z-z_0\right)^2+\left(r+r_0\right)^2}\left(\left(z-z_0\right)^2+\left(r-r_0\right)^2\right)}\right)dz,$$

using $\sigma_0\left(r,z\right)$ calculated before. We are looking for $\frac{\partial u}{\partial n}\left(r,z\right)$ therefore we will use the discretized version:

$$\ln\left(\sigma_0(r_i^M,z_i^M)\right) - \frac{1}{2\pi}\sum_{j=1}^{n-1}\int_{z_j}^{z_{j+1}}\ln\left(\frac{\sigma_0\left(r,z\right)}{\sigma_0(r_i^M,z_i^M)}\right)\left(-\frac{F\left(k\left(r\left(z\right),z,r_i^M,z_i^M\right)\right)}{\sqrt{\left(z-z_i^M\right)^2+\left(r+r_i^M\right)^2}}\right.$$

$$\left.+\frac{E\left(k\left(r\left(z\right),z,z_i^M,r_i^M\right)\right)\left[\left(z-z_i^M\right)^2+2\left(z-z_i^M\right)r\left(z\right)r'\left(z\right)+\left(r_i^M-r\right)\left(r_i^M+r\right)\right]}{\sqrt{\left(z-z_i^M\right)^2+\left(r+r_i^M\right)^2}\left(\left(z-z_i^M\right)^2+\left(r-r_i^M\right)^2\right)}\right)dz$$

$$= -\frac{1}{\pi}\sum_{j=1}^{n-1}\left(\frac{\partial u}{\partial \mathbf{n}}\right)_j\int_{z_j}^{z_{j+1}}\frac{F\left(k\left(r\left(z\right),z,r_i^M,z_i^M\right)\right)}{\sqrt{\left(z-z_i^M\right)^2+\left(r+r_i^M\right)^2}}\sqrt{1+r'\left(z\right)^2}r\left(z\right)dz,$$

where $\left(\frac{\partial u}{\partial \mathbf{n}}\right)_j$ is an approximation of the normal derivative at the middle points. As before, we can invert numerically to obtain an approximate $\mathcal{N}\left(\ln\left(\sigma_0\right)\right) = \frac{\partial u}{\partial n}\left(r,z\right)$ using the same techniques than for σ_0 for the calculation of the integrals, inverting the matrix etc. For approximating $\ln\left(\frac{\sigma_0(r,z)}{\sigma_0(r_i^M,z_i^M)}\right)$ we interpolate linearly using the discretized version found previously.

5.3   Obtaining the Boundary Condition $F\left(V\right)$

We know

$$\sigma_1\left(x_S\right) = -\frac{2\int_{\partial\Omega}\mathcal{N}\left(\ln\left(\sigma_0\right)\right)}{Q}\sigma_0\left(x_S\right) + 2\mathcal{N}\left(\ln\left(\sigma_0\right)\right) + O\left(\varepsilon\right),$$

and now we have the functions that we need to calculate it. Therefore we can obtain the values for the boundary conditions to be used in the Stokes system.

5.4 Details on the Numerical Implementation

We will include the principal algorithm (with only the principal parameters) to illustrate the basic idea followed for generating the evolution of the drops.

Algorithm 1 Input parameters:
μ_1 viscosity of the drop.
μ_2 viscosity of the fluid surrounding the drop.
Q initial charge of the droplet.
ε dimensionless parameter associated with the Debye length.
Configuration parameters:
n number of nodes.
e eccentricity of the spherical harmonic for the initial mesh $\Omega(0)$

1. $t \leftarrow t_0$
2. **while** $t < t_{\max}$
3. Calculate the surface charge density σ_0 at the midpoints of the mesh.
4. Calculate the correction σ_1 for the boundary condition $F(V)$.
5. Calculate the mean curvature at the midpoints of the mesh.
6. Calculate the velocity field at the midpoints of the mesh.
7. Interpolate the velocity to the nodes and project it to the normal.
8. Calculate an appropriate time step for determining the new mesh.
9. We move the mesh using the interpolated velocity to find the position of the nodes at the new time $t + \Delta t$
10. Smoothing the grid, moving the nodes to the direction of maximum curvature.
11. $t \leftarrow t + \Delta t$

Output: The position of the nodes at a final time $t_{\max}$.

6 Numerical Results: The Evolution of a Droplet

6.1 Stability Analysis

We started using the algorithm for the case $\varepsilon = 0$, i.e. assuming that the drop is a perfect conductor (and the corresponding equations to the potential) and using a similar argument to the bisection method we found that the critical charge to 3 decimals for dimensionless variables and equations is $Q_{c,0} = 12.123$. Using the same bisection idea, the algorithm with the force term in the boundary and the correction

σ_1 to the surface charge density (i.e. the case $\varepsilon \neq 0$) we found different values for the critical charge.

Critical charge (to three decimals) depends on ε and we used the perfect conductor case to express it relative to the critical charge for $\varepsilon = 0$:

ε	0	0.01	0.011	0.012	0.013	0.014	0.015	0.016
$Q_{c,\varepsilon}$	12.123	12.478	12.515	12.551	12.587	12.623	12.660	12.696
$\dfrac{Q_{c,\varepsilon}}{Q_{c,0}}$	1	1.0293	1.0323	1.0353	1.0382	1.0412	1.0442	1.0473
X_{ε}	1	1.0594	1.0656	1.0718	1.0778	1.0840	1.0903	1.0968

If we take a charge greater or equal than the critical charge for the respective case of ε, we have instability. In the calculation of X_{ε} we are using that $X \sim Q^2$.

Fitting quadratically we obtained

$$\frac{Q_{c,\varepsilon}}{Q_{c,0}} = \frac{44.893}{12.123}\varepsilon^2 + \frac{35.108}{12.123}\varepsilon + 1,$$

with a norm of residuals 0.00086283.

6.2   The Jets

If we take a value of charge that exceeds the critical charge we can see a deformation in the droplet, different than those observed in the numerical experiments in Fontelos et al. (2008) and in Betelú et al. (2006) done considering the perfect conductor case (Figs. 3 and 4).

Fig. 3 Some of the last profiles in the simulation
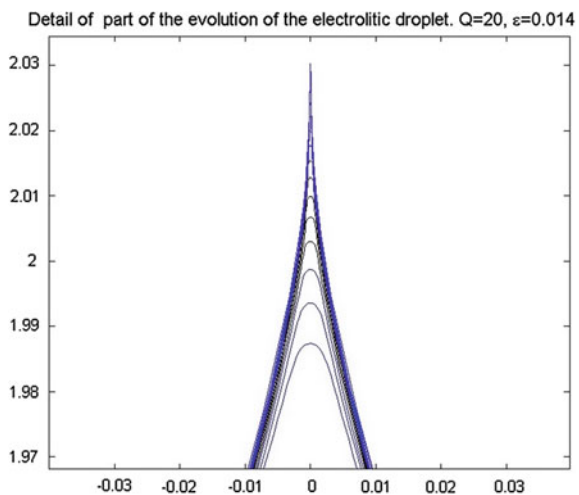
Fig. 4 Part of the behavior of the electrolytic drop

Part of the evolution of the electrolitic droplet. Q=20, ε=0.02
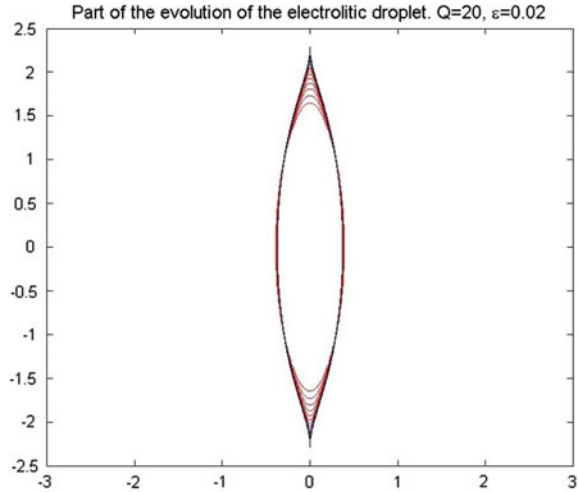
6.3 The Velocity of the Jet Using Dimensional Arguments

We are interested in knowing the relation between the Debye-Length and the velocity of the jet, that is, the dependence in the distribution of the charges in the boundary with the jet. Therefore, for a fixed charge, we will investigate the relation between ε and the component z of the velocity, i.e., v_z in the jet.

We have not defined what a jet is, and we will not define it but empirically, we will use an informal idea that comes from the observation of the experiments and comparing them with the evolution of the droplet in time with the simulations. To define it more properly we could use the evolution of the simulations and identifying the outputs for large times with small numerical error, the curvature in the apex, or also relate to the outputs the physical quantities associated to the drop, like for instance the charge in the "body" of the drop and comparing it with the charge in the part of the drop which we could call a "jet" (Figs. 5 and 6).

Some of the results obtained in simulations about the velocity are represented in Fig. 7

Let us observe in Fig. 5 the presence of jets as observed in the experiments reported, for instance, in Duft et al. (2003), Beauchamp and Grimm (2003).

We will analyze, based on the numerical simulations and asymptotic analysis, the main features of these jets as a function of ε (which is proportional to the absolute temperature) and ion concentration.

As we can observe, jets are emitted with a constant velocity (see Fig. 7). If we plot the velocity of the jet v_z as a function of ε, we can detect a scaling law

$$v_z \sim \frac{C}{\varepsilon}, \tag{27}$$

Fig. 5 Formation of a jet
from an electrically charged
viscous droplet. Numerical
simulation from our model
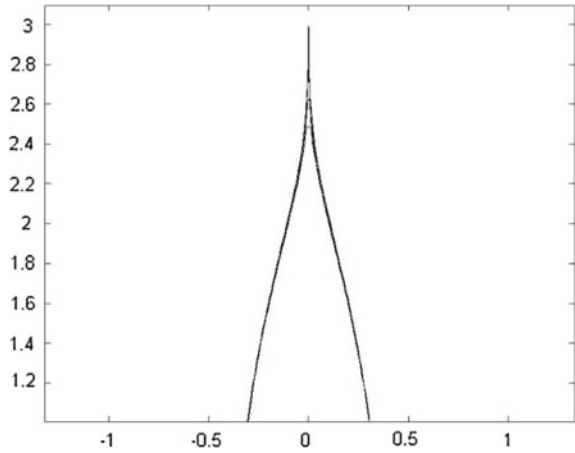
Fig. 6 Experiment from
Beauchamp and Grimm
(2003)
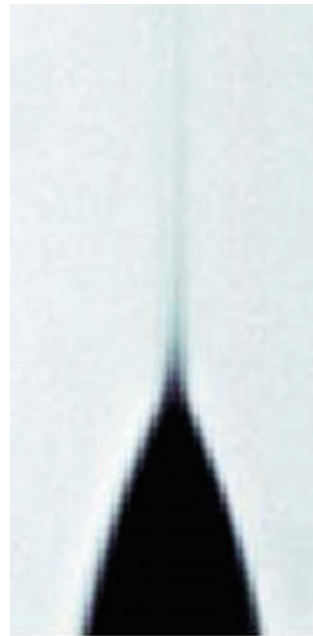
so that jets are emitted faster as ε decreases. Of course, very large velocities as $\varepsilon \to 0$
are not realistic, since inertial terms that have been neglected under Stokes approxi-
mation would then become dominant. Nevertheless, (27) provides an important qual-
itative result: the jet's velocity is inversely proportional to ε. Notice that in the limit
$\varepsilon = 0$, which corresponds to the perfect conductor, the velocity becomes singular as
shown in Fontelos et al. (2008) with the formation of a conical tip. It is then expected

Eps=0.016. Q=20. Iterations from 26,000 to 30,000.
$z = p_1 t + p_2$
Coefficients: $p_1 = 57.084$, $p_2 = -87.009$
Norm of residuals = 0.00086609
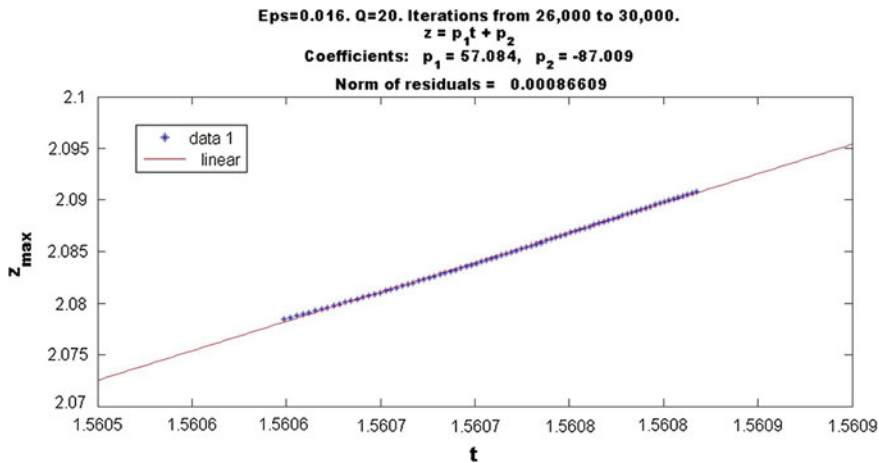
Fig. 7 Possition of the apex of the drop as a function of time for $\varepsilon = 0.016$, $Q = 20$. Observe that the position grows linearly in time indicating the appearance of a jet with $V \simeq 57.084$

that the radius of the jet collapses to zero as $\varepsilon \to 0$. This fact is observed numerically as represented in Fig. 5. A clear cone-jet structure can clearly be observed in Figs. 3 and 5: a cone whose vertex connects with a thin jet. By mass conservation, the flux of mass across a cross-section of the cone (which is independent of ε as the jet develops) equals the flux of mass over a cross-section of the jet. Therefore, if the radius of the jet is r, then

$$\rho \pi r^2 v_z = Const,$$

which implies, by (27), a jet's radius

$$r \propto \varepsilon^{\frac{1}{2}}. \tag{28}$$

Since, for a given solution, ε is proportional to the absolute temperature, we can conclude that the jet's radius decreases with the absolute temperature or, in other words, decreases when the Debye layer's thickness decreases. This is a common experimental observation in the electrokinetic context.

The origin of the scaling law (27) for the velocity of the jet can be understood from the following simple heuristic argument: the jet appears when the correction due to the Debye layer becomes of the same order of magnitude than the capillary force. Since, for $\varepsilon = 0$, conical singularities develop as demonstrated in Betelú et al. (2006) and in Fontelos et al. (2008) and they are such that

$$\mathscr{H} \propto \frac{1}{(t_0 - t)^{\frac{1}{2}}}, \quad \sigma \propto \frac{1}{(t_0 - t)^{\frac{1}{2}}}, \quad v_{z,tip} \propto \frac{1}{(t_0 - t)^{\frac{1}{2}}}$$

close to the singularity time t_0, we can now compare the terms

$$\gamma \mathcal{H} = O((t_0 - t)^{-\frac{1}{2}})$$
$$\varepsilon \sigma \mathcal{H} = \varepsilon O((t_0 - t)^{-1})$$

to conclude that jet starts to form when

$$\varepsilon = O((t_0 - t)^{\frac{1}{2}})$$

so that, the velocity is then

$$v_z \propto \frac{1}{(t_0 - t)^{\frac{1}{2}}} = O(\varepsilon^{-1})$$

Then it is reasonable to assume that the velocity of the jet behaves like:

$$v_z \sim C\varepsilon^{\alpha},$$

now if we use the simulations obtained with the algorithm, we would have

$$\ln\left(v_z\right) \sim \alpha \ln(\varepsilon) + \ln C,$$

therefore, if we use a linear fitting to the graph of $\ln\left(v_z\right)$ against $\ln(\varepsilon)$ we can obtain an approximate value of α using the values obtained from the simulations.

6.4   The Velocity Using the Simulations

We will use now the simulations and an empiric definition of "jet" that includes using some of the last outputs and observing the change in the curvature in the apex. Considering outputs inside the formation that behaves like a jet, we use for all the ε cases, the times corresponding to iterations from 26,000 to 30,000, i.e., the same interval of time for all the analyzed cases. Using the respective height of the droplet, we can approximate the velocity for each case.

Considering the time against the height and fitting linearly, we can obtain an approximate velocity for each case considered, see for example in Fig. 7 the graph for the case of $\varepsilon = 0.016$.

We obtained the velocity for physically relevant cases of ε, and the residual in the respective linear fitting.
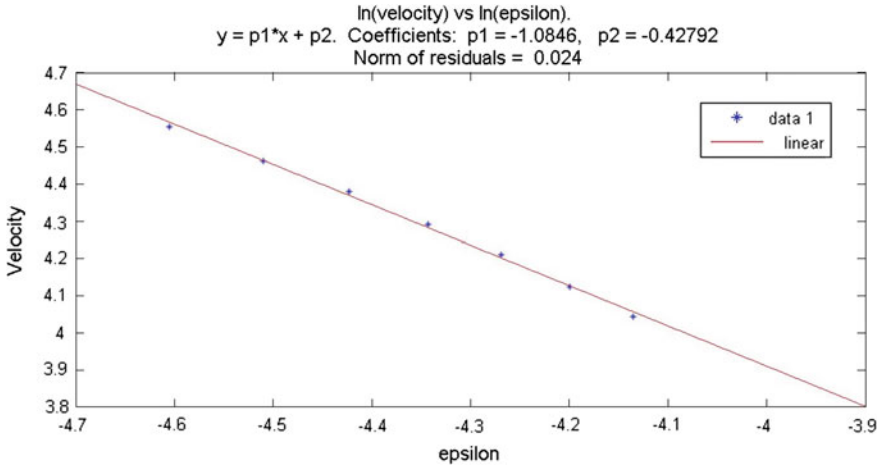
Fig. 8 Approximating ε exponent considering cases with physical relevance

ε	0.01	0.011	0.012	0.013	0.014	0.015	0.016
v_z	95.092	86.737	79.79	73.039	67.418	61.791	57.084
Residual	0.0002694	0.0003053	0.0003684	0.0004626	0.000572	0.000714	0.0008660

If we now consider the linear fitting of the logarithms of ε and v_z obtained before, we can see in Fig. 8 an approximate value to α using the coefficient of the independent variable.

$$v_z \sim \frac{1}{\varepsilon}.$$

7 Conclusions

The critical charge increases with ε. This fact agrees with the observation in Duft et al. (2003) that water droplets, containing always a certain amount of ions, are able to hold an amount of charge slightly larger than Rayleigh's limit (that is, a charge corresponding to, $Q_{c,0}$).

We can strongly suspect that we already have a relation between the velocity and the Debye-Length, i.e., the velocity will grow with smaller values of ε.

References

Beauchamp JL, Grimm RL (2003) Field-induced droplet ionization mass spectrometry. J Phys Chem B 107:14161

Beauchamp JL, Grimm RL (2005) Dynamics of field induced droplet ionization: Time-resolved studies of distortion, jetting, and progeny formation from charged and neutral methanol droplets exposed to strong electric fields. J Phys Chem B 109:8244–8250

Betelú SI, Fontelos MA, Kindelán U, Vantzos O (2006) Sigularities on charged drops. Phys Fluids 18:051706

Duft D, Achtzehn T, Müller R, Huber BA, Leisner T (2003) Rayleigh jets from levitated micro-droplets. Nature 421:128

Fontelos MA, Kindelán U, Vantzos O (2008) Evolution of neutral and charged droplets in an electric field. Phys Fluids 20:092110

Fontelos MA, Gamboa LB (2012) On the structure of double layers in Poisson-Boltzmann equation. Discrete Contin Dyn Syst Ser B 17(6):1939–1967

Garzon M, Gray LJ, Sethian JA (2014) Numerical simulations of electrostatically driven jets from nonviscous droplets Phys. Rev E 89:033011

Pozrikidis C (1992) Boundary integral and singularity methods for linearized viscous flow., Cambridge texts in applied mathematicscambridge University Press, Cambridge

Pozrikidis C (2009) Fluid dynamics: theory, computation, and numerical simulation, 2nd edn. Springer

Rayleigh L (1882) On the equilibrium of liquid conducting masses charged with electricity. Philos Mag 14:184

Sethian JA (1999) Level set methods and fast marching methods: evolving interfaces in computational geometry, Fluid mechanics. Computer vision and materials science. Cambridge University Press

Flow Measurement at the Inlet and Outlet Zones of an Automotive Brake Disc with Ventilation Post Pillars, Using Particle Image Velocimetry Technique

C.A. Jiménez García, G.J. Gutiérrez Paredes, J.E. Rivera López, A. López Villa and J.M. Casillas Navarrete

Abstract Brake system has an impact on the dynamic behavior of the vehicle, during brake episodes, the disc rotor can reach 900 °C, this rise of temperature could cause loss of brake response or failure of the braking system; to reduce overheating problems on disc rotors it is important to increase the air flux through the ventilation posts or vanes, which are between the braking surfaces of the disc brake rotors. Within this research, it is designed, produced and validated an internally ventilated disc brake rotor with a geometric configuration of 22 circular arrays of 9 ventilation pillars with drop tear shape of pillar posts, which increase air speed; to validate the model, it was produced by additive manufacturing, a prototype, to which, were carried out Particle Image Velocimetry tests on a wind tunnel to determine the distribution of air speed at the inlet and outlet of the disc, under three different rotation conditions: 187.2, 561.6 and 748.8 rpm. The results show that the geometric array has higher air speed in comparison with models, which have similar configurations.

C.A. Jiménez García (✉) · G.J. Gutiérrez Paredes · J.E. Rivera López · A. López Villa · J.M. Casillas Navarrete
Instituto Politécnico Nacional SEPI-ESIME. U.P. Azcapotzalco,
Av. de las Granjas 682 Col. Santa Catarina, C.P., 02250,
Delegación Azcapotzalco, Mexico
e-mail: tempoura@hotmail.com

G.J. Gutiérrez Paredes
e-mail: ggutierrezp@ipn.mx

J.E. Rivera López
e-mail: jriveral@ipn.mx

A. López Villa
e-mail: abelvilla77@hotmail.com

J.M. Casillas Navarrete
e-mail: casillas.juan@hotmail.com

323

1 Introduction

One of the most important devices of a car is the braking system due it's wide impact on the dynamic behaviour and on the passenger security. During severe brake episodes, like sudden stop or during continuous braking, kinetic energy is transformed into thermal energy, due to friction between brake rotor and pad, and can reach temperatures of 900 °C, according to (Talati and Jalifar 2008). The 90 % of heat is distributed and absorbed by the brake rotor; the pad absorbs the rest of heat. The rise of temperature on the brake rotors has adverse consequences, like Thermo-Elastic Instability (TEI), which causes cracking on the braking surfaces, hot spots, early wear, over heat of brake fluid and failure of braking components (Limpert 1975), such problems are reduced using vented brake rotors, which increase air flux through pillars or vanes, which are between the contact surfaces of the disc.

Talking about ventilated disc brakes, there are two internal configurations: fins and pillars (Fig. 1a). The fins, extends radially from the inner diameter of the braking track (inlet zone), to the outer diameter of the braking track (outlet zone) this is the most common configuration used in cars, but their main drawback is that under certain design conditions like low number of fins (under 20 fins) or under high angular velocities (Tirovic 2007), the air through the fins can recirculate and reduce the ventilation performance of the rotor, this problem is controlled with the rotors with pillar post configuration (Fig. 1b) which can be designed with different geometries and arrays which can increase air velocity under high angular velocities.

Different authors have focused their research on quantify, or reduce over-heat problems due to high thermal loads; Mc Phee and Jhonson (2008), used 2 dimension Particle Image Velocity (PIV) to measure air velocity through the ventilation fins of the disc rotor; Lisa Wallis et al. (2002) used CFD, to calculate heat transfer coefficient and air velocity, of three different geometry configurations and under three different angular speeds.

Taking into consideration the advantages of internally ventilated rotors with pillars, in this chapter is proposed and validated a new design of disc brake rotor
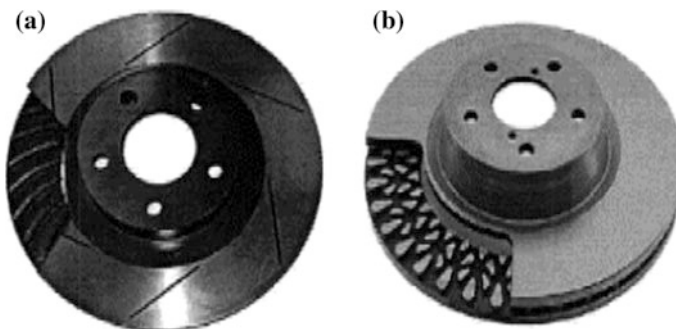
Fig. 1 **a** Brake rotor with ventilation fins. **b** Brake rotor with pillar post

with pillar posts with the aerodynamic shape of profiles NACA 4418 and NACA 66-219 (Abbott et al. 1945) which have drop tear shape. To validate the geometric array, it was produced a full scale prototype using additive manufacturing; also were built two different experimental set ups in order to measure the velocity field at the inlet and outlet zones using PIV.

2 Geometric Design

Considering the thermal distribution studied by (Jimenez 2011), on an automotive disc brake which is tested under severe braking episodes, where can be seen three thermal bands with high thermal gradients (Fig. 2a), the width of the bands is 10 mm, and have an approximate separation between bands of 12 mm (Fig. 2b). It was designed a geometric array with pillars which were located where the thermal rings appear.
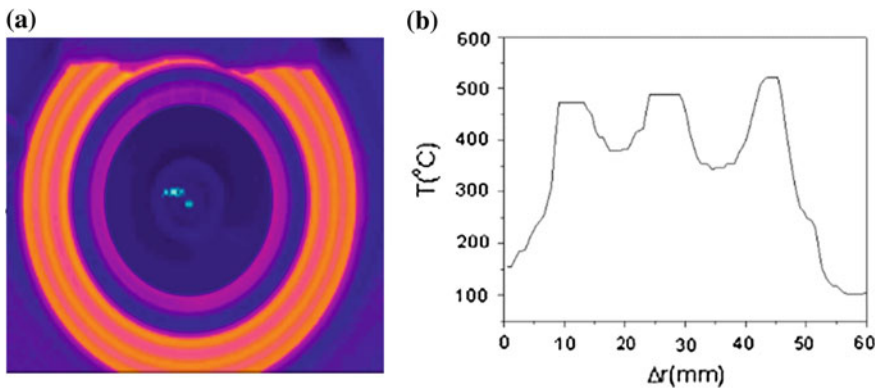
Fig. 2 a Infrared thermography of disc brake. **b** Temperature profile along the braking track

Fig. 3 Geometric array of the disc brake
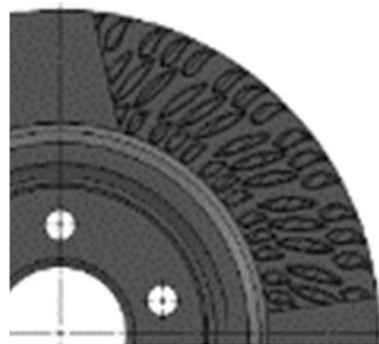
Fig. 4 Assembly process of the disc brake

On Fig. 3 is shown the array of pillars, which are distributed on 22 regular arrays of nine pillars each one. The pillars are placed on three concentric distributions, which extend from the inner diameter of the disc, to the outer diameter of the disc.

3 Prototype Manufacturing

Once modelled the disc brake, was used additive manufacturing to build a full scale prototype, using a 3D printer model Z Printer 310, due to the size limitations of the machine, the prototype was printed in three parts which were assembled, the assembly process in shown on Fig. 4.

4 Experimental Development

To measure the flow field by PIV technique, it was used the equipment described on Table 1, the tracer was glycerine smoke; the measure at the inlet and outlet zones was carried out under three different rotational speeds: 187, 561 and 748 rpm.

Table 1 PIV characteristics

Cameras	Brand	Hamatsu photonics Nikon Hi sense
	Description	Digital Camera CCD
	Model	MKll C8484-03C
	Output (pixels)	1344 × 1024
Laser source	Brand	Litron Laser
	Laser type	Nd:Yag
	Maximum power output	1200 mJ
	Length pulse	4 μs
	Wavelength	1064 nm
Positioning system (traverse)	Brand	Isel 3D traverse
	Degrees of freedom	3

Number	Description
1	Wind Tunnel
2	Camera CCD
3	Shaft
4	Motor CA
5	Disc prototype
6	Windows
7	Smoke machine
8	Flux aligners
9	Laser
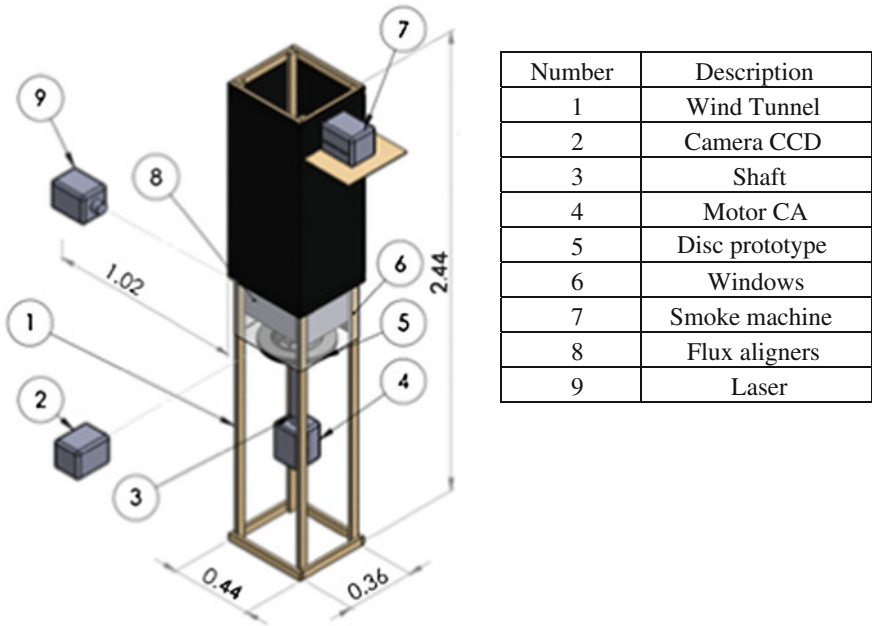
Fig. 5 Wind tunnel

4.1 Experimental Set Up

To measure the flow field at the inlet zone, it was built a wind tunnel (Fig. 5), which has flow aligners, which are separated 10 cm from the disc, the disc prototype is connected to a monophasic motor and to a voltage inverter whose function is to control the angular velocity of the disc.

To measure the flow field at the outlet zone, the set up was turned horizontally as shown in Fig. 6.

On the Table 2 are described the different measuring conditions, all the measures were made with a laser intensity of 35 %.

To calibrate both experimental set ups, first were fixed the RPMs of the disc, using a tachometer and a voltage inverter, the second parameter to calibrate is the scale factor, which consist on showing the software (Dynamic Studio) the relationship between the amount of pixels of a picture recorded by the cameras, with a length parameter.

Fig. 6 Experimental set up
to measure outlet zone

Table 2 Measuring
conditions

Condition	RPM	Time between pulses (μs)
Inlet	187	3500
	541	3000
	748	1500
Outlet	187	500
	541	250
	748	100

5 Results

Figure 7 shows the velocity field measured at the inlet zone, for each measuring points, the black vertical lines represent the limits of the inlet zone, the horizontal white rectangles indicate the brake tracks. For each rotation condition of the disc, can be seen that velocity increments at the limits of the inlet zone, the increment is due to the drag caused between the brake track and the viscous effects of the air. Not considering the drag effects, under the regime of 187 rpm, the velocity is 0.22 m/s, for 561 rpm the velocity is 0.26 m/s and finally for 748 rpm the air velocity is 0.75 m/s.

The velocity field at the outlet zone, for the three angular speeds, is shown on Fig. 8, for the angular speed of 187 rpm, the outlet velocity is 2.59 m/s, for 561 rpm the velocity is 4.7 m/s and for 748 rpm the velocity is 5.16 m/s. It is important to say that the length where the outlet flux reaches its maximum deceleration is 70 mm, this condition is due to the design of the disc which conducts the air to the external part of the rim.
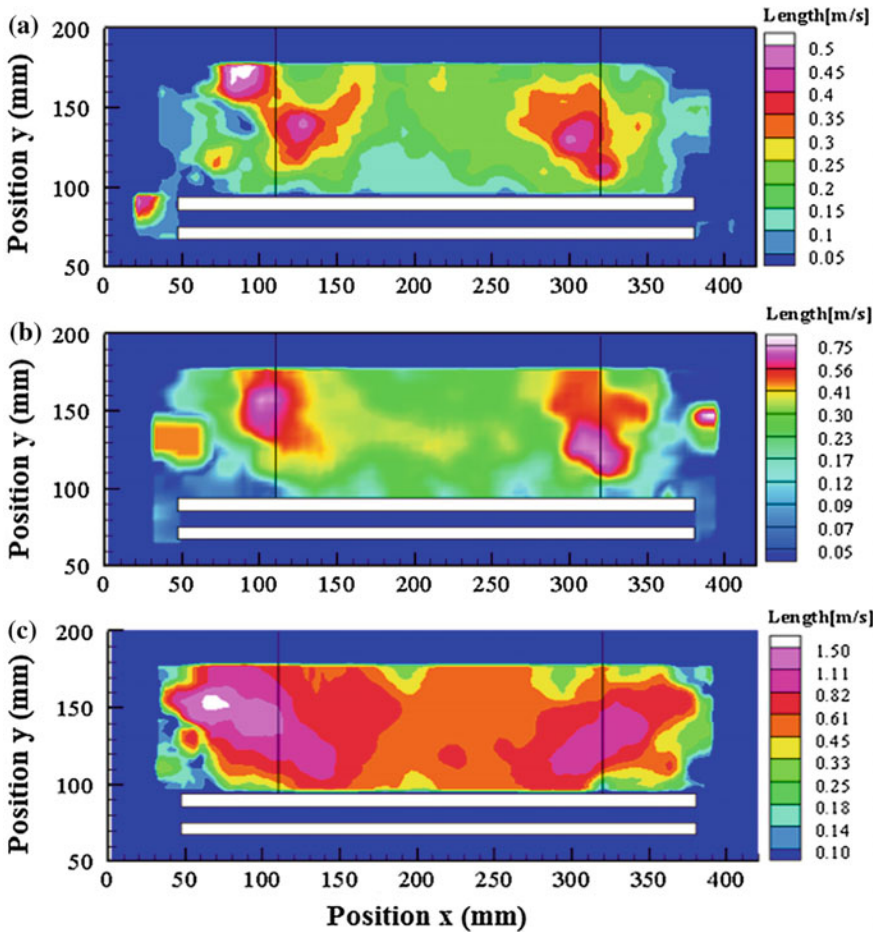
Fig. 7 Velocity field at the inlet zone. **a** 187 rpm, **b** 561 rpm, **c** 748 rpm

The velocity profiles at the inlet (Fig. 9a) and outlet (Fig. 9b) zones; at the inlet zone the rise of velocity is not significant (0.22 m/s for 187 rpm and 0.24 m/s for 561) however, at a rotational speed of 748 m/s the velocity has an increment of 47 % compared with the lowest angular speed (187 rpm), this is due to the mass conservation principle and the design of the pillars.

At the outlet zone, there is an important rise of velocity respect to the inlet zone, the increment is due to the centrifugal force through the pillars this would have an impact on the dissipation of heat by forced convection.

Fig. 8 Velocity field at the outlet zone
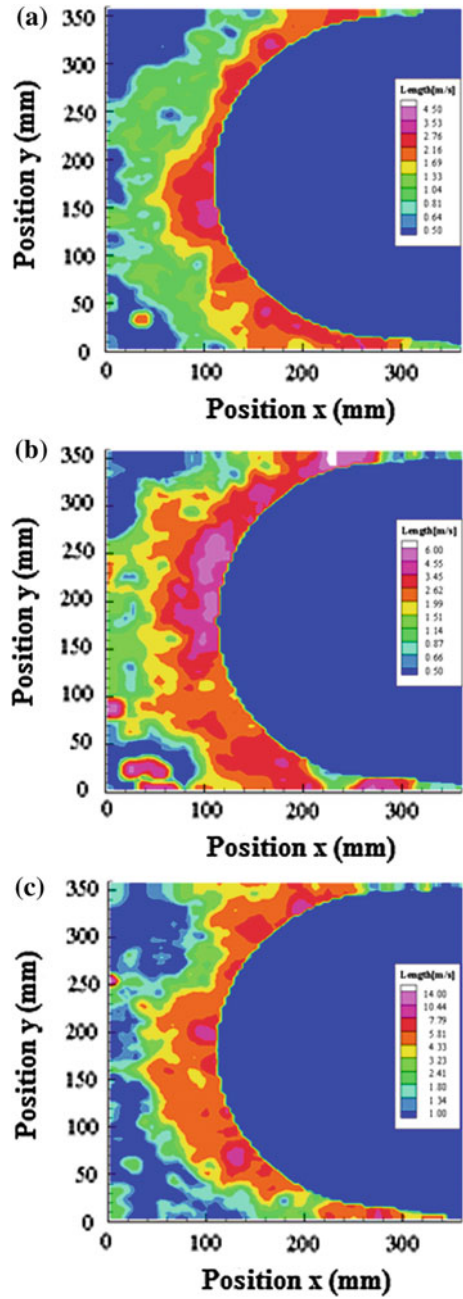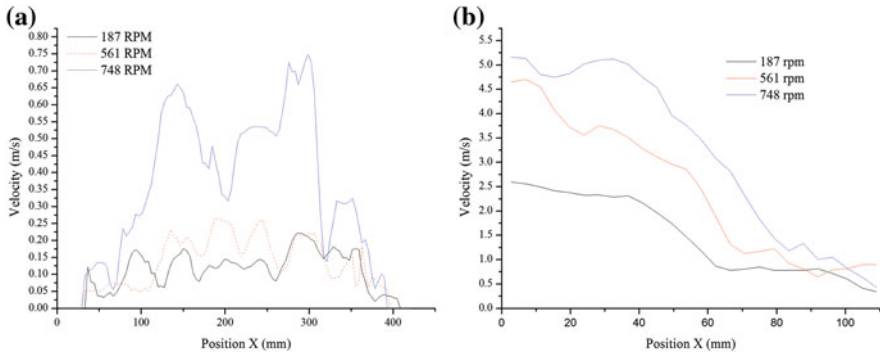
Fig. 9 **a** Velocity at inlet zone. **b** Velocity at outlet zone

6   Conclusions

PIV technique is a non-invasive method to measure velocity fields without disturbing air flux.

Additive manufacturing process, is a method which reduces the time to get the disc brake prototype.

On the measure, is not taken into account the affectation of other components on the brake system like transmission shafts or suspension components.

At the inlet zone the air flux is not affected by rotational effects of the brake disc track.

In the case of the outlet zone, the flow velocity is approximately equal to the stagnation conditions of the environment; this condition occurs at 110 mm of the disc, this indicates that the flow is three-dimensional.

Comparing the speed of 4.76 m/s under a regime of 960 rpm by (Lisa Wallis) with the speed of 5.16 m/s under a regime of 748 rpm of the proposed configuration, it has a difference of 0.4 m/s higher, this indicates that the proposed prototype is able to provide better conditions for pumping through the ventilation pillars at lower rotational speed.

The results reported by Wallis, Lisa (Wallis, Leonardi, Milton, and Joseph, Air flow and heat transfer in ventilated disc brake rotors with diamond and tear-drop pillars, 2002) using diamond-pillars, shows speeds of 0.87 m/s at187 rpm and 4.76 m/s at 560 rpm; to the proposed design was found at a point with similar speed (187 rpm) a difference of 1.72 m/s higher than reported by Lisa Wallis, for the second speed (560 rpm) there is a difference of 0.02 m/s which is lower than the reported. For practical purposes there is no difference, but it is important to note that the rate reported by Lisa Wallis is obtained by a numerical method.

Finally the geometric design has optimal ventilation characteristics, according to the experimental results.

References

Abbott IH, Von Doenhoff AE, Stivers L Jr (1945) NACA Report 824 summary of airfoil data. langley field. National Advisory Committee for Aeronautics, USA

Jimenez R (2011) Influencia de los elementos grafitizantes sobre las propiedades mecánicas y térmicas de un disco de freno de hierro gris hipereutéctico. Tesis SEPI ESIME UA, Mexico

Limpert R (1975) Cooling analisis of disc brake rotors. In: Truck meeting. Society of Automotive Engineers, Philadelphia

McPhee A, Johnson D (2008) Experimental heat transfer and flow analysis of a vented brake rotor. Int J Therm Sci 47(4):458–467. doi:10.1016/j.ijthermalsci.2007.03.006

Talati F, Jalifar S (2008) Investigation of heat transfer phenomena in a ventilated disc brake rotor with straight radial rounded vanes. J Appl Sci 8(20):3583–3592. doi:10.3923/jas.2008.3583.3592

Tirovic M (2007) Development of ventilated brake discs. In: JUMV International automotive conference with exhibition, Beograd, Servia

Wallis L, Leonardi E, Milton B, Joseph P (2002) Air flow and heat transfer in ventilated disc brake rotors with diamond and tear-drop pillars. Numer Heat Transf, Part A: Appl 41(6–7):643–655

Part IV
General Fluid Dynamics
and Applications

Bouncing Droplets, Pilot-Waves, and Quantum Mechanics

Tomas Bohr, Anders Andersen and Benny Lautrup

Abstract Bouncing droplets on a fluid surface have recently been shown to provide a surprising analogy to quantum behaviour. Here we discuss the limitation of this analogy in the context of the double-slit experiment, which our colleagues and we have analysed in a recent paper [Phys. Rev. E **92**, 013006 (2015)]. The present paper is based on the talk given by Tomas Bohr at the XX Congreso de la División de Dinámica de Fluidos, Sociedad Mexicana de Física, Centro Mesoamericana de Física Teórica, Tuxtla Gutiérrez, November 2014.

1 Introduction

Recently, it has been suggested that it is possible to "simulate" quantum mechanics by wave-driven particles (droplets) bouncing on a fluid surface (Eddi et al. 2009, 2012; Fort et al. 2010; Bush 2010, 2015a, b; Couder and Fort 2012; Harris and Bush 2014; Oza et al. 2014; Perrard et al. 2014a, b). Indeed it has been possible to demonstrate typical quantum effects such as discrete orbits and tunnelling. Furthermore, experimental results have provided evidence that the famous double-slit experiment could be reproduced in this way (Couder and Fort 2006). The fact that quantum particles can show interference just like light waves, lies at the heart of quantum mechanics, since it shows that quantum particles, although retaining their integrity and remaining localized, can interfere like waves. Thus the realization of the double-slit experiment with bouncing droplets would be a strong indication of a deep correspondence between the two systems. In a recent paper (Andersen et al.

T. Bohr (✉) · A. Andersen
Department of Physics, Technical University of Denmark, Kgs. Lyngby, Denmark
e-mail: tbohr@fysik.dtu.dk

A. Andersen
e-mail: aanders@fysik.dtu.dk

B. Lautrup
Niels Bohr International Academy, The Niels Bohr Institute, Copenhagen, Denmark
e-mail: lautrup@nbi.dk

2015), our colleagues and we have, however, argued that the double-slit experiment will be qualitatively different for quantum particles and bouncing droplets. The very fact that we can determine the precise paths followed by the droplets makes it impossible to reproduce the quantum results with such "wave-driven" particles.

In 1913, when Niels Bohr published his trilogy *On the Constitution of Atoms and Molecules*, where the structure of atoms and their characteristic spectra are derived on the basis of two novel postulates that clash violently with classical mechanics and electromagnetism, he knew that the incorporation of such new phenomena would require a radical rethinking of the basic laws of physics. Decoupling the orbital period of the electron around the nucleus from the frequency of the radiation it emits or absorbs, actually implies that the very notion of an *orbit* is ill-defined. To him it was therefore no great surprise that the new "Quantum Mechanics", when it finally emerged in 1925–26 turned out to be a *statistical* theory, only able to predict the *probability* for the time and place of certain events, and not the detailed outcome of a single event. Even though Schrödinger's wave mechanics has the appearance of a classical wave equation, these waves are not "real" waves, but probability amplitudes, complex fields, whose square modulus is a probability density.

This created a rift through the physics community between the majority, led by Heisenberg and Bohr, who believed that it was a necessity—or at least, a pragmatic approach allowing very successful calculations and predictions—and those, like Einstein, de Broglie, and Schrödinger—who felt that denouncing "realism" in such a radical fashion was not the right way forward.

In 1927, de Broglie published his reaction to the work of Schrödinger and the statistical interpretation of Born, claiming that a deterministic interpretation of the wave equation could be maintained if particles were introduced as singularites in the wave field (Broglie 1927). On p. 226, he writes: *Pour M. Born il n'y a que des probabilités ; la déterminisme des phénomènes individuels devrai être abandonné, la probabilité des phénomènes statistiques étant seule déterminée. De la manière de voir adoptée ici, au contraire, le point matériel est un réalité essentielle et son mouvement est entièrement déterminé comme étant celui d'une singularité d'amplitude dans une onde qui se propage.*

Niels Bohr reacted to this idea in an unpublished draft for his Como lecture (Bohr 1985, p. 92): *Our point of view is essentially different from that taken by de Broglie in a recent article. This author attempts to reconcile the two apparently contradictory sides of the phenomena by regarding the individual particles or light quanta as singularities in the wave field. It does not seem, however, that any such view resting on the concepts of classical physics is suited to help us over the fundamental difficulties referred to. On the contrary, the dilemma of the nature of light and material particles seems, as far as classical concepts are used, to be unavoidable and to constitute an adequate summary of the analysis of experiments.*

Later, after the work of Bohm in the 1950's, de Broglie returned to his early ideas and came up with his "double solution theory" (Broglie 1987), where he, in addition to the statistical Schrödinger wave, proposed that particles would locally excite a "real" wave field which would simultaneously guide the particle. In de Broglie's lifetime no system was known where his ideas could be tested. This changed suddenly

around 2005, when Yves Couder, Emmanuel Fort, and co-workers started looking carefully at something as far from quantum systems as droplets of silicone oil bouncing on the surface of the same fluid (Couder et al. 2005a).

2 Bouncing Droplets, Walkers, and Pilot-Waves

If a droplet of silicone oil is placed on a vertically vibrating bath of the same fluid, it can bounce and surprisingly start "walking" horizontally across the bath (Couder et al. 2005a). If the amplitude of the vibration is large enough, the bouncing droplet will never coalesce with the bath, due to the small lubricating air cushion between the droplet and the bath (Couder et al. 2005b). Increasing the amplitude of the vibration, the system will finally undergo a Faraday instability, where standing surface waves with half of the driving frequency spontaneously appear throughout the bath. Remaining close to but below this instability, one can observe a period-doubling transition, where the bouncing frequency of the droplet and the frequency of the surface waves become equal. In this regime, a symmetry breaking bifurcation can take place, where the droplet starts moving horizontally across the surface with a characteristic speed, an order of magnitude smaller than the phase velocity of the waves. The wave pattern generated by these "walkers" consists of standing waves with the Faraday wavelength, i.e., the wavelength selected by the imminent Faraday instability (Eddi et al. 2011).

Couder and Fort were immediately struck by the similarity between the walkers and de Broglie's pilot waves: the droplet creates waves in the region around it and these waves then propagate the droplet. Consequently, they set out to explore the strength of this analogy, and how closely this system could imitate quantum behaviour. They could together with their co-workers demonstrate the existence of discrete states when they rotated the oscillating bath around a central vertical axis (Fort et al. 2010), and tunnelling across a "barrier", i.e., a subsurface structure that decreases the depth of the fluid layer and thereby increases the threshold for the Faraday instability (Eddi et al. 2009). Using subsurface barriers with slit openings Couder and Fort also imitated the double-slit experiment (Couder and Fort 2006), and they fitted the single-particle statistics, i.e., the number of droplets deflected in a given angle, by a Fraunhofer diffraction and interference curve

$$f(\alpha) \; = \; A \left| \frac{\sin\left[\pi(L/\lambda_F)\sin\alpha\right]\cos\left[\pi(d/\lambda_F)\sin\alpha\right]}{\pi(L/\lambda_F)\sin\alpha} \right|, \tag{1}$$

where L is the width of each slit, d the distance between the slits, λ_F the Faraday wavelength, and A a normalization constant that depends on the total number of counts (Fig. 1). Based on the experimental data and the fit of the Fraunhofer curve, (Couder and Fort 2006, p. 3) concluded on their double-slit experiment with walkers: *The interference fringes are clearly observed and well fitted by this expression. It can be noted that a given droplet is observed to go through one or the other of the slits.*
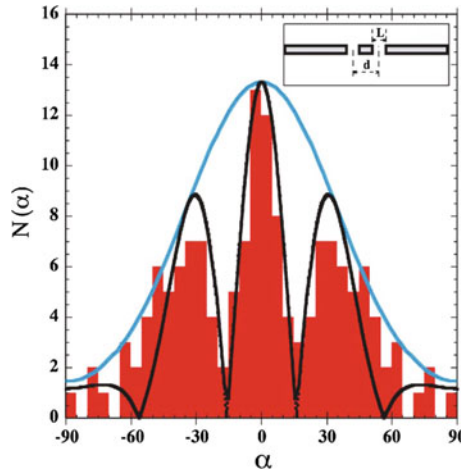
Fig. 1 Single-particle statistics for the droplets in the double-slit experiment with walkers by Couder and Fort. Experiment (*red*), Fraunhofer diffraction and interference curve (1) for a double-slit with $L/\lambda_F = 0.9$ and $d/\lambda_F = 1.7$ (*black*), and Fraunhofer diffraction curve for a comparable single-slit experiment (*blue*). Reproduced with permission from (Couder and Fort 2006)

However its associated wave passes through both slits and the interference of the resulting waves is responsible for the trajectory of the walker.

However, as pointed out in (Andersen et al. 2015), the 75 recorded droplet passages constitute a small data set with on average only approximately two counts for each of the 36 bins in the histogram (Fig. 1). The size of the data set was "doubled" by left-right symmetrization of the histogram, but that did not increase the "true" size of the data set, since the additional 75 data points were not independent. Also, the single-slit diffraction result is not backed by the experiment, since data for a comparable single-slit with the same L/λ_F value are not given by Couder and Fort (2006). Replacing the Fraunhofer curve (1) by a Gaussian distribution with zero mean value and thus deleting all the interference maxima and minima actually gives a fit that is
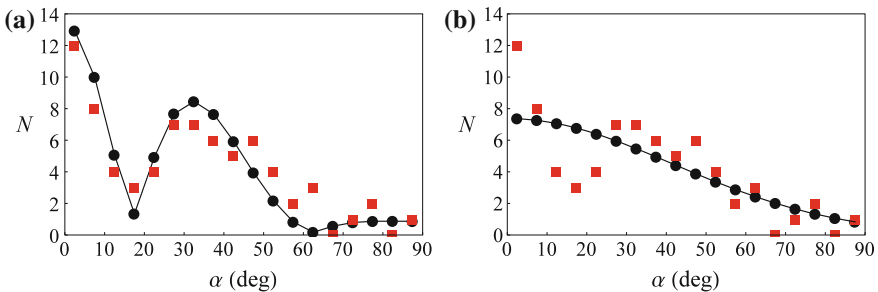
Fig. 2 **a** Fraunhofer diffraction and interference fit (black line and circles) and **b** Gaussian distribution fit (black line and circles) of the data (*red squares*) from the double-slit experiment by Couder and Fort extracted from (Couder and Fort 2006, Fig. 3)

just as good (Fig. 2). Since we do not have access to the non-symmetrised data, we fit only one half of the histogram, where there are 75 data points distributed over 18 bins. A standard approach to determine the goodness-of-fit is to use Pearson's chi-square $\chi_P^2 = \sum_{i=1}^{n_b} (O_i - E_i)^2 / E_i$, where n_b is the number of bins, O_i the observed bin counts, and E_i the modelled bin counts (Baker and Cousins 1984). To assess the quality of the fit we determine the reduced chi-square, i.e., the ratio between χ_P^2 and the number of degrees of freedom $\nu = n_b - n_c$, where n_c denotes the number of constraints, i.e., the number of parameters in the fit that are extracted from the data. A good fit should have a value of χ_P^2/ν close to unity (Bevington and Robinson 2003; Taylor 1997). For the Fraunhofer fit (1) with $L/\lambda_F = 0.9$ and $d/\lambda_F = 1.7$ as chosen by (Couder and Fort 2006), we have $\nu = 17$, since the total number of counts is known. In the Gaussian case we have $\nu = 16$, since both the total number of counts and the standard deviation of the distribution are determined from the data. We find $\chi_P^2/\nu = 3.3$ for the fit to the Fraunhofer curve and $\chi_P^2/\nu = 0.9$ for the Gaussian fit with standard deviation equal to 42 deg. The use of Pearson's chi-square for goodness-of-fit tests is well-established for large data sets, but it may not be appropriate here due to the small number of counts. An alternative method is to use the multinomial maximum likelihood estimator $\chi_{\lambda,m}^2 = 2 \sum_{i=1}^{n_b} O_i \ln (O_i/E_i)$
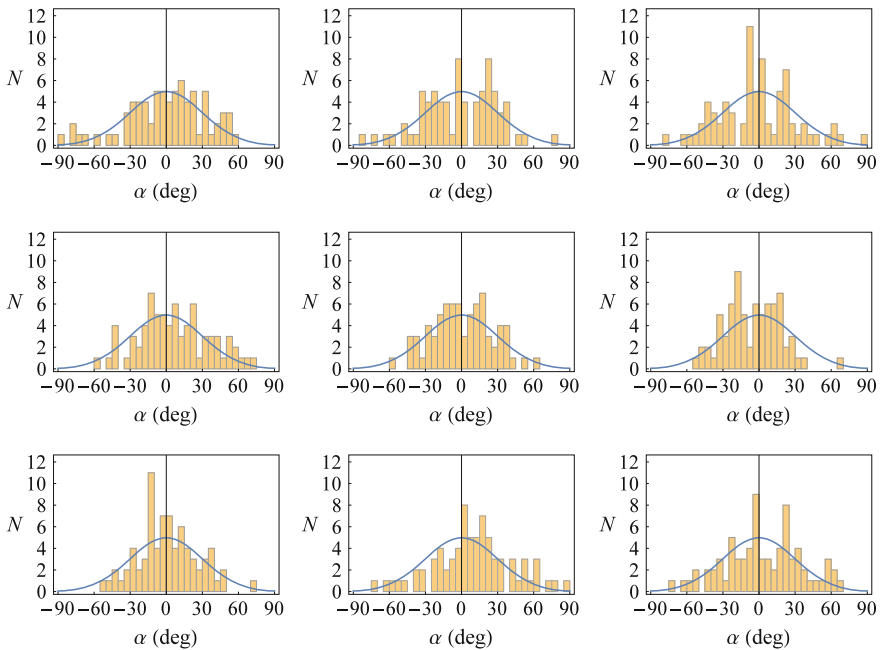
Fig. 3 Histograms (*yellow*) for an ensemble of nine independent data sets each consisting of 75 random angles drawn from a Gaussian distribution (*blue*) with zero mean value and standard deviation 30 deg. The data are binned with the same bin width as the one used by Couder and Fort for their double-slit experiment (Couder and Fort 2006, Fig. 3)
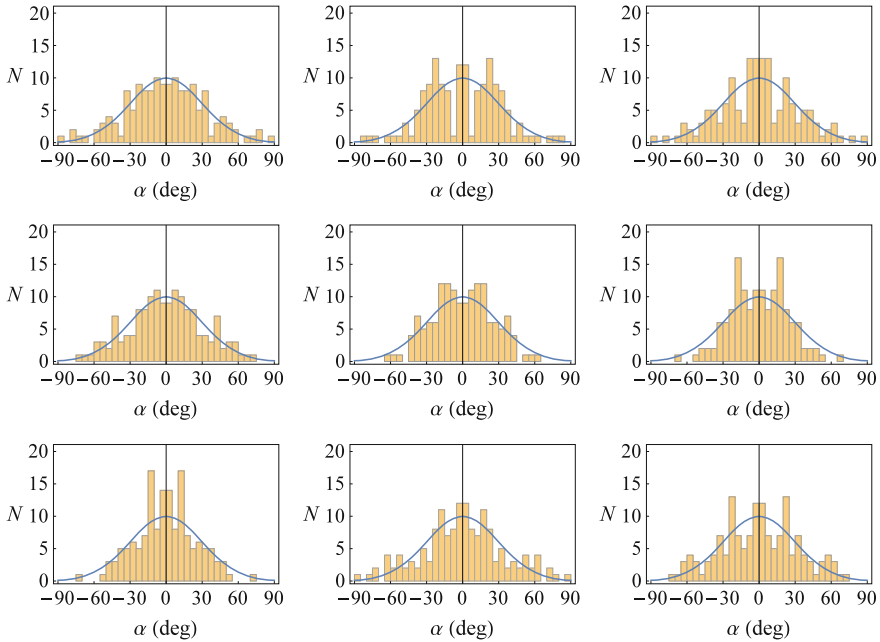
Fig. 4 Histograms (*yellow*) based on the same nine data sets as in Fig. 3 each consisting of 75 random angles drawn from a Gaussian distribution (*blue*) with zero mean value and standard deviation 30 deg, but now left-right symmetrized, thus doubling the number of data points in each data set to 150 as done by Couder and Fort for the data in their double-slit experiment (Couder and Fort 2006, Fig. 3)

when computing the reduced chi-square (Baker and Cousins 1984). Notice that in the limit of a large number of counts $\chi^2_{\lambda,m}$ degenerates to χ^2_P provided that we have $\sum_{i=1}^{n_b} O_i = \sum_{i=1}^{n_b} E_i$. We find $\chi^2_{\lambda,m}/\nu = 1.3$ for the fit to the Fraunhofer curve and $\chi^2_{\lambda,m}/\nu = 1.1$ for the Gaussian fit with standard deviation equal to 42 deg. Given the small data set, Monte Carlo simulations should ideally be used to obtain precise assessments of the goodness-of-fit for the two models (Baker and Cousins 1984).

The deceiving appearance of histograms based on small data sets can be further illustrated by ensembles of data drawn at random from a known distribution. In Fig. 3, 75 angles have been drawn from a Gaussian distribution and binned in a histogram with the same bin width as the one used by Couder and Fort for the data in their double-slit experiment (Couder and Fort 2006). This is shown for nine independent data sets and leads in some cases to histograms with strong left-right asymmetry.[1] In Fig. 4 we have left-right symmetrized the nine data sets, and we see that, in, say, one out of three cases, one might superficially find evidence for interference maxima and minima—simply due to the small number of counts.

---

[1]Note that some counts may fall outside the interval covered by the histogram, and that the number of counts in the histogram may therefore be less than 75 in some cases.

Fig. 5 Example of the wave field during slit passage in the double-slit experiment with walkers carried out by our colleagues and us. The droplet is highlighted in *red* and the subsurface barrier has been accentuated in *white*. Reproduced with permission from (Andersen et al. 2015)
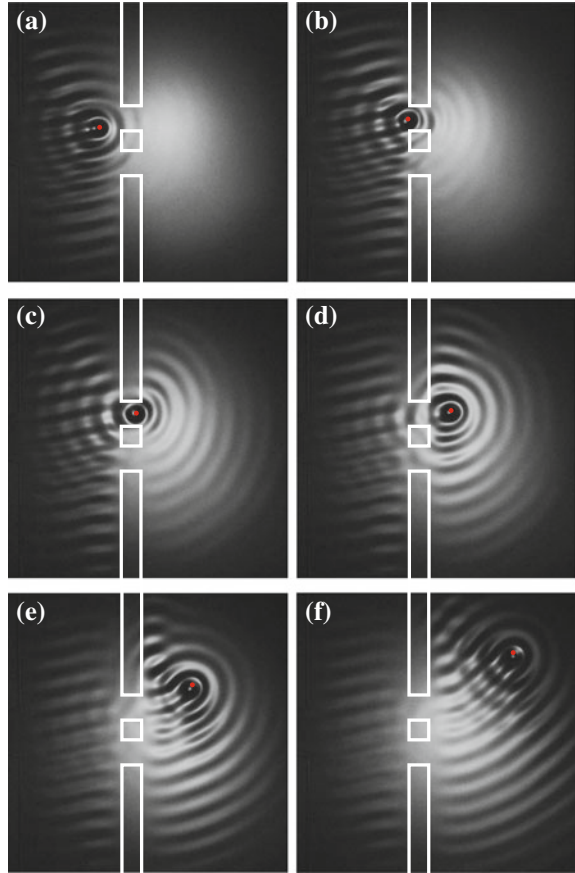
In Fig. 5 we show the wave field and the slit passage of a droplet in the double-slit experiment carried out by our colleagues and us (Andersen et al. 2015) and made with parameters similar to those in the experiment by Couder and Fort (2006). The experimental data presented in (Andersen et al. 2015) shows no evidence for interference in the single-particle statistics and indeed the wide range of passage times through the slit and the weakness of the wave passing through the slit that is not chosen by the droplet cast strong doubt on the interference claimed by Couder and Fort (2006).

3 The Double-Slit Experiment and Its Interpretation

The quantum mechanical description of the double-slit experiment is deceptively simple. One simply has to determine the wave function Ψ by solving the time-dependent Schrödinger equation

$$\left(i\hbar\frac{\partial}{\partial t} + \frac{\hbar^2}{2m}\nabla^2 \right) \Psi(\mathbf{r}, t) \; = \; 0, \tag{2}$$

where m is the mass of the quantum particle and $\hbar$ Planck's constant. The Schrö-dinger equation is a linear differential equation with properties similar to many other dispersive wave equations. In Fig. 6 we show a two-dimensional numerical solution of Eq. (2) with appropriate boundary conditions on barriers and walls for a quantum particle moving in towards a barrier with two slits. In quantum mechanics, one cannot specify both position and velocity simultaneously. The incoming quantum particle is thus represented by a wave packet. The height of the potential barriers were twice the mean energy of the wave packet. As one can see, this wave packet behaves very much like a water wave: when it reaches the two slits, part of it is reflected and the rest goes through the slits. After the slits, interference takes place and breaks the two wave packets emerging from the slits into a series of small wave packets around the interference maxima at the location of the "measuring" screen.

The strangeness arises when one tries to interpret this result in the light of the fact that the double-slit experiment with, e.g., electrons, does not lead to the formation of many small new particles. An electron is always detected as a localized particle with the same mass and charge. Thus one is forced to accept that the solution of the Schrödinger equation only leads to a statistical prediction, the probabil-
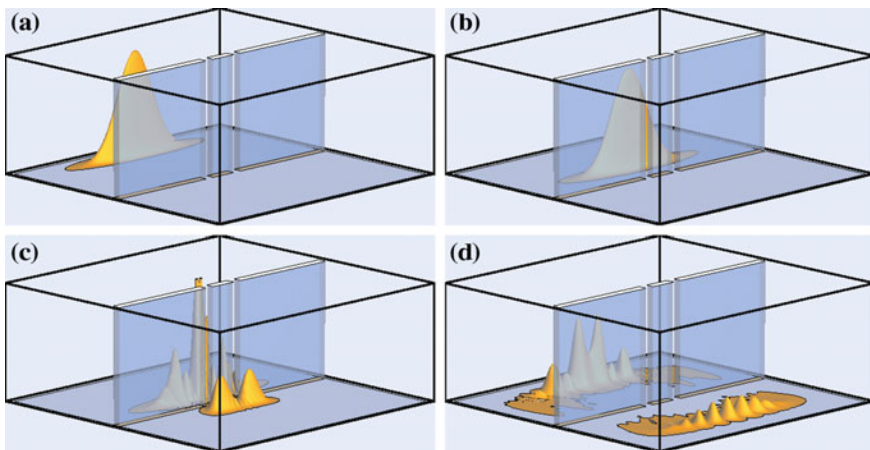
Fig. 6 Time evolution of the probability density in the double-slit experiment in quantum mechanics. Numerical solution of the time-dependent Schrödinger equation with an initial wave packet, which splits on passing the slits. Reproduced with permission from (Andersen et al. 2015)

Fig. 7 Build-up of interference pattern in the quantum mechanical double-slit experiment with electrons performed by Tonomura and co-workers (1989). Numbers of electrons are 10 (**a**), 200 (**b**), 6000 (**c**), 40000 (**d**), and 140000 (**e**). Reproduced with permission from (Tonomura 2005). Copyright (2005) National Academy of Sciences, USA
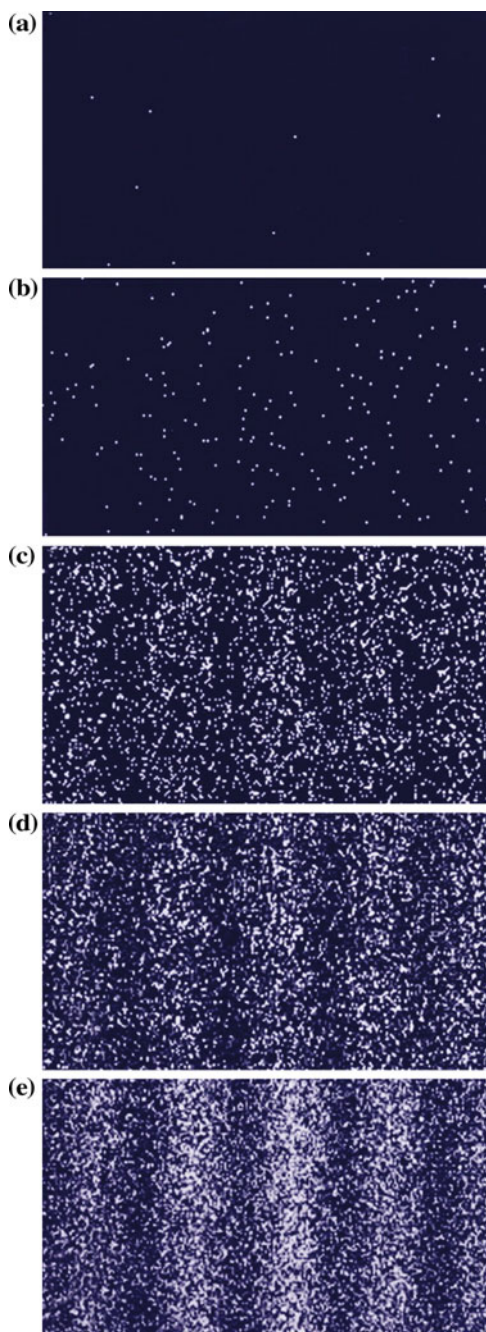
ity of a certain outcome. This is illustrated in Fig. 7 taken from the experiment by
Tonomura (1989, 2005), where an electron microscope was used to create a double-
slit experiment with one electron passing through at a time. Each bright spot (elec-
tron) apparently arrives at a random position on the screen, but after some time an
interference pattern with clear maxima and minima emerges.

These strange correlations are at the heart of quantum mechanics and they are
closely related to the existence of "entanglement", where two particles remain cor-
related despite their lack of precise orbits. Such states were introduced theoretically
by Einstein et al. (1935) to point out the "incompleteness" of quantum mechanics.
In his response, Bohr (1935) made an analogy to the double-slit experiment in a
situation, where one tries to measure the path taken by the particle by allowing the
"diaphragm" containing the two slits to recoil - thus creating a "two-particle" system
consisting of the particle and the diaphragm.

4 Quantum Mechanics with "Real" Particles

The walking droplets have been successfully modelled in situations where no bound-
aries or barriers need to be taken into account. The current status is forcefully re-
viewed in (Bush 2015a, b). In this way one can model, e.g., the discrete Landau-like
circular orbits found when the oscillating bath is rotated around a central vertical axis
(Fort et al. 2010) or the hydrogen-like states found in a central force-field created by
adding magnets (Perrard et al. 2014a). In the double-slit experiment, however, we
cannot neglect boundaries and barriers, so in (Andersen et al. 2015), we have taken a
very different approach, further separated from the experiments. Following the ideas
of de Broglie we have tried to write down a simple model explicitly containing par-
ticles, which might, in an average sense, contain standard quantum mechanics. As
our wave equation we choose

$$\left(i\hbar \frac{\partial}{\partial t} + \frac{\hbar^2}{2m} \nabla^2 \right) \Psi(\mathbf{r}, t) \; = \; A(\mathbf{r}, t)\, \delta[\mathbf{r} - \mathbf{R}(t)], \tag{3}$$

where a particle is present at position $\mathbf{R}(t)$, which creates an inhomogeneity in the
form of a δ-function with amplitude A at the position of the particle. The choice
of the Schrödinger equation as the homogeneous wave equation is mostly a matter
of convenience: it should be a non-dissipative, dispersive equation. Of course, the
experiment *is* damped (and forced), but this is probably not a feature to emulate,
if we want a fundamental equation underlying quantum mechanics. The dispersive
nature is dictated by observation: we know from de Broglie's association of particle
and wave properties, that the wavelength λ of a quantum particle should be related
to its momentum p as:

$$\lambda = \frac{h}{p} \tag{4}$$

and thus waves with different wavelengths should travel with different speeds.

Now, the wave equation (3) introduces a particle position, and thus we need another equation to determine the particle dynamics. A natural choice is the "guiding" equation used by de Broglie and Bohm, relating the velocity of the particle to the phase Φ of the complex wave field Ψ

$$\dot{\mathbf{R}}(t) = \frac{\hbar}{m}\nabla\Phi\bigg|_{\mathbf{r}=\mathbf{R}(t)}. \tag{5}$$

The dynamical equations (3) and (5) constitute two strongly non-linear coupled equations, which are obviously very hard to solve. In (Andersen et al. 2015) it is shown that one can solve for a free particle moving on a straight line, and also that, for a particle executing a classical bound orbit, e.g., in the harmonic oscillator, one obtains discrete states satisfying a condition like the Bohr-Sommerfeld quantisation rule of the old quantum mechanics. For this latter result, it is, however, important that the equations obey Galilean covariance, which dictates the choice of the amplitude $A(\mathbf{r}, t)$.

We should note that, although the above dynamical equations are inspired by de Broglie's work, they are not to be found there. In particular, we have not found an equation in his work, like our Eq. (3), relating the field to the particle position. So this is entirely our own responsibility. We should also stress the strong difference to Bohmian mechanics (Bohm 1952a, b), where the standard, homogeneous Schrödinger equation (2) is retained without any reference to the particle position. In Bohm's theory the particle is moved by the wave, but the wave is not created by the particle.

5 A Modified Double-Slit Experiment

To directly solve Eqs. (3) and (5) for the double-slit experiment seem forbiddingly hard—even numerically. What we can do instead is to give a simple argument, that shows why this type of dynamics can never reproduce the quantum behaviour in all its strangeness. To do that, we modify the double-slit experiment slightly, so as to enhance the strange quantum behaviour. Before the barrier with the two slits we insert between the slits a long "splitter plate" perpendicular to the barrier (Fig. 8). Thereby we effectively "split the world" before the particle reaches the two slits, and thus force it to "choose its path" already when it reaches the up-stream end of the splitter plate.

In quantum mechanics such a splitter plate presents no more problems than it would for water waves. The wave simply moves around the plate, retaining the symmetry between the slits and the interference maxima and minima are basically unchanged (Fig. 9). This is not so for the walking droplets or for our "quantum" particles described by Eqs. (3) and (5). Here, when a particle reaches the splitter plate, its path must be deflected either toward one or the other of the slits. Let us say that it moves
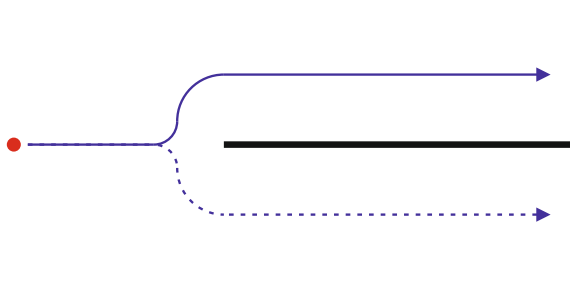
Fig. 8 The modified double-slit experiment with a splitter place inserted before the slits. Reproduced with permission from (Andersen et al. 2015)
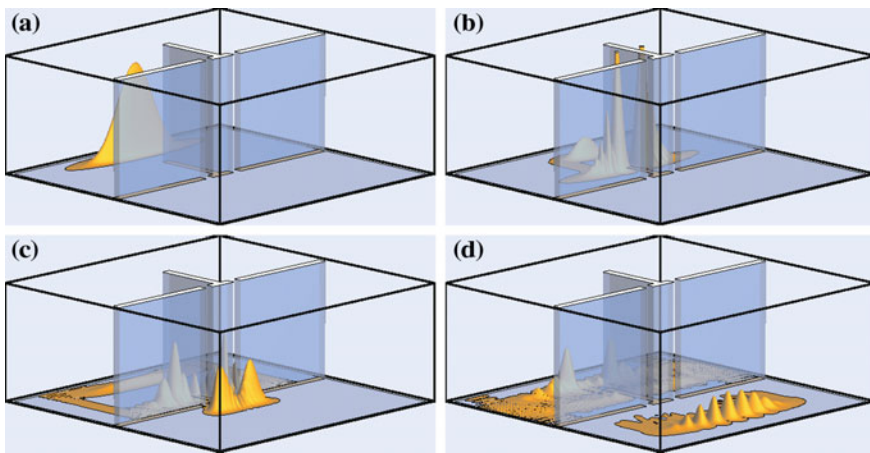
Fig. 9 Time evolution of the probability density in the modified double-slit experiment with a splitter plate in quantum mechanics. Reproduced with permission from (Andersen et al. 2015)

toward the upper slit as shown in Fig. 8. On this path the wave field resembling that of a free particle (perhaps with the addition of an image field to give the right boundary condition on the plate) will move with the speed of the particle. The lower path, however, is in a region where there is no particle and thus no forcing. Thus the initial wave field will decay there, due to its dispersive nature: the initial, localized wave field will have components moving with different velocities, which implies that the wave field will spread and decay. Thus, if the plate is long, and the time to move along it correspondingly large, the particle that finally emerges from the upper slit will see a very weak and dispersed field from the other slit, which cannot change its direction significantly. In fact part of the wave field from the lower slit might emerge only after the particle has hit the measuring screen.

Thus, even though a walking droplet can of course interfere with its own wave going through the other slit, the effect will be far from the quantum mechanical version. In quantum mechanics, Feynman's path integral formulation implies that all

possible paths leading, say, from the starting point where the wave packet is introduced (the red dot in Fig. 8) to a point on the screen contribute according to their "action", irrespective of whether a particle has actually chosen that path or not. This equality of paths is broken in the experiment and in our extended quantum theory, since one of the paths is singled out due to the presence of the "real" particle. In the experiment, such a splitter plate would effectively destroy the contribution from the "other" slit if it is long enough. Here "long enough" means that the time it takes the particle to move the length of the splitter plate should be much longer than the *memory time* that determines for how long the wave field created by a droplet will persist (Eddi et al. 2011).

6 Discussion

In conclusion we see that the very fact that the particles' orbits remain well-defined while they generate the "pilot-waves" around them leads to non-quantum behaviour. Both Couder and Fort (2012) and Bush (2010) note that the uncertainty principle obviously does not work here: we can see the orbits of droplets because the photons that we use to observe them impart negligible momentum compared to that of the droplet. However, they envisage that a quantum like uncertainty might reappear if one could only observe the droplets by, say, making them collide with similar droplets in the spirit of Heisenberg's famous γ-ray microscope. However, as stressed by Bohr in the draft for the Como lecture mentioned in the beginning (Bohr 1985), uncertainty is not a question of the limitation of specific measurements. It is an intrinsic property of the particle due to wave mechanics, meaning that it does not even make sense to think of quantum particles in a "realistic" way, i.e., one where they are attributed a well-defined space-time trajectory. Thus, in the aforementioned draft, after introducing Heisenberg's recent uncertainty relations, Bohr continues (p. 93): *It must be remembered, however, that the uncertainty in question is not a simple consequence of a discontinuous change of energy and momentum say during an interaction between radiation and material particles employed in measuring the space-time coordinates of the individuals. According to the above considerations the question is rather that of the impossibility of defining rigorously such a change, when the space-time coordination of the individuals is also considered.*

That deterministic wave-driven particle systems like walking droplets are not capable of reproducing the strangeness of the quantum mechanical double-slit experiment does not render such systems unworthy of attention. Walking droplets are spectacular fluid dynamical systems in their own right, and, e.g., the interaction of walkers with subsurface obstacles and boundaries form fascinating and at present basically unexplored sets of research problems. Wave-driven particle systems may help us in pinpointing the fundamental differences between quantum mechanics and classical physics and form an instructive classical analogy for some quantum phenomena such as orbital quantisation and possibly for many-particle systems for which the analogy is largely unexplored.

We are thankful to Jacob Madsen, Sonja Rosenlund Ahl, Christian Reichelt, Clive Ellegaard, and Mogens T. Levinsen for the fruitful collaboration leading to our joint work (Andersen et al. 2015). We also thank Yves Couder and John Bush for inspiration and for many stimulating discussions.

References

Andersen A, Madsen J, Reichelt C, Rosenlund Ahl S, Lautrup B, Ellegaard C, Levinsen MT, Bohr T (2015) Double-slit experiment with single wave-driven particles and its relation to quantum mechanics. PRE 92:013006

Baker S, Cousins RD (1984) Clarification of the use of chi-square and likelihood functions in fits to histograms. Nucl Instrum Methods Phys Res 221:437–442

Bevington PR, Robinson DK (2003) Data reduction and error analysis for the physical sciences, 3rd edn. McGraw-Hill Higher Education

Bohm D (1952a) A suggested interpretation of the quantum theory in terms of hidden variables. i. Phys Rev 85:166–179

Bohm D (1952b) A suggested interpretation of the quantum theory in terms of hidden variables. ii. Phys Rev 85:180–193

Bohr N (1935) Can quantum-mechanical description of physical reality be considered complete? Phys Rev 48:696–702

Bohr N (1985) Collected works, vol 6. North Holland

Bush JWM (2010) Quantum mechanics writ large. Proc Natl Acad Sci USA 107:17455–17456

Bush JWM (2015a) Pilot-wave hydrodynamics. Ann Rev Fluid Mech 47:269–292

Bush JWM (2015b) The new wave of pilot-wave theory. Phys Today 68(8):47–53

Couder Y, Fort E (2006) Single-particle diffraction and interference at a macroscopic scale. Phys Rev Lett 97:154101

Couder Y, Fort E (2012) Probabilities and trajectories in a classical wave-particle duality. J Phys: Conf Ser 361:012001

Couder Y, Protière S, Fort E, Boudaoud A (2005a) Walking and orbiting droplets. Nature 437:208

Couder Y, Fort E, Gautier C-H, Boudaoud A (2005b) From bouncing to floating: noncoalescence of drops on a fluid bath. Phys Rev Lett 94:177801

de Broglie L (1927) Le mécanique ondulatoire et la structure atomique de la matière et du rayonnement. Le Journal de Physique et le Radium, VII I(5):225–241

de Broglie L (1987) Interpretation of quantum mechanics by the double solution theory. Ann Fond Louis de Broglie 12(4):1–23

Eddi A, Fort E, Moisy F, Couder Y (2009) Unpredictable tunneling of a classical wave-particle association. Phys Rev Lett 102:240401

Eddi A, Sultan E, Moukhtar J, Fort E, Rossi M, Couder Y (2011) Information stored in Faraday waves: the origin of a path memory. J Fluid Mech 674:433–463

Eddi A, Moukhtar J, Perrard S, Fort E, Couder Y (2012) Level splitting at macroscopic scale. Phys Rev Lett 108:264503

Einstein A, Podolsky B, Rosen N (1935) Can quantum-mechanical description of physical reality be considered complete? Phys Rev 47:777–780

Fort E, Eddi A, Boudaoud A, Moukhtar J, Couder Y (2010) Path-memory induced quantization of classical orbits. Proc Natl Acad Sci USA 107:17515–17520

Harris DM, Bush JWM (2014) Droplets walking in a rotating frame: from quantized orbits to multimodal statistics. J Fluid Mech 739:444–464

Oza AU, Harris DM, Rosales RR, Bush JWM (2014) Pilot-wave dynamics in a rotating frame: on the emergence of orbital quantization. J Fluid Mech 744:404

Perrard S, Labousse M, Miskin M, Fort E, Couder Y (2014a) Self-organization into quantized eigenstates of a classical wave-driven particle. Nature Comm 5:3219

Perrard S, Labousse M, Fort E, Couder Y (2014b) Chaos driven by interfering memory. Phys Rev Lett 113:104101

Taylor JR (1997) An introduction to error analysis, 2nd edn. University Science Books

Tonomura A (2005) Direct observation of thitherto unobservable quantum phenomena by using electrons. Proc Natl Acad Sci USA 102:14952–14959

Tonomura A, Endo J, Matsuda T, Kawasaki T (1989) Demonstration of single-electron buildup of an interference pattern. Am J Phys 57:117–120

Phenomena of a Miscible Drop Through a Stratified Fluid

A. Zarazúa Cruz, C. Echeverría Arjonilla, D. Porta Zepeda and C. Stern Forgach

Abstract This work describes the dynamics of a drop of benzyl alcohol, (partially miscible in water), as it traverses a stratified fluid formed by two layers, water on the top and salted water with a 1.68 molar concentration on the bottom. The width and stability of the interface depends on the temperature and on the way the upper layer mixes as it is introduced into the container. In this case, the procedure was controlled to produce a stable interface for several minutes, and to have a repeatable experiment. The width and position of the interface was measured each time through shadowgraphs. The processes that occur during the fall of the drop depend on various parameters like its geometry, the width of the upper layer and the density of the lower layer. First the drop seems to have a free fall. After it enters in contact with the interface, the behavior is similar to a damped harmonic oscillator. The drag force was calculated using models for a rigid sphere and for an ellipsoid with varying dimensions. A comparison between the measured and the calculated values is presented in a graph.

1 Introduction

The first analytical solution for the drag force about a sphere for Reynolds numbers equal or smaller than one, was given by Stokes in 1851. Stoke's law has many applications, including the falling-sphere viscometer, understanding the swimming of microorganisms and sperm the stationary behavior of droplets and small crystals

A. Zarazúa Cruz (✉) · C. Echeverría Arjonilla · D. Porta Zepeda · C. Stern Forgach
Facultad de Ciencias, UNAM, Ciudad Universitaria, Av. Universidad 3000,
Circuito Exterior S/N Delegación Coyoacán, C.P. 04510 Mexico D.F., Mexico
e-mail: zarknj@gmail.com

C. Echeverría Arjonilla
e-mail: carlosea1982@gmail.com

D. Porta Zepeda
e-mail: alviond@gmail.com

C. Stern Forgach
e-mail: catalina@ciencias.unam.mx

in the clouds and the determination of the terminal velocity of a sphere falling through a stationary fluid. However, for Reynolds numbers larger than one and for geometries other than a sphere, several models have been suggested.

With the contributions of Basset (1888), Boussinesq (1895) and Oseen (1927) the equation of motion known as BBO, for a spherical particle, was proposed. Based on this equation, Tchen suggested in (1949) an equation of motion for a particle in a turbulent flow. This work was further developed by Corrsin and Lumley (1956) and later by Beuvich (1966). Finally in 1983, Maxey and Riley proposed the following equation for small particles in non-uniform and unsteady flows:

$$
\frac{m\,dv_i}{dt} =
\begin{cases}
mg_i & \textbf{I} \\
+ V_d\left(-\frac{\partial p}{\partial x_i} + \frac{\partial \tau_{ij}}{\partial x_j}\right) & \textbf{II} \\
+ 3\mu\pi D\left[(u_i - v_i) + \frac{D^2}{24}\nabla^2 u_i\right] & \textbf{III} \\
+ \frac{1}{2}\rho V_d \frac{d}{dt}\left[(u_i - v_i) + \frac{D^2}{40}\nabla^2 u_i\right] & \textbf{IV} \\
+ \frac{3}{2}\mu\pi D^2 \int_0^t \left[\frac{\frac{d}{d\tau}\left((u_i - v_i) + \frac{D^2}{40}\nabla^2 u_i\right)}{\mu v(t-)^{\frac{1}{2}}}\right] d\tau & \textbf{V}
\end{cases}
\tag{1}
$$

The net force on the body, left hand side of Eq. (1) depends on five terms:

I. The first term represents the force due to gravity, that is, the weight.
II. The second term represents the pressure and shear stresses due to the undisturbed flow.
III. The third term represents the form drag force; it depends on the geometry of the particle within the flow.
IV. The fourth term is known as the virtual or added mass, and corresponds to the fluid that is accelerated at the expense of the work done by the body.
V. The fifth term is known as the historical or Basset term, and takes into account the time delay due to the development of the boundary layer.

The last two terms are very difficult to evaluate experimentally. This paper is focused on possible models for the third term. Model predictions for different geometries are compared to experimental measurements.

1.1 Drag Force

1.1.1 Spherical Model

In the case of a solid sphere, the general drag formula given by Crowe et al. (2011) is:

$$
F_D = \frac{1}{2}\rho C_D A |u_i - v_i|(u_i - v_i)
\tag{2}
$$

where C_D is the drag coefficient, ρ the density, A the area of the cross section perpendicular to the motion, u_i *and* v_i the speeds of the medium and of the drop respectively.

The drag coefficient is a function of the Reynolds number Re_r, based on the relative speed defined as:

$$Re_r = \frac{\rho D_n |u_i - v_i|}{\mu} \tag{3}$$

where D_n is the sphere diameter, and μ is the dynamic viscosity of the fluid.

For a wide range $0 < Re_r < 2 \times 10^5$, the functional form of the drag coefficient C_d is given by Timmerman and Van der Weele (1998), can be written as:

$$C_D \approx \frac{24}{Re_r} + \frac{6}{1 + \sqrt{Re_r}} + 0.4 \tag{4}$$

1.1.2 Ellipsoid of Revolution Model

The use of oblate and prolate coordinates at low Reynolds numbers, leads to the drag force around an ellipsoid of revolution (Happel and Brenner 1983):

$$FD = 6\mu\pi(u - v)ka \tag{5}$$

where k is a constant that depends on whether the horizontal (a) or vertical (b) axes are aligned with the flow (Fig. 1).

For Re > 1, the drag coefficient according to Militzer et al. (1988) is defined as

$$
\begin{aligned}
C_D = &\left[\frac{24}{Re} \left(1 + 0.15 Re^{0.687} \right) + \frac{0.42}{(1 + 42500 Re^{-1.16})} \right] \left(\frac{4+E}{5} \right) \\
&\left[1 + \frac{0.00069 Re}{E} - 0.000754 Re\, E + \frac{0.0924}{Re} + 0.00276 E^2 \right]
\end{aligned}
\tag{6}
$$

Fig. 1 Ellipsoid moving inside a fluid in the Z direction
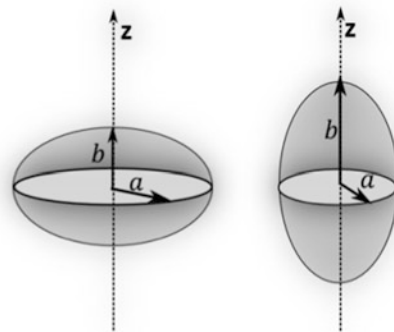
where E is the ratio between the vertical and horizontal diameters

$$E = \frac{2b}{2a} \tag{7}$$

However, for $E = 1$, the drag does not collapse to that of a sphere.

1.1.3 Model for Variable Geometry

A more general formula for the drag force for any geometry is:

$$F_D = \frac{1}{2}\rho C_D A |u_i - v_i|(u_i - v_i) \tag{8}$$

That can be rewritten as:

$$F_D = 3D\pi\mu(u_i - v_i)f \tag{9}$$

where f is the drag factor. So:

$$f = \frac{C_D Re_r}{24} \tag{10}$$

Hölzer and Sommerfeld (2008) obtained the drag coefficient for any value of the Reynolds number:

$$\begin{aligned} C_D = {} & \frac{8}{Re_r}\frac{1}{\sqrt{\phi}} + \frac{16}{Re_r}\frac{1}{\sqrt{\psi}} \\ & + \frac{3}{\sqrt{Re_r}}\frac{1}{\psi^{3/4}} + \frac{1}{\phi}0.4210^{0.4(-\log\psi)^{0.2}} \end{aligned} \tag{11}$$

where, according to expressions (9) and (10), the drag factor becomes:

$$\begin{aligned} f = {} & \frac{1}{3\sqrt{\phi}} + \frac{2}{3\sqrt{\psi}} + \frac{Re_r^{\frac{1}{2}}}{8\psi^{\frac{3}{4}}} \\ & + 0.0175\frac{Re_r}{\phi}10^{0.4(-\log\psi)^{0.2}} \end{aligned} \tag{12}$$

In Eq. (13), ϕ is the crosswise sphericity

$$\phi = \left(\frac{D_n}{D_A}\right)^2 \tag{13}$$

D_n the diameter of the equivalent volume:

$$D_n = \left(\frac{6V_c}{\pi}\right)^{1/3} \tag{14}$$

and D_A the diameter of the equivalent area:

$$D_A = \left(\frac{4A_p}{\pi}\right)^{1/2} \tag{15}$$

A_p is the projected area, represents the sphericity given by the quotient between A_s (the area of a surface with the same volume) and A (the actual area):

$$\Psi = \frac{A_s}{A} \tag{16}$$

If the volume of the falling drop is modeled as an ellipsoid, such that when a = b the model collapses to that of a sphere, then the drag force obtained changes with geometry as a function of time.

2 Experimental Set-up

In this work, the medium where the drop falls is a stratified fluid made by two layers. The upper one is pure water with volume V and density ρ values of 96.387 cm^3 and 0.9928 g/cm^3, respectively. The bottom layer has salt and the corresponding values are 269.883 cm^3 and 1.3879 g/cm^3.

To maintain an interface as thin and stable as possible, the following procedure was established: first the more dense water was introduced. Then pure water is deposited over the bottom layer through a porous medium. Figure 2 shows the width and position of the interface obtained with this technique, over time.

Fig. 2 The shadowgraphs show the interface every 5 min. Its width remains at 2 ± 0.5 mm

Interface
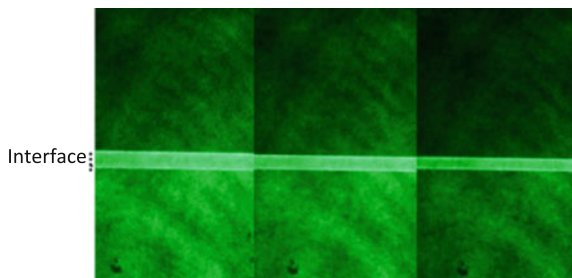
Finally, drops of benzyl alcohol are injected with a syringe that is pushed by a micrometer screw controlled by a computer, to assure that they always have the same volume.

3   Results

The coordinates of the trajectories of the drops were obtained with a 100 fps video camera and the commercial "Tracker" software. Four points were marked and monitored along the fall (Fig. 3), from time t_0 when the motion starts, until the drop stops completely.

The drop is considered symmetric with respect to the vertical axis all through the trajectory; that is, J_i and L_i remain on the axis; N_i and K_i deform the same way. The geometric center of the drop, is obtained with J_i and L_i (Fig. 3).

The trajectory of the drop is shown in Fig. 4.

Figure 5 shows a change in the geometry as the drop traverses the stratified medium. It elongates sometimes along the x axis, and sometimes along the y axis. To determine the changes in geometry, the radii along both axes were measured through the trajectory.

Fig. 3 *Four points* are followed along the trajectory of the drop; i goes from de 0 to 1372 and an image is taken every 0.01 s
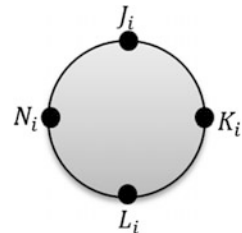
Fig. 4 Graph of the trajectory of the geometric center of the drop. The *blue lines* show the location of the interface
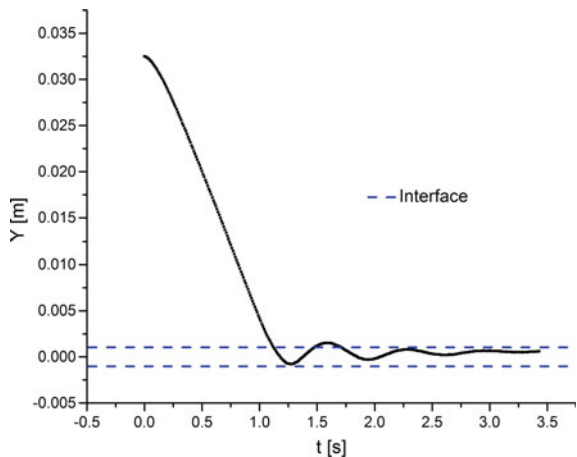
Fig. 5 Time sequence of the fall of the drop

$t_0 = 0s$

$t_1 = 1.27s$

$t_2 = 1.58s$

$t_3 = 1.95s$

$t_4 = 2.28s$

$t_5 = 2.58s$
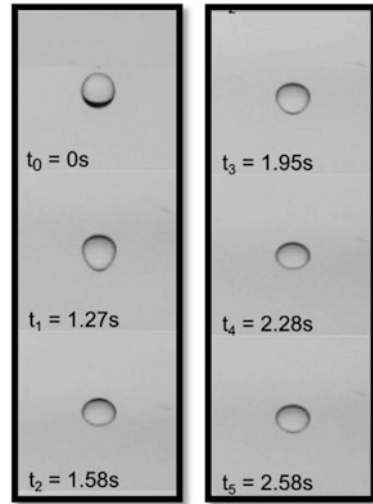
Fig. 6 Changes in the radii of the drop as a function of time
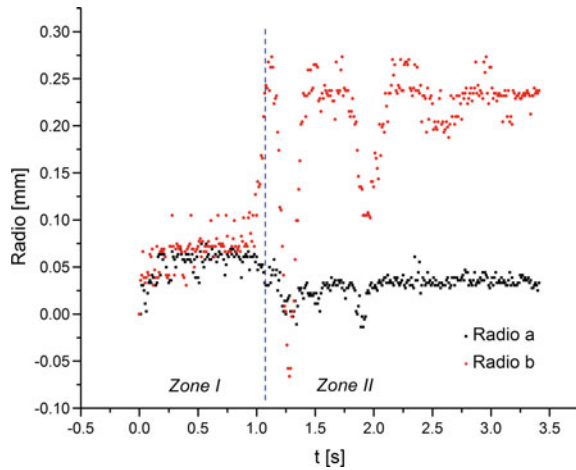
Two clearly different regions can be identified in Fig. 6, the first before the drop interacts with the interface, the second after this interaction occurs and the drop eventually stays at rest.

Before the interface, changes in a and b are small, the drop is almost spherical. The largest deformation occurs mainly along radius b (that is parallel to the stratification) 0.18 s after the drop touches the interface, that is, it does not occur immediately at the entrance of the interface. Due to the stratification, the conditions of pressure and viscosity are different at L_i and J_i when the drop enters the interface.

After the largest deformation, the drop starts to oscillate inside the interface, where it stays trapped and eventually comes to rest.

Fig. 7 Drag force for the three models
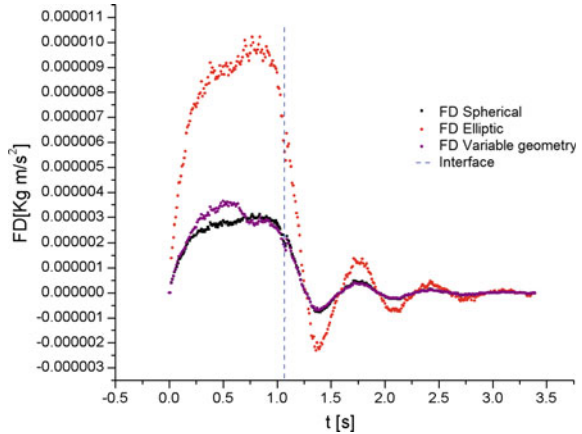
To understand the dynamics of the drop with the BBO equation, it is necessary to calculate the drag from the models suggested: a spherical rigid body, an ellipsoid of revolution and with a form factor for variable geometry. In all cases, the following hypothesis will be made.

- The viscosity and the density of the fluid correspond to those of the upper fluid.
- After point L_i touches the interface, the values of density and viscosity that will be used are those of the bottom fluid, even though it is known that this is not exact.
- The symmetry along the vertical axis is maintained.

3.1 Comparison Between Models

The drag force for each model is shown in Fig. 7.

Figure 7 shows that the drag force increases during the free fall. Inside the interface the drop seems to behave like a damped harmonic oscillator. The graph of the velocity is analogous to this figure.

The elliptic model gives the highest value for the drag, and the sphere gives the smallest.

3.2 Net Force

The net force, shown in Fig. 8, was calculated from the acceleration with the assumption that no mass is lost during the trajectory.

Fig. 8 Net force as a function of time
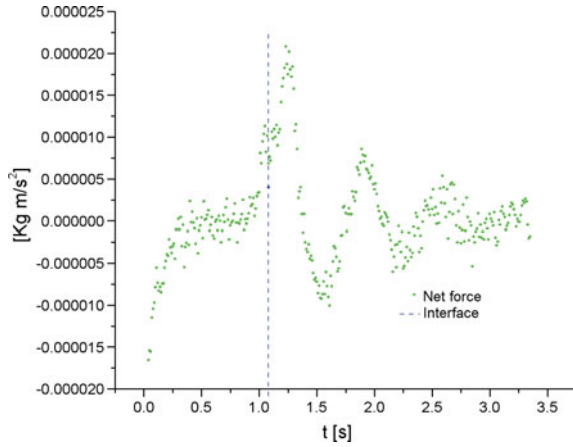
As for the drag, two well defined regions can be found, with an oscillation inside the interface. There is also a time of retardation with respect to the instant the drop touches the interface.

3.3 Comparison Between the Drag Force and the Net Force

In Fig. 9 the drag force evaluated with the different models presented in Sect. 1.1, is compared to the net force evaluated from the mass and the acceleration. In all cases, both forces are out of phase.

In is interesting to note that the three models of the drag force intercept at certain points that correspond to those instants of the trajectory where the drop is a sphere.

Fig. 9 Comparison between the net force and the drag force
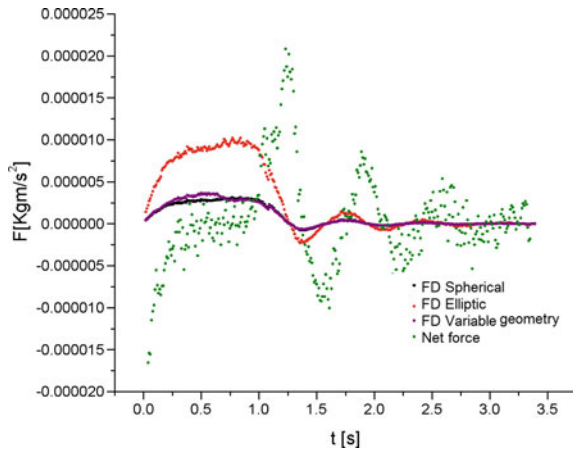
3.4 The Remaining Force

Figures 10, 11 and 12 show the difference between the net force and the drag for each of the three drag models. The remaining force is the sum of the virtual mass, Basset's historical term, the weight and the buoyancy.

In all cases, in region one, the remaining force has approximately the same size and opposite sign as the drag force. The total force is close to zero, there is no acceleration; the drop attains very fast a constant terminal velocity. The drag force increases with speed, so do both the Basset term and the added mass but in the opposite direction. The weight and the pressure terms remain constant, so they are not responsible for this effect.

In region two, the drag is negligible (almost zero) and the remaining force is of the same order of magnitude as the net force.

Fig. 10 Remaining force for the spherical model
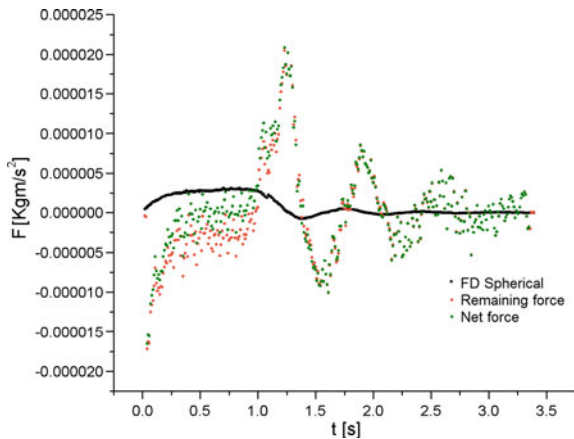
Fig. 11 Remaining force for the ellipsoid of revolution
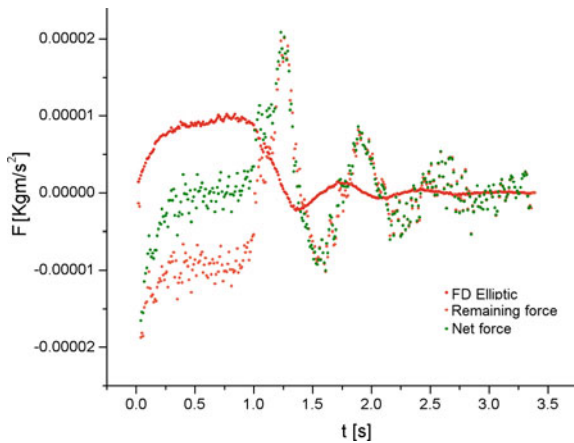
Fig. 12 Remaining force for the variable geometry model
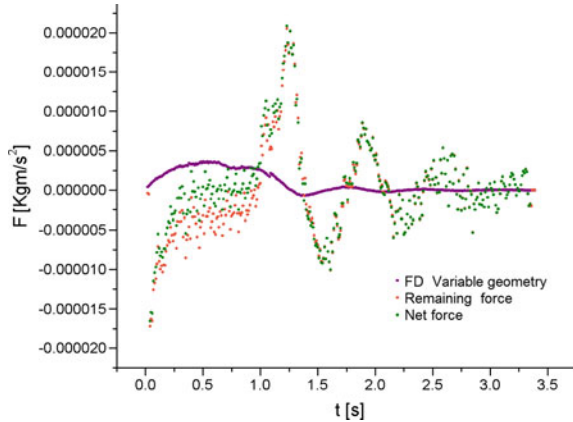
It is interesting to note that the particle does not respond instantly as it enters the interface. The time of response is probably due to the Basset and added mass terms, because the drop moves parcels of fluid behind it.

Once in the interface, the drop starts to oscillate. The density gradients in this region are very large. The Basset term doesn't play a role anymore, but the added mass does. Besides, as the density diminishes, the weight is larger than the buoyancy term and pushes the drop down; when the density increases, the buoyancy makes the drop go up. Eventually the friction stops the oscillation and the drop achieves mechanical equilibrium.

4 Conclusions

A procedure was established to create a stable interface in a stratified fluid, in location and width, for about 15 min. This allows for repeatable experiments.

The trajectories were obtained with a video of the drop as it traverses the stratified fluid and the Tracker© software. Four points on the surface of the drop were followed, and it was shown that the geometry of the drop changes along the path.

Due to the fact that the drag force is related to the geometry, it was calculated with three different models: spherical, ellipsoid of revolution and for a variable geometry. The values obtained with the elliptic model are much larger than those obtained with the other two, but they follow the same trend.

The net force that acts on each drop was determined by evaluating the acceleration of the geometric center. This force was compared at each point of the trajectory with the drag. The remaining force, calculated as the difference between the net force and the drag, changes its behavior before and after the interaction with the interface.

In region one, the drag is important but it is compensated by the remaining term so the net force is almost zero, the drop arrives very fast to a terminal velocity. At the entrance of region two, the drop does not react instantly to the change of density.

In all cases, in region one, the remaining force has approximately the same size and opposite sign as the drag force. The total force is close to zero, there is no acceleration; the drop attains very fast a constant terminal velocity. The drag force increases with speed, so do both the Basset term and the added mass but in the opposite direction. The weight and the pressure terms remain constant, so they are not responsible for this effect.

In region two, the drag is negligible (almost zero) and the remaining force is of the same order as the net force.

It is interesting to note that the particle does not respond instantly as it enters the interface. This time of reaction is probably described by the Basset term and the added mass because parcels of fluid keep moving after the drop's passage.

Once in the interface, the drop starts to oscillate. The Basset term doesn't play a role anymore, but the added mass does. Besides, the density gradients inside are very large so probably as the density diminishes, the weight is larger and pushes the drop down, when the density increases, the buoyancy makes the drop go up. Eventually the friction stops the oscillation, the drop reaches mechanical equilibrium and doesn't move any more.

5   Future Work

To generalize these observations it will be important to study drops with different volumes.

The models do not take into account the loss of mass as the drop traverses the fluid. The changes in the radii indicate that the size of the drop changes along the trajectory; this is due to a loss of mass and should be taken into account in new models. Schlieren images of the drop show this effect.

An experimental method to evaluate the Basset and virtual mass terms should be found.

References

Basset AB (1888) Treatise on hydrodynamics. Deighton Bell, London, pp 232–302
Beuvich YuA (1966) Motion resistance of a particle suspended in a turbulent medium. Fluid Dyn 1:119
Boussinesq J (1895) Théorie Analytique de la Chaleur. L'École Polytechnique, Paris 2:224
Corrsin S, Lumley J (1956) On the equation of motion for a particle in turbulent fluid. Appl Sci Res 2–3:114

Crowe CT, Schwarzkopf D, Sommerfeld M, Tsuji Y (2011) Multiphase flows with droplets and particles, 2nd edn, pp 67–96

Happel J, Brenner H (1983) Low Reynolds number hydrodynamics. 145–149:154–156

Hölzer A, Sommerfeld M (2008) New simple correlation formula for the drag coefficient of non-spherical particle. Powder Tech 184:361

Maxey MR, Riley JJ (1983) Equation of motion for a small rigid sphere in a nonuniform flow. Phys Fluids 26(4):883

Militzer J, Kan JM, Hamdullahpur F, Amyotte PR, AL Taweel AM (1988) Drag coefficient for axisymmetric flow around individual spheroidal particles. Technical University of Nova Scotia

Oseen CW (1927) Hydrodynamik. Akad. Verl.-Ges, Leipzig

Tchen, CM (1949). Mean values and correlation problems connected with the motion of small particles suspended in a turbulent fluid, Doctoral Dissertation, Delft, Holland

Timmerman P, Van der Weele J (1998) On the rise and fall of a ball with linear or quadratic drag. Centre for Theoretical Physics, University of Twente

Astrophysical Fluids of Novae: High Resolution Pre-decay X-Ray Spectrum of V4743 Sagittarii

J.M. Ramírez-Velasquez

Abstract Eight X-ray observations of V4743 Sgr (2002), observed with *Chandra* and *XMM-Newton*, are presented, covering three phases: Early optically thin hard emission (day 50.2), photospheric emission from the ejecta (days 180.4, 196.1, 301.9, 371, 526), and faint post-outburst emission (days 742 and 1286). The flux level at Earth during the first and last phase is of order $10^{-12}\,\mathrm{erg\,cm^{-2}\,s^{-1}}$ over the energy range 0.3–2.5 keV. These values are higher than an upper limit obtained in September 1990 with ROSAT. The nova thus continued fading in the soft band (0.1–2.4 keV). The nova turned off some time between days 301.9 and 371, and the X-ray flux subsequently decreased from day 301.9–526, following an exponential decline time scale of (96 ± 3) days. We use the absorption lines present in the SSS spectrum for diagnostic purposes, and characterize the physics and the dynamics of the expanding atmosphere during the explosion of the nova. The information extracted from this first stage is then used as input for computing full photoionization models of the ejecta in V4743 Sgr. The SSS spectrum is modeled with a simple black-body and multiplicative Gaussian lines, which provides us of a general kinematical picture of the system, before it decays to its faint phase (Ness et al. 2003). In the grating spectra taken between days 180.4 and 370, we can resolve the line profiles of absorption lines arising from H-like and He-like C, N, and O, including transitions involving higher principal quantum numbers. Except for a few interstellar lines, all lines are significantly blue-shifted, yielding velocities between 1000 and 6000 $\mathrm{km\,s^{-1}}$ which implies an ongoing mass loss. It is shown that significant expansion and mass loss occur during this phase of the explosion, at a rate $\dot{M} \approx (3-5) \times 10^{-4}\,(L/L_{38})\,M_{\odot}/yr$. Our measurements show that the efficiency of the amount of energy used for the motion

J.M. Ramírez-Velasquez (✉)
Physics Centre, Venezuelan Institute for Scientific Research (IVIC),
PO Box 20632, Caracas 1020A, Venezuela
e-mail: josem@ivic.gob.ve

Departamento de Matemáticas, Cinvestav del I.P.N., 07360 Mexico, D.F., Mexico

365

of the ejecta, defined as the ratio between the kinetic luminosity $L_{\rm kin}$ and the radiated luminosity $L_{\rm rad}$, is of the order of one.

1 Introduction

Dr. Jan-Uwe Ness (ORCID 0000-0003-0440-7193)

Classical Novae (CNe) are the historically longest-known eruptive sources in the sky. They occur in binary systems consisting of a white dwarf (WD) and a normal star with typical orbital periods of a few hours. Mass lost by the star leads to accumulation of a hydrogen-rich layer on the WD surface that erupts in a thermonuclear explosion after nuclear ignition conditions are reached (Starrfield and Swift-Nova-CV group 2008). The radiative energy output of the outburst is large enough to eject both accreted material and some dredged up WD material into space. This envelope resembles a stellar atmosphere of an F giant (Payne-Gaposchkin 1964). Early in the evolution, the ejecta are bright in the optical, and no high-energy radiation is expected. As the expansion continues, the density drops, the photosphere moves inward in mass, exposing successively hotter plasma, and the effective temperature rises. This process leads to the commonly observed decline in optical, while the peak of the spectral energy distribution (SED) moves to higher energies. In this standard picture, at some point in the evolution the peak is expected to reach the X-ray regime, and several novae have been observed to emit a supersoft X-ray spectrum, similar to those of the class of supersoft X-ray binary sources (SSS) such as Cal 83 (Starrfield et al. 2004). These are extremely luminous sources ($\log L_{\rm bol} \approx 37$) with effective temperatures $\sim$30–40 eV ($T_{\rm eff} \approx (3-5) \times 10^5$ K). Such high luminosities and temperatures, if observed in systems with WDs, can only be powered by nuclear burning, and when a nova is emitting an SSS spectrum, nuclear burning near the surface of the WD must still be continuing. The time at which a nova ceases to emit an SSS spectrum can be considered as the time when nuclear burning has turned off.

The first detailed X-ray study of a nova during outburst was carried out for V1974 Cyg (Krautter et al. 1996). While X-ray emission was not expected to be observable before the photosphere receded to sufficiently hot layers within the envelope, V1974 Cyg exhibited an early hard X-ray spectrum, apparently with the characteristics of a collisional, optically-thin plasma (Krautter et al. 1996; Balman et al. 1998a). Such early X-ray emission has now been seen in other novae, e.g., V838 Her (Lloyd et al. 1992), V382 Vel (Orio et al. 2001), several CNe in a sample of novae observed with *SWIFT* (Ness et al. 2007), and, recently, V2491 Cyg (Page et al. 2010), and V458 Vul (Tsujimoto et al. 2009).

X-ray observations during the SSS phase yield a physical description of the innermost regions. X-ray spectra yielding color-equivalent temperatures in excess of $\sim(2-3) \times 10^5$ K imply that nuclear burning is the energy source (Ness et al. 2008). The evolution of the SSS is governed by the evolution of the nuclear-burning envelope that remains on top of the WD. Models of post-outburst WD envelopes with steady H-burning show that envelopes with smaller masses have smaller photosph-

eric radii and higher effective temperatures. As the H-rich envelope mass decreases due to mass loss and conversion of H to He, the effective temperature is predicted to increase at constant bolometric luminosity, reaching maximum temperature just before turn-off. This has recently been observed by Page et al. (2010) in V2491 Cyg. The evolution of the effective temperature is faster at low temperatures, slowing down at high temperatures, with its pace depending on the WD mass and the particular envelope composition (Sala and Hernanz 2005). For data with sufficient signal-to-noise ratio and spectral resolution, non-LTE atmosphere models allow quantitative conclusions. However, Ness et al. (2009) found significant blue shifts in all available high-resolution X-ray spectra of novae, indicating continuing expansion and probably mass loss, such that rigorous application of such methods must include the expansion (van Rossum and Ness 2010).

An alternative route is the use of expanding photoionized envelope models, for the characterization of the main kinematics and physical parameters of the system. And that is the main goal of the work we introduce in this chapter. Here, we present an analysis of the X-ray spectra from the *Chandra* and *XMM-Newton* monitoring observations of V4743 Sgr (2002) that were carried out between days 50.2 and 1286 after discovery.

2   Observations

Dr. Jan-Uwe Ness (ORCID 0000-0003-0440-7193)

Altogether, five observations with *Chandra* and three with *XMM-Newton* were obtained between days 50 and 1286 after outburst, probing different phases of the evolution. In Table 1 we list the journal of observations with day after discovery.

2.1   *Observing Instruments*

The ACIS-S is an array of CCD chips, sensitive between 0.1–10 keV with an effective area ranging from 110–600 cm^2 from 0.5–1.5 keV and an energy resolution of roughly 100 eV. The HRC (High-Resolution-Camera) is a microchannel plate imaging detector that records the dispersed photons of the Low Energy Transmission Grating Spectrometer (LETGS). The LETGS covers a wavelength range of 1–170 Å with an effective area of 10–30 cm^2 in the 19–40 Å range and a wavelength resolution of 0.05 Å. Since the dispersion angle is proportional to wavelength, the grating spectra are extracted in wavelength units. The Reflection Grating Spectrometer (RGS) on board *XMM-Newton* is sensitive between 1–38 Å with an effective area between 20–60 cm^2 in the 19–40 Å range and a wavelength resolution of 0.05 Å. The European Photon Imaging Camera (EPIC) consists of two MOS (Metal Oxide Semi-conductor) CCD detectors and a pn detector. The MOS are sensitive between

Table 1 Observation summary. (*Source* Jan-Uwe Ness)

Day[a]	ObsID	Detector/mode	Start date	Exp. time (ks)	Count rate	Flux[h]	Flux[i]
50.23	3774	ACIS-S[b]/FAINT	2002-11-09.24	5.30	0.3[g]	1.8 ± 0.6	1.3 ± 0.2
180.39[d]	3775	HRC[b]/LETGS	2003-03-19.40	14.7	44.0[e]	2022 ± 450	1815 ± 400
180.56[d]	3775	HRC[b]/LETGS	2003-03-19.55	5.6	0.62[e]	32 ± 15	24.1 ± 8
196.14	0127720501	RGS[c]	2003-04-04.93	35.2	51.9[f]	1709 ± 573	1709 ± 573
301.88	3776	HRC[b]/LETGS	2003-07-18.90	11.7	43.5[e]	2006 ± 190	1810 ± 170
370.98	4435	HRC[b]/LETGS	2003-09-25.99	12.0	22.6[e]	1044 ± 350	928 ± 300
526.05	5292	HRC[b]/LETGS	2004-02-28.06	10.3	5.05[e]	230 ± 40	172 ± 30
741.98	0204690101	MOS1[c]/THIN	2004-09-30.77	22.1	0.086[g]	2.6 ± 1.0	0.6 ± 0.3
1285.9	0304720101	MOS1[c]/THIN	2006-03-28.64	34.1	0.055[g]	1.5 ± 0.5	0.4 ± 0.2

[a]after discovery (2002, September 19.8)

[b]*Chandra*

[c]*XMM-Newton* (combined RGS1 and RGS2)

[d]observation split in high-state and low-state

[e]counts per second from dispersed photon in range 5–55 Å

[f]counts per second from dispersed photon in range 5–38 Å (RGS1)

[g]counts per second (0.2–10 keV = 1.2–62 Å)

[h]absorbed band flux [ranges as in footnotes $e - g$] in units 10^{-12} erg cm^{-2} s^{-1}; error ranges represent peak to peak variations

[i]absorbed band flux [range 5–38 Å = 0.3–2.5 keV] in units 10^{-12} erg cm^{-2} s^{-1}; error ranges represent peak to peak variations

0.2–10 keV with an effective area ranging between 100–600 cm^2 from 0.5–1.5 keV and an energy resolution of roughly 50 eV.

2.2 Extraction Procedures

The main observation product follows the concept of events files, which are tables of events with columns containing positions, arrival times and energies for each individual event. We generated these files from the raw products using standard reduction routines provided by the respective *Chandra* CIAO[1] (v4.2) software and *XMM-*

---

[1]http://cxc.harvard.edu/ciao.

Newton SAS (9.0.0). We extracted average count rates and spectra from the events files by application of filter criteria on photon positions, arrival times, and energy (see below). In the right part of Table 1 we give the count rates and absorbed X-ray band fluxes for the energy ranges indicated in the corresponding footnotes. Absorbed X-ray band fluxes can be obtained from spectral models with fairly good accuracy. As long as the spectra are reasonably well reproduced, the resultant flux does not depend strongly on the model assumptions, and the determination of absorbed fluxes over the energy band covered by the detector is thus robust. Nevertheless, for the grating spectra we made use of the high spectral resolution and determined the fluxes directly from the spectra by integrating the photon fluxes from each spectral bin in a given wavelength range. First, we extracted the fluxes from the entire band pass of each instrument, except for the LETGS fluxes, where significant contamination of second-order photons occurs longwards of 55 Å. For direct comparison of the brightness evolution, we also extracted fluxes over a common band pass for all observations. Since the light curves are highly variable, we consider the range between minimum and maximum count rates as uncertainty ranges. The extracted fluxes are listed in the last two columns of Table 1.

The first X-ray observation was made with low (CCD) spectral resolution with the original purpose to determine whether the brightness level was suitable for high-resolution observations. We have placed a circular extraction region with a radius of 20 pixels around the expected source position and extracted the number of counts in the detect cell. The background was extracted from an adjacent (source-free) region. As can be seen from Table 1, the source was clearly detected. Next, we extracted a spectrum from the photon energies. The spectral analysis is described in 6.1, and the fluxes listed in the last two columns of Table 1 have been directly integrated from the best-fit model.

The time period between days 50.2 and 180.4 was unfortunately not covered with any observations because Sagittarius was behind the Sun. As soon as V4743 Sgr was visible again, a bright SSS spectrum was observed by *Chandra* with high-amplitude oscillations and a sudden, unexpected decay by two orders of magnitude (Ness et al. 2003). We split this observation into two parts (starting on days 180.4 and 180.6) in order to investigate the bright and faint phases separately. Three more *Chandra* LETGS observations were taken on days 301.9, 371, and 526. The spectrum was obtained by following the standard *Science Threads*[2] for extraction of LETG/HRC-S Grating spectra.[3] We use the new spectral extraction region (i.e., a "bow-tie" shaped region), contained in CALDB 4.2. When the LETG (*Low Energy Transmission Grating*) is used with the HRC-S detector (*High Resolution Camera*), this comprises a central rectangle abutted to outer regions whose widths increase as the dispersion distance increases. The background region is taken from above and below the dispersed spectra. The region shape for both, source and background negative and positive orders is precisely given in the CALDB V 4.2. Having properly extracted both, source and background spectra from each arm, we merged them, obtaining added

---

[2] http://cxc.harvard.edu/ciao/threads/spectra_letghrcs.

[3] Along with the calibration data CALDB V 4.2.

source and background spectra. This is intended to increase the signal-to-noise ratio (S/N) of the final spectrum, and the spectral analysis (throughout this work) is based on this co-added spectrum.

The decay phase, which comprises the time interval before the faint-phase (obs day 180.6), of approximately 5 ks of duration will not be analysed here. The pre-decay phase is composed then for the first 15 ks of the observation at day 180.4, which we call epoch 1. Due to similarities with this we also study the spectra at days 301 and 370 called epochs 2 and 3, respectively. The LETGS has an energy coverage range 0.07–10 keV, however, we make use of the energy bandpass 0.2–10 keV, since significant contamination of second and higher orders photons are expected below 0.2 keV. The final spectra is shown using a bin size of 0.0250 Å for epochs 1, 2, and the default bin size of the LEG 0.0125 Å for epoch 3, making use of the high resolution of the spectrometer.

On day 196.1, two weeks after the observation of the steep decay, an *XMM-Newton* ToO observation was carried out, and the nova was again bright in X-rays exhibiting a SSS spectrum. The spectra and count rates were extracted from standard pipeline products. We have corrected the RGS spectra for pile up by reclaiming the first-order photons that were recorded in the second- and third-order RGS spectra. For the calculation of fluxes, we use the "fluxed" spectrum that combines RGS1 and RGS2 spectra. The "fluxed" RGS spectrum is a product of a SAS procedure that fully exploits the redundancy of the two spectrometers onboard *XMM-Newton*.

Two more observations were taken, on days 742 and 1286, with *XMM-Newton*. The RGS spectra do not contain sufficient signal for useful results, and we concentrate on the MOS1 observations. The source is not recorded in the pn detector because the source position coincided with a gap between two CCD chips. The count rates and spectra were extracted from the events file using circular extraction regions with a radius of 200 pixels, again filtering on the coordinates.

2.3   Brightness Evolution

The evolution of the X-ray broad-band fluxes is depicted in the top panel of Fig. 1. From day 50.2 to 180.6, the flux increased by three orders of magnitude. The faint phase on day 180.6 yields a factor ∼75 reduced brightness compared to before the decay, but the flux level is still a factor ∼20 higher than the flux obtained from the pre-SSS observation taken on day 50.2 (see also Table 1). The flux on day 196.1 is slightly lower than the pre-decay flux, while we find the same flux level for day 301.9 as before the decay. We caution that the comparison of fluxes between days 180 and 196.1 is uncertain owing to cross-calibration uncertainties between different instruments and uncertainties arising from the pile up correction of the RGS spectrum. Note that the *Chandra* LETG spectra are not piled up because of the architecture of the HRC detector. The fluxes for days 301.9, 371, and 526.1 follow an exponential decline, $e^{-t/\alpha}$, with $\alpha = (96 \pm 3)$ days (1-σ uncertainty).

The last two *XMM-Newton* observations taken on days 741 and 1286 yield fairly similar flux levels as on day 50.2. In order to determine whether this may be the quiescent level, we checked the ROSAT archive and found no X-ray detection in a

12-ks observation (ObsID 932149) taken 1990 September 17.1. The upper limit of 2×10^{-4} cps over the 0.1–2.4 bandpass corresponds to a *Chandra* and *XMM-Newton* count rate of $<10^{-3}$ cps and is thus well below the count rate level observed on days 50.2, 741, and 1286 encountered for the same band.
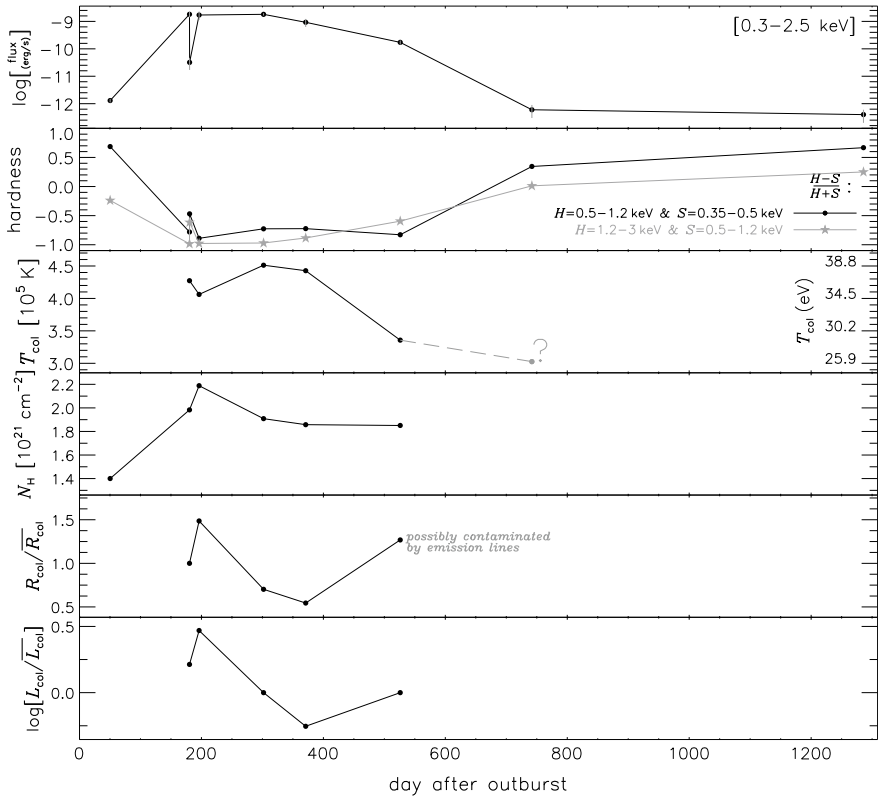
Fig. 1 Evolution of X-ray band fluxes from the last column of Table 1 (*top*) and hardness ratios (second panel). The next four panels show the evolution of color-equivalent temperature, neutral hydrogen column density, N_H, effective radius, and bolometric luminosity. Only relative changes of radii and luminosities are shown because the absolute values are unreliable as a consequence of poor model assumptions. The value of the blackbody temperature found from the model to day 742. The Galactic absorption N_H obtained from the model to day 50.2 as described in Sect. 6.1 are included in the third and fourth panels, respectively. Since the blackbody temperature for day 742 is highly uncertain, it is marked with a *gray question mark*. The normalization for day 526 might be contaminated by emission lines, leading to an overestimated radius (5th panel). (*Source* Jan-Uwe Ness)

2.4 Spectral Evolution

As a first description of the spectral characteristics of the object, we extracted count rates from different energy ranges, and calculated two hardness ratios along the conventional definition $HR = (H - S)/(H + S)$ with H and S being the count rates in two hard and soft bands, respectively. The evolution of the two different hardness ratios are shown in the second panel of Fig. 1, where the energy ranges for H and S are indicated in the bottom right legend. The evolution of both hardness ratios demonstrates the three phases of evolution. We group the observations into an early hard spectrum (day 50), the Super Soft Source phase (days 180–370), and the post-SSS phase (days 526–1285). The panels below show the evolution of the spectral shape of the continuum color and related parameters characterizing the SSS spectra.

The detailed spectra are shown in Fig. 2 in the order of date after discovery from top to bottom (see upper right legends in each panel). While the grating spectra taken between days 180.4 and 526 can be converted to photon flux spectra, this is not possible for the CCD spectra, and the raw counts per bin are plotted instead. Since the CCD spectra are binned on an equidistant *energy* grid, these spectra are not equidistantly binned when plotted in wavelength units, which is chosen here for consistency with the majority of grating spectra. For orientation purposes, the corresponding energies to each given wavelength label on the x-axis are given in the top.

The spectral evolution of novae in X-rays can be divided into three major phases, which can be identified in Fig. 2: an early emission phase that is characterized by "hard" emission (day 50.2), the SSS phase (days 180.4–526), and a late emission phase that is again a harder spectrum (days 742 and 1286). While the SSS emission is photospheric emission from the extended WD, the origin of X-ray emission during the other two phases is less clear. Early "hard" emission is suspected to originate in shocks while the late emission phase could be radiatively cooling nebular ejecta.

The spectrum on day 50.2 is shown in the top panel of Fig. 2. It has very low signal to noise and spectral resolution but significant hard and soft emission can clearly be identified. Some of the features could be emission lines, and this spectrum thus meets expectations of an early hard emission line spectrum.

The LETGS spectrum taken on day 180.4 has already been presented by Ness et al. (2003). The spectrum is clearly significantly softer, and it is a continuum spectrum with absorption lines. On day 180.6, after the steep decay, an emission line spectrum has appeared (Ness et al. 2003). As described above, units of photon fluxes are plotted.

The spectra taken on days 196, 302, 371, and 526 are remarkably similar, and they all originate from the extended WD photosphere. Small differences can be seen in the depth of some absorption lines, and the Wien tail extends to somewhat shorter wavelengths between days 196 and 372, compared to days 180.6 and 526. On day 526, the absorption lines are less deep, and emission line features arise. These emission lines could have been present all the time, and with the lower emission level of the continuum on day 526, they are easier to see. A detailed comparison of the SSS spectra can be found in Sect. 6.

The last two *XMM-Newton* observations are too faint for the high-resolution RGS, and only the low-resolution MOS1 spectra are useful. In the bottom two panels of Fig. 2, the spectra from days 742 and 1286 are shown. Both spectra show no features that could be associated with emission lines like in the ACIS spectrum in the
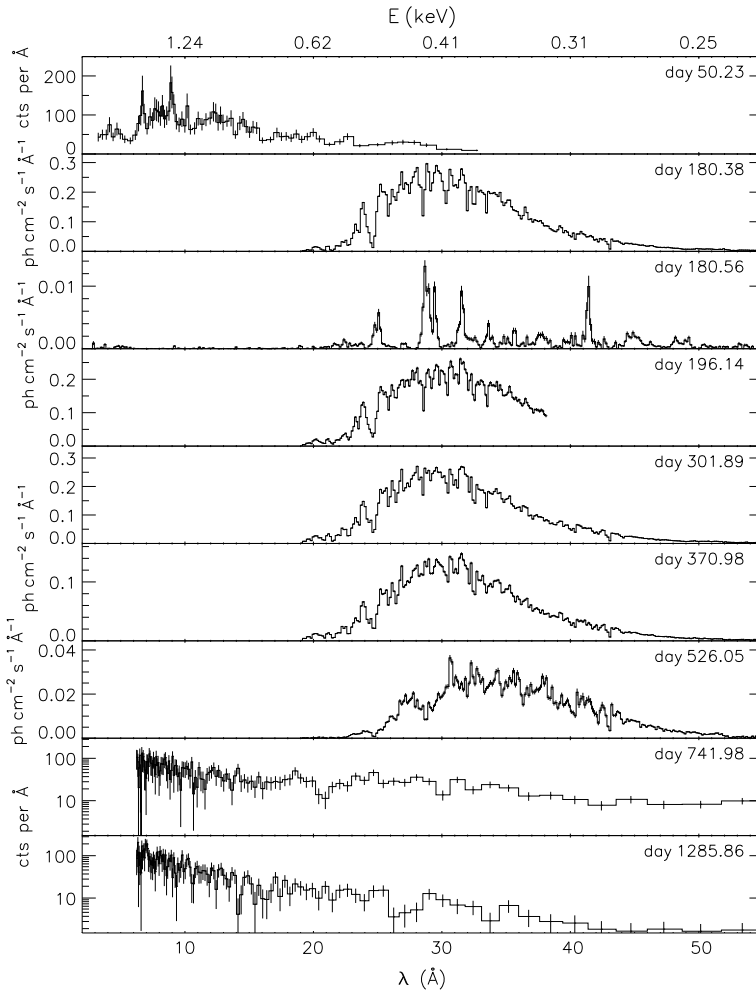
Fig. 2 Comparison of all X-ray spectra with the start times given as fractional days after discovery in the *upper right* legend of each panel. For observation details see Table 1. The grating spectra were converted to photon fluxes (days 180.4–526), and data shortwards of 19 Å were removed as no signal is present. The CCD spectra (days 50.2, 724, and 1286) have been extracted on an equidistant energy grid, but are shown on the same wavelength scale, and in units counts per Å, without background subtraction. In the *bottom two panels*, the spectra are shown on a logarithmic scale. (*Source* Jan-Uwe Ness)

top panel of Fig. 2. Since the MOS1 has a similar resolution as the ACIS, we can conclude that the post-outburst spectra are of a different nature.

2.4.1   Continuum and Detection of X-Ray Lines in the SSS Spectrum

J.M. Ramírez-Velasquez

Here we describe the selection of the continuum and the statistical procedure for the detection of the X-ray lines. We choose a black-body with temperature $kT = 37$ eV ($T = 427000$ K). The column density of neutral hydrogen in the line of sight, $N_{\rm H}$, was found by comparison of the non-absorbed model with $N_{\rm H}$-corrected observed spectra, from different assumed values of $N_{\rm H}$. Other authors argued that $\chi2$ minimization of $N_{\rm H}$ overemphasizes the 25–35-Å region where the highest count rates are encountered, while the importance of $N_{\rm H}$ increases towards longer wavelengths, where the count rate is low, and the contributions to $\chi2$ are small. We use the tbabs[4] model for the interstellar absorption with a column density of $N_H = 2.2 \times 10^{21}$ cm^{-2}. For the continuum described above we look for significant residuals using as general strategy model comparison. The resulting value of 2.2×10^{21} cm^{-2} is between expected values from Galactic neutral hydrogen maps. For the purposes of detecting a spectral feature, i.e., an absorption/emission line (in the count-wavelength space) is at least two *changepoints* (separated by at least a distance equivalent to the resolution of the instrument). In the statistics literature this is a point where the underlying process changes abruptly. The concept, has already been used in time series data (Scargle 2004). Here we apply the idea to grating X-ray data. So we take a "chunk" of data, labeled k, and compute the marginalized likelihood of the model (M_k) given the data (D_k):

$$P(M_k|D_k) = P_0 \frac{\Gamma(N_k + \alpha)}{(\sum \Lambda_n + \beta)^{N_k+\alpha}}, \tag{1}$$

where N_k is the total counts in the chunk of data k. Λ_n is the broad band model count rate in units of counts per bin (n). P_0 forms part of the prior:

$$P_0 l^{\alpha-1} \exp{(-\beta l)}, \tag{2}$$

where

$$P_0 = \frac{\beta^\alpha}{\Gamma(\alpha)}, \tag{3}$$

and Γ is the incomplete gamma function, and β and α are parameters.

Our fitting of the continuum model into the data is made using the Interactive Spectral Interpretation System,[5] and the corresponding subroutines in the library

---

[4]http://space.mit.edu/CXC/ISIS/.

[5]The Tüubingen-Boulder ISM absorption model.
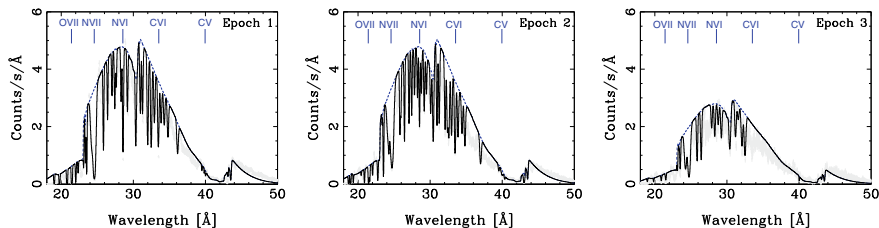
Fig. 3 Chandra LETGS ± 1 order spectrum of V4743 Sgr, in the soft X-rays bandpass, for epochs (1, 2, 3). It is shown the *black-body* continuum as the *thick solid line*. The *dashed line*, is the global `CONTINUUM + LINES` model we use, in order to characterize the absorption of the system

package S-lang/ISIS Timing Analysis Routines.[6] Having computed the *changepoints* of a feature, we take the wavelength center as an input for our `CONTINUUM + LINES` global model. The statistical significance is afterwards measured as the distance from the continuum to the core of the line, in units of the Poissonian error σ_p.

3   Fits to the SSS Spectrum

Figure 3 shows the broad-band X-ray spectra of V4743 Sgr, by epoch, with the continuum described in Sect. 2.4.1 overplotted as a thick blue line. This continuum is then modified by multiplicative Gaussians:

$$M(E) = \exp\left(\tau \times \exp\left[-\frac{(E - E_0)^2}{(2\sigma^2)}\right]\right), \tag{4}$$

with

$$\tau = \frac{\tau_0}{\sqrt{(2\pi)}\sigma}. \tag{5}$$

where τ_0 is the optical depth at the core of the line. The width is given by σ. And the energy at the core is E_0. The number of Gaussians to be used is given by the detection procedure described in Sect. 2.4.1, with $\sigma_p \geq 2$. The measurements of the line parameters along with their identifications are given in Table 4, corresponding to epoch 1 (other Tables are not shown for lack of space).

In the first column we have the observed center of the line, in the second column the statistical significance of the detection. In the third column, the candidate ionic specie for that line. In the fourth, the theoretical wavelength of the transition. In the fifth, the atomic transition of the line. In the sixth, the Doppler shift of the core of the line. In the seventh, the equivalent width of the line (EW) in milli-angstroms, computed with:

---

[6]http://space.mit.edu/CXC/analysis/SITAR/.

$$EW = \int \left[1 - \frac{F_g(E)}{F_c(E)} \right] dE, \tag{6}$$

where $F_g(E) = F_c \times M(E)$, $F_c(E)$ is the continuum at the energy E. The ion column densities (N_j) are derived from the identifications in the Tables, assuming that the equivalent widths lie on the linear part of the curve of growth, and are quoted in column 8. That is we calculate N_j, from:

$$\frac{EW_\lambda}{\lambda} = \frac{\pi e^2}{m_e c^2} N_j \lambda f_{ij}, \tag{7}$$

where m_e is the electron mass, c the speed of light, and f_{ij}, the oscillator strength of the transition between levels, i and j.

4 Kinematic Modeling of the Pre-decay Phase

The SSS spectrum originates from the extended atmosphere of the white dwarf. This is a photoionized optically thick expanding wind (van Rossum and Nes 2010). Here we start by constructing a kinematic model for such a wind, based on the observed spectra, and we use this model to extract various important physical parameters from the observations.

We assume spherically concentric shells photoionized by a simple blackbody with integrated 1–1000 Ryd luminosity $L = 10^{37}$ erg s^{-1}, and temperature of $kT = 37$ eV, which form an expanding envelope. At this point, we do not solve the equations of radiative transfer between spherical clouds, but assume that there is a relation between radial location and velocity field, and the ionizing flux dilute only geometrically as $\propto r^{-2}$. The gas composition is made of H, He, C, N, O, Ne, Mg, Si, S, Ar, Ca and Fe. We use the abundances of Grevesse et al. (1996) in our models (and use the term *solar* for these abundances). From the continuity equation for a constant mass loss rate, we adopt a density profile for the expanding envelope as described by a beta-law,

$$w(x) = w_0 + (1 - w_0) \left(1 - \frac{1}{x} \right)^\beta, \tag{8}$$

where w is the velocity of the wind normalized to the terminal velocity v_∞, w_0 is the normalized velocity at the base of the wind and x is the distance normalized to the radius of the central core $x = r/r_0$. The parameter β is the quantity governing the slope of the velocity with the distance. The other function responsible for the variation of the optical depth with velocity is the ion density. This is given by

$$n_i(x) = A_E \times n_H(x) \times q_i, \tag{9}$$

where $A_E = n_E/n_H$ is the abundance of the element with respect to H, $q_i = n_i/n_E$ is the ionization fraction, and $n_H(x)$ is the gas number density

$$n_H(x) = n_0 x^{-2} w^{-1} = \left(\frac{\dot{M}}{4\pi \mu m_H} r_0^{-2} v_\infty^{-1} \right) x^{-2} w^{-1} \tag{10}$$

where $\dot{M}$ is the mass loss rate and μm_H is the average mass of the particles. At this point we need to adopt a model for the ionization balance. We assume that we can compute the ionization fraction q_i of each specie as a function of an ionization parameter ξ (the ratio of the ionizing flux F to the gas density n_H) at each radial point. ξ for the optically thin case is

$$\xi = \frac{4\pi F}{n_H} = \frac{L_{ion}}{r^2 n_H}, \tag{11}$$

where L_{ion} is the ionizing luminosity of the source, but if the space between the source and the photoionized region is optically thick

$$\xi = \frac{4\pi F}{n_H} = \frac{L_{ion} \times \exp[-\tau(r)]}{r^2 n_H}, \tag{12}$$

where $\tau(r)$ is the optical depth up to the observed gas. By combining equations (10) and (11)

$$\xi = \xi_0 \times \exp[-\tau(r)]w, \tag{13}$$

where $\xi_0 = L_{ion}/(r_0^2 n_0)$. This is what we call, a spherical wind, because the density profile is that of a spherically symmetric shell. Due to additional complexities that can be associated to the expansion of the nova and to take into account deformation of the density profile (due to magnetic fields for instance), we re-write the density as:

$$n_H(x) = n_0 x^{-2+\kappa} w^{-1}, \tag{14}$$

where a positive value of κ implies that the gas flow dilutes more slowly than in a free spherical expansion, i.e. that there are sources of gas embedded in the flow, or that the flow is confined. A negative value corresponds to sinks of gas in the flow, or expansion of an initially confined flow in a flaring geometry. Here and in what follows, we set $w_0 = 0$ for simplicity. We then find that

$$\xi = \xi_0 \times \exp[-\tau(r)]w \times (1 - w^{1/\beta})^\kappa, \tag{15}$$

and this is the relationship between the ionization parameter and the radial velocity for a non-spherical, optically thick wind. The two panels in Fig. 4 shows details of the spectrum and the results of our model. Most of the Gaussian features match well the observed spectrum, more specifically the centroids of the features are well located, a good element for our purposes. However, the fit is far from being statistically acceptable.
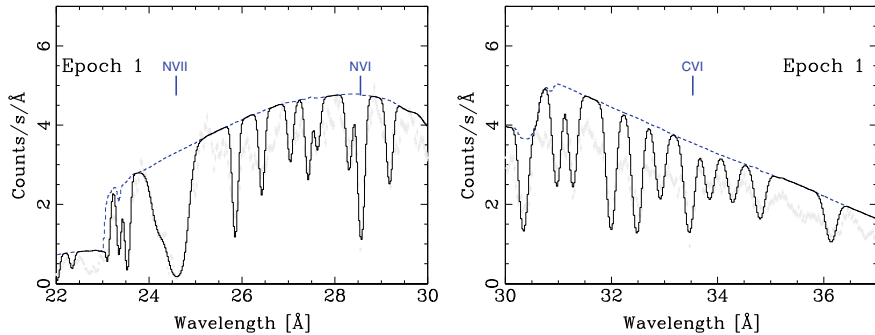
Fig. 4 *Chandra* LETGS ± 1 order spectrum of Sgr. V4723, in the range 22–37 Å, for epoch 1. Several absorption features are identified and modeled with multiplicative Gaussians (*solid line*) modifying a blackbody continuum (*dashed line*)

Table 2 Parameters of the system: Mass loss rate $\dot{M}$, $\dot{M}/L_{ion}$ and L_{kin}/L_{rad}

Epoch	$\dot{M}^a$	$\dot{M}/L_{ion}^b$	L_{kin}/L_{rad}
I (CVI)	4.2	2.63	3.02587
I (NVI)	5.3	3.32	3.52105
I (OVII)	2.5	1.55	1.07782
II (CVI)	4.3	2.71	3.34455
II (NVI)	6.2	3.92	5.77883
II (OVII)	–	–	–
III (CVI)	–	–	–
III (NVI)	0.1	0.09	0.00007
III (OVII)	1.5	0.93	0.23078

[a]In units of $\times 10^{-4}$ $(\frac{L}{L_{38}})$ $M_\odot/yr$

[b]In units of $\times 10^{-16}$ gr/ergs

5　Ionizing Luminosity, Mass Loss Rate, and Kinetic Luminosity of the Flow

We seek to constrain key physical parameters of the wind such as its mass loss rate and kinetic luminosity from the observed spectra and the relations derived above (see Table 2 for a summary). But, first one needs to answer a basic question, is the wind optically thin or optically thick?

To answer this we look for possible changes in the ionization of the spectra among the three epochs of observation. In Fig. 5 we look at the relative column densities of S XVI and N VI resonant lines versus apparent luminosity for the three epochs of observation.

These two column densities are easily measured in the spectra and expand a large range in ionization. The ratio of column densities is notoriously flat, and so are the ionization of the spectra, while the apparent luminosity changes by a factor of ≈2.

This means that the three spectra steam from different radial distance, being the region farthest from the source in epoch 1 when the luminosity is maximum and nearest in epoch 3. It also means that if ξ is to remain constant for varying L_{rad} and the wind is spherical it cannot be optically thin, but thick (see Eq. 11).

From Eqs. 10 and 12 one can write the mass loss rate as

$$\dot{M} = 4\pi\mu m_H L_{\mathrm{ion}} \times \exp(-\tau) \left(\frac{v}{\xi}\right) \qquad (16)$$

where μm_H is the average mass of the particles. The ratio (v/ξ) can be independently determined from observations for each of the species observed in the spectra. The values of v were measured from the centroids of the lines; C VI $\lambda33.734$, N VI $\lambda28.787$ and O VII $\lambda21.602$ for the three epochs under consideration (see Tables 3 and 4). The values of ξ are taken from the ionization balance curves of Kallman and Bautista (2001). Figure 6 presents the results for $\dot{M}$ as derived from different species and on

Fig. 5 Column densities of S XVI and N VI resonant *lines* versus apparent luminosity for the three epochs of observation. These two column densities are easily measured in the spectra and span a large range in ionization
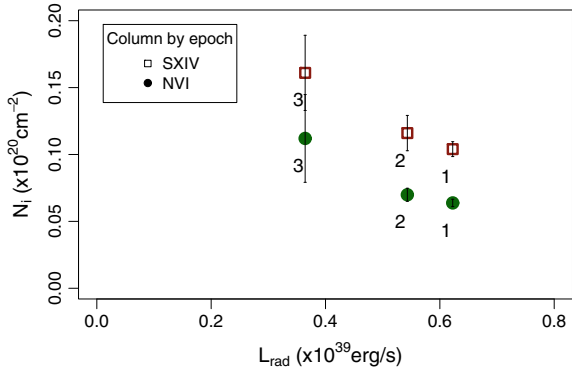
Table 3 Models to ACIS spectrum (50.2 days after discovery). (*Source* Jan-Uwe Ness)

Param.	Unit	Value[a]
kT_1	keV	$0.25 - 0.35$
$\log(VEM_1)^c$	cm^{-3}.............	$56.97 - 57.35$
kT_2	keV	$2.7 - 15$
$\log(VEM_2)^c$	cm^{-3}............	$56.05 - 56.28$
N_{H}	cm^{-2}............	$(1.4 \times 10^{21})^b$
flux^d	10^{-12} erg cm^{-2} s^{-1}	$1.2 - 2.4$
$L_X^{c,d}$	10^{32} erg s^{-1}......	$1.7 - 3.5$
$\chi2_{\mathrm{red}}$ (dof)	....	1.16 (64)

[a]90 % uncertainty ranges
[b]fixed
[c]assuming distance 3.9 kpc
[d]0.2–10 keV
Abundances of N, O, Ne, Mg, Si, S, and Fe were varied (see text)

Table 4 Line properties of V4743 Sgr., LETGS epoch 1 (day 180.39). (*Source* Jan-Uwe Ness)

λ_{obs}^{a}	σ_p^{b}	Ion^c	λ_0^{d}	Atomic transition	Velocity (km s^{-1})	EW (mÅ)	N_i^e	flag
19.768 ± 0.003	8	N VII	19.826	1s ^{2}S - 4p ^{2}P	−873 ± 51	88 ± 10	0.52 ± 0.06	i
20.818 ± 0.003	10	N VII	20.910	1s ^{2}S - 3p ^{2}P	−1312 ± 45	98 ± 13	0.19 ± 0.03	i
21.470 ± 0.001	11	O VII	21.602	1s^2 ^{1}S - 1s 2p ^{1}P	−1832 ± 16	104 ± 1	0.03 ± 0.01	s
22.021 ± 0.002	11	O VI	22.020	1s^2 2s ^{2}S - 1s 2s(3P) 2p ^{2}P	11 ± 25	215 ± 31	0.05 ± 0.01	i
22.345 ± 0.004	12	O V	22.360	1s^2 2s^2 ^{1}S - 1s2p ^{1}P	−334 ± 47	281 ± 76	*NA*	i
23.106 ± 0.001	20	N VI	23.277	1s^2 ^{1}S - 1s 5p ^{1}P	−2202 ± 19	271 ± 30	2.00 ± 0.22	i
23.355 ± 0.002	17	O I	23.450	1s^2 2s^2 2p^4 - 1s 2s^2 2p^5	−1215 ± 20	291 ± 32	0.42 ± 0.05	g
23.534 ± 0.001	22	N VI	23.771	1s^2 ^{1}S - 1s 4p ^{1}P	−2989 ± 13	257 ± 18	0.88 ± 0.06	i
24.604 ± 0.002	24	N VII	24.779	1s ^{2}S - 2p ^{2}P	−2121 ± 19	975	0.26 ± 1.86	s
25.856 ± 0.001	24	Ca XI	26.442	2p^6 ^{1}S-2p^5 4s ^{1}P	−6644 ± 13	351 ± 20	1.50 ± 0.09	i
26.430 ± 0.002	20	Ca XI	26.962	2p^6 ^{1}S - 2s 2p^{6}3p ^{1}P	−5915 ± 20	407 ± 35	0.17 ± 0.01	s
27.044 ± 0.003	21	Si XIII	27.341	1s 2s ^{3}S - 1s 4p ^{3}P	−3259 ± 31	452 ± 57	0.37 ± 0.05	i
27.429 ± 0.002	22	Ar XIV	27.464	2s^2 2p ^{2}P - 2s^2 3d ^{2}D	−382 ± 22	447 ± 41	0.04 ± 0.01	i
27.629 ± 0.003	18	Ar XIV	27.636	2s^2 2p ^{2}P - 2s^2 3d ^{2}D	−76 ± 36	480 ± 71	0.23 ± 0.03	i
28.309 ± 0.002	21	C VI	28.465	1s ^{2}S - 3p ^{2}P	−1645 ± 23	484 ± 46	0.51 ± 0.05	s
28.570 ± 0.001	29	N VI	28.787	1s^2 ^{1}S - 1s 2p ^{1}P	−2261 ± 11	419 ± 18	0.06 ± 0.01	s
30.346 ± 0.002	21	S XIV	30.427	1s^2 2s ^{2}S - 1s^2 3p ^{2}P	−799 ± 15	507 ± 27	0.10 ± 0.01	s
30.975 ± 0.002	23	Si XII	31.012	1s^2 2s ^{2}S - 1s^2 4p ^{2}P	−359 ± 17	558 ± 33	0.44 ± 0.03	i
31.277 ± 0.002	26	N I	31.223	1s^2 2s^2 2p^3 - 1s 2s^2 2p^4	518 ± 18	572 ± 35	0.13 ± 0.01	g
31.996 ± 0.001	26	S XIII	32.239	2s^2 ^{1}S - 2s 3p ^{1}P	−2261 ± 13	551 ± 23	0.10 ± 0.01	i

(continued)

Table 4 (continued)

λ_{obs}^{a}	σ_{p}^{b}	Ion[c]	λ_{0}^{d}	Atomic transition	Velocity (km s^{-1})	EW (mÅ)	N_i^e	flag
32.483 ± 0.001	24	Ca VIII	32.770	3p ^{2}Po - ∞	−2626 ± 12	567 ± 24	0.21 ± 0.01	i
32.921 ± 0.002	19	Ca VIII	33.120	3p ^{2}Po - ∞	−1801 ± 22	645 ± 45	*NA*	i
33.469 ± 0.002	26	C VI	33.734	1s ^{2}S - 2p ^{2}P	−2357 ± 16	619 ± 30	0.09 ± 0.01	i
33.850 ± 0.003	17	S XII	34.533	2s^2 2p ^{2}P - 2s 2p(3P) 3p ^{2}D	−5928 ± 30	703 ± 67	0.12 ± 0.01	i
34.286 ± 0.004	16	C V	34.973	1s^2 ^{1}S - 1s 3p ^{1}P	−5887 ± 34	727 ± 75	0.32 ± 0.03	i
34.799 ± 0.003	16	Ar IX	35.024	2p^6 ^{1}S - 2p^5 4d ^{1}P	−1926 ± 28	728 ± 60	0.10 ± 0.01	i
36.138 ± 0.003	15	S XII	36.398	2s^2 2p ^{2}P - 2s^2 3d ^{2}D	−2142 ± 27	764 ± 57	0.04 ± 0.01	i
39.508 ± 0.007	18	Mg X	39.668	1s^2 2s ^{2}S - 1s^2 5p ^{2}P	−1212 ± 54	266 ± 88	0.31 ± 0.10	i
40.012 ± 0.008	8	C V	40.268	1s^2 ^{1}S - 1s 2p ^{1}P	−1905 ± 58	395 ± 80	0.03 ± 0.01	i
39.832 ± 0.006	9	Si XI	40.286	2s^2 ^{1}S - 2p 3p ^{3}D	−3379 ± 46	68 ± 334	*NA*	i

Errors are 1σ, computed individually for each of the parameters. [a]Observed wavelength in Å.
[b]Statistical significance of the detection.
[c]Probable ion identification.
[d]The latest laboratory wavelength (in Å) taken from the National Institute of Standars and Technology (`NIST`: http://physics.nist.gov/PhysRefData/ASD/lines_form.html).
The K-shell wavelength of the oxygen ions (O VI and O V), are taken from (García et al., 2005).
[e]Measured column density for the ion in units of ×10^{20} cm^{-2}.
[f]This is a broad feature, not actually associated to any atomic transition.
Column `flag`: *s* Secure identification *i* Insecure identification *vi* Very insecure identification: means that there is no reliable atomic data for this ion. *g* Galactic line.

different epochs. The spread in values from different species is probably due to variations in the optical depth up to the regions where different ions form. The optical depth τ is a complex function that depends on the column density of gas and its physical conditions up to the region responsible for the observed absorption troughs. The overall results are for an upper limit to $\dot{M} \approx 4 \times 10^{-4}$ ($\frac{L}{L_{38}}$) $M_\odot/yr$.

The kinetic energy of the flow is defined as

$$L_{kin} = \frac{1}{2}\dot{M}v^2. \qquad (17)$$

Our results for the ratio of (L_{kin}/L_{rad}) × exp τ in epochs 1–3 are depicted in Fig. 7. The numeric values in this figure can be regarded as upper limits to the ratio of kinetic

to radiative energy in the wind. Interestingly, this ratio is less than one in epoch 3, suggesting that the flow has fallen out of equipartition. This can be understood if by this time in the expansion radiative pressure has become insufficient to overcome the gravitacional potential. If this result is applicable to other novae it means that ejecta mass determinations based on the assumption of equipartition are only reliable when near the spectral peak, which is also the kinetic peak. During other phases, the mass outflow is very small.

6 Analysis and Discussion

Dr. Jan-Uwe Ness (ORCID 0000-0003-0440-7193)

Here we present an analysis and following of a discussion of the: (1) early hard spectrum, (2) sss-phase and (3) the post-sss phase.

6.1 Analysis of Early Hard Spectrum

V4743 Sgr is not the first nova for which a hard X-ray spectrum was found before the WD has become visible in X-rays. Spectral model fits to such spectra imply that the X-ray emission originates from an optically thin collisional plasma, leading to the interpretation of shock fronts within the ejecta (O'Brien et al. 1994).

For this reason, we chose a model that produces an emission line spectrum arising in an optically thin plasma with an isothermal electron temperature, T_e, in order to model the ACIS-S spectrum taken on day 50.2. We have used xspec to fit the model to the data while accounting for all instrumental effects. The vapec model is based on atomic data calculated by the Astrophysical Plasma Emission Code (APEC, v1.3:, Smith et al. 2001) and allows the abundances of He, C, N, O, Ne, Mg, Al, Si, S, Ar,

Fig. 6 Mass loss rate during days 180.4, 301 and 371 after outburst. We use three spectral absorption *lines* to compute this quantity: C VI $\lambda 33.734$, N VI $\lambda 28.787$ and O VII $\lambda 21.602$. Because of the luminosity is model-dependent, $\dot{M}$ is give as a function of it. L_{38} is luminosity in units of 10^{38} erg s^{-1}
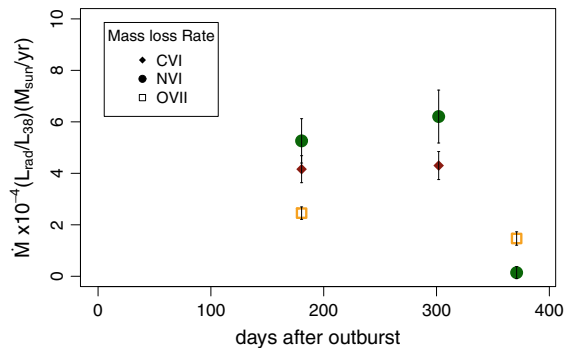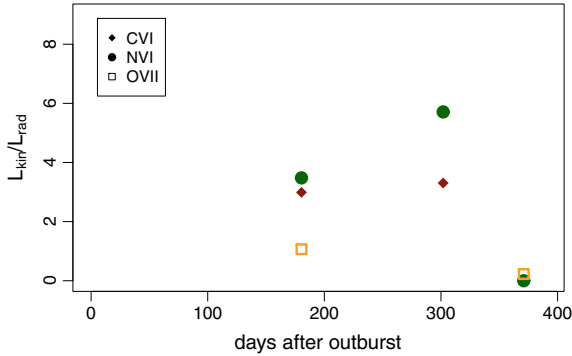
Fig. 7 Efficiency of the amount of energy used for the motion of the ejecta, measured as the ratio between the kinetic luminosity L_{kin} and the radiated luminosity L_{rad}. We use three spectral absorption lines to compute this quantity: C VI $\lambda 33.734$, N VI $\lambda 28.787$ and O VII $\lambda 21.602$. The three lines are consistent with an efficiency of the order of one. See text for details

Ca, Fe, and Ni to vary. The associated database, APED, is a more recent compilation of the atomic data contained in the MEKAL database which was used by Balman et al. (1998b) for the early emission of V1974 Cyg. The underlying assumptions are the same, i.e., the plasma is optically-thin and in collisional equilibrium. The principal parameters are temperature, normalization, and abundances relative to Solar. Since the plasma is unlikely to be isothermal, the sum of several APEC models can be used as an approximation of a continuous distribution of temperatures.

We have corrected for interstellar absorption assuming a fixed value of $N_{\text{H}} = 1.4 \times 10^{21} \, \text{cm}^{-2}$ Lyke et al. 2002), using the absorption model tbabs. The normalization parameter can be converted to volume emission measure (*VEM*, units cm^{-3}), assuming a distance of 3.9 kpc. We found isothermal models statistically unsatisfactory with none achieving a reduced $\chi 2$ better than $\chi 2_{\text{red}} = 1.70$ (66 degrees of freedom, $dof = N - n_p$). With 2-temperature (2-*T*) models, we found significantly better fits (see Table 3). For the best-fit model, we found an F-test value of 64 and a probability of 1.8×10^{-6}, thus the second model component is statistically justified. We found no further improvement with 3-*T* models.

We first assumed solar abundances, scaled with a single factor for all abundances, but we found poor fits. Next we iterated the abundances of N, O, Ne, Mg, Si, S, and Fe, with other elements fixed at their solar values because no strong lines from these species are observable. The values of the abundances are poorly constrained. For Fe we find only an upper limit of <0.04. We caution, however, that the low Fe abundance may be an artifact from approximating a continuous temperature distribution with only two isothermal components. Likewise, the abundances of the other elements are poorly constrained, and no robust conclusions can be drawn from the best-fit values. The model parameters are listed in Table 3.

6.2 Discussion of Early Hard Spectrum

The optically thin models used for fitting the early hard spectrum have originally been developed for the X-ray spectra of the Solar and stellar coronae. Our spectrum differs only in the X-ray luminosity and the likely different chemical composition of nova ejecta. The possibility could be considered that the early hard emission is of a similar origin. The Solar corona is powered by magnetic fields that are generated in the tachocline, the sheer layers between the inner radiation zone and the outer convection zone. In a nova, magnetic fields could be generated by a similar dynamo, located in the interface between the ejected envelope and the WD surface that is rigidly rotating underneath the ejecta. If V4743 Sgr is an intermediate polar as suggested by Kang et al. (2006), and Dobrotka and Ness (2010), the permanent magnetic field of the WD could amplify dynamo-generated magnetic fields that power a corona. However, these considerations are solely based on plausibility arguments and are difficult to test, as no coherent models for the production of coronal emission exist. While the influence of magnetic fields can not necessarily be discarded, magnetic fields are not part of the models assumptions of the optically thin thermal models. Other possibilities can thus be considered.

More commonly accepted is the idea of interpreting the collisional nature as originating from a shock-heated plasma, although it is not clear whether the shocks originate from within the ejecta or from interactions with circumstellar material or the stellar wind of the companion.

Shocks with the stellar wind of the companion can only produce X-ray emission that is strong enough to be detectable at the given large distance if the stellar wind is sufficiently thick, and that requires a symbiotic nova such as RS Oph (Ness and Starrfield 2009). In those systems, the companion is an evolved giant or subgiant. The ejecta run into this medium and dissipate some of their kinetic energy in the form of X-ray emission in the resulting shock (O'Brien et al. 1992). In Classical Novae like V4743 Sgr, no strong stellar wind is present and no hard X-ray emission is expected from this production mechanism. One indication that V4743 Sgr is not a symbiotic nova is its short orbital period of 6.7 h (Kang et al. 2006), which is much shorter than typical orbital periods of symbiotic novae of several hundred days. We also consider shock interactions with circumstellar material unlikely, since the required density is higher than models of nova binary systems would suggest (Lloyd et al. 1992). We have no reason to assume a higher density of the ambient medium as believed in GK Per (Bode 2004) or V458 Vul (Tsujimoto et al. 2009), where a planetary nebula was found to surround the nova.

O'Brien et al. (1994) developed a shocked-gas model for the specific case of V838 Her and argued that the shock-heating must take place as a result of the interaction of different components *within* the ejecta. This "interacting winds" model has been refined by Lloyd et al. (1995). The complexity of the absorption lines that we found in the later SSS spectra indicates that the ejecta are not homogeneous, which is an important ingredient for this model. The presence of different velocity components could aid the development of shocks within the ejecta.

On the other hand, in order to produce enough X-ray emission in a shock, sufficiently high densities are needed, which unavoidably also have a high opacity. It has not been tested whether X-ray resonance lines of H-like ions can escape such a plasma. Furthermore, at least two distinct episodes of ejection are needed, providing slow-moving ejecta from an earlier outburst and fast-moving ejecta from a later ejection event. While this has been observed in V2362 Cyg, no explanation on how such secondary events could occur have been found. It could be possible, on the other hand, that some material is falling back, colliding with the expanding ejecta.

With all the given arguments, the cause for the early hard emission can not be identified with certainty. At this time, no deep X-ray spectrum of the early hard emission phase of a nova has been taken that could be used to pose constraints on the different causes.

6.3 Analysis of the SSS Phase

The details of the grating spectra confront us with a high degree of complexity. The continuum has the shape of a stellar atmosphere in all observations between days 180.4 and 370, but the absorption lines are blue-shifted and highly structured. The blue-shifts of all photospheric lines indicate that expansion is still continuing during the SSS phase, bringing about (as we will show later) a significant mass loss (Ness et al. 2009). The line profiles are extremely complex, and not all lines have the same profile. Globally, up to three different velocity-bands can be observed: $v_1 \sim -1000$ km s^{-1}, $v_2 \sim -2500$ km s^{-1} and $v_3 \sim -6000$ km s^{-1}, coming from ionic species spanning a wide range of ionization states, from C V to S XIV (see Table 4).

The distinctness of three velocity components as seen in Fig. 4, suggests that three (or more) concentric shells with low-density plasma in between are present. On the other hand, some lines are much narrower with only one or two components. Clearly, not all lines originate from the same region, indicating that a large range of different plasma regions are visible at the same time.

The amount and duration of mass-loss during the SSS phase can only be determined from detailed, physically plausible models. NLTE effects have proven to be crucial Hartmann and Heise (1997), and minimum requisite of the model has to be that it is spherically symmetric and expanding van Rossum and Ness (2010). See also Sect. 4 for evidences of this latest assumption.

6.4 Discussion of the SSS Phase

This is the first time that such results is extracted from observations, and a direct comparison with other works is not possible at the moment, but it implies that the kinematics of the ejecta comes from the radiation supplied by the central source; *suggesting the validity of the equipartition of energy* Shara et al. (2010a).

We assume an *ad hoc* efficiency of the radiation to ionization $L_{ion}/L_{rad} = 0.41$. A precise determination of L_{rad} is not simple, but we explore plausible values of it. We make use of the grid of novae models from Yaron et al. (2005), to estimate the mass of the white dwarf, M_{WD}, the temperature of its isothermal core, T_{WD}, and the mass transfer rate, $\dot{M}_{WD}$. If we take the average of $m_{ej} \approx 4 \times 10^{-4} \, M_\odot$ (assuming $L = 10^{38}$ erg s^{-1}), and look for the "best"-fit with the m_{ej} in Table 2 of Yaron et al. (2005), we find that the best- set of parameters is: $M_{WD} = 0.4$, $T_{WD} = 10^7$ K and $\log_{10}(\dot{M}_{WD}) = -9$ ($M_\odot/yr$). That would imply that we are in the presence of a low-mass ($\lesssim 0.5 \, M_\odot$) WD close binary system Yaron et al. (2005). On the other hand, if we look for parameters with $m_{ej} \approx 6 \times 10^{-4} \, M_\odot$, then $M_{WD} = 0.65$, $T_{WD} = 10^7$ K and $\log_{10}(\dot{M}_{WD}) = -12$ ($M_\odot/yr$). However assuming we take our computed luminosity of $L \approx 6 \times 10^{38}$ erg s^{-1}, then our estimation of m_{ej}, would be $\approx 2 \times 10^{-3} \, M_\odot$ and the extended grid of models Shara et al. (2010b) is required instead. In that case $M_{WD} = 0.5$, $T_{WD} = 3 \times 10^6$ K and $\dot{M}_{WD} = 5 \times 10^{-11}$ ($M_\odot/yr$), posing our object at the border of a very luminous red novae. This is certainly an upper limit since $L \approx 6 \times 10^{38}$ erg s^{-1} is only for epoch 1 and not for the whole time-interval of the mass loss. At the moment more precise estimations of the luminosity are required to characterize the set of physical parameters of the system V4743 Sgr. More work on that regard might take place in the near future.

6.5 Discussion Post SSS Phase

The basic idea of the final stages of nova evolution is that the ionized ejecta are radiatively cooling. Kinetic energy is successively converted to radiation via bound-bound collisional excitations followed by radiative deexcitations. As discussed in Sect. 6.2, charge exchange may also be an efficient cooling mechanism. In any way, the typical spectrum of a radiatively cooling plasma is an emission line spectrum,
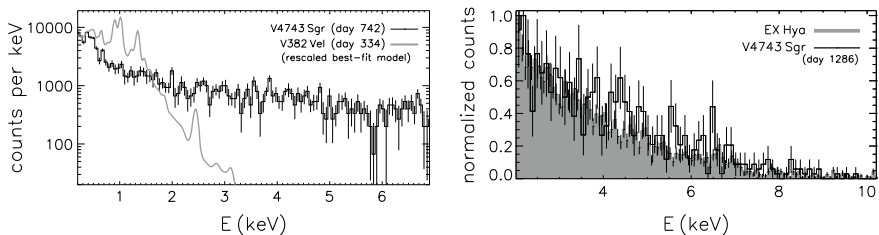
Fig. 8 Comparison between the X-ray spectrum of V4743 Sgr taken on day 742 and a post-SSS nova spectrum (*top*) and that of the intermediate polar EX Hya (*bottom*). The *thick grey line* in the *top panel* is a rescaled best-fit model to an X-ray spectrum of V382 Vel taken 334 days after discovery after convolution through the MOS1 response. In the *bottom panel*, normalized counts from our MOS1 spectrum and a *SWIFT*/XRT count spectrum are compared. (*Source* Jan-Uwe Ness)
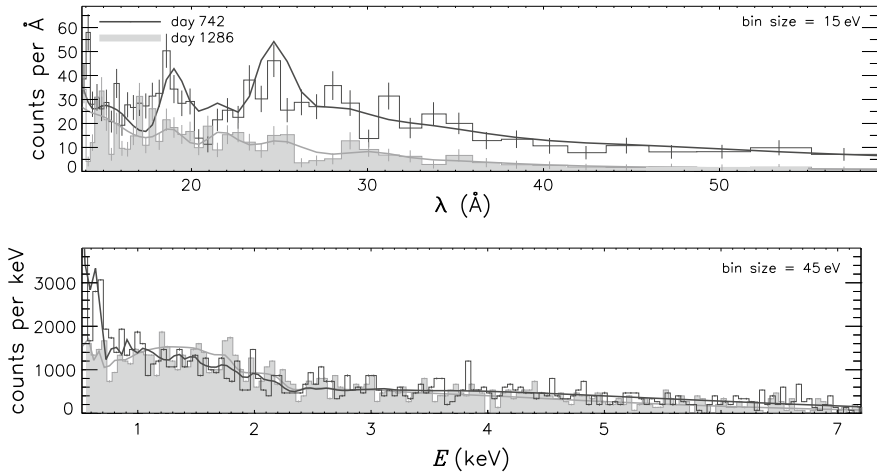
Fig. 9 *XMM-Newton*/MOS1 spectra taken on days 742 and 1286, plotted with *dark and light colors*, respectively (see *top left* legend). In the *top panel*, the soft part is shown in units wavelength, and in the *bottom* part the hard part in units keV. Best-fit models are included with continuous lines. (*Source* Jan-Uwe Ness)

and appropriate models are thin-thermal models as, e.g., implemented in the `apec` module in `xspec`.

A good example of a spectrum of radiatively cooling ejecta are post-SSS *Chandra* observations of the nova V382 Vel, taken on days 268, 334, and 450 after discovery. The first of these spectra was analyzed by Ness et al. (2005), and the assumption of a radiatively cooling plasma proved valid. The other two observations were successfully modeled with thin-thermal plasma models by Burwitz et al. (2002), who also found a slow power-law decline from all three observations.

Both post-SSS spectra of V4743 Sgr are different to V382 Vel. In order to compare these spectra, we show in the top panel of Fig. 8 the *XMM-Newton*/MOS1 spectrum of V4743 Sgr taken on day 742 and a rescaled model that fits the *Chandra* spectrum of V382 Vel, taken on day 334, after convolution through the instrumental response of the MOS1 detector. The spectrum of V382 Vel contains strong emission lines that are resolvable with the MOS1 detector, and no significant emission arises above ∼2 keV. Meanwhile, our spectrum is dominated by featureless emission, including a hard tail extending up to 10 keV. We were unable to find a satisfactory fit to the spectrum using an optically thin, thermal plasma model. Furthermore, no significant fading of the hard emission can be identified between days 742 and 1286 (see Fig. 9), while considerable fading was seen in V382 Vel (Burwitz et al. 2002). All evidence we have thus indicates that the hard component is not typical post-nova emission.

It is also of interest to note that no X-ray emission was seen in a deep ROSAT observation in 1990, twelve years before outburst. The nova has thus not returned to quiescence yet. Since the ROSAT band only covers the energy range 0.1–2.4 keV,

this non-detection only indicates the absence of soft emission, while the hard tail could have been present at that time. We thus predict that at least the soft component will eventually disappear.

7 Summary and Conclusions

Dr. Jan-Uwe Ness (ORCID 0000-0003-0440-7193)

We studied the hardness and brightness evolution using eight X-ray observations of V4743 Sgr and found three main stages of evolution.

(1) One X-ray spectrum was taken during the first phase and is an optically thin emission line spectrum which can be modeled by a thin-thermal plasma model, indicating that collisional processes are involved. Shock interactions of different components within the ejecta are the most commonly accepted model, but the presence of strong magnetic fields could lead to coronal emission that is heated in magnetically confined loops, similar to stellar coronae. V4743 Sgr has been proposed to be an intermediate polar, and we found supporting evidence (see below), thus magnetic fields may be present and relevant.

(2) The five high-resolution spectra obtained during the brightest SSS phase provide the largest amount of detail. The spectrum resembles a stellar atmosphere, but the absorption lines are blue shifted, and their complex profiles indicate that we are dealing with an expanding atmosphere, and the ejecta are inhomogeneous. Our technique of line identification, allow us to identify lines coming from H- and He-like ions of C,N,O blueshifted by ~2500 km s^{-1}, lead us to estimate a mass loss rate of $\dot{M} \approx (3-5) \times 10^{-4} \left(\frac{L}{L_{38}}\right) M_{\odot}/yr$. The total ejected mass is $m_{\mathrm{ej}} \approx (2-3) \times 10^{-4} M_{\odot}$, which locate V4743 Sgr., as a low-mass WD CO system. However due to uncertainties in the intrinsic luminosity of the source others (extreme?) positions in the parameter space of the grid of classical novae models, cannot be ruled out.

(3) The final phase is different from that observed in other novae, for which radiative cooling of the ionized ejecta has been observed. While significant fading of emission below ~2 keV is seen, the harder part of the spectrum does not change and resembles that of the intermediate polar EX Hya. ROSAT has detected no soft X-ray emission before the outburst that could have swept away material that blocks all soft emission. As this material replenishes, all emission below 2 keV might eventually disappear. This can be tested with further observations. Meanwhile, the hard emission could stay, which would support the intermediate polar nature of V4743 Sgr.

References

Balman S, Krautter J, Oegelman H (1988a). The X-ray spectral evolution of classical Nova V1974 Cygni 1992: a reanalysis of the ROSAT data. Astrophys J **499**: 395–+. https://doi.org/10.1086/305600

Balman S, Krautter J, Oegelman H (1988b) The X-ray spectral evolution of classical Nova V1974 Cygni 1992: a reanalysis of the ROSAT data. Astrophys J 499:395–+. https://doi.org/10.1086/305600

Bode MF (2004) The Evolution of Nova Ejecta. In: Meixner M, Kastner JH, Balick B, Soker N (eds) Asymmetrical Planetary Nebulae III: Winds, Structure and the Thunderbird, volume 313 of Astronomical Society of the Pacific Conference Series, pp 504–+

Burwitz V, Starrfield S, Krautter J, Ness J-U (2002) Chandra ACIS-I and LETGS X-ray observations of Nova 1999 Velorum (V382 Vel). In: Hernanz M, José J (eds) Classical Nova Explosions, volume 637 of American Institute of Physics Conference Series, pp 377–380. https://doi.org/10.1063/1.1518233

Dobrotka A, Ness J-U (2010) Multifrequency nature of the 0.75 mHz feature in the X-ray light curves of the nova V4743 Sgr. MNRAS 405:2668–2682. https://doi.org/10.1111/j.1365-2966.2010.16654.x

García J, Mendoza C, Bautista MA, Gorczyca TW, Kallman TR, Palmeri P (2005) K-Shell Photoabsorption of Oxygen Ions. Astrophys J Supplement 158:68–79. https://doi.org/10.1086/428712

Grevesse N, Noels A, Sauval AJ (1996) Standard abundances. In: Astronomical society of the Pacific conference series, p 117

Hartmann HW, Heise J (1997) Hot high-gravity NLTE model atmospheres as soft X-ray sources. A&A 322:591–597

Kallman T, Bautista M (2001) Photoionization and high-density gas. Astrophys J Supplement 133:221–253

Kang TW, Retter A, Liu A, Richards M (2006) Nova V4743 Sagittarii 2002: an intermediate polar candidate. Astron J 132:608–613. https://doi.org/10.1086/505174

Krautter J, Oegelman H, Starrfield S, Wichmann R, Pfeffermann E (1996) ROSAT X-ray observations of Nova V1974 Cygni: the rise and fall of the brightest supersoft X-ray source. Astrophys J 456:788–+. https://doi.org/10.1086/176697

Lloyd HM, O'Brien TJ, Bode MF, Predehl P, Schmitt JHMM, Truemper J, Watson MG, Pounds KA (1992) X-ray detection of Nova Herculis 1991 five days after optical outburst. Nature 356:222–224. https://doi.org/10.1038/356222a0

Lloyd HM, O'Brien TJ, Bode MF (1995) Interacting winds in classical nova outbursts. Ap&SS 233:317–321. https://doi.org/10.1007/BF00627366

Lyke JE, Kelley MS, Gehrz RD, Woodward CE (2002) Free-free turnover in Nova V4743 Sgr 2002 #3. In: Bulletin of the American Astronomical Society, volume 34 of Bulletin of the American Astronomical Society, pp 1161–+

Ness J-U, Starrfield S (2009) The X-ray Spectra of the Shock Systems in RS Oph. In: Murphy SJ, Bessell MS (eds) Astronomical Society of the Pacific Conference Series, volume 404 of Astronomical Society of the Pacific Conference Series, pp 77–+

Ness J-U, Starrfield S, Burwitz V, Wichmann R, Hauschildt P, Drake JJ, Wagner RM, Bond HE, Krautter J, Orio M, Hernanz M, Gehrz RD, Woodward CE, Butt Y, Mukai K, Balman S, Truran JW (2003) A chandra low energy transmission grating spectrometer observation of V4743 Sagittarii: a supersoft X-ray source and a violently variable light curve. Astrophys J Lett 594:L127–L130. https://doi.org/10.1086/378664

Ness J-U, Starrfield S, Jordan C, Krautter J, Schmitt JHMM (2005) An X-ray emission-line spectrum of Nova V382Velorum 1999. MNRAS 364:1015–1024. https://doi.org/10.1111/j.1365-2966.2005.09664.x

Ness J-U, Schwarz GJ, Retter A, Starrfield S, Schmitt JHMM, Gehrels N, Burrows D, Osborne JP (2007) Swift X-ray observations of classical novae. Astrophys J 663:505–515. https://doi.org/10.1086/518084

Ness J-U, Schwarz G, Starrfield S, Osborne JP, Page KL, Beardmore AP, Wagner RM, Woodward CE (2008) V723 CASSIOPEIA still on in X-rays a bright super soft source 12 years after outburst. Astron J 135:1328–1333. https://doi.org/10.1088/0004-6256/135/4/1328

Ness J-U, Drake JJ, Beardmore AP, Boyd D, Bode MF, Brady S, Evans PA, Gaensicke BT, Kitamoto S, Knigge C, Miller I, Osborne JP, Page KL, Rodriguez-Gil P, Schwarz G, Staels B, Steeghs D, Takei D, Tsujimoto M, Wesson R, Zijlstra A (2009) Swift X-ray and ultraviolet monitoring of the classical Nova V458 Vul (Nova Vul 2007). Astron J 137:4160–4168. https://doi.org/10.1088/0004-6256/137/5/4160

O'Brien TJ, Bode MF, Kahn FD (1992) Models for the remnants of recurrent novae. III—Comparison with the X-ray observations of RS Ophiuchi (1985). MNRAS 255:683–693

O'Brien TJ, Lloyd HM, Bode MF (1994) An interacting winds model for the X-ray emission from V838 Her (Nova Herculis 1991). MNRAS 271:155–160

Orio M, Parmar A, Benjamin R, Amati L, Frontera F, Greiner J, Ögelman H, Mineo T, Starrfield S, Trussoni E (2001) The X-ray emission from Nova V382 Velorum-I. The hard component observed with BeppoSAX. MNRAS 326:L13–L18. https://doi.org/10.1046/j.1365-8711.2001.04448.x

Page KL, Osborne JP, Evans PA, Wynn GA, Beardmore AP, Starling RLC, Bode MF, Ibarra A, Kuulkers E, Ness J-U, Schwarz GJ (2010) Swift observations of the X-ray and UV evolution of V2491 Cyg (Nova Cyg 2008 No. 2). MNRAS 401:121–130. https://doi.org/10.1111/j.1365-2966.2009.15681.x

Payne-Gaposchkin C (1954) The galactic novae

Sala G, Hernanz M (2005) Envelope models for the supersoft X-ray emission of V1974 Cyg. A&A 439:1057–1060. https://doi.org/10.1051/0004-6361:20042587

Scargle JD (2004) Data analysis through segmentation: bayesian blocks and beyond. In: Bulletin of the American Astronomical Society, volume 36 of Bulletin of the American Astronomical Society, p 1200–+

Shara MM, Yaron O, Prialnik D, Kovetz A (2010a) Non-equipartition of energy, masses of Nova Ejecta, and Type Ia Supernovae. Astrophys J Lett 712:L143–L147. https://doi.org/10.1088/2041-8205/712/2/L143

Shara MM, Yaron O, Prialnik D, Kovetz A, Zurek D (2010b) An extended grid of nova models. III. Very Luminous, Red Novae. ArXiv e-prints

Smith RK, Brickhouse NS, Liedahl DA, Raymond JC (2001) Collisional plasma models with APEC/APED: emission-line diagnostics of hydrogen-like and helium-like ions. Astrophys J Lett 556:L91–L95. https://doi.org/10.1086/322992

Starrfield S, Timmes FX, Hix WR, Sion EM, Sparks WM, Dwyer SJ (2004) Surface hydrogen-burning modeling of supersoft X-ray binaries: are they type ia supernova progenitors? Astrophys J Lett 612:L53–L56. https://doi.org/10.1086/424513

Starrfield S, Swift-Nova-CV group (2008) Classical Novae in the Swift Era. In: AAS/High energy astrophysics division, volume 10 of AAS/High Energy Astrophysics Division, pp 19.04–+

Tsujimoto M, Takei D, Drake JJ, Ness J-U, Kitamoto S (2009) X-ray spectroscopy of the c lassical Nova V458 Vulpeculae with Suzaku. PASJ 61:69–+

van Rossum DR, Ness J-U (2010): Expanding atmosphere models for SSS spectra of novae. Astron Nachr 331:175–+. https://doi.org/10.1002/asna.200911321

Yaron O, Prialnik D, Shara MM, Kovetz A (2005) An extended grid of nova models. II. The parameter space of nova outbursts. Astrophys J 623:398–410. https://doi.org/10.1086/428435

X-Ray Outflows of Active Galactic Nuclei Warm Absorbers: A 900 ks Chandra Simulated Spectrum

J.M. Ramírez-Velasquez and J. García

Abstract We report on the performance of the statistical X-ray absorption lines identification procedure XLINE-ID. As illustration, it is used to estimate the time averaged gas density $n_H(r)$ of a representative AGN's warm absorber ($T \approx 10^5$ K) X-ray simulated spectrum. The method relies on three key ingredients: (1) a well established emission continuum level; (2) a robust grid of photoionization models spanning several orders of magnitude in gas density (n_H), plasma column density (N_H), and in ionization states; (3) theoretical curves of growth for a large set of atomic lines. By comparing theoretical and observed equivalent widths of a large set of lines, spanning highly ionized charge states from O, Ne, Mg, Si, S, Ar, and the Fe L-shell and K-shell, we are able to infer the location of the X-ray warm absorber.

1 Introduction

In active galactic nuclei (AGNs), photoionization has been recognized as the main mechanism for the formation of Ultraviolet (UV) and X-ray lines (Bahcall and Kozlovsky 1969). If the photo-ionized plasma reaches a stable state for their ion populations, they are said to be in photo-ionization equilibrium (PIE). Under the assumption of PIE, one of the principal parameters describing the physical condition of the plasma is the ionization parameter ξ:

J.M. Ramírez-Velasquez (✉)
Physics Centre, Venezuelan Institute for Scientific Research (IVIC),
PO Box 20632, Caracas 1020A, Venezuela
e-mail: josem@ivic.gob.ve

J.M. Ramírez-Velasquez
Departamento de Matemáticas, Cinvestav del I.P.N., 07360 Mexico, D.F., Mexico

J. García
Harvard-Smithsonian Center for Astrophysics, 60 Garden Street,
Cambridge, MA 02138, USA
e-mail: javier@head.cfa.harvard.edu

$$\xi(r) = \frac{L}{n_H(r)r^2}, \qquad (1)$$

where L is the ionizing luminosity of the primary source, $n_H(r)$ is the gas density, and r is the distance from the ionizing source to the interacting shell/slab of plasma. Therefore, spectral fitting to the observational data in the X-ray band of a given source combined with a measurement of its luminosity L provides constrains on the degenerated quantity $n_H(r)r^2$. Moreover, in order to have an estimate of the spatial location of the gas absorbing/emitting photons from the primary underlying source, an independent determination of the gas density $n_H(r)$ is required.

Curve of growth (COG) (Spitzer 1998) is a useful tool to gather information from astrophysical spectra, like ion column density (N_{ion}) using the strength of absorption lines. However, the technique is full of exact requirements and limitations. In order for a line to be used as COG diagnostic tool, firstly (1) a well defined continuum level has to be known prior any construction of the COG. Secondly (2) the synthetic COGs, are usually compared with real measurements of equivalent widths (EWs) of lines. Third (3) the chosen lines must be not saturated respect to the variable we wish to contrast to. Furthermore (4), a reliable *identification* procedure *must be* built on the grounds of a well constructed photoionization modelling (Kallman and Bautista 2001) which in turn needs a well established set of atomic data. For instance, Badnell (2006) pointed out about the inappropriate use of some dielectronic recombination (DR) rates, which are later discussed by Kallman (2010) in the context of photoionization modelling and the correct use of atomic data (now implemented in the latest version of XSTAR) (Bautista and Kallman 2001).

Following a series of papers related with the computations of K lines of Fe (Palmeri et al. 2002, 2003a), and K-shell photoabsorption of O ions atomic data (energies, cross sections, lifetimes) (Ramírez and Bautista 2002; García et al. 2005, 2011), Palmeri et al. (2008) discuss in detail the reliability and accuracy of some sets of these data (medium-Z elements), currently observed in the X-ray spectrum of active galactic nuclei (AGNs, e.g., NGC 3783 Kaspi et al. 2002, Ramírez et al. 2005, Ramírez 2011, MR 2251−178 Ramírez et al. 2008, APM 08279+5255 Ramírez et al. 2008, Ark 564 Ramírez 2013), in the form of K-absorption lines of H- and He-like Ne,Mg,Si,S, possibly Ar and Ca, and also from lower and medium ionization stages of Si and S (e.g., for MCG-g-30-15 and IRAS 13349 + 2438) (Holczer et al. 2007), with the aim of improving the atomic database of the XSTAR modelling code.

We report on the accuracy of the statistical method, XLINE-ID, which allows us to extract time averaged gas density n_H of interacting material surrounding UV+X-rays sources, from EW measurements and *detection* of unsaturated absorption lines respect n_H.

The paper is organized as follows: in the first section, we present the set of data used, next the details of the method, and finally we delineate the results of the distribution of Doppler velocities found, and compute gas densities. We also discuss the results and conclude. Throughout this paper, we use a cosmology with $H_0 = 70$ km s^{-1} Mpc^{-1}, $\Omega_M = 0.3$ and $\Omega_\lambda = 0.7$.

2 The Set of Data and the Emission Continuum Level

One of the main problems in the identification of narrow spectral features in X-ray sources, is the impossibility of contrasting the final atomic identification (ID) of a feature with an input feature, once it has passed through all the instrumentation (effective areas, re-distribution matrix, etc.). This is why we aim at assessing this problem, generating a spectrum, over which we have absolute control of every single feature (absorption lines and edges). For that purpose we have created an artificial first dispersion order ± 1 HETG+MEG 900 ks (HETGS with medium energy grating [MEG]), where we know exactly where every feature is located, and described in more detail as follows.

We begin by building a physical model (pow)*wabs1*wabs2 constituted by an UV+X-rays source, redshifted by $z = 0.00976$, emitting a powerlaw (pow), modified by two constant-density (log$[n_H] = 12$ [cm^{-3}]) absorbers (wabs1, with ionization parameter log$\xi = 2.08$ [erg cm s^{-1}], column densities $N_H = 10^{22}$ cm^{-2}, and wabs2, with ionization parameter log$\xi = 1.15$ [erg cm s^{-1}], column densities $N_H = 10^{21}$ cm^{-2}).[1] We call this model A. We then use XSPEC 12 to generate a 900 ks MEG spectrum, using appropriate +1 and –1 dispersion orders of MEG effective areas and 1st order response matrix (see science threads in the CIAO main page, http://cxc.harvard.edu/ciao/).

Table 1 gives the physical parameters of model A to produce one of the spectra we use in the analysis. Figures 1 and 2 show: the simulated ± 1 MEG spectrum, (points with error bars); how wabs1 and wabs2 (solid red line) modify the Spectral Energy Distribution (SED)[2] pow.

In order to analyze an X-ray spectrum more similar to a real observation (Pérez and Ramírez 2014), we introduce an outflow velocity to each absorber, $z_{\text{out}-\text{wabs1}} = 0.00876$ (300 km s^{-1}) for wabs1, and $z_{\text{out}-\text{wabs2}} = 0.00836$ (420 km s^{-1}) to wabs2.

Finally, one additional complication is introduced in model B. We add absorption due to interstellar medium (ism), ism*(pow)*wabs1*wabs2, so we can study the effect of measuring equivalent widths, with and without consider the unabsorbed continuum emission. Table 2 gives parameters for model B. Each case will be carefully analyzed in the next sections.

---

[1] Computed using the code XSTAR and described in more detail in the section **Models: The grid**.

[2] We refer also as the unabsorbed emission continuum from the primary source as seen by the absorber (dashed line in the figures).

Table 1 Physical parameters of model A

Component	Value	Units
Γ_x	2	–
N^a	0.010	Photons keV^{-1}cm^{-2} s^{-1} at 1 keV
z_{pow}	0.00976	–
$\log \xi(1)$	2.08	erg cm s^{-1}
$N_H(1)$	10^{22}	cm^{-2}
$z_{out-wabs1}$	0.00876	–
$\log \xi(2)$	1.15	erg cm s^{-1}
$N_H(2)$	10^{21}	cm^{-2}
$z_{out-wabs2}$	0.00836	–

Fig. 1 The continuum emission seen by the material surrounding the UV+X-rays source (1–13 Å). Points with *error bars* are the 900 ks simulated redshifted *Chandra* observation. *Solid lines* photoionization model of the absorber (*red*), and *dashed line* the SED

3   The XLINE-ID Method: General Picture

Our goal is to compare measured line equivalent widths (EWs) with synthetic curves generated as functions of the main physical parameters of the system: column density in the line of sight (N_H), (log of) ionization parameter ($\log \xi$), and gas density (n_H).
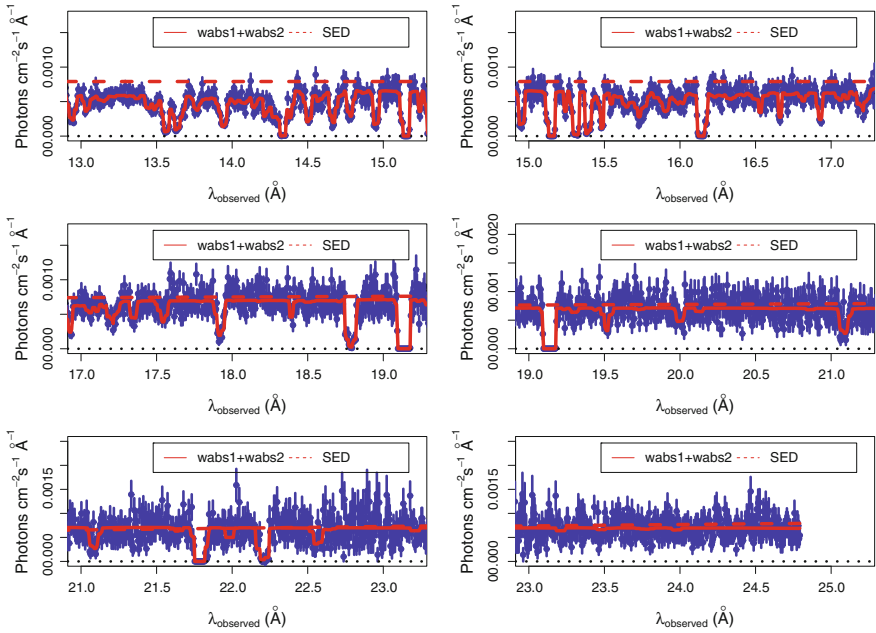
Fig. 2 The continuum emission seen by the material surrounding the UV+X-rays source (13–25 Å). Points with *error bars* are the 900 ks simulated redshifted *Chandra* observation. *Solid lines* photoionization model of the absorber (*red*), and *dashed line* the SED

Table 2 Physical parameters of model B

Component	Value	Units
ism	9.91×10^{20}	cm^{-2}
Γ_x	2	–
N^a	0.010	Photons $keV^{-1}cm^{-2}s^{-1}$ at 1 keV
z_{pow}	0.00976	–
$\log \xi(1)$	2.08	erg cm s^{-1}
$N_H(1)$	10^{22}	cm^{-2}
$z_{out-wabs1}$	0.00876	–
$\log \xi(2)$	1.15	erg cm s^{-1}
$N_H(2)$	10^{21}	cm^{-2}
$z_{out-wabs2}$	0.00836	–

The first step to achieve this is to generate a grid of photoionization models (as in AGNs, photoionization is the dominant mechanism for production of spectral lines). Secondly, we define the line profile and compute the integrals involved in the EWs of the lines of interest (a list of *detected* features is required as input for XLINE-ID). This is a critical step, since none of the main photoionization codes (e.g., CLOUDY,

XSTAR), compute this quantity (by default) for the thousands of lines usually included in the run of the grids, mainly for computational efficiency. The third step is to compare measured EWs with theoretical EWs in order to draw out the parameters of interest.

3.1   Models: The Grid

Here we describe the building of the grid of models. We use the photoionization code XSTAR[3] v 2.2 with the most up-to-date atomic database v 2.2.1bn20 (Bautista and and Kallman 2001).

The code includes all the relevant atomic processes, including inner shell processes (Palmeri et al. 2003a, b). It computes the emissivities and optical depths of the most prominent X-ray and UV lines identified in AGN spectra. Our models are based on spherical slabs illuminated by a point-like X-ray continuum source. The input parameters are the source spectrum, the gas composition, the gas density n_H, the column density in the line of sight N_H and the ionization parameter ξ. The source spectrum is described by the spectral luminosity $L_\epsilon = L_{ion}f_\epsilon$, where L_{ion} is the integrated luminosity from 1 to 1000 Ryd, and $\int_1^{1000\ \mathrm{Ryd}} f_\epsilon d\epsilon = 1$. The spectral function f_ϵ is taken to be a powerlaw $\sim \epsilon^\alpha$ with $\alpha = -1$ (photon index $\Gamma_x = 2$). The gas consists of the following elements, H, He, C, N, O, Ne, Na, Mg, Si, S, Ar, Ca and Fe. We use the abundances of Grevesse et al. (1996) in all our models (and the term *solar* for these abundances). We adopt a turbulent velocity of 200 km s^{-1}. The total ionizing luminosity used is $L_{ion} = 2.5 \times 10^{44}$ erg s^{-1}.

We have taken two representative ionization parameters: $\log \xi = 2.08$ [erg cm s^{-1}], and $\log \xi = 1.15$ [erg cm s^{-1}]. We call them medium ionization plasma (MIP, represented by wabs1) and low ionization plasma (LIP, represented by wabs2), respectively. Finally due to our interest in testing the sensitivity of the line strengths with the gas density, we run $log_{10}(n_H) = 5 - 18$ [cm^{-3}], and $N_H = [1, 0.1] \times 10^{22}$ cm^{-2}, for each of the two ionization states, resulting in 28 points in the grid, making it a modest resolution density-COG grid for warm absorber in AGNs.

3.2   TRUNK-1: The Identification List Model

We have developed a simple algorithm to identify observed absorption spectral features. The identification is performed by comparing both the line wavelength and optical depth with those computed theoretically in our grid of models. For each model we choose the 500 strongest features, which results in a total of 14,000 theoretical absorption lines ($500 \times 14n_H \times 2N_H$). We shall refer to this as our *identification*

---

[3]https://heasarc.gsfc.nasa.gov/docs/software/xstar/xstar.html.

list. The simplest way to identify an observed line is to compare its measured wavelength with the theoretical values. However, one must also allow for the possibility of wavelength shifts due to velocity components in the absorbing material. Thus, starting with the best-fit for the line centroid λ_0 of a given observed line, we search for theoretical lines within a $\pm\Delta\lambda_0$ identification window (IW) around λ_0. This allows for the identification of blue or redshifted lines. If more than one theoretical line is present in the identification window, we choose the line with the largest optical depth at the core (τ_0).

A second observed feature can be found close enough such that its identification window cover a similar range, including the same strong lines. If the next observed feature is identified by the same theoretical line as in the feature just before, we do not allow for repetition but rather choose the second strongest line in the identification window. This allows for the detection of duplets. Nevertheless, this constrain is only applied to two consecutive lines. Thus, if a third consecutive observed line (i.e. two features next) is identify with the same strongest theoretical lines as the first, this one is assigned again. This allows the detection of more than one velocity component. The result is an identification list based on the strongest predicted absorption line, $\pm\Delta\lambda_0$ Å around a feature detected at λ_0 Å, truncated only *once* for repetition if two features are too close. We call this identification list model TRUNK-1.

Similar studies have been carried out in the past where measured absorption features are compared with a theoretical features in a given identification list (e.g., Krongold et al. 2003; Netzer et al. 2003). However, these studies present two important limitations: the identification list employed typically contain a relatively small number of theoretical features (e.g., ∼50), and their identification is based on comparing the wavelength position of the observed feature with those calculated theoretically using undefined identification window (how much is allowed for an observed feature to be compared with theory, e.g., 0.1 Å, is too large). The latter restriction is particularly important because the larger the identification window becomes, the more are the chances of an incorrect identification. To demonstrate the efficacy of our methodology, we have applied the TRUNK-1 algorithm to the synthetic spectra produced with Model A, i.e., the model consisting of two warm absorbers (Table 1).

Because we know exactly which lines are contained in the synthetic spectra, we can then assess how well TRUNK-1 identify the observed lines. Figure 3 shows the level of matching in percent achieved by TRUNK-1. The upper panel in Fig. 3 shows the level of matching achieved when the identification is performed solely based on the line position. A good matching is only possible when the identification window is set to the smallest value ($\Delta\lambda_0 = 10^{-4}$ Å). For wider windows the quality of the identification becomes rapidly poor. A much better performance is achieved when, in addition to line positions, line strengths are also compared with the theoretical predictions. This agreement is shown in the lower panel of Fig. 3, where is clear that the full TRUNK-1 method is capable to correctly identify no less of 90 % of the lines, even for the largest identification window considered ($\Delta\lambda_0 = 0.2$ Å).

The synthetic spectra discussed above contains 239 absorption lines produced with the MIP (wabs 1), and 115 lines produced with the LIP (wabs 2). Although the identification is somewhat better for the lines produced in the absorption component

Fig. 3 *Top panel* Only first stage of the matching lists process input/TRUNK-1, for the list of the strongest lines coming from our simulation. In the X-axis we open the identification window ($\Delta\lambda$) from 10^{-4} to 0.2 Å. In *blue* we present matching process for wabs1, and in *red* for wabs2. *Bottom panel* Second stage of the matching lists process input/TRUNK-1. In the X-axis we open the identification window ($\Delta\lambda$) from 10^{-4} to 0.2 Å. In *blue* we present matching process for wabs1, and in *red* for wabs2 (see Y-axis scale)
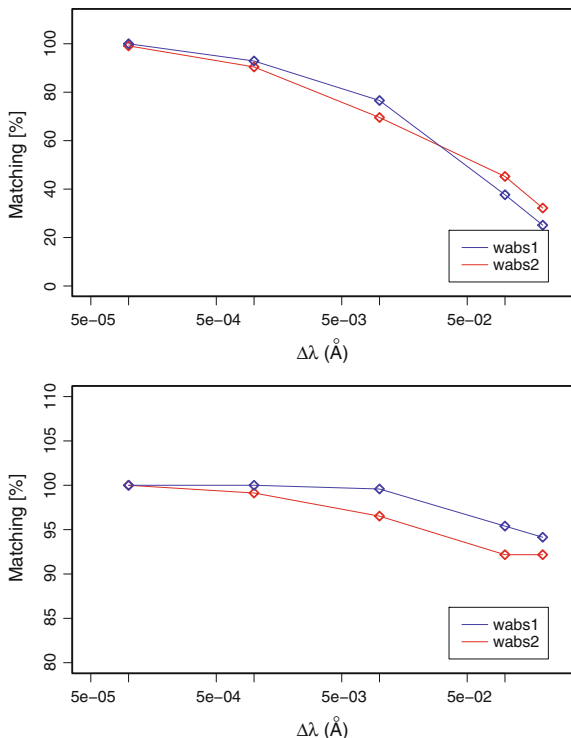
with the smaller redshift (wabs 1), these results indicate that our algorithm can be successfully implemented to real X-ray observations where complex mixture of absorption components can be present. Figure 5 shows the 11–12 Å band of the synthetic spectra, where the known absorption features and those identified by TRUNK-1 are indicated.

Our method correctly identifies 100 % of the lines in this band, which we have tested for different widths of the identification window. A similar analysis is performed using a synthetic spectra based on Model B (Table 2), where on top of the two warm absorber components, a third component due to galactic absorption is included (ism). This latter component only includes the continuum (bound-free) photoelectric absorption, thus while it modifies the model continuum it does not introduces any additional absorption features.

In order to illustrate the virtues and caveats of the method we show in Fig. 4, six possible cases which are easily solved by it. In panel (a) we have the simplest possible case. One observed feature $\lambda(O)_1$, has an IW $\Delta\lambda_0$, and only the theoretical line $\lambda(T)_1$ is within the IW. Then $\lambda(O)_1$ is easily identified as $\lambda(T)_1$.

In panel (b), theoretical lines $\lambda(T)_1$ and $\lambda(T)_2$ are within $\Delta\lambda_0$. In this case we simply take the one with the largest optical depth. If we assign τ_1 to $\lambda(T)_1$ and τ_2 to $\lambda(T)_2$ with $\tau_1 > \tau_2$, then $\lambda(O)_1$ is simply identified as $\lambda(T)_1$.
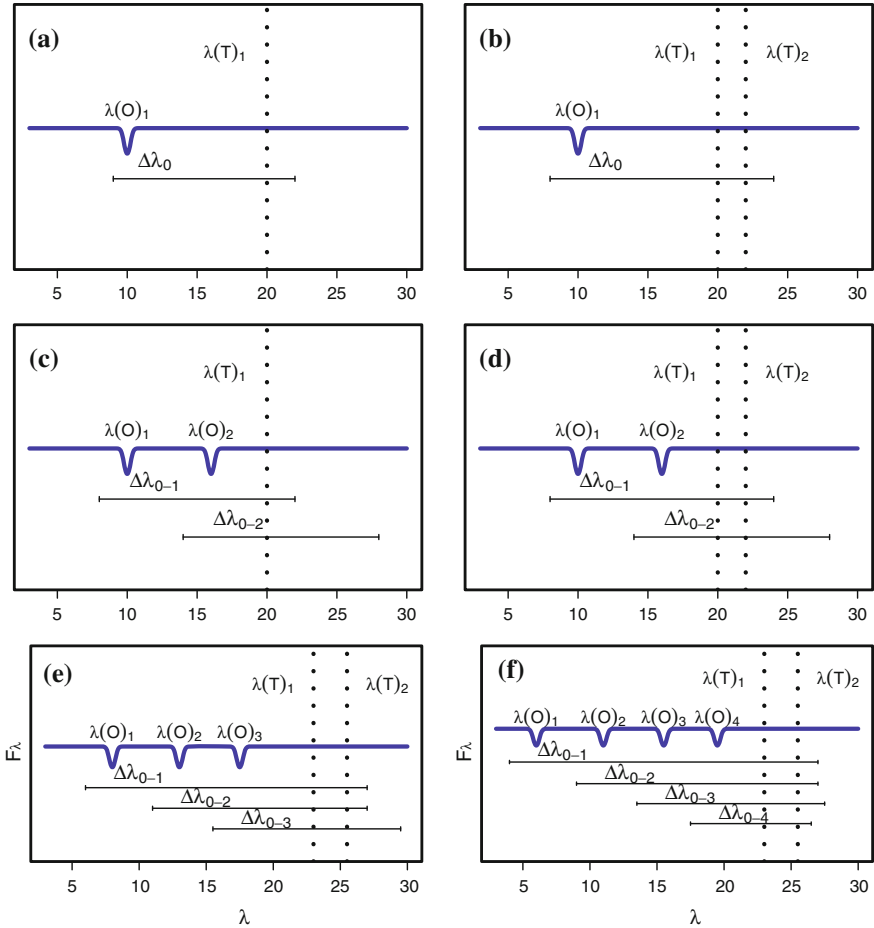
Fig. 4 Complex cases treated by TRUNK-1 for the ID of lines. Panel **a** the simplest case. Panel **b** two candidate lines case. Panel **c** two observed lines have one theoretical line as candidate. Panel **d** two- features, two- candidates (duplets). Panel **e** two velocity-component case. Panel **f** two velocity-component duplets case. See text for details

In panel (c) we now have a second observed feature $\lambda(O)_2$. Assuming $\lambda(O)_1$ was already identified as $\lambda(T)_1$ and $\Delta\lambda_{0-2}$ does not contain another theoretical line, $\lambda(O)_2$ will be marked as UNKNOWN. Although this is a rare case, it can be mentioned as a caveat of the algorithm (which also happens with regular ID methods) (Fig. 5).

In panel (d) a second theoretical line $\lambda(T)_2$ is now in the list of candidates for $\lambda(O)_2$. Assuming $\lambda(O)_1$ was already identified as $\lambda(T)_1$, the TRUNK-1 will force to $\lambda(O)_2$ to be identified as $\lambda(T)_2$ and not as $\lambda(T)_1$, missing the "unlikely" possibility of $\lambda(O)_2$ being a second velocity-component of $\lambda(O)_1$, and by some unknown mechanism $\lambda(T)_2$ was remove from our line-of-sight. Although rare, this also has to be mentioned as a caveat of the method.

Fig. 5 Simulated spectrum (11–12 Å) showing the input "full-list" given to the procedure TRUNK-1 for wabs1, and the output identification list, using $\Delta\lambda = 10^{-4}$ Å (*vertical black dashed lines* for wabs1). The absorption lines are enumerated in increasing strength order from 1 to 13

In panel (e), we allow the possibility of $\lambda(O)_1$ to have a second velocity-component, if $\lambda(O)_1$ was already identified as $\lambda(T)_1$, and $\lambda(O)_2$ as $\lambda(T)_2$, then $\lambda(O)_3$ will be identified as $\lambda(T)_1$.

And finally in panel (f), there will be two duplets velocity-components with $\lambda(O)_1$ and $\lambda(O)_3$ identified as $\lambda(T)_1$, and $\lambda(O)_2$ and $\lambda(O)_4$ identified as $\lambda(T)_2$.

Although not complete, the list of possible cases cover the situations given in the present work. More cases and/or possibilities can be added to the algorithm in the future, but the results given by Fig. 3 (bottom panel), show the method's performance is at the level of ≈ 90 %.

In summary we list the limitations of the method:

1. From the beginning, if the photoionization components (e.g., wabs1 and/or wabs2) are not globally fitting the spectrum, the ID process will be dubious.
2. The method expects a list of detected features. If as part of a blend, only one feature is given, the method will ID it as the strongest one, regardless the micro-physics of the blend.
3. The method will not identify a case where the physics changes the ratio $\lambda(T)_1/\lambda(T)_2 > 1$ to < 1 (e.g., case b of Fig. 4).

4. Naturally, if the continuum is not well established in the building of the physical model, at the beginning of the process, the absolute measurement of EWs will be wrong (though the comparison between them will be good since they all use the same continuum).

5. The algorithm does not allow the ID of two-velocity component of a feature under the configuration given by case c) of Fig. 4. In all those cases visual and manual inspections are required.

3.3 Line Profile and EWs

Our procedure receive a list of lines (previously produced in the ID step) and applies the following treads: Each transition produces an absorption optical depth computed with:

$$\tau_\lambda = \tau_0 \phi_\lambda, \tag{2}$$

the optical depth at the core of the line is $\tau_0 = \int_0^{\Delta R} \tau_0(r)dr = N_{\text{ion}}^0 \frac{\pi e^2}{mc} f_{\text{lu}}$, where $\Delta R = N_H/n_H$ is the thickness of the slab, N_{ion}^0 is the column density of the ion at the line core (i.e., $\lambda = \lambda_0$), m is the electron mass, e is the electron charge, c is the speed of light, and f_{lu} is the oscillator strength of the transition. The line profile ϕ_λ, is assumed to be a Voigt profile (Rybicki and Lightman 1979). The Doppler broadening parameter $v_{\text{Dop}}^2 = v_{\text{turb}}^2 + v_{\text{therm}}^2$, is the combination of microturbulent (v_{turb}) and thermal broadening (v_{therm}). The last one is computed with $v_{\text{therm}} = \sqrt{\frac{2k_B T}{\mu m_H}}$, where k_B is the Boltzmann constant, μm_H is the average mass per particle; $\mu \simeq 0.6$ for fully ionized solar-metallicity gas. The temperature T is taken from our XSTAR calculations. The microturbulent velocity v_{turb} is set to 200 km s^{-1}. Then, we build absorption spectrum for each line (F_λ around each feature) and compute EWs:

$$EW = \int 1 - \exp(-\tau_\lambda)d\lambda. \tag{3}$$

One important problem we are able to address here, is the difference of measuring absorption line EWs taking into account all the relevant atomic physics, i.e., bound-bound and bound-free transitions, which extend from the SED, in contrast with measurements of EWs made using as the continuum the absorbed SED. We call the first type unabsorbed EWs and the second one absorbed EWs. Figure 6, depicts this problem in a visual manner.

For instance in a model where a single absorber is present (wabs1), we find difference between the level of SED (red dashed line in figures), and the level of the absorbed SED (gray dashed line), which is the result of the SED's radiation passing through wabs1. It is clear that measuring EWs using these two different continuum levels will give different results.
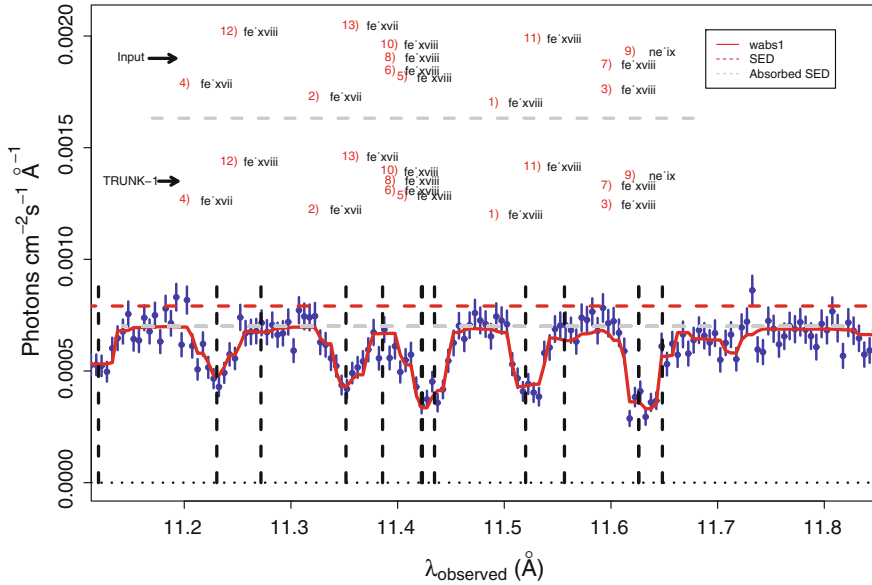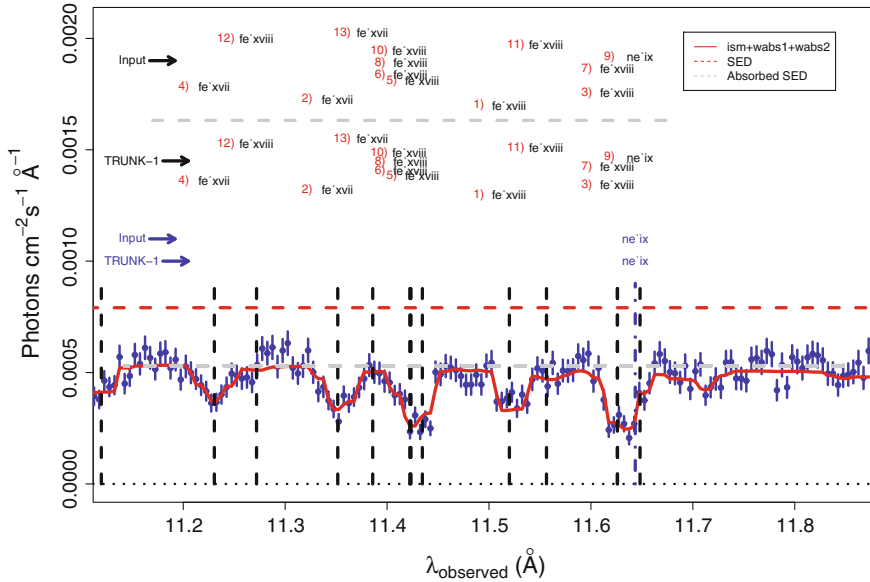
Fig. 6 Simulated spectrum (11–12 Å) showing the input "full-list" given to the procedure trunk-1 for ism+wabs1+wabs2, and the output identification list, using $\Delta\lambda = 10^{-4}$ Å (*vertical black dashed lines* for wabs1, and *vertical blue dashed lines* for wabs2). The absorption lines are enumerated in increasing order from 1 to 13

Likewise applied to a real observation, the method identifies and present results from H- and He-like ions falling in the X-rays regime, and differences among 6 % at $\lambda \approx 20$ Å in lines like Ly_α and Ly_β of OVIII, to 24 % at $\lambda \approx 10$ Å in lines like MgXI and L-shell of FeXVI-FeXIX, are attributable to the chosen continuum level.

The situation becomes more dramatic as the complexity in absorption increases for model A and model B. We quantify how important this continuum level problem results, where ISM is taking into account. Up to 80 % differences, in both absorbers wabs1 and wabs2, of EW measurements are observed, and it serves as benchmark for comparison of EWs measured using the free-line region (FLR) technique, which make use of absorbed SED as continuum level, as for instance in Kaspi et al. (2002), for measuring line properties of NGC 3783 (see their Table 1).

4   Results: Deducing Distance from the Supermassive Black Hole

In this section we apply our method to the X-ray 900 ks spectrum, introduced in the first section.

4.1 Measured Versus Theoretical EWs

Theoretical curves of the Ratio $= \frac{EW_{meas}}{EW_{theo}}$ (measured EW to theoretical EW) *versus* n_H, for each of the identified features included in the simulation, are compared for wabs1 and wabs2. In Fig. 7 (bottom panel) we plot all the Ratios produced through identification of lines (239) using the TRUNK-1 model and the absorber wabs1 ($\log \xi = 2.08$, $N_H = 10^{22}$ cm^{-2}, $n_H = 10^{12}$ cm^{-3}). A wavelength-color map has been placed at the right side, so one can read which lines are causing the deviations from 1, that is obtained when $EW_{meas} = EW_{theo}$. It is natural from this plot to infer what is the spectrum that matches better the observation, i.e., the one with the smaller standard deviation (SD, top axis on the plot) from the mean equal to 1. The same type of graphics has been plotted in Fig. 8 for wabs2 ($\log \xi = 1.15$, $N_H = 10^{21}$ cm^{-2}, $n_H = 10^{12}$ cm^{-3}), where again we reach the conclusion that the best-fit n_H is the one with smallest SD for Ratio, with mean 1. An analysis of these results will be given in the next section.

4.2 COG Analysis

In order for a line to be used as density diagnostic, it must be not saturated, and its ratio with measured EWs sensitive respect to n_H. In Fig. 8 we present the ratio of measured to theoretical EWs for each of the feature identified and included in building of the spectrum, given by the LIP, with IW, $\Delta\lambda = 10^{-4}$ Å. This plot infers that the plasma gas density reproducing best the observation is $n_H = 10^{12}$ cm^{-3}, where SD = 0.0. Fitting procedures allow us to set limits on SD in order to achieve confidence level in therms of χ^2. SD of 0.12–0.15 produce changes >90 % confidence level on measurements of n_H. We are able to infer the gas density of the spectrum to be $n_H = (2.4 \times 10^{10}, 1.2 \times 10^{13})$ cm^{-3}, for the LIP component of the absorbing complex in model B.

The COG ratio shown by the MIP is an excellent case of highly sensitive curve with n_H (see Fig. 7). The envolvent (irregular gray polygon) makes a strong constrain of the gas density to be $n_H \approx 10^{12}$ cm^{-3}. Again limits on the measurements using SD = 0.15–0.17 ($\chi^2 > 2.79$) reports $n_H = (1.9 \times 10^{10}, 3.1 \times 10^{12})$ cm^{-3}, for the MIP component of model B.

We checked for the robustness of these measurements with the building of a 2D contours, produced by computing a grid of photoionization models for wabs1 (MIP) and wabs2 (LIP), varying $\log(n_H) = 5 - 18$ [cm^{-3}], with one point per decade. The result is plotted at the top panel of Fig. 7 (for wabs1). From the best-fit $n_H \approx 10^{12}$ cm^{-3}, $\chi^2 \approx 4845$ using 4604 PHA bins (and two free parameters), we compute contour level of confidences 63, 90 and 95 % for n_H and the normalization parameter of the powerlaw.

We remark here, that in an independent way, we are obtaining results that are in agreement with the measurements given by our own method. In the bottom panel we
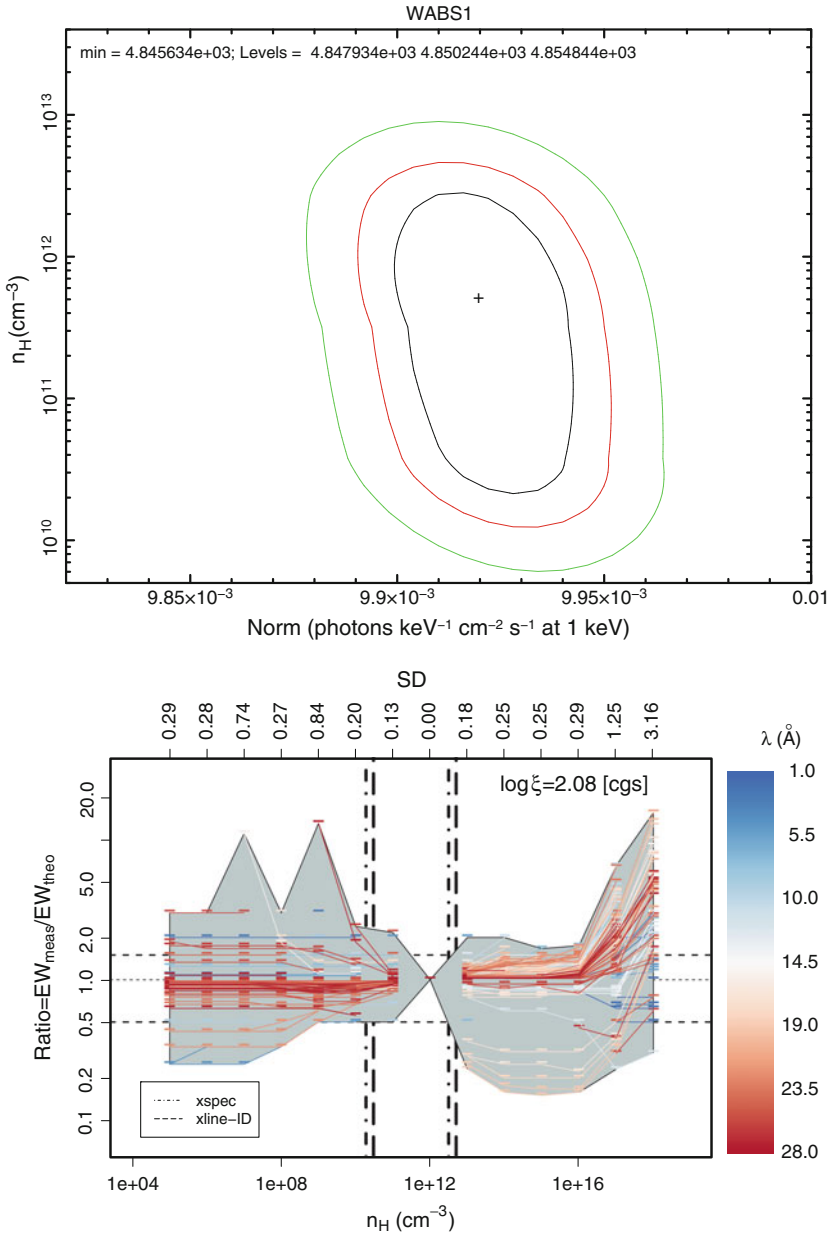
Fig. 7 *Top panel* 63, 90 and 95 % 2D confidence level contours on the gas density, n_H, and normalization parameter infer for wabs1. *Bottom panel* Ratio $= \frac{EW_{meas}}{EW_{theo}}$ versus n_H, covering 14 order of magnitudes. At the *right side* there is a wavelength-color map for the 239 spectral lines detected for the wabs1. Top axis presents the standard deviation (SD) from the mean 1, for each set of lines given by each n_H. *Vertical dot-dashed lines* are lower- and upper limits computed using spectral fitting within xspec. *Vertical dashed lines* are lower- and upper limits computed using xline-ID
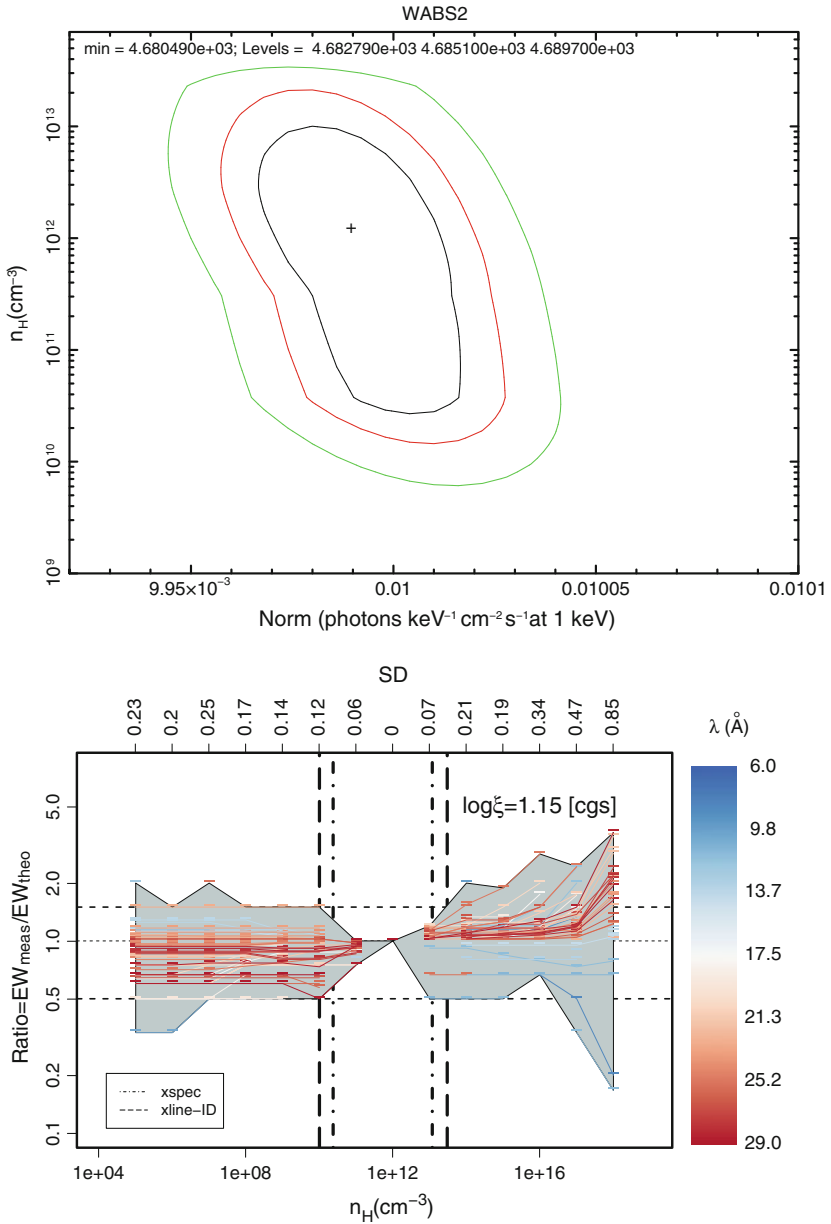
Fig. 8 *Top panel* 63, 90 and 95 % 2D confidence level contours on the gas density, n_H, and normalization parameter infer for wabs2. *Bottom panel* Ratio = $\frac{EW_{meas}}{EW_{theo}}$ versus n_H, covering 14 order of magnitudes. At the *right side* there is a wavelength-color map for the 115 spectral lines detected for the wabs2. Top axis presents the standard deviation (SD) from the mean 1, for each set of lines given by each n_H. *Vertical dot-dashed lines* are lower- and upper limits computed using spectral fitting within xspec. *Vertical dashed lines* are lower- and upper limits computed using xline-ID

compare these XSPEC measurements, i.e., single parameter 90 % confidence level on n_H (vertical dot-dashed line), against the XLINE-ID results. The obvious advantage of our method, is that we can track each of the absorption line which is contributing to the COG ratio density diagnostic, overcoming problems like several χ^2-minima, double evaluated best-fit parameter, lack of ability to evaluate what are the spectral ranges contributing to χ^2, among others.

4.3 Velocity Density Distribution

The second main result of the present analysis can be drawn from Fig. 9. There we plot the univariate kernel density estimators (k.d.e) for the Doppler velocity distribution:

$$\hat{f}_{\text{kern}}(v, h) = \frac{1}{nh} \sum_{i=1}^{n} K\left(\frac{v - V_i}{h}\right), \qquad (4)$$

where the kernel function K is a Gaussian and normalized to unity, i.e., $\int K(x)dx = 1$, h is the (constant) bandwidth set to 300 km s^{-1}, and $V_1, V_2, \ldots V_n$ is our random sample of velocities of size n. Each possible identification list has the 500 strongest lines for each point of the grid and, as mentioned in section **Models: The grid**, there are 28 grid points. Whenever a detected feature is out of the identification window ($\Delta\lambda$ Å around the feature), is flagged as UNKNOWN and is not taken into account in the probability distribution function (p.d.f) analysis. As we may observe from Fig. 9,
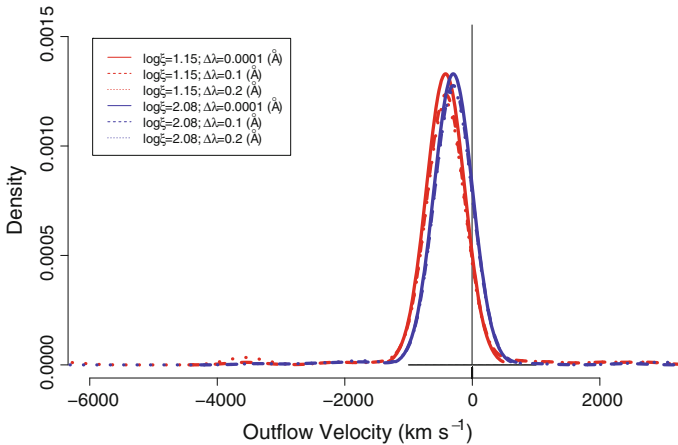
Fig. 9 Probability distribution function (p.d.f) for the flowing velocity of the material absorbing X-rays in the 900 ks *Chandra* simulated spectrum. *Solid*, *dashed* and *dotted lines* are smoothed p.d.fs for the $\Delta\lambda = 10^{-4}, 0.1, 0.2$ respectively. It is used a Gaussian kernel with the best bandwidth of $h = 300$ km s^{-1}. *Red* and *blue* are LIP and MIP plasmas respectively

one of the main components have peaks at $v_{out} \approx 300$ (wabs1) and 420 (wabs2) km s^{-1}, confirming the expected result, as this is what we introduce as outflow velocity in our simulated data (see Table 2).

A closer examination also reveals densities different from zero for higher velocity outflows, for instance exhibits by the LIP Si IX $\lambda 6.938$ Å outflowing at $v_{out} \simeq 3600$ km s^{-1}, and Si VIII $\lambda 7.005$ Å with $v_{out} \simeq 3200$ km s^{-1}, which are clearly wrong identifications, consequence of the identification window scheme (for the two plasma, solid line has $\Delta\lambda = 10^{-4}$ Å, dashed line with $\Delta\lambda = 0.1$ Å, and dotted line with $\Delta\lambda = 0.2$ Å). However we see that the density function of these velocities are very small compared with the components made by right identification.

5 Discussion and Conclusions

In this paper we show how important is to correctly define the level of continuum for EW measurements, which could differ up to ∼80 %, including or not interstellar absorption. We also show that XLINE-ID is better than 90 % in the identification of absorption lines, where more than one absorber is present.

Once we have inferred the gas density from the spectral lines, we can take Eq. (1) and compute r from it. What is deduced, using the relation $n_H \propto r^{-2}$, and Fig. 10, is a suggestion of the MIP located at distances of $r_{MIP} \simeq (0.18 - 1.80)$ lt-days ($\log r \simeq 14.7 - 15.7$ [cm]), and the LIP located at distances of $r_{LIP} \simeq (0.51 - 5.13)$ lt-days ($\log r \simeq 15.1 - 16.1$ [cm]). The global picture that emerges from this is that highly ($\log \xi \sim 2$) ionized material with gas density ($n_H \sim 10^{12}$ cm^{-3}) is located closer than the less ionized (colder $\log T \sim 4.7$ K) gas. There was no attempt to introduce any pre-established density profile or velocity law in the procedure, and the final relationship between n_H and r was self-consistently achieved.

Fig. 10 Spatial location of the absorbers in the analyzed data. The gas density n_H is independently inferred from our COG ratio method. *Horizontal lines* MIP (*red*) and LIP (*black*). *Vertical lines* are lower and upper limits on r deduced from Eq. (1)
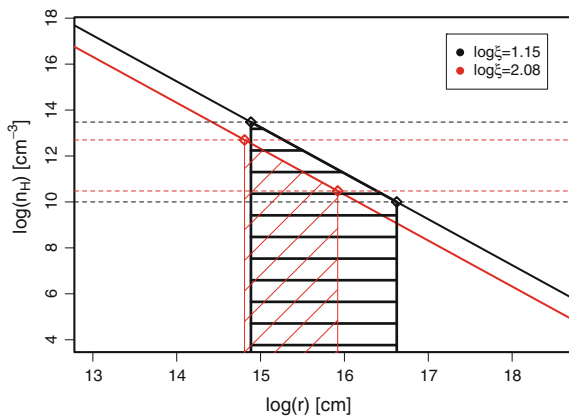
References

Badnell NR (2006) Dielectronic recombination of Fe 3p^q Ions: a key ingredient for describing x-ray absorption in active galactic nuclei. Astrophys J Lett 651:L73–L76. doi:10.1086/509739

Bahcall JN, Kozlovsky B-Z (1969) Some models for the emission-line region of 3c 48. Astrophys J 158:529. doi:10.1086/150216

Bautista MA, Kallman TR (2001) The XSTAR atomic database. Astrophys J S. 134:139–149

García J, Mendoza C, Bautista MA, Gorczyca TW, Kallman TR, Palmeri P (2005) K-Shell Photoabsorption of oxygen ions. Astrophysl J S. 158:68–79. doi:10.1086/428712

García J, Ramírez JM, Kallman TR, Witthoeft M, Bautista MA, Mendoza C, Palmeri P, Quinet P (2011) Modeling the oxygen K absorption in the interstellar medium: an XMM-Newton view of Sco X-1. Astrophys J Lett 731:L15. doi:10.1088/2041-8205/731/1/L15

Grevesse N, Noels A, Sauval AJ (1996) Standard Abundances. In: Astronomical Society of the Pacific Conference Series, p 117

Holczer T, Behar E, Kaspi S (2007) Absorption Measure Distribution of the Outflow in IRAS 13349+2438: Direct Observation of Thermal Instability? Astrophys J 663:799–807. doi:10.1086/518416

Kallman TR (2010) Modeling of photoionized plasmas. Space Sci Rev 157:177–191. doi:10.1007/s11214-010-9711-6

Kallman T, Bautista M (2001) Photoionization and high-density gas. Astrophys J S 133:221–253

Kaspi S, Brandt WN, George IM, Netzer H, Crenshaw DM, Gabel JR, Hamann FW, Kaiser ME, Koratkar A, Kraemer SB, Kriss GA, Mathur S, Mushotzky RF, Nandra K, Peterson BM, Shields JC, Turner TJ, Zheng W (2002) The ionized gas and nuclear environment in NGC 3783. I. Time-averaged 900 Kilosecond Chandra grating spectroscopy. Astrophys J 574:643–662

Krongold Y, Nicastro F, Brickhouse NS, Elvis M, Liedahl DA, Mathur S (2003) Toward a Self-Consistent Model of the Ionized Absorber in NGC 3783. Astrophys J 597:832–850

Netzer H, Kaspi S, Behar E, Brandt WN, Chelouche D, George IM, Crenshaw DM, Gabel JR, Hamann FW, Kraemer SB, Kriss GA, Nandra K, Peterson BM, Shields JC, Turner TJ (2003) The ionized gas and nuclear environment in NGC 3783. IV. Variability and modeling of the 900 Kilosecond Chandra spectrum. Astrophys J 599:933–948. doi:10.1086/379508

Palmeri P, Mendoza C, Kallman TR, Bautista MA (2002) On the Structure of the Iron K Edge. Astrophys J Lett 577:L119–L122. doi:10.1086/344243

Palmeri P, Mendoza C, Kallman TR, Bautista MA (2003a) A complete set of radiative and Auger rates for K-vacancy states in Fe XVIII-Fe XXV. A&A 403:1175–1184. doi:10.1051/0004-6361:20030405

Palmeri P, Mendoza C, Kallman TR, Bautista MA, Meléndez M (2003b) Modeling of iron K lines: Radiative and Auger decay data for Fe II-Fe IX. A&A 410:359–364. doi:10.1051/0004-6361:20031262

Palmeri P, Quinet P, Mendoza C, Bautista MA, García J, Kallman TR (2008) Radiative and Auger Decay of K-Vacancy Levels in the Ne, Mg, Si, S, Ar, and Ca Isonuclear Sequences. Astrophys J S. 177:408–416. doi:10.1086/587804

Pérez LF, Ramírez JM (2014) Statistical Methods for the Detection of Flows in Active Galactic Nuclei Using X-Ray Spectral Lines. Sigalotti L, Klapp J, Sira E (eds) Computational and Experimental Fluid Mechanics with Applications to Physics, Engineering and the Environment. Springer International AG, pp 521

Ramírez JM (2008) Physical and kinematical properties of the X-ray absorber in the broad absorption line quasar APM 08279+5255. A&A 489:57–68. doi:10.1051/0004-6361:200810264

Ramírez JM (2011) Kinematics from spectral lines for AGN outflows based on time-independent radiation-driven wind theory. Rev Mexicana Astron. Astrofis 47:385–399

Ramírez JM (2013) Chandra LETGS observation of the variable NLS1 galaxy Ark 564. A&A 551:A95. doi:10.1051/0004-6361/201220424

Ramírez JM, Bautista MA (2002) Resolving resonances in R-matrix calculations. J Phys B Atomic Mol Phys 35:4139–4146. doi:10.1088/0953-4075/35/20/302

Ramírez JM, Bautista M, Kallman T (2005) Line asymmetry in the seyfert galaxy NGC 3783. Astrophys J 627:166–176. doi:10.1086/430202

Ramírez JM, Komossa S, Burwitz V, Mathur S (2008) Chandra LETGS spectroscopy of the Quasar MR 2251–178 and its warm absorber. Astrophys J 681:965–981. doi:10.1086/587949

Rybicki GB, Lightman AP (1979) Radiative processes in astrophysics

Spitzer L (1998) Physical processes in the interstellar medium

Comparative Analysis of the Air Flow in Different Cultures Inside a Greenhouse Using CFD

J. Flores-Velázquez, W. Ojeda B and A. Rojano

Abstract The air-flow dynamics in crops (cultures), when a crop is considered as porous media, is determined by factors depending of the phenological stage which define size and shape of the leaves. Leaves topology with respect to the wind direction determines the porosity of the media and in consequence the flow rate. This flow rate is a function of the porosity and permeability, which determines the dragging coefficient. The presence of crops in a greenhouse causes a consumption of momentum due to the resistance that the leaves offer for the friction force (drag forces). In this paper the greenhouse airflow dynamics is analyze for four different crops with different leaf configurations. Computational Fluid Dynamics (CFD) was used to model the airflow dynamic behavior considering a crop as porous media. The pressure reduction due to the effect of inertial force is represented by a Forcchaimer equation, which describe dragging forces (drag effect) depending on the crop density foliar area. The results indicate a reduction of 33 % in the wind speed along the cropped area; this causes a thermal gradient increase of 6 K in a length of 34 m.

1 Introduction

The greenhouse's ventilation system is one of the basic factors to climate control in semiarid and tropical zones. Due to high costs of installation and maintenance, natural ventilation prevails in the majority of these production systems. Natural ventilation can generate good crop conditions depending of external weather

J. Flores-Velázquez (✉) · W. Ojeda B · A. Rojano
Coordinación de Riego y Drenaje, Instituto Mexicano de Tecnología del Agua, Paseo
Cuauhnáhuac 8532, Col. Progreso, C.P. 62550 Jiutepec, Mor, Mexico
e-mail: jorge_flores@tlaloc.imta.mx

W. Ojeda B
e-mail: wojeda@tlaloc.imta.mx

A. Rojano
e-mail: abrojano@hotmail.com

variables. Nevertheless, the use of anti-insect mesh windows under crops fully developed can have as a negative side effect due to the drastic reduction in the ventilation rate (Perez-Parra et al. 2004; Majdoubi et al. 2009).

A limited ventilation area and the presence of anti-insect mesh windows are factors that reduce the ventilation rate (h^{-1}) up to 60 % (Perez-Parra et al. 2004; Romero-Gómez et al. 2010). Common cooling alternatives are *pad* or *fog systems*, screens shades and natural or mechanical ventilation. However, the prevalent ventilation system is natural one (Flores-Velazquez 2010).

In addition to factors that induce pressure reduction and consequently block air flow, inside the greenhouse the air does not have a free flow due to the presence of crop canopy. Air must overcome the crop resistance principally in fully developed crop with high foliar index such as the case for tomato or pepper crops.

In this paper, Computational Dynamics of Fluids (CFD) was used to study the spatial temperature variation in a roof-windows greenhouse with three spans. Four crops were studied considered a greenhouse with natural ventilation system and screen mesh windows, under semiarid conditions located in the center of Mexico.

2 Problem Formulation

Theoretical approach

A new approach in the analysis of greenhouse ventilation consists in establishing a reliable methodology that describes the interactions that are taking place in the interface porous matrix-fluid.

The flow characteristics in a permeable material can be described in terms of permeability and porosity (Miguel et al. 1997). If a specific volume is considered, the porosity is represented by the space for which the fluid flows in relation with the total space contained in this volume. In a closed conduit, the porosity is 0 and when it does not exist flow restrictions, the porosity will be 1. The permeability is defined as the ability of the material to flow across itself, analogous when a conduit is totally opened the permeability tends to infinite.

One of the first works to model the flow was published by Hsu and Chang (1990) and later was used by Michael et al. (1997), who indicated that Eq. 1 can be used for analysis of one-dimensional mass transfer across a permeable material:

$$\frac{\rho}{\varepsilon}\frac{\partial u}{\partial t} + \frac{\rho}{\varepsilon^2}u\frac{\partial u}{\partial x} = -\frac{\partial p}{\partial x} - \frac{u}{K}u - \rho\frac{Y}{\sqrt{K}}u|u| + \frac{\mu}{\varepsilon}\frac{\partial^2 u}{\partial x^2} \tag{1}$$

where $u = \varepsilon\ u_i$; u = is the superficial fluid speed (ms^{-1}), u_i = speed across the material (ms^{-1}); ε = porosity $(m^2 m^{-2})$, ρ = density of the fluid $(kg\ m^{-3})$, P = pressure (Pa), μ = dynamic viscosity $(kg\ m^{-1}s^{-1})$, Y = factor of inertia (adim), x = flow direction (m) and K = media permeability (m^{-1}).

Equation 1 is a general equation and it explicitly shows how the fluid velocity is related to the gradient of the pressure through convective inertia effects (Miguel et al. 1997)

$$\frac{\rho}{\varepsilon^2} u \frac{\partial u}{\partial x}$$

And, the pore inertia effects

$$\rho \frac{Y}{\sqrt{K}} u|u|$$

represents the flow of pressure inertial loss, the force of viscous resistance due to the transfer at the moment in the interface matrix-fluid is included as

$$\frac{\mu}{K} u$$

and the resistance for viscosity of the flow of the fluid as

$$\frac{\mu}{\varepsilon} \frac{\partial^2 u}{\partial x^2}$$

The equation of fluid movement across a porous media can be derived from this equation.

Crops (Porous Zone)

To analyze the effects of crop canopy in the airflow inside a greenhouse, Haxaire (1999), led an experiment in a wind tunnel to determine the speed loss (drag effect) due to the presence of plants. He also analyzed the effect on the pressure drop (Dp) and the density of foliar area (L) due to changes in the air speed. The determination of the drag coefficient has allowed new incursions in the study of the d fluid dynamics; such studies have been conducted introducing this coefficient (Haxaire 2000; Lee and Short 2000; Bartzanas et al. 2004; Fatnassi et al. 2003; Molina Aiz et al. 2004).

The analysis and calculation of the effect of crops can be realized adding the term source into the Navier Stokes's Equation (Eq. 2):

$$\frac{\partial(\rho\phi)}{\partial t} + \nabla(\partial\overline{u}\phi) = \nabla(\Gamma\nabla\phi) + S_\phi \tag{2}$$

The source term $S\phi$, contains the variable of interest (ϕ), which represents the moment consumption due to the effect of dragging (drag effect) of the crop. This friction force can be expressed as unit of volume of coverage using the Wilson formula (1985) (Eq. 3):

$$S_\varphi = -LC_D v^2 \qquad (3)$$

where ν is the speed of the air (ms^{-1}); L refers to the canopy density $(\mathrm{m}^2\mathrm{m}^{-3})$, and C_D is the friction coefficient (drag coefficient) which Haxaire (1999) experimentally established as 0.32. In order to include the effect of dragging or friction (drag effect) proportionally to the density of foliate area, the crop (cultures) were considered as porous media and it can be described by Darcy-Forcchaimer equation (CFD manual, 1997).

$$S_\varphi = -\left[\frac{\mu}{K}U +\right]\rho\frac{C_f}{K}U_2 \qquad (4)$$

where, U = is the wind speed, μ = is the fluid dynamic viscosity, K = is the permeability of the porous zone and C_f = is the loss coefficient assuming a non linear moment.

In greenhouse ventilation studies, the wind speed is such that the quadratic term of Eq. 4 dominates over the linear term. This term can be neglected due to the small lost coefficient in the not linear moment equation. The intrinsic permeability K can be deduced combining Eqs. 3 and 4 by the following relation (Eq. 5).

$$\frac{C_f}{K} = LC_D \qquad (5)$$

Construction of the Computational Model

Computational Fluid Dynamics (CFD) was used for the construction of the model, using the version 14.5 of the program ANSYS-WorkBench FLUENT. The computational model (Fig. 1) was generated from the physical model. The analyzed greenhouse is located in the Faculty of Agronomy of the University of San Luis Potosí, Mexico. It is a 3-multispan greenhouse, each span with $27 \times 34 \times 6.5$ m dimensions and with lateral ventilation and a roof window. For the simulation, boundary conditions were established using external weather data supplied by an outside meteorological station.

Fig. 1 Construction of the computational model

Table 1 Characterization of four crops with different leave shape (Adapted of Molina-Aiz 2006)

Crop	LAD ($m^2 m^{-3}$)	Cd	Sϕ
Tomato	5.6	0.26	2.9
Pepper	5.8	0.23	2.7
Egg plant	3.7	0.23	1.7
Beans	3.0	0.22	1.6
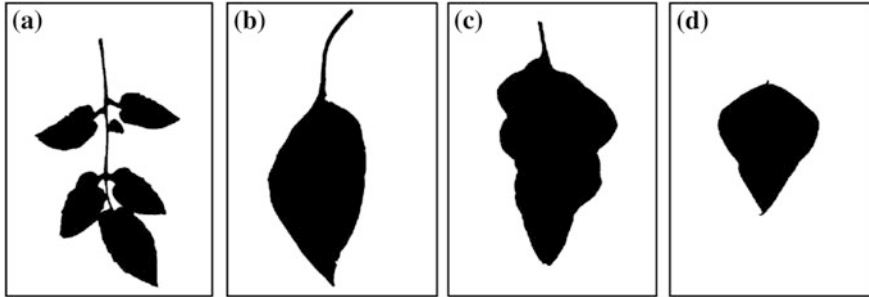
Fig. 2 Morphology of the leaves of **a** tomato, **b** pepper, **c** egg plant **d** beans (Molina-Aiz 2006)

Dragging coefficients were estimated using experimental data for each crop as shown in Table 1, by applying Eqs. 1 and 3. The flow reduction due to crop, was simulated in the source term (Sϕ) in Eq. 5.

The leaves shape determines air flow. Different crop shapes are shown in Fig. 2.

3 Results and Discussion

The unload coefficient is the factor that determines momentum loss according the transport equation; when insect mesh windows are used, the pressure drop ranges between 80 %, with a variation of 8 % depending on the mesh porosity (Flores and Montero 2008). This implies that air speeds inside the greenhouse usually are less than 1 ms^{-1}. Nevertheless, this reduction is accentuated along the cropped area from the air inlet, depending on cropped length and in a staked crop.

In this study, the wind speed drop, for two crops studies, are shown in Fig. 3. The results show that even if the leaves configuration is different, the pressure drop depends principally on canopy density. This can attributed that differences in wind speed are not significant. In addition, we have the hypothesis that at the first contact with the crop (Fig. 3), airflow modifies the angle inducing a leaves "alignment" that favor the flow and becomes constant and less restrictive. The presence of crop canopy represents a reduction in airflow, which increases as moved away from the wind-inlet window. In this study, an immediate drop was of 0.1 ms^{-1}, but as
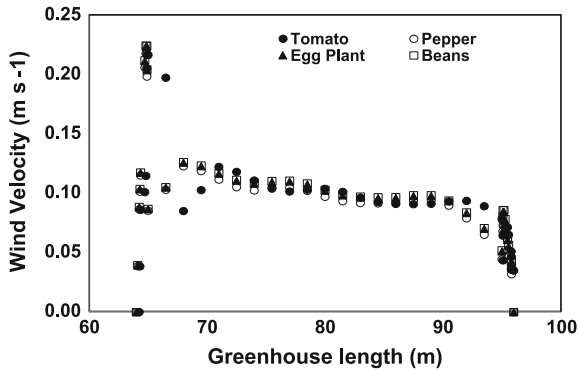
Fig. 3 Longitudinal variation of the wind speed for two crops
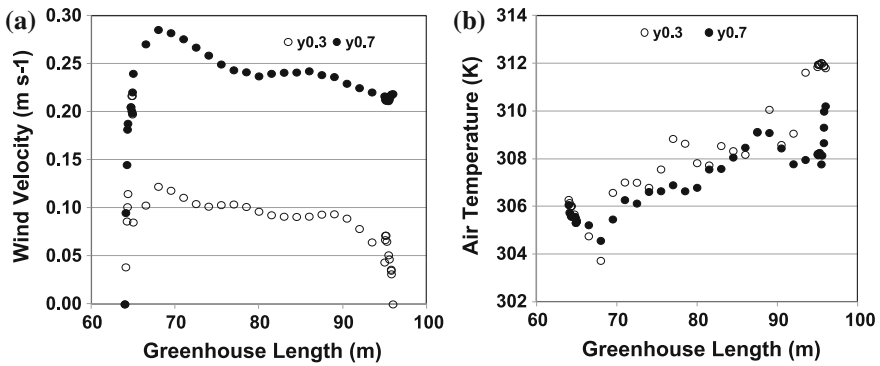
Fig. 4 Variation of the wind velocity (ms^{-1}) **a** and temperature (K) **b** in the cropped area along the greenhouse (m)

becomes stable, the speed variations are of ± 0.05 ms^{-1} in 34 m of greenhouse length.

Due to presence of canopy, there is a speed reduction of 33 % between the inlet and outlet windows (above) through crop canopy (Fig. 4a). Inside the canopy the wind speed is about 0.1 ms^{-1}, but above increases very small up to 0.25 %, this can be very important for best placement of sensors to measure transpiration. This process is directly related to wind speed (Stanghellini 1987).

As a consequence of flow variation, the temperatures showed an increase towards the windows outlet. A 6 K increase was estimated (Fig. 4b) with the particularity that this variable is dependent of the canopy height. This indicates the convective transport of the heat inside the greenhouse can be more homogeneous and independent from the air flow rate as becomes stable.
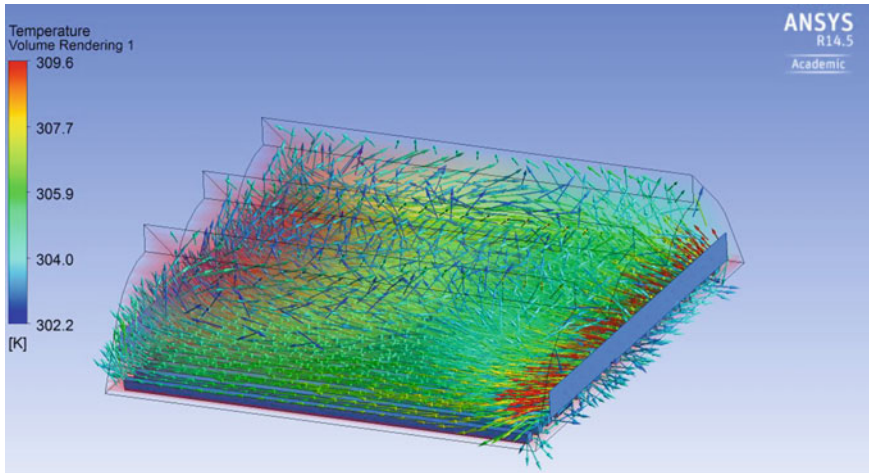
Fig. 5 Spatial distribution of wind speed vectors (ms^{-1}) and temperature (K)

Schematically, Fig. 5 shows the distribution of the speed vectors in the dominant wind direction, and spatial distribution of the temperature in the greenhouse ambient.

4 Conclusions

Null or very low wind speeds less then to 2 ms^{-1} with crop canopy in a greenhouse can cause a drop of 30 % in wind speed and in consequence an increase in the temperature. For the simulated conditions, it was found a 6 K thermal gradient, along 34 m length, between the window of air entry and exit.

In spite of the difference in leaf shape, no difference was observed in the rate of air renovation between crop studied. This promotes the theory that wind becomes stable once the leaves "align" to air flow. In consequence the flow rate is independent from the unload coefficient, associate to the leave crops.

References

Bartzanas T, Boulard T, Kittas C (2004) Effect of vent arrangement on winward ventilation of a tunnel greenhouse. Biosyst Eng 88(4):479–490

Flores-Velazquez J, Montero JI (2008) Computational fluid dynamics CFD study of large-scale screenhouse. Acta Hort 797:117–122

Flores-Velazquez J (2010) Anisáis de la ventilación en los principales modelos de invernaderos en Mejico mediante dinámica de fluidos computacional (CFD). Tesis doctoral. Universidad de Almería. Almería, España

Fatnassi H, Boulard T, Bouirden L (2003) Simulation of climatic conditions in full-scale greenhouse fitted with insect-proof screens. Agric For Meteorol 118:97–111

Hsu C, Cheng P (1990) Thermal dispersion in a porous medium. Int J Heat Mass Transf 33:1587–1597

Haxaire R (1999) Caractérisation et Modélisation des écoulements d'air dans une serre. [Characterization and modelling of the air flows within a greenhouse.] Thèse de Docteur en Sciences de l'Ingénieur de l'Université de Nice, Sophia Antipolis, 148 pp

Haxaire R, Boulard T, Mermier M (2000) Greenhouse natural ventilation by wind forces. Acta Hortic 534:31–40

Lee IB, Short TH (2000) Two-dimensional numeric simulation of natural ventilation in a multi-span greenhouse. T ASAE, 43(3):745–753

Majdoubi H, Boulard T, Bouirden L (2009) Airflow and microclimate patterns in a one-hectare Canary type greenhouse: an experimental and CFD assisted study. Agric For Meteorol 149(6–7):1050–1062

Miguel AF, Vande Braak NJ, Bot GP (1997) Analysis of the airflow characteristic of greenhouse screening materials. J Agric Eng Kes 67:105–112

Molina-Aiz FD, Valera DL, Alvarez AJ (2004) Measurement and simulation of climate inside almeria-type greenhouse using computational fluid dynamics. Agric Forest Meteorol 125:33–51

Molina-Aiz FD, Valera DL, Alvarez AJ, Madueno A (2006) A wind tunnel study of airflow through horticultural crops: determination of the drag coefficient. Biosystem Eng 93(4): 447–457

Pérez-Parra JJ, Baeza E, Montero JI, Bailey BJ (2004) Natural ventilation of parral greenhouses. Biosyst Eng 87(3):89–100

Romero-Gomez P, Choi YC, Lopez CIL (2010) Enhancement of the greenhouse air ventilation rate under climate conditions of central Mexico. Agrociencia 44(1):1–15

Stanghellini C (1987) Transpiration of greenhouse crops: an aid to climate management. Phd Thesis, Agricultural University of Wageningen, The Netherlands, p 150

Wilson JD (1985) Numerical studies of flow through a windbreak. J Wind Eng Aerodyn 21:119–154

Numerical Modeling of the Knee Synovial Joint Under Deformation Using the Finite Volume Method

N. Martínez-Gutiérrez, L.A. Ibarra-Bracamontes,
S.R. Galván-González, A. Aguilar-Corona
and G. Viramontes-Gamboa

Abstract The human knee synovial joint is considered one of the three joints having the higher damage or injury incidence, along with the hip and the ankle. Here, a 2D model of a knee synovial junction is presented, where the Condyle is modeled by a mobile circular wall, the condylar concave cavity by a larger circular wall, the Articular Cartilage with a porous medium, and the Synovial Fluid by a high viscosity Newtonian fluid. The model focuses in the study of the angular pressure distribution along the Synovial Fluid/Cartilage interface when the fluid zone undergoes a deformation in the direction of the symmetry axis due to simulated loads. The model equations were solved using FLUENT® as a numerical tool for the study of biological systems, considering small deformations at the fluid zone, low deformation rates, high fluid viscosities, constant porous fractions and different initial thickness. The results show that the pressure decreases gradually from the center of the join to its ends. The maximum values obtained were in the order of 10^9 for the dimensionless pressure (i.e. the total pressure with respect to dynamic pressure), these values correspond to 10^3 Pa for the total pressure. The greater the fluid zone to cartilage thickness ratio the lower the maximum pressure. The numerical model was validated with an analytical model previously proposed by Jurczak in (2006).

Keywords Synovial fluid · Articular cartilage · 2D numerical model

N. Martínez-Gutiérrez · L.A. Ibarra-Bracamontes (✉) · S.R. Galván-González
A. Aguilar-Corona
Faculty of Mechanical Engineering, Universidad Michoacana de San Nicolás
de Hidalgo, Ciudad Universitaria, Av. Francisco J. Mugica S/N,
C.P. 58030 Morelia, Michoacán, Mexico
e-mail: laibarrab@gmail.com

G. Viramontes-Gamboa
Faculty of Physics and Mathematics, Universidad Michoacana de San Nicolás
de Hidalgo, Ciudad Universitaria, Av. Francisco J. Mugica S/N,
C.P. 58030 Morelia, Michoacán, Mexico

1   Introduction

In general terms a joint is the junction between two or more bones of the skeleton. The joints show a variety of forms and functions, some allow moderate movements while others remain permanently static. In the case of synovial joints, they have two main components: Articular Cartilage and Synovial Fluid (Moore and Dalley 2007; Katta et al. 2008).

The bearing materials in synovial joints are Articular Cartilage, supported by subchondral bone and lubricated by Synovial Fluid. The load experienced in hip joints during normal walking can reach up to 3–5 times body weight (Jin 2010). Healthy synovial joints can last for more than 70 years with minimum friction and wear. However, disease or trauma can severely impair the normal function of synovial joints, resulting in the loss of Articular Cartilage, consequently causing pain and restricted movements. Currently various treatment options are available, from conservative approaches including defect repair of cartilage surface and hemi-arthroplasty, where only the diseased cartilage is replaced with a biomaterial, to end-stage total joint replacements. Synovial Fluid is a clear viscous fluid, a dialysate of plasma with mucopolysaccharides or glycosaminoglycans added. Synovial Fluid usually exhibits a non-Newtonian shear thinning behavior, however, under high shear rates, the viscosity of Synovial Fluid approaches a constant value, not much higher than that of water. Therefore, a Newtonian lubricant model has often been used for Synovial Fluid in lubrication modeling (Gale 2007).

An important aspect of Synovial Fluid is how it lubricates the Articular Cartilage, thereby permitting a decrease in friction between the contact surfaces. Synovial Fluid also helps load distribution during movements or displacements. Meanwhile, the Articular Cartilage is a tissue layer which covers the joint surface acting as cushion and reducing the joint wear, and then avoiding collision against the other end. Articular Cartilage is also considered as a viscoelastic material showing deformations by applying a constant load stress. The Articular Cartilage is a permeable medium where Synovial Fluid flows through when a pressure gradient is applied. The Synovial Fluid flux depends on cartilage porosity and stress applied. There is a straight relationship between permeability and water content, and conversely with proteoglycan content. The tissue response to a solicitation follows a time-dependent viscoelastic behavior. That is, it depends on the deformation of the permeable solid matrix over time and the interstitial fluid through pores. When the charges disappear, cartilage re-absorbs the fluid and recovers its initial dimensions, which can be from 2 to 4 mm thick (Forriol-Campos 2002).

Recently there has been a considerable development in analytical and numerical models that help in describing the physiological behavior of joints (Walicki and Walicka 2000; Jurczak 2006; Ruggiero and D'Amato 2010; Dabiri and Li 2013). Current numerical modeling of joints is limited by the complexity of the system and the wide variety of factors affecting joint´s behavior. Some analytical models have been proposed taking into account deformability and poroelastic properties of the

Articular Cartilage allowing for a better distribution of mechanical loads (Di Paolo and Berli 2004).

In 2000 Walicki and Walicka proposed a mathematical model for an ankle, modelled as a bio-bearing including the behaviour of a squeezable fluid film. However, in their model the existence of a cartilage zone was not considered (Walicki and Walicka 2000). Later in 2006, the pressure distribution in a bio-bearing consisting of a porous media lubricated by a thin fluid film was presented by P. Jurczak, his analytical model was restricted to low porosity values, and presented results for 0 and 0.2 (Jurczak 2006).

The Patrachari's work focuses on fluid dynamics studies applied on tissue engineering and it highlights the importance to develop numerical models applicable to physiological studies (Patrachari et al. 2012). In 2013, Dabiri and Li implemented numerical models using Finite Element Methods for the study of joints (Dabiri and Li 2013). They analyzed mechanically the knee with moderate movements considering the cartilage wear by osteoarthritis and determined the pressure change in a three-dimensional geometric model. Because of the tiny deformations only qualitative results were obtained, showing a redistribution of stresses.

As more models and research are developed, the behavior of the synovial joints will be better understood, which in turn will contribute to the development of better medical treatments for degenerated joints. This contribution has the purpose to show the results obtained by a numerical model proposed to study a 2D model knee synovial joint, which considers two essential components of a real joint: a region for the Synovial Fluid and another one for the Cartilage. This novel study focuses on the behavior of the fluid zone, which can be deformed, producing an influx into the porous medium. The Finite Volume Method was employed using FLUENT® to solve the numerical equations. The effect of the following parameters of interest was established: the magnitude of the induced deformation in the fluid region, the deformation rate, the fluid viscosity, and the porosity of the cartilage. The calculated values of the dimensionless pressure near the *Synovial Fluid/Articular Cartilage* interface are presented, as part of the results.

2 Methodologies

In Jurczak's work the bio-bearing model consist of two regions: a fluid region of variable thickness h, and a porous region of constant thickness H (Jurczak 2006). Jurczak's geometry is shown in Fig. 1. The numerical model for the knee synovial joint, here presented, solves the governing fundamental equations of fluid mechanics for this geometry, making it one of its foundations. The model finds the angular distribution of pressure through the simulated Synovial Fluid and the Cartilage when the mobile circular wall moves down at controlled velocities. The real physiological dimensions needed to adapt the geometry of Fig. 1 were estimated using the anthropometric data published by Ziylan and Murshid (2002),

Fig. 1 Bio-bearing geometry proposed by Jurczak (2006)
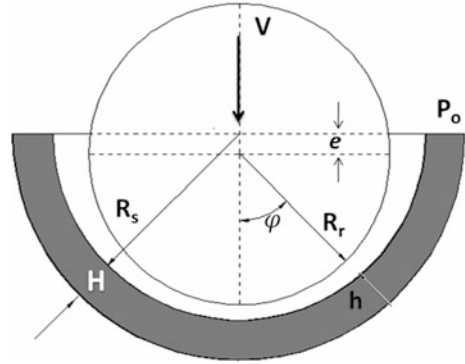
whom studied lower extremities from individuals of various ages (see data used for boundary conditions).

In the Finite Volume Method or Control Volume Method, the domain is divided into a finite number of non-overlapping cells. The conservation of a discrete variable, β, is imposed all over the domain. The differential equation:

$$\frac{d\beta}{dx} + \beta = 0; \qquad 0 \le x \le 1; \qquad \beta(0) = 1, \tag{1}$$

is integrated over the one-dimensional control volume P (see Fig. 2)

$$\int_{W}^{E} \frac{d\beta}{dx} dx + \int_{W}^{E} \beta dx = 0, \tag{2}$$

to give the discrete expression (Fernandez 2012):

$$\frac{\beta_E - \beta_P}{\Delta x} - \frac{\beta_P - \beta_W}{\Delta x} + \beta \Delta x = 0. \tag{3}$$

CFD codes are structured around the numerical algorithms that can tackle fluid flow problems. In order to provide easy access to their solving power all commercial CFD packages include sophisticated user interfaces to input problem parameters and to examine the results (Versteeg and Malalasekera 1995).

Figure 3 shows the geometry and mesh generated for the numerical study.

Fig. 2 Schematic representation of a one-dimensional discretization in the Finite Volume Method
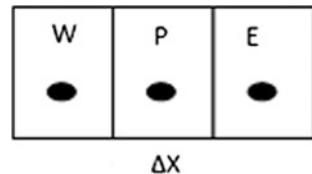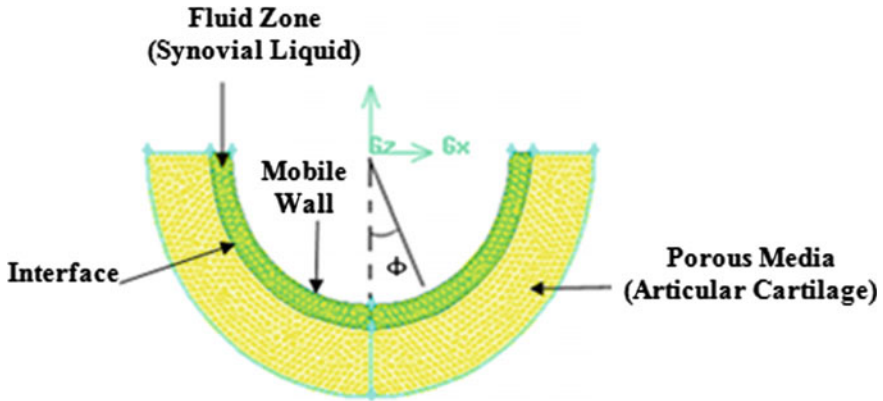
Fig. 3 Geometry and mesh. The fluid zone corresponds to the synovial fluid and the porous region corresponding to the articular cartilage

The validation of the numerical model was performed using the equation for the dimensionless angular pressure $\tilde{p}$ given by Jurczak (2006):

$$\tilde{p} = \frac{(p - p_0)c^2}{\mu R_r^2 \dot{\varepsilon}} \tag{4}$$

where p_0 is the pressure at $\phi = \pm 90°$, the angular ends of the fluid zone, $p = p(\phi)$ is the angular pressure, μ is the fluid viscosity, and R_r is the curvature radius of the mobile wall. c is the thickness of the initial semicircular-shaped fluid zone, given by the difference between R_s (the radial distance measured from the origin to the *Synovial Fluid/Articular Cartilage* interface) and R_r the mobile wall's curvature radius (see Fig. 1).

$$c = R_s - R_r \tag{5}$$

Finally, $\dot{\varepsilon}$ is the deformation rate of the fluid zone (induced by the movement of a mobile wall) given by:

$$\dot{\varepsilon} = \frac{d\varepsilon}{dt} \tag{6}$$

The deformation rate is calculated based on e, the total downward displacement of the mobile wall with respect to c. This dimensionless displacement of the mobile wall is called the fluid thickness reduction, ε, it is given by:

$$\varepsilon = \frac{e}{c} \tag{7}$$

and its value is always between 0 and 1. For example, a value of $\varepsilon = 0.1$ indicates a 10 % reduction in the thickness of the fluid zone along the y symmetry axis ($\phi = 0$), due to the downward displacement of the mobile wall. Note that for $\phi \neq 0$ the fluid zone reduction is lower.

The following assumptions and initial and boundary conditions were considered:

- At $t = 0$, the fluid zone shape is a semicircular shell because the radii R_s and R_r are concentric, the porous medium is filled with air, $c = 0.1062$ mm, $R_r = 38.62$ mm, and the Cartilage thickness $H = 6.0$ mm.
- At $\phi = \pm 90°$, $P_0 = 0$ Pa for all t. The pressure at the angular ends of the fluid zone remains null.
- The Cartilage is modeled as a porous medium having uniform porosity.
- The Synovial Fluid is modeled as a Newtonian fluid that fills a space region that can be deformed.
- The deformation rate is constant in the negative direction of the y symmetry axis, $\dot{\varepsilon} = $ constant.
- An interface that separates the Synovial fluid zone and a Cartilage zone can be defined.

The Dynamic Mesh Technique was implemented in order to control the movement of the mobile wall, using a User-defined Function based on the In-cylinder tool provided by FLUENT, inducing deformations in the fluid zone.

The calculation of the fluid angular pressure distribution was obtained close to the fluid/cartilage interface, and the effects of varying ε, $\dot{\varepsilon}$, μ, k (the cartilage's porosity) and α were systematically studied. This last parameter is the fluid zone to cartilage thickness ratio; it defines the exact position of the *Fluid Zone/Cartilage* interface, and is expressed by:

$$\alpha = \frac{c}{H} \qquad Keeping \qquad H + c = Const. \tag{8}$$

Varying α can help to compare the effect of different initial geometries on the fluid pressure distribution. For example, $\alpha = 1.0$ indicates that the initial thicknesses of the fluid zone and the cartilage are the same; $\alpha = 0.5$ indicates that the initial fluid thickness is half of the cartilage's.

3   Results

3.1   Validation of the Numerical Model Using an Analytical Model

Typical angular pressures of Jurzack's approximate analytical model, given by Eq. 4, are presented in Fig. 4. Some results obtained with the present numerical model for the angular dimensionless pressure are also shown in Fig. 4. The pressure plotted in

Fig. 4 Dimensionless angular pressure obtained from the numerical model with $\varepsilon = 0.1$ and 0.5. Comparison of the numerical results (*dotted lines*) and Jurczak's analytical results (*solid lines*). The results correspond to a Newtonian fluid with a low modified Reynolds number (Re ≈ 0, a constant deformation rate, and a low porosity $k = 0.2$ (Jurczak 2006)
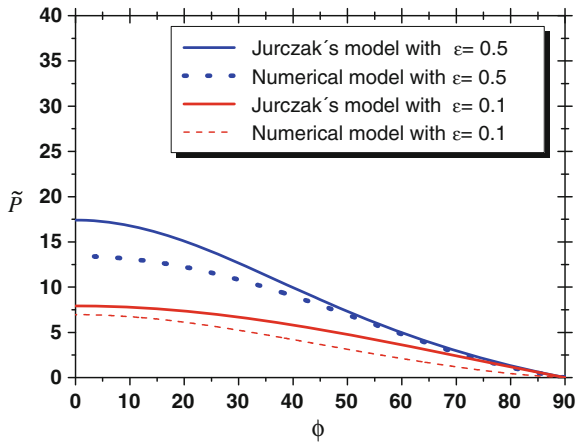
this figure is also normalized with $\mu R_r^2 \dot{\varepsilon}$. These results were calculated with $k = 0.2$, $\dot{\varepsilon} = 0.05 \text{ s}^{-1}$, water viscosity, $\alpha = 0.0177$, and $\varepsilon = 0.1$ and 0.5 respectively. Comparing the behavior and tendencies of both models, it can be seen that there is great agreement between them. It is not possible to expect precise numerical coincidence of pressure values because Jurzack did not report the viscosity and the deformation rate used for his calculations, precluding exact reproductions of his results.

By symmetry, the results are presented only for ϕ values between $0°$ and $90°$ (see Figs. 1 and 3). $\phi = 0°$ corresponds to the direction of maximum deformation (vertical axes), while $\phi = 90°$ corresponds to the direction of minimal deformation (horizontal axis).

3.2 Dimensionless Parameters

To calculate the dimensionless parameters, a modified Reynolds number proposed by Jurczak was used:

$$Re = \frac{\rho \dot{\varepsilon} c^2}{\mu} \qquad (9)$$

where ρ is the density of the fluid, μ is the dynamic viscosity, and c is the characteristic length of the system, which corresponds to the initial thickness of the fluid zone for our model. Because the fluid is in relative motion to a surface, in this study the velocity of the mobile wall, v, is given by:

$$v = \dot{\varepsilon} c. \qquad (10)$$

Table 1 Modified Reynolds numbers for different values of fluid viscosity (at multiples of water viscosity μ_w)

Viscosity μ (Kg/m · s)	Re
$1\ \mu_w = 0.001003$	5.62×10^{-4}
$10\ \mu_w = 0.01003$	5.62×10^{-5}
$100\ \mu_w = 0.1003$	5.62×10^{-6}

Values of modified Reynolds number that were obtained for different viscosities are shown in Table 1. These calculations were obtained using the following values: $\rho = 1000$ kg/m^3 (water density), $c = 0.1062$ mm, and $\dot{\varepsilon} = 0.05$ s^{-1} (equivalent to $v = 5.31$ m/s).

Low Reynolds number indicates a laminar flow regime, where viscous forces are dominant. In this case the Synovial Fluid is modeled as a highly viscous Newtonian fluid.

The dimensionless pressure proposed by Jurczak is directly proportional to c, the initial thickness of the fluid zone (see Eq. 4). As a result the greater c is, the higher the obtained dimensionless pressure, which is counterintuitive. Therefore in this work a more convenient expression for pressure normalization is proposed, according to:

$$p^* = \frac{p - p_0}{\rho(\dot{\varepsilon}c)^2}.$$ (11)

The normalizing factor is proportional to the fluid density and to the square of the mobile wall speed.

3.3 Effects of Reducing the Synovial Fluid Thickness

In everyday life the knee undergoes different stresses, causing a redistribution of the Synovial Fluid into the join. In the present model, this redistribution of the fluid is induced through the impermeable mobile wall whose movements deform the fluid zone. Due to these deformations, a portion of the fluid flows away from the region of maximum pressure and another part of the fluid enters into the porous cartilage region.

In order to analyze the effect of the displacement of the mobile wall on the angular dimensionless pressure, p^*, calculations were made with three different values for ε: 0.1, 0.4, and 0.5, keeping $\dot{\varepsilon} = 0.05$ s^{-1}, fluid viscosity equal to water's, and $k = 0.2$. Figure 5 shows the numerical results. Accordingly, the pressure increases all over the joint by increasing the degree of deformation. Maximum dimensionless pressures are observed at $\phi = 0$, close to 10^8 along the vertical axes for $\varepsilon = 0.5$. As the angle approaches to the joint ends, pressure changes gradually decrease, reaching up 0 at the joint ends.

Fig. 5 Angular dimensionless pressure versus ϕ for $\varepsilon = 0.1$, 0.4 and 0.5. Other parameters: $\dot{\varepsilon} = 0.05$ s^{-1}, water viscosity, and $k = 0.2$
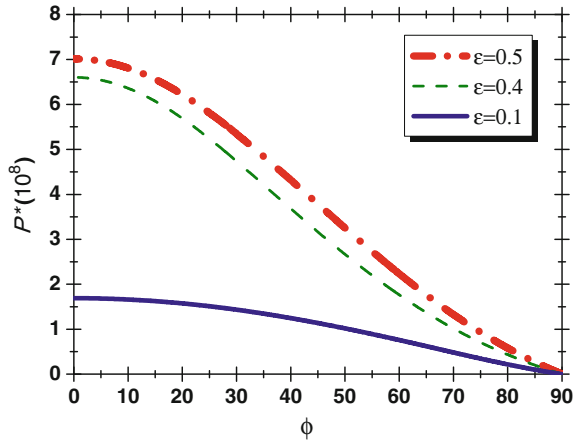
A contour plot of the pressure after a 10 % reduction of the fluid thickness ($\varepsilon = 0.1$) with $\dot{\varepsilon} = 0.05$ s^{-1}, $k = 0.2$, and a fluid viscosity 100 times greater than water's is presented in Fig. 6. The maximum total pressure reached in this case is $\sim 10^3$ Pa, also at $\phi = 0$.

Figure 7 shows the distribution pattern of velocity vectors for the same conditions of Fig. 6. When the fluid zone is deformed, the fluid flows from the central region towards the joint ends. The pattern shows important features in the porous region, as expected the fluid flows from areas of higher pressure to those of lower pressure.
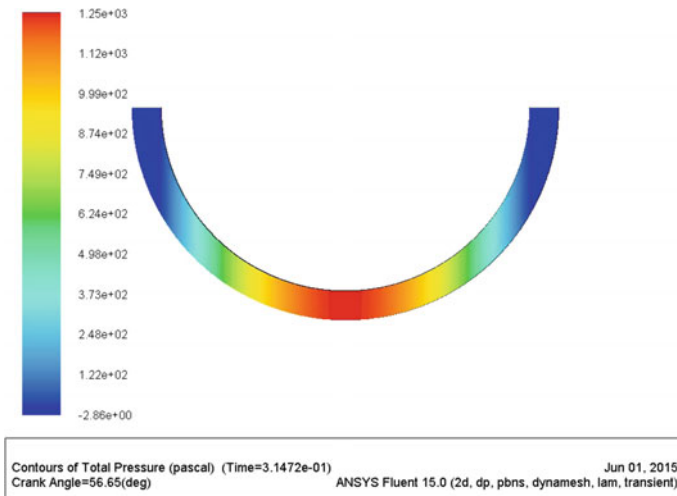
Fig. 6 Contour plot of total pressure for a fluid thickness reduction of 10 % ($\varepsilon = 0.1$), $\dot{\varepsilon} = 0.05$ s^{-1}, $k = 0.2$. The fluid viscosity is 100 times the viscosity of water (μ_w)
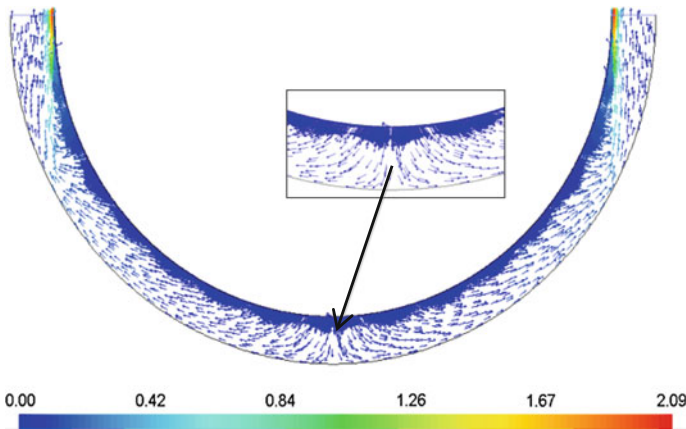
Fig. 7 Field of velocity vectors in the fluid and porous zones. Same conditions of Fig. 6. Speeds are expressed in m/s

3.4 Effects of Viscosity Variations

The high viscosity of the Synovial Fluid is critical for an accurate cartilage lubrication and for supporting large loads. Several health conditions impair this function affecting the viscosity; a well known example is the loss of nutrients. Numerical methods are quite important because with them it is very easy to stablish the effect of viscosity in the distribution of pressure along the joint, which in turn affects important biomechanical properties of the cartilage and the joint as a whole.

To analyze the effect of viscosity in the synovial joint model, the three different viscosity listed in Table 1 were considered, taking the water viscosity, μ_w, as reference. The angular dimensionless total pressure for these viscosities is shown in Fig. 8.

Fig. 8 Angular dimensionless pressure versus ϕ, for $\mu = 1\ \mu_w$, 10 μ_w, and 100 μ_w. Other parameters are $\varepsilon = 0.1$, $\dot{\varepsilon} = 0.05$ s^{-1}, and $k = 0.2$
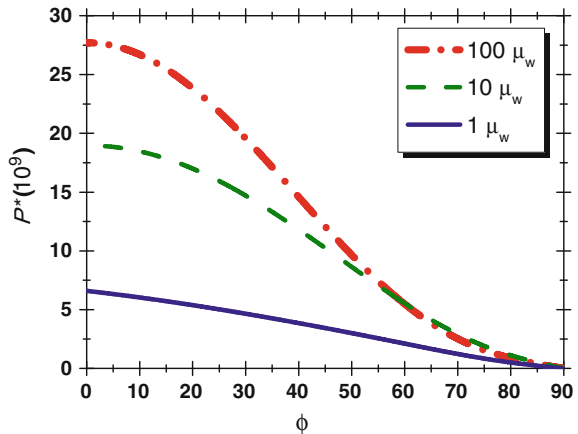
It shows that for angles lower than 60°, as the fluid viscosity increases the fluid pressure increases too. The maximum dimensionless pressure along the vertical axis increases considerably, reaching values up to 2.7×10^{10}. The higher the viscosity the greater the flow resistance, then an increase in fluid pressure occurs. Due to the increased resistance, the fluid flowing towards areas of lower pressure slows down. At the same time the amount of fluid entering into the porous medium along the vertical axis increases.

3.5 Variations in the Deformation Rate

Everyday workout, like walking, jogging or running, changes the compression rate of the joint. The effect of these compressions at three different rates of $\dot{\varepsilon} = 0.033$, 0.05, and 0.167 s^{-1} is shown in Fig. 9. These rates correspond to $v = 3.53 \times 10^{-6}$, 5.31×10^{-6}, and 17.39×10^{-6} m/s, respectively.

For higher deformation rates higher pressures are reached in the fluid zone. The order of the maximum dimensionless pressure is $\sim 10^{10}$ for the range of deformation rates considered. In this case the maximum total pressure obtained with $v = 17.39 \times 10^{-6}$ m/s was 2.48×10^{3} Pa. As in the previous figures, the pressure decreases as the angular position gets close to the end of the joint.

3.6 Porosity Variations

It has been reported that for a healthy Articular Cartilage the porosity ranges around 0.75–0.80 (Geneser 2000). In this study two values for the porosity parameter have

Fig. 9 Angular dimensionless pressure versus ϕ for mobile wall velocities of $v = 3.53 \times 10^{-6}$, 5.31×10^{-6}, and 17.39×10^{-6} m/s. Other parameters are $\varepsilon = 0.1$, $\mu = 10\ \mu_w$, and $k = 0.2$
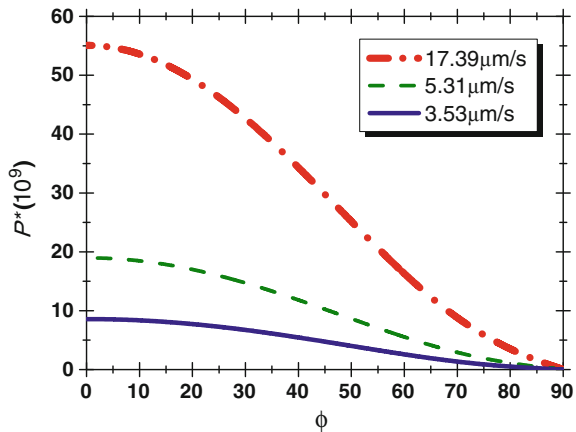
Fig. 10 Angular
dimensionless pressure versus
ϕ for $k = 0.2$ and 0.8. Other
parameters are $\varepsilon = 0.1$,
$\dot{\varepsilon} = 0.05\ s^{-1}$, and $\mu = \mu_w$
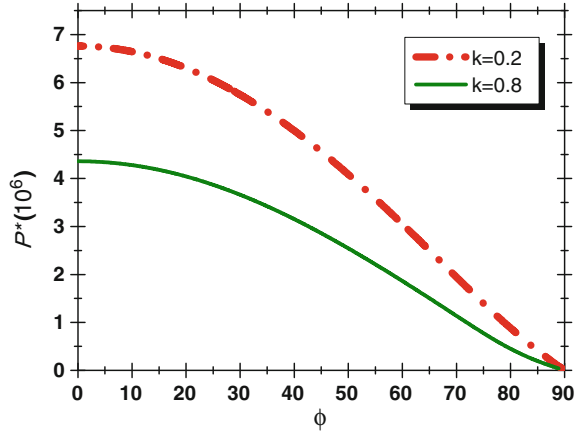
been considered: 0.2 and 0.8. The former because it was used by Jurczak, and the
latter because it is associated to a healthy knee. The results obtained are shown in
Fig. 10. Pressure increases as Cartilage porosity decreases. In a highly porous
cartilage, the fluid flows easily into the porous medium, achieving greater velocities
and consequently reducing the fluid pressure. The order of the maximum dimen-
sionless pressure is $\sim 10^6$, in this case the maximum total pressure obtained with
$k = 0.2$ was 1.25×10^3 Pa.

3.7 Variations in Thickness Ratio

As noted above, small values of α (for $\alpha < 1.0$) indicate that the fluid thickness is
thinner than the cartilage. $\alpha = 1.0$ indicates that the initial thicknesses of the fluid
zone and the cartilage are the same. $\alpha > 1.0$ indicates that the fluid zone is thicker
than the cartilage. Figures 11 and 12 show the dependence of the angular pressure
with the fluid to cartilage thickness ratio.

As α increases, the maximum pressure decreases. The maximum pressure is
highly sensitive to the thickness of the fluid zone, through α. Note that the order of
magnitude decreases drastically from 10^6 for $\alpha = 0.1$ to 10^3 for $\alpha = 5.0$. High
pressures are related to joint protection, since bones do not touch each other.
Oppositely, at low pressures it is easier for the bones to get closer. Figure 12 shows
in a semi-log scale the maximum pressure versus the thickness ratio α. If the
damping generated by the fluid is insufficient ($\alpha > 1$), the risk of a cartilage wear
may occur favoring an eventual contact between surfaces bones.

Fig. 11 Angular pressure distribution versus ϕ for **a** $\alpha = 0.1$, 0.25 and 0.5; **b** $\alpha = 0.75$, 1.0 and 5.0. Other parameters are $\varepsilon = 0.1$, $\dot{\varepsilon} = 0.05 \text{ s}^{-1}$, $\mu = \mu_w$, and $k = 0.2$
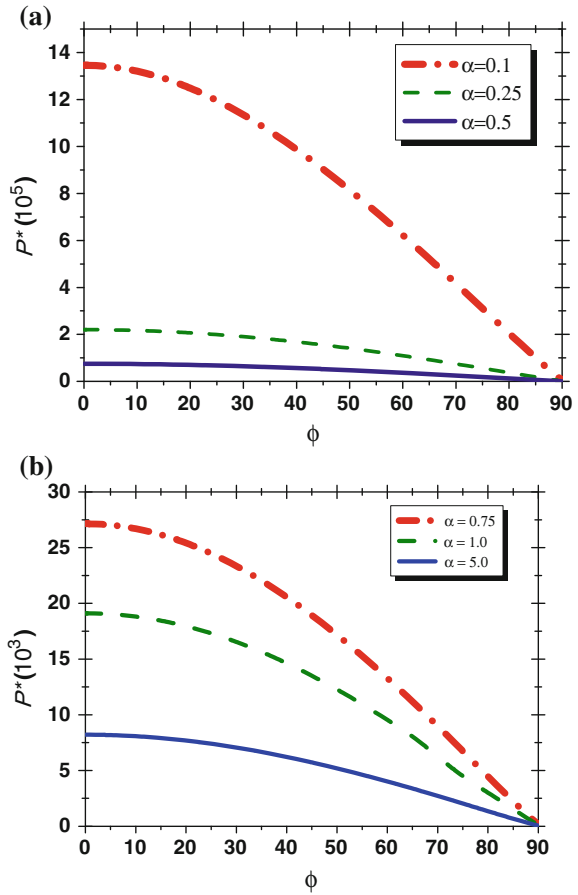
Fig. 12 Semi-log graph of the maximum dimensionless pressure values as a function of the thickness ratio α. Same conditions as Fig. 11
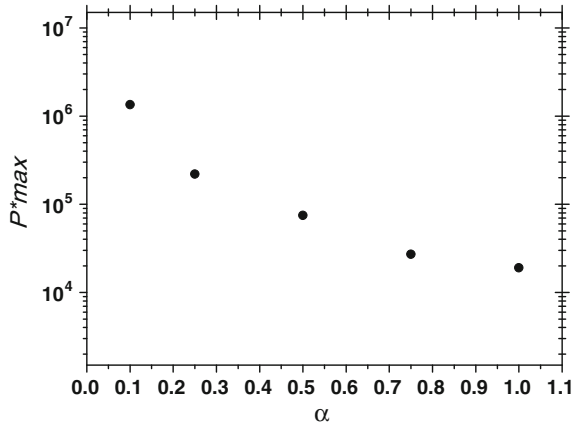
4 Conclusions

- The maximum angular pressure is always obtained at $\phi = 0$, due to the geometry of the model and to the imposed fact that the displacement of the mobile wall is always downwards. Lateral movements are not considered. This would correspond to a vertical position in a human knee.
- Pressure increases as a response to the following events:

  (a) Greater deformations induced in the fluid zone.
  (b) By increasing the deformation rate on the fluid zone.
  (c) By increasing the viscosity of the synovial fluid.
    Greater deformations and greater deformation rates produced by the mobile wall simulate greater loads and faster load application, respectively, on the Synovial joint. These differences would resemble different activities such as weight lifting, walking or jogging, among others.
    A reduction in the fluid viscosity implies a faster flow, decreasing the pressure. In real life, the Synovial fluid is a highly viscous fluid and is able to withstand high stresses. A reduction in real viscosity generally is a manifestation of an unhealthy Synovial Fluid, this situation would allow lower pressures, favoring the friction and wear of the Articular Cartilage.

- With the numerical model here proposed, it is very easy to study the effect of the cartilage porosity, unlike other reported models that are only valid for low porosities.
- The effect of the fluid zone to cartilage thickness ratio is the most prominent of all. As the fluid thickness increases, the pressure drops abruptly at the interface. Some health conditions may produce $\alpha > 1$, like severe joint inflammation, or severe wear of the cartilage. Under this conditions the pressure drops down, and the joint losses protection, acting as a positive feedback for the advance of the adverse condition.
- The parameters that affect more significatively the pressure of the Synovial joint are: (a) the viscosity, (b) the deformation rate and (c) the fluid to cartilage thickness ratio.

References

The authors acknowledge the Mexican National Council for Science and Technology (CONACyT) and the Coordination for Scientific Research of the UMSNH for the support on this project. The corresponding author Laura Ibarra-Bracamontes acknowledges to the Pennsylvania State University, USA, for her Sabbatical stay as Visiting Professor at the Pritchard Fluid Mechanics Laboratory in the Department of Mathematics.

Di Paolo J, Berli ME (2004) Predicciones numéricas de una prótesis total de rodilla con elemento tibial deformable y microporoso. Mecánica Computacional, XXIII, pp 1491–1504

Fernández JM (2012) Técnicas numéricas en Ingeniería de Fluidos: Introducción a la Dinámica de Fluidos Computacional (CFD) por el Método de Volumen Finito. Reverte

Forriol-Campos F (2002) El cartilago articular: aspectos mecánicos y su repercusión en la reparación tisular (Articular cartilage: mechanical factors and their effects on tissue repair). Rev Ortop Traumatol 5:380–390

Gale LR (2007) Biotribological assessment for artificial synovial joints: the role of boundary lubrication. Doctoral Thesis, Institute of Health and Biomedical Innovation, Queensland University of Technology, Brisbane

Geneser F (2000) Histología. Médica Panamericana, Argentina

Jin Z (2010) Lubrication of synovial joints. Advanced tribology proceedings, pp 871–872. Springer, Berlin

Jurczak P (2006) Pressure distribution in a squeeze film biobearing lubricated by a synovial fluid. Int J Appl Mech Eng 11(4):857–864

Katta J, Jin Z, Ingham E, Fisher J (2008) Biotribology of articular cartilage—A review of the recent advances. Med Eng Phys 30:1349–1363

Moore KL, Dalley AF II (2007) Anatomía con orientación clinica. Médica Panamericana, México

Patrachari AR, Podichetty JT, Madihally SV (2012) Application of computational fluid dynamics in tissue engineering. J Biosci Bioeng 114(2):123–132

Ruggiero A, D'Amato R (2010) Squeeze—film lubrication of the human ankle joint: a simplified analytical model during walking. Ann Fac Eng Hunedoara. Int J Eng VIII(2):73–80

Versteeg HK, Malalasekera W (1995) An introduction to computational fluid dynamics: the finite volume method. Longman Scientific and Technical, England

Walicki E, Walicka A (2000) Mathematical modelling of some biological bearings. Smart Mater Struct 9:280–283

Ziylan T, Murshid KA (2002) An analysis of anatolian human femur anthropometry. Turk J Med Sci 32:231–235

Causal Propagation of Heat and Thermohaline Instability in Quasi-static Phenomena

A. Aguirre-Guzman and N. Falcón

Abstract Double diffusive convection is discussed in context of the simultaneity problem emerged from the thermal energy flux, where the temperature gradient (the cause) and the energy flux (the effect) appear at the same time. We used Cattaneo's law, as a correction of the conventional Fourier's law for thermal transport, in order to consider a delay time in the interaction, the so called relaxation time. For the sinking of a convective blob in a Newtonian fluid, Fourier's equation describes a steady state flow, however the Cattaneo's law predicts damped oscillations for times of the order of this relaxation time. Physical systems as the salt-finger phenomenon (for the Fourier regime), and the superfluid Helium II and pulsars micro-oscillations (for the Cattaneo regime) are studied through simulations of the temporal evolution of the speed of the convective blobs. Concluding that the dynamic of convective blobs in systems where the relaxation time is important presents quasi-static oscillations, even for degenerate matter. A further study about the complete description of the light curve of pulsars is suggested.

1 Introduction

In fluid dynamics, double diffusive convection stands over recent developments of convection, which studies fluid distributions with two gradients of diffusivities (usually thermal and molecular). When these gradients determine the vertical distribution of density, the Rayleigh-Taylor instability may be present. This process mainly consists in a transient effect of convection originated in the interface of layer of fluids initially stables with different diffusivities. Throughout the transitory regime, the sinking of filaments can be observed from the upper layer to the lower one. This process concludes when the homogenization of the fluid is reached, leading to thermal and mechanical equilibrium.

A. Aguirre-Guzman (✉) · N. Falcón
Laboratorio de Física de la Atmósfera Y El Espacio Ultraterrestre,
Universidad de Carabobo, Valencia 2001, Venezuela
e-mail: aaguirre3@uc.edu.ve

In a system of two different layers of fluid (e.g. with different thermal and molecular diffusivities), the layer with high molecular weight on the cooler layer of lower molecular weight may remain in dynamic equilibrium, because the high temperature of the upper layer increases its buoyancy despite its high molecular weight. However, a small blob of the upper fluid can be displaced into the lower one due to perturbations at the interface. The molecular diffusion of heat is approximately a hundred times greater than the molecular diffusion of mass, so the blob loses its temperature faster than its mass, the buoyancy decreases, and the blob sinks.

In fluids where molecular weight is determined by salt content, the sinking of blobs (or filaments) of the hotter and salty upper fluid is known as "salt-finger" phenomenon, while the double diffusivity process (of temperature and salinity) is the so called *thermohaline instability*, which is a particular case of Rayleigh-Taylor instability.

The phenomenon of sinking of blob (or filaments) can be observed in a wide range of natural system, e.g. in oceans (Stern 1960) (in the Strait of Gibraltar where hot and salty water layers of the Mediterranean Sea are on the coolest and less salty water layers of the Atlantic Ocean), in the metallurgical industry (Sarkar and Phillips 1992) (when residual minerals sink into a tank of molten iron, then they mix with the iron in the process of manufacturing of steal), in geophysics (Singh et al. 2011) (in the formation of basaltics during the cooling of magma called basalt fingers, and the oil extraction), and even in stars (Grossman and Taam 1996) (when Hydrogen is transformed in Helium into the star forming carbon blobs).

For the mathematical description of the thermal diffusion (i.e. heat conduction) from the blob to its surrounding, it is usual to use Fourier's law, which establishes that the rate of heat transfer through a material is proportional to the negative gradient of the temperature. However, in this equation the underlying assumption is that particles carrying the radiated energy propagate with infinite speed. This assumption becomes a fundamental problem where the cause (the temperature gradient) and the effect (the energy flux) appear at the same time, yielding a *simultaneity problem*.

This problem has been treated since mid-19th century, where a more realistic scenario has been presented by considering a relaxation time, that represents a delay time between the cause and the effect. In this context, the modification of the Fourier's equation was made by Cattaneo (1948), by introducing an additional term as depending of this relaxation time. Since its derivation from the kinetic theory of gases, it is well known that Cattaneo's equation keeps a very well agreement with experiments.

In this paper, we will show the simulations of the behavior of the sinking of a blob by a double diffusion process in both the Fourier and the Cattaneo regime. To this end, in Sect. 2 we will review the mathematical formalism to describe the sinking of a blob in both regimens. In Sect. 3, we will discuss some physical systems where the double diffusion phenomenon is presented and later we will simulate some of these systems with the determined equations. Finally, conclusions are given in Sect. 4.

2 Fourier and Cattaneo Regime

In this section we will review the classical mathematical formalism for deriving the sinking speed of a blob in a Newtonian fluid by using Fourier's law for the thermal conduction.

In order to describe mathematically the diffusion process in the system, we will consider the heat transfer (by conduction) from the blob to the isotropic surrounding as described by Fourier's law

$$F = -k\,|\nabla T| \simeq -k\frac{DT}{d/2}, \tag{1}$$

where F is the heat flux per unit of surface of the blob (in W/m^2), k is the thermal conductivity of the blob (in W/(m K)), ∇T is the temperature gradient (in K/m), DT is the difference of temperature between the blob and its surrounding (in K), and d is the diameter of the blob (in mm). However, this heat flux (or radiated energy) is equal to the temporal change of thermal energy of the blob. Hence, Eq. (1) can be written as

$$\frac{\partial(DT)}{\partial t} = -\frac{DT}{\tau_{adj}}, \tag{2}$$

which allows us to obtain an expression for DT as

$$DT(t) = DT(0)\exp(-t/\tau_{adj}), \quad \tau_{adj} \equiv \frac{d^2}{12\alpha}, \tag{3}$$

where τ_{adj} is the thermal adjustment time (time to reach the thermal equilibrium), and α is the thermal diffusivity of the blob (in m^2/s).

Therefore, the *total* rate of change of the temperature of the blob (where we can also use the total derivative of DT, because the temperature of the surrounding is constant) is given by this radiation of thermal energy, and additionally by the adiabatic compression due to changes of the pressure. Thus, the equation of state is

$$\frac{1}{T}\frac{d(DT)}{dt} = \left(\nabla_{ad}\frac{d\ln P}{dt} + \nabla\frac{d\ln\rho}{dt}\right) - \frac{DT}{T\tau_{adj}}, \tag{4}$$

where we defined the temperature gradients ∇_{ad} (adiabatic) and ∇ as

$$\nabla_{ad} \equiv \left(\frac{\partial\ln T}{\partial\ln P}\right)_S \quad \text{(at constant entropy)} \tag{5}$$

$$\nabla \equiv \left(\frac{\partial\ln T}{\partial\ln\rho}\right)_m \quad \text{(derived on the surrounding)} \tag{6}$$

here P is the pressure on the blob (in Pa) and ρ its density.

From the conservation of energy, in Eq. (4), we impose that $d(DT)/dt = 0$. Additionally, we can use the Pascal's equation (in the quasi-static case) to write $d \ln \rho / dt = -d \ln P / dt$. Under these assumptions we obtain an expression for the sinking speed of the blob

$$v_\mu = -\frac{H_p}{(\nabla_{ad} - \nabla)\tau_{adj}} \frac{DT}{T}, \tag{7}$$

with DT defined by the Eq. (3), and the pressure scale height, H_p (in cm), is given by

$$H_p \equiv -\frac{dr}{d \ln P}, \tag{8}$$

where r (in cm) is the distance between the interface and the blob (note that $v_\mu = dr/dt$). See Kippenhahn and Weigert (1990) for a detailed deduction of the Eq. (7).

At this point, we have obtained remarkable results from the Fourier's law (as given by the Eq. (1)) in the characterization of the motion of the blob, but as we discussed in the preceding section, this becomes a simultaneity problem. For a more real situation we may consider the Cattaneo's equation

$$\tau \frac{\partial F}{\partial t} + F = -k \left| \nabla T \right|, \tag{9}$$

where τ is the relaxation time, and k is defined as in Eq. (1). The physical systems where the transitory effects before the relaxation time are important will be discussed in the next section. Here, we will treat the mathematical issues only.

This work is not intended to demonstrate the mathematical details of the corresponding deduction of the speed from Eq. (9) as we did for the Fourier regime, so the details of this deduction can be seen in the full paper of Herrera and Falcón (1995). Taking their results, we have that the speed of the blob is

$$\begin{aligned} v = v_\mu + v_\mu \exp[x(2\tau/\tau_{adj} - 1)] \\ \times \cdots [(1 + \tau_{adj}/\tau)\cos(\omega x) + (1 - \tau_{adj}/\tau)\sin(\omega x)/\omega] \end{aligned} \tag{10}$$

with the following definitions $x \equiv t/2\tau$ and $\omega \equiv \sqrt{4\tau/\tau_{adj} - 1}$. Here, v_μ is given by Eq. (7) with DT as defined by Eq. (3). Furthermore, we imposed that the Eq. (10) should converge to the Fourier solution for long time scales, i.e. times greater than the relaxation time (as in Eq. (7)).

In this context, the Cattaneo contribution given by the second term in the right hand side of the Eq. (10) represents a transient effect for initial times less than the relaxation time. This additional term exposes the purely oscillatory behavior of the blob with the amplitude determined by the exponential term. The frequency of oscillation of the two harmonic functions is given by ω, which clearly depends on the relation between the relaxation time and the thermal adjustment time. Even more, the exponential term that modulates the amplitude of the oscillations also behaves

differently according to the τ-τ_{adj} relation. In fact, this last dependence provides three different cases:

1. For $\tau \gg \tau_{adj}$, the thermal energy flows slowly from the blob to the surrounding but the system reaches the thermal equilibrium immediately after the establishment of this gradient. This means that the blob won't sink immediately but first it will oscillate (due to the early perturbation) about its position of equilibrium (the interface between the two fluids). Eventually, the blob will sink due to the thermohaline instability. This behavior is reflected in the speed of the blob

$$v = v_\mu + v_\mu(0)\cos(t/\sqrt{\tau\tau_{adj}}), \tag{11}$$

where the oscillations has period $2\pi\sqrt{\tau\tau_{adj}}$.

2. Now, when $\tau \simeq \tau_{adj}$ a transitory effect is observed: the blob oscillates as before, but this periodical motion is damped by a factor of $\exp(-t/2\tau_{adj})$ as we can see in its speed

$$v = v_\mu + 2v_\mu(0)\exp(-t/2\tau_{adj})\cos(\sqrt{3}t/2\tau_{adj}), \tag{12}$$

and the period is now $4\pi\tau_{adj}/\sqrt{3}$. In both cases (1 and 2), the period of oscillation is proportional to the relaxation time.

3. Finally, with $\tau \ll \tau_{adj}$ the speed of the blob is given by

$$v = v_\mu + v_\mu(0)(\tau_{adj}/\tau)\exp(-t/\tau), \tag{13}$$

but the relaxation time is small enough as the decreasing exponential makes the last term disappears, and the Fourier solution is recovered.

In this paper, we are focused on the study of systems where the relaxation time is comparable with the thermal adjustment time, i.e. where transient oscillatory effects are observed. Thus, Eqs. (3), (7) and (12) will be important in the study of the behavior of the blob sinking via computational plotting as we will see in the next section.

3 Simulations of the Speed of Convective Blobs

In the preceding sections we studied the Fourier's law, and it was said that particles carrying the thermal energy from the blob to the surrounding move with infinite speed, so the temperature gradient and the thermal energy flux occur simultaneously. This assumption works for most materials where relaxation times are very small, e.g. in phonon-phonon interaction and free electron interaction, these are of the order of $\sim 10^{-13}$ s (at room temperature) (Peierls 1995). However, there are some physical systems where the mean free path of the particles in propagation is short enough, so the relaxation time cannot be neglected, e.g. in superfluid Helium II where $\tau \sim 10^{-3}$ s (at 1, 2 K) (Band and Meyer 1948). In this section, we will simulate some

physical scenarios for both systems: where relaxation times can be neglected (as in most Newtonian fluids), and where they introduce important effects.

3.1 Salt-Finger Phenomenon as Physical Scenario for Fourier Regime

In order to study Fourier regime ($\tau = 0$ s) we consider the difference of temperature between the blob and its surrounding, DT, in a physical system corresponding to salt-finger experiments made by Chiang et al. (2007), where they laid a solution of Methyl violet ($C_{25}H_{30}N_3Cl$) at 293 K on fresh water (273 K). They slightly perturbed this initially stable system, then the convective blobs (in practice, filaments or fingers) appear and start to sink into the cooler water. This process continued until the fluid reached the thermal and mechanical equilibrium for times greater than 20 s. In their experiments, Chiang et al. (2007) also reported the sinking of thick and thin blobs, with mean diameters of $d = 0, 2$ cm and $d = 0, 1$ cm, respectively.

To describe the time evolution of DT for the thick and thin blobs we can use Eq. (3), where we can additionally consider two different salt concentrations to illustrate the sensibility of DT respect to changes in the different thermal diffusivity, α.

The corresponding simulations to the Salt-finger phenomenon are shown in Fig. 1. As we expected there is an exponential decrement of DT with time, which correspond to the usual exponential decreasing predicted by the Newton's law of cooling. Furthermore, we note that the thermal adjustment time is very sensible to changes in the diameter of the blob, i.e. for thick blobs $\tau_{adj} \simeq 2$ s, and for thin blobs $\tau_{adj} \simeq 0, 5$ s, which comes from the increasing in heat capacity of the blob with its diameter.

Fig. 1 Difference of temperature between the blob and its surrounding for *thick* and *thin* blobs, with different thermal diffusivities
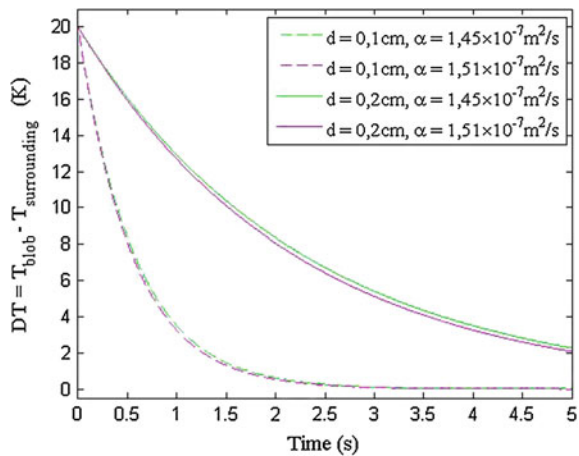
On the other hand, from the Eq. (7), we note that the speed of the blob inherits the exponential decreasing behavior from the temperature difference DT, therefore it is expected that v_μ also decreases exponentially.

3.2 Cattaneo Regime and Degenerate Matter

Now, we study the scenarios where $\tau \neq 0$ s, i.e. the Cattaneo regime. As we discussed before, in superfluid Helium II the relaxation time is of the order of 10^{-3} s at 1, 2 K, so we can briefly study this system by considering thick and thin blobs as before, in order to illustrate the characteristic times.

In the Fig. 2, we plot the speed of the blob for the case of Helium II by using Eq. (12). There, the speed describes damped oscillations as we discussed in the preceding section, where it is important to remark that this transient effect occurs for times shorter than or of the order of the relaxation time. Now, just like in Fourier regime, the behavior of the blob is very sensitive to changes in its thickness, i.e. in its heat capacity which acts as a kind of "thermal inertia".

On the other hand, these rapid oscillations may be present also into degenerate matter. For example, in an astrophysical scenario, we can study a neutron star where the matter in it is degenerate. In this case there exists a region rich in neutrons (a layer of superfluid neutrons) and another one below it less doped (nearest to the nucleus). As before, we can think in a convective globule of high content of neutrons that is pushed downward into the poor-neutron region, so that this difference of thermal and composition (of neutrons) diffusivities is quite similar to that presented in the salt-finger phenomenon, where early oscillations in the Cattaneo regime might also be presented. Even more, these (damped) oscillations might occur in the radial direction, so it is possible to describe them by using the Eq. (12).

Fig. 2 Speed of *thick* and *thin* blobs in the Cattaneo regime
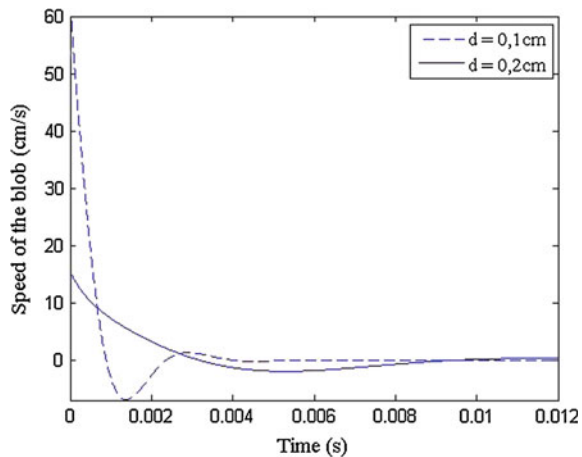
In a rotating neutron star or pulsar, the radial oscillatory motion of a convective globule may change its moment of inertia, which can be reflected in the frequency emission and subsequently observed in the luminosity function. On the other hand, this luminosity function $L(t)$ is proportional to the angular velocity $\Omega(t)$ of the pulsar, and because the angular momentum is conserved, we can write

$$L(t) \propto \Omega(t) = \Omega_0 \frac{I_0}{I(t)}, \tag{14}$$

where $I(t)$ is the moment of inertia of the pulsar, and the subscript 0 indicates the initial values for these two quantities. Thus, when the globule approaches to the nucleus, the inertia decreases and the angular velocity increases. In the opposite case, when the globule moves away from the nucleus the angular velocity decreases. These temporal variations in $\Omega(t)$ might induce periodic perturbations in the luminosity function. Therefore, the oscillatory behavior of the convective globule produced in the Cattaneo regime could be observed in the light curve of the pulsar.

By studying the pulsar PSR 2016+28, Cordes et al. (1990) could observe periodic variations of its luminosity function. These micro oscillations are also known as *micro glitching*. They observed a main pulse produced by the rotation of the pulsar. However, after the filtering of the natural noise, they also observed a secondary pulse with a well defined structure. This subpulse behaved like damped oscillations at times of the order of milliseconds, which can be thought as the transitory effect seen in the Cattaneo regime.

If we assume that the micro glitching is produced by Cattaneo-like oscillations, this phenomenon might be governed by the Eq. (12), by assuming a relaxation time of the order of the thermal adjustment time. So that the period of the micro glitching is given by $4\pi\tau/\sqrt{3}$. Therefore, from the results of Cordes et al. (1990), we can infer a period of $\sim 10^{-3}$ s for the pulsar PSR 2016+28, leading to a relaxation time is of the order of 10^{-4} s.

A remarkable result comes from Eq. (14), where the moment of inertia as a function of the position of the globule can be completely determined by integrating Eq. (12), so the luminosity function could be obtained for the description of the light curve of a given pulsar.

4   Conclusions

Cattaneo's law may be understood as the first order term of a Taylor series expansion of the heat flux in the Fourier's equation. Although for most of the applications this first order correction may be neglected, there exist several physical systems where the relaxation time is long enough, so that it is measurable. In fact, a second order correction can be considered, but the order of its contribution could be quietly ignored without remove any physics from the system.

An important outcome is that the dynamic of the convective globule is very different before and after the relaxation time, e.g. for times shorter than it indeed the globule can be displaced against the gradient of temperature, an unexpected behavior if Newton's law for thermal transport is only considered.

According to the model assumed here, inside neutron stars, Cattaneo-type oscillations of convective globules could introduce periodic variations in the rotation rate of such pulsars. Thereby, this could be the origin of the secondary pulse (i.e. the quasiperiodic microstructure) in radio pulsar emissions observed today. In fact, the mathematical formalism of that model is exposed in this work, where the use of the Cattaneo's law allows to determine the displacement of the globule and so describe the variations on the moment of inertia, thus the subsequent subpulse in the luminosity function is completely determined as well. This topic is beyond the aims of this work, but represents an open field for researching.

References

Band W, Meyer L (1948) Second sound and the heat conductivity in Helium H. Phys Rev 73:226–229

Cattaneo C (1948) Sulla conduzione del calore. Atti del Semin. Mat. e Fis. Univ. Modena 3:83

Chiang C, Labrador J, Orozco E, Falcón N (2007) Medición de velocidad en un fenómeno de Salt-Finger. Ciencia 15:68–72

Cordes JM, Weisberg JM, Hankins T (1990) H: quasiperiodic microstructure in radio pulsar emissions. Astron J 100:1882–1891

Grossman SA, Taam RE (1996) Double-Diffusive mixing-length theory, semiconvection and massive star evolution. Mon Not R Astron Soc 283:1165–1178

Herrera L, Falcón N (1995) Heat waves and thermohaline instability in a fluid. Phys Lett A 201:33–37

Kippenhahn R, Weigert A (1990) Stellar structure and evolution. Springer, Berlin

Peierls RE (1995) Quantum theory of solids. Oxford University Press, Oxford

Sarkar A, Phillips OM (1992) Effects of horizontal gradients on thermohaline instabilities in a thick porous layer. Phys Fluids A 4:1165–1175

Singh OP, Ranjan D, Srinivasan J, Sreenivas KR (2011) A study of Basalt fingers using experiments and numerical simulations in double-diffusive systems. J Geograp Geol 3:42–50

Stern ME (1960) The Salt-Fountain and Thermohaline convection. Tellus 12:172–175

Dynamics of Noncohesive Confined Granular Media

N. Mujica and R. Soto

Abstract Despite the ubiquitousness and technological and scientific importance of granular matter, our understanding is still very poor compared to molecular fluids and solids. Until today, there is no unified description, which indeed seems unreachable. However, it has been proposed that important advances could be attained for noncohesive, hard-sphere like systems, by combining fluid dynamics with phase-field modeling through an appropriate order parameter (Aranson and Tsimring 2006). Here, we present a review of the dynamics of confined granular matter, for which this systematic approach has proven its value. Motivated by the pioneering work of Olafsen and Urbach (1998), many experimental, theoretical and numerical studies of model confined granular systems have been realized, which have unveiled a very large variety of fundamental phenomena. In this review, we focus on few of these fundamental aspects, namely phase coexistence, effective surface tension, and a detailed description of the liquid state.

1 Introduction

Granular materials are ubiquitous in nature and in everyday life, including industrial applications. Examples are sand dunes, avalanches, granular food of daily usage, transport of grains in food and pharmaceutical industry, transport of grains in the mining industry, granular flow in block caving extraction in a mine, dust disks at the astrophysical scale, and so forth. However, compared to the liquid and vapor states of matter, which flow is well described by the hydrodynamic conservation equations, our understanding of the dynamics of granular matter is very limited (Andreotti et al. 2013). It is the athermal nature of the macroscopic constituents of granular matter and their dissipative interactions that generate the main differences with molecular fluids. The fact is that there is no unified description for the collective motion of

N. Mujica (✉) · R. Soto
Facultad de Ciencias Físicas y Matemáticas, Departamento de Física,
Universidad de Chile, Santiago, Chile
e-mail: nmujica@dfi.uchile.cl

granular systems. This is a key problem for the industry, where these materials are the second most important after fluids. Scientifically, granular materials are a prototype of matter far from equilibrium. Advances in our current knowledge of these systems will also strongly impact the general field of non-equilibrium statistical physics. It is known that granular matter can exist in solid, liquid or gaseous states depending on how we force it (Jaeger et al. 1996) or the three states can coexist, as during an avalanche. Also, they undergo instabilities and pattern formation (Aranson and Tsimring 2006).

Granular systems are simply defined as a collection of macroscopic solid particles for which thermal fluctuations are negligible. Typical sizes range from 1 μm to cm scale, or much larger for geophysical and other natural phenomena. Additionally, the individual constituents have contact forces that are intrinsically dissipative, given by friction and inelastic collisions. Particles can also interact via electrostatic, van der Waals, magnetic or hydrodynamic forces (e.g. air drag), or even through capillary bridges. Here, for this review, we use the classification given by Andreotti et al. (2013), where particles of size larger than 100 μm are considered as granular media, for which in many situations dissipative collisions and frictional contacts are dominant. In this classification, particles of sizes between 1 and 100 μm are considered as powders and below 1 μm we refer to colloids. For the former, van der Waals forces, capillary bridge forces and air drag are more relevant than the collisional interactions. For the latter, the thermal nature of the systems is recovered.

The athermal nature of granular media is a consequence of the macroscopic size of its constituents. Indeed, the potential energy that is required to lift a glass bead of diameter $d = 100$ μm to a height comparable with this lengthscale is 10^8 times larger than the thermal energy scale $k_B T$ at ambient temperature. As energy is dissipated at grain-grain and grain-boundary collisions, dynamic states can be obtained injecting energy by different mechanisms, typically via boundaries (vibration or shear) or external fields (e.g. air fluidization) acting on the bulk and, therefore, the detailed balance condition is not fulfilled. However, a global balance between dissipation and energy injection can be made such that the system reaches a steady state.

Since some years there has been a large amount of interest in the study of the dynamics of confined, quasi-two-dimensional (Q2D) granular systems, initiated by Olafsen and Urbach (1998), who studied clustering, order and collapse in a vibrated granular monolayer. Since then, simple model experiments and simulations have been developed that allow for a detailed understanding of basic granular physics, with interest for non-equilibrium statistical mechanics and nonlinear physics. More specifically, researchers have focused on the study of vibrated Q2D and Q1D granular systems composed by several hundreds to several thousands spherical particles (of size ∼1 mm in most experiments). The cell's height H is much smaller than the lateral dimensions L_x and L_y (in many cases $L_x = L_y \equiv L$). Energy injection is provided by sinusoidal oscillation of the complete setup, with an imposed vibration $z(t) = A \sin(\omega t)$. In some simulation studies it is provided by a "thermal" wall, for which particle's velocities are obtained from a Maxwellian flux distribution after a wall collision. From an experimental point of view, the confined geometry has a great advantage because it allows the observation of both individual trajectories and

collective behavior, which enables one to study both the microscopic and macroscopic dynamics. In general, the focus is on the effective one or two-dimensional system. This dimensional reduction is appropriate as the dynamical time scale of interest is larger than the fast vertical motion, which acts as an energy source. In addition, experiments are also ideal for comparisons with molecular dynamic simulations, which, for example, can explore the vertical motion. Figure 1 presents the setup used by the authors in various experiments using the Q2D geometry.

In these model systems, individual grains interact solely via collisions. Other forces are negligible except when explicitly introduced, as with electrostatic (Aranson et al. 2000; Howell et al. 2001) or magnetic interactions (Oyarte et al. 2013; Merminod et al. 2014). The choice of particle size insures that van der Waals forces and air drag effects are negligible. Also, the use of electrically conducting boundaries (like indium tin oxide, ITO, coated glass plates and metallic walls) minimizes electrostatic interactions. The choice of the particle material allows to avoid magnetic dipolar interactions. Experiments are performed at ambient (low) humidity, so capillary bridge interactions are negligible. Thus, our focus is the study of noncohesive granular matter, which are dominated by dissipative collisions as the main interaction between particles.

Although there is no unified description of granular matter, which does seems unreachable for all types of granular systems, Aranson and Tsimring (2006) proposed that important advances could be attained for dense noncohesive, hard-sphere like systems, by combining fluid dynamics with phase-field modeling through an appropriate order parameter. In this review, we present a set of results concerning the dynamics of confined granular matter for which this systematic approach has proven to work satisfactory. Additionally, these confined systems serve then as a basis for understanding a variety of fundamental phenomena. Here, we will focus on a few of
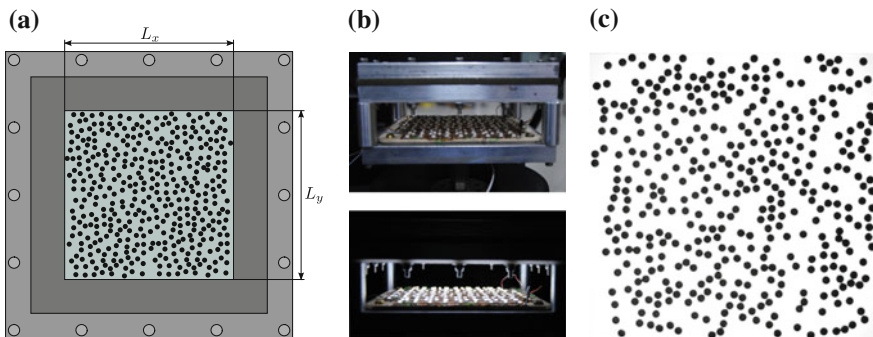
Fig. 1 Quasi two dimensional (Q2D) geometry using in confined granular experiments. **a** General scheme of the experimental cell, showing the horizontal dimensions and the frame that holds the *bottom* and *top* glass plates; **b** *side view* pictures of the cell and the base with the illumination LED array off (*above*) and on (*below*); **c** typical image used for particle position detection. From two consecutive images particle velocities are measured as well. Figure from Néel et al. (2014). ©2014 American Physical Society

these fundamental aspects, namely phase coexistence, effective surface tension, and detailed description of the liquid state.

In order to guide the reader to a broader range of phenomena, we provide here a more comprehensive list (still incomplete!) of other fundamental issues that arise in these systems: crystallization (Reis et al. 2006), caging dynamics (Reis et al. 2007), KTHNY-type (Olafsen and Urbach 2005) and surface melting (May et al. 2013), superheating (Pacheco-Vázquez et al. 2009), phase separation and coarsening in electrostatically driven systems (Aranson et al. 2000; Howell et al. 2001) and in dipolar liquids (Oyarte et al. 2013), the dynamics of "polymer-like" granular chains (Ben-Naim et al. 2001; Safford et al. 2009), the occurrence of giant number fluctuations in nematic monolayers (Narayan et al. 2007, 2008; Aranson et al. 2008), segregation in a binary system (Rivas et al. 2011a) and related "granular explosions" (Rivas et al. 2011b, 2012). Also, the crucial role of vertical dynamics has been put in evidence (Rivas et al. 2011b; Roeller et al. 2011; Pérez-Ángel and Nahmad-Molinari 2011; Rivas et al. 2012; Néel et al. 2014).

2 Granular Phase Coexistence in Confined Systems

2.1 Clustering in Unforced Systems

A remarkable collective effect that is observed in noncohesive granular matter is clustering under certain conditions. A free cooling (unforced) granular gas shows the formation of dense clusters. These clusters are not cohesive and fragment into pieces due to shear stresses but new clusters form dynamically. The mechanism, proposed by Goldhirsch and Zanetti (1993), is that dense regions created by fluctuations have a higher dissipation rate and therefore cool faster than less dense regions, leading to progressive cooling and clustering. A hydrodynamic analysis shows that this picture is indeed correct, where the clustering is associated to a hydrodynamic instability for long wavelengths (Orza et al. 1997). Beyond a critical system size that depends on density and inelasticity, the compression waves are unconditionally unstable generating the clustering instability and no metastability is observed. In this instability there is no stable phase separation and no order parameter presents any non-analytic behavior. Also, there is no evidence of a surface tension that stabilises the interface as it is the case for the transitions described below, which take place in forced confined systems.

2.2 Liquid-Vapor Transition

Forced granular systems that can reach fluid-like steady states also show clustering and phase separation. Some mechanisms are shared with the unforced case but the

picture is quite different. Argentina et al. (2002) introduced a simple model were through molecular dynamic simulations it was shown that a heated granular system in 2D can undergo a phase separation, analogous to the spinodal decomposition of the gas-liquid transition in the van der Waals model (see Fig. 2). This phase separation is triggered by a negative compressibility. The control parameter is the restitution coefficient; at low dissipation, the effective pressure is a monotonically increasing function of density, whereas for larger dissipation a decreasing pressure as function of density is observed. At the onset of this phase transition, the system reveals rich dynamic behavior characterized by the appearance, coalescence, and disappearance of clusters. Clusters undergo a coarsening process that can not be explained by a standard diffusion mechanism. Instead, it was shown that the system sustains waves, which in turn cause clusters to interact and coarsen much more effectively than through pure diffusion.

Considering the observed propagating waves, which are created through density fluctuations, an order parameter was defined as the density difference with respect to a critical value. Using symmetry arguments, Argentina et al. (2002) deduce an effective non-linear wave equation, which includes an interface energy term and dissipation. This modified wave equation was named the van der Waals normal form. This theoretical model recovers well the observations obtained by molecular dynamic simulations. In particular, the phase diagram can be computed, displaying a critical point, the spinodal and coexistence curves, with the bistability region in between. Cartes et al. (2004) deduced the same van der Waals normal form starting from a one-dimensional granular hydrodynamical model. The equation of state, postulated
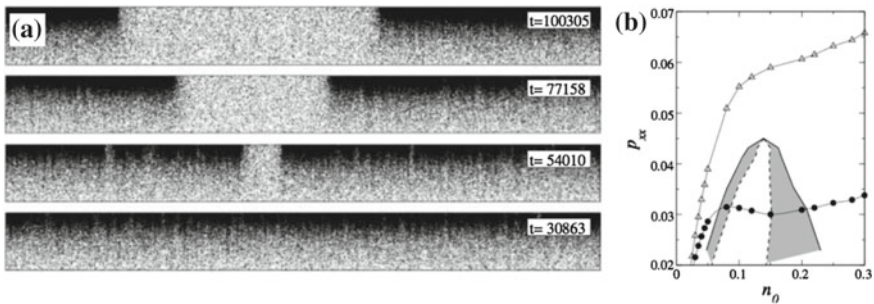
Fig. 2 **a** Snapshots of the quasi-1D granular system from simulations, with $L \sim 10000d$ and $H \sim 100d$ (Argentina et al. 2002). *Black dots* correspond to particles. The *bottom* wall heats the systems with a "thermal" boundary condition and periodic boundary conditions are imposed laterally. At the *top* wall, collisions are elastic. The systems is initially homogeneous in the longitudinal direction, with a density gradient in the transverse one due to the asymmetry of energy injection. Between the first and second frame a low density "bubble" nucleates and grows until a stationary coexisting state is attained. **b** Pressure versus filling density computed for a small system, what prevents the instability to develop. At low dissipation, pressure is a monotonic function of density; at larger dissipation, a negative compressibility regions develops. The *continuous line*, *dashed line* and the *gray* region in between correspond to the coexistence line, spinodal line and the bistability region respectively. Copyright ©2002, American Physical Society

as the one of a hard-sphere disk system in 2D, can present a negative compressibility region as a consequence of the granular temperature being a decreasing function of density.

This liquid-gas phase separation was also studied experimentally and numerically by Roeller et al. (2011) in a Q2D configuration. Submillimeter glass spheres are vertically shaken in a box with large horizontal dimensions, $L \approx 210d$ and much smaller height $H \sim 10d$. For a given particle volume fraction, the system displays an homogeneous liquid state at low vibration amplitudes and a coherent gas state at high amplitudes. The liquid-gas phase separation is observed at intermediate amplitudes; the transitions between the homogeneous states and the phase separation can be obtained by either varying the driving amplitude or the particle volume fraction, with a larger coexistence region for larger H. Their event-driven simulations suggest that the phase separation is driven by spinodal decomposition and pressure measurements for small systems display a negative compressibility region.

2.3 Solid-Fluid Transitions

2.3.1 Clustering and Collapse of Submonolayers for Low Vibration Amplitudes

In their pioneering work, Olafsen and Urbach (1998) demonstrated that a 2D granular gas can undergo a clustering and ordering transition by adjusting very carefully the forcing amplitude. A submonolayer of stain-less steel particles is placed on a sinusoidally vibrating plate. At fixed frequency, by decreasing the normalized acceleration, $\Gamma = A\omega^2/g$, to values <1, a gas state will phase separate into a gas phase and an hexagonally packed solid cluster. Previous to this phase separation, small density fluctuations are observed, which also present lower velocities. These dense clusters serve as nucleation points for a collapse, from which the hexagonally ordered cluster will grow until it reaches a stable size, in mechanical equilibrium with the gas, low density phase. This dense phase is what they refer as a collapsed state, mainly because of its low kinetic energy. An example of the coexistence of the two phases is shown in Fig. 3a, b. At higher filling densities, the system shows the presence of an hexagonally ordered phase that extends over the entire cell, with no gas phase in equilibrium. In this state, particles fluctuate around average positions but with much larger kinetic energy than the so called collapsed state. Two phase diagrams, for low and high filling densities, are presented in Fig. 3c, with vibration frequency $\nu = \omega/2\pi$ and acceleration Γ as control parameters. At low densities, the transitions present hysteresis.

Olafsen and Urbach (1998) also present a detailed statistical analysis of the gas positional structure. The experimentally computed pair correlation function was shown to be quantitatively similar to the one obtained with a Monte Carlo calculation of a 2D gas of elastic hard disks in equilibrium for a the same filling density of the experiment, with no adjustable parameters, showing that the structure of the
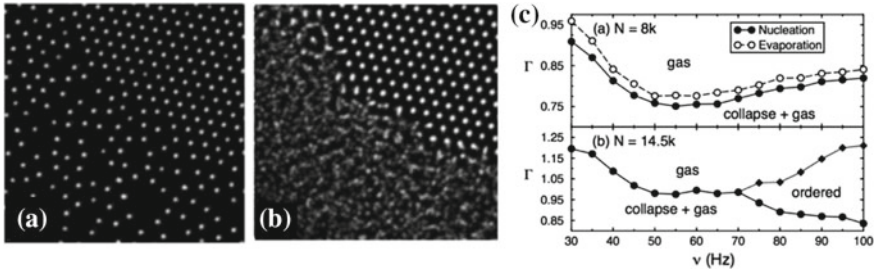
Fig. 3 Instantaneous (**a**) and average (**b**) photographs of part of the 2D granular system at $\nu = \omega/2\pi = 70$ Hz and $\Gamma = 0.76$. The less dense, gas phase is at the *bottom-left* half of the image and the more dense, solid cluster at the other half, which is more evident in the average image. Particles in the solid cluster have much lower velocities. **c** Phase diagrams obtained at low (*top*) and high filling density (*bottom*). The control parameters are the vibration frequency ν and normalized acceleration Γ. Figures from Olafsen and Urbach (1998). Copyright ©1998, American Physical Society

2D granular gas is dominated by excluded volume effects. Additionally, spatial correlations were shown to increase when the system is cooled to a lower Γ, closer to the transition line.

Losert et al. (1999) studied a reverse phase transition in the same experimental configuration. Instead of cooling the granular gas to a collapse, they started with an amorphous submonolayer of particles at rest with $\Gamma \lesssim 1$, which in our current context can be considered as the condensed, solid phase. In a region of the frequency-amplitude parameter space, when an external perturbation is applied to a group of grains, these start to bounce and trigger a transition to a gas state that involves all the particles. The authors focus on the front propagation of this gas state that grows within the also stable amorphous state. At low coverages, they show that these two metastable dynamical states can simultaneously coexist, inferred from observations of particle trajectories; some correspond to stationary particles and some to moving, bouncing particles.

The coexistence of two metastable states was confirmed recently by Pérez-Ángel and Nahmad-Molinari (2011). Using 3D molecular dynamic simulations of a granular system that is vertically vibrated, they demonstrated the coexistence of two type of dynamical modes. Some particles rebound on the vibrating plate ("bouncers"), conforming collectively the gas state, while others remain always in contact with the plate and roll on it ("rollers"). Their respective population depends on the initial conditions that are set. The bouncers in fact bounce with the same period of the vibrating plate. Clusters of rollers and bouncers can form depending on which has the largest initial population; in both cases, clusters form due to the external pressure exerted by the other species. When the largest initial population corresponds to bouncers, the clusters of rollers that are formed end up with an hexagonal order, as in the original experiments by Olafsen and Urbach (1998).

In the Q2D geometry, individual grains can reach a simple limit cycle where they bounce back and forth with the top and bottom walls with the same period of the

vibrating cell. When the particle concentration is large, this limit cycle is difficult to reach because collisions with other grains are more probable. The fluid state and the synchronized limit cycle coexist. The later state is absorbing—defined as one from which the system cannot escape—with no residual horizontal dynamics. The former is metastable and after long, but finite, times the system transits from the fluid to the absorbing state. Only large perturbations, that appear in experiments due to imperfections are able to refluidize the system (Néel et al. 2014).

2.3.2 Ordering for Large Vibration Amplitudes

When a Q2D monolayer of mono-disperse noncohesive spherical particles is vertically vibrated, a solid-liquid-like transition occurs when the driving amplitude or filling density exceeds a critical value (Prevost et al. 2004; Melby et al. 2005). This is very counter-intuitive, because the system suffers a transition from a liquid phase to a coexisting solid-liquid state when the vibration amplitude is increased for a fixed density. Thus, solidification occurs while the injected kinetic energy is increased above a certain threshold. Here, we stress that the physical mechanism underlying particle clustering relies on the strong interactions mediated by grain dissipative collisions in a confined geometry, rather than on grain-grain cohesive forces in a non-confined system (Royer et al. 2009). Varying the filling fraction and box height, different possible solid phases are observed (Melby et al. 2005). The effect of inelasticity was studied experimentally and numerically by Reyes and Urbach (2008); two sets of experiments were performed, with stain-less steel and brass particles, which are less and more dissipative respectively. They showed that inelasticity has a strong effect on the phase diagram, pushing the transition lines to higher critical accelerations for the more dissipative, brass particles. They also demonstrated that the solid cluster can melt again for higher vibration amplitudes or lager inelasticity.

This phase separation is triggered by the negative compressibility of the effective 2D equation of state and the associated transient dynamics is governed by waves. Indeed, following the pressure measurement setup proposed by Géminard and Laroche (2004), Clerc et al. (2008) demonstrate that the pressure versus density curve reaches a *plateau* precisely at the solid-liquid phase coexistence. They also performed 2D and 3D event driven simulations from which pressure measurements confirm the van der Waals scenario for this transition. Using a Q1D setup they demonstrate trough a coarse-graining procedure that waves are induced by fluctuations, but are only observable in the longitudinal momentum field. In this case, solid clusters interact and merge, also much more effectively than a pure diffusive process, as for the liquid-gas van der Waals transition (Argentina et al. 2002; Cartes et al. 2004).

The effect of forcing and dissipation were studied numerically by Lobkovsky et al. (2009). They report results from two numerical studies, namely soft-sphere molecular dynamics using a vibrating wall as the forcing mechanism and hard-sphere event driven simulations with random energy injection. For both types of forcing, inelasticity suppresses the transition to the solid-liquid coexistence, shrinking the phase

coexistence region for lager dissipation. However, for the random forcing there is no clear phase separation as there is for the vibrating case; indeed, these authors conjecture the existence of an effective surface tension for the latter, although no measurement was proposed. They relate this surface tension to the observation that there is a strong phase-dependence of energy injection, which is minimum at the solid cluster.

To correctly describe the solid-liquid transition a new order parameter was required. Castillo et al. (2012) introduced an orientational order parameter (see Fig. 4), which shows that the transition can be either of first or second order type (see Fig. 5). Depending on the cell's height and filling density, the transition can be abrupt or continuous. The two configurations that lead to each type of transition referred to as C1 and C2. The 4-fold bond-orientational order parameter per particle is defined

$$Q_4^j = \frac{1}{N_j} \sum_{s=1}^{N_j} e^{4i\alpha_s^j}, \tag{1}$$

where N_j is the number of nearest neighbors of particle j and α_s^j is the angle between the neighbor s of particle j and the x axis. For a particle in a square lattice, $|Q_4^j| = 1$, and the complex phase measures the square lattice orientation respect to the x axis. Figure 4a, b present results from molecular dynamic simulations obtained by
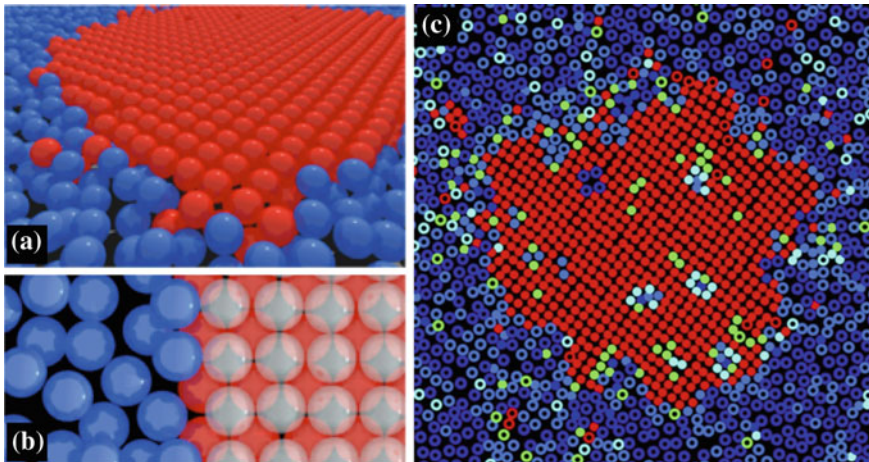
Fig. 4 **a**, **b** Visualization of solid and liquid phases (*red-white* and *blue* respectively) from molecular dynamic simulations. The *bottom panel* shows that the solid cluster is composed by two interlaced layers (*white* on *top* and *red below*). Figure from Prevost et al. (2004). Copyright ©2004, American Physical Society. **c** Experimental colormap of the bond-orientational order parameter Q_4, from Castillo et al. (2012). *Red color* indicates particles with local order close to a square lattice; *blue*, those with order far from the square lattice. *Solid symbols* (•) represent dense regions, measured through de Voronoi area; *open symbols* (○) correspond to less dense regions. ©2012, American Physical Society
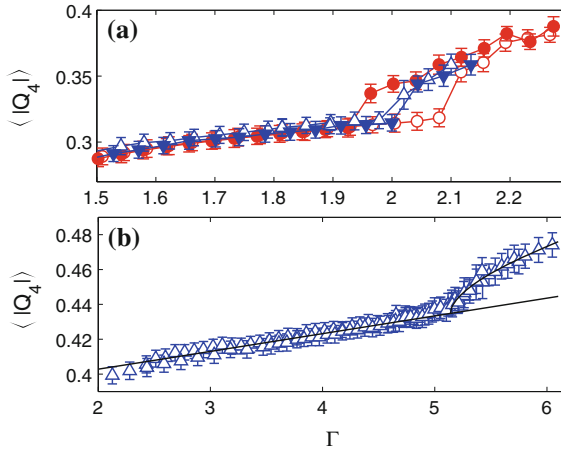
Fig. 5 Average global 4-fold bond-orientational order parameter $\langle|Q_4|\rangle$ versus Γ for C1 (**a**) and C2 (**b**). Open (*solid*) symbols represent data obtained for increasing (decreasing) Γ ramps, with the following rates: $\Delta\Gamma/\Delta t \approx 0.005$ min^{-1} ($\triangle$, $\blacktriangledown$) and $\Delta\Gamma/\Delta t \approx 0.02$ min^{-1} ($\circ$, $\bullet$). *Continuous lines* in (**b**) correspond to fits of the linear trend $Q_4^L = a\Gamma + b$ for $2.5 < \Gamma < 5$, with $a = 0.011 \pm 0.001$ and $b = 0.380 \pm 0.002$, and a supercritical-like behavior $\langle|Q_4|\rangle = Q_4^L + c(\Gamma - \Gamma_c)^\beta$, with $\beta = 1/2$, observed for $\Gamma \gtrsim 5$. Figure from Castillo et al. (2012). ©2012, American Physical Society

Prevost et al. (2004). Here, the double layered solid cluster can be clearly observed. Figure 4c presents a representation of local order $|Q_4^j|$ in the experimental system (Castillo et al. 2012). Only part of the system is shown, approximately $L_x/3 \times L_y/3$. From this figure it is evident that the denser regions are where the system is more ordered.

For the second order-type transition, criticality has been reported and five independent critical exponents have been measured (Castillo et al. 2012). These critical exponents are associated to different properties of Q_4: the correlation length, relaxation time, vanishing wavenumber limit (static susceptibility), the hydrodynamic regime of the pair correlation function, and the amplitude of the order parameter. The results are consistent with model C of dynamical critical phenomena (Hohenberg and Halperin 1977), valid for a non-conserved critical order parameter (bond-orientation order) coupled to a conserved field (density). An example of the observed critical behavior is presented in Fig. 5b, in this case for the amplitude of the order parameter.

More recently, Castillo et al. (2015) tested the universality of this transition by changing the system's dissipation parameters. The top and bottom glass plates have an ITO coating on their inner surfaces that minimizes electrostatic charges. Thus, two different thicknesses of this coating were used, with a thicker (thinner) coating having lower (larger) effective dissipation parameters. The difference between the dissipation parameters is in fact deduced from the difference in the critical accelerations, with a ratio of about 0.87. Within experimental errors, these authors demonstrate

the agreement of all five critical exponents. This is an exigent test for the universality of the transition. Thus, while dissipation is strictly necessary to form the crystal, the path the system undergoes toward the phase separation is part of a well-defined universality class.

2.4 Effective Surface Tension

Although our focus is on phase coexistence, we must note that clustering may also occur without phase separation, through capillary effects induced by an effective surface tension. The sole existence of this property is counterintuitive because, due to the dominance of collisional, dissipative interactions, for a long time granular matter has been considered to have no surface tension at all. However, experiments performed with tapped powders show a Rayleigh-Taylor-like instability (Duran 2001). Also, interface fluctuations and droplet formation in granular streams have been reported both in air (Amarouchene et al. 2008) and vacuum (Royer et al. 2009), and their origin seems to be the surface-tension-driven Plateau-Rayleigh instability.

In all these systems, effective surface tensions have been estimated, being as low as $0.1\,\mu$N/m for the granular free-falling jet in vacuum (Royer et al. 2009). This is about 10^6 times lower than the surface tension of a pure air-water interface ($\gamma_w \approx 70$ mN/m). Such low surface tension is induced by nanoNewton level cohesion forces, which result from a combination of van der Waals interactions and capillary bridges. In other cases, for the so called strongly forced systems for which momentum transfer dominates other forces, granular matter has shown to behave as a zero-surface-tension liquid, as for particle sheets created by a granular jet impacting a target (Cheng et al. 2007) and fingering in a granular Hele-Shaw system (Cheng et al. 2008). In some cases, an hydrodynamic derivation taking the zero-surface-tension limit succeeds in describing the observations (Cheng et al. 2007, 2008) but in others a finite surface tension is needed (Ulrich and Zippelius 2012). The key point is to understand how capillary-like features can emerge out of collections of particles that are completely noncohesive or that have very low interaction forces.

The systems presented in the two previous subsections do present features that are related to the existence of an interface energy, for which surface tensions can be defined and measured. Both system classify as strongly forced systems for which momentum transfer trough collisions dominates other forces. Nonetheless, low surface tensions—of the order of 1 mN/m—have also been measured in these strongly agitated noncohesive granular systems that phase separate (Clewett et al. 2012; Luu et al. 2013). To our knowledge, these two systems are the only examples that have shown the emergence of an effective surface tension induced by dissipative collisions rather than by low cohesive forces (Royer et al. 2009) or by air drag (Duran 2001; Amarouchene et al. 2008).

Using experiments and soft-sphere molecular dynamic simulations Clewett et al. (2012) show that at the liquid-gas coexistence, stable liquid droplets have in average a circular shape. A pressure difference between the liquid drop and the surrounding gas

was measured in the molecular dynamic simulations. It was shown to be consistent with a Laplace law, $\Delta P \sim 1/R_0$, with R_0 the average radius. This method gives a surface tension $\gamma = 1.0 \pm 0.1$ mN/m for the particular parameters that were used (geometry, filling fraction, forcing frequency and amplitude). Computations of the pressure tensor at the interface showed that the surface tension is mainly given from an anisotropy in the kinetic energy part of the pressure tensor. For a circular drop, surface tension is known to have a mechanical definition, namely

$$\gamma = R_0 \int_0^\infty \frac{p_N(r) - p_T(r)}{r} dr, \tag{2}$$

where p_N (p_T) is the normal (tangential) component of the pressure tensor. Evaluating this integral over several drop sizes, they obtained $\gamma = 0.94 \pm 0.05$ mN/m, consistent with the value computed from the Laplace pressure difference.

At the solid-liquid coexistence, Luu et al. (2013) show that a solid cluster, in average, resembles a drop, with a striking circular shape. The coarse-grained solid-liquid interface fluctuations turn out to be well described by the capillary wave theory, which allows to define an effective surface tension and interface mobility for this noncohesive granular system. More specifically, by computing the Fourier modes of the interface radial fluctuations $\delta R(\theta, t) = R(\theta, t) - R_0$ and kinetic energy K, they demonstrated that the system obeys a capillary spectrum

$$\langle |\widetilde{\delta R}_{|m| \geqslant 2}|^2 \rangle = \frac{\langle K_{|m| \geqslant 2} \rangle R_0}{\pi \gamma_{2D}(m^2 - 1)}, \tag{3}$$

where m is the Fourier mode number. For the continuous transition—configuration C2 of Castillo et al. (2012)—and an acceleration well above the critical value ($\Gamma = 6.3$, $\Gamma_c \approx 5.1$), the effective surface tension was determined, $\gamma_{2D} = 2.9 \pm 0.1$ μN in two-dimensions. Using H as the third dimension, Luu et al. (2013) obtained $\gamma \equiv \gamma_{2D}/H = 1.5 \pm 0.1$ mN/m in 3D. Additionally, the mobility parameter M, which relates the interface speed with its curvature and surface tension, was measured by demonstrating the each mode obeys a Langevin-type equation. Finally, both γ and M are consistent with a simple order of magnitude estimation considering the characteristic energy, length, and time scales, which is very similar to what can be done for atomic systems.

3 The Liquid Phase

3.1 Velocity Distribution

There is a wide range of parameters where the liquid phase is stable, which is simpler to characterize. Measurements of this state serve as tests for theories of confined

granular matter. Using a high speed camera (normally operated using sequences of two rapid triggers) it is possible to measure the in-plane speed of all the particles. The resulting velocity distribution function $P(v)$ deviates strongly from a Maxwell–Boltzmann. This deviation is characterized by two properties. For small velocities the kurtosis $\kappa = \langle v^4 \rangle / \langle v^2 \rangle^2$, which equals 3 for a Maxwellian, takes values larger than 3 for a broader distribution and smaller than three for a narrow one, being particularly sensitive to the range of small velocities. Experiments give $\kappa > 3$ for all densities and particles used, with decreasing values for increasing Γ. The results differ, however, if the system has or has not a top lid where, in the later case, the confinement is produced as a balance between energy injection, dissipation and gravity. In absence of a top lid the kurtosis approaches 3 for increasing acceleration, therefore recovering a Maxwellian distribution. But when the lid is present, finite asymptotic values are obtained, different from 3 (Olafsen and Urbach 1999, 2001).

For large velocities, the deviation from a Maxwellian distribution is characterized by the tails of $P(v)$ in log scale (shown in Fig. 6). In systems with a top lid a slower than Maxwellian decay is observed, which is given roughly by $P(v) \sim e^{-v^{1.5}}$ (Losert et al. 1999; Olafsen and Urbach 2001). These overpopulated tails appear also in other configurations, as in free cooling granular gases. The overpopulated tails disappear at high frequencies when the top lid is removed (Olafsen and Urbach 1999, 2001). Together with the result for the kurtosis, the conclusion is that systems without lid at high frequencies are well described by a Maxwellian distribution.

The difference between experiments with and without top lid, indicates that the strong deviation from a Maxwell–Boltzmann distribution is related to the energy transfer mechanism from the vertical to the horizontal scale, where the anisotropy between the vertical and horizontal distributions becomes relevant. Under confinement, the vertical velocities are dominated by the walls and there is no thermalization

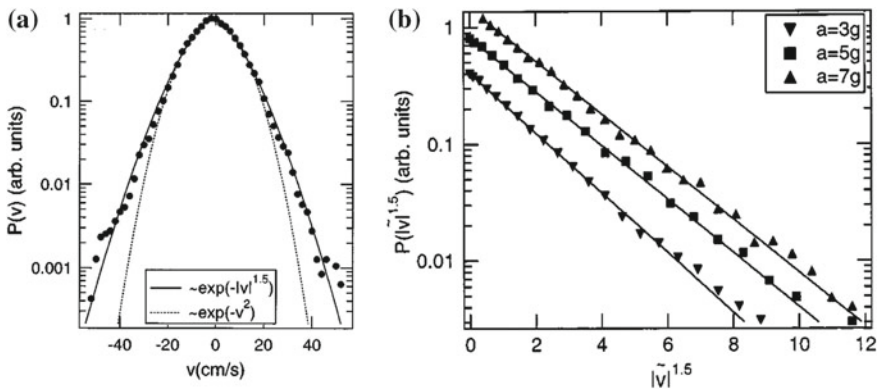**Fig. 6** Probability distribution function (PDF) of the in-plane velocities $P(v)$ for a system with a top lid. **a** PDF in log-scale as a function of the velocity, where it is compared with a Maxwellian distribution. **b** PDF in log-scale as a function of $v^{1.5}$, where the linear trend is evident. Figure reprinted with permission from Losert et al. (1999). Copyright 1999, AIP Publishing LLC

(equipartition) between the two directions. Indeed, the velocity distribution for the vertical direction, which can be measured in simulations, gives a vertical granular temperature that is much larger than the horizontal one (Rivas et al. 2011a).

At the phase-separated regime, Olafsen and Urbach (1998) measured velocity distribution functions for the gas, collapsed and ordered states. The distributions collapse on a single curve when appropriately rescaled and show clear deviations from Maxwell statistics: a pronounced cusp is observed at low velocities and exponential tails at large velocities. The authors suggest that both types of deviations may be a consequence of clustering in momentum space, understood as the correlation between high density and low velocity when particles condense in real space. These dense regions in turn allow the other particles to access to larger velocities because of the reduction of the collisional frequency. Later, a more detailed study of the density and velocity statistics and correlations was reported (Olafsen and Urbach 1999). They demonstrated that the non-Gaussian nature of the velocity distribution increases as the acceleration is decreased from an homogeneous gas state ($\Gamma \approx 3$) down to the collapse transition line ($\Gamma \lesssim 1$), being almost Gaussian at larger accelerations. It was also shown that velocity and density correlations become strong near this transition but for larger accelerations these quantities become uncorrelated.

3.2 Effective Two-Dimensional Models

Grains loose energy at collisions and the Q2D geometry allows granular matter to remain in fluidized states by the continuous transfer of energy from the top and bottom walls to the vertical degrees of freedom and, from these, to the in-plane horizontal degrees of freedom. Besides the direct simulation of three-dimensional systems that include naturally these processes, there has been an important effort in building effective two-dimensional models that include energy source terms.

The first model of this sort consists on adding random kicks to the grains, which are superimposed to the usual collisional dynamics (Peng and Ohta 1998; van Noije and Ernst 1998). It is shown that, for all densities and inelasticities, the granular fluids adopts homogeneous steady states. Kinetic theory analysis of this model predicts that the distribution function is well approximated by a Maxwellian, except for an overpopulated tail $P(v) \sim \exp(-Av^{3/2})$ (van Noije and Ernst 1998). The steady state presents fluctuations that are of large amplitude and long correlation lengths, which is a result of the dynamics not conserving momentum (van Noije et al. 1999).

In the random kick model energy is injected to individual grains, while in the Q2D geometry grains gain energy at collisions. As an improved approach to solve this problem, Barrat and Trizac (2001) and Barrat et al. (2001) introduced the random restitution coefficient model. Here grains move in two dimensions but the restitution coefficient that characterize collisions is a random variable that can adopt values larger than one, hence injecting energy. Different probability distributions for the restitution coefficient are used with the sole condition that the average injected energy vanishes to obtain steady states with finite energy. In all cases, the conclusions

are qualitatively similar. Namely, that the velocity distribution function departs from a Maxwellian with a kurtosis larger than 3 and long tails for large velocities. The tails decay as $P(v) \sim e^{-Av^B}$, where the exponent B depends on the probability distribution used for the restitution coefficient and lay in the range [0.8–2]. The advantage of this model over the random kick description is that it correctly includes the energy injection in the horizontal dynamics at collision events. However, in the long term, the total energy of the system performs a random walk because the inelastic hard sphere model with a random restitution coefficient does not present any characteristic intrinsic scale.

Finally, Brito et al. (2013) introduced a model that solves the problems of the previous models to describe the in-plane dynamics in the Q2D geometry. Grains collide in two-dimensions and, besides the restitution coefficient α that is constant and smaller than one, a kick of a fixed speed Δ is given at the collision events, which are modeled by the collision rule

$$\mathbf{v}_1^* = \mathbf{v}_1 - \frac{1}{2}(1 + \alpha)(\mathbf{v}_{12} \cdot \hat{\sigma})\hat{\sigma} - \hat{\sigma}\Delta, \tag{4}$$

$$\mathbf{v}_2^* = \mathbf{v}_2 + \frac{1}{2}(1 + \alpha)(\mathbf{v}_{12} \cdot \hat{\sigma})\hat{\sigma} + \hat{\sigma}\Delta, \tag{5}$$

where $\mathbf{v}_{12} = \mathbf{v}_1 - \mathbf{v}_2$ is the relative velocity and $\hat{\sigma}$ points from particle 1 to 2. The system reaches stable steady states with a characteristic granular temperature that scales as $T \sim [\Delta/(1 - \alpha^2)]^2$. Here, however, as a result of fixing an energy scale, the velocity distribution does not present long tails and the distribution resembles a Maxwellian. It could be possible that using a distribution for the values of Δ could change the situation.

3.3 Hydrodynamics

At the large, hydrodynamic scale the confined granular fluids present features characteristic of non-equilibrium systems. Prevost et al. (2002) measured the in-plane velocity–velocity correlations when the bottom layer is smooth or rough. It is found that for the smooth surface the correlations are long-ranged, decaying approximately as $1/r^2$. When the rough surface is used the correlations decay exponentially with a correlation length that is larger for the longitudinal velocity (compression modes) compared with the transverse one (shear modes). The drastic difference between the two cases is due to the momentum dissipation in the later.

Using a rough bottom wall, which injects momentum randomly while dissipating it by friction, Gradenigo et al. (2011) and Puglisi et al. (2012) studied experimentally and in simulations the role of friction in the development of velocity correlations in the hydrodynamic scale. The origin of the correlation is related to the absence of a fluctuation–dissipation relation between noise and friction. In all cases, correlations

decay exponentially, and an algebraic decay is only obtained in absence of friction, consistent with the simulation of the random kick model (van Noije et al. 1999).

Different hydrodynamic models have been formulated to describe the long-scale properties of confined systems. Khain and Aranson (2011) emphasized the relevance of the vertical motion, writing separate equations for the vertical and horizontal temperatures. Energy transfer mechanisms were included which resulted in an effective negative compressibility for the in-plane pressure. In a more general approach, Brito et al. (2013) consider a generic energy injection–dissipation mechanism, which is coupled to standard hydrodynamic equations for granular fluids. Two regimes are found. For large dissipations or wavelengths the dynamics is dominated by dissipation and the longitudinal dynamics is governed by damped sound waves. In the opposite case, the diffusive energy transfer dominate the longitudinal modes.

Finally, hydrodynamic equations can be obtained from effective two-dimensional models using the tools of kinetic theory. In particular, this program has been achieved in detail for the model presented at the end of the last section (Brito et al. 2013; Brey et al. 2014, 2015; Soto et al. 2015). The recently obtained equations have been completed with the corresponding transport coefficients. Adding the appropriate fluctuating terms these equations could be analyzed to compare with the experimental results. In the case of the solid-liquid transition, these equations must be coupled with one describing the bond-orientational order parameter evolution.

4   Conclusions

Granular media in confined quasi two-dimensional geometry allows for a simultaneous study of the microscopic and collective dynamics, with the aim of finding models that describe the various phenomena that granular media present. We adopt the proposal that advances in the description of dense granular media could be attained by combining fluid dynamics with appropriate order parameters. In the confined geometry, grains are placed in a shallow box of only a few grains in height, while the lateral dimensions are large. The full box is vibrated periodically and the energy is injected by collisions of the grains with the walls, and later transferred by grain–grain collisions to the horizontal motion. This horizontal motion is monitored experimentally by optical means and is the main object of study.

For box heights of some tens of diameters, the vibrated granular fluid presents a liquid–vapor transition. The system is described by the integrated density over the vertical dimension as the order parameter. The average temperature is obtained from the balance between injection and dissipation and results to be a decreasing function of density. Consequently, the effective pressure presents regions of negative compressibility, which is the responsible of the phase separation.

By decreasing the confining height, the granular layers show a liquid–solid transition. Depending on the vibration amplitude and frequency, the solid can occupy one or two layers, with different crystallographic symmetries. Qualitatively, the origin of the transition is similar to the previous case with negative compressibility

being the responsible of the transition. However, to characterize it, it is found that besides density, the crystalline order should be used as order parameter. With this appropriate order parameter, the transition can be classified as being continuous or discontinuous. In the former case, critical exponents have been measured.

For both the liquid–vapor and liquid–solid transitions the phase separation is stable, with both phases coexisting. The interfaces fluctuate but are otherwise stable and the denser phase presents circular shapes, indicating that an effective surface tension exists. For the liquid–vapor transition, this effective tension was included in the model for the order parameter and, later, it was measured in simulations by using the Laplace law and the anisotropy of the stress tensor. For the liquid–solid transition, the spectral analysis of interface capillary waves allowed the experimental measurement of the effective surface tension.

In the homogeneous liquid phase, the in-plane velocity distribution functions deviate strongly from a Maxwellian. Long tails and kurtosis larger than for a Maxwellian are obtained in experiments. The origin of these deviations is the anisotropy between the vertical and horizontal motion. Effective two-dimensional models that incorporate the energy injection from the vertical to the horizontal motion describe some properties of the full three dimensional systems, particularly some features of the distribution function, but still the complete transfer mechanism is not captured. These effective models, because of their simplicity compared to the case of three dimensions, allows the construction of hydrodynamic equations that are coupled to different mechanisms of energy injection. To fully describe the phase transitions, the crystalline order parameter remains to be included.

References

Amarouchene Y, Boudet JF, Kellay H (2008) Capillarylike fluctuations at the interface of falling granular jets. Phys Rev Lett 100:218001

Andreotti B, Forterre Y, Pouliquen O (2013) Granular media: between fluid and solid. University Cambridge Press, Cambridge

Aranson IS, Blair D, Kalatsky VA, Crabtree GW, Kwok WK, Vinokur VM, Welp U (2000) Electrostatically driven granular media: phase transitions and coarsening. Phys Rev Lett 84:3306–3309

Aranson IS, Tsimring LS (2006) Patterns and collective behavior in granular media: theoretical concepts. Rev Mod Phys 78:641–692

Aranson IS, Snezhko A, Olafsen JS, Urbach JS (2008) Comment on "Long-lived giant number fluctuations in a swarming granular nematic". Science 320:612c–612c

Argentina M, Clerc MG, Soto R (2002) van der Waals-like transition in fluidized granular matter. Phys Rev Lett 89:044301

Barrat A, Trizac E (2001) Inelastic hard spheres with random restitution coefficient: a new model for heated granular fluids. Adv Complex Syst 4:299–307

Barrat A, Trizac E, Fuchs JN (2001) Heated granular fluids: the random restitution coefficient approach. Eur Phys J E 5:161–170

Ben-Naim E, Daya ZA, Vorobieff P, Ecke RE (2001) Knots and random walks in vibrated granular chains. Phys Rev Lett 86:1414–1417

Brey JJ, García de Soria MI, Maynar P, Buzón V (2014) Memory effects in the relaxation of a confined granular gas. Phys Rev E 90:032207

Brey JJ, Buzón V, Maynar P, García de Soria MI (2015) Hydrodynamics for a model of a confined quasi-two-dimensional granular gas. Phys Rev E 91:052201

Brito R, Risso D, Soto R (2013) Hydrodynamic modes in a confined granular fluid. Phys Rev E 87:022209

Castillo G, Mujica N, Soto R (2012) Fluctuations and criticality of a granular solid-liquid-like phase transition. Phys Rev Lett 109:095701

Castillo G, Mujica N, Soto R (2015) Universality and criticality of a second-order granular solid-liquid-like phase transition. Phys Rev E 91:012141

Cartes C, Clerc MG, Soto R (2004) van der Waals normal form for a one-dimensional hydrodynamic model. Phys Rev E 70:031302

Cheng X, Varas G, Daniel C, Jaeger HM, Nagel SR (2007) Collective behavior in a granular jet: emergence of a liquid with zero surface tension. Phys Rev Lett 99:188001

Cheng X, Xu L, Patterson A, Jaeger HM, Nagel SR (2008) Towards the zero-surface-tension limit in granular fingering instability. Nat Phys 4:234–237

Clerc MG, Cordero P, Dunstan J, Huff K, Mujica N, Risso D, Varas G (2008) Liquid-solid-like transition in quasi-one-dimensional driven granular media. Nat Phys 4:249–254

Clewett JPD, Roeller K, Bowley RM, Herminghaus S, Swift MR (2012) Emergent surface tension in vibrated, noncohesive granular media. Phys Rev Lett 109:228002

Duran J (2001) Rayleigh-Taylor instabilities in thin films of tapped powder. Phys Rev Lett 87:254301

Géminard JC, Laroche C (2004) Pressure measurement in two-dimensional horizontal granular gases. Phys Rev E 70:021301

Goldhirsch I, Zanetti G (1993) Clustering instability in dissipative gases. Phys Rev Lett 70:1619–1622

Gradenigo G, Sarracino A, Villamaina D, Puglisi A (2011) Non-equilibrium length in granular fluids: from experiment to fluctuating hydrodynamics. EPL 96:14004

Hohenberg PC, Halperin BI (1977) Theory of dynamic critical phenomena. Rev Mod Phys 49:435–479

Howell DW, Aronson IS, Crabtree GW (2001) Dynamics of electrostatically driven granular media: effects of humidity. Phys Rev E 63:050301

Jaeger HM, Nagel SR, Behringer RP (1996) Granular solids, liquids, and gases. Rev Mod Phys 68:1259–1273

Khain E, Aranson IS (2011) Hydrodynamics of a vibrated granular monolayer. Phys Rev E 84:031308

Lobkovsky AE, Vega-Reyes F, Urbach JS (2009) The effects of forcing and dissipation on phase transitions in thin granular layers. Eur Phys J Special Topics 179:113–122

Losert W, Cooper DGW, Gollub JP (1999a) Propagating front in an excited granular layer. Phys Rev E 59:5855–5861

Losert W, Cooper DGW, Delour J, Kudrolli A, Gollub JP (1999b) Velocity statistics in excited granular media. Chaos 9:682–690

Luu L-H, Castillo G, Mujica N, Soto R (2013) Capillarylike fluctuations of a solid-liquid interface in a noncohesive granular system. Phys Rev E 87:040202

May C, Wild M, Rehberg I, Huang K (2013) Analog of surface melting in a macroscopic nonequilibrium system. Phys Rev E 88:062201

Melby P, Vega Reyes F, Prevost A, Robertson R, Kumar P, Egolf DA, Urbach JS (2005) The dynamics of thin vibrated granular layers. J Phys Cond Mat 17:S2689–S2704

Merminod S, Berhanu M, Falcon E (2014) Transition from a dissipative to a quasi-elastic system of particles with tunable repulsive interactions. EPL 106:44005

Narayan V, Ramaswamy S, Menon N (2007) Long-lived giant number fluctuations in a swarming granular nematic. Science 317:105–108

Narayan V, Ramaswamy S, Menon N (2008) Response to comment on "Long-lived giant number fluctuations in a swarming granular nematic". Science 320:612d–612d

Néel B, Rondini I, Turzillo A, Mujica N, Soto R (2014) Dynamics of a first order transition to an absorbing state. Phys Rev E 89:042206

Olafsen JS, Urbach JS (1998) Clustering, order, and collapse is a driven granular monolayer. Phys Rev Lett 81:4369–4372

Olafsen JS, Urbach JS (1999) Velocity distributions and density fluctuations in a granular gas. Phys Rev E 60:R2468–R2471

Olafsen JS, Urbach JS (2001) Experimental observations of non-equilibrium distributions and transitions in a 2D granular gas, granular gases. In: Pöschel T, Luding S (eds). Springer, pp 410–428

Olafsen JS, Urbach JS (2005) Two-dimensional melting far from equilibrium in a granular monolayer. Phys Rev Lett 95:098002

Orza JAG, Brito R, Van Noije TPC, Ernst MH (1997) Patterns and long range correlations in idealized granular flows. Int J Mod Phys C 8:953–965

Oyarte L, Gutiérrez P, Aumaître S, Mujica N (2013) Phase transition in a out-of-equilibrium monolayer of dipolar vibrated grains. Phys Rev E 87:022204

Pacheco-Vázquez F, Caballero-Robledo GA, Ruiz-Suárez JC (2009) Superheating in granular matter. Phys Rev Lett 102:170601

Peng G, Ohta T (1998) Steady state properties of a driven granular medium. Phys Rev E 58:4637

Pérez-Ángel G, Nahmad-Molinari Y (2011) Bouncing, rolling, energy flows, and cluster formation in a two-dimensional vibrated granular gas. Phys Rev E 84:041303

Prevost A, Melby P, Egolf DA, Urbach JS (2004) Non-equilibrium two-phase coexistence in a confined granular layer. Phys Rev E 70:050301(R)

Prevost A, Egolf DA, Urbach JS (2002) Forcing and velocity correlations in a vibrated granular monolayer. Phys Rev Lett 89:084301

Puglisi A, Gnoli A, Gradenigo G, Sarracino A, Villamaina D (2012) Structure factors in granular experiments with homogeneous fluidization. J Chem Phys 136:014704

Reis P, Ingale RA, Shattuck MD (2006) Crystallization of a quasi-two-dimensional granular fluid. Phys Rev Lett 96:258001

Reis P, Ingale RA, Shattuck MD (2007) Caging dynamics in a granular fluid. Phys Rev Lett 98:188301

Reyes FV, Urbach JS (2008) Effect of inelasticity on the phase transitions of a thin vibrated granular layer. Phys Rev E 78:051301

Rivas N, Cordero P, Risso D, Soto R (2011a) Segregation in quasi two-dimensional granular systems. New J Phys 13:055018

Rivas N, Ponce S, Gallet B, Risso D, Soto R, Cordero P, Mujica N (2011b) Sudden chain energy transfer events in vibrated granular media. Phys Rev Lett 106:088001

Rivas N, Cordero P, Risso D, Soto R (2012) Characterization of the energy bursts in vibrated shallow granular systems. Granul Matter 14:157–162

Roeller K, Clewett JPD, Bowley RM, Herminghaus S, Swift MR (2011) Liquid-gas phase separation in confined vibrated dry granular matter. Phys Rev Lett 107:048002

Royer JR, Evans DJ, Oyarte L, Guo Q, Kapit E, Möbius ME, Waitukaitis SR, Jaeger HM (2009) High-speed tracking of rupture and clustering in freely falling granular streams. Nature 459:1110–1113

Safford K, Kantor Y, Kardar M, Kudrolli A (2009) Structure and dynamics of vibrated granular chains: comparison to equilibrium polymers. Phys Rev E 79:061304

Soto R, Risso D, Brito R (2015) Shear viscosity of a model for confined granular media. Phys Rev E 90:062204

Ulrich S, Zippelius A (2012) Stability of freely falling granular streams. Phys Rev Lett 109:166001

van Noije TPC, Ernst MH (1998) Velocity distributions in homogeneous granular fluids: the free and the heated case. Granul Matter 1:57–64

van Noije TPC, Ernst MH, Trizac E, Pagonabarraga I (1999) Randomly driven granular fluids: large-scale structure. Phys Rev E 59:4236

Equations to Determine Energy Losses in Sudden and Gradual Change of Direction

J.J. Villegas-León, A.A. López-Lambraño, J.G. Morales-Nava, M. Pliego-Díaz, C. Fuentes and A. López-Ramos

Abstract Equations to estimate the K coefficient have been obtained for devices of change direction of ducts under forced regime. For this approach, a state of art was carried out where it was noticed that the traditionally utilized methods that evaluate the losses of the devices needed tables and/or graphics when estimating the K coefficient, which is singular to each accessory. Each theory was analyzed and classified accordingly to each piece whenever these are present in sudden or gradual conditions. The data was homogenized with the purpose to obtain average curves values of the coefficient. The results were used as data in methods of multiple linear regressions until obtain a representative equation for each case studied. These equations have the advantage of being reliable to determine the loss of K coefficient without having to manipulate tables and graphics; this allows saving time when designing and testing the hydraulic behavior in forced ducts. Finally, these equations can be implemented in advanced computational algorithms which will allow the analysis and modeling of the losses caused by friction in different scenarios.

J.J. Villegas-León · A.A. López-Lambraño (✉)
Facultad de Ingeniería, Universidad Autónoma de Baja California (UABC),
Blvd. Benito Juárez S/N, C.P., 21280 Mexicali, BC, Mexico
e-mail: altoti@gmail.com
URL: http://www.hidrusmx.com

J.G. Morales-Nava
Facultad de Ingeniería Arquitectura Y Diseño, Universidad Autónoma de Baja California,
Km. 103 Carretera Tijuana—Ensenada, C.P., 22860 Ensenada, BC, Mexico

M. Pliego-Díaz
Instituto Tecnológico de Querétaro. Ciencias Básicas. Av. Tecnológico S/N,
Centro 76000, Santiago de Querétaro, Mexico

C. Fuentes
Instituto Mexicano de Tecnología del Agua. Paseo Cuauhnahuac 8532 Progreso, 62550
Jiutepec, MOR, Mexico

A. López-Ramos
Escuela de Ingenierías y Arquitectura Facultad de Ingeniería Civil,
Universidad Pontificia Bolivariana-Seccional Montería, Km. 8 vía a Cereté,
Montería, Córdoba, Colombia

465

1 Introduction

The loss of hydraulic energy is vital to quantify, because it is necessary to know the amount of available hydraulic energy in order to use it in a system such as: the conveying lines in industrial plants (Anaya-Durand et al. 2014), internal distribution networks in geothermal centrals (Di Maria 2000), ducts in hydroelectric plants (Elbatran et al. 2015), water distribution networks to populations (Yıldırım and Singh 2010), drip irrigation systems (Sesma et al. 2015), and many more which can be cited.

The study of energy losses is divided in: friction losses and local losses, both having a different origin (Liu et al. 2013), and with reference to the latter the present work is concentrated. Local losses take place when the fluid flows in a duct which has a constant diameter and suddenly, the duct changes direction or it exist an expansion, reduction, bifurcation, or obstruction (accessory). This generally happens in the surroundings of the element that causes it and its magnitude, origins and quantification depends of the specific characteristics of the device (Bariviera et al. 2013; Fuentes and Rosales 2004). Our investigation focuses on the study of energy losses caused by a change in direction of the flow (curves) of circular conduits, being this device the highly used in the building of forced conductions.

A change in direction can occur in sudden or gradual conditions. In a sudden direction change, the direction of the fluid is abruptly modified which causes a detachment or separation of the fluid in the internal part of the curve and a pressure increase in the external part caused by the intensity of the impact (Fig. 1a). This causes that, after the curve the motion of the flow change into a spiral form up to lengths equal 50 times the diameter of the conduction (Hellström et al. 2013; Sotelo 2013). However, when the direction change is performed in gradual form (Fig. 1b), the phenomenon of the fluid's alteration is similar to the abrupt change, but it happens in lower magnitude according to how smooth the curve is produced (Sotelo 2013).

Recent investigations carried out by: Csizmadia and Hős (2014), Gasljevic and Matthys (2009), Hellström et al. (2013), Ji et al. (2010), Noorani et al. (2013),
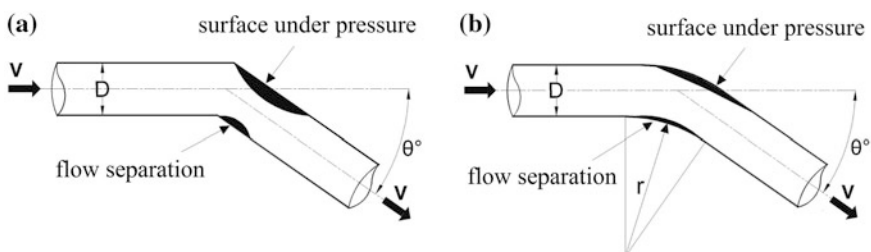

Fig. 1 Behavior of circulating flow in: **a** Sudden change of direction. **b** Gradual change of direction. θ is the deflection angle of the *curve*, r is curvature's ratio and D the diameter of the conduit

Shi et al. (2013), Ulusarslan (2010); among others, support the importance of studying the phenomenon and the way energy losses in a change of direction are quantified. Despite having an array of analytical and experimental results to obtain the losses of K coefficient for this device, there is no generalized value for the geometrical and physical conditions on which these devices are being used.

In this investigation are obtained equations to determine the K coefficient of a sudden and gradual change of direction, providing an average value using experimental information.

2 Theory

2.1 *Estimation of Energy Losses*

In literature (Acero and Rodríguez 2008; Bariviera et al. 2013; Sotelo 2013; Streeter et al. 2000; USACE 1980; USBR 1985; Yıldırım and Singh 2010)—among others —local energy losses have been determined as follows:

$$h_L = K \frac{V^2}{2g} \tag{1}$$

where: h_L is the loss of hydraulic charge (m); g is the acceleration of gravity (m/s^2); V is the average speed of flow (m/s) which, in a change of direction is the one produced in the upstream above the accessory; K is the coefficient of losses in the accessory (dimensionless) which is obtained by employing tables or graphics from experimental results who are often combined with empirical equations whose values are dependent to physical and geometrical parameters and, in occasions of the Reynolds Number (Bae and Kim 2014). This number is calculated as follows:

$$R_e = \frac{DV}{v} \tag{2}$$

where: R_e is the Reynolds Number (dimensionless); D is the diameter of the conduit (m); V is the average speed of flow (m/s); v is t kinematic viscosity of the fluid (m^2/s).

2.2 *Estimation of the K Coefficient*

(*a*) *Sudden Change of Direction*
Sotelo (2013) and USACE (1980) recommended the use of a graphical method to estimate the K coefficient, using the laboratory results of Kirchbach and Schubart. This graphic has curves for three Reynolds numbers (20000, 60000, and 250000) and relate to the deflection angle (θ) to obtain the coefficient of interest. On the other hand,

in CFE (1983) and Miller (1978), the K losses coefficient is obtained from a graphic for $R_e = 1000000$, where the value of K is subjected to the deflection angle (θ_b).

(b) Gradual Change of Direction

In USACE (1980), it is said that the coefficient of loss can be estimated using a Wasieliewski's graphic which depends on the deflection of the angle (θ) and to the relation of the curve's ratio according to the diameter of the device (r/D). Based on USBR (1985), it has been suggested a graphic to obtain the experimental coefficient value when the central angle of the curve is 90°. This graphic has several curves proposed by various researchers and a curve fitting proposed by the author of this paper which will be also considered as part of the article itself. To this point, the losses coefficient depends on the ratio of the curvature and the diameter of the accessory (R_b/D). Subsequently, the author proposes other graphic with a correction factor for a change in direction with other curvature angle different of 90°. In order to obtain the most adequate K coefficient, the correction factor proposed by the author is proportional to the resulting coefficient of the curve with an angle of 90°. In Sotelo (2013), the K coefficient can be determined as follows:

$$K = C_c \frac{\theta°}{90°} \tag{3}$$

where; K is the experimental coefficient; θ is the inner angle of the curvature, and C_c is a coefficient for curves presenting a constant diameter and for the Reynolds number $>2.2 \times 10^5$. This number has been obtained from the Hoffman graphic which depends the ratio of the curve and the diameter of the conduit (r/D), and at the same time, it depends on the relation between the roughness and the diameter (ε/D). In order to obtain the same amount of parameters, this research considers the average curve of ε/D. Considering CFE (1983) and Miller (1978), the experimental coefficient can be obtained in a graphic representation when the flow reaches its standarization and the Reynolds' number is equal to 10^6. On this graphic, the coefficient is governed by the deflection angle and the relation between the ratio of the curve and the diameter of the conduit (r/D). The authors of the current research suggest three other graphics where correction coefficients can be obtained for the Reynolds Number, by the length after the curve, and by the roughness of the conduit. However, this current research will not consider these corrections in order to maintain a degree of uniformity on the parameters regarding the other authors. According to SARH (1984), the K coefficient in a change of direction, presenting a deflection of 90°, can be estimated through a tabulation which is governed by the relation between the ratio of the curvature and the diameter of the conduit (r/D). Nevertheless, if the deflection is different from 90°, the obtained coefficient should be proportional to a η factor which can be determined with a second tabulation and it will depend on the magnitude of the deflection angle (θ).

3   Estimation and Analysis of the K Coefficient

Based on what has been found in the literature, the study of energy losses on devices which have direction changes are divided according to sudden conditions and gradual conditions. Based on this criterion.

(a) Sudden Change of Direction

In order to estimate the K coefficient in sudden conditions, the methods suggested in CFE (1983), Miller (1978), Sotelo (2013) and USACE (1980) were choose to work with. All of them employ graphics to estimate the losses coefficient dependent to the deflection angle (θ). Using the graphs, coordinates were obtained showing the points on the curves; afterwards, this information was homogenized in such manner that, for each method, values of the K coefficient were obtained for values of θ. from 0 to 90°, in 5° increments. Based on the obtained data, using the previously described process, average values were estimated and subsequently proposed in this research, indicated as K_{CB}. Figure 2 shows the behavior of the values—represented by curves-of the K coefficient; the coefficients and the curve of the average losses coefficient (K_{CB}) were determined by the employment of the previously selected methods. Furthermore, this figure shows the tendency of the K coefficient of a given value of θ and R_e, whereas the K_{CB} coefficient depends just to the angle θ.

A multiple linear regression was carried out using the values of the K_{CB} coefficient. Figure 3 shows the curve fitting and its equation in order to estimate the coefficient of a device which makes an abrupt direction change (K_{CB}) with a confidence of 99.9 %

$$K_{CB} = \frac{0.0031960558 + 0.0030444516\,\theta}{1 - 0.014390831\,\theta + 0.00006719314\,\theta^2} \tag{4}$$

where: K_{CB} is the coefficient of an abrupt change of direction; θ is the deflection angle of the curve (degrees). In order to apply this equation it suffices to know the angle θ. This equation is suggested to obtain the values with previously exposed level of trust/confidence only in the cases when the angle is greater than 0 and lesser or equal to 90°.

(b) Gradual Change of Direction

In order to estimate the K coefficient in gradual conditions, methods proposed in CFE (1983), Miller (1978), SARH (1984), Sotelo (2013), USACE (1980) and USBR (1985) were employed; these methods involved graphics, tables, and equations.

Values of the losses coefficient were obtained for each method in a relation to the curvature ratio regarding to a diameter (r/D) of 1 and to values of the deflection angle (θ) from 0 to 90° in steps of 5°. K values were obtained in a similar way corresponding to the relations of r/D 1.5, 2, 4, 6, and 10. Once having these results, average values of the losses coefficient were determined for each value of θ for r/D = 1; each increment is represented as K_{CG1}. This average was also carried out
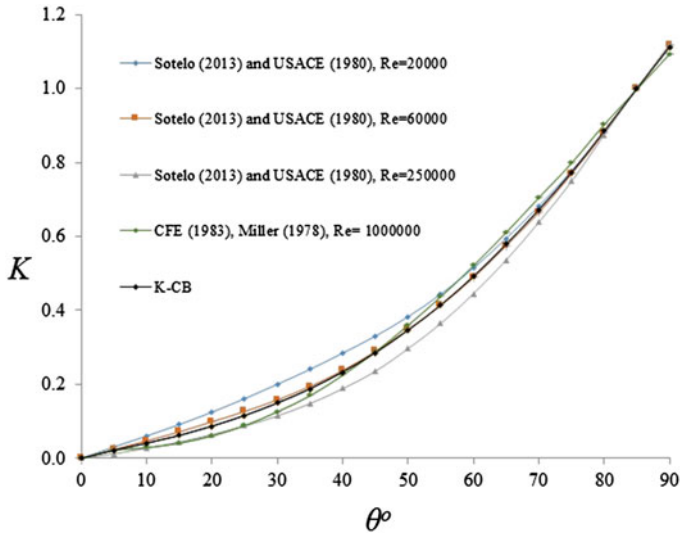
Fig. 2 Curves of the *K* coefficient in an abrupt change of direction corresponding to the angle of the deflection curve in degrees. The *K-CB* curve represents the average values
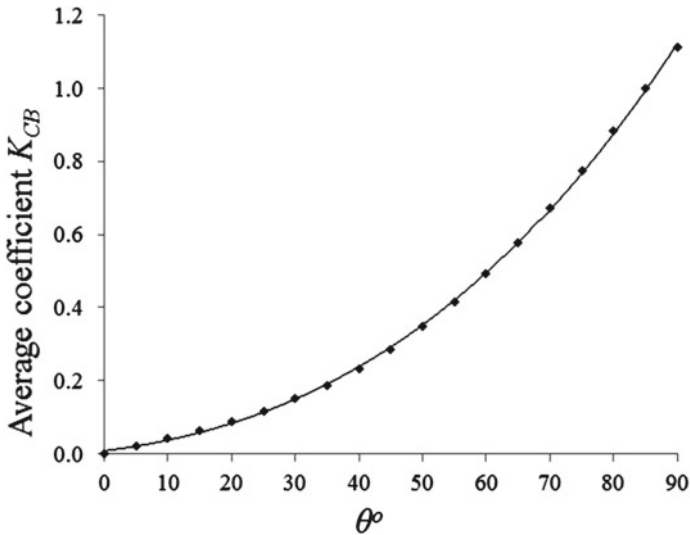
Fig. 3 Fitting curve and the equation of the K_{CB} coefficient regarding the deflection angle of the curve (θ)

in the case that *r/D* might be of 1.5, 2, 4, 6, and 10; these average values are represented as K_{CG2}, K_{CG3}, K_{CG4}, K_{CG5}, and K_{CG6}, respectively, Fig. 4 shows the

tendency of the average values of the K_{CG} coefficient with respect to the variation of the curve's deflection angle (θ).

Once all the average values were obtained, a multiple linear regression was carried out where a fitting curve was selected for the 6 classifications of K_{CG}, i.e. a fitting curve of 99.9 % was obtained for the K_{CG1} values (Fig. 5). This resulted in the same curve for the other 5, but with a different fitting on each one of them.

In general, the equation of the fitting curve for all 6 classifications of K_{CG} can be represented as follows:

$$K_{CG} = \frac{(a + c\theta)}{(1 + b\theta)} \tag{5}$$

where: K_{CG} is the losses coefficient in gradual direction change with a fixed value of r/D; a, b, and c are constants that vary in relation to r/D; θ is the value of the deflected angle in degrees. Since the values of the constants (a, b, c) vary on each classification of the K_{CG} coefficient, a fitting curve was defined for each of the constants regarding the relation r/D. Figure 6 shows the fitting curve with the values of constant a and the Eq. (6) which defines its value with a 99.9 % confidence. Equations for constant b and c are represented in (7) and (8), respectively.
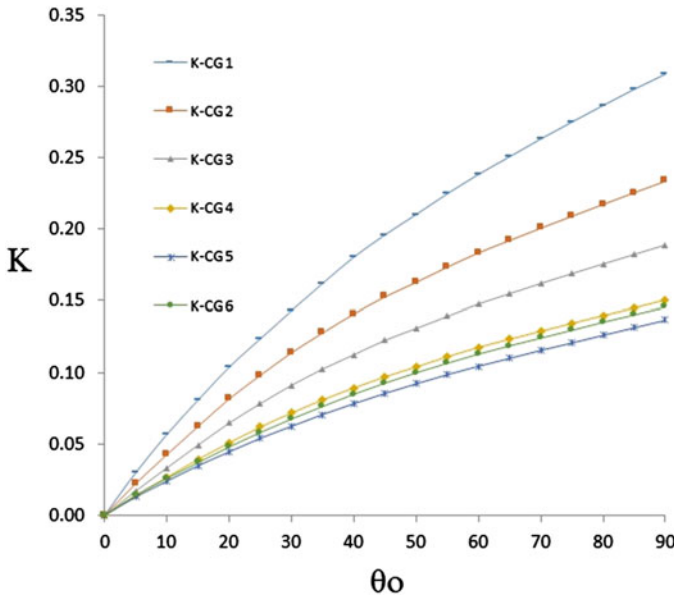
Fig. 4 Behavior of the average values in a gradual direction change of different relations between the ratio of the curve regarding the diameter of the conduit (r/D) according to the curve's deflection angle θ. Curves K-CG1, K-CG2, K-CG3, K-CG4, K-CG5, and K-CG6 correspond to the ratio r/D = 1, 1.5, 2, 4, 6, and 10, respectively
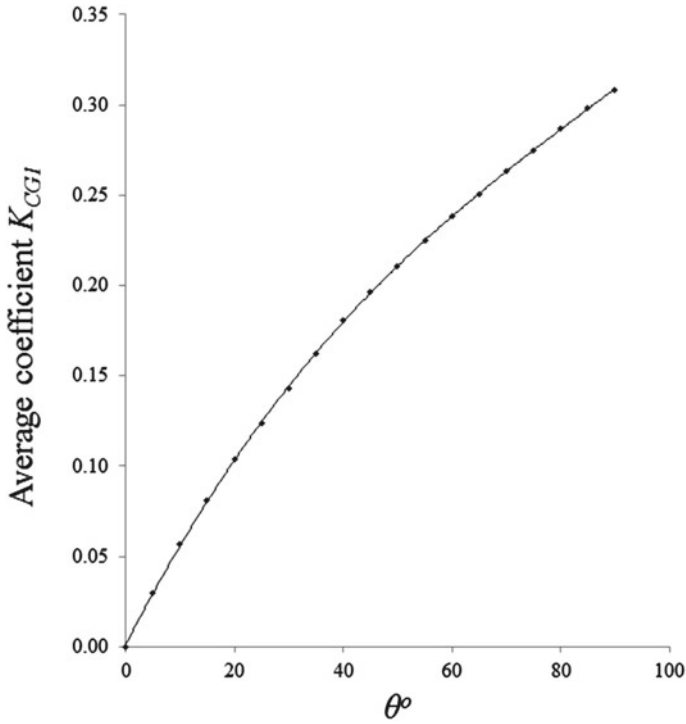
Fig. 5 Fitting curve to estimate the K_{CGI} coefficient as a function of the curve's deflection angle θ
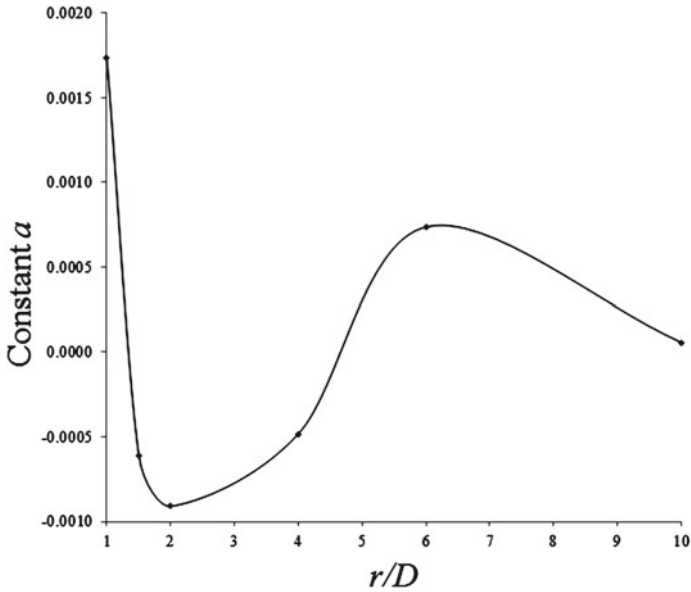
Fig. 6 Fitting curve of the constant a in Eq. 5 with respect between the curvature's ratio and the diameter of the conduit r/D

$$a = -0.0573379 + 0.00496834(r/D) - 0.00001716(r/D)^3$$
$$+ \frac{0.07867083}{(r/D)^{0.5}} - \frac{0.066727}{e^{(r/D)}} \tag{6}$$

$$b = 0.20495202 + 0.05446522(r/D) - 0.08723377(r/D)^{0.5}\ln(r/D)$$
$$- \frac{0.45002930\ln(r/D)}{(r/D)} - \frac{0.25130468}{(r/D)^2} \tag{7}$$

$$c = -0.01383436 - 0.01385106(r/D) + 0.00051449(r/D)^2$$
$$+ 0.04504019ln(r/D) + \frac{0.08991395}{e^{(r/D)}} \tag{8}$$

Considering the equations for constants *a, b,* and *c,* Eq. (5) is presented as follows:

$$K_{CG} = \left\{ \left[-0.0573379 + 0.00496834(r/D) - 0.00001716(r/D)^3 + \frac{0.07867083}{(r/D)^{0.5}} - \frac{0.066727}{e^{(r/D)}} \right] \right.$$
$$+ \left[-0.01383436 - 0.01385106(r/D) + 0.00051449(r/D)^2 + 0.04504019\ln(r/D) + \frac{0.08991395}{e^{(r/D)}}(\theta) \right] \right\} /$$
$$\left\{ 1 + \left[0.20495202 + 0.05446522(r/D) - 0.08723377(r/D)^{0.5}\ln(r/D) - \frac{0.45002930\ln(r/D)}{(r/D)} + \frac{0.25130468}{(r/D)^2} \right](\theta) \right\} \tag{9}$$

where: K_{CG} is the losses coefficient in a gradual direction change; This equation should be used under the following conditions: $1 \leq r/D \leq 10$ and $5 \leq \theta \leq 90$. The aim of these conditions is to obtain results under a confidence of 99 %.

By running the Eqs. (4) and (9) the K_{AB} and K_{AG} coefficients are obtained, respectively, which are substituted in Eq. (1) order to obtain energy losses in a sudden change direction and gradual change direction, respectively, without using tables and graphs.

4 Conclusions

By reviewing the literature, we realized different methods are suggested in order to determine the losses coefficient (K) for each studied device. After analyzing such methods, it was determined that different values of *K* can be obtained with the use of one or other method; therefore, no standard values were registered. The implemented equations generate average *K* values of the analyzed methods with a determination of 0.99 and they not requires any handling of documents to determine its losses coefficient safely, exact and practical. Mathematical models implemented in this research can be applied jointly with Eq. (1) to obtain energy losses in the

studied devices and save time in the design and testing of hydraulic behavior of forced conduits. Likewise, the equations can be implemented in advanced calculation algorithms that allow the analysis and modeling of losses caused by friction in different scenarios.

References

Acero, MF, Rodríguez, D (2008) Determinación experimental del coeficiente de pérdidas menores km en accesorios de agua potable de PVC. In: XVIII seminario nacional de hidráulica e hidrología, sociedad colombiana de ingenieros, Bogotá, D.C. 22–24 de mayo de

Anaya-Durand AI, Cauich-Segovia GI, Funabazama-Bárcenas O, Gracia-Medrano-Bravo VA (2014) Evaluación de ecuaciones de factor de fricción explícito para tuberías. Rev Mexicana Ing Química 25:128–134

Bae Y, Kim Y (2014) Prediction of local loss coefficient for turbulent flow in axisymmetric sudden expansions with a chamfer: effect of Reynolds number. J. Ann Nucl Energy 73:33–38

Bariviera D, Frizzone JA, Rettore NO (2013) Dimensional analysis approach to estimate local head losses in microirrigation connectors. J Irrig Sci 32:169–179

CFE (1983) Conducciones a Presión, tomo 2.3, Hidrotecnia Comisión Federal de Electricidad, Instituto de Investigaciones Eléctricas, Manual de Obras Civiles

Csizmadia P, Hős C (2014) CFD-based estimation and experiments on the loss coefficient for Bingham and power-law fluids through diffusers and elbows. J Comput Fluids 99:116–123

Deniz Ulusarslan D (2010) Effect of diameter ratio on loss coefficient of elbows in the flow of low-density spherical capsule trains. Part Sci Technol Int J 28:348–359

Di Maria F (2000) Design and off design pipe network geothermal power plant analysis with power pipe simulator. Energy Convers Manag 41:1223–1235

Elbatran AH, Yaakob OB, Ahmeda YM, Shabara HM (2015) Operation, performance and economic analysis of low head micro-hydropower turbines for rural and remote areas: a review. Renew Sustain Energy Rev 43:40–50

Fuentes OA, Rosales IL (2004) Estimación de pérdidas locales de energía e domiciliarias de agua potable. Rev Mexicana Ingeniería Hidráulica en México 19:65–73

Gasljevic K, Matthys EF (2009) Friction and heat transfer in drag-reducing surfactant solution flow through curved pipes and elbows. Eur J Mech B/Fluids 28:641–650

Hellström LHO, Zlatinov MB, Cao G, Smits AJ (2013) Turbulent pipe flow downstream of a 90° bend. J Fluid Mech 735(R7):1–12

Ji C, Zhang X, Jiang M, Yan P (2010) Numerical simulation of influence of 90°-bend pipeline geometric shape on local loss coefficient. In: 2010 International conference on mechanical and electrical technology (ICMET 2010), pp 668–672

Liu SH, Xue J, Fan M (2013) The calculation of mechanical energy loss for incompressible steady pipe flow of homogeneous fluid. J Hydrodyn 25:912–918

Miller DS (1978) Internal flow systems. BHRA (information services)

Noorani A, El Khoury GK, Schlatter P (2013) Evolution of turbulence characteristics from straight to curved pipes. Int J Heat Fluid Flow 41:16–26

SARH (1984) Obras de Toma para Presas de Almacenamiento. Dirección General de Obras Hidráulicas y de Ingeniería Agrícola para el Desarrollo Rural, Distrito Federal, Mexico

Sesma J, Molina-Martínez JM, Cavas-Martínez F, Fernández-Pacheco DG (2015) A mobile application to calculate optimum drip irrigation laterals. Agric Water Manag 151:13–18

Shi H, Chen G, Wang Y, Chen X (2013) Ratcheting behavior of pressurized elbow pipe with local wall thinning. Int J Press Vessels Pip 102–103:14–23

Sotelo AG (2013) Hidráulica general, vol 1. LIMUSA

Streeter VL, Wylie EB, Bedford KB (2000) Mecánica de fluidos, 9th edn. Mc Graw-Hill International, SA

USACE (1980) Engineering and design, hydraulic design of reservoir outlet department of the army. Corps of Engineers, USA

USBR (1985) Diseño de presas pequeñas, united states department of the interior, bureau of reclamation, 13th edn. Compañía Editorial Continental, SA de CV

Yildirim G, Singh VP (2010) A MathCAD procedure for commercial pipeline hydraulic design considering local energy losses. J. Adv Eng Softw 41:489–496

Parallel CPU/GPU Computing for Smoothed Particle Hydrodynamics Models

J.M. Domínguez, A. Barreiro, A.J.C. Crespo, O. García-Feal and M. Gómez-Gesteira

Abstract Smoothed Particle Hydrodynamics (SPH) is a numerical method particularly suitable to describe a variety of complex free-surface flows with large discontinuities. However, SPH simulations are computationally expensive and typical runtimes are too high to study real problems with high resolution. The proposed solution is the parallel computation to accelerate the SPH executions. This work introduces several high performance techniques applied to SPH to allow simulation of real problems at reasonable time. In this way, OpenMP was used to exploit all cores in the classical CPUs. On the other hand, CUDA language was used to take advantage of the high parallel computing power of GPUs (Graphics Processing Units). Finally, Message Passing Interface (MPI) was implemented to combine the power of several machines connected by network. These parallelization techniques are implemented in the code DualSPHysics and results are shown in terms of performance, efficiency and scalability using different CPU and GPU models.

1 Introduction

Smoothed Particle Hydrodynamics (SPH) is a Lagrangian meshless method developed during seventies (Gingold and Monaghan 1977) in astrophysics. This technique has been successfully applied to a wide variety of fields, in particular to free surface hydrodynamics such as the study of wave breaking, wave-structure interactions.

SPHysics is an SPH numerical model developed to study free-surface flows and is the product of a collaborative effort amongst researchers at the Johns Hopkins University (US), the University of Vigo (Spain) and the University of Manchester

J.M. Domínguez (✉) · A. Barreiro · A.J.C. Crespo · O. García-Feal · M. Gómez-Gesteira
EPhysLab Environmental Physics Laboratory, Universidad de Vigo,
Edificio de Física, Campus As Lagoas s/n, Ourense 32004, Spain
e-mail: jmdominguez@uvigo.es

(UK). The original serial open-source code, written in FORTRAN, is available for public use at http://www.sphysics.org. Although the SPHysics method can provide an accurate description of the flow (Gómez-Gesteira and Dalrymple 2004; Dalrymple and Rogers 2006; Crespo et al. 2007; Rogers et al. 2010; Narayanaswamy et al. 2010; Gómez-Gesteira et al. 2012a, b) its main drawback is the slowness, which makes virtually impossible to use for practical engineering problems.

Graphics Processing Units (GPUs) are a new technology imported from the computer games industry that can be used for scientific computing. GPUs offer now a higher computing power than CPUs and they are an affordable option to accelerate SPH with a low economic cost. One of the first schemes implementing a classical SPH approach on the GPU was performed by Harada et al. (2007). A remarkable added value of their work is the implementation before the appearance of Compute Unified Device Architecture (CUDA) and the ease of the software development kits (SDKs). A new CPU-GPU code based on SPHysics and named DualSPHysics has been developed using C++ and CUDA for operation on CPUs and GPUs, respectively.

The DualSPHysics code (Crespo et al. 2015) has been developed to use SPH for real engineering problems. DualSPHysics is open source and can be freely downloaded from http://www.dual.sphysics.org. Recently, DualSPHysics code was applied to study the run-up on a real armour block coastal breakwater in Altomare et al. (2014) and the estimation of sea wave impact on coastal structures in Altomare et al. (2015).

In the present work, the DualSPHysics solver is presented describing the different parallel codes implemented for several CPU cores and one or more GPUs. The achieved speedups comparing CPU and GPU are addressed in this work to investigate the efficiency of this new technology in CFD problems.

2 Theory

Smoothed Particle Hydrodynamics is a meshless method that describes a fluid by dividing it into a set of discrete elements (named *particles*). Each particle has an area of influence over which its physical magnitudes are known. The physical quantities of a particle (a) can be computed as an interpolation of the values of the nearest neighbouring particles. Mathematically, the contribution of the neighbouring particles is weighted according to their distance for particle a using a kernel function (W) and a smoothing length (h). Herein, the distance from particle a at which the interaction with the rest of the particles can be neglected is $2h$.

The fundamental principle is to approximate any function by the integral approximation:

$$F(\mathbf{r}) = \int F(\mathbf{r}') W(\mathbf{r} - \mathbf{r}', h) d\mathbf{r}' \qquad (1)$$

This equation can be expressed in a discrete form, where the approximation of the function is interpolated at a given location (or particle a) and a summation is performed over all the particles within the region of compact support of the kernel:

$$F(\mathbf{r}_a) \approx \sum_b F(\mathbf{r}_b) W(\mathbf{r}_a - \mathbf{r}_b, h) \Delta v_b \tag{2}$$

so that

$$\sum_b W(\mathbf{r}_a - \mathbf{r}_b, h) \approx 1 \tag{3}$$

Thus, Eq. (2) becomes:

$$F(\mathbf{r}_a) \approx \sum_b F(\mathbf{r}_b) \frac{m_b}{\rho_b} W(\mathbf{r}_a - \mathbf{r}_b, h) \tag{4}$$

being m and ρ, the mass and the density of particle b.

Thus, the conservation laws of continuum fluid dynamics, in the form of differential equations, are transformed into their particle forms by the use of these interpolation functions that give the kernel estimate of the field variables at a point. In the classical SPH formulation, the Navier-Stokes equations are solved and the fluid is treated as weakly compressible. A detailed description of the main features of the SPH method can be found in the literature (Monaghan 1992, 1994; Liu 2003; Monaghan 2005; Gómez-Gesteira et al. 2010).

3 DualSPHysics Implementation

The DualSPHysics code is the result of an optimised implementation that uses the best approaches for CPU and GPU computation of SPH, with simulation accuracy, reliability and numerical robustness given precedence over computational performance where necessary. SPH software frameworks (such as DualSPHysics) can be split into three main steps (Fig. 1); (i) generation of a neighbour list (NL), (ii) computation of forces between particles and solving momentum and continuity equations (PI) and (iii) integrating in time to update all the physical properties of the particles in the system (SU). Running a simulation therefore means executing these steps in an iterative manner.

During the first step the neighbour list is generated. Particles only interact with neighbouring particles located at a distance less than $2h$. Thus, the domain is divided into cells of size ($2h \times 2h \times 2h$) to reduce the neighbour search to only the adjacent cells and the cell itself. The Cell-linked list described in Domínguez et al. (2011) was implemented in DualSPHysics. Another traditional method to perform a neighbour search is creating an array with all the real neighbours of each particle of

Fig. 1 Conceptual diagram summarising the implementation of a SPH code
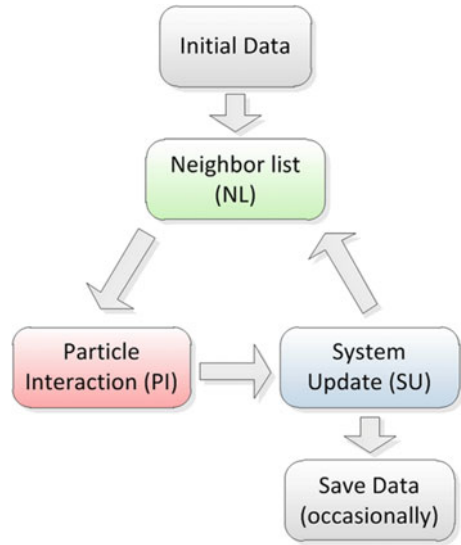
the system (named Verlet list), however the main drawback of this approach is its higher memory requirements compared to the Cell-linked list. In the DualSPHysics, two different cell lists were created; the first one with fluid particles and the second one with boundary particles. Therefore, this process can be divided into different operations: (i) domain division into square cells of side *2h*, (or the size of the kernel domain), (ii) determining the cell to which each particle belongs, (iii) reordering the particles according to the cells, (iv) ordering all arrays with data associated to each particle and, finally, (v) generating an array with the position index of the first particle of each cell. Note that an actual neighbour list is not created, but also a list of particles reordered according to the cell they belong to, which facilitates the identification of real neighbours during the next step.

Secondly, the force computation is performed so that all particle interactions are solved according to the SPH equations. Each particle interacts with all neighbouring particles located at a distance less than *2h*. Only particles inside the same cell and adjacent cells are candidates to be neighbours. Kernel and kernel gradient symmetry, avoids unnecessary repetition of particle interactions leading to a minor improvement in performance. When the force interaction of one particle with a neighbour is calculated, the force of the neighbouring particle on the first one is known since they have the same magnitude but opposite direction. Thus, the number of adjacent cells to search for neighbours can be reduced if the symmetry in the particle interaction is considered, which reduces the computational time. The equations of conservation of momentum and mass are computed for the pair-wise interaction of particles.

Finally, the system is updated. New time step is computed and the physical quantities are updated in the next step starting from the values of physical variables at the present time step, the interaction forces and the new time step value. In addition, particle information (position, velocity and density) are saved on local storage (the hard drive) at defined times.

4 DualSPHysics Acceleration

This section describes the different parallel implementations applied to the Dual-SPHysics code. Thus, most of the sequential tasks and operations that involve a loop over all particles in a serial code are instead executed using the multiple cores of a CPU, or multiple cores of one or more GPUs.

4.1 Multi-core CPU Parallelization

Firstly, the work load is distributed among the different cores of a multicore CPU using the parallel programming framework OpenMP. The physical domain is divided into sub-domains, and the computations of different sub-domains are executed by different threads of the CPU. A dynamic load balancing between the sub-domains is also implemented. This multi-core code does not present significant changes in comparison to the single-core version. One of the main advantages of this technique is the reduction in the time dedicated to communication between different cores since they share the same memory space, however the main limitation that exists is the number of cores on a single CPU.

4.2 GPU Parallelization

The new GPU technology is also used in this work to parallelize the SPHysics model. The parallel programming architecture CUDA developed by Nvidia is used to obtain an efficient and extensive use of the capabilities of the GPU architecture. In this case, the sequential tasks over the particles are performed using different execution threads of the GPU. The three main steps of SPH described in Sect. 3 are implemented on the GPU. In this approach, there is first a memory transfer of particle data from CPU to GPU and then all particle information remains on the GPU memory throughout the simulation. When saving simulation information, such as particle positions, velocities, etc., only the necessary data is transferred from GPU to CPU. Since this task is not performed often, the computationally expensive CPU $\leftrightarrow$ GPU data transfers are minimized, making the program more efficient. Therefore, the most efficient option is to keep all data in the memory of the GPU

where the three main SPH processes are executed in parallel. The same type of neighbour list implemented on CPU is also used on the GPU; the creation of a Cell-linked list where the domain is subdivided into cells dimension of $2h$. Updating the physical quantities of the particles can be easily parallelized using different execution threads of the GPU. Particle interaction, which is the most expensive computationally, is implemented on the GPU by executing one thread to compute the force for only one particle resulting from the interaction with all its neighbours. The thread looks for the neighbours of each particle among the adjacent cells and computes the resulting force from all the interactions. Due to the Lagrangian nature of the method, different problems appear such as lack of balancing, code divergence and lack of perfect coalescent access to the global memory of the device. A more complete description of the GPU implementation can be found in Dominguez et al. (2013a).

4.3 Multi-GPU Parallelization

The third massively parallel technique presented in this work implements SPH across multiple GPUs. The motivation of implementing a multi-GPU scheme is that the memory capacity of a single-GPU still imposes a limitation on the maximum number of particles. The use of more than one GPU enables larger domains to be simulated and accelerating the SPH scheme beyond the performance of only one GPU.

A novel SPH implementation is here presented that utilizes MPI and CUDA to combine the power of different devices making possible the execution of SPH on heterogeneous clusters (Fig. 2). Specifically, the proposed implementation enables communications and coordination among multiple CPUs, which can also host GPUs, making possible multi-GPU executions.
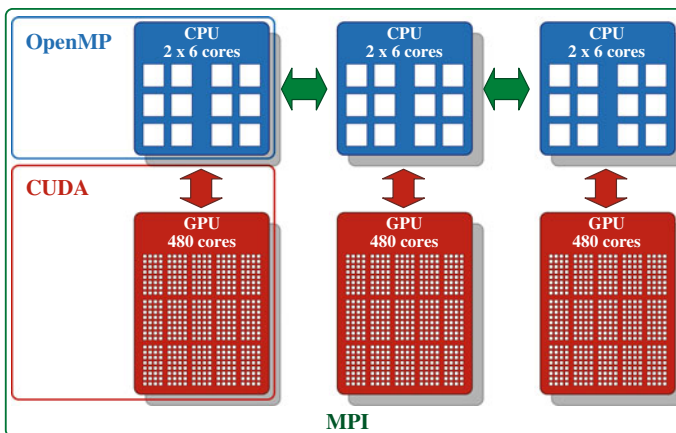

Fig. 2 Scheme of technologies and its scope of application

A scheme for multi-GPU SPH simulations was presented by Valdez-Balderas et al. (2013). In that work, a spatial decomposition technique was described for dividing a physical system into fixed sub-domains, and then assigning a different GPU of a multi-GPU system to compute the dynamics of particles in each of those sub-domains. The Message Passing Interface (MPI) was used for communication between devices, i.e. when particles migrate from one sub-domain to another, and to compute the forces exerted by particles on one sub-domain onto particles of a neighbouring sub-domain. The algorithm was only tested up to 32 million particles on 8 GPUs at a fraction of the computational cost of a conventional HPC cluster.

The implementation is based on a spatial decomposition where the domain is divided into subdomains or blocks of particles that are assigned to the different MPI processes. This division can be performed in any direction (X, Y or Z) adapting to the nature of the simulation case. In this way, each subdomain has two neighbouring subdomains, one on either side, except those subdomains at the perimeter of the simulation box, which have only one neighbour. Each MPI process needs to obtain, at every time step, the data of neighbouring particles from the surrounding processes within the interaction distance ($2h$ here). Therefore, to calculate the forces exerted on the particles within its assigned subdomain, each process needs to know the data of particles from the neighbouring subdomains that are located within the interaction distance. We call this the *halo* of the process (or subdomain) existing on the *edge* of the neighbouring process (or subdomain).

This approach to divide the domain among the MPI processes where particles are reordered according to the direction of the domain subdivision gives rise to interesting advantages that increase performance:

(a) If particles of a subdomain are not merged with particles of the halo, no time is wasted in reordering all particles when receiving data from the halo before a force computation, and no time is wasted in separating them after the force computation. The memory usage is also reduced since only the basic properties of halo particles need to be stored (position, velocity and density).

(b) Each process can adjust the size of its subdomain with the limits of the fluid particles inside. With the number of cells minimized for each subdomain, the total number of cells over the entire is also minimized leading to a reduction of the execution time and memory requirements.

(c) Particle data of the subdomains is stored in slices. Data existing in the edges can be sent to the neighbouring processes much faster since all data are grouped in consecutive memory positions.

(d) This reordering system also enables automatic identification of particles contained in a subdomain needing to interact with the halo. Thus, task overlapping is possible by computing particle interactions of particles not on an edge, while simultaneously performing the reception of the halo (needed only by edge particles), thereby inherently saving the communication time. For example, the particles that belong to the left edge of the subdomain 1 also form the halo of subdomain 0 and force interactions between particles not on the edge of subdomain 0 can be computed while they wait for the halo.

(e) Symmetry of pairwise interactions is not necessary for the particles of the halo since halo and edge particles only interact once in each process. This is relevant to the GPU implementation since symmetry is not applied for the pair-wise computations and does not represent any loss of performance in comparison to single-GPU version.

Reducing time dedicated for exchanging data among MPI processes is essential to increase the number of processes without drastically decreasing efficiency. One method to achieve this is by overlapping the communication with the computation using asynchronous communications. Hence, asynchronous send operations and synchronous receptions are used in the present algorithm. In this way, one process can send information to another while carrying out other tasks without waiting for the end of the transfer. This is an improvement over an algorithm that uses synchronous operations, in which an MPI process cannot continue execution of tasks until the operation is complete, implying a wait to receive data from another process or processes, thereby rendering computational resources idle, and consequently causing loss of efficiency.

Due to the Lagrangian nature of SPH, particles move through space during the simulation so the number of particles must be redistributed after some time steps to maintain a balanced work load among the processes and minimise the synchronisation time. Most of the total execution time is spent on force computation, and this time depends mainly on the number of fluid particles. For an equal load per processor, the domain must be divided into subdomains with the same number of fluid particles (including particles of the *halos*) or with the number of particles appropriate to the computing power of the device assigned to it. Two different dynamic load balancing algorithms are used. The first one assigns the same number of fluid particles to each computing device, and is suitable when the simulation is executed on machines that present the same performance. The second load balancing algorithm is used when hardware of different specifications and features are combined, such as different models of GPU. This second approach takes into account the execution time on each device. In particular, a weighted average of the computing time per integration step over several steps (on the order of 30) is used, with a higher weight to the most recent steps. An average over many time steps is chosen because a single time step presents large fluctuations. This average time is used to distribute the number of particles so that the fastest devices can compute subdomains with more particles than the slowest devices. This second type of dynamic load balancing enables the adaptation of the code to the features of a heterogeneous cluster achieving a better performance.

A more complete description of the Multi-GPU implementation can be found in Dominguez et al. (2013b).

5 Results

5.1 Testcase

The experiment of Yeh and Petroff at the University of Washington, also described in Gómez-Gesteira and Dalrymple (2004) for validation of their 3D SPH model, will be used here to analyse the performance of GPU code. In the experiment, a dam break was reproduced within a rectangular tank, with a volume of water initially contained behind a thin gate at one end of the box and a tall structure placed inside the tank. A similar validation was carried out by Crespo et al. (2011) using data from the experiment of Kleefsman et al. (2005) to show the accuracy of DualSPHysics. A validation of DualSPHysics using this testcase has already been shown in Barreiro et al. (2013) where experimental forces exerted onto the structure were in good agreement with the numerical values. Figure 3 shows different instants of the simulation involving one million particles.

As mentioned above, the SPH method is expensive in terms of computational time. For example, a simulation of this dam break evolution during 1.5 s of physical time using 300,000 particles (Fig. 3) takes more than 15 h on a single-core machine. The first limitation is the small time step (10^{-6}–10^{-5} s) imposed by forces and velocities (Monaghan et al. 1999). Thus, in this case, more than 16,000 steps are needed to complete the 1.5 s of physical time. On the other hand, each particle interacts with more than 250 neighbours, which implies a large number of interactions (operations) in comparison with the methods based on a mesh (Eulerian methods) where only a few grid nodes are taken into account. In this case, as it will be shown, the particle interaction takes more than 90 % of the total computational time when executed on a single-core CPU. Thus, all the efforts to increase the performance of the code must be focused on reducing the execution time of the particle interaction stage.
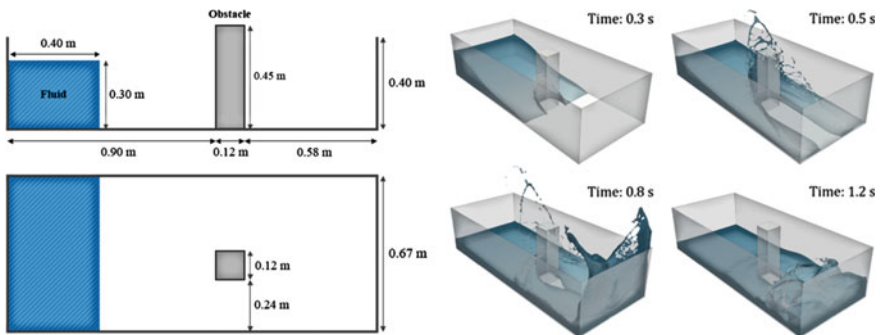

Fig. 3 Dam break flow impacting on a structure

5.2   *GPU Results*

Using the validation case shown in Fig. 3 and varying the number of particles (N) of the simulation, a comparison of the runtimes of the different parallel codes (multi-core, GPU and multi-GPU) is analysed. DalSPHysics is executed on a CPU and different GPU cards whose specifications can be seen in Table 1.

The performance of different simulations of the same case is presented for 1.5 s of physical time. The performance is analysed for different resolutions by running calculations with different numbers of particles. Computational times of the executions on CPU and GPU are shown in Fig. 4 where it can be noticed that for a simulation of 3 million particles takes 1 h using the GTX Titan GPU card while it takes almost 2 days using a CPU.

In Fig. 5, the speedups of different GPUs are shown by comparing their performance against the CPU device using a single core and also the full 8 physical cores of the Intel Xeon X5500. For the case chosen here, the use of a GPU can accelerate the SPH computations by almost two orders of magnitude, e.g. the GTX Titan card is 149 times faster than the single core CPU and 24 times faster than the CPU using all 8 cores.

Figure 6 shows the runtime distribution of the three main SPH steps; neighbour list (NL) creation, particle interaction (PI) and system update (SU) when simulating one million particles. The particle interaction takes 98.5 % of the total

Table 1 Specifications of different execution devices

	Number of cores	Processor clock (GHz)	Memory space	Compute capability
Xeon X5500	1–8	2.67	–	–
GTX 480	480	1.40	1.5 GB	2.0
GTX 680	1536	1.14	2 GB	3.0
Tesla K20	2496	0.71	5 GB	3.5
GTX Titan	2688	0.88	6 GB	3.5

Fig. 4 Runtime for CPU and different GPU cards
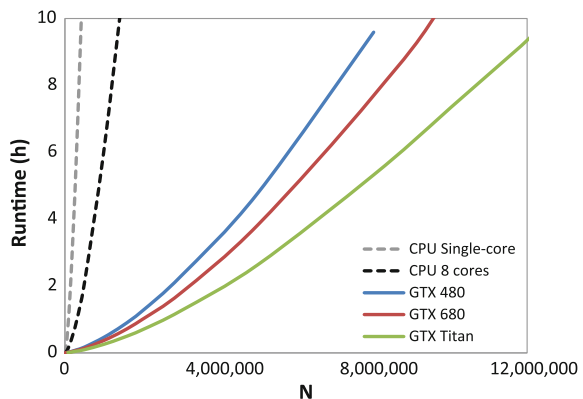
Fig. 5 Speedups of GPU against CPU simulating 1 million particles
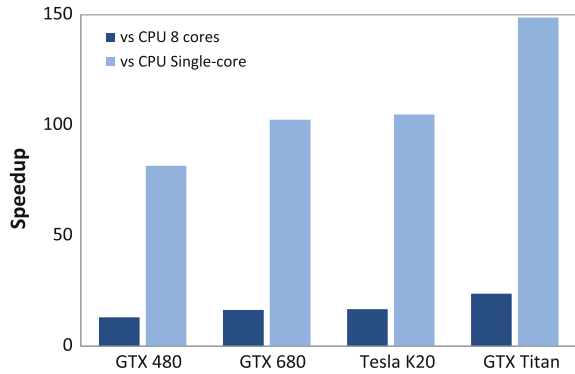
Fig. 6 Computational runtime distribution on CPU and GPU simulating 1 million particles
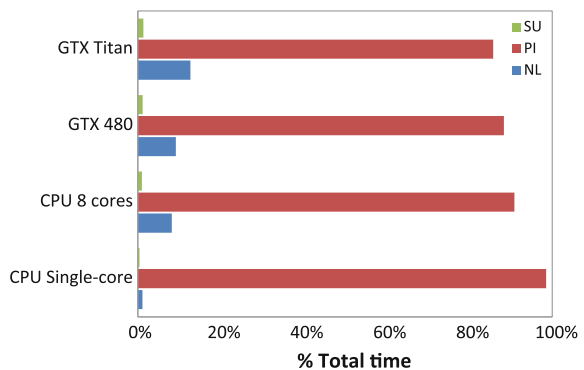
computational time when using a CPU single-core and this percentage decreases when the code is parallelized. Hence PI takes 90.8 % when using the 8 cores of the CPU and it is reduced to 88.3 and 85.7 % when using GPU cards (GTX 480 and GTX Titan, respectively). On the other hand the percentages of NL and SU increase with the number of cores to parallelize over.

Figure 7 gives an idea of how many particles can be simulated on the different GPU devices employed when using the DualSPHysics code. It can be observed that the difference in terms of speedup between GTX 680 and Tesla K20 is negligible (see Fig. 5) and the main difference of using these two GPU cards lies in the memory space that allows simulating more than 28 million particles in one Tesla K20 while less than the half can be simulated with a GTX 680.

5.3   Multi-GPU Results

First, the results when using the dynamic load balancing according to the number of particles are presented. The test-case (Fig. 3) is simulated using 3GPUs (3× GTX 480) so the domain is divided in 3 processes along the x-direction. Different instants
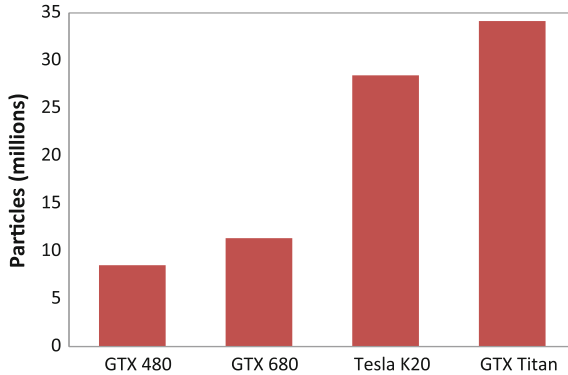
Fig. 7 Maximum number of particles simulated with different GPU cards using DualSPHysics code
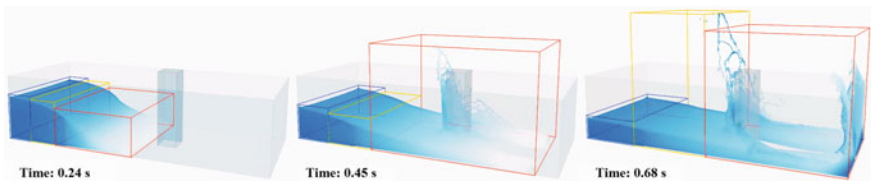
Fig. 8 Different instants of the simulation of testcase when using the dynamic load balancing according to the number of particles ($3 \times$ GTX 480)

of the simulations are shown in Fig. 8. The limits of the three different subdomains are depicted using coloured boxes. The size of the different subdomains changes with time to keep the workload evenly distributed among processes (similar number of particles per process).

The dynamic load balancing scheme was also applied in the same testcase but using a system with 3 different GPU cards (GTX 285, GTX 480 and GTX 680) which is a heterogeneous system since the 3 GPUs present different specifications and performances. The execution with only one GTX 680 card takes 5.8 h; combining this GPU with GTX 285 and GTX 480, whose performance characteristics are lower, the run takes 4.6 h applying the dynamic load balancing according to the number of fluid particles, and only 2.8 h applying the balancing based on the computation time of each device. Figure 9 summarises the execution times of the 3 GPUs used individually and together.

One of the main objectives of the proposed multi-GPU implementation using MPI is the possibility of simulating large systems (10^7–10^9 particles) at reasonable computational times, which is imperative to use the model in real-life applications that require high resolutions. An efficient use of the resources to minimise the computational and economical cost will make these large scale simulations viable. Therefore, a study of the efficiency and scalability of the multi-GPU implementation is shown.
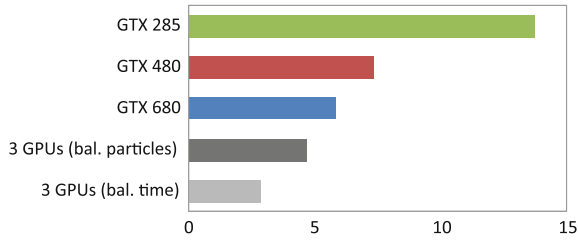
Fig. 9 Execution times of 3 different GPUs used individually and together applying the two different approaches of dynamic load balancing

A slightly different testcase is now used to evaluate the performance using the different number of GPUs. This second testcase is also a dam break similar to the previous one, but the main differences are that there is no obstacle in the middle of the numerical tank and the width of the tank can be modified according to the number of particles to be simulated. Note that modifying the width, the number of particles can vary keeping the same number of steps to complete the simulation and the same number of neighbouring particles of each particle. Thus, this testcase is used to analyse the performance for different numbers of particles (from 1 to 1,024 million) to simulate 0.6 s of physical time.

The achieved speedups are shown in Fig. 10 analysing the weak scaling using a maximum of 128 T M2090 GPUs of the Barcelona Supercomputing Center. The multi-GPU implementation has shown a high efficiency using a significant number of GPUs. Thus, using 128 GPUs, an efficiency of 92.1 % has been achieved simulating 1 M/GPU but an efficiency close to 100 % simulating 4M/GPU and 8M/GPU.

The possibility of combining the resources of several GPUs and the efficient use of the memory enables simulations with a huge number of particles. For example, more than 2000 million particles can be simulated with 64 GPUs Tesla M2090.
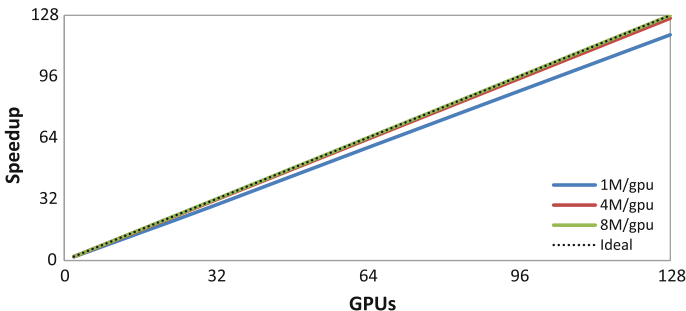
Fig. 10 Speedup for different number of GPUs using weak scaling with a GPU cluster of Tesla M2090

6   Conclusions

The DualSPHysics code has been developed to study complex free-surface flows requiring high computational resources.

CUDA is used to exploit the huge parallel power of present-day Graphics Processing Units for general purpose applications such as DualSPHysics. However, an efficient and full use of the capabilities of the GPUs is not straightforward.

The efficiency and performance of the new MPI-CUDA implementation of DualSPHysics are presented and analysed. The main contributions can be summarised as follows:

- A dynamic load balancing is implemented to distribute work load across the multiple processes to achieve optimal resource utilization and minimise response time.
- Overlapping between data communications and computations tasks is introduced to balance latency and to reduce computational times.
- The proposed multi-GPU code can be executed on different GPUs with identical specifications or old and new cards can be exploited together. Thus, the heterogeneous version allows a more efficient use of different machines with different GPU cards.
- The scalability is analysed in terms of weak scaling, indicating how the runtime varies with the number of processes for a fixed total problem size and how varies with the number of processes for a fixed problem size per processor.
- The simulation of billion particles is possible in medium-size clusters of GPUs.

References

Altomare C, Crespo AJ, Rogers BD, Domínguez JM, Gironella X, Gómez-Gesteira M (2014) Numerical modelling of armour block sea breakwater with smoothed particle hydrodynamics. Comput Struct 130:34–45

Altomare C, Crespo AJC, Domínguez JM, Gómez-Gesteira M, Suzuki T, Verwaest T (2015) Applicability of smoothed particle hydrodynamics for estimation of sea wave impact on coastal structures. Coast Eng 96:1–12. doi:10.1016/j.coastaleng.2014.11.001

Barreiro A, Crespo AJC, Domínguez JM, Gómez-Gesteira M (2013) Smoothed particle hydrodynamics for coastal engineering problems. Comput Struct 120(15):96–106. doi:10.1016/j.compstruc.2013.02.010

Crespo AJC, Gómez-Gesteira M, Dalrymple RA (2007) Boundary conditions generated by dynamic particles in SPH methods. CMC: Comput Mater Contin 5(3):173–184

Crespo AJC, Domínguez JM, Barreiro A, Gómez-Gesteira M, Rogers BD (2011) GPUs, a new tool of acceleration in CFD: efficiency and reliability on smoothed particle hydrodynamics methods. PLoS ONE 6(6):e20685

Crespo AJC, Domínguez JM, Rogers BD, Gómez-Gesteira M, Longshaw S, Canelas R, Vacondio R, Barreiro A, García-Feal O (2015) DualSPHysics: open-source parallel CFD solver on smoothed particle hydrodynamics (SPH). Comput Phys Commun 187:204–216. doi:10.1016/j.cpc.2014.10.004

Dalrymple RA, Rogers BD (2006) Numerical modelling of water waves with the SPH method. Coast Eng 53:141–147

Domínguez JM, Crespo AJC, Gómez-Gesteira M, Marongiu JC (2011) Neighbour lists in smoothed particle hydrodynamics. Int J Numer Meth Fluids 67(12):2026–2042

Domínguez JM, Crespo AJC, Gómez-Gesteira M (2013a) Optimization strategies for CPU and GPU implementations of a smoothed particle hydrodynamics method. Comput Phys Commun 184(3):617–627

Domínguez JM, Crespo AJC, Rogers BD, Gómez-Gesteira M (2013b) New multi-GPU implementation for smoothed particle hydrodynamics on heterogeneous clusters. Comput Phys Commun 184:1848–1860

Gingold RA, Monaghan JJ (1977) Smoothed particle hydrodynamics: theory and application to non-spherical stars. Mon Not R AstrSoc 181:375–389

Gómez-Gesteira M, Dalrymple RA (2004) Using a 3D SPH method for wave impact on a tall structure. J Waterway Port Coast Ocean Eng 130(2):63–69

Gómez-Gesteira M, Rogers BD, Dalrymple RA, Crespo AJC (2010) State-of-the-art of classical SPH for free surface flows. J Hydraul Res 48:6–27. doi:10.3826/jhr.2010.0012

Gómez-Gesteira M, Rogers BD, Crespo AJC, Dalrymple RA, Narayanaswamy M, Domínguez JM (2012a) SPHysics—development of a free-surface fluid solver-Part 1: theory and formulations. Comput Geosci 48:289–299

Gómez-Gesteira M, Crespo AJC, Rogers BD, Dalrymple RA, Domínguez JM, Barreiro A (2012b) SPHysics—development of a free-surface fluid solver-Part 2: efficiency and test cases. Comput Geosci 48:300–307

Harada T, Koshizuka S, Kawaguchi Y, (2007) Smoothed particle hydrodynamics on GPUs. Comput Graph Intl 63–70

Kleefsman KMT, Fekken G, Veldman AEP, Iwanowski B, Buchner B (2005) A volume-of-fluid based simulation method for wave impact problems. J Comput Phys 206:363–393

Liu GR (2003) Mesh free methods: moving beyond the infinite element method. CRC Press

Monaghan JJ (1992) Smoothed particle hydrodynamics. Annu Rev Astron Appl 30:543–574

Monaghan JJ (1994) Simulating free surface flows with SPH. J Comput Phys 110:399–406

Monaghan JJ (2005) Smoothed particle hydrodynamics. Rep Prog Phys 68:1703–1759

Monaghan JJ, Cas RF, Kos A, Hallworth M (1999) Gravity currents descending a ramp in a stratified tank. J Fluid Mech 379:39–70

Narayanaswamy MS, Crespo AJC, Gómez-Gesteira M, Dalrymple RA (2010) SPHysics-funwave hybrid model for coastal wave propagation. J Hydraul Res 48:85–93. doi:10.3826/jhr.2010.0007

Rogers BD, Dalrymple RA, Stansby PK (2010) Simulation of caisson break water movement using SPH. J Hydraul Res 48:135–141. doi:10.3826/jhr.2010.0013

Valdez-Balderas D, Domínguez JM, Rogers BD, Crespo AJC (2013) Towards accelerating smoothed particle hydrodynamics simulations for free-surface flows on multi-GPU clusters. J Parallel Distrib Comput 73(11):1483–1493. doi:10.1016/j.jpdc.2012.07.010

Aquathemolysis Reaction of Heavy Oil by a MoWNiC Nanocrystalline Catalyst Produced by Mechanical Alloying

G.J. Gutiérrez Paredes, J.N. Rivera Olvera, A. López Villa and L. Díaz Barriga Arceo

Abstract MoWC-NiC-WC was produced by mechanical alloying at the following grinding times: 0, 40, 80, 120, 160, 200 and 240 h. XRD results indicated that by increasing the milling time from 0 to 240 h, the nanostructured carbide phases were synthesized with a crystal size ranging from 125.6 to 10.1 nm. The performance of the nano-catalysts in the heavy oil before and after the reaction was analyzed by Fourier transform infrared spectroscopy (FTIR), Viscosimetry, SARA method analysis by Thin-layer chromatography-flame ionization detection (TLC-FID), elemental (EL) analysis, and gas chromatography/mass spectroscopy (GC/MS). As the milling time increased, the ratio of the viscosity reduction of the heavy oil increased from 80.4 to 97.1 % by using the catalyst milled for 240 h. In addition, the results showed that some reactions were observed during the aquathermolysis: pyrolysis, depolymerization, hydrogenation, isomerization, ring opening, desulphurization, etc. It was also found that the catalysts at short milling times caused more changes in the resin, saturated hydrocarbon, and oxygen-containing groups, whereas the 240 h catalyst led to more changes in the asphaltene, aromatic hydrocarbon, and sulfur-containing groups.

G.J. Gutiérrez Paredes (✉) · A. López Villa
Instituto Politécnico Nacional SEPI-ESIME, U.P. Azcapotzalco,
Av. de Las Granjas 682, Col. Santa Catarina, Delegación Azcapotzalco,
México D.F. C.P. 02250, Mexico
e-mail: ggutierrezp@ipn.mx

A. López Villa
e-mail: abelvilla77@hotmail.com

J.N. Rivera Olvera
Centro Conjunto de Investigación en Química Sustentable UAEM-UNAM, Carretera
Toluca-Atlacomulco, Toluca C.P. 50200, Estado de México, Mexico
e-mail: rivter12@yahoo.com

L. Díaz Barriga Arceo
ESIQIE, Instituto Politécnico Nacional, México D.F. C.P. 07738, Mexico

493

1 Introduction

In the past decades, the rate of discovery of accessible high quality petroleum resources has consistently lagged behind the rate of world consumption (Gray 2015). As a result, the more viscous crude oils (i.e. heavy oils, extra-heavy oils and bitumens) present a considerable challenge. However, the high viscosity and solidification of these resources cause difficulties in their exploitation. Consequently, reducing their viscosity to enhance oil recovery is an important focus of study (Rivera 2014). In the 1980s; some researchers explored the details of the chemical reactions between steam, heavy oil and minerals and described all of these reactions collectively as aquathermolysis (Hyne 1982). They discovered that the injection steam can reduce the viscosity of heavy oil and react with the heavy oil, so that leading to changes in their properties. In the literature various studies about aquathermolysis have been reported. Ultrasonic has been studied to assist the catalytic aquathermolysis reaction of heavy oil on the effect of catalyst and ultrasonic on the physical and chemical properties of a heavy oil. They found that the viscosity of heavy oil was reduced by 86.2 %, and the composite technology can further decrease the average molecular weight of heavy oil, increase the saturate and aromatic contents, decrease the resin and asphaltene contents (Xu and Pu 2011). In other work, it was synthesized a new type of catalyst aromatic sulfonic copper and tested in aquathermolysis reaction (Kun Chao 2012). The experimental results showed that, using 0.2 wt% catalyst and 25.0 wt% water at 280 °C for 24 h, the viscosity of oil sample could be decreased by 95.5 %, with 13.72 % in the conversion of heavy content to light content. Most of these synthesis methods used to prepare catalysts are expensive and produce low catalyst volumes. Mechanical Alloying (MA) is an alternative, simple and useful technique for synthesizing different catalysts at room temperature from elemental powders and can also be used to synthesize novel alloys (Rivera 2014). In this work was studied the performance of a nano crystalline NiWMoC in the catalytic aquathermolysis of a heavy oil as well as to determine the relationship between the phases obtained during MA and the viscosity reduction of the heavy oil.

2 Experimental Details

Pure tungsten (99.9+ %), molybdenum (99.8+ %), graphite (99+ %) and nickel (99.8 + %) from Sigma Aldrich Company were used as raw materials. The nickel powder featured particles measuring approximately 11 ± 3 μm with an irregular morphology. The tungsten powder particles showed an irregular shape with a mean size of approximately 5 ± 2 μm. The molybdenum powder showed a particle size of 25 ± 3 μm. The graphite showed a mean particle size of 50 ± 2 μm. The starting powders were mixed in a molar ratio 10:1 at room temperature in a low energy ball mill for 0, 40, 80, 120, 160, 200 and 240 at rotational speed of 500 rpm. Cylindrically

shaped zirconia (ZrO_2) grinding media with a high density and two different sizes ($1/2 \times 1/2$ and $3/8 \times 3/8$ in.) were used to avoid cross contamination. The structural study of the samples at every stage of milling was carried out in a Bruker AXS D8 Focus diffractometer using CuKα ($\lambda = 1.5406$ Å) in a radiation over a 2θ range from 20° to 110° at a speed of 4 min^{-1}. XRD patterns were analyzed using the data base software from the international center for diffraction data: ICDD PDF-2 (2003). Scanning electronic microscopy (SEM) was carried out using a JEOL-6300 at a voltage of 5 kV. The average particle size calculations for the different milling times were carried out using the ImageJ software. To evaluate their catalytic performance, the samples were tested in the aquathermolysis reaction of the heavy oil UTSIL, which has a viscosity of 1.13 Pa s. The experiments were carried out by places 50 g of oil, 50 g of sea water and 50 g of oil, 50 g of sea water and 0.5, 0.8, 1 and 1.2 g of catalyst into a reactor at a pressure of 3 MPa. The temperature of the reaction system was held at 50, 100, 150, 200 °C for 24 h. The viscosity of the resulting heavy oil was determined by a BROOKFIELD DV-II + PRO Viscometer before and after the reaction with samples submitted to different milling times. The ratio of the viscosity reduction was calculated according to the following equation: $\Delta\eta \% = ((\eta o - \eta)/\eta o) \times 100$ where, $\Delta\eta \%$ is the ratio of viscosity reduction, ηo is the viscosity of the oil before the reaction, and η is the viscosity of the oil after the reaction. Changes in the structures of the resins and asphalthenes in the heavy oil were analyzed before and after the reaction using a PerkinElmer 200 Spectrum Two FT-IR spectrometer. The reaction parameters (temperature and catalysts concentration) were optimized in preliminary tests to study the best catalyst. The group compositions of the heavy oil were carried out before and after reaction on an Iatroscan MK6 thin-layer chromatography—flame ionization detection (TLC-FID). The oil was further analyzed for structural changes and group compositions: asphaltenes, resins, saturated hydrocarbons, and aromatic hydrocarbons using the column chromatography-based SARA method according the ASTM D-3279-07, IP 143 y IP-368 standard methods.. Elemental analyses of the resins and asphaltenes before and after reaction were performed on an EA 5000 elemental analyzer. To study the hydrocarbons, aromatic, and organic content in reaction water before and after catalytic were performed on an Agilent 6890 gas chromatograph and a Agilent HP 5973 mass spectroscope.

3 Results and Discussion

3.1 X Ray Diffraction

To evaluate the microstructural evolution of the powder particles, the Fig. 1 shows the X-ray results obtained at different stages of milling. Sharp peaks corresponding to C, Ni, W and Mo were observed before the milling of the starting powders (0 h), which is related to very crystallized samples. The strongest peaks corresponding to C, Ni, W and Mo are (002), (111), (100), (100), respectively. With increasing

Fig. 1 X-ray diffraction patterns of NiWMoC at different milling times

milling time, the diffraction peaks of the powders decreased in their intensity and showed significant broadening as a result of the increase in internal strain and the refinement of the crystal size produced by the increase of kinetic energy from mechanical impacts (Rivera 2015). The peaks associated with carbon disappeared completely in the sample milled for 240 h. The disappearance of carbon characteristic diffraction peaks suggests that the carbon is dissolved in the metallic matrix in MoW, Ni. After 120 h of milling, a weak reflection at 35.8° from the (100) plane was observed corresponding to the WC phase (PCPDWIN 65-4539). The presence of the (001), (100), (101), (002) and (200) planes corresponds to the WC phase, which has a hexagonal Bravais lattice. After 240 h of milling, the formation of a WC solid solution was also detected (87.8° and 100.2°). The sample milled at 240 h exhibited a Ni peak (111) that was shifted to a lower diffraction angle, which may be due to the dissolution of carbon into the FCC structure of Ni (see Fig. 1b).

According to interstitial structures, carbon occupies certain interstitial sites within a metal lattice (Ni). The ratio of the radius of the interstitial atom to the radius of the atom must be less than 0.59 for the formation of an interstitial phase.

The atomic radii ratio between C/Ni is approximately 0.627(>0.59), which indicates that the nickel atomic radii are too small to accommodate the carbon in the interstitial position without distortion of the lattice. The formation of the WC phase from W and C can be divided into three main stages: (1) nucleation from available sites for nucleation due to the inter-layer spacing decreases and the number of layers in a particle increase, (2) growth of the nucleated particles and finally (3) welded particles when steady-state equilibrium is attained. Furthermore, after 160 h of milling peak non-overlapping diffraction (40.39°) suggests the formation of W-Mo bimetallic phase, and after 200 and 240 h of milling this reflection was significantly shifted towards lower angles diffraction, suggesting dissolution of carbon in the crystal lattice of the W-Mo bimetallic phase to form carbide. The W-Mo phase tends to form a substitutional solid solution.

3.2 Scanning Electron Microscopy

The SEM micrographs of the catalysts after different milling times can be observed in Fig. 2. At 80 h of milling (Fig. 2a), the particles are flake-like, and their average size is approximately 20.41 μm. Figure 2a also shows some ductile particles that were flattened by a forging process. A decrease in the particle size was observed after 120 h of milling (Fig. 2b) with some flattened and welded agglomeration of the particles. The average particle size after 120 h of milling was approximately 16.11 μm. After 160 and 200 h of milling, the particle size (Fig. 2c, d) decreased considerably as a function of reinforcement. The particles were work hardened and fracture via a fatigue mechanism. The 160 and 200 h milled alloy powders had an
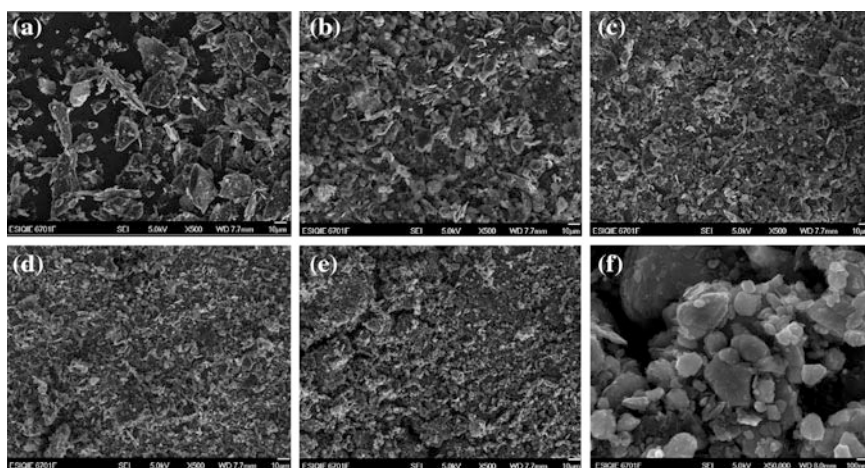

Fig. 2 SEM micrographs of the powder particles after **a** 80 h, **b** 120 h, **c** 160 h, **d** 200 h, **e** and **f** 240 h of milling

average particle size of approximately 11.16 and 10.32 μm, respectively. After 240 of milling, an average particle size of less than 5.23 μm was observed, as shown in Fig. 2e. The agglomeration of smaller particles was also observed. The sample that was milled for 240 h (see Fig. 2f) also exhibited agglomeration of particles in the range 88–832 nm. The dominant mechanism during mechanical milling after 160 h involves fracture. Due to the continued impact of grinding balls for 200 and 240 h of milling, the structure of the particles is steadily refined, but the particle size continues to remain the same. Therefore, the inter layer spacing decreases, and the number of layers in a particle increases. Alloying begins to occur at this stage due to a combination of increased lattice defect density and decreased diffusion distances during the milling process (Rivera 2015).

3.3 Catalytic Performance

The temperature and catalyst-heavy oil ratio concentration are important parameters in the emulsion that affect the viscosity and hydrotreating process (Yufeng Yi 2009). The viscosity results on the catalytic aquathermolysis in the emulsion: heavy oil UTSIL, (starting viscosity 113 mPa s) + water + catalyst concentrations of 0.5, 0.8, 1 and 1.2 g are shown in Fig. 3. By comparing the results, both temperature and catalysts synthetized at different milling times, affect the oil viscosity. As the concentration of catalyst is increased, the viscosity decreased. In example, when 0.5 g of catalyst was used, the viscosity decreased from 113 to 14 mPa s, whereas for 0.8, 1 and 1.2 g decreased to 11.16, 3.28 and 5.86 mPa s, respectively. The greater reduction in viscosity was obtained using the combination of temperature at 200 °C and 1 g of catalyst.

The best result was observed with 1 g of catalyst concentration (see Fig. 3c), which was obtained at 200 h of milling with a viscosity from 13.58 to 3.28 mPa s. This reduction is associated to the combination of factors as follows: the thermolysis of heavy oil at high temperatures and the catalytic properties showed by the sample prepared by mechanical alloying. In Fig. 2a, b the viscosity increased slightly for the same milling time (240 h) compared to those heated at 200 and 250 °C. Anyway, we expected to have a greater viscosity reduction at 250 °C compared to 200 °C as observed in the results in Fig. 2a–d, but the results were very similar between these temperatures. This probably is related to the different concentrations of catalysts and because the heteroatoms in the heavy oil molecules interacted very quickly with other groups via hydrogen bonding or van der Waals forces and polymerize to form larger molecules, thus leading to a viscosity regression. Anyway, at 250 °C the reactions turned very violent, causing the experiment was dangerous, this fact is probably related to the accelerated kinetics in the rapid separation of large chains from the organic molecules in contact with the catalyst reactivity became very high, so it was impossible to conduct a proper analysis of conversion of asphaltenes and resins at this temperature. Based on these results, a temperature of 200 °C and 1 g of catalyst
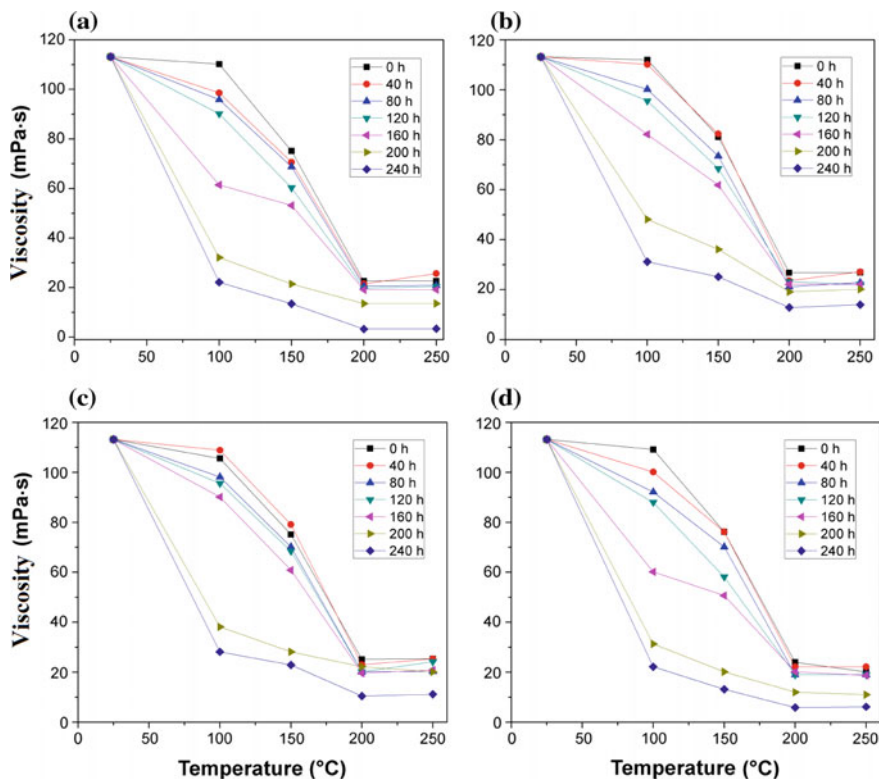
Fig. 3 Viscosity of the emulsion water + heavy oil + catalyst NiWMoWC at different milling times and concentrations: **a** 0.5 g, **b** 0.8 g, **c** 1 g y **d** 1.2 g

concentration at different milling times were selected in order to carry out the analysis of IR, CG and SARA analysis.

Figure 4 shows the dependence of oil was reduced from a reduction ratio of 80.4–97.1 %, and the best catalyst was produced after 240 h of milling. The results regarding the viscosity reduction are supported by the changes in the contents of resins and asphalthenes during the catalytic aquathermolysis reaction analyzed by FT-IR spectroscopy (see Fig. 5). The ratios of viscosity reduction ranged from 80.4 to 97.1 %. The similar activities of the materials milled from 0 to 120 h can be attributed to the mix effect of thermal cracking: as the particle size decreases, sea water acts as an ionic liquid and the formation of WC. The catalyst synthesized by 240 h of milling exhibited a high catalytic activity, which can be attributed to the formation of nanostructured WMoC, NiC and WC phases. However, nickel promotes the hydrotreating process, and the presence of NiC alloy probably prevented the catalysts from being poisoned leading to an increase in catalytic activity performance. The changes in the viscosity indicate that the viscosity is strongly dependent on the MA milling time due to the increase in the number of defects in

Fig. 4 Ratio of viscosity reduction of NiWMoC catalyst synthesized at different milling times
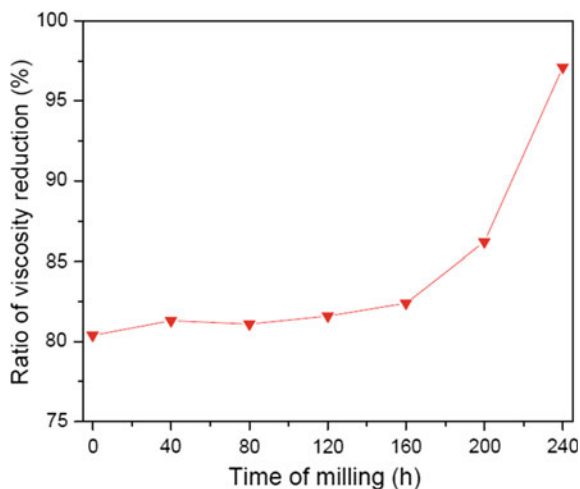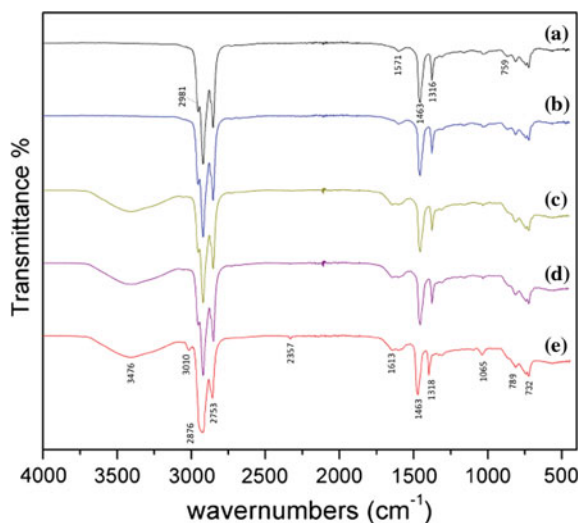

Fig. 5 IR spectra of NiWMoC catalyst **a** before reaction and at **b** 0 h; **c** 160 h; **d** 200 h; **e** 240 h of milling after aquathermolysis reaction

the crystalline phase, which can improve the number of active sites in the catalysts, the crystal size and the formation of metallic carbide phases, mainly over the longest milling period.

Figure 4 shows the FT-IR spectrum of the heavy oil after different milling times of mechanical alloying. The bands 2981, 2876 and 2753 cm^{-1} peaks observed before reaction are the characteristic absorption peaks of methyl and methylene groups, and the peaks at 1463 and 1318 cm^{-1} indicate that the oil samples contain a condensed aromatic ring. The weak peak at 3476 cm^{-1} indicates a series of alcohol reactions which only appeared for the catalyst after 160 h of milling and can be attributed to structural changes of NiWMoC catalyst during the reaction. The weak

peak at 2357 cm^{-1} vibration gained intensity for the catalyst after 240 h of milling, which indicates an increasing of saturate content from heavy oil due to the hydrogenation reaction of unsaturated content from C and H bonds. The strong bands at 2876 and 2753 cm^{-1} observed after the reaction are the absorption peaks of methylene groups indicating that the hydrogenation reaction occurred due to the breakage of C-O bonds in heavy oil molecules. It can also be attributed to the mix of metals and metallic carbide phases synthesized during mechanical alloying, mainly during the final stages and the refinement of crystal size for the catalyst after 240 h of milling and during catalytic aquathermolysis. The absorption peaks at 1463 and 1318 cm^{-1} is associated to the presence of condensed aromatic rings while the peak at 1613 cm^{-1} obtained after 160 h of milling suggests the reduction of the aromatic content of reacted samples, which could be attributed to the probable pyrolysis of C-O. After the reaction, the 1065 cm^{-1} peak became appreciably strong, suggesting that decarboxylation, hydrodesulfurization and the aromatic ring of the reacted samples were reduced as the heavy oil was cracked during the aquathermolysis, promoting the transformation from content of heavy species to one of light species, such as resins and asphaltene containing groups (Rivera 2014). The thin-layer chromatography—flame ionization detection (TLC-FID) was used to obtain the group compositions (SARA) of heavy oil before and after de aquathermolysis reaction is show in Table 1. Before the aquathermolysis reaction, the asphaltene content was 35.4 % and decreased up to 4.3 % by using the catalyst milled at 240 h, and the resins content, aromatics and saturated changed 18.6 %, 21.5 % and 24.5 % to 5.1 %, 38.4 % and 52.2 % respectively for the same catalyst synthetized at 240 h. By increasing the MA time, the asphaltenes and resins containing groups decreased, whereas aromatic and saturated groups increased. This behavior is related to the conversion of large to lighter molecules, resulting in reducing the oil viscosity. It was also observed that resin containing group after using the catalyst 160–200 h increased from 5.2 to 6.8 %, respectively, and decreased again to 5.1 % with the catalyst at 240 h. This behavior is associated with oil polymerization, probably caused by the catalyst poisoning by concentrations of Ni atoms at the edges of the surface of the bimetallic catalyst to form Ni-W

Table 1 SARA composition of heavy oil UTSIL before and after reaction

Catalyst	Asphaltenes (%)	Resins (%)	Aromatics (%)	Saturated (%)
Before the aquathermolysis	35.4	18.6	21.5	24.5
After the aquathermolysis				
0 h	21.6	17.6	26.5	34.8
40 h	18.1	12.8	27.8	41.3
80 h	18.0	12.1	28.6	41.3
120 h	17.0	10.1	30.4	42.5
160 h	6.8	5.2	32.8	55.2
200 h	6.1	6.8	36.6	50.5
240 h	4.3	5.1	38.4	52.2

Fig. 6 Conversion percentage of Saturate, Aromatic, Resin and Asphaltene (SARA) of heavy oil by catalysts milled at various times
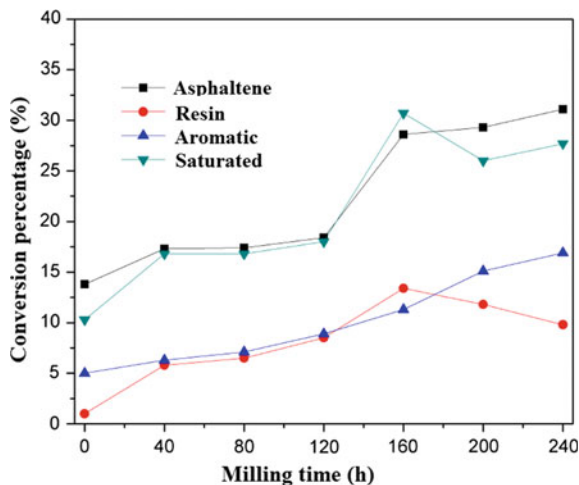
or Ni-Mo sulfides. This probably happen because there is a strong interaction between the nickel dispersed and heteroatoms N and S with asphaltene molecules, resulting in the formation of intermediate complex phases of nickel-asphaltenes bonds. Ni-asphaltenes complex phases may be capable of dissociating water in the emulsion, so that the asphaltene molecules may have been more easily hydrogenated. Anyway, this did not significantly affect the rate of viscosity reduction when the catalyst to 160 to 200 h was used, because the heavy oil was catalyzed with greater selectivity on the asphaltene containing groups compared to resins resulting in simultaneous reactions to enhance oil flow.

Figure 6 shows the conversion rates with different mechanically alloyed catalysts. After the aquathermolysis reaction by using the catalyst at 0 h of milling, showed 13.8 % conversion, 1, 5 and 10.3 % for asphaltenes, resins, aromatics and saturates, respectively. These conversion rates increased by 18.4, 8.5, 8.9 and 18 % by the catalysts synthesized at 120 h of MA. The higher conversion efficiency was observed when asphaltene content decreased by 31.1 %, and the resin content decreased by 9.8 %, while the content of saturated and aromatic increased by 27.7 % and 16.9 %, respectively, using the catalyst at 240 h of milling. Comparing the results, the catalysts acted on asphaltenes and saturated containing group. In the example, the catalyst at 160 h of milling is likely to act on saturated, while the catalyst milled at 240 h catalysts is likely to act on asphaltenes containing group. This suggests that the catalysts caused structural changes on asphaltenes to convert to saturated structures of H/C, which indicates the breaking of heteroatoms and ring opening.

Tables 2 and 3 lists the results for elemental analysis (C, H, O, H and S) of asphaltenes and resins groups, respectively. Regarding asphaltene fractions (see Table 2), after the aquathermolysis the catalysts obtained at different milling times have a strong effect on the heteroatoms (O, N and S), suggesting that after the reaction multiple reactions occurred. The content of S was reduced from 3.51 to

Table 2 Elemental content of asphaltene of UTSIL heavy oil before and after aquathermolysis reaction

Catalyst	C (%)	H (%)	O (%)	N (%)	S (%)
Before the aquathermolysis	74.16	11.15	8.84	2.34	3.51
After the aquathermolysis					
0 h	75.22	11.16	8.26	2.23	3.13
40 h	76.33	10.18	8.31	2.18	3.00
80 h	76.18	11.19	8.42	2.01	2.22
120 h	77.18	10.54	8.23	1.87	2.18
160 h	77.84	11.18	8.15	1.82	1.01
200 h	77.87	12.31	7.18	1.72	0.92
240 h	78.24	12.48	7.21	1.45	0.62

Table 3 Elemental content of resin of UTSIL heavy oil before and after aquathermolysis reaction

Catalyst	C (%)	H (%)	O (%)	N (%)	S (%)
Before the aquathermolysis	76.17	9.77	9.18	1.56	3.32
After the aquathermolysis					
0 h	78.91	10.18	7.87	1.18	1.86
40 h	77.84	11.37	8.15	1.24	1.40
80 h	78.15	11.58	7.81	1.21	1.25
120 h	78.36	11.50	7.51	1.20	1.43
160 h	78.42	11.77	7.15	1.15	1.51
200 h	79.10	11.81	7.10	0.98	1.01
240 h	81.15	11.98	6.15	0.34	0.38

0.62 % by using the catalyst at 0 and 240 h of milling, respectively. The reduction of S kept held constant for each catalyst synthesized at various stages of milling. A similar behavior is observed for the N and O content, where the concentration ranged from 2.34 % and 8.84 % to 1.45 % and 7.24 %, respectively.

Furthermore, the concentration of C-H structures increased by increasing the milling time of the catalysts.

Therefore, comparing the results observed in Table 2, indicate that after the catalytic aquathermolysis, the asphaltenes containing groups became gas products, saturated, aromatic and possibly small amounts of insoluble toluene (coke). Table 3 shows the elemental composition C, H, O, N and S fractions from resins. A similar behavior is observed compared to asphaltene fractions elemental contents with different catalyst milled, however, is important to emphasize some differences. The resins containing groups showed a greater decreasing on sulfur and nitrogen structures compared to asphaltenes, observing a better catalytic efficiency in breaking S structures (like thiophene) for all catalysts. In the example, the catalyst milled at 0 h, the S asphaltene fraction was reduced to 3.13 %, while the S for resin fraction amount was reduced to 1.86 %. This behavior could be associated that resins chains have larger oxygen concentration and H/C ratio is greater than asphaltenes.

The structural changes show that catalysts promoted hydrogenation during the reaction and they acted on heteroatom containing groups (S, O and N), causing the breaking of asphaltenes and resins from large molecular chains resulting in the production of pyrolytic gas and water reaction. It can be observed (see Tables 2 and 3), the reduction of oxygen content from asphaltenes and resins after the aquathermolysis reaction, indicates pyrolysis of CO_2, decomposition of C-S, H-S, C-N and H-N bonds, corresponding to desulfurization and denitrogenation.

In order to determinate what reactions are occurring during the catalytic aquathermolysis, the chromatography (GC/MS) spectrum before and after the reaction with the use of the catalyst milled at 240 h of MA is shown in Fig. 7. The Table 4 lists the corresponding composition of the pyrolytic gas after aquathermolysis reaction. The result revealed the appearance of new peaks and the increasing of intensities of some peaks compared to before the aquathermolysis (see Fig. 7a). This demonstrate that gas molecules with low boiling point such as alcohols, phenols, olefins, alkanes, thioesters, ethers, etc., appeared after the
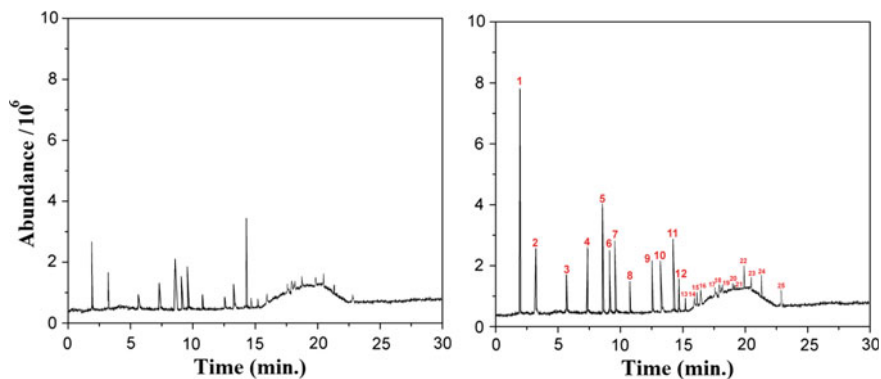

Fig. 7 GC/MS spectra of pyrolytic gas **a** before and **b** after the aquathermolysis reaction by the catalyst synthesized at 240 h

Table 4 Compositions of the pyrolytic gas after aquathermolysis reaction by the catalyst NiWMoC synthesized at 240 h

Peak	structure	Peak	structure	Peak	structure
1	$C_7H_{16}O$	11	$C_{13}H_{26}S$	21	CO_2
2	$C_8H_{14}O_2$	12	$C_{18}H_{36}$	22	$C_{18}H_{32}O$
3	$C_{10}H_{18}O$	13	$C_{12}H_{20}O$	23	$C_{19}H_{36}O$
4	C_9H_{18}	14	$C_{13}H_{22}$	24	$C_{20}H_{28}O$
5	C_9H_{16}	15	$C_{14}H_{24}$	25	$C_{20}H_{26}O$
6	$C_{15}H_{26}O$	16	$C_{13}H_{22}$		
7	$C_{17}H_{34}O$	17	$C_{19}H_{36}$		
8	$C_{10}H_{20}$	18	$C_{15}H_{28}$		
9	$C_{18}H_{34}O$	19	$C_{15}H_{24}$		
10	$C_{10}H_{18}$	20	$C_{16}H_{28}$		

catalytic aquathermolysis. These results indicate that changes occurred mainly on molecules with oxygen containing groups (Yanling Chena 2009).

The GC/MS analysis suggests that the nano NiWMoC 240 h catalyzed by the pyrolysis of heavy contents to light hydrocarbons, resulting in bond C-O, C-C breaking, removing phenols, ethers, etc., of the heavy oil molecules, probably including various reconstructions between asphaltenes and resins given the different structures observed in the pyrolysis showed in Table 4. These changes are attributed to the novel catalytic properties of nanocrystalline NiWMoC milled at 240 h, where the results demonstrate changes in the oxygen-containing groups. Figure 8 and Table 5 show the organic compounds in reaction water after aquathermolysis. The results showed that after the reaction catalyzed by the NiWMoC milled at 240 h, the oxygen structures indicates the presence of alcohols, ethers, esters, etc., and small compounds of saturated and aromatic hydrocarbons in the reacted water. Also the appearance of structures containing nitrogen was also detected. In the literature it has been reported that the presence of Mo catalyst can promote changes

Fig. 8 Spectra of the organic compounds in reaction water after aquathermolysis by the catalyst NiWMoC synthesized at 240 h
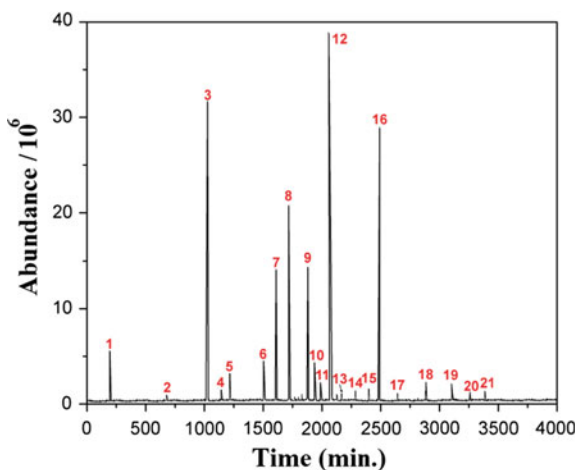
Table 5 Organic compounds in reaction water after aquathermolysis by the catalyst NiWMoC synthesized at 240 h

Peak	structure	Peak	structure	Peak	structure
1	$C_{10}H_{22}O_4$	11	$C_{18}H33O_4$	21	$C_{18}H_{31}$
2	$C_{10}H_{23}O_2$	12	$C_6H_9NO_2$		
3	$C_7H_{12}N_4O_4$	13	$C_{21}H_{38}O$		
4	$C_{16}H_{34}$	14	$C_{17}H_{16}$		
5	$C_{17}H_{28}$	15	$C_{18}H_{38}$		
6	$C_6H_{12}N_3O_4$	16	$C_{16}H_{22}O_2$		
7	$C_{17}H_{36}$	17	$C_{17}H_{26}O_4$		
8	$C_{12}H_{14}O_4$	18	$C_{22}H_{34}O$		
9	C_5H_8O	19	$C_{17}H_{16}$		
10	$C_{11}H_{12}O_2$	20	$C_{22}H_{44}$		

after aquathermolysis to produce rich oxygen organic structures (Chuan 2009). In addition, this could indicate that the nano composite WMoC obtained by MA promoted oxygenation during catalytic aquathermolysis in heavy oil. These reactions occurred mainly by the effect of oxygen content and sulfur groups of resins and asphaltenes, as well as olefins, alkali alkane chains saturated contents (Celine Fontaine 2010).

4   Conclusions

NiWMoC catalysts were produced by MA. Metallic carbide phases were observed after 160, 200 and 240 h of milling.

The viscosity of heavy oil decreased from 113 mPa s until 3.28 mPa s by using the catalyst milled at 240 h under 200 °C of temperature during the catalytic aquathermolysis.

The viscosity ratio changed from 80.4 to 97.1 %, and the best catalyst was produced after 240 h of milling.

The results regarding the viscosity reduction are supported by the changes in the contents of resins and asphalthenes during the catalytic aquathermolysis reaction analyzed by FT-IR spectroscopy.

The results showed that the main reactions during the aquathermolysis of heavy oil were: pyrolysis, hydrogenation, ring opening, oxygenation and hydrodesulfurization.

References

Celine Fontaine YR (2010) Insight into sulphur compounds and promoter effects on molybdenum-based catalysts for selective HDS of FCC gasoline. Appl Catal A: Gen 188–195

Chuan W (2009) Upgrading and visbreaking of Shengli ultra-heavy oil by aqua-thermolysis with catalyst. Oilfield Chem 121–123

Gray M (2015) Upgrading oilsands bitumen and heavy oil

Hyne (1982) Aquathermolysis of heavy oil. In: Proceedings of the 2th international conference on heavy oil crude and tar sands, pp 25–30

Kun Chao YC (2012) Upgrading and visbreaking of super-heavy oil by catalytic aquathermolysis with aromatic sulfonic copper. Fuel Process Technol 174–180

Rivera J (2014) Use of unsupported, mechanically alloyed NiWMoc nanocatalyst to reduce the viscosity of aquathermolysis reaction of heavy oil. Catal Commun 131–135

Rivera JN (2015) Synthesis and characterization of a MoWC-WC-NiC nanocomposite via mechanical alloying and sintering. Powder Technol 292–300

Xu H, Pu C (2011) Experimental study of heavy oil underground aquathermolysis using catalyst and ultrasonic. J Fuel Chem Technol 606–610

Yanling Chena YW (2009) The viscosity reduction of nano-keggin-K3PMo12O40 in catalytic aquathermolysis of heavy oil. Fuel 1426–1434

Yufeng Yi SL (2009) Change of asphaltene and resin properties after catalytic aquathermolysis. Pet Sci 194–200

Correction to: Astrophysical Fluids of Novae: High Resolution Pre-decay X-Ray Spectrum of V4743 Sagittarii

J.M. Ramírez-Velasquez

Correction to:
Chapter "Astrophysical Fluids of Novae: High Resolution
Pre-decay X-Ray Spectrum of V4743 Sagittarii" in:
J. Klapp et al. (eds.), *Recent Advances in Fluid Dynamics*
with Environmental Applications, **Environmental**
Science and Engineering,
https://doi.org/10.1007/978-3-319-27965-7_27

The original version of this chapter, containing text, tables, and figures, was published without the authorization of the actual author, Dr. Jan-Uwe Ness (ORCID 0000-0003-0440-7193).

Jan-Uwe Ness gives his kind permission to publish the following content retrospectively:

– Text of Sections 1, 2 (except for Subsection 2.4.1), 6, and 7.
– Tables 1, 3, and 4.
– Figures 1, 2, 8, and 9.

Jan-Uwe Ness has now been included as Section Author in the mentioned sections. The permissions have been included in the captions of the mentioned tables and figures.

The corrected chapter has been updated with the changes.